Evaluating the Fracture Potential of Steel Moment Connections with Defects and Repairs

Ryan T. Stevens

Thesis submitted to the Faculty of the
Virginia Polytechnic Institute and State University
in partial fulfillment of the requirements for the degree of

Master of Science
in
Civil Engineering

Matthew H. Hebdon, Chair
Matthew R. Eatherton
Roberto T. Leon

December 17, 2020
Blacksburg, Virginia

Keywords: special moment frames, protected zone, reduced beam section, full-scale testing, low-cycle fatigue, seismic

Evaluating the Fracture Potential of Steel Moment Connections with Defects and Repairs

Ryan T. Stevens

ABSTRACT

Steel moment frames are a popular seismic-force resisting system, but it is believed that they are susceptible to early fracture if there is a stress concentration in the plastic hinge region, also known as the protected zone. If a defect is present in this area, it may be repaired by grinding and/or welding, but little research has investigated how the repairs affect the performance of full-scale moment connections subjected to inelastic rotations. Thus, the goals of this research were to establish the performance of full-scale moment connections with repairs and defects, then develop a method for predicting fracture of the full-scale specimens using more economical cyclic bend tests. To do this, six full-scale reduced beam section (RBS) connections were tested having arrays of repairs or defects applied to the flanges. The repairs were 0.125 in. deep notches ground to a smooth taper and 0.25 in. deep notches ground to a smooth taper, welded, and ground smooth. The defects were sharp 0.25 in. and 0.375 in. notches. In addition, 54 bend tests were conducted on beam flange and bar stock coupons having the same repairs and defects, power actuated fasteners, puddle welds, and no artifacts. Finally, Coffin-Manson low-cycle fatigue relationships were calibrated using results from the cyclic bend tests with each artifact (repair, defect, or attachment method) and used in conjunction with estimates of full-scale plastic strain amplitudes to predict fracture of full-scale specimens. All four of the full-scale moment connections with repairs satisfied special moment frame qualification criteria (SMF). One full-scale specimen with sharp 0.25 in. notches satisfied SMF qualification criteria, but the flexural resistance dropped rapidly after the qualification cycle. On the other hand, the specimen with sharp 0.375 in. notches did not satisfy SMF qualification criteria due to ductile fractures propagating from the notches. The proposed method for predicting fracture of full-scale connections was validated using the six current and six previous full-scale RBS specimens. This method underpredicted fracture for eleven of the twelve specimens. The ratio of the actual to predicted cumulative story drift at fracture had a mean of 1.13 and a standard deviation of 0.19.

Evaluating the Fracture Potential of Steel Moment Connections with Defects and Repairs

Ryan T. Stevens

GENERAL AUDIENCE ABSTRACT

Moment connections in steel structures resist earthquake loads by permanently deforming the material near the connection. This area is called the protected zone and is critical to the safety of the structure in an earthquake. Due to this importance, no defects are allowed near the connection, which can include gouges or notches. If a defect does occur, it must repaired by a grinding or welding. These are the required repair methods, but there have be no tests to determine how the repairs affect the strength and ductility of the connection.

This research tested six full-scale moment connections with defects repaired by grinding and welding, as well as unrepaired defects. A correlation was also developed and validated between the full-scale tests and small-scale bend tests of steel bars with the same defects and repairs. This relationship is valuable because the small-scale tests are quicker and less expensive to conduct than the full-scale tests, meaning other defects or repairs could be easily tested in the future.

All but one of the six full-scale specimens met the strength requirements and had adequate ductility. The one test specimen that failed had an unrepaired defect. The relationship between the full-scale and small-scale tests underpredicted fracture (a conservative estimate) for the five of the full-scale tests and overpredicted fracture (unconservative estimate) for one test.

ACKNOWLEDGMENTS

This research was supported by the American Institute of Steel Construction with in-kind funding provided by Nucor-Yamato Steel and Cives Steel Company.

I would like to thank my advisors, Dr. Matthew Hebdon and Dr. Matthew Eatherton for the opportunity to work on this project, and for serving on my committee. Their support and guidance has made me a better researcher today than when I started. I would also like to thank Dr. Roberto Leon for serving on my committee. Dr. David Mokarem, Garret Blankenship, and Brett Farmer were especially helpful at the lab and I am thankful for all they taught me (and for letting me drive the forklift). Thank you to my colleagues Sam Sherry, Japsimran Singh, and Raul Avellaneda for their humor and their company.

Finally, thank you to my family for their continual support, even when the future seemed uncertain.

Contents

List of Figures

List of Tables

Chapter 1. Introduction

1.1 Background and Motivations

Steel moment frames are a popular seismic-force resisting system, but they are not without limitations. The 1994 Northridge earthquake showed that without proper detailing, steel moment connections can fracture at low rotations (Popov et al. 1998). Following the earthquake, numerous research studies were conducted to identify fracture causes and develop new designs for future construction (Tremblay and Filiatrault 1997; Civjan et al. 2000; Uang and Bondad 1996). One such study suggested that moment connections are susceptible to early fracture if stress concentrations are present in the plastic hinge region (Ricles et al. 2002).

The plastic hinge region of the connection came to be known as the "protected zone", where shear studs, welds, bolts, notches, or gouges are prohibited. Only puddle welds and power actuated fasteners (PAF) up to 0.18 in. diameter are allowed for decking attachment in the protected zone (AISC 2016b). In a previous study, the term "artifacts" was used to describe any defect, fastener, or attachment applied in the protected zone, including the allowable attachment methods or unauthorized studs, welds, or defects (Eatherton et al. 2013). If an unauthorized attachment or defect does occur in the protected zone, the artifact must be repaired by grinding or repair welding (AWS 2016). Repair by grinding requires that the defect be ground to a smooth 1:5 and 1:2.5 taper in the longitudinal and transverse directions, respectively. Repair by welding requires that the defect be ground to a smooth 0.25 in. radius, welded, and ground smooth.

There has been little research to establish the response of full-scale moment connections with repairs subjected to inelastic rotations. Rather, past research has investigated puddle welds and PAFs as decking attachment methods in the protected zone (Eatherton et al. 2013). That study showed that puddle welds and PAFs applied in a conventional configuration for decking would not prevent a connection from satisfying special moment frame (SMF) qualification criteria. This introduced the idea that other artifacts may be acceptable when used in the protected zone.

Currently, full-scale testing is the best method for establishing the performance of moment connections with artifacts in the protected zone, but this testing is time-intensive and expensive. However, an alternative method is small-scale cyclic bend tests of flat bar coupons cut from beam flange material (Abbas and Eatherton 2014; Florig and Eatherton 2015). This involved comparing results from cyclic bend tests of plate specimens with new artifacts to the results of specimens with artifacts that had also been tested on full-scale moment connections, as a means of showing equivalence to artifacts that were acceptable for SMF connections. One limitation though, is that no method exists to correlate results of the full-scale and small-scale tests. Nor is there a way to predict how a full-scale connection would

perform with a certain artifact, using only small-scale testing.

Thus, there is a need to establish the performance of full-scale specimens with repairs and defects to determine if the connections can satisfy SMF qualification criteria. There is also a need to develop a method that correlates the full-scale and small-scale test results, for use in predicting fracture of full-scale moment connections. A method such as this would be valuable because more artifacts could be evaluated quickly and economically.

1.2 Objectives and Scope of Work

The two main objectives of this study were:

1. Evaluate the performance of full-scale moment connections having one of four artifacts applied in the protected zone: 0.125 in. notches repaired by grinding, 0.25 in. notches repaired by welding, and sharp 0.25 in. and 0.375 in. notches.
2. Develop a correlation between the full-scale and small-scale test results, in order to predict fracture of full-scale connections.

To meet these objectives, this work included the following parts:

1. A full-scale experimental program that involved testing six reduced beam section (RBS) moment connection specimens with W24×62 and W36×150 beams. These specimens had an array of either 0.125 in. notches repaired by grinding, 0.25 in. notches repaired by welding, or sharp 0.25 in. or 0.375 in. notches.
2. A small-scale experimental program that involved cyclically testing 54 flat bar coupons of varying thicknesses, with 0.125 in. notches repaired by grinding, 0.25 in. notches repaired by welding, sharp 0.25 in and 0.375 in. notches, Pneutek K66062 and K66075 fasteners, and Hilti X-ENP-19 L15 sheet metal nails. Bare steel specimens were also tested. The results of the cyclic bend tests were used to calibrate Coffin-Manson relationships for each artifact.
3. A finite element and elastic-plastic fracture mechanics analysis to understand how the spacing of artifacts affected the peak stress and strain states, fracture initiation, and fracture propagation on full-scale specimens.
4. Calibration of Coffin-Manson low-cycle fatigue relationships for each artifact using the results of the small-scale tests. The Coffin-Manson relationship is an inverse power law that relates the number of cycles to final fracture to the plastic strain amplitude of a flat bar specimen in the cyclic bend test. This characterizes the fracture resistance of the specimen when an artifact is present. The focus was on final fracture as it was more objective to determine when the small-scale specimens had completely fractured.

5. Development and validation of a method for predicting final fracture of the full-scale specimens. This method used the calibrated Coffin-Manson relationships and estimates of full-scale plastic strain amplitudes to determine the theoretical fatigue life for each displacement step in the full-scale loading protocol. Next, Miner's rule was used to sum the fatigue life used in each step until the all fatigue life was consumed. This gave the predicted cycle and cumulative story drift of final fracture.

1.3 Thesis Organization

This thesis is organized as follows:

- The background, motivations, objectives, and organization of the report are outlined in Chapter 1.
- Previous, relevant research on artifacts in the protected zone, cyclic bend test setups, and the Coffin-Manson low cycle fatigue relationship are discussed in Chapter 2.
- Experimental methods are described in Chapter 3, including setups, test matrices and specimens, loading procedures, and instrumentation plans.
- The results of a finite element study investigating artifact spacing are given in Chapter 4.
- The results of an elastic-plastic fracture mechanics analysis are given in Chapter 5.
- Full-scale and small-scale test results are presented and briefly discussed in Chapter 6.
- A discussion of the full-scale results, calibrated Coffin-Manson relationships, and the method for predicting fracture are given in Chapter 7.
- The testing and major conclusions are summarized in Chapter 8.
- Additional drawings, plots, notes, equations, and pictures are given in the numerous appendices.

Chapter 2. Literature Review

This chapter describes the origins of the protected zone and its restrictions, and relevant research that investigated the effects of puddle welds and power actuated fasteners (PAFs) when used in the protected zone of moment connections. This chapter also presents small-scale experimental programs related to low-cycle fatigue testing, before concluding with a description of the Coffin-Manson relationship.

2.1 Moment Connection Fractures

Steel moment frames dissipate seismic energy by forming plastic hinges in the beam-column connections, but the 1994 Northridge earthquake showed that connections were vulnerable to fracture if not detailed properly. One study conducted after the earthquake identified more than 100 structures in the region where fractures in beam-column connections had occurred without significant inelastic deformations (Youssef et al. 1995). This was a serious concern and was the impetus for the FEMA/SAC Joint Venture research program. A large part of this initiative was testing full-scale beam-column connections to establish the behavior of pre-Northridge connections, and develop retrofits and new designs for future construction (Popov et al. 1998; Uang and Bondad 1996; Civjan et al. 2000; Tremblay and Filiatrault 1997). Multiple connection configurations were tested, including some with composite slabs (Hajjar et al. 1998; Leon et al. 1998). In one such test, the beam fractured at a smaller rotation than a similarly sized noncomposite specimen in the same study (Ricles et al. 2002). The fracture initiated at the base of a welded shear stud, at a distance from the face of the column flange equal to approximately half the depth of the beam. Flange local buckles had also formed near the fracture initiation. The authors concluded that a combination of low-notch toughness in the heat-affected zone of the weld and high inelastic strains due to local buckling led to the sudden fracture. Thus, they recommended that shear studs not be placed in the plastic hinge region of the beam where large inelastic strains are expected.

This raised a concern that other types of welds, attachments, or defects in the plastic hinge region could also cause a premature fracture. Due to these concerns, the plastic hinge region in a moment connection was designated as a "protected zone", where attachment methods are restricted and defects must be repaired (AISC 2016b; AWS 2016).

2.2 The Protected Zone

The plastic hinge region of a moment connection is defined as the "protected zone" in the American Institute of Steel Construction (AISC) 341-16 *Seismic Provisions for Structural Steel Buildings* (AISC 2016b). The connection type

determines the dimensions of the protected zone, as given in AISC 358-16 *Prequalified Connections for Special and Intermediate Moment Frames for Seismic Applications* (AISC 2016a). Two examples are shown in Figure 2.1: a reduced beam section (RBS) connection and an extended end-plate connection. For RBS connections, the protected zone extends from the face of the column to the end of the RBS cut.

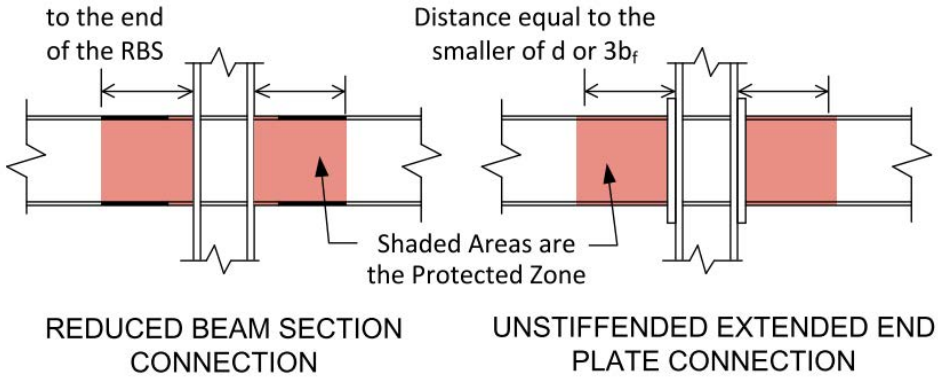

Figure 2.1. Protected zone dimensions for RBS and end-plate connections (Watkins 2013).

The types of authorized attachments in the protected zone are limited. Currently, only arc spot welds (puddle welds) and PAFs up to 0.18 in. diameter are allowed for deck attachment; other attachments like shear studs, welds, and bolts are expressly prohibited. Any defects that occur in the protected zone during fabrication or erection must be repaired. This includes notches, gouges, holes, welds, or erection aids (AISC 2016b).

Two repair methods for gouges and notches are given in the American Welding Society (AWS) D1.8/D1.8M *Structural Welding Code-Seismic*: grinding and repair welding (AWS 2016). When defects are repaired by grinding, they must be ground to have a smooth taper that does not exceed 1:5 parallel to the member axis and 1:2.5 transverse to the member axis. For defects repaired by welding, they must be ground to have a smooth radius of at least 0.25 in. before welding. After welding, the weld is ground flush with the base metal and inspected using a magnetic particle test to identify surface cracks that must be repaired.

These requirements are similar to the repair methods for gouges that occur when cutting the RBS, given in AISC 358-16 (AISC 2016a). Unlike the AWS D1.8 repair requirements, the AISC 358-16 repair requirements for RBS cuts have a maximum allowable depth for repairs by grinding. If a gouge is less than 0.25 in. deep, it can be ground to a smooth 1:5 taper, but deeper gouges must be ground to a smooth 0.25 in. radius and welded. After welding, these repairs are ground flush with the base metal and inspected using a magnetic particle test.

The concept of the protected zone was created out of concern for premature fractures, but there have been no full-scale tests to establish the performance of connections with repairs or to show that unrepaired defects cause early fracture. There has been some previous research of PAFs and puddle welds in the protected zone (Eatherton et al. 2013).

2.3 Protected Zone Research

Studies have investigated the performance of full-scale moment connections with decking attachments in the protected zone (Eatherton et al. 2013) and decking attachments and repairs on small-scale specimens in a setup that simulated local buckles of full-scale tests (Abbas and Eatherton 2014; Florig and Eatherton 2015). The small-scale research involved testing flat bar specimens with artifacts in a cyclic bend test and comparing the results to successful artifacts (ones that had been tested on full-scale moment connections that satisfied special moment frame (SMF) qualifaction). If a coupon with a new artifact sustained at least the same number of cycles as a coupon with a successful artifact, then the a full-scale connection with the new artifact would also likely satisfy SMF criteria.

Full-scale connection testing is the most realistic method for evaluating the effects of artifacts in the protected zone, but few full-scale tests have been conducted. The study by Eatherton et al. (2013) involved testing eight specimens with puddle welds and fasteners, and four specimens without welds or fasteners. These specimens were full-sized RBS and non-RBS connections with W24×62 and W36×150 beams and extended end-plate connections. At the time of the study, puddle welds were the only decking attachment allowed in the protected zone. The fasteners were 0.18 in. diameter, Hilti X-ENP-19 L15 sheet metal nails, driven with a DX 76 PTR powder actuated tool and a 0.27 caliber charge.

These decking attachments were installed in two configurations, shown in Figure 2.2. The first configuration was a typical layout for attaching steel deck, with fasteners or welds spaced 12 in. on-center. The second configuration was a closely-spaced grid of PAFs on both flanges and the web. Eatherton et al. (2013) suggested that the grid of fasteners represented many tests with a single fastener at each location and ensured that a fastener was located near the peak of a local buckle, where fractures typically initiated.

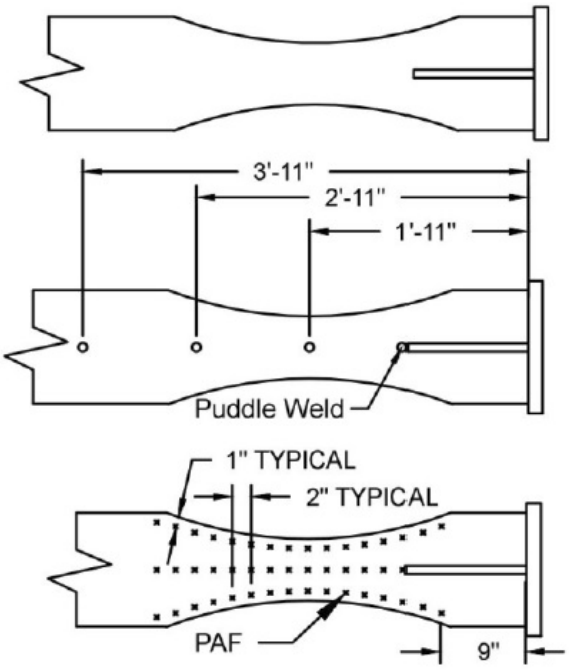

Figure 2.2. Flange layouts of puddle welds and PAFs (Eatherton et al. 2013).

Regardless of the layout, all eight specimens with welds or fasteners SMF qualification criteria and exhibited similar behavior to specimens without fasteners. For SMFs, the qualification criteria is that a connection maintain at least 80% of the nominal plastic flexural strength through the first cycle of 4% story drift (AISC 2010). Failure of specimens was characterized by web and flange local buckling, fracture initiation on the flange tip or face, and fracture propagation across the width of the flange and into the web. Each of the six connections with an RBS fractured, but only one non-RBS specimen fractured; the other tests were stopped when the hysteretic behavior appeared to stabilize. The only non-RBS specimen that failed was a W36×150 beam with a grid of fasteners on the flanges and web, but this specimen still satisfied SMF qualification criteria before fracturing. The authors concluded that moment connections with PAFs applied in the protected zone have adequate ductility for SMFs.

In addition to the full-scale tests, puddle welds and PAFs were tested on flat bar coupons in cyclic bending and monotonic tension. These coupons were cut from the full-scale specimen flanges for direct comparison between the studies. Coupons were also tested with 0.199 in. diameter, 0.625 in. long Pneutek K66062 and 0.75 in. long Pneutek K66075 pneumatic actuated fasteners, and repair methods like ground fillet welds, welded and unwelded notches ground to a taper, and a boat-shaped weld repair (BSWR) (Abbas and Eatherton 2014; Florig and Eatherton 2015). Pneumatic actuated fasteners are another type of PAF that is installed with compressed air. The welded and unwelded notches ground to a taper, shown in Figure 2.3 and Figure 2.4, were two repair methods that met the AWS D1.8 requirements described in the previous section. Runoff tabs were used for the starts and stops on the welded coupons and were ground off when the weld was ground flush. The BSWR, shown in Figure 2.5, also met the AWS D1.8 requirements. It was ground to a depth of 0.25 in., with a 1:5 taper in the longitudinal direction and a 1:2.5 taper in the

transverse direction. On the surface of the coupon, the notch was approximately 3.3 in. long and 1.25 in. wide. Runoff tabs were used for the starts and stops, and were ground off when the weld was ground flush with the base metal.

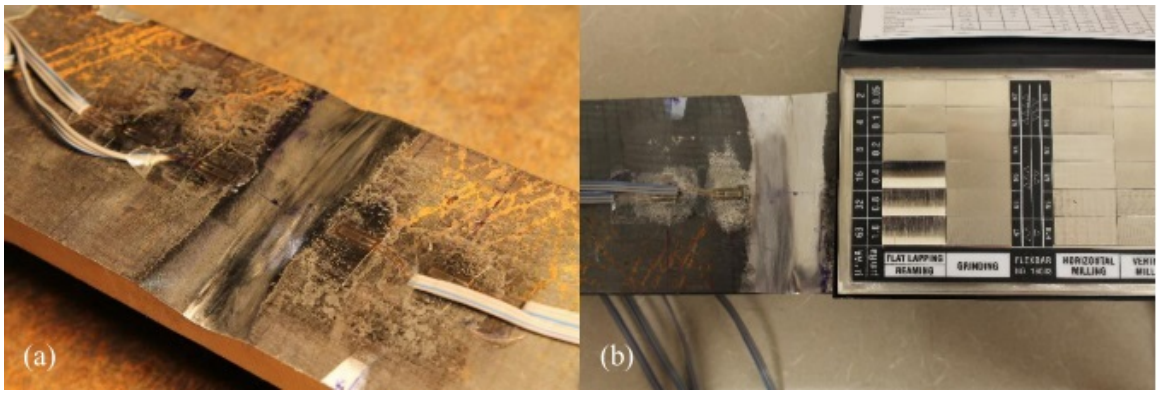

Figure 2.3. V-shaped notch ground to a 1:5 taper (Abbas and Eatherton 2014).

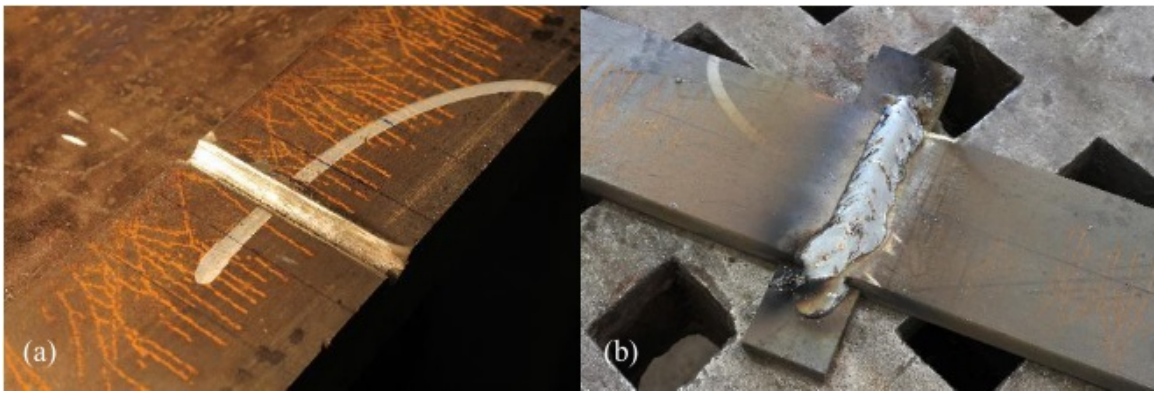

Figure 2.4. U-shaped notch ground to a 0.25 in. radius and welded (Abbas and Eatherton 2014).

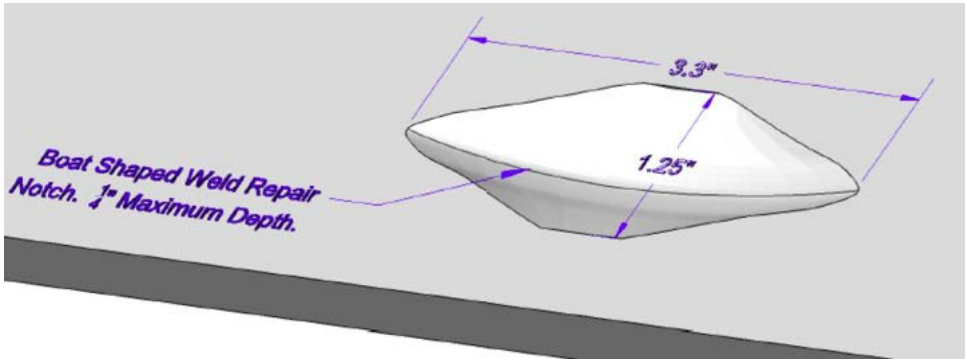

Figure 2.5. Flat bar coupon with BSWR and dimensions (Florig and Eatherton 2015).

The results of the cyclic bend tests are presented in Table 2.1, with thinner coupons generally sustaining more cycles before fracture initiation and failure than thicker coupons. Additional tests were also done with 0.25 in. and 1 in. side notches to vary the stress triaxiality, but are not reported here (Abbas and Eatherton 2014; Florig and Eatherton 2015).

Fracture initiation of BSWR specimens was determined to be the cycle of the first folded steel defect. The folded steel defect was a fracture that initiated in the weld metal that had a raised)(or X shape, with the fracture at the center, shown in Figure 2.6.

Table 2.1. Bend test results from previous research (Abbas and Eatherton 2014; Florig and Eatherton 2015).

Specimen Name	Artifact Type	Coupon Thickness, in.[1,2]	Fracture Initiation Cycle	Final Fracture Cycle
W24-B1-T59-R000	Bare steel	0.59	18	28
W36-B1-T94-R000	Bare steel	0.94	4	7
W24-PAF1-T59-R000	Hilti X-ENP-19-L15	0.59	3	18
W36-PAF1-T94-R000	Hilti X-ENP-19-L15	0.94	4	6
W24-PnAF0625-T59-R000	Pneutek K66062	0.59	3	13
W36-PnAF0625-T94-R000	Pneutek K66062	0.94	3	5
W24-PnAF075-T59-R000	Pneutek K66075	0.59	4	9
W36-PnAF075-T94-R000	Pneutek K66075	0.94	2	5
W24-PW1-T59-R000	Puddle weld	0.59	5	9
W36-PW1-T94-R000	Puddle weld	0.94	4	7
W24-GFW1-T59-R000	Ground fillet weld	0.59	4	9
W36-GFW1-T94-R000	Ground fillet weld	0.94	2	6
W24-NGT1-T59-R000	Notch ground to a taper	0.59	2	5
W36-NGT1-T94-R000	Notch ground to a taper	0.94	2	3
W24-NWG1-T59-R000	Notch ground and welded	0.59	4	14
W36-NWG1-T94-R000	Notch ground and welded	0.94	2	3
W24-BSW-T59-R000	Boat-shaped weld repair	0.59	2	13
W36-BSW-T94-R000	Boat-shaped weld repair	0.94	2	4

[1] 0.59 in. coupons were cut from W24×62 flanges.

[2] 0.94 in. coupons were cut from W36×150 flanges.

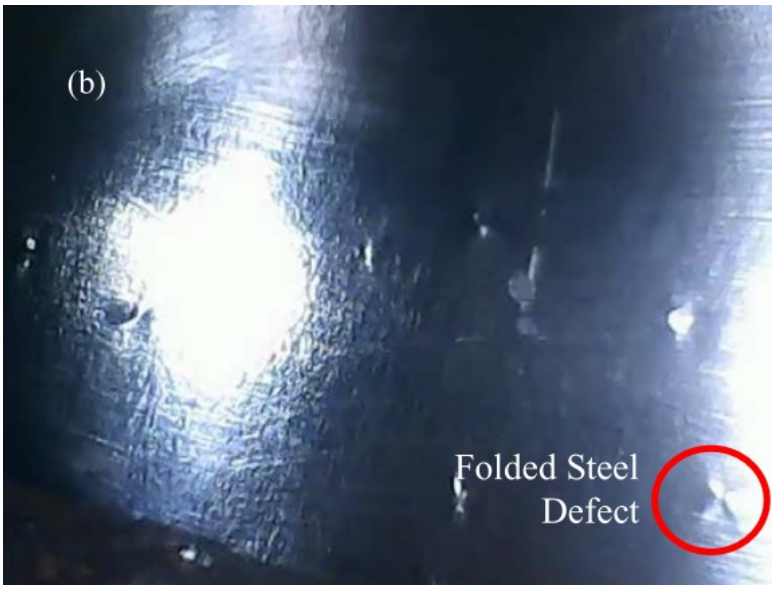

Figure 2.6. Folded steel defect on flat bar specimen with BSWR (Florig and Eatherton 2015).

The results of flat bar specimens with puddle welds and PAFs were used as references, as these artifacts had been tested on full-scale moment connections that had adequate ductility for SMFs (Eatherton et al. 2013). The method for showing equivalence to successful artifacts involved comparing the elongation measured in monotonic tension tests, and the number of cycles to fracture initiation and final fracture from the cyclic bend tests. Using this method, the authors determined that full-scale connections with Pneutek K66062 fasteners or ground fillet welds would likely satisfy SMF qualification criteria (Abbas and Eatherton 2014).

2.4 Low-Cycle Fatigue Tests

Multiple setups have been developed for cyclic testing with the major difference being how the load is applied, either as point loads, end moments, or axial loads. While only one of the setups described in this section has been used for testing flat bar specimens with artifacts, the other methods could be modified for this purpose and then used to calibrate Coffin-Manson relationships.

The setup developed by Abbas and Eatherton (2014) for previous artifact testing is shown in Figure 2.7. With this setup, a 0.5-1.0 in. thick flat bar coupon was held between four 11 in. diameter rollers attached to a movable assembly. During testing, the movable assembly was moved past fixed guides by a servohydraulic actuator, which bent the coupon bent to the radius of the rollers. To apply reverse bending, the actuator was moved in the opposite direction. Six cameras placed in the gap between the rollers captured where fractures initiated and how they propagated during the cyclic loading.

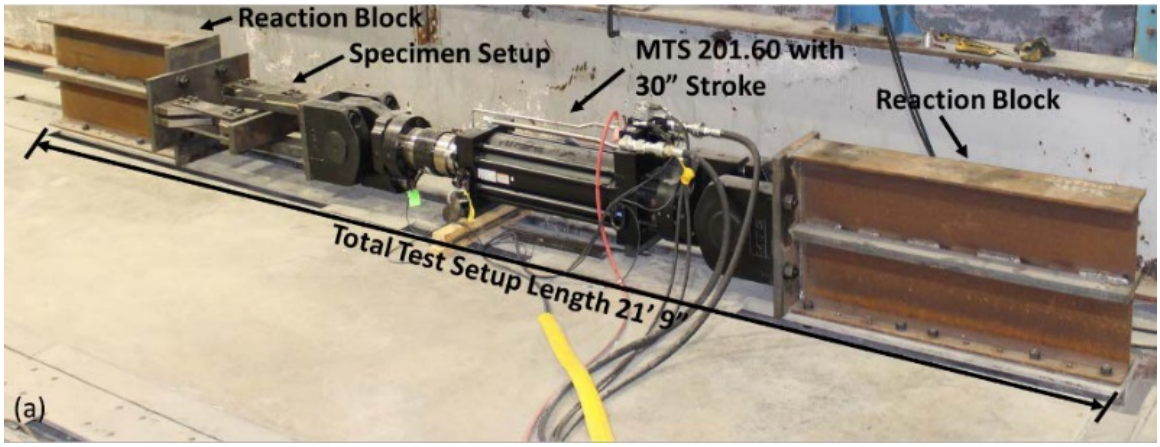

Figure 2.7. Small-scale bend test setup in a horizontal orientation (Abbas and Eatherton 2014).

Other test setups apply bending and reverse bending by generating opposite moments at the ends of the specimen. The setup shown in Figure 2.8 was used for investigating the cyclic buckling behavior of tubes with external and internal pressure (Kyriakides and Shaw 1987; Coronoa and Kyriakides 1991; Limam et al. 2010). In this assembly, the hollow tube slid over tapered mandrels at each end held by rollers and sprockets. A chain wrapped around both sprockets was connected to two pairs of hydraulic cylinders and load cells. When one cylinder was retracted, the sprockets rotated in opposite directions, which generated bending in the tube. Reverse bending was applied by retracting the opposite cylinder. The tension in the chain and the rotation of the sprockets was then related to the moment and curvature applied to the specimen. A similar variant, shown in Figure 2.9, was used for investigating the low-cycle fatigue behavior of tubes, but the specimen was held by large end fixtures rather than sprockets and rollers (Pereira et al. 2016). Four hydraulic cylinders were connected to the end fixtures, and cyclic bending was applied by extending or retracting the cylinders on one side. Another setup, shown in Figure 2.10, was used for investigating the low-cycle fatigue behavior of small steel coupons in a universal testing machine (Tateishi et al. 2006). Bending was applied when the crosshead of the machine moved up or down, which caused the offset cams to rotate the bearings holding the specimen in opposite directions. The end fixtures were set on sliding bearings to accommodate the lateral movement of the supports when the specimen was bent.

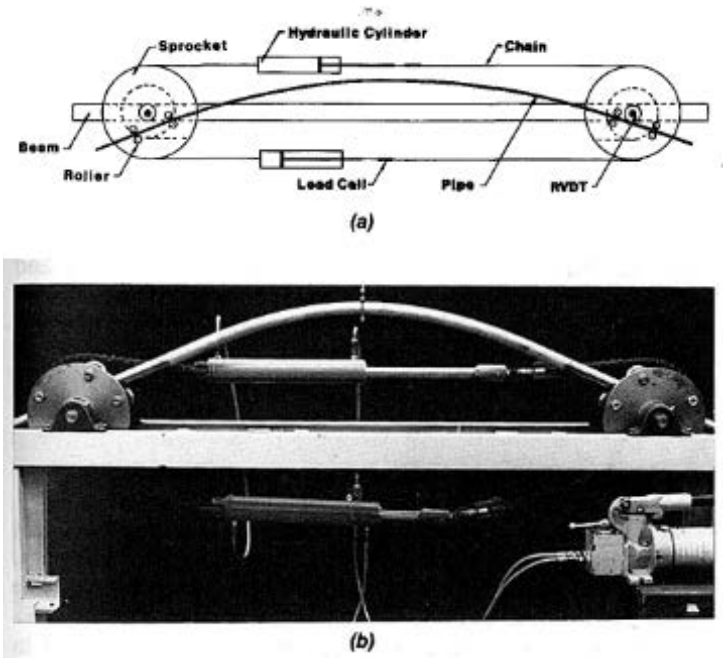

Figure 2.8. Cyclic bend test of tubes using sprockets (Kyriakides and Shaw 1987).

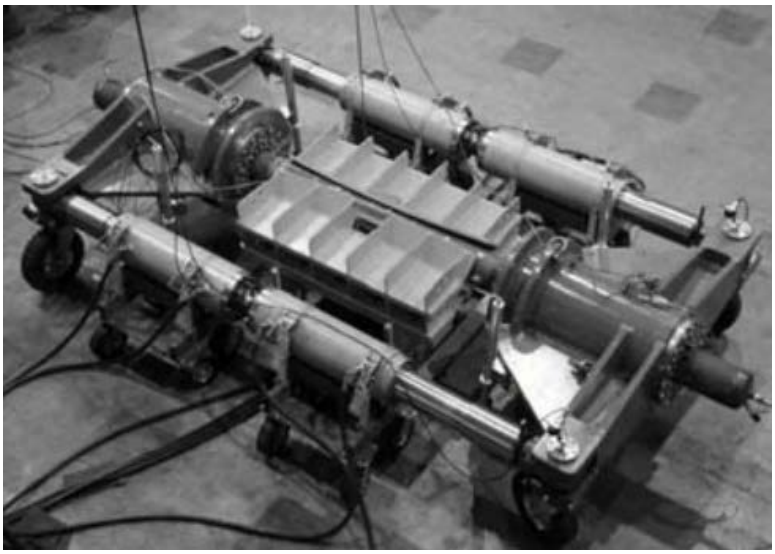

Figure 2.9. Cyclic bend test of tubes using hydraulic cylinders (Pereira et al. 2016).

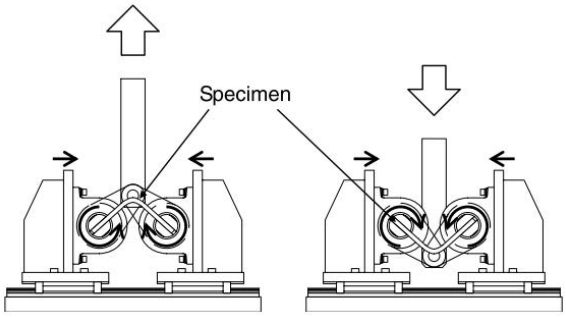

Figure 2.10. Cyclic bend test for use in a universal testing machine (Tateishi et al. 2006).

A method for simulating flange local buckling, shown in Figure 2.11, was used for investigating highly ductile slenderness ratios for beam webs and flanges (Wu et al. 2018). Rather than use flat bar coupons to simulate buckling, this assembly used T-sections with a 1:3 length to depth ratio to create realistic local buckles. With these dimensions, the authors could simulate the buckling response of full-scale moment connections by applying only cyclic axial loads to the T-sections. The specimens were welded to end-plates which were then bolted to the crossheads of a universal testing machine.

Figure 2.11. Flange local buckling of T-sections (Wu et al. 2018).

2.5 Coffin-Manson Relationships

The cyclic bend test used to test flat bar specimens with artifacts was intended to simulate the behavior of a local buckle in a full-scale test, as Eatherton et al. (2013) showed this was the typical location for fracture initiation. While acceptability of flat bar coupons with artifacts was determined by comparing the number of cycles to failure, there is a need for a more robust correlation that can be used to predict when fracture would occur in a full-scale moment connection. A method like this that uses the Coffin-Manson low-cycle fatigue relationship is proposed in Chapter 7.

This relationship characterizes the fracture resistance of flat bar specimens with different artifacts.

While working on independent studies, Manson (Manson 1954, 1953) and Coffin (Coffin 1953) both found that the relationship between plastic strain amplitude, e, and fatigue life, N, could be represented by an inverse power function, given in Eq. (2.1),

$$N = \frac{C}{e^c} \tag{2.1}$$

where C and c are material constants (Manson and Halford 2006). This relationship can also be rewritten as Eq. (2.2),

$$\frac{\Delta\epsilon_p}{2} = \epsilon'_f(2N_f)^c \tag{2.2}$$

where $2N_f$ is the number of load reversals to failure, $\frac{\Delta\epsilon_p}{2}$ is the plastic strain amplitude, c is a material constant, and ϵ'_f is a material constant approximately equal to the fatigue ductility of the material (Suresh 1998).

While the initial studies investigated the effects of cyclic thermal stresses, the inverse power relationship has also been validated for low-cycle fatigue tests conducted at ambient temperatures (Smith et al. 1963). One example of this is shown in Figure 2.12, where the data points represent the response of small-scale cast steel yield links in a yielding brace system (Gray et al. 2012). In this test, the yielding links were bent in constant amplitude cycles at room temperature until failure. The plastic strain range was varied by changing the constant amplitude displacement.

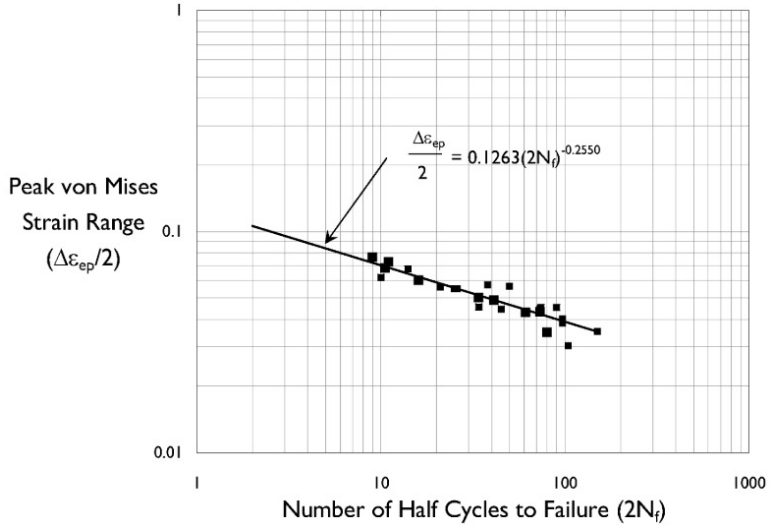

Figure 2.12. Coffin-Manson relationship for low-cycle fatigue of cast steel yielding links (Gray et al. 2012).

Chapter 3. Experimental Methods

This chapter describes the test setup, test specimens, loading protocol, and instrumentation plan for the full-scale moment connection tests and the small-scale cyclic bend tests. All tests were conducted at the Thomas M. Murray Structural Engineering Laboratory at Virginia Tech, in Blacksburg, Virginia.

3.1 Full-Scale Moment Connection Tests

3.1.1 Test Setup

The setup used in this study simulated an exterior moment connection in a structure with 32 ft. wide bays and a 12 ft. story height. A schematic drawing of the test setup is shown in Figure 3.1 and the actual setup is shown in Figure 3.2. Detailed drawings of the setup and reaction frames are provided in Appendix A. Force was applied by an MTS 201.70 servohydraulic actuator with a $\pm$ 10 inch stroke and a 220 kip capacity. This displacement was needed to ensure the test specimens could reach at least 4% story drift, and the capacity was needed to reach the full nominal plastic flexural strength of the largest specimen.

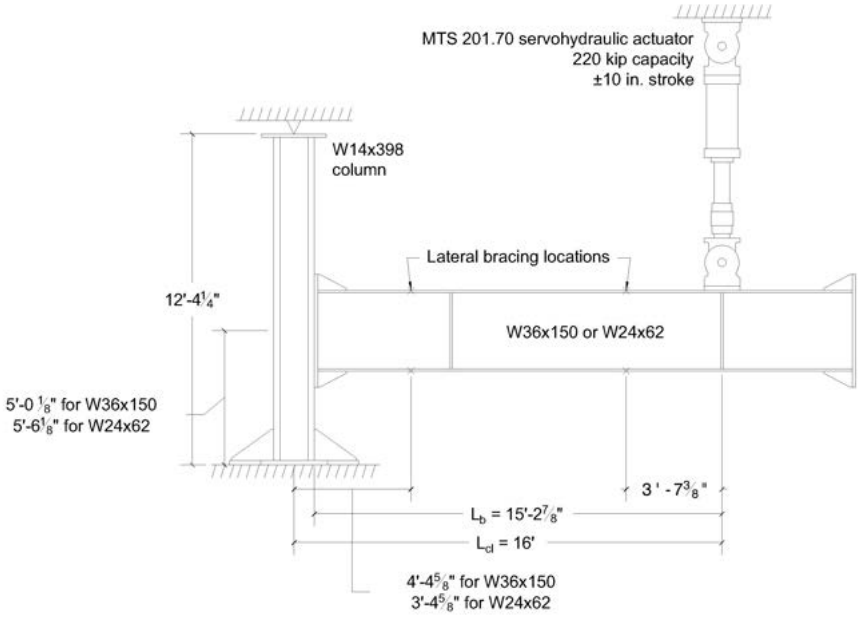

Figure 3.1. Schematic diagram of full-scale moment connection setup.

Figure 3.2. Test setup for full-scale moment connections.

Lateral bracing of the specimen was provided at the loading point and the end of the plastic hinge, shown in Figure 3.3. This bracing consisted of adjustable steel angles that were moved such that the face of the angle was approximately 0.063 in. away from the flange tips. Lithium grease was applied to the face of the angles to reduce friction during the test. To position the bracing at the end of the plastic hinge, the bracing frame was moved such that the distance between the centerline of the bracing frame and the centerline of the reaction column was 4.5 ft. for specimens with W24×62 beams and 5.5 ft. for specimens with W36×150 beams.

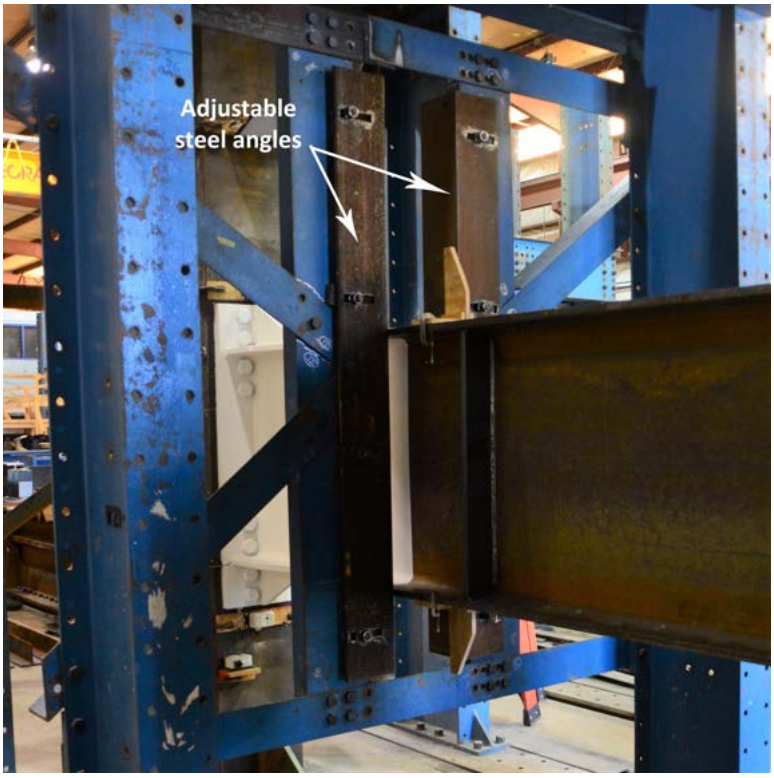

Figure 3.3. Beam lateral bracing with adjustable steel angles.

The reaction column was an ASTM A992 W14×398 bolted to the strong floor. This column was used for all six moment connection tests, and was sized to eliminate continuity and doubler plates. The beam end-plate-to-column bolts were pretensioned using a pneumatic impact wrench and the turn-of-the-nut tightening method. These were 1.5 in. diameter ASTM F3125 A490 bolts.

3.1.2 Test Specimens

The two beam sizes tested, ASTM A992 W24×62 and W360×150, were used because they were the same sizes used in previous research (Eatherton et al. 2013), but also covered a realistic range of beam depths, beam weights, flange widths, and flange thicknesses. The artifacts tested included two repair methods that met AWS D1.8 requirements, a 0.125 in. notch repaired by grinding (0.125NGT) and a 0.25 in. notch repaired by welding (0.25 NGTW), and two sharp notches that were 0.25 in. deep (0.25N) or 0.375 in. deep (0.375N). The test matrix for the large-scale specimens is shown in Table 3.1. The naming is convention is the beam size and connection type (W24RBS or W36RBS), the type of artifact (0.125NGT, 0.25NGTW, 0.25N, or 0.375N), and the thickness of the beam flanges (T59 for 0.59 in. or T94 for 0.94 in.).

Table 3.1. Full-scale test matrix.

Specimen ID	Artifact	Beam Size	Connection Type
W24RBS-0.125NGT-T59	0.125 in. notch repaired by grinding	W24×62	RBS with 4E
W36RBS-0.125NGT-T94	0.125 in. notch repaired by grinding	W36×150	RBS with 8ES
W24RBS-0.25NGTW-T59	0.25 in. notch repaired by welding	W24×62	RBS with 4E
W36RBS-0.25NGTW-T94	0.25 in. notch repaired by welding	W36×150	RBS with 8ES
W24RBS-0.375N-T59	Sharp 0.375 in. notch	W24×62	RBS with 4E
W36RBS-0.25N-T94	Sharp 0.25 in.	W36×150	RBS with 8ES

All specimens had a reduced beam section (RBS) and a four bolt extended (4E) or eight bolt extended-stiffened (8ES) end-plate connection that were designed and detailed following AISC 358-16 procedures (AISC 2016a), shown in Figure 3.4 and Figure 3.5. Detailed drawings of the test specimens are provided in Appendix B. Only RBS specimens were tested because previous tests showed that specimens with an RBS fractured before non-RBS specimens (Eatherton et al. 2013). Applied to this research, this means if a specimen with an artifact and an RBS satisfies special moment frame (SMF) qualification criteria, then a similarly detailed non-RBS specimen with the same artifact would likely satisfy SMF qualification criteria as well. While it is uncommon to use an RBS with an end-plate, the bolted connection meant the same reaction column could be used for all six tests. The two end-plate configurations used, 4E and 8ES, were the appropriate configuration for their respective beam sizes, W24×62 and W36×150, and were the same configurations used by Eatherton et al. (2013).

For RBS connections, the protected zone extended from the face of the column to the farthest end of the RBS cut: 24.5 in or 38.5 in. for specimens with W24×62 or W36×150 beams, respectively.

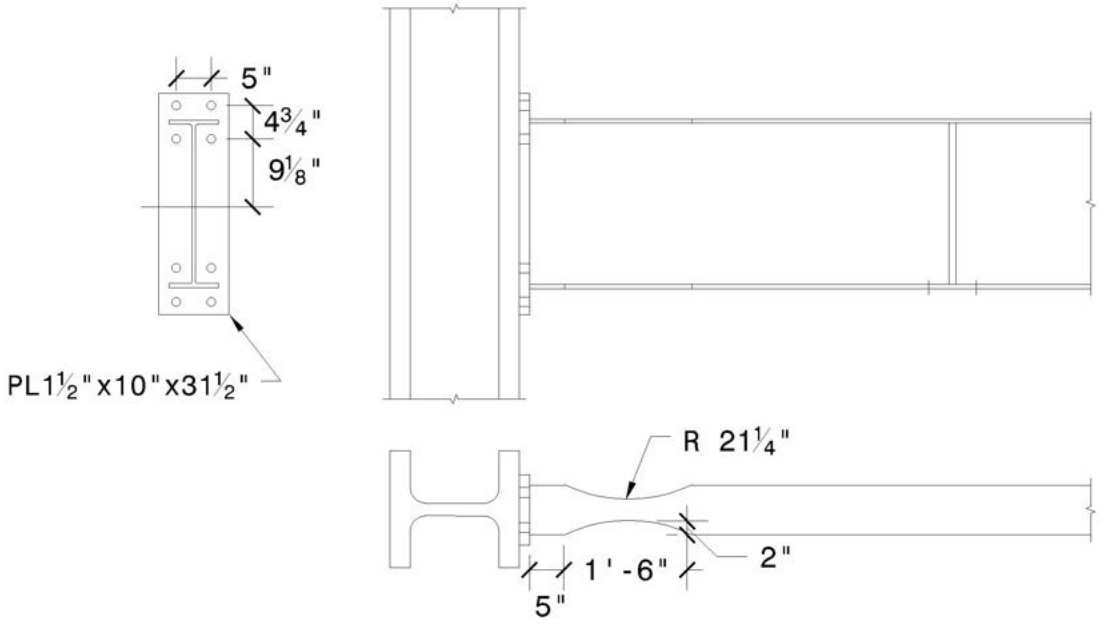

Figure 3.4. RBS connection with a W24×62 beam and 4E end-plate.

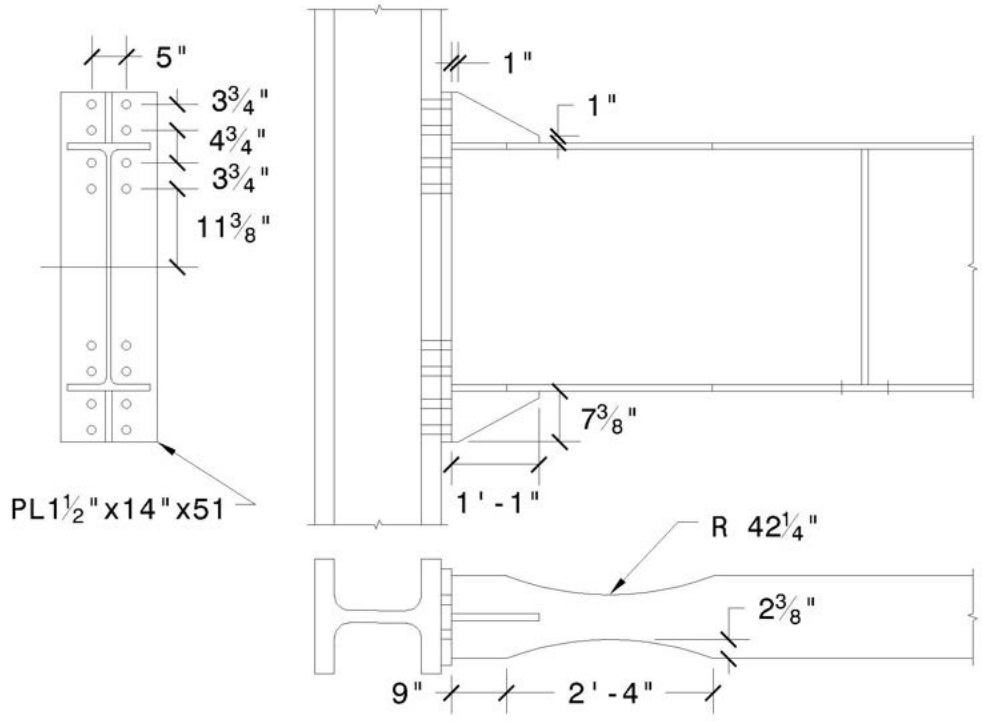

Figure 3.5. RBS connections with a W36×150 beam and 8ES end-plate.

3.1.3 Artifacts

The 0.125 in. notches repaired by grinding were first ground to a 1:5 taper in the longitudinal direction and a 1:2.5 taper in the transverse direction (AWS 2016). Grinding was done using a die grinder and carbide burr or an angle grinder and abrasive grinding wheel. While grinding, the depth was periodically checked using a digital caliper to ensure the final depth was within $\pm$ 0.01 in. of the intended depth. After grinding, the notch was at least 1.25 in. long and 0.63 in. wide, measured on the surface of the flange. Examples of finished artifacts are shown in Figure 3.6.

Figure 3.6. Finished 0.125 in. notches repair by grinding.

The 0.25 in. notches repaired by welding were first ground to a 1:5 taper in the longitudinal direction and a 1:2.5 taper in the transverse direction. This was done using a die grinder and carbide burr or an angle grinder and abrasive grinding wheel. The depth was checked periodically with a digital caliper to ensure that the final depth was within $\pm$ 0.01 in. of the intended depth. After grinding, the notches were at least 2.5 in. long and 1.25 in. wide, measured on the surface of the flange. Examples of 0.25 in. deep notches before welding are shown in Figure 3.7a.

Welding of these artifacts followed the weld procedure specification provided in Appendix C. This involved grinding the surrounding area to bright metal before removing residual dirt and grease on the notch and runoff tabs. The runoff tabs were tack welded at the ends of the notch, shown in Figure 3.7b, before preheat was applied with an oxygen-acetylene torch. Welding commenced when the base metal was at least 150°F but less than the maximum interpass

temperature of 550°F. A weld bead started on one runoff tab and traveled in the longitudinal direction before ending on the opposite runoff tab. In between weld passes, the toe of the weld bead was ground out using a die grinder and carbide burr to remove hard-to-reach slag. Examples of these artifacts after welding but before grinding the welds flush are shown in Figure 3.7c.

After the welds had cooled to ambient temperatures, the runoff tabs were removed and the welds were ground flush with the base metal using an angle grinder and abrasive grinding wheel. The welds were then inspected visually and using a magnetic particle test with a dry iron powder, following the procedure given in ASTM E2034: Standard Practice for Magnetic Particle Testing (ASTM 2016a; AWS 2016). If a defect was found, it was ground out and rewelded following the same weld procedure. Examples of finished 0.25 in. repaired by welding are shown in Figure 3.7d.

(a) Ground 0.25 in. deep notches before welding.

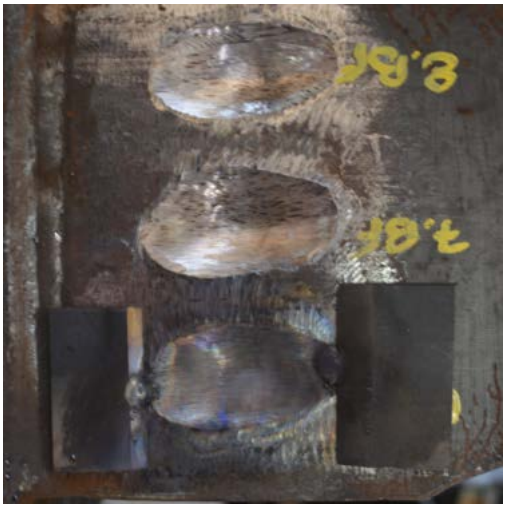

(b) Runoff tabs tacked on 0.25 in. deep notches.

(c) Welded notches before grinding welds flush.

(d) Finished 0.25 in. notches.

Figure 3.7. Ground, welded, and finished artifacts on W24RBS-0.25NGTW-T59.

y

The sharp 0.25 in. and 0.375 in. notches were ground using a Dremel rotary tool and 426B abrasive cutting wheel, with a 1.25 in. diameter and a 0.045 in. kerf. As with the other artifacts, the depth was periodically checked during grinding to ensure the final depth was within $\pm$ 0.01 in. of the intended depth. Examples of finished, sharp 0.375 in. notches are shown in Figure 3.8.

Figure 3.8. Sharp 0.375 in. notches.

Similar to the previous research, the artifacts were applied in an array on the top and bottom flanges of the full-scale specimens. Having many artifacts on one beam is likely unrealistic in practice, but having many artifact on the test specimen meant evaluating many potential artifact locations with a single specimen. This premise was more efficient but is only valid if there is little stress or strain interaction between artifacts. Thus, a finite element study was done at the start of the project to determine if the artifact spacing was sufficient to limit interaction between adjacent artifacts. This study, discussed in Chapter 4, showed that the chosen spacing was adequate for 0.25 in. notches ground to a smooth taper.

The dimensioned layouts for sharp 0.375 in. and 0.25 in. notches on the W24$\times$62 and W36$\times$150 beam specimens are shown in Figure 3.9a and Figure 3.9b, respectively. Layouts for the other artifacts were the same, and are provided in Appendix D. No artifacts were applied on the web of a specimen because the previous research investigating power actuated fasteners (PAF) and puddle welds showed that fractures were unlikely to start in the web (Eatherton et al. 2013). For specimens with a W24$\times$62 beam, a row of artifacts was placed adjacent to the end-plate because the moment is highest in this area. For specimens with a W36$\times$150 beam, an artifact was placed as close to the toe of the stiffener as possible, because this is a likely spot for fractures to initiate. Examples of the finished artifact arrays for all full-scale specimens are shown in Figures 3.10a to 3.10f.

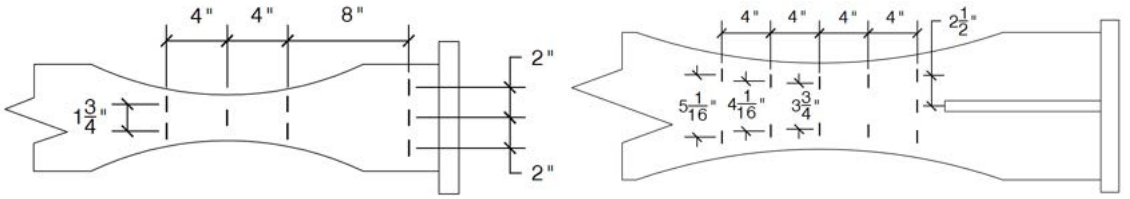

(a) Specimens with W24×62 beams. **(b)** Specimens with W36×150 beams.

Figure 3.9. Dimensioned artifact layouts for full-scale specimens.

(a) W24RBS-0.125NGT-T59 specimen. **(b)** W36RBS-0.125NGT-T94 specimen.

(c) W24RBS-0.25NGTW-T59 specimen. **(d)** W36RBS-0.25NGTW-T94 specimen.

(e) W24RBS-0.375N-T59 specimen. **(f)** W36RBS-0.25N-T94 specimen.

Figure 3.10. Complete artifact arrays for full-scale specimens.

3.1.4 Instrumentation

The instrumentation plan for all tests is shown in Figure 3.11 and included 13 displacement sensors used to decompose the story drift into its components. Decomposing the story drift into components is necessary because there is an SMF qualification requirement that the inelastic rotation in the test specimen must be within 25% of the anticipated inelastic rotation in the prototype connection (AISC 2016b). The equations provided in Appendix E were used to calculate the components of the applied story drift due to panel-zone shear, column flexure, end-plate separation, elastic beam deformation, and plastic hinge rotation.

In Figure 3.11, the string potentiometers used were Celesco model PT101-0010-111-5110 with a 10 in. range, except for SP_05 which was a Celesco model PT101-0040-111-5110 with a 40 in. range. For the first two tests, W24RBS-0.125NGT-T59 and W36RBS-0.125NGT-T94, linear voltage differential transformers (LVDTs) were used in place of LP_01 and LP_02. Celesco CLP-100 and CLP-150 linear potentiometers with 4 in. and 6 in. range, respectively, were used for the remaining tests because they were easier to install and more reliable. Two spring calipers, CLP_01 and CLP_02, were added after the W24RBS-0.125NGT-T59 and W36RBS-0.125NGT-T94 tests to measure the end-plate separation.

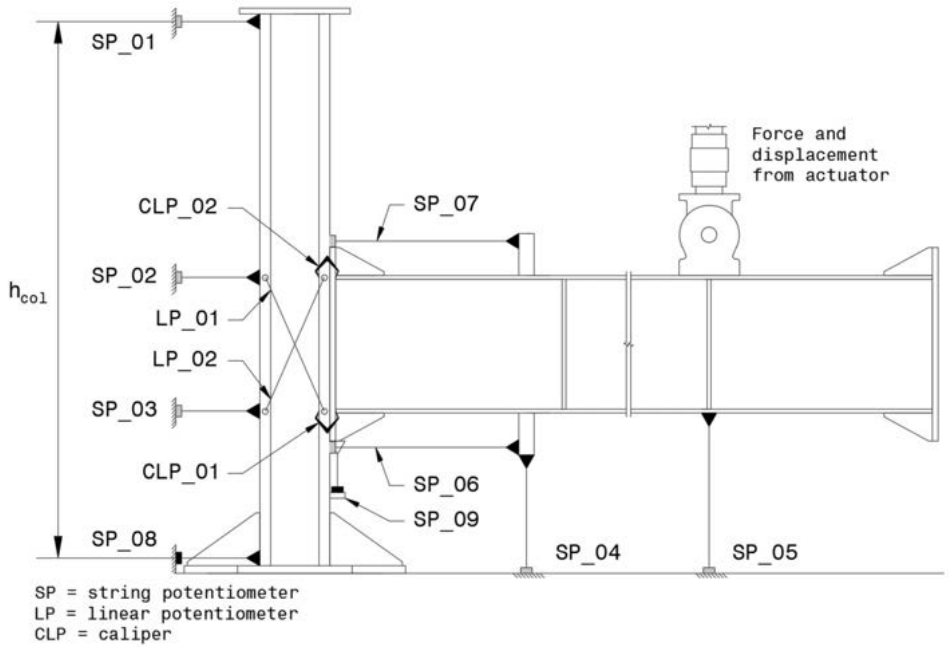

Figure 3.11. Instrumentation plan for the large-scale tests.

The force and displacement applied to the specimens were measured by the actuator's internal load cell and displacement transducer. These sensors, along with SP_01, SP_05, and SP_08, were connected to an MTS FlexTest 60 controller which applied signal conditioning and output the signals to a National Instruments SCXI-1001 chassis. All other sensors were connected directly to the SCXI-1001 chassis. A wiring diagram for all sensors is given in Ap-

pendix F. National Instruments' SignalExpress program on a desktop computer was used to display and record data at 3-5 Hz, depending on the test.

In addition to force and displacement sensors, the tests were documented using Canon digital SLR cameras. Four cameras were positioned to capture the top flange, bottom flange, and both sides of the web, shown in Figures 3.12a to 3.12d. An additional camera captured an overall view of the setup, shown in Figure 3.12e. The cameras were controlled using GBTimelapse software, which took pictures every six seconds. The pictures were then compiled into time-lapse videos to show the response of the specimen during the test. Hydrated lime (whitewash) was also used to show the response of the connection. The 1:1 mixture of lime and water adheres to the beam when applied, but falls off as the mill scale flakes off, indicating where the steel has yielded. However, in areas where the mill scale was ground off, such as around the welded artifacts, the whitewash was not a good indicator of yielding.

(a) West side.

(b) East side.

(c) Top flange.

(d) Bottom flange.

(e) Overall view.

Figure 3.12. Camera views around the connection.

3.1.5 Loading Protocol

The loading protocol from AISC 341-16 for qualification testing of SMF connections is given in Table 3.2 (AISC 2016b). The prescribed loading stops after 0.04 radians, but there is an additional requirement that loading continues in 0.01 radian increments for two cycles each until failure. The maximum story drift that could be applied was 0.05 radians, based on the location and maximum stroke of the actuator. Thus, all specimens were cycled at 0.05 radians until failure, except W24RBS-0.125NGT-T59, which was cycled at 0.045 radians until failure. Similarly, all specimens were loaded at a rate of 0.0002 radians/second through the first two cycles of 5% story drift, except W24RBS-0.125NGT-T59, which was loaded at a rate of 0.0001 radians/second through the first two cycles of 4.5% story drift. These loading rates correspond to a vertical displacement of approximately 2.3 in./min and 1.2 in./min, respectively. If a specimen completed two cycles of 5% story drift, the loading rate doubled for the remainder of the test.

Table 3.2. Loading protocol for full-scale moment connection tests.

Drift Target		Number of
Radians	**Percent**	**Cycles**
0.00375	0.375	6
0.005	0.5	6
0.0075	0.75	6
0.01	1	4
0.015	1.5	2
0.02	2	2
0.03	3	2
0.04	4	2
0.05	5	Varies

The applied story drift was calculated concurrent with the test and used as active feedback to control the movement of the actuator. This ensured that the applied story drift accounted for the deformation of the reaction frame and column sliding. The applied story drift, θ_{APP}, was calculated in the MTS MultiPurpose Testware calculations module using Eq. (3.1),

$$\theta_{APP} = \frac{-\delta_{SP\_05}}{L_{cl}} + \frac{\delta_{SP\_01} - \delta_{SP\_08}}{h_{col}} \tag{3.1}$$

where: h_{col} = distance between SP_01 and SP_08, 11.4 ft.

L_{cl} = distance from the actuator centerline to column centerline, 16 ft.

δ_{SP_01} = displacement measured by SP_01

δ_{SP_05} = displacement measured by SP_05

δ_{SP_08} = displacement measured by SP_08.

In all tests, the free end was displaced upwards in the first cycle, which corresponds to negative story drift. This also puts the top flange in compression first. Based on previous testing, it was believed that loading the top flange in compression first would lead to fractures occurring on the top flange and be more visible to cameras documenting the tests.

3.2 Small-Scale Cyclic Bend Tests

The small-scale cyclic bend test was developed by Abbas and Eatherton (2014) to simulate flexure in the local buckles of a full-scale moment connection test, as this was the typical fracture location identified by Eatherton et al. (2013). A small-scale test that can approximate local buckling would be beneficial because the small-scale tests are quicker and

less expensive than full-scale testing. However, one major difference between the full-scale and small-scale tests is that the strain amplitude of local buckles on a full-scale specimens varies and may not fully reverse, while the small-scale test applies constant strain amplitudes that fully reverse each cycle. In this sense, the small-scale test would not accurately simulate a local buckle, but would be similar enough for calibrating the Coffin-Manson low-cycle fatigue relationship to correlate the full-scale and small-scale tests.

3.2.1 Test Setup

The cyclic bend test setup had a movable assembly and a fixed assembly; both are shown in Figure 3.13. The movable assembly was comprised of two loading arms bolted at one end to an MTS 201.80 servohydraulic actuator with a capacity of 330 kips and a $\pm$ 15 in. stroke. The free end of the loading arms held four 11 in. diameter, 3 in. thick semicircular rollers. Two bottom rollers were secured with a square pin, while the two opposing top rollers were secured with a 1.375 in. bolt in a long slotted hole. The fixed assembly was bolted to the strong floor and consisted of a top and bottom set of fixed guides. The main components of the bend test setup are shown in Figure 3.14. Drawings of the components are also provided in Appendix G

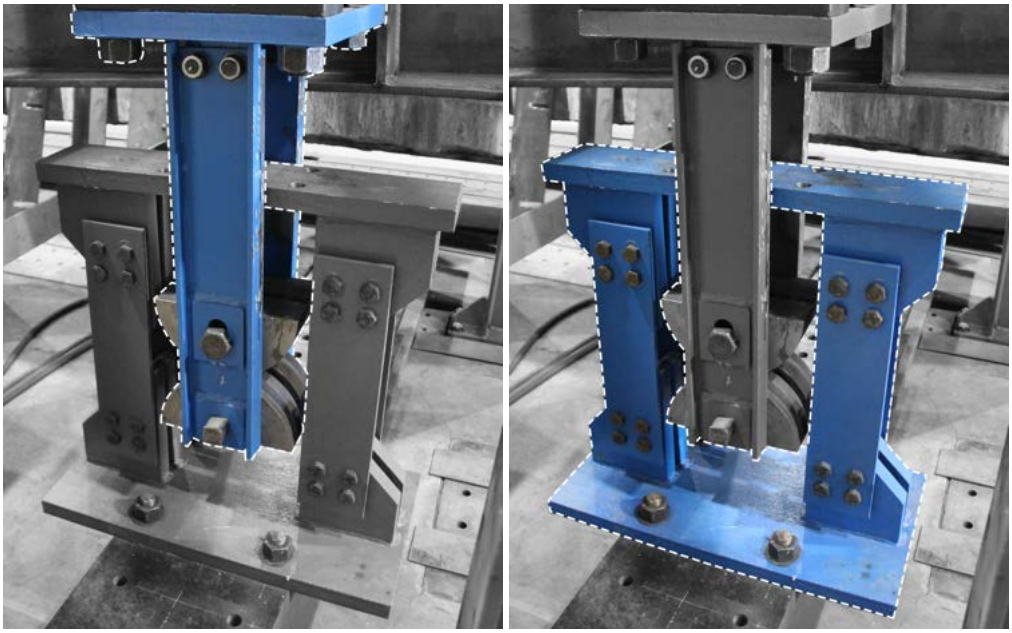

(a) Movable assembly. **(b)** Fixed assembly.

Figure 3.13. Cyclic bend test assemblies.

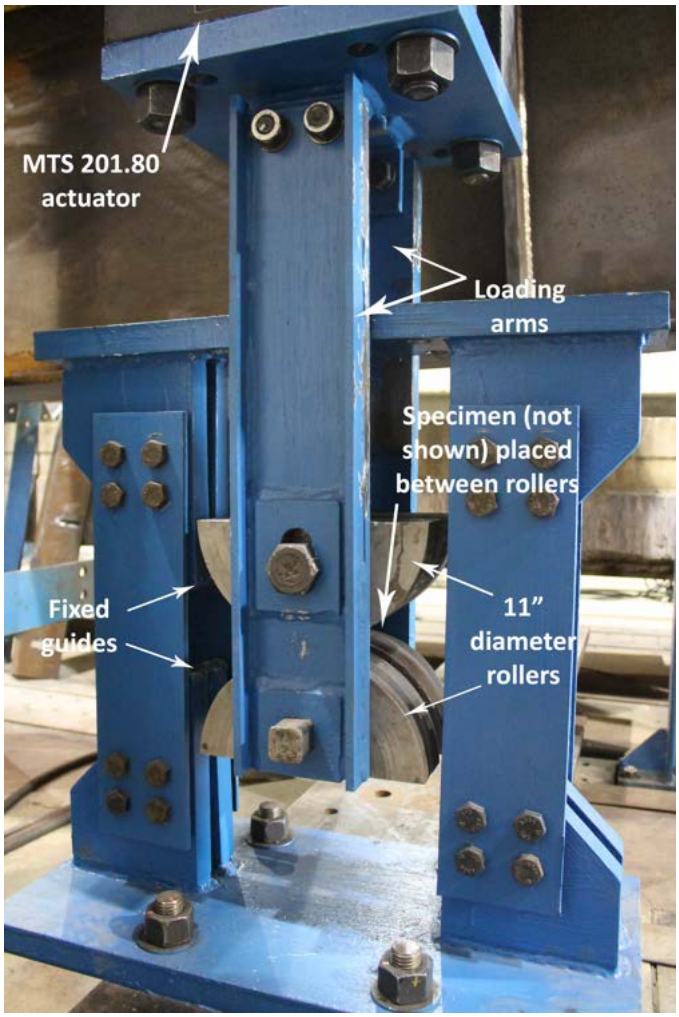

Figure 3.14. Main components of the cyclic bend test setup.

To prepare for a test, a coupon was placed between the top and bottom rollers with the artifact centered on the rollers and facing up. A hydraulic bottle jack was used to apply 9-10 kips to clamp the specimen between the rollers, before the 1.375 in. diameter bolt was tightened and the jack was removed. The pretension in this bolt was insufficient to prevent the top roller from slipping, so a 0.75 in. diameter threaded rod was installed though the loading arms above the top roller for additional bearing resistance. This rod held two angles in contact with the top roller that prevented the roller from slipping in the slotted hole.

During testing, the actuator cyclically moved the loading arms, rollers, and specimen up and down. When the specimen contacted either set of fixed guides, it was forced to bend to the radius of the roller. Reverse bending was applied when the specimen contacted the opposite set of fixed guides. A loading schematic of the small-scale tests is shown in Figure 3.15.

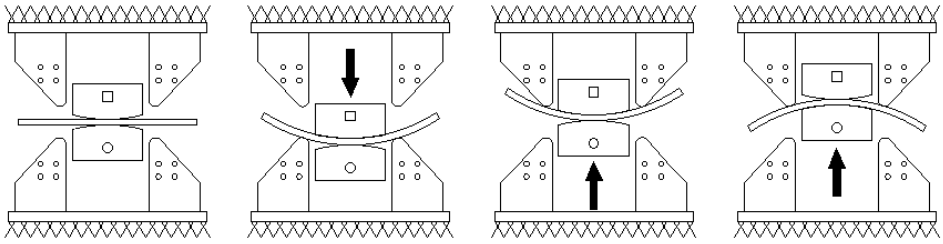

Figure 3.15. Loading schematic of small-scale bend test.

The total strain at the extreme fiber, ϵ_t, for each coupon thickness was calculated using Eq. (3.2),

$$\epsilon_t = \frac{t}{D+t} \tag{3.2}$$

where t is the coupon thickness and D is the roller diameter. The plastic strain amplitude, ϵ_p, was used when calibrating the Coffin-Manson relationships, and was calculated using Eq. (3.3),

$$\epsilon_p = \epsilon_t - \epsilon_{el} \tag{3.3}$$

where ϵ_{el} is the elastic strain, assumed to be 0.002 in./in. The total and plastic strains for various coupon thicknesses are given in Table 3.3.

Table 3.3. Strain per half cycle for small-scale tests.

Coupon Thickness, in.	**Total Strain, ϵ_t in./in.**	**Plastic Strain, ϵ_p, in./in.**
0.4	0.0351	0.0331
0.5	0.0435	0.0415
0.59	0.0509	0.0489
0.94	0.0787	0.0767
1.0	0.0833	0.0813

3.2.2 Test Specimens

Fifty-four flat bar coupons with varying thicknesses and artifacts were tested. The test matrix for coupons with repairs and defects is shown in Table 3.4; the test matrix for additional bare steel specimens and coupons with PAFs or puddle welds is shown in Table 3.5. All coupons were 28 in. long with the artifact centered in the transverse and longitudinal directions. Actual dimensions of the coupons are given in Appendix H, and specimen drawings are given in Appendix I. The 0.59 in. and 0.94 in. thick coupons were cut from the flanges of ASTM A992 W24×62 and ASTM

A992 W36×150 beams, respectively, while 0.5 in. and 1.0 in. thick coupons were cut from ASTM A572 Grade 50 bar stock. Bar stock was used in lieu of beam flange material of the same thickness because it was easier to obtain and had similar material properties; both ASTM A992 and ASTM A572 Grade 50 have a nominal yield stress of 50 ksi and an ultimate strength of 65 ksi. This was assumed to be acceptable at the start of testing, but was confirmed by testing identical, 0.4 in. thick bare steel coupons: the W24-BAR STOCK-T40-R11.02 specimen was milled from 0.5 in. bar stock, while the W24-FLANGE MATERIAL-T40-R11.01 specimen was milled from W24×62 beam flange material.

Table 3.4. Test matrix for flat bar coupons with repairs and defects.

Specimen Name	Artifact	Coupon Thickness, in.	Nominal Width, in.
W24-0.125NGT-T50-R11.01	0.125 in. notch repaired by grinding	0.5	3.5
W24-0.125NGT-T50-R11.02	0.125 in. notch repaired by grinding	0.5	3.5
W24-0.125NGT-T59-R11.01	0.125 in. notch repaired by grinding	0.59	3
W24-0.125NGT-T59-R11.02	0.125 in. notch repaired by grinding	0.59	3
W36-0.125NGT-T94-R11.01	0.125 in. notch repaired by grinding	0.94	4.63
W36-0.125NGT-T94-R11.02	0.125 in. notch repaired by grinding	0.94	4.63
W36-0.125NGT-T100-R11.01	0.125 in. notch repaired by grinding	1.0	5
W36-0.125NGT-T100-R11.02	0.125 in. notch repaired by grinding	1.0	5
W24-0.25NGTW-T50-R11.01	0.25 in. notch repaired by welding	0.5	3.5
W24-0.25NGTW-T50-R11.02	0.25 in. notch repaired by welding	0.5	3.5
W24-0.25NGTW-T59-R11.01	0.25 in. notch repaired by welding	0.59	3
W24-0.25NGTW-T59-R11.02	0.25 in. notch repaired by welding	0.59	3
W36-0.25NGTW-T94-R11.01	0.25 in. notch repaired by welding	0.94	4.63
W36-0.25NGTW-T94-R11.02	0.25 in. notch repaired by welding	0.94	4.63
W36-0.25NGTW-T100-R11.01	0.25 in. notch repaired by welding	1.0	5
W36-0.25NGTW-T100-R11.02	0.25 in. notch repaired by welding	1.0	5
W24-0.25N-T50-R11.02	Sharp 0.25 in. notch	0.5	3.5
W24-0.25N-T50-R11.03	Sharp 0.25 in. notch	0.5	3.5
W24-0.25N-T59-R11.02	Sharp 0.25 in. notch	0.59	3
W24-0.25N-T59-R11.03	Sharp 0.25 in. notch	0.59	3
W36-0.25N-T94-R11.01	Sharp 0.25 in. notch	0.94	4.63
W36-0.25N-T94-R11.02	Sharp 0.25 in. notch	0.94	4.63
W36-0.25N-T100-R11.01	Sharp 0.25 in. notch	1.0	5
W36-0.25N-T100-R11.02	Sharp 0.25 in. notch	1.0	5
W24-0.375N-T50-R11.01	Sharp 0.375 in. notch	0.5	3.5
W24-0.375N-T50-R11.02	Sharp 0.375 in. notch	0.5	3.5
W24-0.375N-T59-R11.01	Sharp 0.375 in. notch	0.59	3
W24-0.375N-T59-R11.02	Sharp 0.375 in. notch	0.59	3
W36-0.375N-T94-R11.01	Sharp 0.375 in. notch	0.94	4.63
W36-0.375N-T94-R11.02	Sharp 0.375 in. notch	0.94	4.63
W36-0.375N-T100-R11.01	Sharp 0.375 in. notch	1.0	5
W36-0.375N-T100-R11.02	Sharp 0.375 in. notch	1.0	5

Table 3.5. Test matrix fasteners and bare steel.

Specimen Name	Artifact	Coupon Thickness, in.	Nominal Width, in.
W24-0.625PnAF-T50-R11.01	Pneutek K66062	0.5	3.5
W24-0.625PnAF-T50-R11.02	Pneutek K66062	0.5	3.5
W36-0.625PnAF-T100-R11.01	Pneutek K66062	1.0	5
W36-0.625PnAF-T100-R11.02	Pneutek K66062	1.0	5
W24-0.75PnAF-T50-R11.01	Pneutek K66075	0.5	3.5
W24-0.75PnAF-T50-R11.02	Pneutek K66075	0.5	3.5
W36-0.75PnAF-T100-R11.01	Pneutek K66075	1.0	5
W36-0.75PnAF-T100-R11.02	Pneutek K66075	1.0	5
W24-PAF-T50-R11.01	Hilti X-ENP-19 L15	0.5	3.5
W24-PAF-T50-R11.02	Hilti X-ENP-19 L15	0.5	3.5
W36-PAF-T100-R11.01	Hilti X-ENP-19 L15	1.0	5
W36-PAF-T100-R11.02	Hilti X-ENP-19 L15	1.0	5
W24-PW-T50-R11.01	Puddle weld	0.5	3.5
W24-PW-T50-R11.02	Puddle weld	0.5	3.5
W36-PW-T100-R11.01	Puddle weld	1.0	5
W36-PW-T100-R11.02	Puddle weld	1.0	5
W24-BAR STOCK-T40-R11.02	Bare steel	0.4	3.5
W24-FLANGE MATERIAL-T40-R11.01	Bare steel	0.4	3
W24-STEEL-T50-R11.01	Bare steel	0.5	3.5
W24-STEEL-T50-R11.02	Bare steel	0.5	3.5
W36-STEEL-T100-R11.01	Bare steel	1.0	5
W36-STEEL-T100-R11.02	Bare steel	1.0	5

3.2.3 Artifacts

The 0.125 in. notches repaired by grinding and 0.25 in. notches repaired by welding applied to the flat bar coupons were the same as those applied to the full-scale specimens. Both artifacts were first ground to a smooth 1:5 taper in the longitudinal direction and a 1:2.5 taper in the transverse direction. Grinding was done with a die grinder and carbide burr until the final depth was within $\pm$ 0.01 in. of the intended depth, measured with a digital caliper. The 0.25 in. notches repaired by welding were then cleaned and welded following the weld procedure specification given in Appendix C and described in Section 3.1.3. For these specimens, the weld passes were parallel to the longitudinal

axis of the coupon. When the welds had cooled to ambient temperature, the runoff tabs were removed, the welds were ground flush with the bar, and the welded area was inspected with a magnetic particle tester. Examples of completed 0.125 in. notches repaired by grinding and 0.25 in. notches repaired by welding are shown in Figure 3.16a and Figure 3.16b, respectively.

The sharp 0.25 in. and 0.375 in. deep notches were ground using an abrasive cutting wheel with a 1.25 in. diameter and 0.045 in. kerf until the depth was within $\pm$ 0.01 in. of the intended depth. For these artifacts, the notches were cut perpendicular to the longitudinal axis of the coupon. An example a completed sharp 0.25 in. notch on a flat bar coupon is shown in Figure 3.16c.

The pneumatic actuated fasteners, Pneutek K66062 and K66075, were installed using a PT-2000Z tool operating at 180 psi. Proper installation of the Pneutek fasteners meant there was tight contact between the collation material, fastener, and steel. The Hilti X-ENP-19 L15 sheet metal nails were installed with a DX 76 PTR powder actuated tool and 0.27 caliber, 6.8/11 M10 powder cartridge. Proper installation of the Hilti fasteners was determined by three criteria: firm contact between the two washers on the fastener, a C-shaped mark on the top washer from the piston ring, and using a penetration adjustment guide. Examples of a properly installed Pneutek and Hilti fasteners are shown in Figure 3.16d and Figure 3.16e, respectively.

To fabricate the puddle weld specimens, a 1 in. by 1 in. square of 20 gauge galvanized deck was welded to the flat bar coupons using a 6010 SMAW electrode. An example of a finished, 0.63 in. diameter puddle weld is shown in Figure 3.16f.

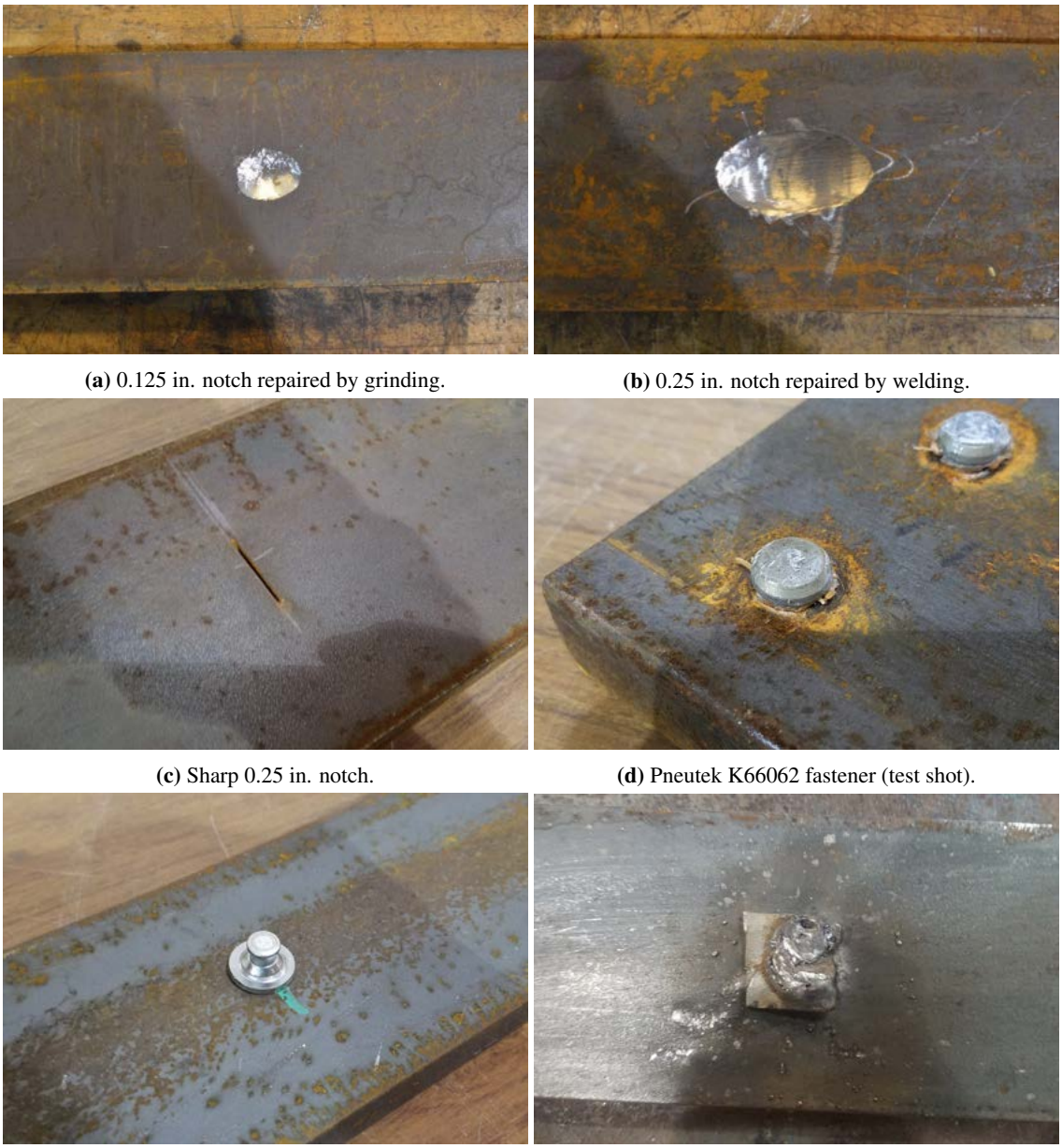

(a) 0.125 in. notch repaired by grinding.

(b) 0.25 in. notch repaired by welding.

(c) Sharp 0.25 in. notch.

(d) Pneutek K66062 fastener (test shot).

(e) Hilti X-ENP-19 L15 fastener.

(f) 0.63 in. diameter puddle weld.

Figure 3.16. Bend coupons with various artifacts.

3.2.4 Instrumentation

The actuator force and displacement were measured by an internal load cell and displacement transducer, respectively, that were connected to an MTS FlexTest 60 controller. Four Microsoft LifeCam webcams were placed in the gap between rollers, in the layout shown in Figure 3.17, to record where fractures initiated and how they propagated. These cameras were connected to a desktop computer and recorded simultaneously using OBS Studio software. The inside of the rollers was painted matte black to reduce the glare in the recordings.

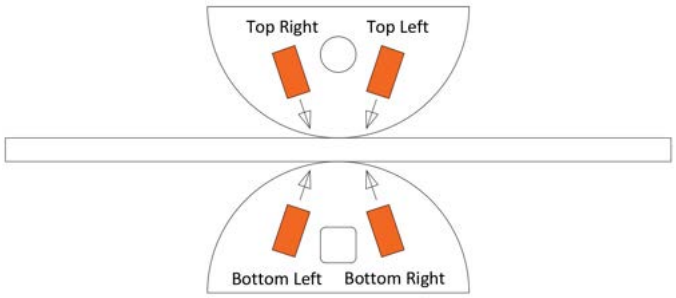

Figure 3.17. Layout and naming of webcams for small scale testing.

3.2.5 Loading Protocol

During testing, the actuator cyclically moved the rollers and specimen ±5 in. at a rate of 10 in./min for the 0.4-0.59 in. thick coupons and at a rate of 5 in./min for the 0.94 in. and 1 in. thick coupons. The loading rate was the same rate used in the previous small-scale studies and was chosen because it was quick, but limited strain rate effects. The loading procedure was controlled using the MTS MultiPurpose TestWare program and an MTS FlexTest 60 controller.

3.3 Material Testing

Tensile coupons were cut from the beams and bar stock to determine the yield stress, ultimate strength, and elongation of the material. Three coupons were cut from the middle of each beam, parallel to the rolling direction: one from each flange and one from the web. The coupons were intended to have the same dimensions as a standard coupon given in ASTM E8: Standard Test Methods for Tension Testing of Metallic Materials (ASTM 2016b), with a total length of 18 in. and a gauge length of 8 in. However, the reduced section was inadvertently cut to be 1 in. wide, rather than 1.5 in. Before testing, the average cross-sectional area of the reduced section was calculated to be used when calculating the applied stress. Punch marks were also spaced 8 in. apart at the end of the gauge length to determine the elongation after testing.

Coupons up to 0.83 in. thick were tested in an MTS Landmark 370.50 servohydraulic universal testing machine with a tension capacity of 110 kips. The crosshead was displaced at a rate of 0.15 in./min until 0.2 in. displacement, at which point the rate increased to 0.5 in./min. The loading was controlled by an MTS FlexTest SE controller and the MultiPurpose TestWare program. Throughout the test, force was measured by an internal load cell and displacement was measured by an internal displacement transducer. An Epsilon axial extensometer, model 3543-0800-400T-ST, with an 8 in. gauge length measured strain. The extensometer and force output from the controller were connected to a National Instruments SCXI-1001 chassis, and were recorded at 10 Hz using National Instruments' SignalExpress program.

Coupons with a thickness greater than 0.83 in. were tested in a SATEC Model M300WHVL servohydraulic universal

testing machine with a tension capacity of 300 kips. The crosshead was displaced at a rate of 0.15 in./min for the entire test and was controlled by an MTS model 407 controller. Force was measured by an internal load cell and displacement was measured by an internal displacement transducer, while the same Epsilon axial extensometer measured strain. The extensometer, load cell, and LVDT were connected to a National Instruments PXI-1052 chassis, and were recorded at 10 Hz using National Instruments' SignalExpress program.

In addition to tensile tests, standard Charpy V-notch (CVN) specimens were cut from the beam flanges and bar stock to determine the impact toughness of the material at room temperature. Three specimens were cut from each of the two beam sizes and two bar stock sizes, for a total of twelve tests. These specimens had the same dimensions as a standard specimen given in ASTM E23: Standard Test Methods for Notched Bar Impact Testing of Metallic Materials (ASTM 2018). The specimens were oriented in the material such that the long dimension was parallel to the rolling direction, and the V-notch was parallel to the thickness dimension of the beam flange or bar stock, shown in Figure 3.18 for specimens cut from beam flange material.

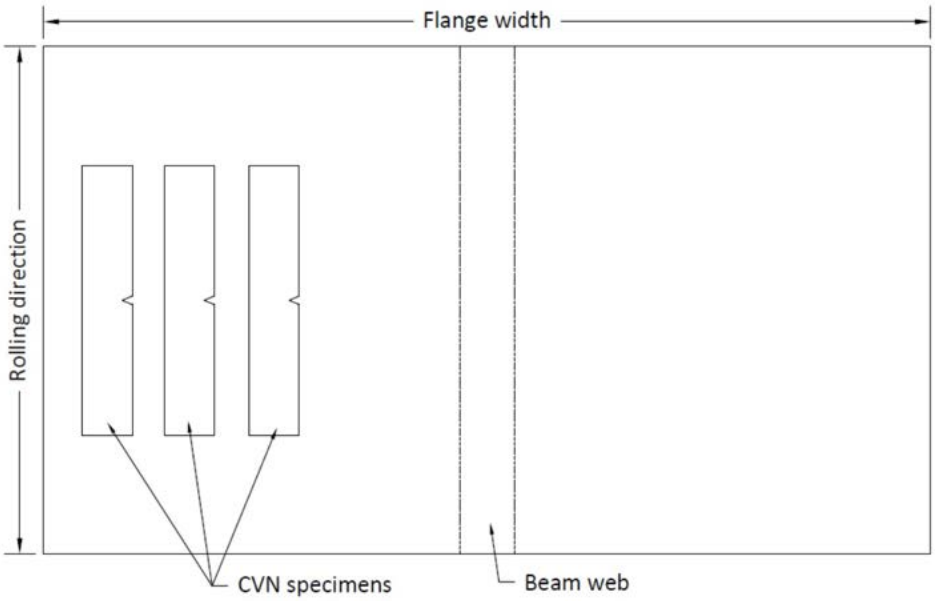

Figure 3.18. Plan view of CVN specimens cut from beam flanges.

Chapter 4. Finite Element Modeling

This chapter describes a brief finite element (FE) study that sought to answer the following research questions:

1. Is the artifact spacing appropriate to limit stress and strain interaction between artifacts?
2. Will fractures initiate in similar locations for specimens with a single artifact or an array?
3. Are the stress and strain states at the initial fracture location similar between the full-scale and small-scale tests?

Four models with solid elements were created using Abaqus 6.14-4: three full-scale moment connections and one small-scale cyclic bend test.

4.1 FE Model Parameters

The full-scale models replicated the W24×62 reduced beam section (RBS) specimens tested by Eatherton et al. (2013), including the W14×257 reaction column. The model with no artifacts is shown in Figure 4.1, but the two models with artifacts were similar. The column was pinned at the top and fixed at the bottom, while out-of-plane displacement was restrained at the lateral bracing points. The artifacts were 1.25 in. by 2.5 in. ellipsoids that were 0.25 in. deep applied on the top flange as a single artifact and as an array, shown in Figure 4.2a and Figure 4.2b. The artifacts in the array had the same spacing given in Figure 3.9a, with two additional lines of three notches at either end of the RBS cut, 8 in. from the center of the RBS. There were six 0.1 in. thick elements through the flange thickness and 11-15 elements across the flange width, depending on the model. These elements were about 0.5 in. by 0.27 in. at the center of the RBS and about 1 in. by 0.66 in. away from the RBS. Farther into the beam the mesh size increased to about 2 in. by 1.65 in., as these areas were expected to remain elastic. The elements in all parts were eight node bricks with reduced integration. The loading protocol was an applied displacement that followed the loading procedure given in Table 3.2, but stopped after completing two cycles of 4% story drift.

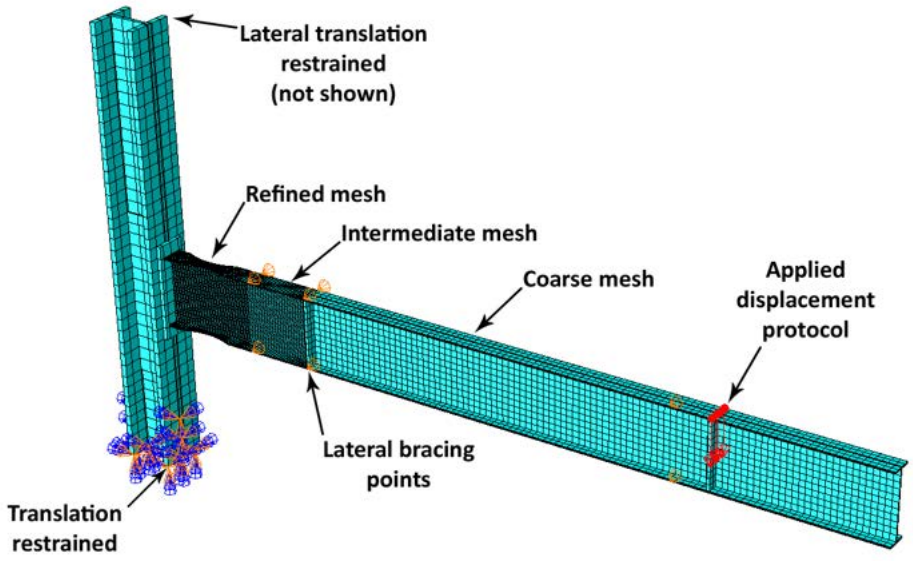

Figure 4.1. Full-scale model of an RBS with a W24×62 beam.

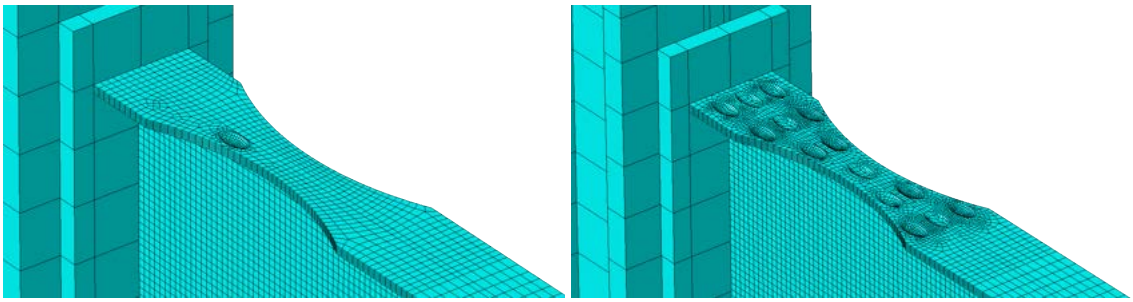

(a) Single 0.25 in. deep notches. **(b)** Array of 0.25 in. deep notches.

Figure 4.2. Artifact meshes for RBS specimens with W24×62 beams.

The model of the small-scale cyclic bend coupon replicated the test described in Section 3.2, shown in Figure 4.3 with pinned ends. The 11 in. diameter rollers were constrained to the coupon, with the coupon being the master surface and the roller being the slave surface. The coupon was 3 in. wide, 28 in. long, and 0.6 in. thick, with a 0.25 in. deep, 1.25 in. wide by 2.5 in. long ellipsoidal artifact centered in both directions. Like the full-scale models, there were six 0.1 in. thick elements through the thickness of the coupon. The mesh of the small scale coupon with an artifact is shown in Figure 4.4. The larger elements were about 0.5 in. by 0.25 in. away from the artifact at the edges of the coupon, while smaller elements were about 0.05 in. by 0.05 in. at the center of the artifact. Like the full-scale models, eight-node bricks with reduced integration were used. The loading protocol for the bend test was an applied displacement that involved cyclically displacing the rollers $\pm$ 5 in.

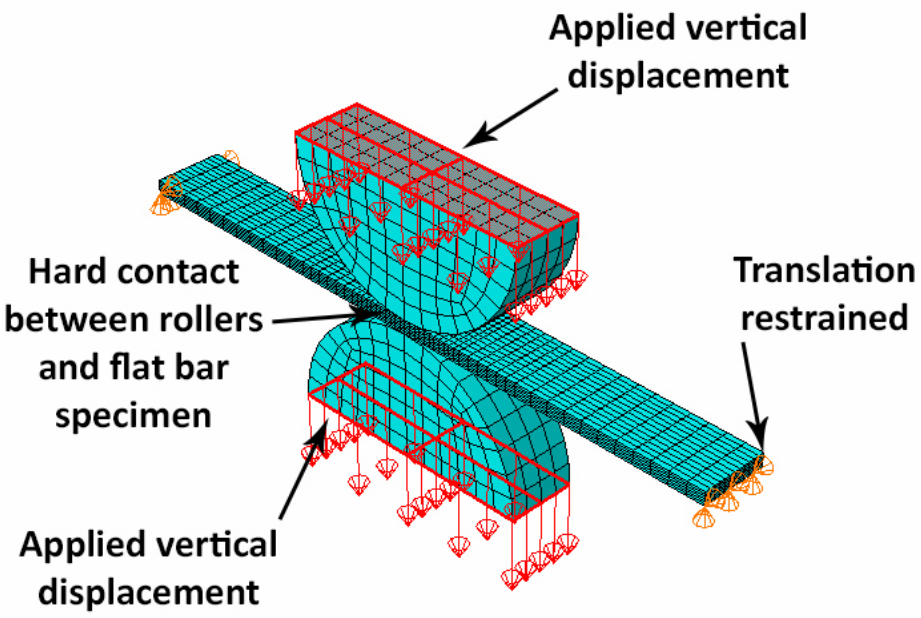

Figure 4.3. Model of a bend coupon cut from a W24×62 flange.

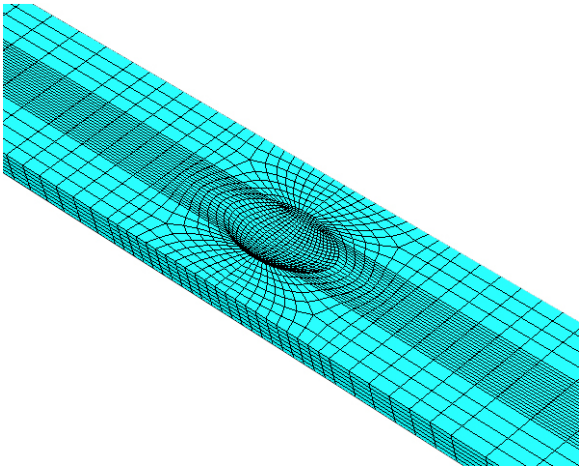

Figure 4.4. Small-scale bend coupon mesh.

The steel material for all four models was modeled with isotropic hardening using the true stress and true plastic strain values given in Table 4.1. This was the same material model used by Toellner (2013).

Table 4.1. Isotropic hardening data (Toellner 2013).

True plastic strain, in./in.	True stress, ksi
0.00	54.09
0.012	54.86
0.013	56.30
0.018	59.16
0.028	63.35
0.038	66.87
0.047	69.51
0.057	71.87
0.075	75.17
0.094	77.55
0.112	79.41
0.261	92.18

4.2 FE Model Results

The von Mises stress and equivalent plastic strain gradients for the four models are shown in Figures 4.5 to 4.8. Regarding the full-scale models, the buckled shape was similar for all three and agreed with the response seen in the full-scale tests by Eatherton et al. (2013). Furthermore, the area of highest equivalent plastic strain was similar: the inside of a local buckle or at the edge of an artifact, if one was present. The maximum equivalent plastic strain was also of the same order of magnitude for the two full-scale models with artifacts. Thus, the spacing of the artifacts was sufficient to limit strain interaction because there was little change in the location and magnitude of maximum equivalent plastic strain between the two models with artifacts.

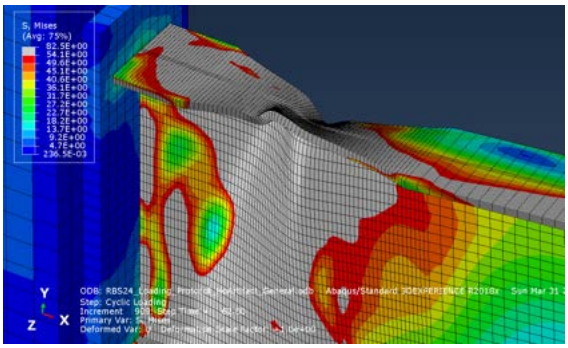

(a) Von Mises stress (yielded material is gray).

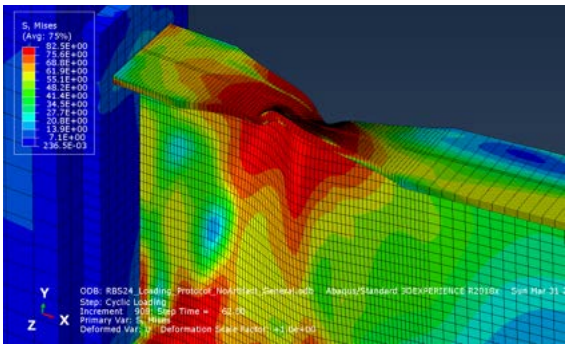

(b) Von Mises stress (gradients beyond yield).

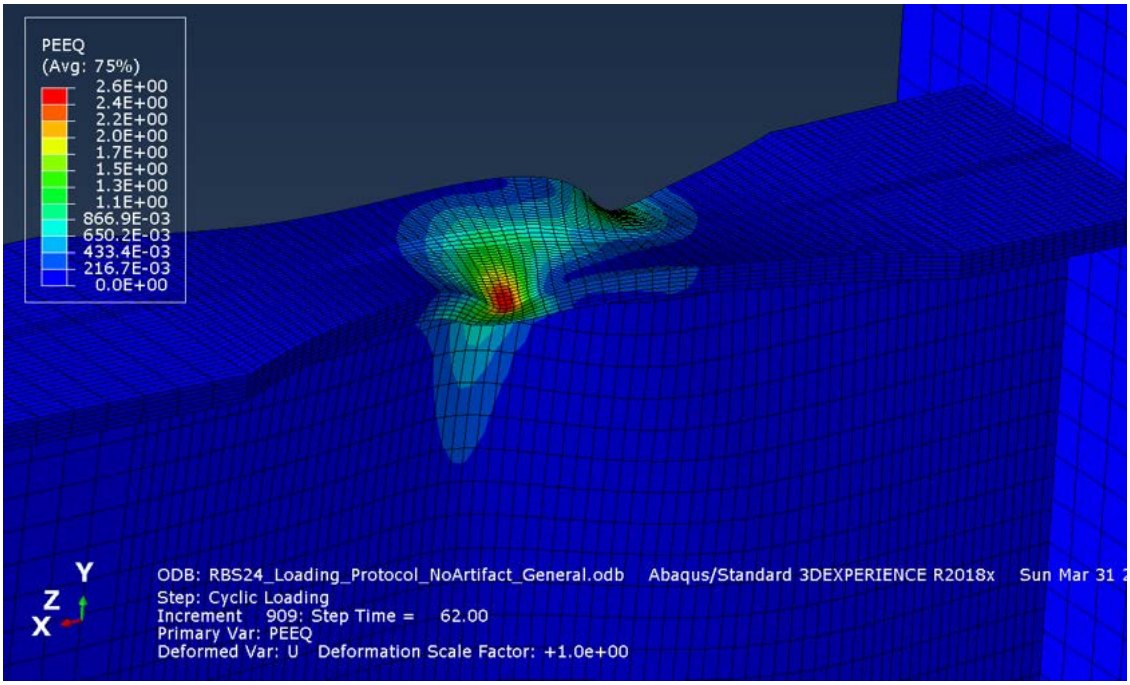

(c) Equivalent plastic strain.

Figure 4.5. Stress, strain, and buckled shape of W24×62 RBS with no artifact.

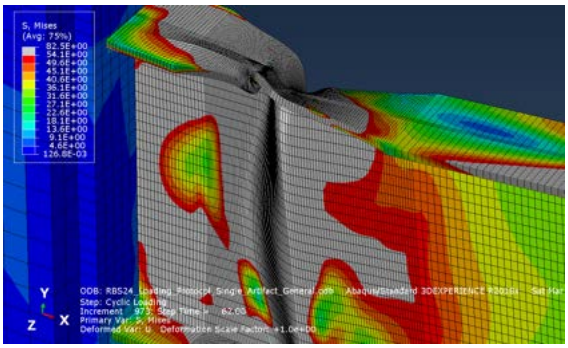

(a) Von Mises stress (yielded material is gray).

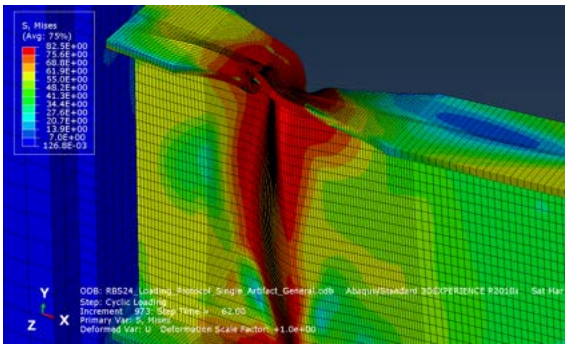

(b) Von Mises stress (gradients beyond yield).

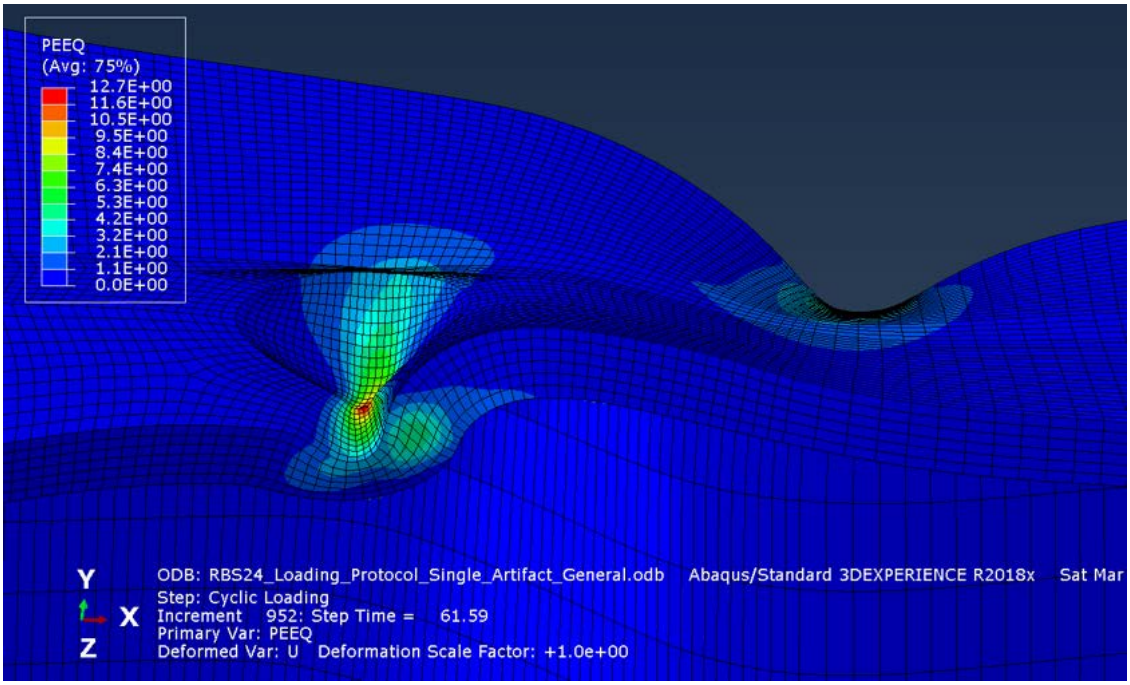

(c) Equivalent plastic strain.

Figure 4.6. Stress, strain, and buckled shape of W24×62 RBS with a single artifact.

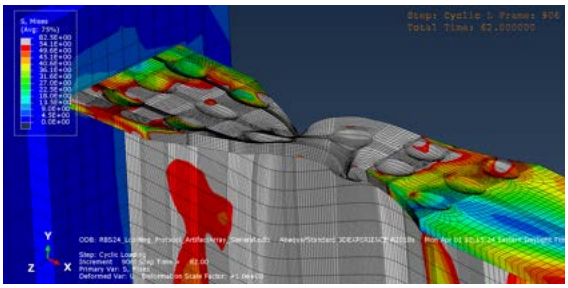

(a) Von Mises stress (yielded material is gray).

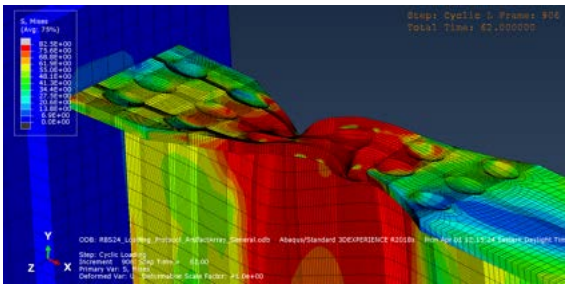

(b) Von Mises stress (gradients beyond yield).

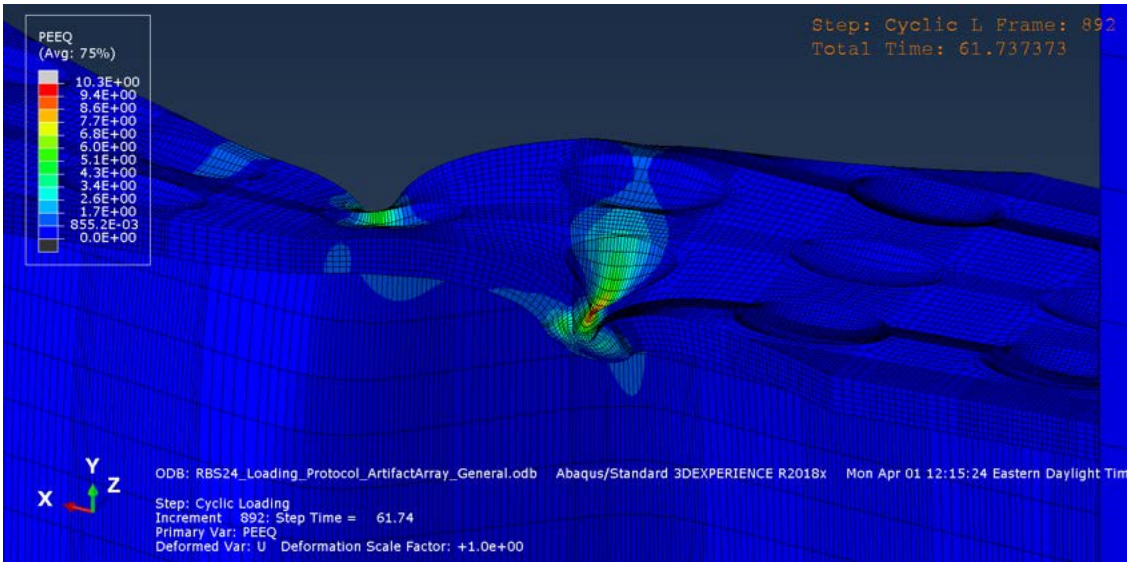

(c) Equivalent plastic strain.

Figure 4.7. Stress, strain, and buckled shape of W24×62 RBS with an array of artifacts.

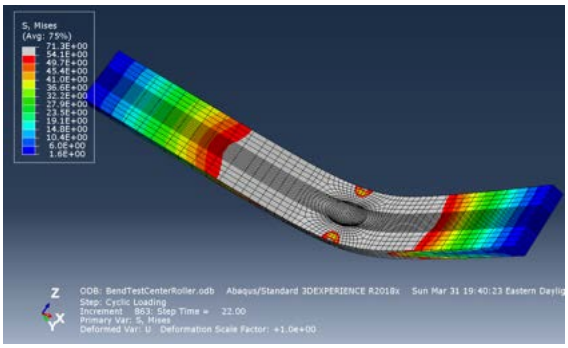

(a) Von Mises stress (yielded material is gray).

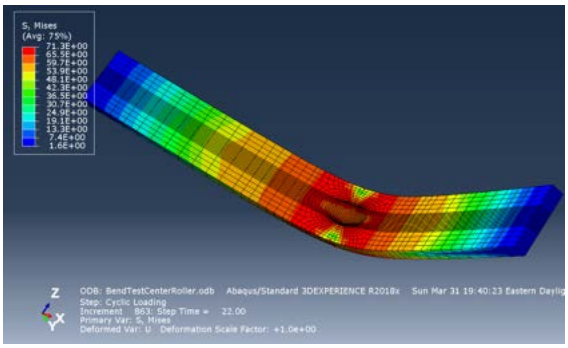

(b) Von Mises stress (gradients beyond yield).

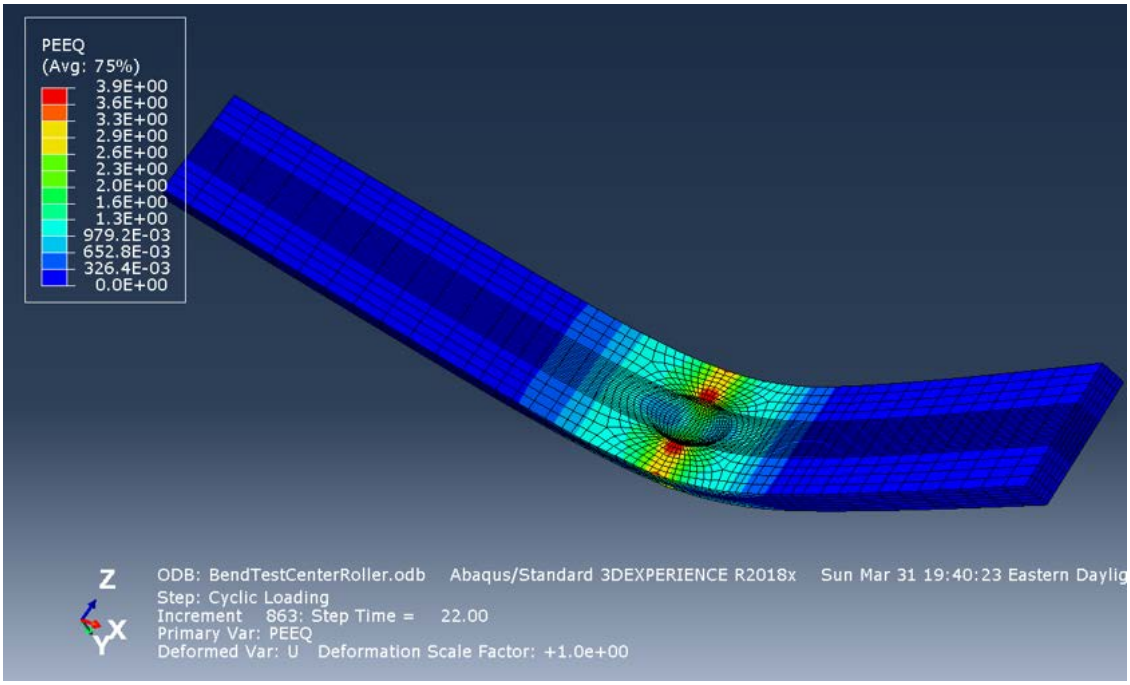

(c) Equivalent plastic strain.

Figure 4.8. Stress, strain, and buckled shape of 0.59 in. bend coupon with a single artifact.

For each of the four models, the principal stress history for the worst-case location (highest equivalent plastic strain) was extracted and used to calculate the stress triaxiality, η, and the Lode angle parameter, ζ, following the method given in Appendix J. Stress triaxiality is the ratio of the mean stress to the von Mises stress, while the Lode angle parameter is related to the J_2 and J_3 invariants by Eq. (J.3). Together, the stress triaxiality and Lode angle parameter are used to represent a stress state in fracture models (Smith et al. 2014). For the full-scale and small-scale FE models, the Lode angle parameter and stress triaxiality were plotted in Figures 4.9a to 4.9d to compare the stress states in the areas with the highest equivalent plastic strain. The additional curve in these plots represents a plane stress condition, given by Eq. (4.1) (Wierzbicki et al. 2005).

$$\zeta = -\frac{27}{2}\eta(\eta^2 - \frac{1}{3}) \tag{4.1}$$

The plots for the two full-scale models with artifacts were similar, which further justifies the conclusion that there is little strain interaction between artifacts. The stress state in the cyclic bend coupon was similar for positive triaxiality but negative triaxiality was absent. In this regard, the cyclic bend test would not be representative of the full-scale tests. This agrees with Toellner (2013), who found that it is difficult to create a small-scale test that replicates the behavior of a local buckle. However, some fracture models have established cutoff values for triaxiality. Smith et al. (2014) proposed a cyclic void growth model that only considered positive triaxiality, while Bao and Wierzbicki (2005) established a cutoff of $\eta = -\frac{1}{3}$. By establishing cutoff values, these models are implying that high magnitude negative triaxiality is less important to damage accumulation. Thus, the lack of negative triaxiality in the cyclic bend coupon model was deemed acceptable.

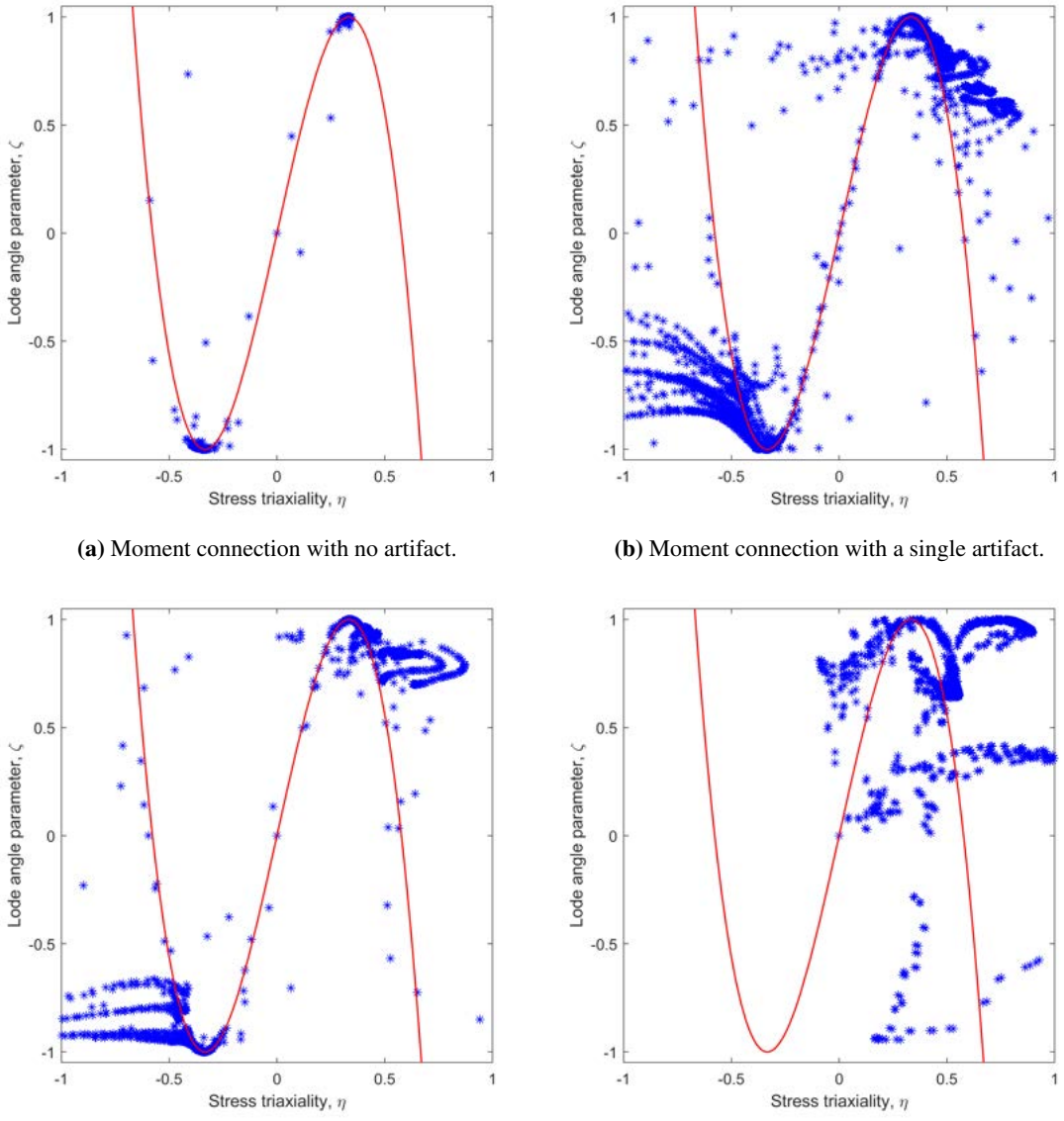

(a) Moment connection with no artifact.

(b) Moment connection with a single artifact.

(c) Moment connection with an artifact array.

(d) Cyclic bend coupon with a single artifact.

Figure 4.9. ζ-η plots for four finite element models.

Chapter 5. Elastic Plastic Fracture Mechanics Analysis

This chapter describes the results of an elastic-plastic fracture mechanics (EPFM) analysis that was done for the W24RBS-0.375N-T59 and W36RBS-0.25N-T94 specimens. This analysis was done after the W36RBS-0.25N-T94 test to predict if the W24×62 specimen with sharp 0.25 in. notches would fracture before satisfying special moment frame (SMF) qualification criteria. These specimens with sharp notches were intended to fail early to provide examples of severe artifacts that cause early fracture and examples of failed specimens when validating the model for predicting fracture of full-scale connections. However, the W36RBS-0.25N-T94 specimen did not fail as intended, so it was important to know if the depth of the notches needed to be increased on the W24×62 beam specimen. If necessary, the depth would be increase from 0.25 in. to 0.375 in., which was the maximum depth possible with the Dremel rotary tool and 426B abrasive cutting wheel.

5.1 EPFM Assumptions

The following assumptions were made when conducting the calculations:

1. The beam flange was modeled as a plate with the same thickness as the beam flange and the same width as the beam flange at the center of the reduced beam section (RBS).
2. One semi-elliptical crack (notch) was applied at the center of each plate.
3. The self-weight of the beam was negligible compared to applied loads (i.e., no initial loading).
4. The applied moment was resolved into an extreme fiber stress that was equivalent to the axial stress in the modeled plate.
5. The bending stress in the plate was zero.
6. The semi-elliptical crack had a sharp tip.
7. Euler-Bernoulli beam theory applies.
8. From the literature, the reference stress was calculated for a rectangular crack that circumscribed the semi-elliptical crack (Goodall and Webster 2001).

Four of these (1, 2, 6, 8) were due to the references used for calculating the stress intensity factor, K_I, and the J integral. The equations for K_I determined by Newman and Raju (1984) were for plates of uniform thickness and width, with a single semi-elliptical crack at the center of the plate. Applied to the RBS specimens with W24×62 and W36×150 beams, these equations ignore the additional thickness over the web and k-area, and the increased flange width away from the center of the RBS. Additionally, the tabulated equations were for cracks with a sharp tip, like fatigue cracks, unlike the ground notches with a wider, blunter tip. Finally, Goodall and Webster (2001) assumed the crack was a rectangle that circumscribed the semi-elliptical crack to simplify the derivation of the reference stress, σ_{ref}.

The other assumptions simplified how the applied load on a fictitious full-scale specimen was resolved into an equivalent axial stress in the plate model for use in the EPFM calculations. It is important to note that the seventh assumption regarding Euler-Bernoulli beam theory would only be valid until the material yielded. At this point, the strain distribution would be nonlinear from the neutral axis to the extreme fiber. However, this was deemed sufficient for elastic and inelastic behavior, given that there were other more conservative assumptions; the objective was to determine if the notch depth should be increased, rather than model the actual behavior.

5.2 EPFM Results

The equations used in the EPFM calculations are given in Appendix K. The reference stress given in the appendix is related to the reference strain using a material model such as a Ramberg-Osgood model, given by Eq. (5.1).

$$\epsilon_{ref} = \frac{\sigma_{ref}}{E} + \left(\frac{\sigma_{ref}}{H}\right)^{\frac{1}{n}} \tag{5.1}$$

The constants H and n were fit to the actual stress-strain behavior of the tensile coupons cut from the W24×62 and W36×150 beam flanges. The constants for the two material models are given in Table 5.1.

Table 5.1. Ramberg-Osgood constants.

Data	H**, ksi**	n
W24×62 top flange	110	0.1515
W36×150 top flange	109	0.1588

After calibrating the material model, a failure assessment diagram (FAD) was created for the sharp 0.25 in. and 0.375 in. notches by plotting the load ratio, L_r, against the K ratio, K_r. These diagrams are shown in Figure 5.1, where the plotted assessment point, P_a, represents the critical load when fracture initiation and propagation occurs. On these plots, the area within the curve represents a safe region where fractures do not propagate, while the area outside the curve represents an unsafe area.

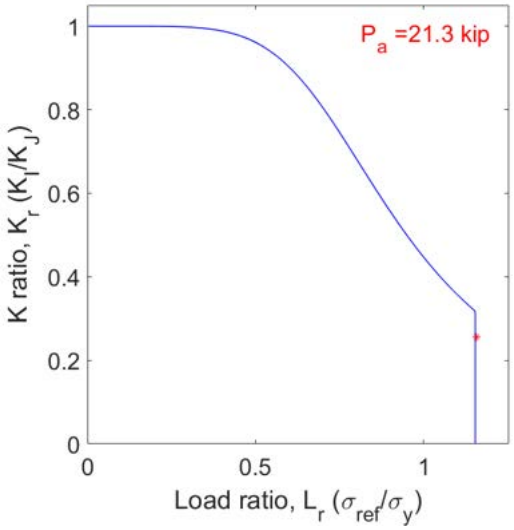

(a) W24×62 flange with a sharp 0.25 in. notch.

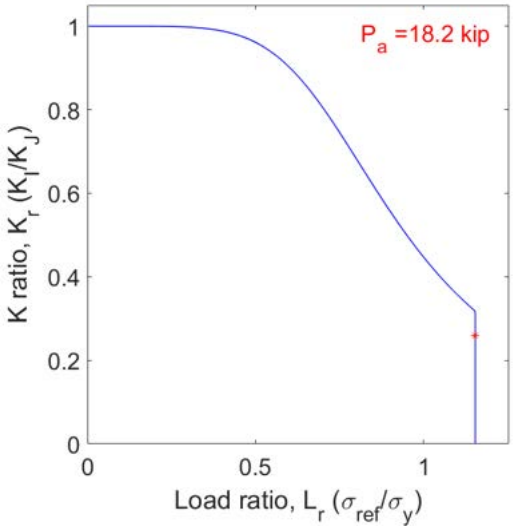

(b) W24×62 flange with a sharp 0.375 in. notch.

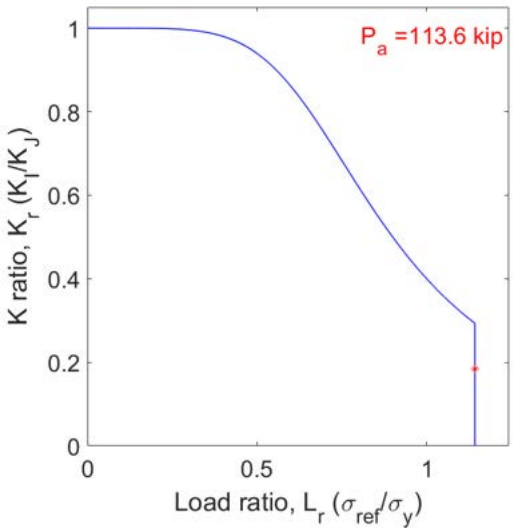

(c) W36×150 flange with a sharp 0.25 in. notch.

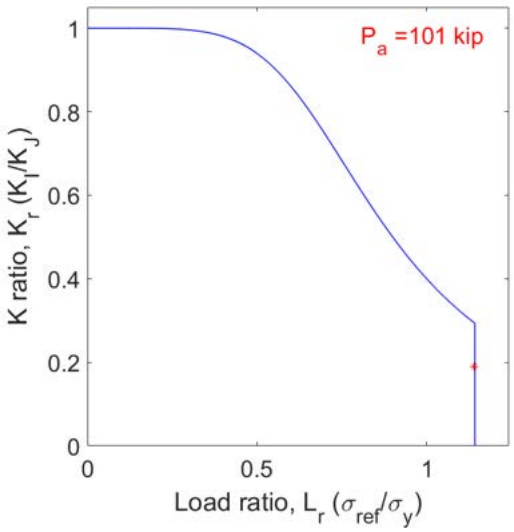

(d) W36×150 flange with a sharp 0.375 in. notch.

Figure 5.1. FADs of beam flange models with 0.25 in. and 0.375 in. notches.

Increasing the depth of the notch reduced the critical load by 14.5%, from 21.3 kips to 18.2 kips for the W24×62 beam flange model. RBS specimens with W24×62 beams experienced loads of similar magnitudes in the 0.75 % and 1% story drift cycles, but both loads are well below the applied load that would cause the extreme fibers to yield, 39.1 kips. This implies that the full-scale specimens would begin to fracture before reaching SMF qualification criteria, as intended. However, all the assumptions made were conservative, meaning the actual critical load was likely larger. Thus, it was decided to increase the depth of the notch to 0.375 in. to increase the likelihood of the W24×62 specimen not satisfying SMF qualification criteria, unlike the W36RBS-0.25N-T94 specimen.

Chapter 6. Experimental Results

This chapter presents the results of the full-scale and small-scale testing, as well as material testing. The results of the full-scale tests include the moment-rotation response, buckling and fracture propagation, fracture surface analysis, and story drift decomposition. The results of the small-scale tests include the fracture initiation and fracture propagation for each artifact. The results of the material testing include yield stress, ultimate strength, elongation, and Charpy V-notch (CVN) toughness of materials used in the full-scale and small-scale tests. This chapter also includes a discussion of subsurface-origin fatigue fractures seen on the full-scale and small-scale specimens with 0.25 in. notches repaired by welding.

Sensor plots for the large scale tests are provided in Appendices L to Q. Force-displacement plots for the small-scale tests are provided in Appendix R.

6.1 Full-Scale Moment Connection Tests

6.1.1 Moment-rotation response

Five of the six specimens met one of the special moment frame (SMF) qualification criteria, as the flexural resistance at the face of the column was at least 80% of the nominal plastic flexural strength through the first cycle of 4% story drift. The flexural resistances at the peaks of the two 4% story drift cycles are shown in Table 6.1, and the moment-rotation response plots are shown in Figures 6.1a to 6.1f. In these plots, the normalized moment, M at the face of the column was calculated using Eq. (6.1),

$$M = \frac{PL_B}{M_p} \tag{6.1}$$

where: P = actuator load

L_B = distance from the actuator centerline to the face of the column, 15.24 ft.

M_p = nominal plastic flexural strength, 638 or 2421 kip*ft.

The applied story drift was calculated using Eq. (3.1). The W24RBS-0.375N-T59 specimen did not meet this SMF qualification criterion because a ductile fracture formed before the 4% story drift cycles, which caused the flexural resistance to drop below 80% of the nominal plastic flexural strength.

Table 6.1. Percent of nominal plastic flexural strength during 4% story drift cycles.

Specimen Name	1st Negative Peak	1st Positive Peak	2nd Negative Peak	2nd Positive Peak
W24RBS-0.125NGT-T59	-79.3[1]	82.2	-74.4	72.7
W36RBS-0.125NGT-T94	-102	98.4	-96.5	91.12
W24RBS-0.25NGTW-T59	-91.2	90.7	-85.6	85.7
W36RBS-0.25NGTW-T94	-105	91.5	-92.7	81.1
W24RBS-0.375N-T59	-48.4[2]	41.9[2]	N/A	N/A
W36RS-0.25N-T94	-104	93.9	-89	57.2

[1] Deemed to be close enough to SMF qualification. Loss of strength was associated with local buckling, rather than fractures at the artifacts.

[2] Failed SMF qualification.

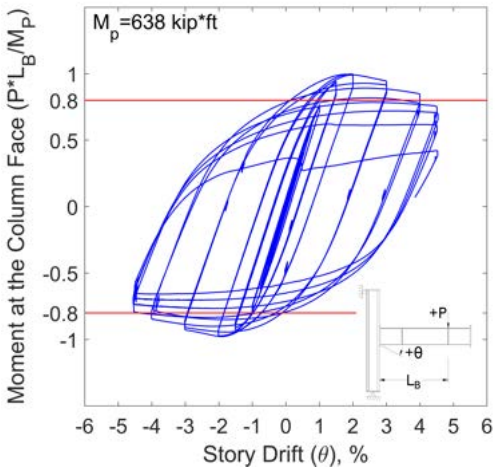

(a) W24RBS-0.125NGT-T59.

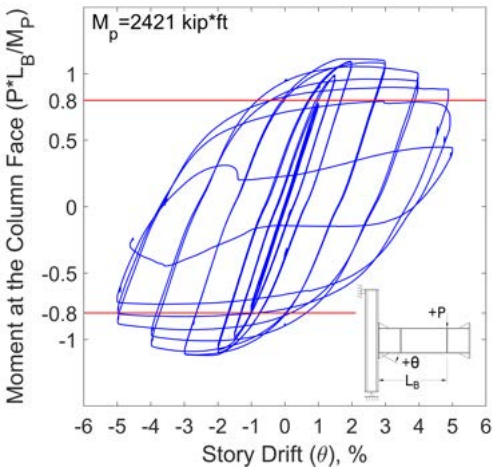

(b) W36RBS-0.125NGT-T94.

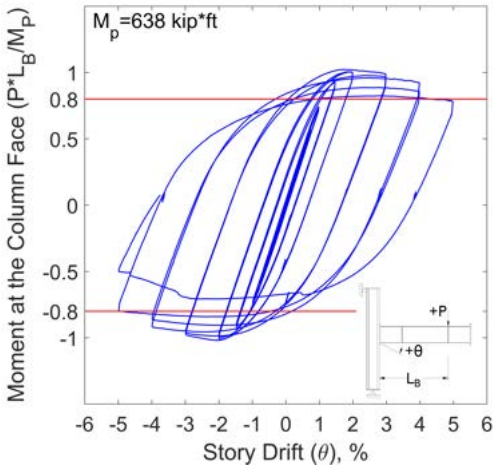

(c) W24RBS-0.25NGTW-T59.

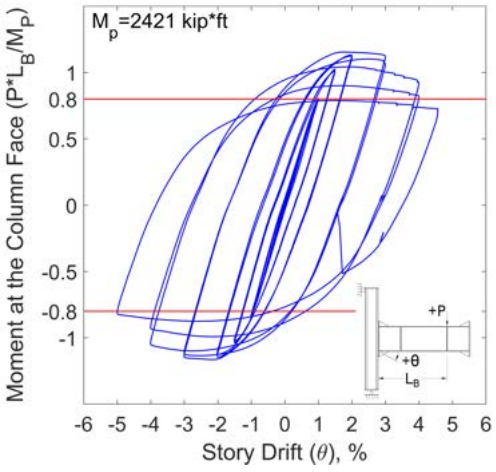

(d) W36RBS-0.25NGTW-T94.

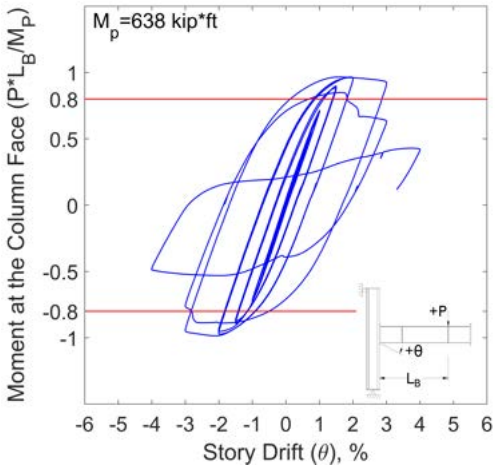

(e) W24RBS-0.375N-T59.

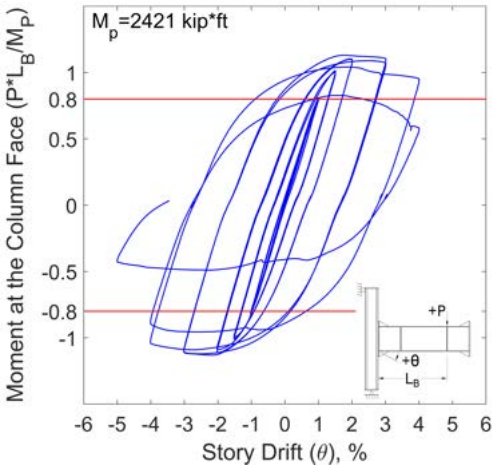

(f) W36RBS-0.25N-T94.

Figure 6.1. Moment-rotation response plots for full-scale specimens.

6.1.2 Buckling and fracture propagation

W24RBS-0.125NGT-T59

The conditions of the specimen before testing and after a ductile tear of the top flange are shown in Figure 6.2. Top flange local buckling started in the first 4% story drift cycle and increased in the following cycles. Fractures were first observed at the flange tip at a local buckle in the second cycle of 4% story drift. In the subsequent cycle, this fracture turned into a ductile tear approximately 1.5 in. long, shown in Figure 6.3a. This fracture was 1 in. from the center of the RBS but did not pass through an artifact. During the fourth cycle of 4.5% story drift, this tear spread across the entire flange and about 3 in. into the web, shown in Figure 6.3.

(a) Undeformed condition. **(b)** Deformed condition.

Figure 6.2. Undeformed and deformed conditions of W24RBS-0.125NGT-T59.

(a) Fracture initiation. **(b)** Final fracture.

Figure 6.3. Fracture propagation of W24RBS-0.125NGT-T59.

After testing was complete, a ductile tear approximately 1 in. long was found in the web at the vertical edge of the "N" in the "NYS-USA" rolling mill stamp, shown in Figure 6.4. The stamp was located in the protected zone, approximately 1 in. from the center of the reduced beam section (RBS) and 4.5 in. below the bottom of the top flange in an area of out-of-plane web buckling. It is unknown when the fracture initiated.

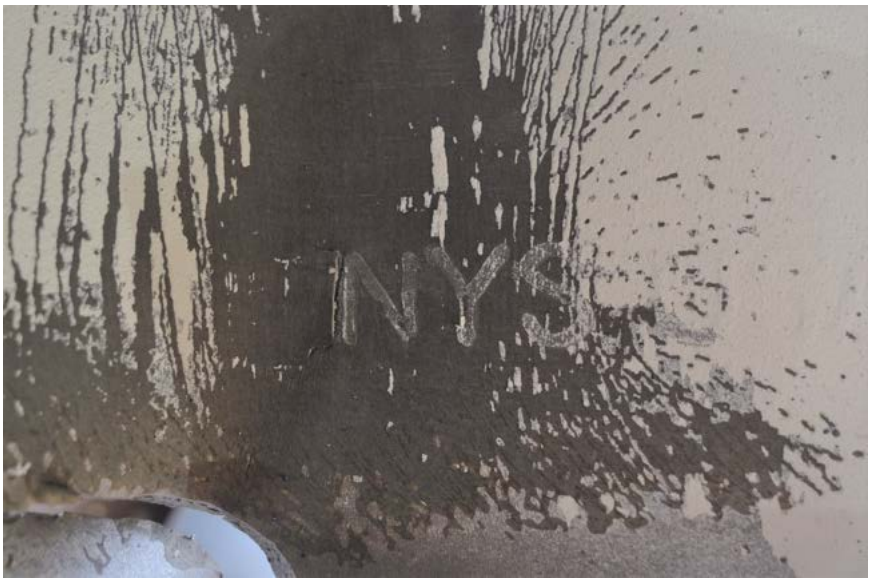

Figure 6.4. Web fracture at a rolling mill stamp on W24RBS-0.125NGT-T59.

The top flange fracture surface is shown in Figure 6.5. Fractures initiated at the flange tip in a local buckle, but the fracture surface was smoothed when the surfaces rubbed together in the subsequent cycles. The web fracture has a similarly smooth surface but is duller because it did not rub against the other side during the test. The region labeled ductile overload indicates where plastic deformation preceded final fracture. There is also a small shear lip along the web that formed when the fracture reached the surface of the web.

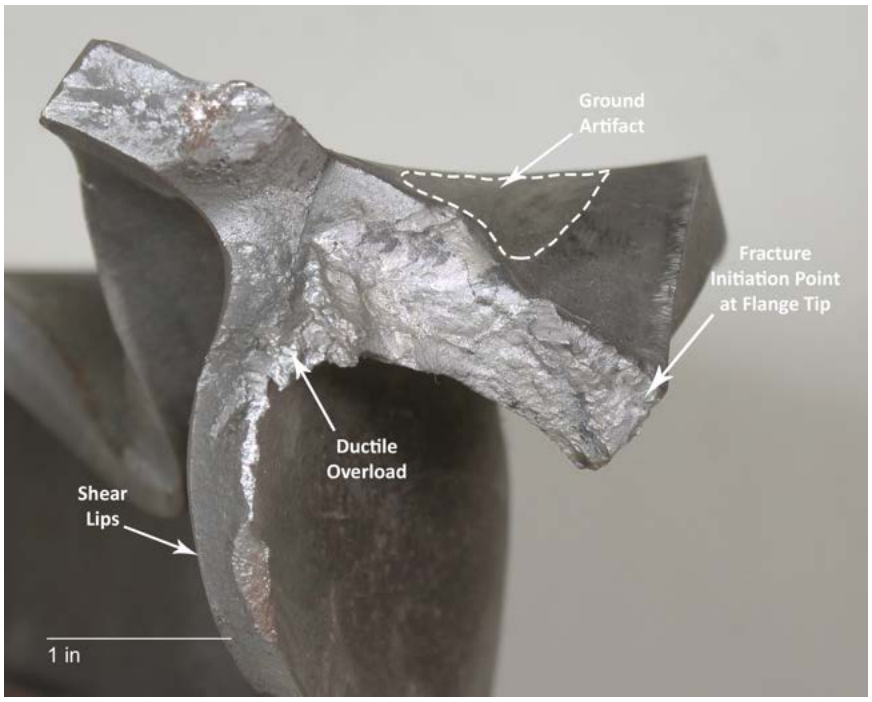

Figure 6.5. W24RBS-0.125NGT-T59 top flange fracture looking towards the end-plate.

W36RBS-0.125NGT-T94

The conditions of the specimen before and after testing are shown in Figure 6.6. Local buckling of both flanges began in the first cycle of 3% story drift and increased in the following cycles. Fractures initiated in artifacts at the center of the RBS on both flanges in the second cycle of 4% story drift, shown in Figure 6.7, and grew in the first cycle of 5% story drift. There was also local buckling in this area. In the second cycle of 5% story drift, a ductile fracture opened up on the bottom flange at the center of the RBS, at the same location as fracture initiation. A complete ductile fracture of the top flange and partial fracture of the web occurred in the third cycle of 5% story drift, while a ductile fracture of the bottom flange and partial fracture of the web occurred in the fourth cycle of 5% story drift. The complete fracture of both flanges is shown in Figure 6.8. The top flange fracture propagated 6.5 in. into the web while the bottom flange fracture only propagated 3 in. into the web.

(a) Undeformed condition. **(b)** Deformed condition.

Figure 6.6. Undeformed and deformed conditions of W36RBS-0.125NGT-T94.

(a) Top flange. **(b)** Bottom flange.

Figure 6.7. Fracture initiation of W36RBS-0.125NGT-T94.

(a) Top flange. **(b)** Bottom flange.

Figure 6.8. Final fracture of W36RBS-0.125NGT-T94.

The top and bottom flange fracture surfaces are shown in Figure 6.9 and Figure 6.10, respectively. During testing, fractures initiated at the edges of the ground artifacts at the center of the RBS. The smooth, shiny areas in Figure 6.9 are areas where the fracture surfaces rubbed together in the cycles after fracture.

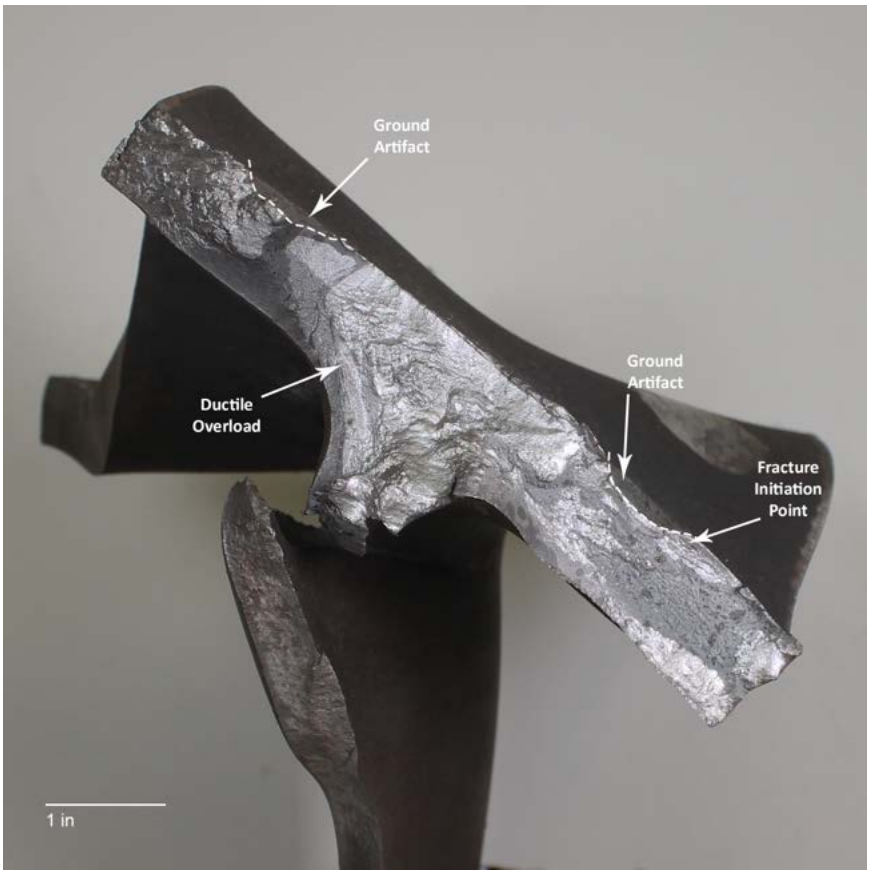

Figure 6.9. W36RBS-0.125NGT-T94 top flange fracture looking towards the end-plate.

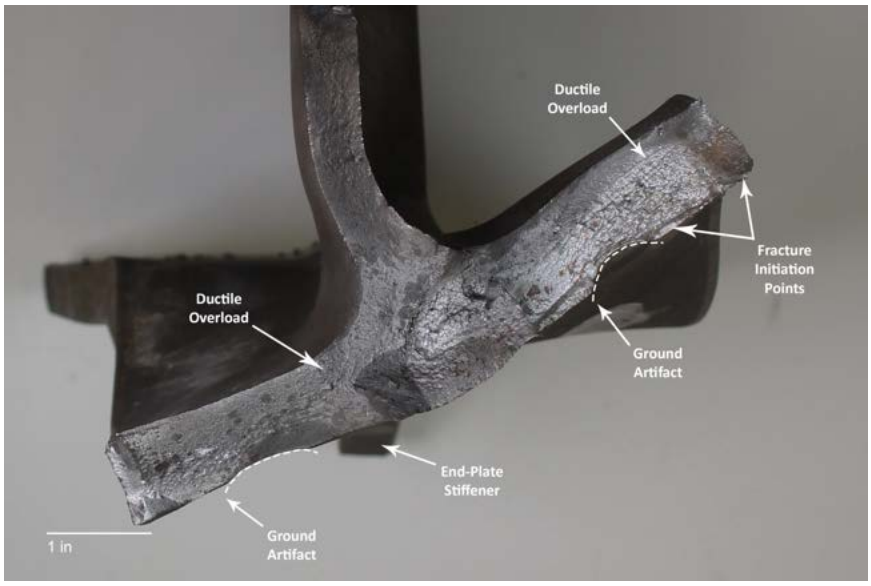

Figure 6.10. W36RBS-0.125NGT-T94 bottom flange fracture looking towards the end-plate.

W24RBS-0.25NGTW-T59

Four additional surface cracks were found after the welds were ground flush. More information about the size and location of the cracks is given in Appendix S, but they were ground out and repaired using the same weld procedure described in Chapter 3 and Appendix C.

The conditions of the specimen before testing and after a ductile fracture of the bottom flange are shown in Figure 6.11. Local buckling of both flanges started in the first 3% story drift cycle. In the second cycle of 3% story drift, fractures initiated on the top flange. Fractures initiated on the bottom flange in the following cycle, in the weld metal of the artifacts on the bottom flange near the end of the RBS cut. These fractures were 0.25 to 0.5 in. long and are shown in Figure 6.12a. They were also similar to the folded steel defects that were observed in the previous small-scale tests. Fractures also formed on the bottom flange between the artifact and the flange tip at the center of the RBS, shown in Figure 6.12b. The bottom flange fractures at the center of the RBS grew slowly in the 4% story drift cycles until a ductile tear spread almost entirely across the flange and 2.5 in. into the web. This is shown in Figure 6.13.

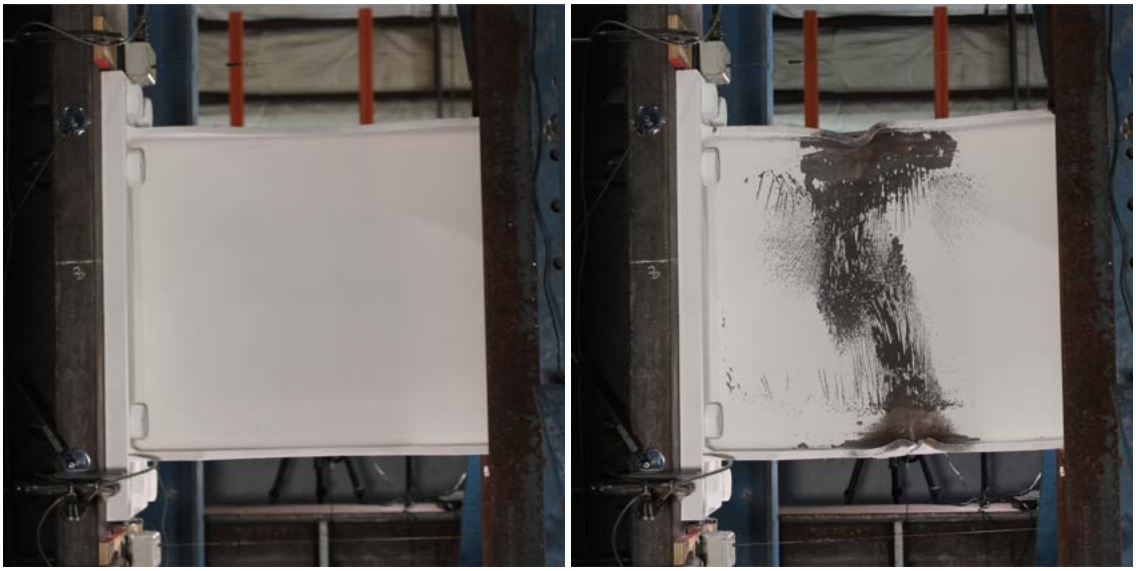

(a) Undeformed condition. **(b)** Deformed condition.

Figure 6.11. Undeformed and deformed conditions of W24RBS-0.25NGTW-T59.

(a) Weld metal. **(b)** Base metal.

Figure 6.12. Fracture initiation of W24RBS-0.25NGTW-T59.

Figure 6.13. Bottom flange fracture of W24RBS-0.25NGTW-T59.

The bottom flange fracture surface is shown in Figure 6.14. During the test, fractures initiated in the base metal on the flange surface, between a welded artifact and the flange tip. These fractures had a smoother finish because the two sides rubbed together after fracture initiation. A small circular fracture was also found in the weld metal. This fracture is similar to a subsurface-origin fatigue fracture because it has a small, circular appearance distinct from the surrounding material. Other fractures like this were found in the welded small-scale specimens, discussed in Section 6.2.2.

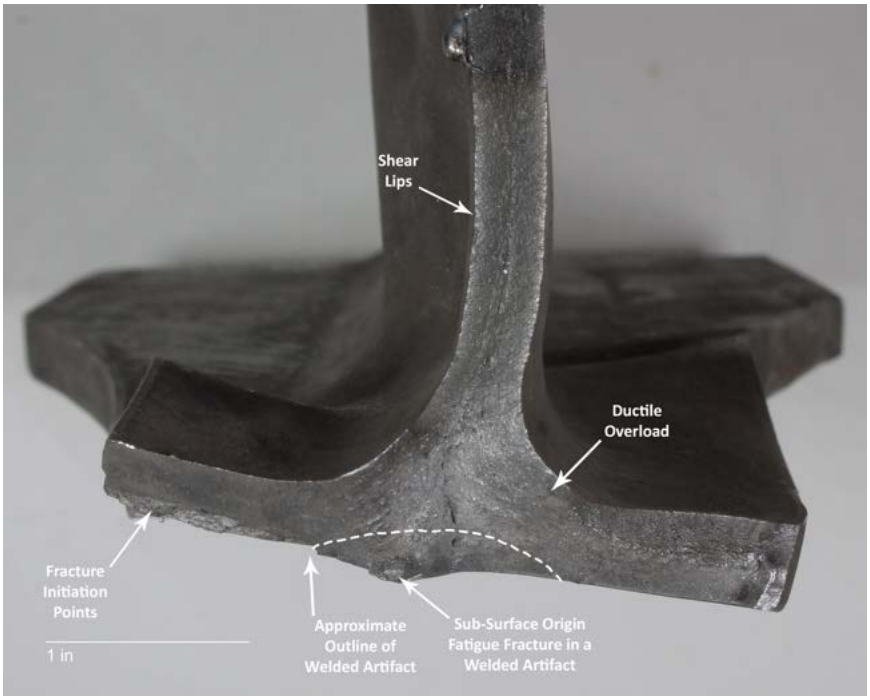

Figure 6.14. W24RBS-0.25NGTW-T59 bottom flange fracture looking towards the end-plate.

W36RBS-0.25NGTW-T94

Numerous defects were found after the weld runoff tabs were removed during the repair process. These defects were repaired following the weld procedure described in Chapter 3 and Appendix C; more information about the defects is available in Appendix S.

The conditions of the specimen before testing and after a brittle fracture of the bottom flange are shown in Figure 6.15. Flange local buckling began in the 3% story drift cycles, while the first fractures were observed in artifacts on the bottom flange at the end of the first 4% story drift cycle. The fractures were seen in the artifacts at the center of the RBS and in the artifacts at the end of the RBS cut closest to the stiffener, shown in Figure 6.16. These artifacts were also near local buckles. An additional fracture was found at the toe of the top flange stiffener, but no fractures were seen in the artifacts on the top flange. The bottom flange fractures grew in the following cycles until there was a sudden brittle fracture of the bottom flange after the first 5% story drift cycle. The flange fractured at two places simultaneously, shown in Figure 6.17, which was at the same artifacts and local buckles where fractures were first observed. These fractures propagated 7.5 in. across the flange and 3 in. into the web. They grew slightly in the second cycle of 5% story drift but did not propagate across the entire flange.

(a) Undeformed condition. **(b)** Deformed condition.

Figure 6.15. Undeformed and deformed conditions of W36RBS-0.25NGTW-T94.

(a) Center of the RBS. **(b)** End of the RBS, near the stiffener.

Figure 6.16. Bottom flange fractures at the end of the 3% story drift cycles on W36RBS-0.25NGTW-T94.

Figure 6.17. Bottom flange fractures on W36RBS-0.25NGTW-T94.

The fractures surfaces of both bottom flange fractures are shown in Figure 6.18 and Figure 6.19. During the test, fractures were first observed in the welded artifacts. In Figure 6.18 and Figure 6.19, these are smooth, relatively dull areas where the surfaces rubbed against one another in subsequent cycles before the brittle fracture initiated. The chevron marks on both fracture surfaces indicated that the brittle overload originated at the base of a welded artifact and then propagated rapidly into the web and the opposite side of the flange. The brittle fracture also appeared to propagate around the welded artifact at the toe of the stiffener in Figure 6.18. Shear lips were visible around the edge of the surface where the fracture was more ductile. Testing continued after the brittle fractures, resulting in the ductile overload of the web.

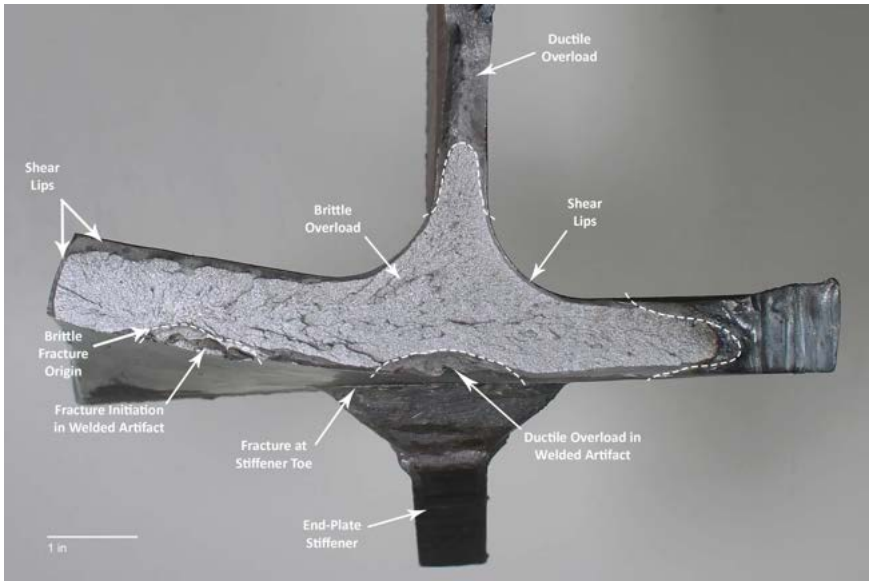

Figure 6.18. Bottom flange fracture closest to the end-plate, looking towards the end-plate.

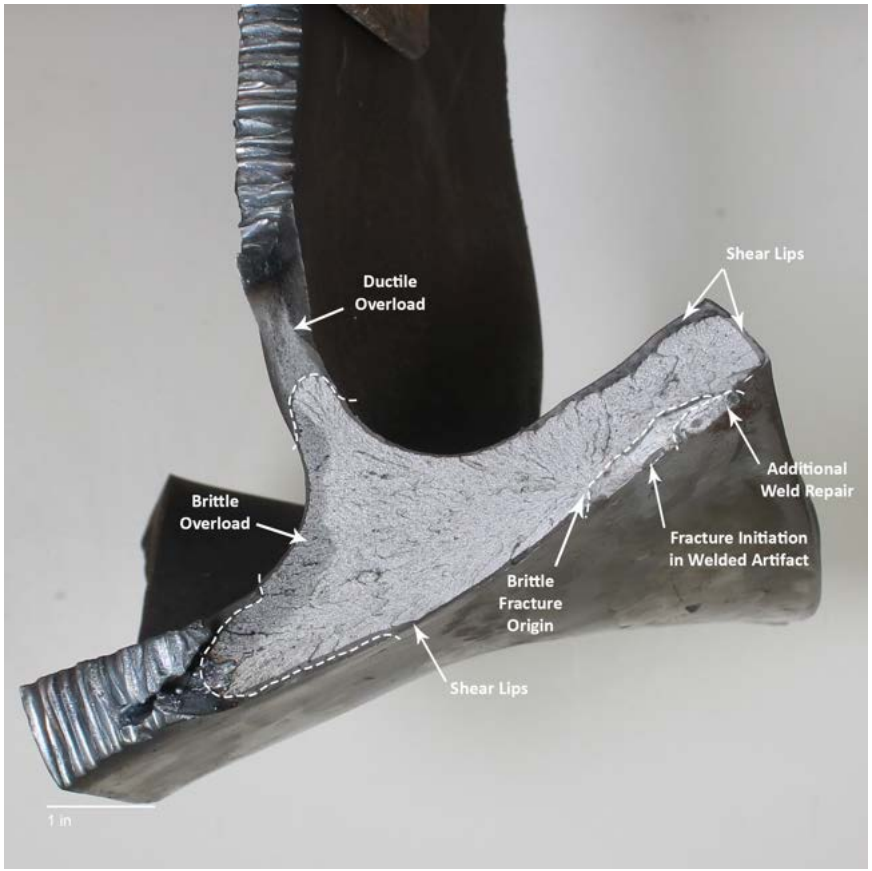

Figure 6.19. Bottom flange fracture farthest from the end-plate, looking towards the end-plate.

W24RBS-0.375N-T59

The conditions of the specimen before testing and after ductile fractures of the top and bottom flanges are shown in Figure 6.20. Flange buckling began in the first 3% story drift cycle, at which point the notches on the bottom flange closed up. Fractures also initiated in the bottom of notches on the top flange at the end of 1.5% story drift cycles, shown in Figure 6.21. In the second cycle of 3% story drift, a ductile fracture propagated through two notches on the bottom flange, while an additional ductile fracture propagated through two notches on the top flange. In the first 4% story drift cycle, the bottom flange fracture propagated across the remainder of the flange. Both flange fractures grew into the web: 2.75 in. at the top flange fracture and 5 in. at the bottom flange fracture. The final fractures of both flanges are shown in Figure 6.22.

(a) Undeformed. **(b)** Deformed.

Figure 6.20. Undeformed and deformed conditions of W24RBS-0.375N-T59.

Figure 6.21. Fracture initiation in the bottom of a notch.

(a) Bottom flange. **(b)** Top flange.

Figure 6.22. Final fracture after first 4% story drift cycle.

The fracture surfaces of the top and bottom flange fractures are shown in Figure 6.23 and Figure 6.24, respectively. During the test, fractures initiated in the bottoms of the notches and grew rapidly in the following cycles. This meant only one distinct striation was visible at the bottom flange notches. The ductile overload region propagated from the notches and into the web on both the top and bottom flanges.

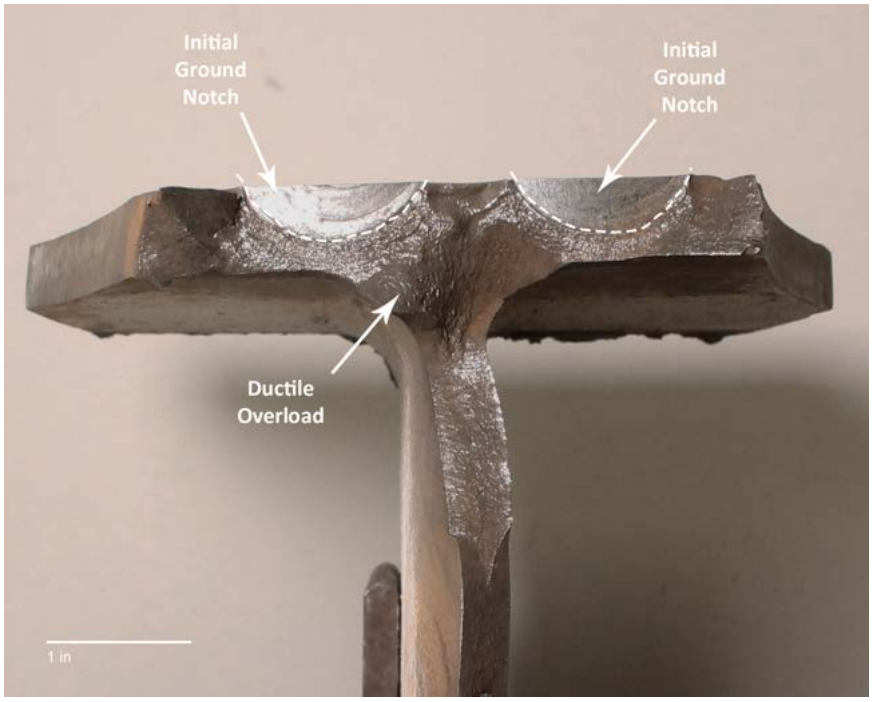

Figure 6.23. W24RBS-0.375N-T59 top flange fracture looking towards the end-plate.

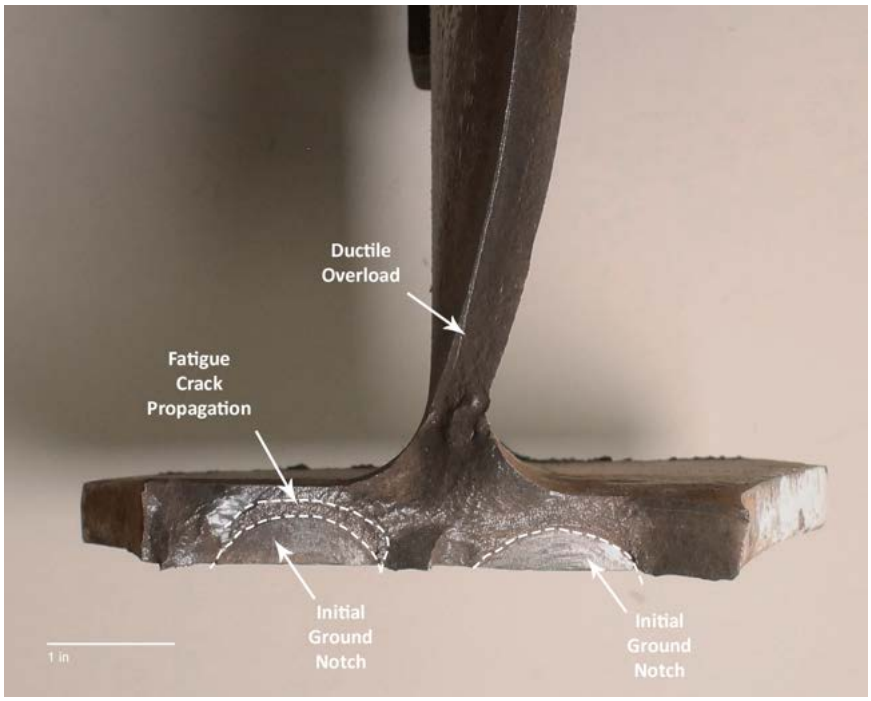

Figure 6.24. W24RBS-0.375N-T59 bottom flange fracture looking towards the end-plate.

W36RBS-0.25N-T94

The conditions of the specimen before testing and after ductile fractures of the top and bottom flanges are shown in Figure 6.25. Flange buckling began in the first cycle of 3% story drift, which caused some notches near the local buckles to close up, shown in Figure 6.26. At the end of the 3% story drift cycles, ductile fractures were found in the bottom of some notches on the top flange, shown in Figure 6.27. In the first cycle of 4% story drift, a ductile tear initiated at one of these fractures located at the inside of a local buckle and propagated through the flange. In the following cycle, a similar ductile tear formed on the bottom flange at a notch located on the inside of a local buckle. Both fractures, shown in Figure 6.28, were approximately 3 in. long and spread to the flange tip and the edge of the web. In the same cycle, the ductile tear on the top flange spread across the entire flange and 5 in. into the web but did not pass through another notch. In the first cycle of 5% story drift, the bottom flange fracture propagated past the web while a third ductile tear formed at the adjacent bottom flange notch. The two bottom flange fractures coalesced and then spread to the flange tip and 7.5 in. into the web before the test was stopped. The final fractures on the top and bottom flanges are shown in Figure 6.29.

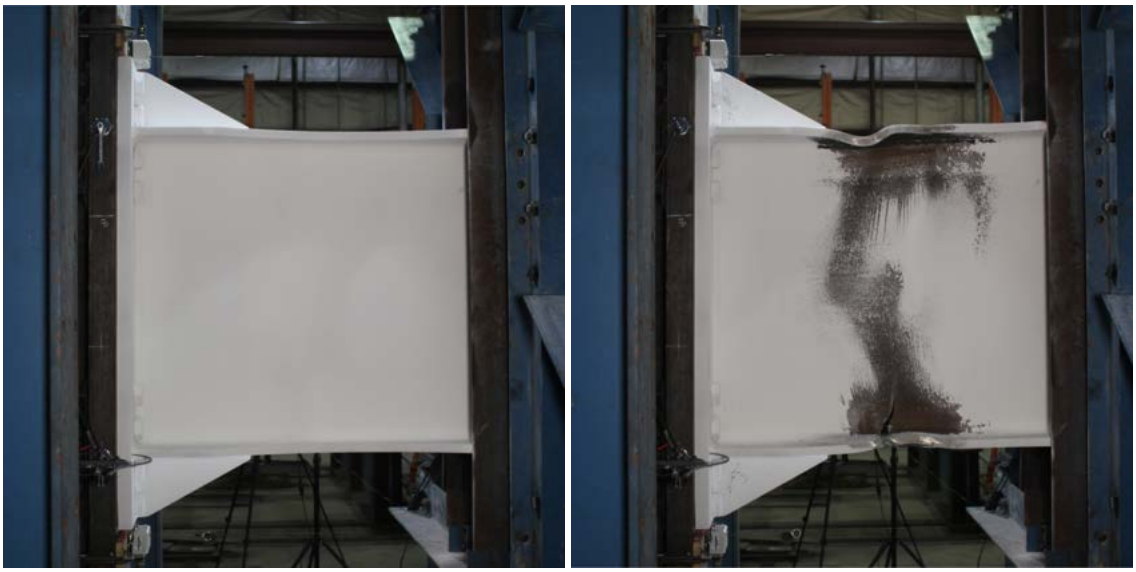

(a) Undeformed. **(b)** Deformed.

Figure 6.25. Undeformed and deformed conditions of W36RBS-0.25N-T94.

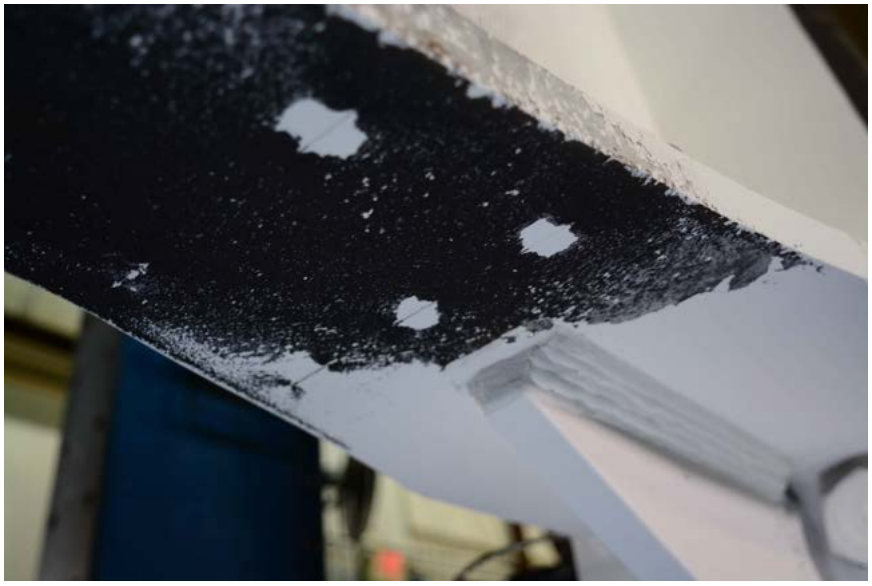

Figure 6.26. Notches closed up due to local buckling..

Figure 6.27. Fracture initiation in the bottom of notches on W36RBS-0.25N-T94.

(a) Top flange fracture. **(b)** Bottom flange fracture.

Figure 6.28. Fractures initiating at notches on W36RBS-0.25N-T94.

(a) Top flange. **(b)** Bottom flange.

Figure 6.29. Final fractures of the flanges and web on W36RBS-0.25N-T94.

The fracture surfaces of the top and bottom flange fractures are shown in Figure 6.30 and Figure 6.31, respectively. During the test, fractures were first observed at the bottom of the ground notches. These initial fractures show up as distinct striations at the bottom of the notch on the fracture surfaces, indicating fractures grew over multiple cycles. The ductile overload regions surrounding the ground notches have a smooth texture because the two sides of the fractures rubbed together in the cycles after the fractures formed. Only small shear lips formed in the k-area of Figure 6.30 and along the web in Figure 6.31

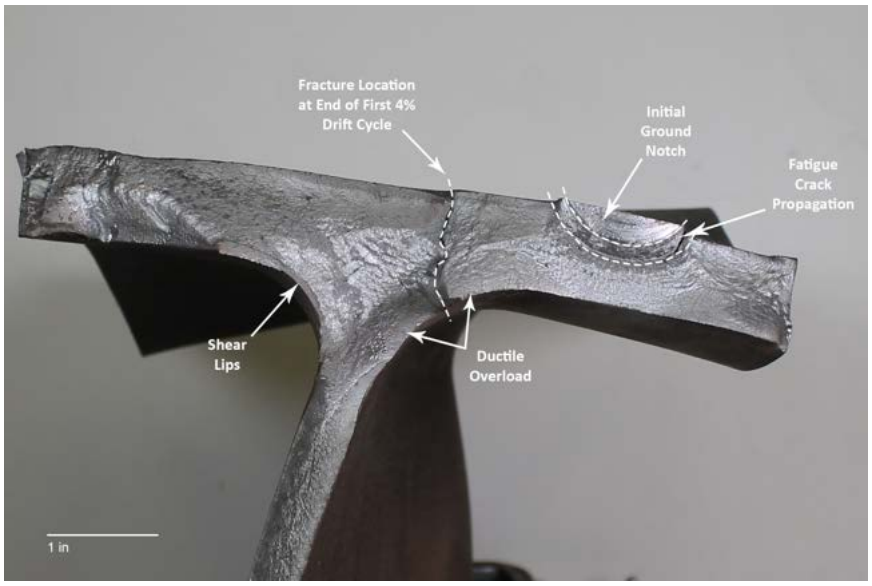

Figure 6.30. W36RBS-0.25N-T94 top flange fracture looking towards the end-plate.

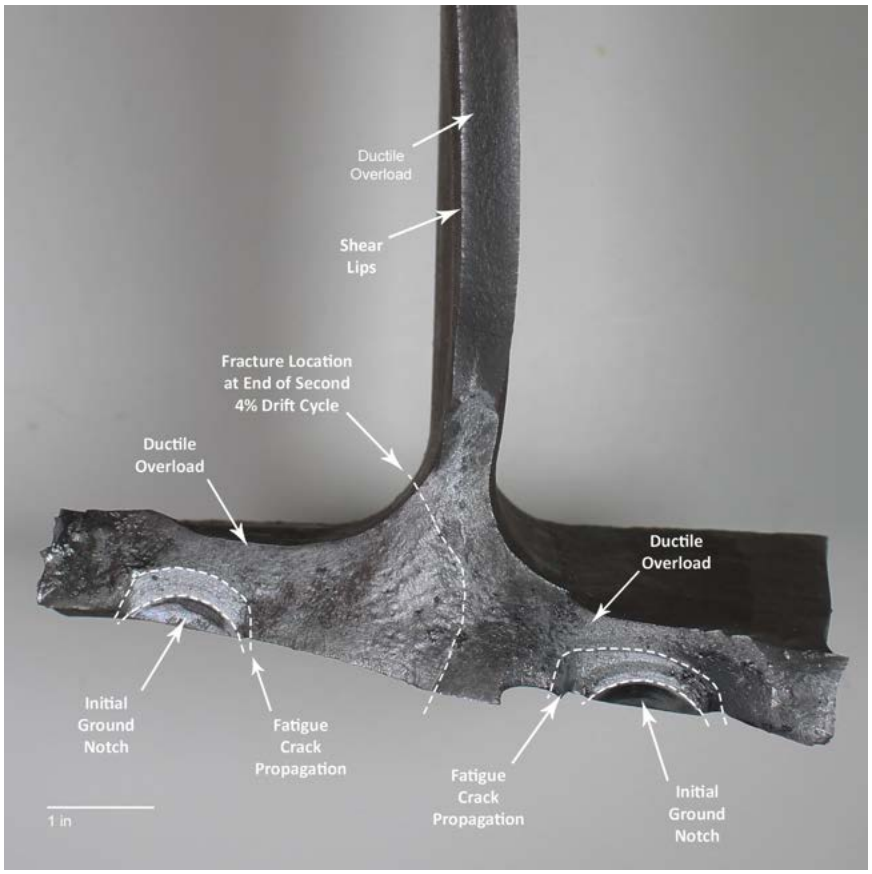

Figure 6.31. W36RBS-0.25N-T94 bottom flange fracture looking towards the end-plate.

6.1.3 Story Drift Decomposition

As mentioned in Section 3.1.4, one SMF qualification criterion is that the test specimen must develop inelastic rotations that are within 25% of the anticipated inelastic rotation in the prototype connection (AISC 2016b). Since the full-scale specimens had both an RBS and an end-plate, it was necessary to determine how much of the total story drift was due to plastic hinge rotation and ensure it was not reduced by the end-plate connection. The applied story drift was split into components using the data measured by the displacement sensors described in Section 3.1.4 and the equations given in Appendix E. In an idealized moment connection subjected to 4% story drift, it might be anticipated that elastic deformations account for 1% story drift (25% of the applied drift), with the remainder due to plastic hinge rotation. Thus, the target plastic hinge rotation was at least 75% of the applied story drift in the qualification cycle.

As shown in Table 6.2, plastic hinge rotation contributed to 84-94% of the applied story drift for all specimens. This is also shown graphically in Figures 6.32a to 6.32f, where a cumulative story drift of 1.11 radians corresponds to the first negative peak of the first 4% story drift cycle.

Table 6.2. Percentage of applied story drift due to plastic hinge rotation.

Specimen Name	1st Negative Peak	1st Positive Peak	2nd Negative Peak	2nd Positive Peak
W24RBS-0.125NGT-T59	88.9	86.9	89.1	89.2
W36RBS-0.125NGT-T94	84.4	87.6	85.4	88.3
W24RBS-0.25NGTW-T59	86.1	83.7	87.2	85
W36RBS-0.25NGTW-T94	86.1	88.4	86.6	89.6
W24RBS-0.375N-T59	92.4	94.0	N/A	N/A
W36RBS-0.25N-T94	84.7	88.5	87.8	93.4

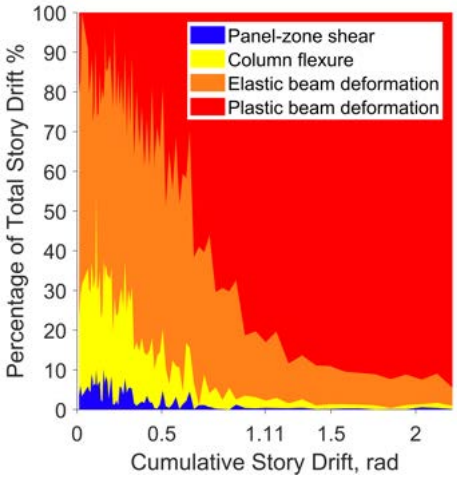

(a) W24RBS-0.125NGT-T59.

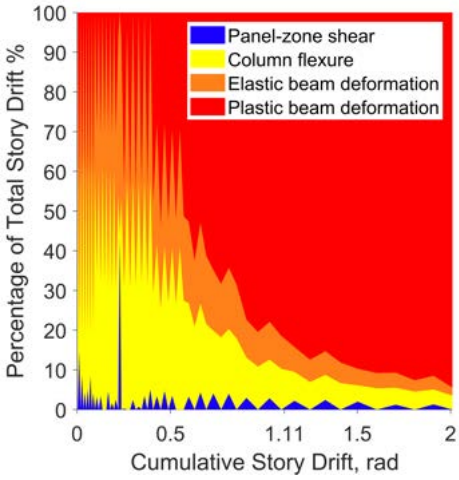

(b) W36RBS-0.125NGT-T94.

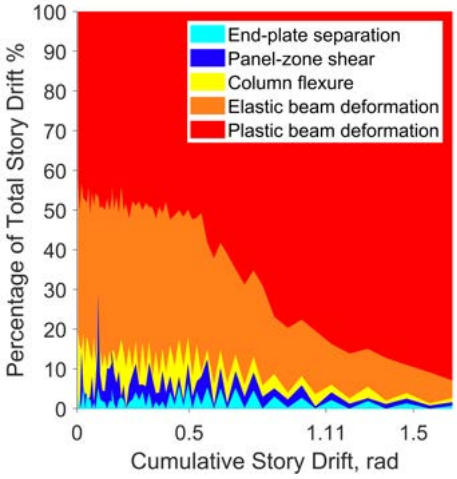

(c) W24RBS-0.25NGTW-T59.

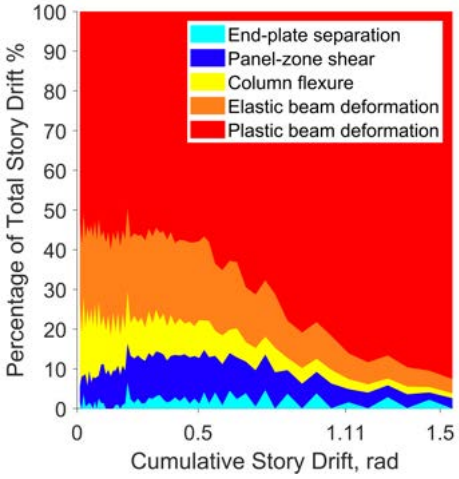

(d) W36RBS-0.25NGTW-T94.

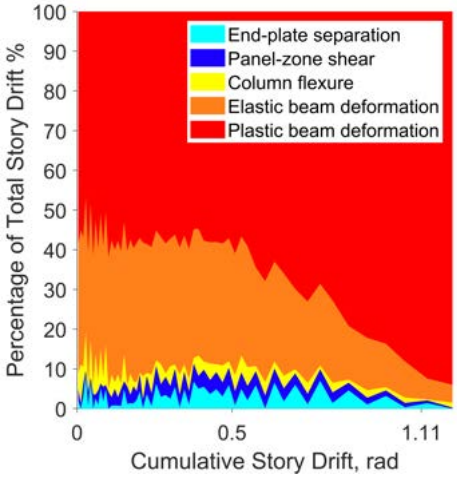

(e) W24RBS-0.375N-T59.

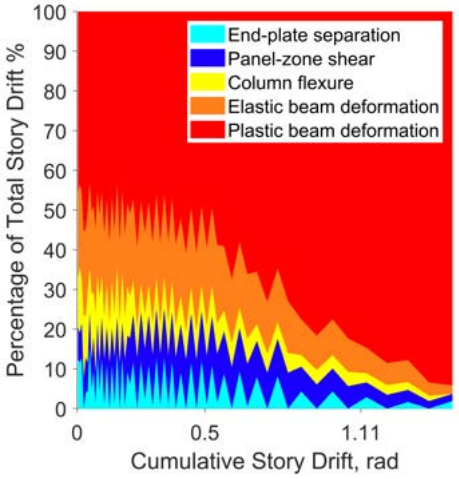

(f) W36RBS-0.25N-T94.

Figure 6.32. Story drift component area plots for full-scale tests.

6.2 Small-Scale Cyclic Bend Tests

Thirty-four bend tests were conducted to establish the low-cycle fatigue behavior of flat bar coupons with 0.125 in. notches repaired by grinding, 0.25 in. notches repaired by welding, and sharp 0.25 in. and 0.375 in. notches. An additional 22 bend tests were conducted with bare steel coupons, coupons with power actuated fasteners (PAF), and coupons with puddle welds to augment the results from the previous research discussed in Section 2.3. Additional information about individual specimens is given in Appendix V.

Results for coupons with repairs and defects are shown in Table 6.3. Results for the bare steel coupons and coupons with PAFs and puddle welds are shown in Table 6.4. Fracture initiation was defined as the cycle when a fracture was first captured by the video cameras, estimated to be 0.008 in. wide, and final fracture was defined as the cycle when the coupon was in two pieces. For coupons with 0.25 in. notches repaired by welding, fracture initiation was defined as the cycle when the first folded steel defect formed (see Section 6.4).

Material testing discussed in Section 6.3 showed that bar stock and beam flange material had similar yield stresses (1.1-5.2% difference), and ultimate strengths (3.4-8.7% difference). However, the CVN toughness was 51.8% and 74.6% smaller for bar stock when compared with beam flange material from W24×62 and W36×150 rolled shapes. In this sense, the bar stock and beam flange material would not be analogous, but this difference was not reflected in the results of the small-scale tests. When two specimens were milled to the same thickness, one from 0.5 in. bar stock and one from W24×62 flange material, there was only a two cycle difference (about 3%) for final fracture of the two specimens.

Table 6.3. Bend test results for flat bar coupons with repairs and defects.

Specimen Name	Artifact	Coupon Thickness, in.	Fracture Initiation Cycle	Final Fracture Cycle
W24-0.125NGT-T50-R11.01	0.125 in. notch repaired by grinding	0.5	11	18
W24-0.125NGT-T50-R11.02	0.125 in. notch repaired by grinding	0.5	11	17
W24-0.125NGT-T59-R11.01	0.125 in. notch repaired by grinding	0.59	8	12
W24-0.125NGT-T59-R11.02	0.125 in. notch repaired by grinding	0.59	7	11
W36-0.125NGT-T94-R11.01	0.125 in. notch repaired by grinding	0.94	4	6
W36-0.125NGT-T94-R11.02	0.125 in. notch repaired by grinding	0.94	4	6
W36-0.125NGT-T100-R11.01	0.125 in. notch repaired by grinding	1.0	3	5
W36-0.125NGT-T100-R11.02	0.125 in. notch repaired by grinding	1.0	2	4
W24-0.25NGTW-T50-R11.01	0.25 in. notch repaired by welding	0.5	8	35
W24-0.25NGTW-T50-R11.02	0.25 in. notch repaired by welding	0.5	7	33
W24-0.25NGTW-T59-R11.01	0.25 in. notch repaired by welding	0.59	5	13
W24-0.25NGTW-T59-R11.02	0.25 in. notch repaired by welding	0.59	6	13
W36-0.25NGTW-T94-R11.01	0.25 in. notch repaired by welding	0.94	2	5
W36-0.25NGTW-T94-R11.02	0.25 in. notch repaired by welding	0.94	3	6
W36-0.25NGTW-T100-R11.01	0.25 in. notch repaired by welding	1.0	3	6
W36-0.25NGTW-T100-R11.02	0.25 in. notch repaired by welding	1.0	3	5
W24-0.25N-T50-R11.02	Sharp 0.25 in. notch	0.5	1	9
W24-0.25N-T50-R11.03	Sharp 0.25 in. notch	0.5	1	8
W24-0.25N-T59-R11.02	Sharp 0.25 in. notch	0.59	1	4
W24-0.25N-T59-R11.03	Sharp 0.25 in. notch	0.59	1	4
W36-0.25N-T94-R11.01	Sharp 0.25 in. notch	0.94	1	3
W36-0.25N-T94-R11.02	Sharp 0.25 in. notch	0.94	1	4
W36-0.25N-T100-R11.01	Sharp 0.25 in. notch	1.0	1	2
W36-0.25N-T100-R11.02	Sharp 0.25 in. notch	1.0	1	2
W24-0.375N-T50-R11.01	Sharp 0.375 in. notch	0.5	1	8
W24-0.375N-T50-R11.02	Sharp 0.375 in. notch	0.5	1	6
W24-0.375N-T59-R11.01	Sharp 0.375 in. notch	0.59	1	5
W24-0.375N-T59-R11.02	Sharp 0.375 in. notch	0.59	1	6
W36-0.375N-T94-R11.01	Sharp 0.375 in. notch	0.94	1	4
W36-0.375N-T94-R11.02	Sharp 0.375 in. notch	0.94	1	3
W36-0.375N-T100-R11.01	Sharp 0.375 in. notch	1.0	1	2
W36-0.375N-T100-R11.02	Sharp 0.375 in. notch	1.0	1	2

Table 6.4. Bend test results for bare steel coupons and coupons with PAFs and puddle welds.

Specimen Name	Artifact	Coupon Thickness, in.	Fracture Initiation Cycle	Final Fracture Cycle
W24-BAR STOCK-T40-R11.02	Bare steel	0.4	28	67
W24-FLANGE MATERIAL-T40-R11.02	Bare steel	0.4	30	69
W24-STEEL-T50-R11.01	Bare steel	0.5	31	33
W24-STEEL-T50-R11.02	Bare steel	0.5	35	37
W36-STEEL-T100-R11.01	Bare steel	1.0	5	6
W36-STEEL-T100-R11.02	Bare steel	1.0	4	5
W24-0.625PnAF-T50-R11.01	Pneutek K66062	0.5	2	13
W24-0.625PnAF-T50-R11.02	Pneutek K66062	0.5	2	12
W36-0.625PnAF-T100-R11.01	Pneutek K66062	1.0	2	3
W36-0.625PnAF-T100-R11.02	Pneutek K66062	1.0	3	4
W24-0.75PnAF-T50-R11.01	Pneutek K66075	0.5	1	18
W24-0.75PnAF-T50-R11.02	Pneutek K66075	0.5	1	12
W36-0.75PnAF-T100-R11.01	Pneutek K66075	1.0	2	3
W36-0.75PnAF-T100-R11.02	Pneutek K66075	1.0	2	3
W24-PAF-T50-R11.01	Hilti X-ENP-19 L15	0.5	7	17
W24-PAF-T50-R11.02	Hilti X-ENP-19 L15	0.5	5	17
W36-PAF-T100-R11.01	Hilti X-ENP-19 L15	1.0	3	4
W36-PAF-T100-R11.02	Hilti X-ENP-19 L15	1.0	2	2
W24-PW-T50-R11.01	Puddle weld	0.5	3	18
W24-PW-T50-R11.02	Puddle weld	0.5	4	22
W36-PW-T100-R11.01	Puddle weld	1.0	2	4
W36-PW-T100-R11.02	Puddle weld	1.0	3	4

6.2.1 0.125 in. Notches Repaired by Grinding

For all specimens with a 0.125 in. notches repaired by grinding, the fracture initiated in the ground notch, either at the edge or in the middle. Typically, fractures initiated in marks left by the die grinder. An example of fracture initiation is shown in Figure 6.33a and the fracture surface is shown in Figure 6.33b.

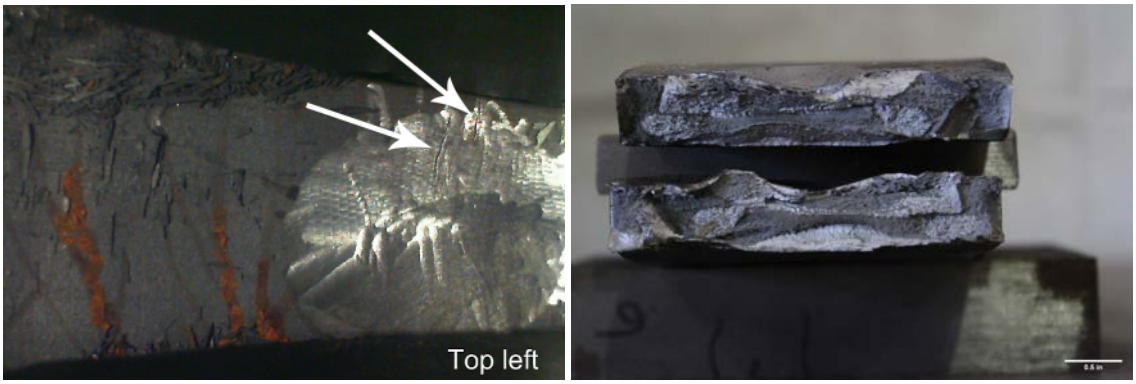

(a) Fracture initiation. **(b)** Fracture surface.

Figure 6.33. Fracture of a plate specimen with 0.125 in. notches repaired by grinding.

6.2.2 0.25 in. Notches Repaired by Welding

Fractures of the welded specimens initiated as folded steel defects that grew and coalesced to form the final fracture. See Section 6.4 for more discussion of folded steel defects. The only exception to this was the W36-0.25NGTW-T94-R11.01 specimen, which had a rougher surface finish than the other specimens, shown in Figure 6.34a. On this specimen, multiple fractures initiated in the marks left by the grinder. These fractures then combined to form the final fracture, but without forming folded steel defects. A similar specimen, W36-0.25NGTW-T94-R11.02, had a finer surface finish, shown in Figure 6.34b, and sustained one more cycle to failure than W36-0.25NGTW-T94-R11.01 before fracturing.

(a) W36-0.25NGTW-T94-R11.01. **(b)** W36-0.25NGTW-T94-R11.02.

Figure 6.34. Surface roughness of small-scale coupons.

The fracture surface of one of these specimens is shown in Figure 6.35. In the weld metal, there were numerous small, circular fracture patterns, similar to the fracture pattern shown in Figure 6.14. As mentioned in Section 6.1.2, these fractures are considered to be subsurface-origin fatigue fractures that formed and grew in the weld metal before appearing as folded steel defects on the surface. From the recorded fracture propagation of the welded specimens, it was apparent that the folded steel defects formed at the same places as the circular fracture patterns. Hydrogen

embrittlement is also known to create small, circular fracture patterns, but that is discussed and refuted in Section 6.4.

Figure 6.35. Fracture surface of W24-0.25NGTW-T59-R11.01.

6.2.3 Sharp 0.25 in. Notches

Due to the nature of this defect, fracture initiation was assumed to occur in the first cycle in the bottom of the notch where it was not visible. Final fracture of coupons with 0.25 in. notches always occurred when the top side was in tension. In most tests, there was visible fracture initiation and propagation on the bottom side that preceded the full fracture of the coupon. The only exceptions were the two specimens cut from 1 in. bar stock (W36-0.25N-T100-R11.01 and R11.02), which fractured suddenly in the second cycle. The fracture surface of one of these specimens, shown in Figure 6.36a, is compared with a more ductile fracture surface of a W36-0.25N-T94-R11.01 coupon.

(a) Fracture surface of W36-0.25N-T100-R11.01. **(b)** Ductile fracture of W36-0.25N-T94-R11.01.

Figure 6.36. Fractures surfaces of coupons with sharp 0.25 in. notches.

6.2.4 Sharp 0.375 in. Notches

Similar to the coupons with sharp 0.25 in. notches, fracture initiation was assumed to occur in the first cycle but in the bottom of the notch where it was not visible. However, there was visible fracture initiation on the bottom side that preceded complete fracture. Unlike the specimens with 0.25 in. notches, specimens with 0.375 in. notches cut from 1 in. bar stock had a more ductile failure mode, shown in Figure 6.37.

Figure 6.37. Fracture surface of W36-0.375N-T94-R11.01.

6.2.5 Bare Steel

Fracture of bare steel coupons was characterized by numerous fractures forming on the faces of the coupons. These fractures grew and coalesced in subsequent cycles until complete fracture. An example of these fractures is shown in Figure 6.38. In addition to the 0.5 in. and 1 in. bar stock, two 0.4 in. thick bare steel coupons were also tested to determine if there was a difference between the bar stock and beam flange material. There was only a 3% (two cycles) difference between the final fracture cycle of these specimens, and the behavior during testing was similar. Thus, the differences between flange material and bar stock are due to the different thickness of the coupons.

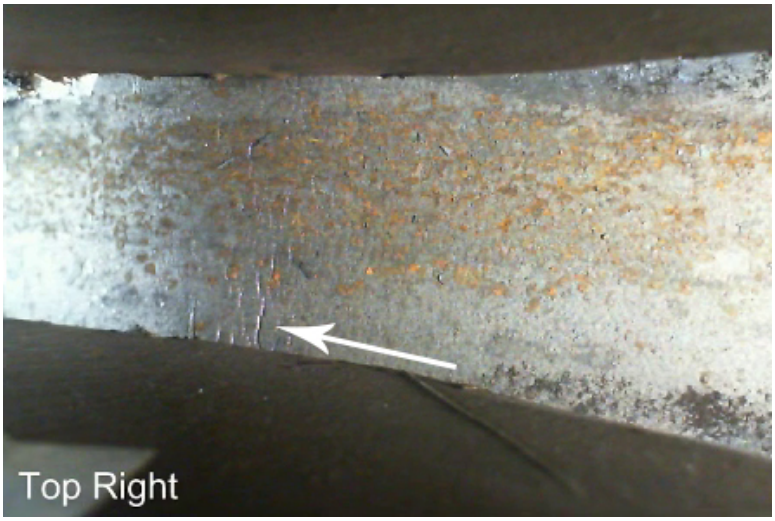

Figure 6.38. Fracture initiation of W24-STEEL-T50-R11.02.

6.2.6 Power actuated fasteners

Just as Abbas (2015) observed, the fracture initiation of specimens with PAFs was dependent on the material thickness. On 0.5 in. bar stock, the 0.625 in. long Pneutek K66062 fasteners and the Hilti X-ENP-19 L15 sheet metal nails created a noticeable bump on the bottom side, while the 0.75 in. long Pneutek K66075 fasteners broke through the bottom side. This is shown in Figure 6.39a. During testing, fractures initiated at the bump on the bottom side around the tip of the fastener and propagated outwards, eventually forming the final fracture. On the other hand, fracture initiation on the 1.0 in. bar stock coupons formed at the edge of the hole formed by the fastener, shown in Figure 6.39b. These fractures propagated and eventually formed the final fracture.

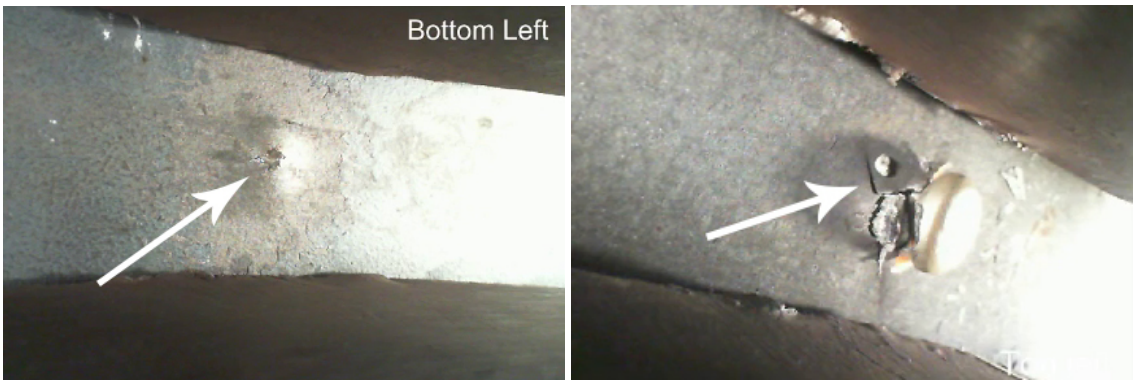

(a) Fastener protruding from 0.5 in. coupon.

(b) Fracture initiation under the fastener head.

Figure 6.39. Fracture initiation of 0.5 in. and 1 in. coupons with K66075 fasteners.

6.2.7 Puddle welds

Fractures on puddle weld specimens always initiated at the edge of the weld on the top side, even on the 0.5 in. bar stock coupons, shown in Figure 6.40. These findings conflict with the findings of the previous research in that fractures on 0.59 in. coupons initiated on the bottom side, opposite the puddle weld (Abbas 2015). The fracture on 1.0 in. bar stock coupons was similar between the past and current research.

Figure 6.40. Fracture initiation under a puddle weld.

6.3 Material Testing

The yield stress, ultimate strength, and elongation values for the eight monotonic tension coupons tested are given in Table 6.5 and results of the CVN tests are given in Table 6.6. Additional mill certificates and CVN test reports are provided in Appendix T and Appendix U. The stress-strain curves for tension coupons cut from the W24×62 beam are shown in Figure 6.41a and the curves for coupons cut from the W36×150 beam are shown in Figure 6.41b . Stress-strain curves for the tension coupons cut from the bar stock material are shown in Figure 6.42.

As mentioned in Section 3.2, 0.5 in. and 1 in. bar stock was used in lieu of beam flange material of the same thickness because it was easier to obtain and both materials had similar yield stress and ultimate strength requirements. The yield stress requirement for ASTM A992 beam flange material and ASTM A572 Grade 50 bar stock was 50 ksi and the ultimate strength requirement was 65 ksi. The material testing confirmed that the yield stress and ultimate strength were similar, with only a 1.1-5.2% difference in yield stresses and a 3.4-8.7% difference in ultimate strength. Furthermore, the stress-strain curves showed a similar response.

Based on the results of the tension coupon tests, the bar stock and beam flange material were analogous, but there was a more substantial difference between the CVN toughness of the two materials: the CVN toughness of bar stock was

51.8% and 74.6% lower than the toughness of W24×62 and W36×150 beam flanges, respectively. This could affect the fracture propagation and lead to more brittle fractures for flat bar coupons cut from bar stock, but this was not reflected in the small-scale results as only two of the 37 specimens cut from bar stock experienced brittle fractures. One possible explanation for the low number of brittle fractures was that the strain rate of the cyclic bend test was slow enough to allow fractures to propagate in the bar stock, but the fast strain rate of the CVN test did not. A brittle fracture was considered to be one where there was no fracture initiation before final fracture, while a ductile fracture was one in which fracture initiation on either side of the coupon preceded final fracture. The two specimens that experienced brittle fractures were the specimens cut from 1 in. bar stock with sharp 0.25 in. notches.

Table 6.5. Tension coupon results.

Coupon location	Yield stress, ksi	Ultimate strength, ksi	Elongation, %
W24×62 top flange	53.9	70.5	30.6
W36×150 top flange	53.9	69.2	28.6
0.5 in. bar stock	55.5	75.2	30.6
1 in. bar stock	53.2	73.4	26.2

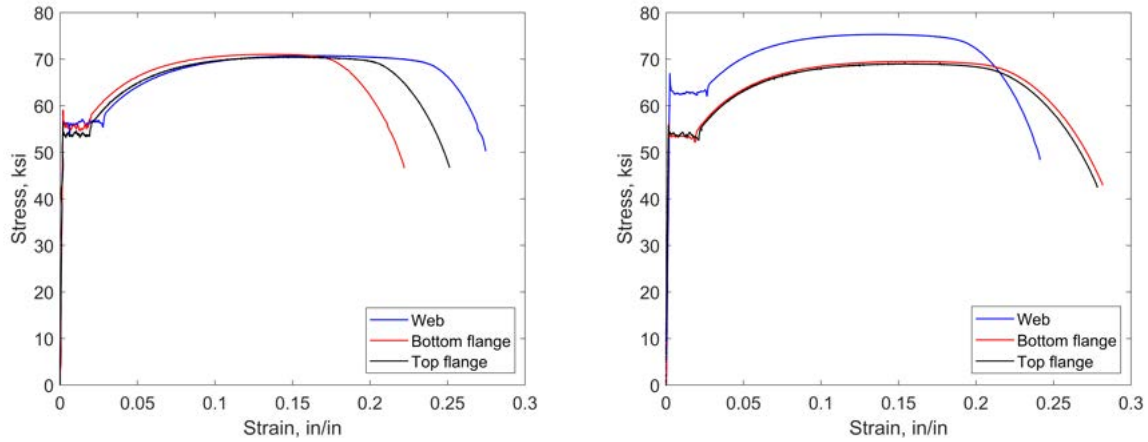

(a) W24×62. **(b)** W36×150.

Figure 6.41. Stress-strain plots of beam material.

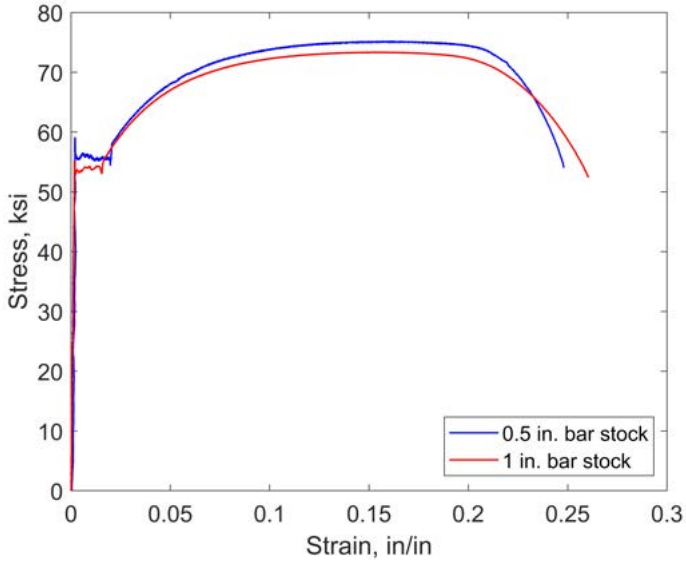

Figure 6.42. Stress-strain curves for bar stock material.

Table 6.6. CVN test results.

Coupon location	Absorbed energy[1], ft*lb			
	Specimen 1	Specimen 2	Specimen 3	Average
W24×62 beam flange	104	113	119	112
W36×150 beam flange	234	206	200	213
0.5 in. bar stock	59	68	35	54
1 in. bar stock	86	40	34	53

[1] Specimens were tested at room temperature.

6.4 Subsurface-Origin Fatigue Fractures

As mentioned briefly in Section 6.2.2, an interesting fracture surface was seen on the small-scale coupons with 0.25 in. notches repaired by welding. This was a series of small circular fractures in the weld metal, believed to be subsurface-origin fatigue fractures (Wulpi 1985). An example of these fractures on the fracture surface of a small-scale coupon are shown in Figure 6.43. A similar fracture was also seen on the full-scale specimen with a W24×62 beam, shown in Figure 6.44. On the small-scale coupons, folded steel defects formed on the top side at the same locations as the subsurface fractures, shown in Figures 6.45a to 6.45b. The folded steel defect was a fracture that initiated in the weld metal that had a raised)(or X shape, with the fracture at the center. Fractures initiated on the welded flat bar coupons sooner than on bare steel coupons, but the number of cycles of final fracture was similar for coupons with the same

thickness.

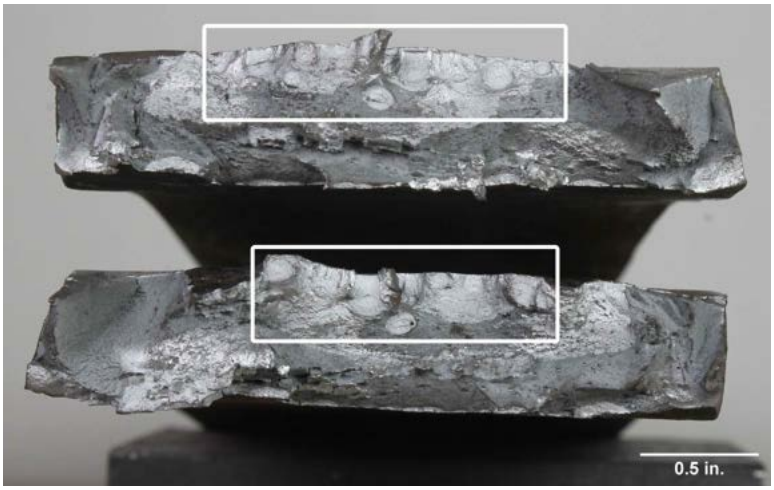

Figure 6.43. Subsurface-origin fatigue fractures on a welded bend coupon.

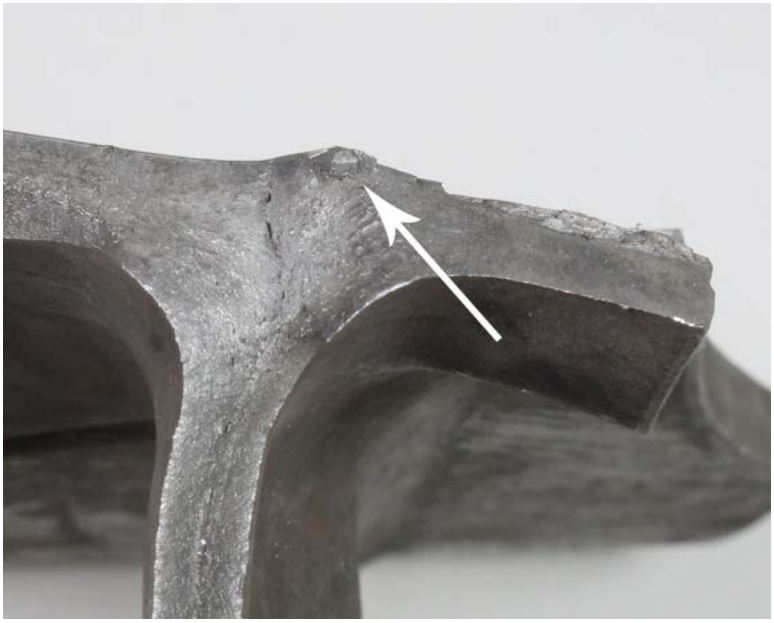

Figure 6.44. Subsurface-origin fatigue fracture on a full-scale specimen with welded artifacts.

(a) Folded steel defects forming on a welded bend coupon. **(b)** Subsurface fractures formed at folded steel defects.

Figure 6.45. Fracture initiation and propagation for coupon with a 0.25 in. notch repair be welding.

Hydrogen embrittlement is also known to appear as small, relatively circular indications on the fracture surface, but they are not the same as the fractures shown in Figure 6.43 and Figure 6.44. This kind of fracture surface is characterized by a fisheye, shown in Figure 6.46. The fisheye has a blowhole at the center, with a silvery appearance, and a surrounding embrittled region with a shiny texture (Zapffe and Sims 1940, 1941). There are also fissures leading away from the blowhole. On the welded bend coupons, the circular fractures did not have a distinct blowhole or fissures, and the surface was smooth and dull, unlike the shiny, textured surface of a brittle fracture. Furthermore, the welding wire used had a low diffusible hydrogen content, H4, and was stored in a dry environment. The coupons were also cleaned and dried before welding commenced, all of which suggests the coupons should not have had hydrogen embrittlement.

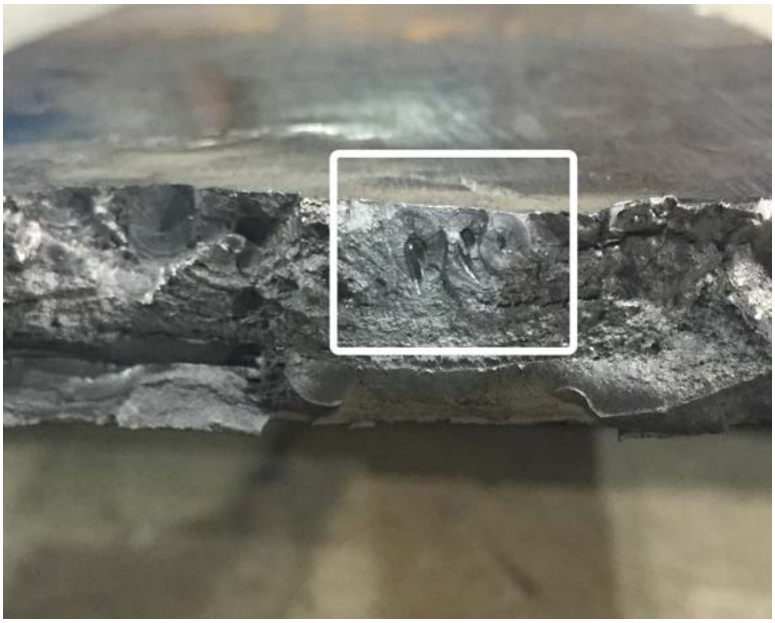

Figure 6.46. Hydrogen embrittlement of a welded coupon.

Chapter 7. Discussion

This chapter use the results of the full-scale experimental program to evaluate the acceptability of the four repairs and defects in the protected zone. A method for correlating the full-scale and small-scale tests is proposed using Coffin-Manson relationships and estimates of plastic strain amplitudes from full-scale tests. This method is then used for predicting final fracture of full-scale specimens.

7.1 Evaluating Repair Methods on Full-Scale Moment Connections

The results of the six full-scale moment connection tests are summarized in Table 7.1. From AISC (2016b), the requirements for qualifying special moment frame (SMF) connections are:

1. The connection must maintain at least 80% of the nominal plastic flexural strength through the first cycle of 4% story drift (qualification cycle);
2. The inelastic rotation in the test specimen must be within 25% of the anticipated inelastic rotation in the prototype connection.

Overall, the two repair methods, 0.125 in. notches repaired by grinding and 0.25 in. notches repaired by welding, did not prevent the four repaired specimens from satisfying SMF criteria. The W24RBS-0.125NGT-T59 specimen had a flexural resistance of 79.3% of the nominal plastic flexural strength at the first negative peak in the qualification cycle, and a flexural resistance of 82.2% of the nominal strength at the first positive peak. Since the reduction in strength was associated with local buckling rather than fracture, this was deemed to satisfy SMF qualification criteria.

Given the performance of the test specimens with repairs, it is concluded that reduced beam section (RBS) moment connections with similarly sized beams are acceptable for SMFs with the two repair methods, 0.125 in. notches repaired by grinding and 0.25 in. notches repaired by welding. The same can be said for non-RBS specimens, since tests by Eatherton et al. (2013) showed that RBS connections on W24×62 and W36×150 beams fractured before non-RBS connections with the same beam sizes.

Table 7.1. Results of full-scale moment connection tests.

Specimen Name	Beam Size	Artifact	Cycle of Final Fracture	Satisfy SMF Qualification
W24RBS-0.125NGT-T59	W24×62	0.125 in. notch repaired by grinding	4th cycle of 4.5% drift	Yes
W24RBS-0.25NGTW-T59	W24×62	0.25 in. notch repaired by welding	2nd cycle of 5% drift	Yes
W24RBS-0.375N-T59	W24×62	Sharp 0.375 in. notch	1st cycle of 4% drift	No
W36RBS-0.125NGT-T94	W36×150	0.125 in. notch repaired by grinding	3rd cycle of 5% drift	Yes
W36RBS-0.25NGTW-T94	W36×150	0.25 in. notch repaired by welding	1st cycle of 5% drift	Yes
W36RBS-0.25N-T94	W36×150	Sharp 0.25 in. notch	1st cycle of 5% drift	Yes

When the two repairs were applied to the specimens with W24×62 beams, the specimens had a similar performance as specimens with no artifacts. For comparison, a W24×62 beam with an RBS and no artifacts fractured in the second cycle of 4.7% story drift (Eatherton et al. 2013). As shown in Table 7.1, the W24RBS-0.125NGT-T59 specimen fractured after more cycles at a slightly lower maximum story drift, while the W24RBS-0.25NGTW-T59 specimen fractured after the same number of cycles at a higher maximum story drift. The performance of the two specimens was also similar to that of specimens with puddle welds and power actuated fasteners (PAF), which are currently the only decking attachments allowed in the protected zone. Fracture initiation was comparable, in that fractures formed on the flange face on the inside of a local buckle, but the final fracture of repaired specimens was more ductile than specimens with puddle welds and PAFs. Fractures also formed in an artifact on W24RBS-0.25NGTW-T59, unlike the W24RBS-0.125NGT-T59 specimen, but these fractures did not contribute to the final fracture.

The performance of specimens with W36×150 beams and repair methods was more variable. For comparison, a similar specimen with no artifacts fractured in the fifth cycle of 4.7% story drift, while two specimens with puddle welds or PAFs both fractured in the first cycle of 4.7% story drift. The repaired specimens performed as well as or better than specimens with puddle welds and PAFs, but while both specimens satisfied SMF qualification, they fractured in fewer cycles than a connection with no artifacts. Unlike the specimens with W24×62 beams, the two repair methods did affect fracture initiation and propagation on the specimens with larger beams. For W36RBS-0.125NGT-T94, the final fracture initiated at the edge of the ground notches at the center of the RBS, while the brittle fractures of W36RBS-0.25NGTW-T94 initiated at the bottom of the welded artifacts.

Contrary to the two repair methods, specimens with sharp notches are not acceptable for SMFs. Specimen W36RBS-0.25N-T94, satisfied the SMF qualification criteria, but a 3 in. long ductile fracture formed on the top flange in the first cycle of 4% story drift. In the second cycle of 4% story drift, a similar fracture formed on the bottom flange, while the top flange fracture propagated across the flange. This caused the flexural resistance to quickly drop below 80% of the nominal plastic flexural strength after the qualification cycle. On the other hand, specimen W24RBS-0.375N-T59 did not satisfy SMF qualification criteria because fractures formed on both flanges in the second cycle of 3% story drift, causing the flexural resistance to drop below 80% of the nominal strength. For both of these specimens, fractures initiated and propagated from the bottom of the sharp notches. While the sharp 0.25 in. notches did not prevent the specimen from satisfying SMF qualification criteria, both of the sharp notches are examples of defects that should be repaired because the they can cause a rapid decline in flexural resistance after the qualification cycle or lead to an early fracture.

7.2 Correlating Full- and Small-Scale Response

7.2.1 Coffin-Manson Relationships

As mentioned briefly in Section 2.5, low-cycle fatigue can be represented by an inverse power function known as the Coffin-Manson relationship, given in Eq. (2.2). Given that the functions are only valid for a certain geometry and material, an individual relationship was calibrated for each artifact using the cyclic bend test results from Table 2.1, Table 6.3, and Table 6.4. The plastic strain amplitudes from Table 3.3 were also used. Values for the constants ϵ'_f and c were found using the Matlab to conduct regression analysis, and are given in Table 7.2 for final fracture. Plots of the individual relationships with data points are shown in Figure 7.1.

As mentioned in Section 6.2 and Section 6.3, the bar stock and beam flange material had similar yield stresses and ultimate strengths, but the CVN toughness of the bar stock was much lower than that of the beam flange material. This would suggest that there would be an obvious difference between the bar stock and beam flange specimens, but that was not the case. When the thickness of the specimens was the same, there was only a 3% difference between the number of cycles to failure for bar stock and beam flange specimens. There were also very few brittle fractures, only two out of 37 specimens, even though the low notch toughness would indicate a propensity for brittle fractures of bar stock specimens. Additionally, when the number of cycles to failure was plotted against the plastic strain amplitude, as in Figure 7.1, there were no apparent outliers. The lack of outliers indicates that the varying plastic strain amplitudes (i.e. coupon thicknesses) were the reason for the difference in the number of cycles to failure for bar stock and beam flange material specimens.

Table 7.2. Coffin-Manson coefficients for final fracture.

Artifact	ϵ'_f	c
0.125 in. notch repaired by grinding	0.2527	-0.5065
0.25 in. notch repaired by welding	0.1997	-0.3949
Sharp 0.25 in. notch	0.1599	-0.4737
Sharp 0.375 in. notch	0.1675	-0.4885
Pneutek K66062	0.1979	-0.4533
Pneutek K66075	0.1784	-0.4245
Hilti X-ENP-19 L15	0.1342	-0.2904
0.63 in. puddle weld	0.2027	-0.4313
Bare steel	0.1659	-0.3261

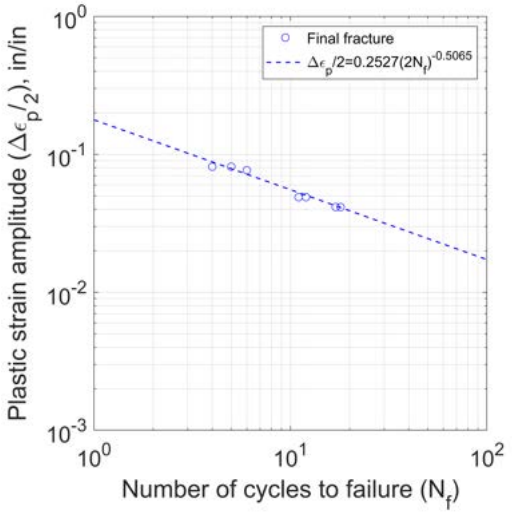

(a) 0.125 in. notch repaired by grinding.

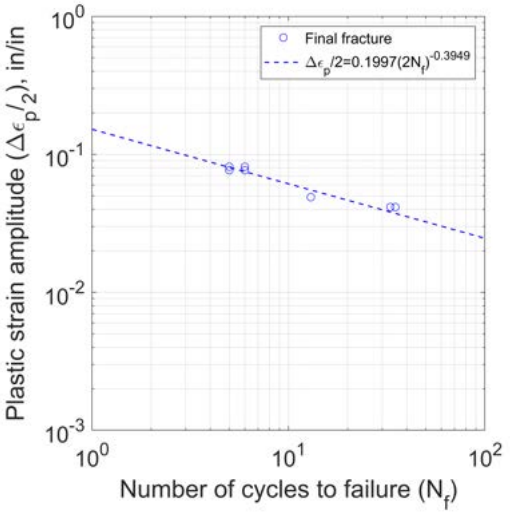

(b) 0.25 in. notch repaired by welding.

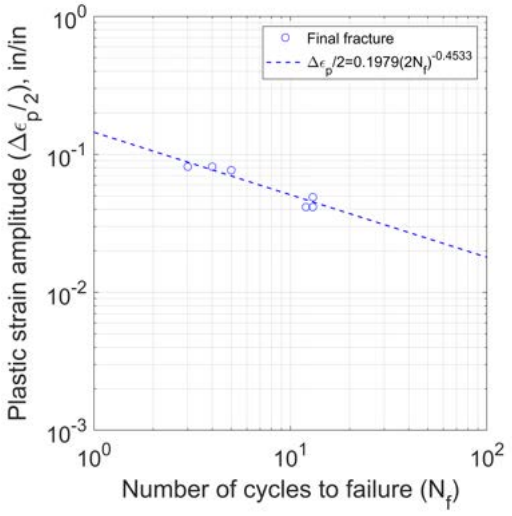

(c) Sharp 0.25 in. notch.

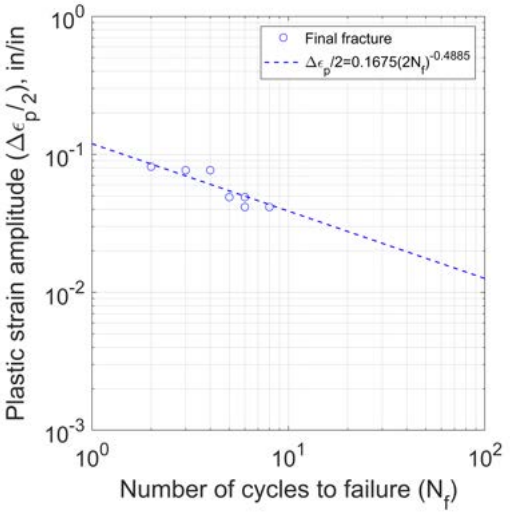

(d) Sharp 0.375 in. notch.

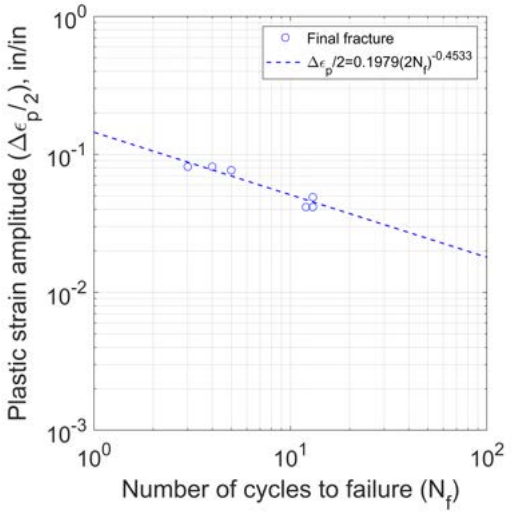

(e) Pneutek K66062 fastener.

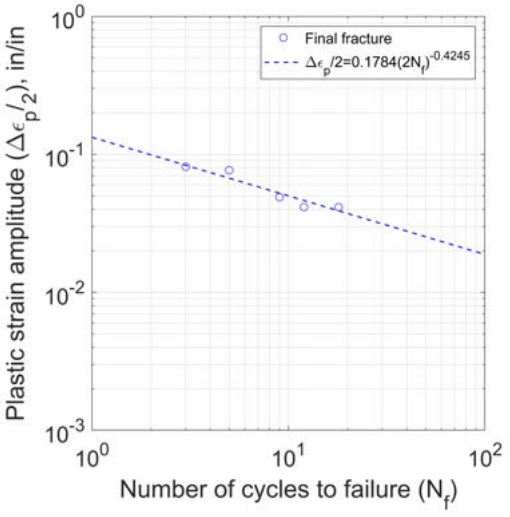

(f) Pneutek K66075.

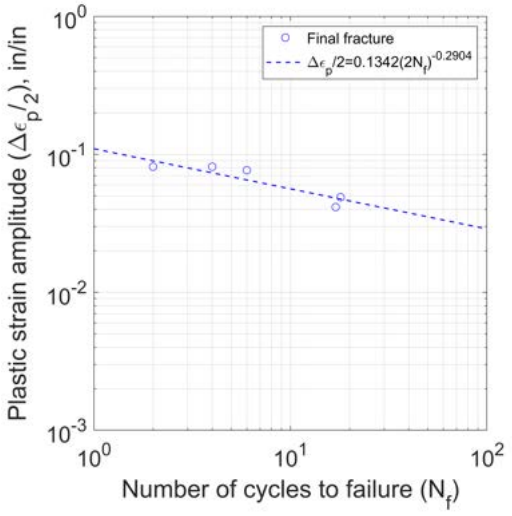

(g) Hilti X-ENP-19 L15.

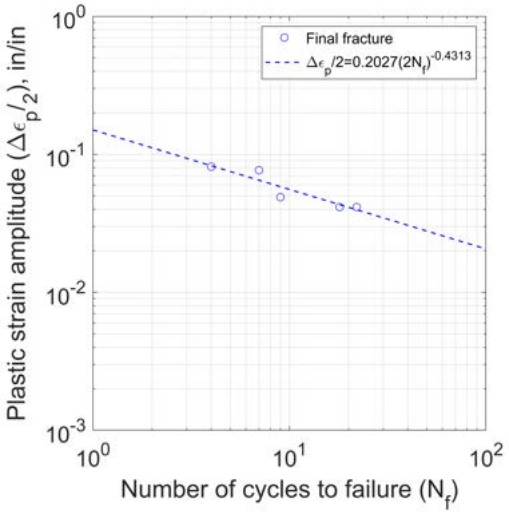

(h) 0.75 in. puddle weld.

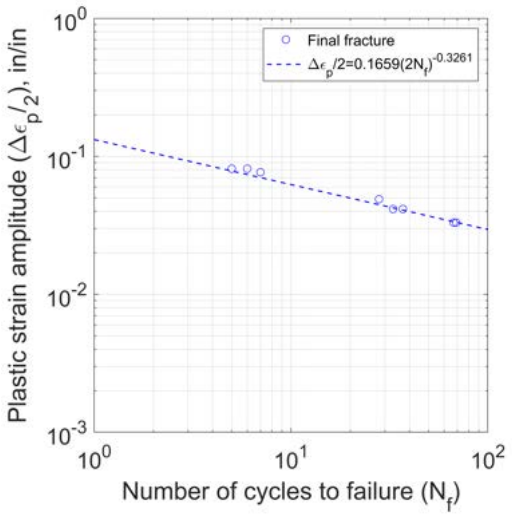

(i) Bare steel specimens.

Figure 7.1. Coffin-Manson relationships for final fracture of flat bar specimens.

The correlation between the full-scale and small-scale tests was calibrated for final fracture because it was easier to objectively identify when final fracture occurred. In the full-scale tests, this was when a fracture propagated across the width of the flange and into the web, and for small-scale tests this was when the coupon was in two pieces. Fracture initiation of full-scale tests was more difficult to identify because the full-scale tests were not stopped after every loading cycle. Additionally, fracture initiation of small-scale specimens with sharp 0.25 in. and 0.375 in. notches did not follow the inverse power law of the Coffin-Manson relationship. Fracture initiation was assumed to occur in the first cycle for all specimens, regardless of thickness, due to the nature of the sharp notch. The correlation was applied for fracture initiation though, with the results provided in Appendix W.

7.2.2 Plastic Strain Amplitudes for Full-Scale Tests

The coefficients in Table 7.2 represent one part of a proposed correlation between the full-scale moment connection tests and the small-scale cyclic bend tests. The second part of the correlation are estimates for plastic strain amplitudes during each cycle of the full-scale testing. When used in conjunction with the calibrated Coffin-Manson relationships, the plastic strain amplitudes give an estimate of the fatigue life for each story drift cycle of the full-scale tests. Only cycles after yielding were of interest, as the plastic strain was assumed to be zero before yielding. Yielding started in the 0.75% story drift cycles for RBS specimens with W24×62 beams and in the 1% story drift cycles for RBS specimens with W36×150 beams.

Plastic strain was estimated before the onset of local buckling using the plastic hinge rotation, θ_{PH}, calculated using Eq. (7.1). As shown in Figure 3.11, SP_06 is placed below the beam and SP_07 is placed above the beam. Both string potentiometers measure the elongation and shortening of the plastic hinge region. The plastic strain at the extreme fiber was then calculated using Eq. (7.2). For all specimens, the plastic hinge was assumed to form at the center of the RBS.

$$\theta_{PH} = \frac{\delta_{SP\_06} - \delta_{SP\_07}}{L_{sp2}} - \theta_{EP} \tag{7.1}$$

$$\epsilon_p = \frac{\theta_{PH} d_b}{2L_p} - \epsilon_{el} \tag{7.2}$$

where: d_b = beam depth, 24 or 36 in.
L_p = distance from the plastic hinge to the face of the column, 15.5 or 24.5 in.
L_{sp2} = distance between SP_06 and SP_07, 36 or 55.5 in.
δ_{SP_06} = displacement of SP_06
δ_{SP_07} = displacement of SP_07
ϵ_{el} = elastic strain, 0.002 in./in.
ϵ_p = plastic strain
θ_{EP} = story drift due to end-plate separation, from Eq. (E.6).

Between the onset of local buckling and fracture, plastic strain was estimated using scaled pictures of the local buckle where the final fracture occurred. Visually observable local buckling began in the 3% story drift cycles for all specimens except W24RBS-0.125NGT-T59, when flange buckling was observed in the first cycle of 4% story drift. Using the scaled pictures, the radius of curvature was estimated for the top and bottom flange at the peaks of each story drift cycle and then converted to curvature using Eq. (7.3). The plastic strain was calculated using Eq. (7.4).

$$c = \frac{1}{\rho} \tag{7.3}$$

$$\epsilon_p = \frac{ct}{2} - \epsilon_{el} \tag{7.4}$$

where: c = curvature

t = beam flange thickness, 0.59 or 0.94 in.

ϵ_{el} = elastic strain, 0.002 in./in.

ϵ_p = plastic strain

ρ = radius of curvature

The plastic strain amplitudes from Eq. (7.2) and Eq. (7.4) were used with the calibrated Coffin-Manson relationships to determine the theoretical fatigue life for the story drift cycles after yielding. Miner's rule was then used to calculate how much of the theoretical fatigue life was used in each cycle. The plastic strain amplitudes for cycles after the onset of local buckling were scaled down such that all of the fatigue life was used when the flange fracture propagated through the thickness of the flange, and extended from the flange tip into the web. Only plastic strain amplitudes determined for cycles after the onset of local buckling were scaled down because using Miner's rule suggested that the majority of the theoretical fatigue life (i.e. >95%) was used in the large displacement cycles after the onset of local buckling. The scaling factors ranged from 0.07-0.96 for specimens with W24×62 beams and 0.06-0.94 for specimens with W36×150 beams. The strain amplitudes were then averaged for the individual story drift cycles and beam sizes. These values are given in Table 7.3. To expand the correlation and fracture prediction to RBS specimens tested in previous research, plastic strain amplitudes for 4.7% story drift cycles were included, as this was the maximum story drift applied in that research (Eatherton et al. 2013). Values for plastic strain amplitude at 4.7% story drift were linearly interpolated between the values for 4% and 5% story drift.

Table 7.3. Estimated plastic strain amplitudes.

Story Drift, rad.	**Plastic Strain Amplitude[1], in./in.**	
	W24×62 RBS	**W36×150 RBS**
0.0075	0.0031	N/A
0.01	0.0045	0.0045
0.015	0.0075	0.0079
0.2	0.0113	0.0116
0.03	0.0202	0.0714
0.04	0.0530	0.0875
0.045	0.0930	N/A
0.047	0.1097	0.1033
0.05	0.1340	0.1100

[1] Shading denotes plastic strain amplitudes after local buckling.

7.3 Predicting Fracture of Full-Scale Moment Connections

The Coffin-Manson relationships and the plastic strain amplitudes for each story drift cycle can be used with Miner's rule to predict when final fracture would occur on full-scale specimens. An example of this process is given for W24RBS-0.125NGT-T59, an RBS connection on a W24×62 beam with an array of 0.125 in. notches repaired by grinding. The Coffin-Manson relationship for final fracture is given in Eq. (7.5).

$$\frac{\Delta\epsilon_p}{2} = 0.2527(2N_f)^{-0.5065} \tag{7.5}$$

The process for predicting fracture was iterative, and is shown in Table 7.4. First, Eq. (7.5) was rearranged to give the number of cycles to failure, N_f, for a given plastic strain amplitude, $\frac{\Delta\epsilon_p}{2}$. Next, Miner's rule was used to calculate the amount of fatigue life used for each story drift cycle, given the theoretical fatigue life and the number of cycles from Table 3.2. Finally, the percent of fatigue life used in each story drift cycle was summed to give the total fatigue life used. To find the predicted cycle of final fracture, the number of cycles for the maximum story drift was decreased until the sum of fatigue life used was equal to 1. If the sum of fatigue life was greater than one but the number of cycles at the maximum story drift was zero, then the cycles for the next largest story drift were reduced.

Table 7.4. Prediction of final fracture for W24RBS-0.125NGT-T59.

Story Drift, rad	Plastic Strain Amplitude, in./in.	Theoretical Fatigue Life (cycles)	Applied Cycles	Fatigue Life Used	Cumulative Fatigue Life Used
0.0075	0.0031	2968	6	0.002	0.002
0.01	0.0045	1422	4	0.003	0.005
0.015	0.0075	519	2	0.004	0.009
0.02	0.0113	231	2	0.009	0.018
0.03	0.0202	73	2	0.027	0.045
0.04	0.0530	11	2	0.183	0.228
0.045	0.0930	4	2.8	0.772	1.000

Based on Table 7.4, final fracture is predicted to occur after 2.8 cycles of 4.5% story drift. In this example, this means final fracture would occur in the third cycle of 4.5% story drift at an approximate cumulative story drift of 1.89 radians. In actuality, specimen W24RBS-0.125NGT-T59 fractured in the fourth cycle of 4.5% story drift, one cycle after the predicted fracture.

Final fracture was predicted using this process for all full-scale tests with no artifacts, puddle welds, PAFs, and 0.25 in. notches repaired by welding. Final fracture was not predicted for Pneutek K66062 or K66075 fasteners, as no

full-scale specimens have been tested with those artifacts. Only RBS specimens with W24×62 and W36×150 beams were included, as the plastic strain amplitudes in Table 7.3 were calibrated to RBS specimens with these beam sizes. The results of these predictions are given in Table 7.5. For most specimens, fracture was predicted for the same cycle or one cycle before when the specimen actually fractured during testing. The mean cumulative story drift ratio was 1.13 and the standard deviation was 0.19.

Table 7.5. Final fracture prediction for full-scale RBS specimens.

Specimen Name	Artifact	Actual Result		Predicted Result		Cumulative Story Drift Ratio
		Fracture Cycle	Cumulative Story Drift, rad.	Fracture Cycle	Cumulative Story Drift, rad.	
RBS24[1]	None	2nd cycle of 4.7% drift	1.77	2nd cycle at 4.7% drift	1.68	1.05
RBS24-PW12[1]	4 puddle welds at 12 in. spacing	3rd cycle of 4.7% drift	1.85	2nd cycle at 4.7% drift	1.70	1.09
RBS24-PAF12[1]	4 PAFs at 12 in. spacing	2nd cycle of 4.7% drift	1.58	1st cycle at 4.7% drift	1.55	1.02
W24RBS-0.125NGT-T59	0.125 in. notch repaired by grinding	4th cycle of 4.5% drift	2.07	3rd cycle of 4.5% drift	1.89	1.10
W24RBS-0.25NGTW-T59	0.25 in. notch repaired by welding	2nd cycle of 5% drift	1.65	2nd cycle of 5% drift	1.63	1.01
W24RBS-0.375N-T59	Sharp 0.375 in. notch	1st cycle of 4% drift	1.20	1st cycle of 5% drift	1.49	0.81
RBS36[1]	None	5th cycle of 4.7% drift	2.21	1st cycle at 4.7% drift	1.44	1.53
RBS36-PW12[1]	4 puddle welds at 12 in. spacing	1st cycle of 4.7% drift	1.59	1st cycle at 4.7% drift	1.42	1.12
RBS36-PAF_ARRAY[1]	Grid of PAFs	1st cycle of 4.7% drift	1.48	2nd cycle at 4% drift	1.26	1.17
W36RBS-0.125NGT-T94	0.125 in. notch repaired by grinding	4th cycle of 5% drift	2.04	1st cycle of 5% drift	1.49	1.37
W36RBS-0.25NGTW-T94	0.25 in. notch repaired by welding	1st cycle of 5% drift	1.58	1st cycle of 5% drift	1.49	1.06
W36RBS-0.25N-T94	Sharp 0.25 in. notch	1st cycle of 5% drift	1.46	1st cycle of 4% drift	1.15	1.27

[1] From Eatherton et al. (2013).

A plot of the actual and predicted cumulative story drifts at final fracture is given in Figure 7.2. This plot has a diagonal 1:1 correlation line where points above the line represent an overprediction of final fracture and points below the line represent an underprediction of final fracture. Overpredictions represent unconservative estimates, where fracture was predicted to occur after actual fracture in full-scale tests. Underpredictions are conservative estimates, where fracture was predicted to occur before actual fracture in full-scale tests. The plot also has solid horizontal lines indicating the cumulative story drift at the end of the 0.75%, 1%, 1.5%, 2%, 3%, and 4% story drift cycles, which are 0.39, 0.55, 0.67, 0.83, 1.07, and 1.39 radians, respectively. The dashed horizontal lines indicate the intermediate 1.5%, 2%, 3%, and 4% story drift cycles.

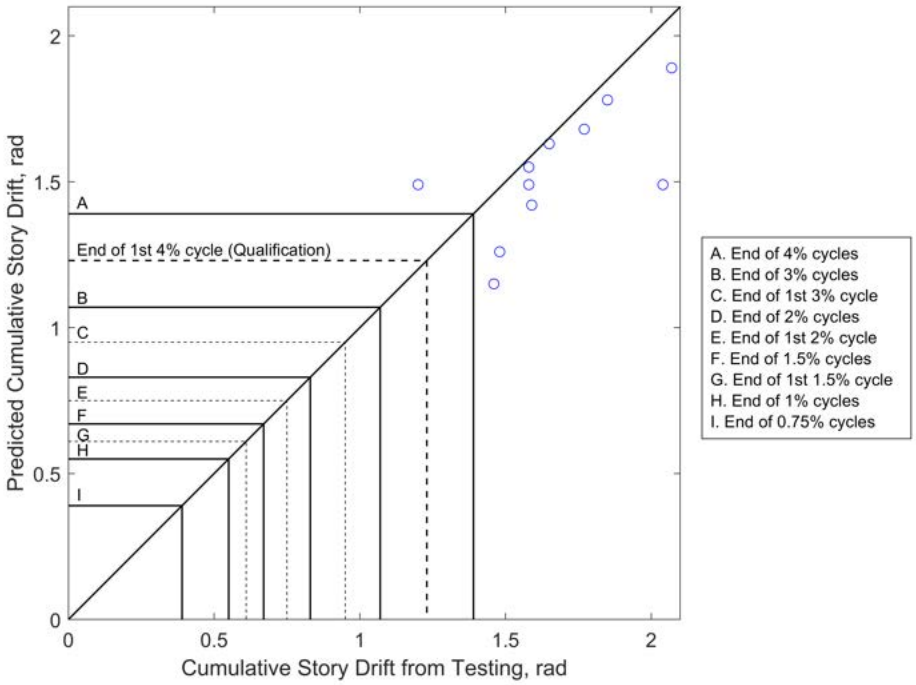

Figure 7.2. Correlation plot of actual and predicted final fracture of full-scale RBS specimens.

It is evident from Figure 7.2 that the proposed correlation between full-scale and small-scale tests underpredicted the final fracture for all but one specimen. The only exception was W24RBS-0.375N-T59: a specimen with a W24×62 beam and an array of sharp 0.375 in. notches. One possible limitation of this correlation is the number of small-scale tests conducted to calibrate the Coffin-Manson relationships. More accurate estimates of the plastic strain amplitudes for each loading cycles would also improve the correlation.

7.4 How to Evaluate other Artifacts

One of the primary goals of this research was to develop a method for using small-scale cyclic bend tests to evaluate the fracture potential of SMF connections with artifacts in the protected zone. A correlation like this is valuable because the cyclic bend tests are quicker and less expensive than full-scale tests, meaning artifacts could be tested more easily in the future.

The procedure for evaluating new artifacts is as follows. First, a set of flat bar specimens would be created with a single artifact centered on one side. A minimum of eight specimens (two for each of four bar thicknesses) is recommended, with the range of bar thicknesses covering the flange thickness of interest. Bar stock was determined to be an appropriate substitute for beam flange material because there was little difference between the low-cycle fatigue response of coupons with the same thickness cut from bar stock or beam flange material. The number of cycles to final fracture, N_f, should be recorded for each specimen, along with the plastic strain amplitude, $\frac{\Delta\epsilon_p}{2}$, calculated using Eq. (3.2) and Eq. (3.3) based on the roller diameter and coupon thickness.

Next, a Coffin-Manson relationship would be calibrated using regression analysis. The equation for the Coffin-Manson relationship is given by Eq. (2.2), and the regression results in constants ϵ'_f and c. The amount of theoretical fatigue life for story drift cycle of a full-scale specimen would then be calculated using the plastic strain amplitudes in Table 7.3 and the process described in Section 7.3. Finally, Miner's rule would be used to sum the fatigue life used in cycle and determine the predicted cycle of final fracture, as demonstrated in Table 7.4. If final fracture is predicted to be after the 4% story drift cycles, then a full-scale specimen with the same artifact would be expected reach 4% story drift without fracturing. However, this would not give an indication of the flexural resistance at the time of fracture.

As an example, the predicted cycle of final fracture and cumulative story drift for RBS specimens with Pneutek fasteners are given Table 7.6. Full-scale specimens with these fasteners have not been tested, but this method for predicting fracture suggests that full-scale specimens would not experience an early fracture before the SMF qualification cycle. It is also expected that full-scale specimens with the same beam size would have a similar response for either the K66062 or K66075 fasteners.

Table 7.6. Predicted cycle of final fracture for RBS specimens with Pneutek fasteners.

Fastener Type	**W24×62 RBS**		**W36×150 RBS**	
	Fracture Cycle	**Cumulative Story Drift, rad**	**Fracture Cycle**	**Cumulative Story Drift, rad**
K66062	1st cycle of 5% drift	1.56	2nd cycle of 4% drift	1.35
K66075	1st cycle of 5% drift	1.54	2nd cycle of 4% drift	1.30

Chapter 8. Conclusions

8.1 Summary

Six full-scale reduced beam section (RBS) moment connection specimens were tested to evaluate the performance of special moment frame (SMF) connections with repair methods and defects applied to the flanges and subjected to large inelastic rotations. The repair methods were 0.125 in. notches repaired by grinding and 0.25 in. notches repaired by welding, while the defects were sharp 0.25 in. and 0.375 in. notches. Small-scale cyclic bend tests of bar stock and beam flange coupons with the same repair methods and defects, power actuated fasteners (PAF), puddle welds, and bare steel specimens were also tested. Coffin-Manson low-cycle fatigue relationships were calibrated for each repair method, defect, or fastener using the results of the bend tests. These relationships were then used with estimates of the plastic strain amplitudes from the full-scale tests to develop a method for predicting fracture of full-scale tests. Finally, the proposed method was validated for the six full-scale tests in this research, as well as six full-scale tests from a previous study.

8.2 Conclusions

All four full-scale specimens with repairs satisfied the SMF qualification criteria. The flexural resistance of the specimen with a W24×62 beam and 0.125 in. notches repaired by grinding was 79.3% of the nominal plastic flexural strength at the first negative peak in the qualification cycle, and 82.2% at the first positive peak. While this is slightly smaller than the qualifiction criterion of 80% of the nominal plastic flexural strength, this specimen was deemed acceptable because the loss of strength was associated with local buckling rather than fracture. Plastic hinge rotation made up between 84% and 94% of the applied story drift at the end of the tests.

The specimens with repairs performed as well as similarly sized connections with puddle welds and PAFs, which are currently the only decking attachment methods allowed in the protected zone. The specimens with W24×62 beams performed as well as specimens with no artifacts, but the specimens with W36×150 beams fractured in fewer cycles than specimens with no artifacts. Fracture propagation was more ductile for specimens with repairs compared to puddle welds and PAFs, with one exception: the RBS specimen with a W36×150 beam and 0.25 in. notches repaired by weldingl experienced a brittle fracture in the first cycle of 5% story drift.

Based on these tests, the AWS D1.8 repair methods, where defects are repaired by grinding or repair welding, are satisfactory for SMF connections in seismic zones. This is expected to be true for RBS and non-RBS specimens, since

the tests were on RBS connections and Eatherton et al. (2013) showed that RBS specimens fractured before non-RBS specimens.

The two specimens with sharp notches did not have an adequate response, and thus sharp notches are not acceptable in SMF connections. The RBS specimen with a W24×62 beam and sharp 0.375 in. notches did not satisfy SMF qualification criteria, as the flexural resistance was well below 80% of the nominal plastic flexural strength before the qualification cycle. The RBS specimen with a W36×150 beam and sharp 0.25 in. notches did satisfy SMF qualification criteria, but a 3 in. long fracture formed on the top flange in the first cycle of 4% story drift. This led to a rapid decline in flexural resistance in the following cycle as the fracture propagated.

Small-scale cyclic testing of flat bar specimens with similar artifacts showed that the relationship between plastic strain amplitude and fatigue life followed an inverse power law that could be fit to the Coffin-Manson relationship. Coffin-Manson relationships were calibrated for the plate specimens with 0.125 in. notches repaired by grinding, 0.25 in. notches repaired by welding, sharp 0.25 in. and 0.375 in. notches, puddle welds, Pneutek K66062 and K66075 fastener, Hilti X-ENP-19 L15 sheet metal nails, and bare steel coupons.

A method was developed that used the calibrated Coffin-Manson relationships and estimates of plastic strain amplitudes to predict fracture of full-scale moment connections. When applied to the twelve full-scale RBS connections tested with the same artifacts, this method underpredicted fracture for all but one specimen. The only exception was the specimen with a W24×62 beam and sharp 0.375 in. notches, which had a ratio of actual to predicted cumulative story drift of 0.81. All other specimens had a ratio greater than 1, with the mean of 1.13 and the standard deviation of 0.19.

This method is valuable because the fracture potential of other artifacts could be evaluated without having to conduct time-intensive and expensive full-scale testing, but there are limitations. While the yield stress and ultimate strength of ASTM A572 Grade 50 bar stock was similar to that of the ASTM A992 beam flange material, the Charpy V-notch toughness was substantially lower. This could affect fracture propagation on small-scale specimens regarding brittle fractures, but this was not reflected in the results of the small-scale tests. However, strains developed in coupons in the cyclic bend test are different from those in a local buckle of full-scale specimens. In the cyclic bend test, strains have constant amplitude and fully reverse each cycle, while strains in a local buckle have variable amplitudes, do not fully reverse, and have an additional inelastic tensile component. Plate specimens in the cyclic bend test also only experience positive stress triaxiality, but finite element modeling suggests local buckles in a moment connection experience both positive and negative stress triaxaility. This may not be a concern because most low-cycle fatigue models apply cutoff values for negative stress triaxiality, implying that it is less important for damage accumulation.

Future research could focus on expanding the data set of artifacts that have been tested on flat bar specimens in the cyclic bend test and have valid Coffin-Manson relationships. Additional research could also refine the estimates for plastic strain amplitudes of the full-scale tests to improve the method for predicting fracture. The estimates for plastic strain amplitude could also be expanded to account for non-RBS specimens.

References

Abbas, E. (2015). "A Low Cycle Fatigue Testing Framework for Evaluating the Effect of Artifacts on the Seismic Behavior of Moment Frames." Ph.D. thesis, Virginia Tech, Blacksburg, VA (October).

Abbas, E. and Eatherton, M. R. (2014). "A Low Cycle Fatigue Testing Framework for Evaluating the Effect of Artifacts on the Seismic Behavior of Moment Frames." *Report No. CE/VPI-ST-14/06*, Virginia Tech, Blacksburg, VA (December).

AISC (2010). *Seismic Provisions for Structural Steel Buildings*. American Institute of Steel Construction, Chicago, IL.

AISC (2016a). *Prequalified Connections for Special and Intermediate Steel Moment Frames for Seismic Applications*. American Institute of Steel Construction, Chicago, IL.

AISC (2016b). *Seismic Provisions for Structural Steel Buildings*. American Institute of Steel Construction, Chicago, IL.

AISC (2017). *Steel Construction Manual*. American Institute of Steel Construction, Chicago, IL, 15th edition.

Anderson, T. L. (2017). *Fracture Mechanics*. CRC Press, Boca Raton, FL, 4th edition.

ASTM (2016a). "Standard practice for magnetic particle testing." *E3024/E3024M-16*, ASTM International, West Conshohocken, PA.

ASTM (2016b). "Standard test methods for tension testing of metallic materials." *E8/E84M-16a*, ASTM International, West Conshohocken, PA.

ASTM (2018). "Standard test methods for notched bar impact testing of metallic materials." *E23-18*, ASTM International, West Conshohocken, PA.

AWS (2015). *Structural Welding Code-Steel*. American Welding Society, Miami, FL, 23rd edition.

AWS (2016). *Structural Welding Code-Seismic*. American Welding Society, Miami, FL, 3rd edition.

Bao, Y. and Wierzbicki, T. (2005). "On the cut-off value of negative triaxiality for fracture." *Engineering Fracture Mechanics*, Elsevier, 72, 1049–1069.

Barsom, J. M. and Rolfe, S. T. (1999). *Fracture and Fatigue Control in Structures-Applications of Fracture Mechanics*. ASTM International, West Conshohocken, PA, 3rd edition.

Civjan, S. A., Engelhardt, M. D., and Gross, J. L. (2000). "Retrofit of Pre-Northridge Moment-Resisting Connections." *Journal of Structural Engineering*, ASCE, 126(4), 445–452.

Coffin, J. L. F. (1953). "A Study of the Effects of Cyclic Thermal Stresses on a Ductile Metal." *Report No. KAPL-853*, Knolls Atomic Power Laboratory, Schenectady, NY (June).

Coronoa, E. and Kyriakides, S. (1991). "An Experimental Investigation of the Degradation and Buckling of Circular Tubes Under Cyclic Bending and External Pressure." *Thin-Walled Structures*, Elsevier, 12, 229–263.

Dowling, N. E. (2013). *Mechanical Behavior of Materials*. Pearson, Upper Saddle River, NJ, 4th edition.

Eatherton, M. R., Toellner, B. W., Watkins, C. E., and Abbas, E. (2013). "The Effect of Powder Actuated Fasteners on the Seismic Performance of Protected Zones in Steel Moment Frames." *Report No. CE/VPI-ST-13/05*, Virginia Tech, Blacksburg, VA (July).

Florig, S. H. and Eatherton, M. R. (2015). "Evaluation of the Effect of Boat-Shaped Welds and Pneumatic Power Actuated Fasteners on the Seismic Behavior of Moment Frames." *Report no.*, Virginia Tech, Blacksburg, VA (December).

Goodall, I. W. and Webster, G. A. (2001). "Theoretical determination of reference stress for partially penetrating flaws in plates." *International Journal of Pressure Vessels and Piping*, Elsevier, 78, 687–695.

Gray, M. G., Christopoulos, C., Packer, J. A., and Lignos, D. G. (2012). "Development, Validation and Modeling of the new Cast Steel Yielding Brace System." *20th Analysis & Computation Specialty Conference*, ASCE, Reston, VA, 71–82.

Hajjar, J. F., Leon, R. T., Gustafson, M. A., and Shield, C. K. (1998). "Seismic Response of Composite Moment-Resisting Connections ii: Behavior." *Journal of Structural Engineering*, ASCE, 124(8), 877–885.

Kyriakides, S. and Shaw, P. K. (1987). "Inelastic buckling of tubes under cyclic bending." *Journal of Pressure Vessel Technology*, ASME, 109, 169–178.

Leon, R. T., Hajjar, J. F., and Gustafson, M. A. (1998). "Seismic Response of Composite Moment-Resisting Connections ii: Performance." *Journal of Structural Engineering*, ASCE, 124(8), 868–876.

Limam, A., Lee, L.-H., Corona, E., and Kyriakides, S. (2010). "Inelastic wrinkling and collapse of tubes under combined bending and internal pressure." *International Journal of Mechanical Sciences*, Elsevier, 52(5), 637–647.

Manson, S. S. (1953). "Behavior of Materials under Conditions of Thermal Stress." *Technical Note 2933*, NACA, Washington, DC (July).

Manson, S. S. (1954). "Behavior of Materials under Conditions of Thermal Stress." *Technical Report 1170*, NACA, Washington, DC.

Manson, S. S. and Halford, G. R. (2006). *Fatigue and Durability of Structural Materials*. ASM International, Cleveland, OH.

Newman, J. C. and Raju, I. S. (1984). "Stress-intensity factor equations for cracks in three-dimensional finite bodies subjected to tension and bending loads." *Technical Memorandum 85793*, NASA, Washington, DC (April).

Pereira, J. C. R., Van Wittenberghe, J., Jesus, A., Thibaux, P., and Fernandes, A. A. (2016). "Ultra-low cycle fatigue behavior of full-scale straight pipes under alternating bending." *Proceedings of the ASME 2016 Pressure Vessels and Piping Conference*, ASME, New York, NY, 1–9.

Popov, E. P., Yang, T.-S., and Chang, S.-P. (1998). "Design of steel MRF connections before and after 1994 Northridge earthquake." *Engineering Structures*, 20(12), 1030–1038.

Ricles, J. M., Fisher, J. W., Lu, L.-W., and Kaufmann, E. J. (2002). "Development of improved welded moment connections for earthquake-resistant design." *Journal of Constructional Steel Research*, Elsevier, 58, 565–604.

Rolfe, S. T. and Novak, S. R. (1970). "Slow-Bend Kic Testing of Medium-Strength High-Toughness Steels." *Review of Developments in Plane Strain Fracture Toughness Testing, ASTM STP 463*, American Society for Testing and Materials, 124–159.

Smith, C. M., Deierlein, G., and Kanvinde, A. M. (2014). "A Stress Weighted Damage Model for ductile fracture initiation in structural steel under cyclic loading and generalized stress states." *Report No. 187*, Stanford University, Stanford, CA (September).

Smith, R. W., Hirschberg, M. H., and Manson, S. S. (1963). "Fatigue Behavior of Materials under Stress Cycling in Low and Intermediate Life Range." *Technical Note D-1574*, NASA, Washington, DC (April).

Suresh, S. (1998). *Fatigue of Materials*. Cambridge Univ. Press, Cambridge, UK.

Szabo, T. A. (2017). "Development and Validation of a Twelve Bolt Extended Stiffened End-Plate Moment Connection." M.S. thesis, Virginia Tech, Blacksburg, VA (May).

Tateishi, K., Hanji, T., and Minami, K. (2006). "A prediction model for extremely low cycle fatigue strength of structural steel." *International Journal of Fatigue*, Elsevier, 29, 887–896.

Timoshenko, S. (1955). *Strength of Materials*. Robert E. Krieger Publishing Co., Huntington, NY.

Toellner, B. W. (2013). "Evaluating the Effect of Decking Fasteners on the Seismic Behavior of Steel Moment Frame Plastic Hinge Regions." M.S. thesis, Virginia Tech, Blacksburg, VA (April).

Tremblay, R. and Filiatrault, A. (1997). "Seismic performance of steel moment resisting frames retrofitted with a locally reduced beam section connection." *Canadian Journal of Civil Engineering*, NRC Canada, 24.

Uang, C.-M. and Bondad, D. (1996). "Static Cyclic Testing of Pre-Northridge and Haunch Repaired Steel Moment Connections." *Report No. SSRP-96/02*, Univ. of California, San Diego, La Jolla, CA (February).

Watkins, C. E. (2013). "Developing a Full-Scale Test Setup to Study the Effects of Fasteners on the Protected Zone of Steel Moment Frames." Project and report, Virginia Tech, Blacksburg, VA (May).

Wierzbicki, T., Bao, Y., Lee, Y.-W., and Bai, Y. (2005). "Calibration and evaluation of seven fracture models." *International Journal of Mechanical Sciences*, Elsevier, 47, 719–743.

Wu, T.-Y., El-Tawil, S., and McCormick, J. P. (2018). "Experimental Study of Cyclic Flange Local Buckling." *Structures Congress 2018*, ASCE, Reston, VA, 49–57.

Wulpi, D. J. (1985). *Understanding How Components Fail*. American Society for Metals, Metals Park, OH.

Youssef, N. F. G., Bonowitz, D., and Gross, J. L. (1995). "A Survey of Steel Moment-Resisting Frame Buildings Affected by the 1994 Northridge Earthquake." *Report No. NISTIR 5625*, Building and Fire Research Laboratory, NIST, Gaithersburg, MD.

Zapffe, C. A. and Sims, C. E. (1940). "Defects in weld metal and hydrogen in steel." *Welding Journal*, American Institute of Mining and Metallurgical Engineers, 19, 377–395.

Zapffe, C. A. and Sims, C. E. (1941). "Hydrogen Embrittlement, Internal Stress and Defects in Steel." *Metals Technology*, American Institute of Mining and Metallurgical Engineers, 8(5), 1–37.

Appendices

Appendix A. Full-Scale Test Setup Drawings

This appendix includes all drawings for the full-scale moment connection test setup, including the actuator frame, the lateral-torsional buckling frame, and the reaction frame. The actuator frame held the servohydraulic actuator used to apply force, the bracing frame limited lateral-torsional buckling outside of the plastic hinge region, and the reaction frame supported the beam-column subassemblage. The actuator and bracing frames are shown in Figure A.1a and Figure A.1b, respectively.

(a) Actuator frame viewed from the south end. **(b)** Bracing frame viewed from the south end.

Figure A.1. Test setup components.

The actuator was bolted to a W14×257 header supported by two pairs of W21×62 crossheads. These crossheads were in turn supported by two pairs of W21×62 columns bolted to the strong floor. Diagonal bracing on the south side stiffened the frame, while additional longitudinal beams tied the actuator frame to the reaction frame. X-bracing on the south side also stiffened the frame in the transverse direction. Lateral bracing on the north side of the frame

consisted of two C10×30 channels bolted to top and bottom shelf angles. An L8×8×3/4 with slotted holes was bolted to each channel and acted as an adjustable shim to account for test specimens with varying flange widths.

An additional set of lateral bracing was installed on the north side of the bracing frame. This bracing was similar to that on the actuator frame but the channels were stiffened with k-braces to account for the higher out-of-plane forces closer to the plastic hinge. This frame was moved to position the brace points at the end of the plastic hinge. This meant the centerline of the bracing frame was 4.5 ft. from the centerline of the reaction column for W24×62 beam specimens and 5.5 ft. for W36×150 beam specimens.

Finally, the reaction frame supported the W14×398 column that was reused for each test. The column was bolted to a stub section in the strong floor below and a W36×150 header at the top. This header was supported by W21×62 columns stiffened by two pairs of diagonal bracing.

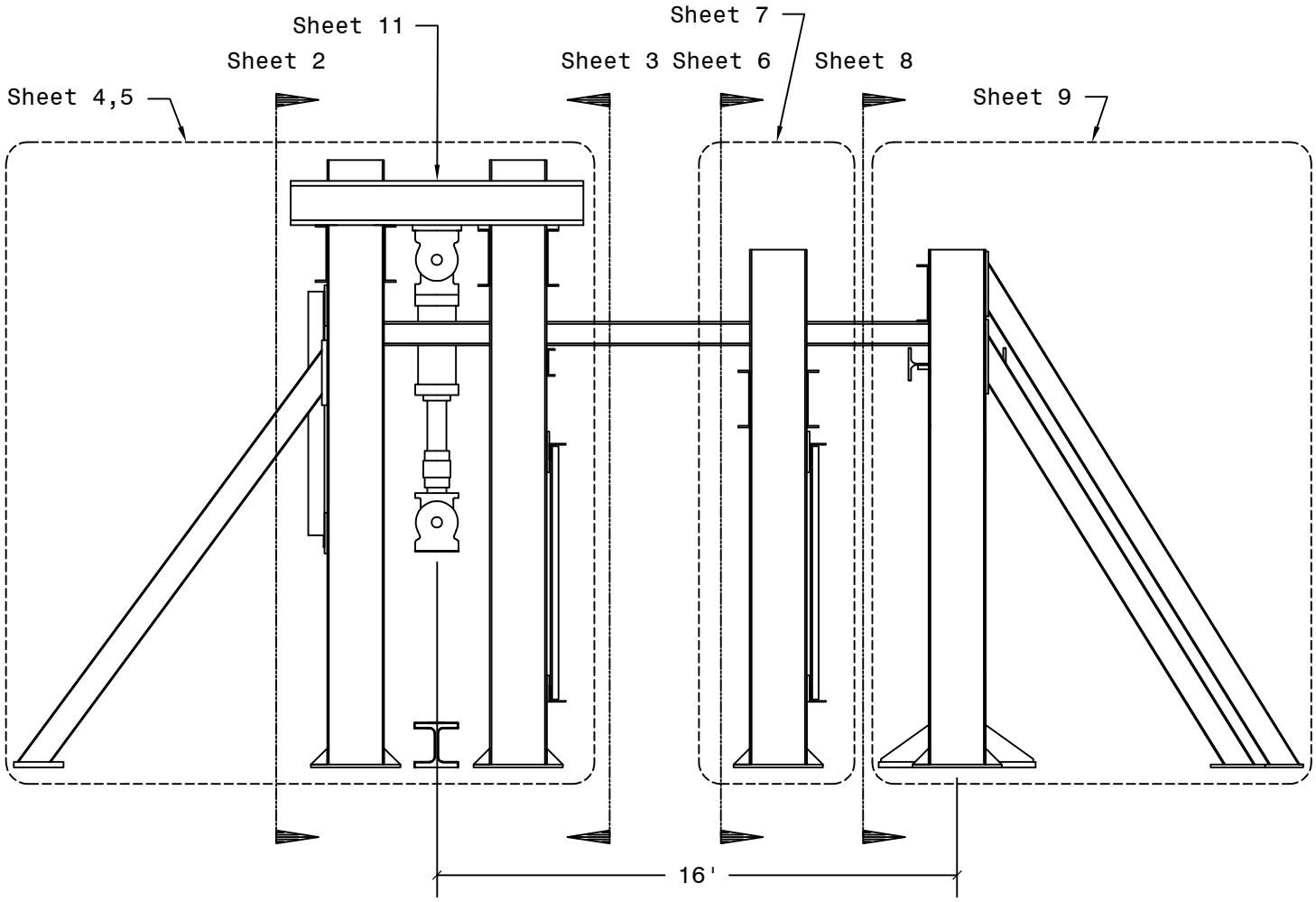

VIRGINIA TECH
CHARLES E. VIA JR. DEPARTMENT OF CIVIL & ENVIRONMENTAL ENGINEERING
200 PATTON HALL
BLACKSBURG, VA 24061
P: 540-231-6635

PROJECT:

MRF Protected Zone/Low-Cycle Fatigue

SHEET NOTES:

1. Scale is 3/8"=2'
2. See Sheet 10 for reaction column details

REVISIONS:

NO.	DATE	BY

DESIGNED BY:
DRAWN BY: R. Stevens
CHECKED BY:
DATE: 7/30/2020
PROJECT NO.:

SHEET TITLE:

Moment connection test setup

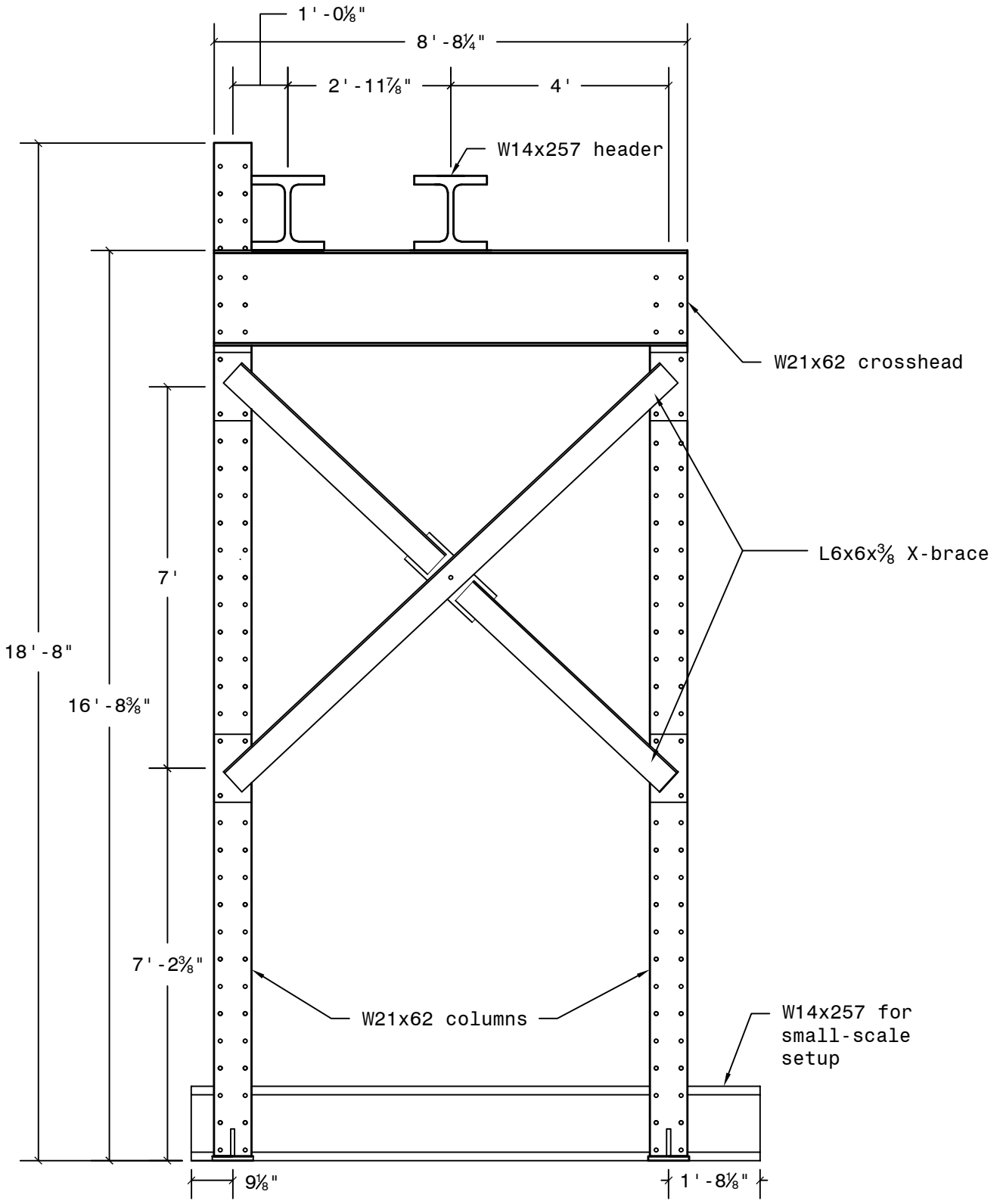

VIRGINIA TECH

VIRGINIA TECH
CHARLES E. VIA JR. DEPARTMENT OF CIVIL & ENVIRONMENTAL ENGINEERING
200 PATTON HALL
BLACKSBURG, VA 24061
P: 540-231-6635

PROJECT:

MRF Protected Zone/Low-Cycle Fatigue

SHEET NOTES:

1. Scale is 3/8"=1'
2. MTS 201.70 and 201.80 actuators not shown

REVISIONS:

NO.	DATE	BY

DESIGNED BY:

DRAWN BY: R. Stevens

CHECKED BY:

DATE: 7/30/2020

PROJECT NO.:

SHEET TITLE:

South elevation of actuator frame

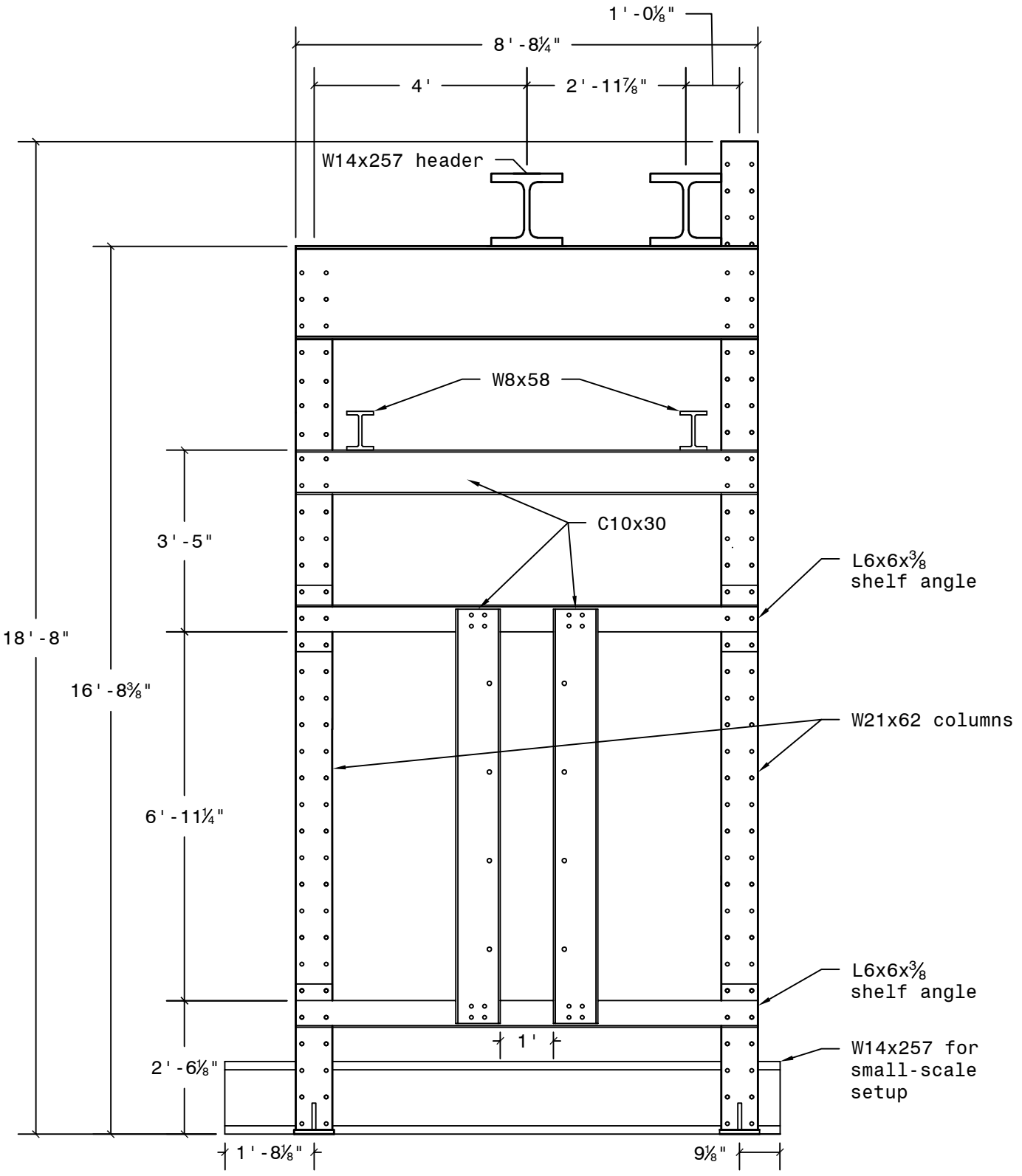

VIRGINIA TECH

VIRGINIA TECH
CHARLES E. VIA JR. DEPARTMENT OF CIVIL & ENVIRONMENTAL ENGINEERING
200 PATTON HALL
BLACKSBURG, VA 24061
P: 540-231-6635

PROJECT:

MRF Protected Zone/Low-Cycle Fatigue

SHEET NOTES:

1. Scale is 3/8"=1'
2. MTS 201.70 and 201.80 actuators not shown

REVISIONS:

NO.	DATE	BY

DESIGNED BY:
DRAWN BY: R. Stevens
CHECKED BY:
DATE: 7/30/2020
PROJECT NO.:

SHEET TITLE:

North elevation of actuator frame

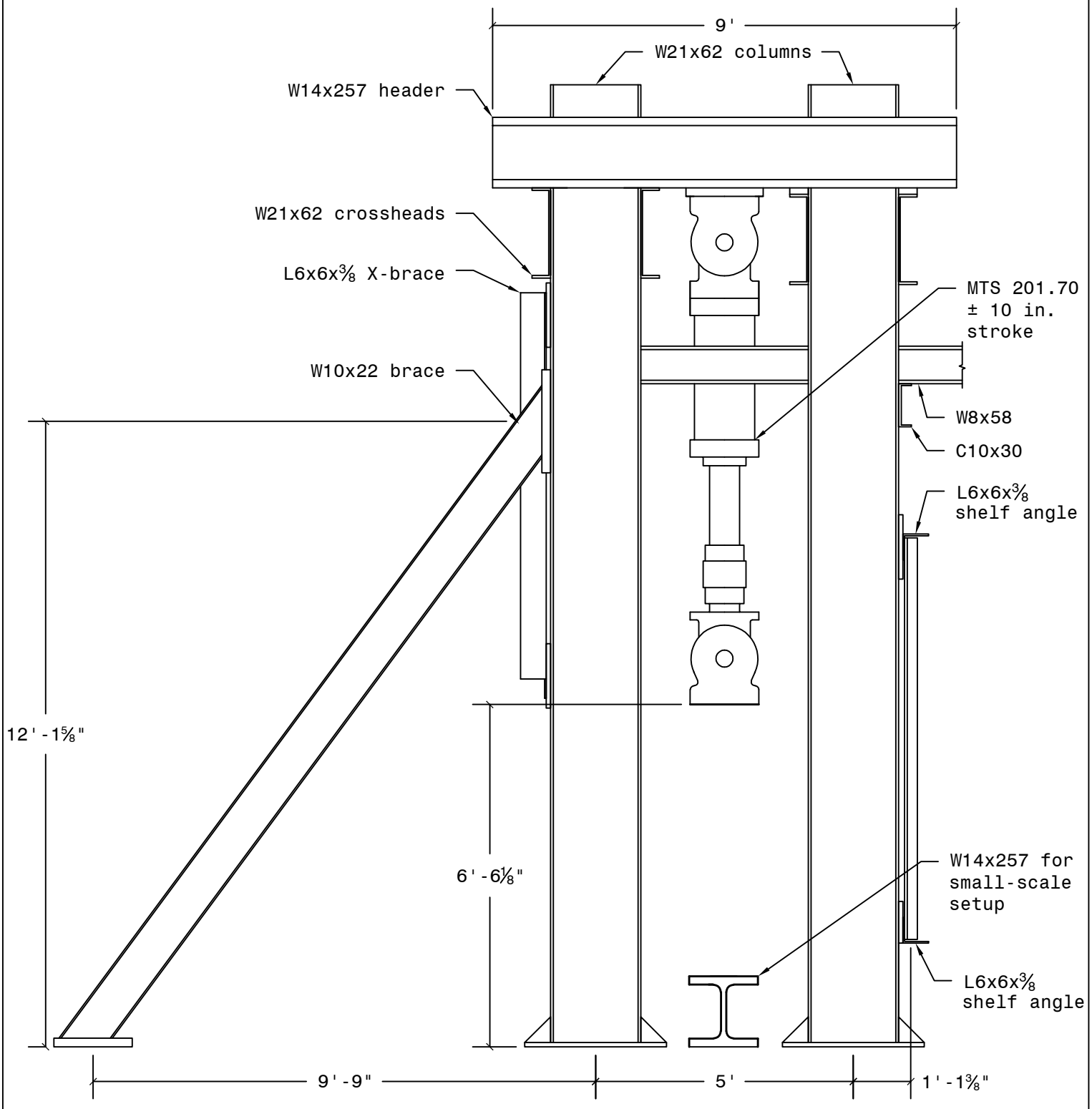

VIRGINIA TECH

VIRGINIA TECH
CHARLES E. VIA JR. DEPARTMENT OF
CIVIL & ENVIRONMENTAL
ENGINEERING
200 PATTON HALL
BLACKSBURG, VA 24061
P: 540-231-6635

PROJECT:

MRF Protected Zone/Low-Cycle Fatigue

SHEET NOTES:

1. Scale is 3/8"=1'

REVISIONS:

NO.	DATE	BY

DESIGNED BY:

DRAWN BY: R. Stevens

CHECKED BY:

DATE: 7/30/2020

PROJECT NO.:

SHEET TITLE:

East elevation of actuator frame

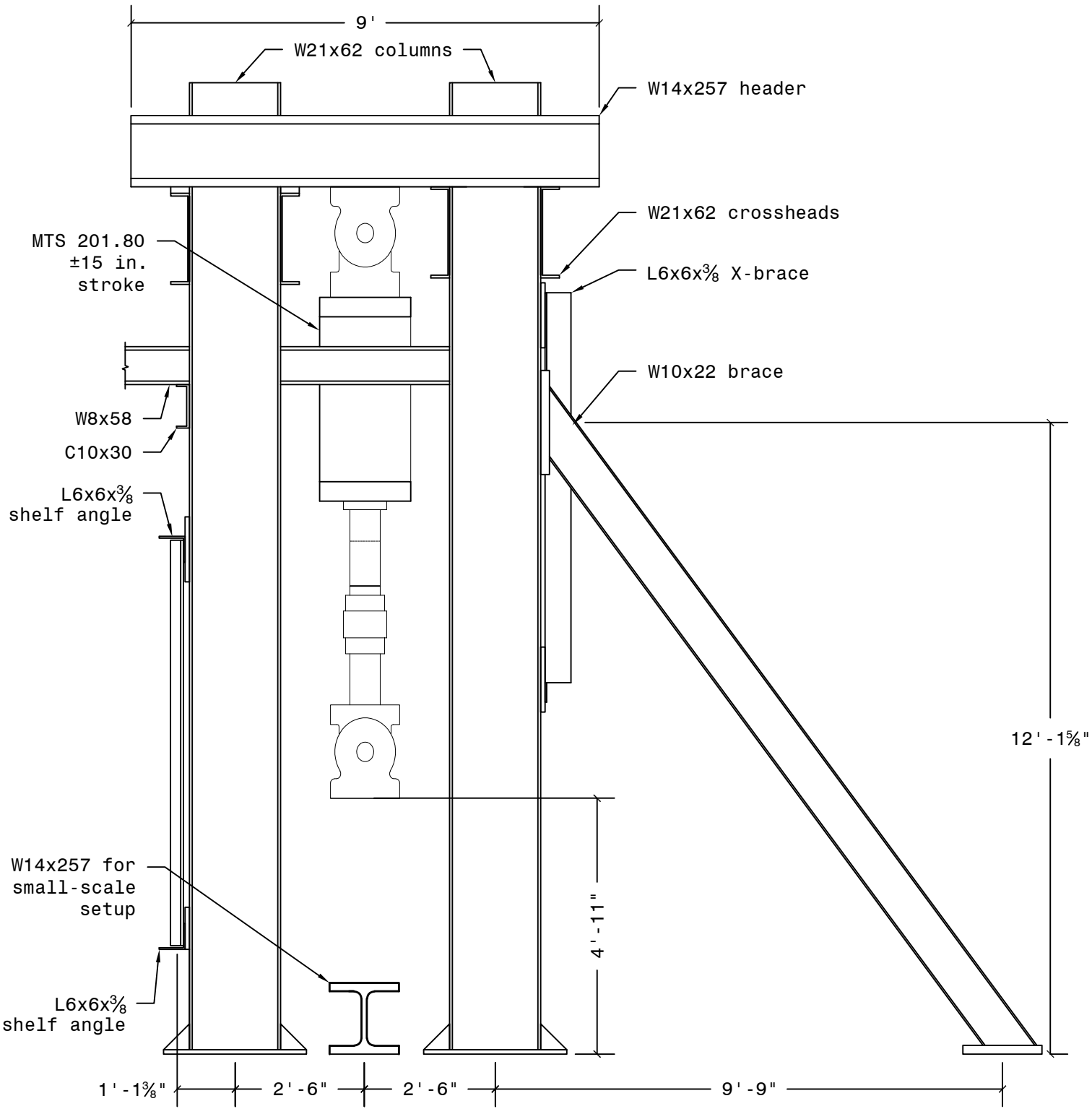

VIRGINIA TECH

VIRGINIA TECH
CHARLES E. VIA JR. DEPARTMENT OF CIVIL & ENVIRONMENTAL ENGINEERING
200 PATTON HALL
BLACKSBURG, VA 24061
P: 540-231-6635

PROJECT:

MRF Protected Zone/Low-Cycle Fatigue

SHEET NOTES:

1. Scale is 3/8"=1'
2. Small-scale setup not shown

REVISIONS:

NO.	DATE	BY

DESIGNED BY:

DRAWN BY: R. Stevens

CHECKED BY:

DATE: 7/31/2020

PROJECT NO.:

SHEET TITLE:

West elevation of actuator frame

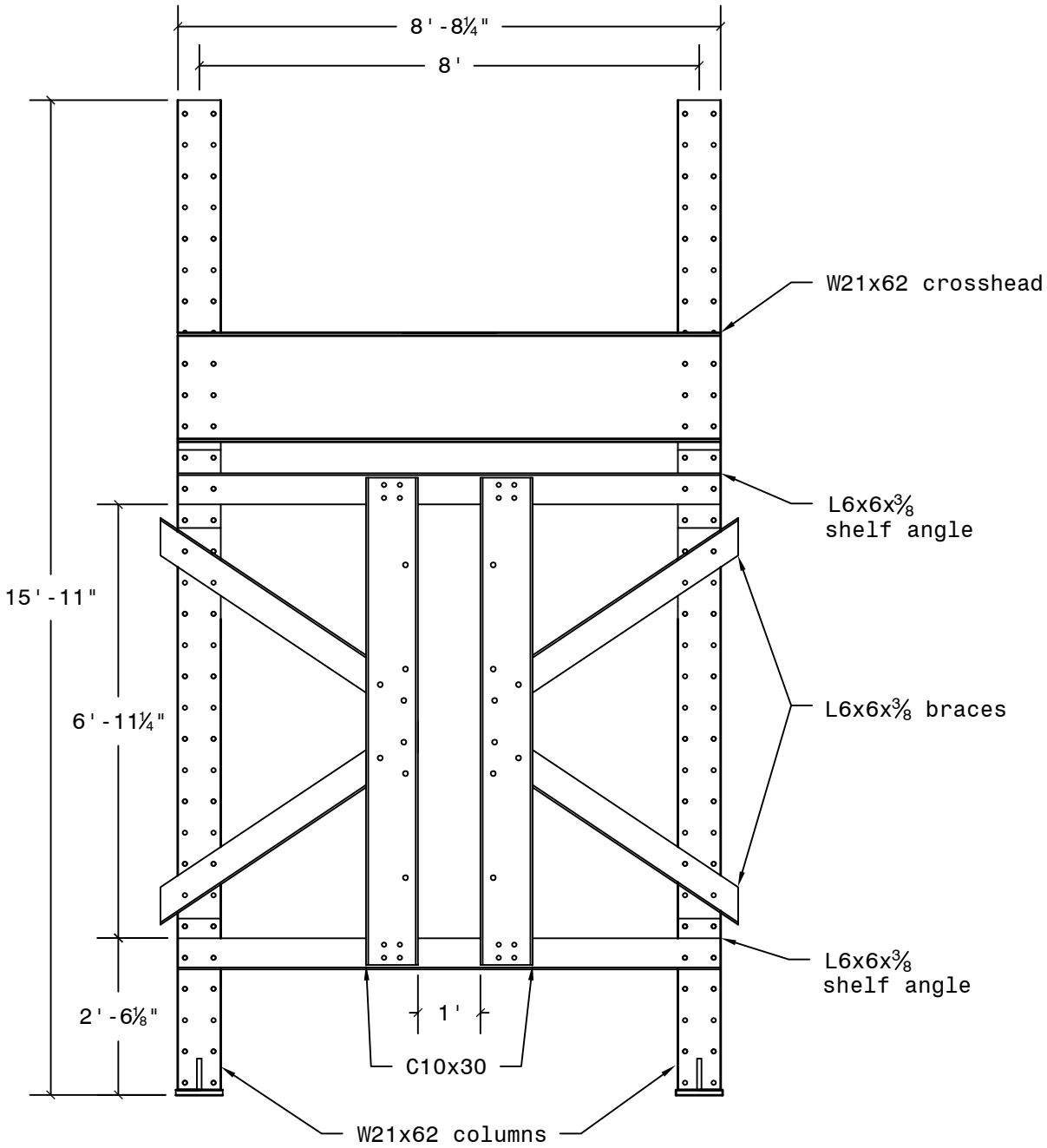

VIRGINIA TECH

VIRGINIA TECH
CHARLES E. VIA JR. DEPARTMENT OF CIVIL & ENVIRONMENTAL ENGINEERING
200 PATTON HALL
BLACKSBURG, VA 24061
P: 540-231-6635

PROJECT:

MRF Protected Zone/Low-Cycle Fatigue

SHEET NOTES:

1. Scale is 3/8"=1'
2. W8x58 not shown

REVISIONS:

NO.	DATE	BY

DESIGNED BY:

DRAWN BY: R. Stevens

CHECKED BY:

DATE: 7/30/2020

PROJECT NO.:

SHEET TITLE:

North elevation of lateral-torsional buckling bracing frame

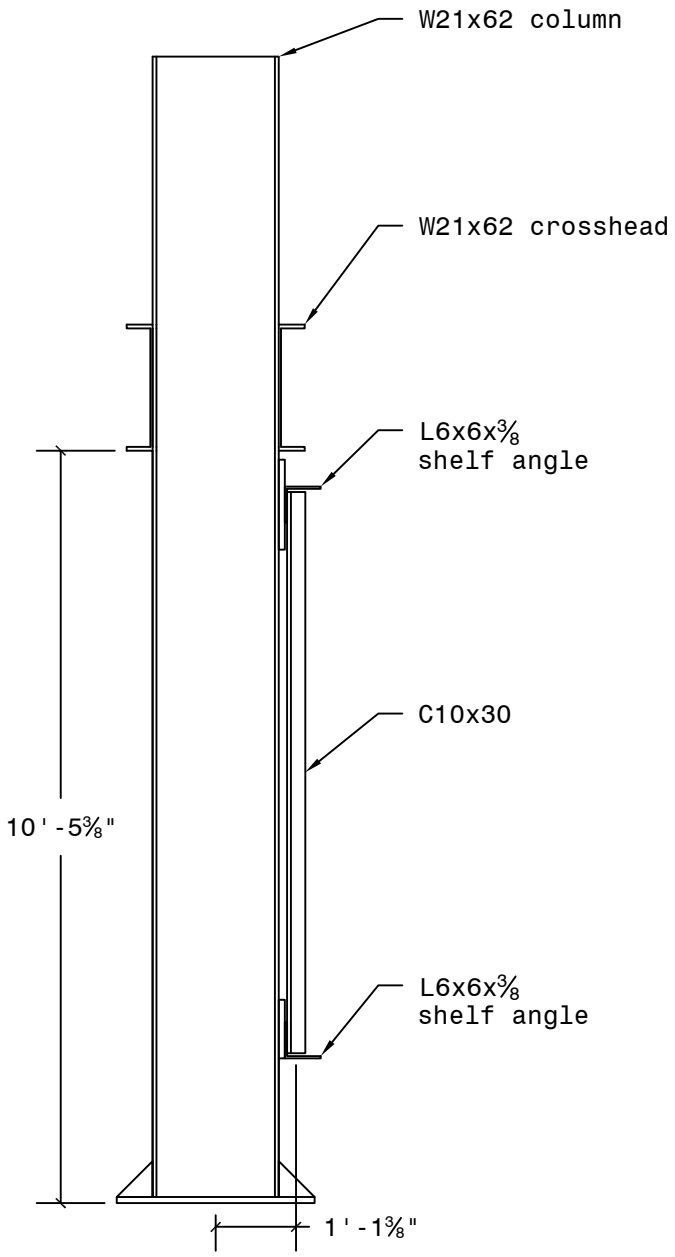

VIRGINIA TECH
CHARLES E. VIA JR. DEPARTMENT OF CIVIL & ENVIRONMENTAL ENGINEERING
200 PATTON HALL
BLACKSBURG, VA 24061
P: 540-231-6635

PROJECT:

MRF Protected Zone/Low-Cycle Fatigue

SHEET NOTES:

1. Scale is 3/8"=1'
2. W8x58 not shown

REVISIONS:

NO.	DATE	BY

DESIGNED BY:
DRAWN BY: R. Stevens
CHECKED BY:
DATE: 7/30/2020
PROJECT NO.:

SHEET TITLE:

East elevation of lateral-torsional buckling bracing frame

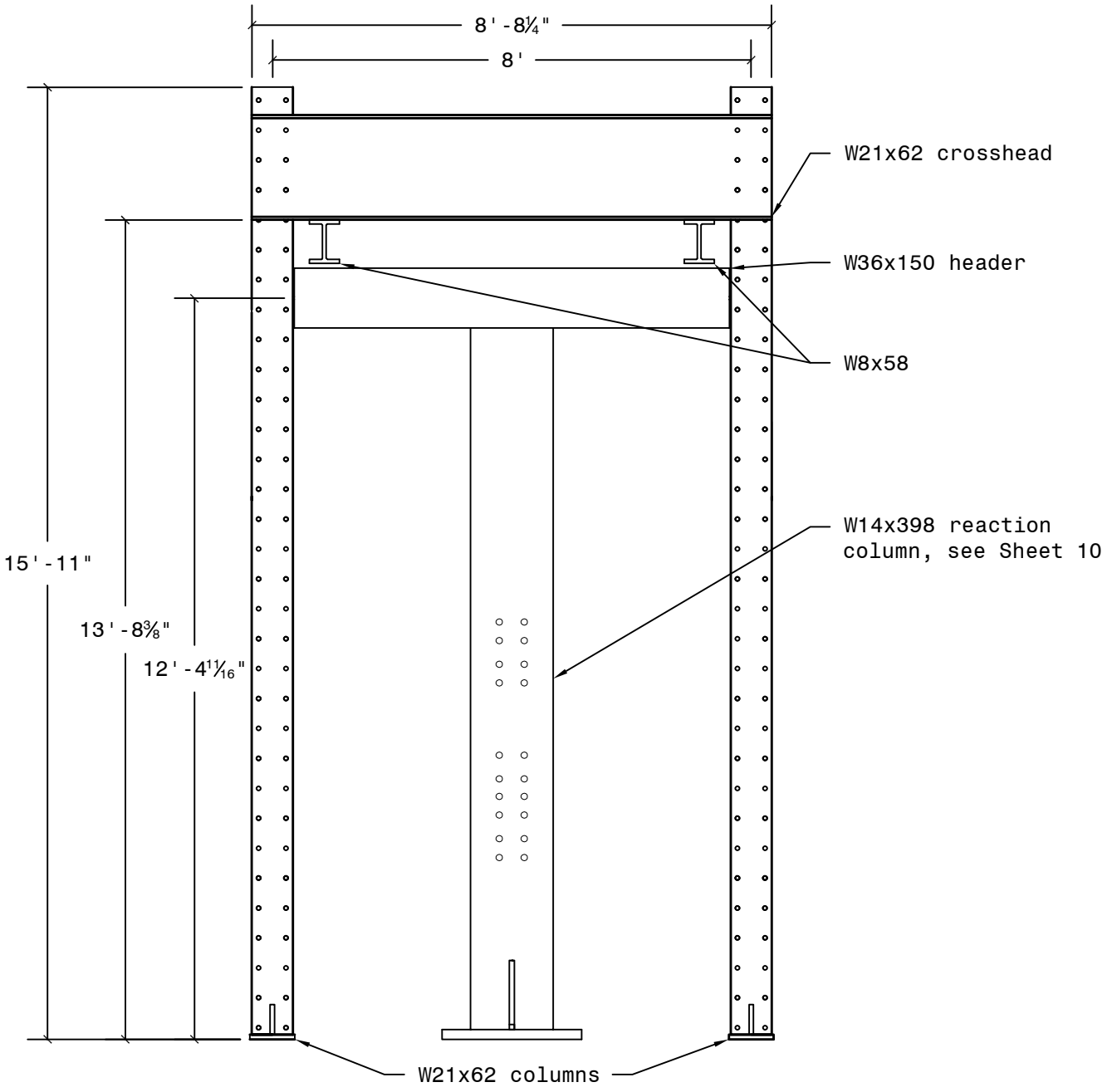

VIRGINIA TECH
CHARLES E. VIA JR. DEPARTMENT OF CIVIL & ENVIRONMENTAL ENGINEERING
200 PATTON HALL
BLACKSBURG, VA 24061
P: 540-231-6635

PROJECT:
MRF Protected Zone/Low-Cycle Fatigue

SHEET NOTES:
1. Scale is 3/8"=1'

REVISIONS:

NO.	DATE	BY

DESIGNED BY:
DRAWN BY: R. Stevens
CHECKED BY:
DATE: 7/30/2020
PROJECT NO.:

SHEET TITLE:
South elevation of column frame

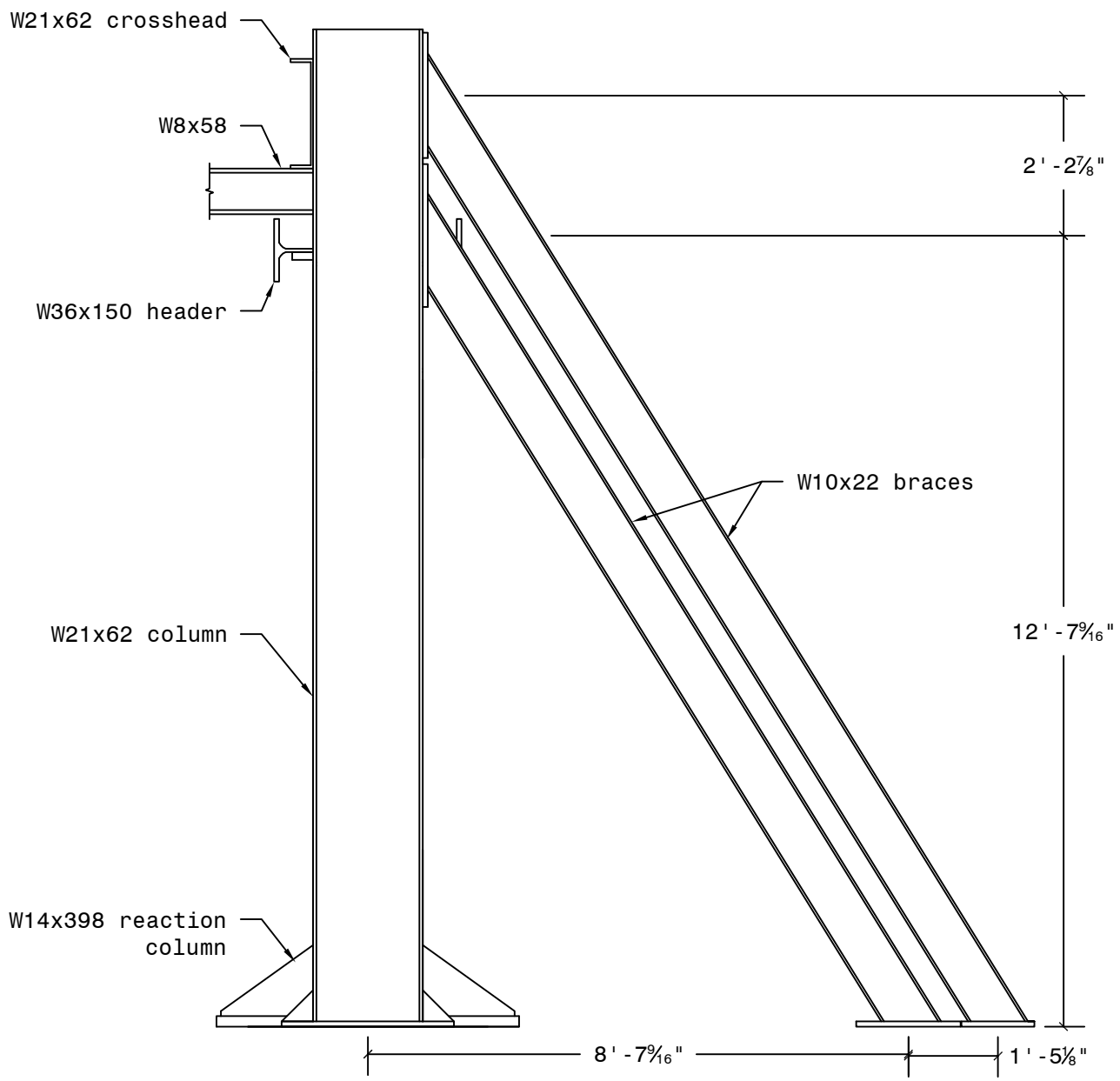

VIRGINIA TECH
CHARLES E. VIA JR. DEPARTMENT OF CIVIL & ENVIRONMENTAL ENGINEERING
200 PATTON HALL
BLACKSBURG, VA 24061
P: 540-231-6635

PROJECT:
MRF Protected Zone/Low-Cycle Fatigue

SHEET NOTES:
1. Scale is 3/8"=1'

REVISIONS:

NO.	DATE	BY

DESIGNED BY:
DRAWN BY: R. Stevens
CHECKED BY:
DATE: 7/30/2020
PROJECT NO.:

SHEET TITLE:
East elevation of column frame

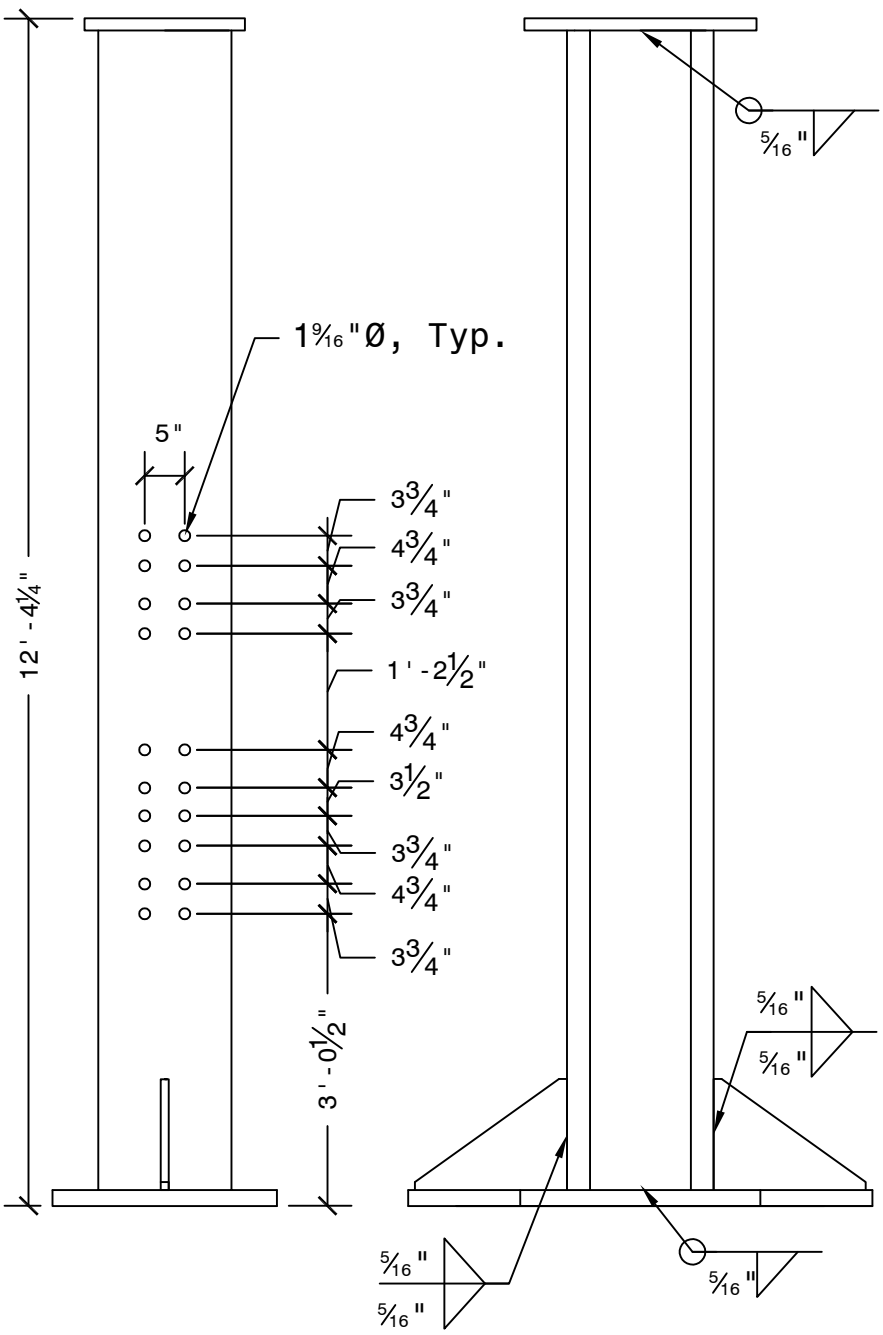

Column Elevations

Scale: 1/2" = 1'-0"

1 S10

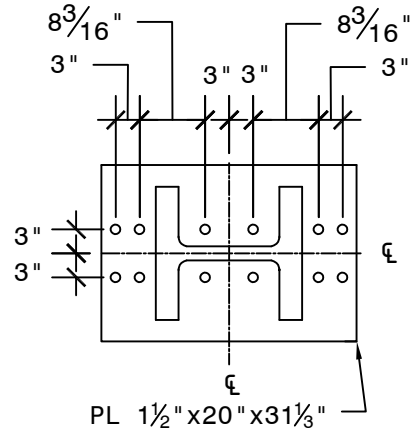

Top Plate

Scale: 1/2" = 1'-0"

2 S10

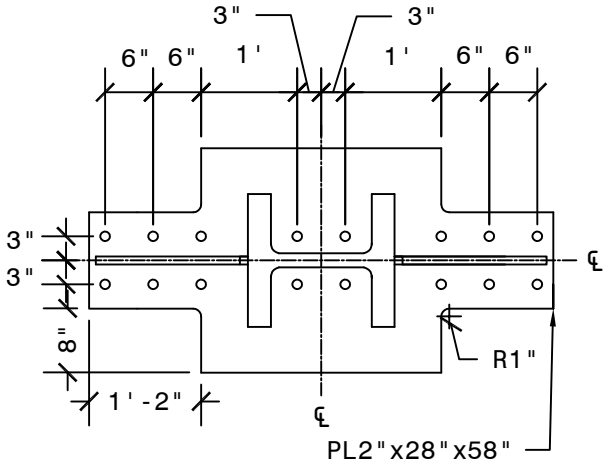

Base Plate

Scale: 1/2" = 1'-0"

3 S10

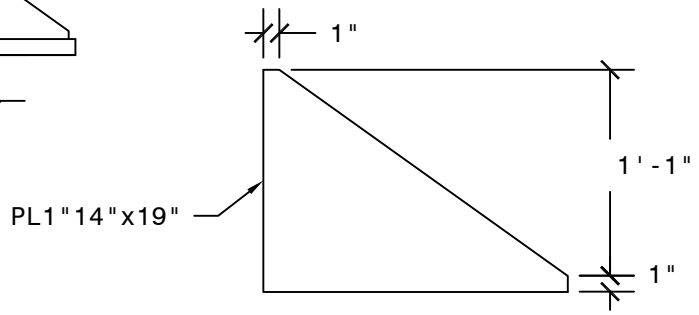

Base Plate Stiffeners

Scale: 1/2" = 1'-0"

4 S10

ADDITIONAL SHEET NOTES:
1. Holes in the column flange are centered horizontally on the flange.
2. Base plate and top plate holes are 1 1/16" Ø.

VIRGINIA TECH

VIRGINIA TECH
CHARLES E. VIA JR. DEPARTMENT OF CIVIL & ENVIRONMENTAL ENGINEERING
200 PATTON HALL
BLACKSBURG, VA 24061
P: 540-231-6635

PROJECT:

MRF Protected Zone/Low-Cycle Fatigue

SHEET NOTES:
1. The column shall be centered on the base plate and top plate in both directions.
2. Holes in the column are only drilled on one flange, as shown.

REVISIONS:

NO.	DATE	BY

DESIGNED BY:
DRAWN BY: R. Stevens
CHECKED BY:
DATE: 7/1/2020
PROJECT NO.:

SHEET TITLE:

W14x398 reaction column

SHEET NO.: 10 of 11

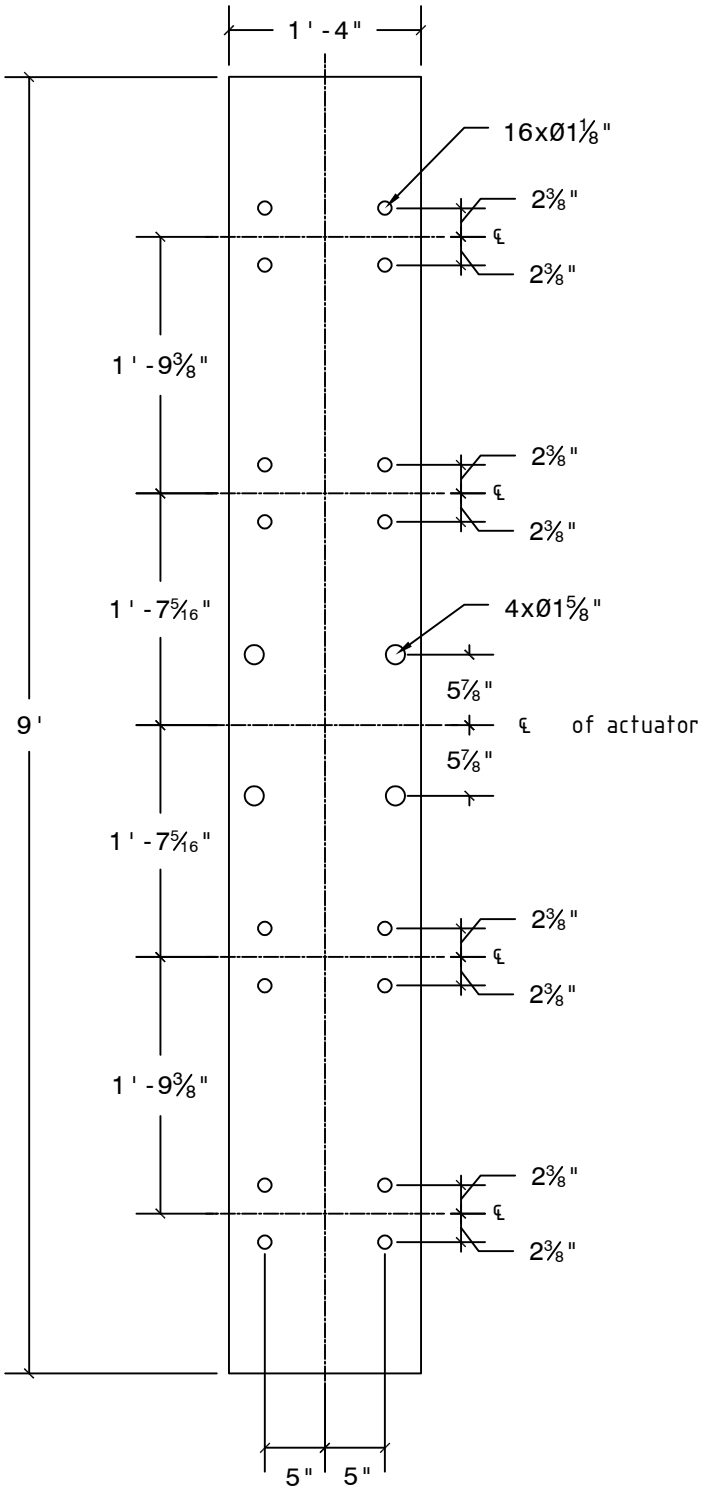

VIRGINIA TECH
CHARLES E. VIA JR. DEPARTMENT OF CIVIL & ENVIRONMENTAL ENGINEERING
200 PATTON HALL
BLACKSBURG, VA 24061
P: 540-231-6635

PROJECT:

MRF Protected Zone/Low-Cycle Fatigue

SHEET NOTES:

1. Scale is 3/4"=1"

REVISIONS:

NO.	DATE	BY

DESIGNED BY:

DRAWN BY: R. Stevens

CHECKED BY:

DATE: 7/30/2020

PROJECT NO.:

SHEET TITLE:

W14x257 actuator header

SHEET NO.: 11 of 11

Appendix B. Full-Scale Specimen Drawings

This appendix includes drawings for the W24×62 and W36×150 full-scale specimens.

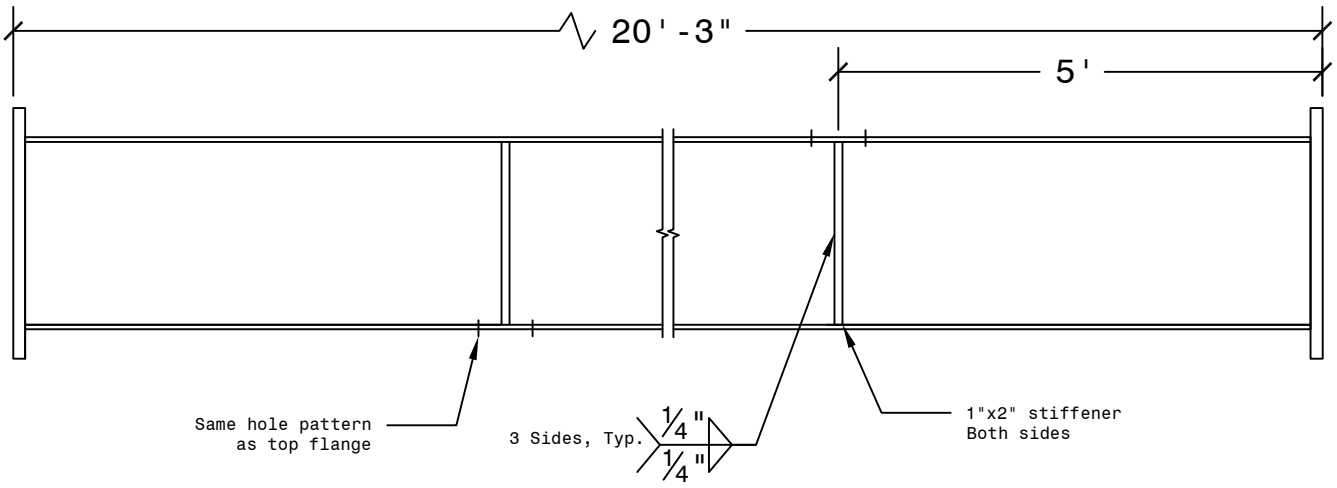

Elevation

Scale: 1/2" = 1'-0"

1

S1

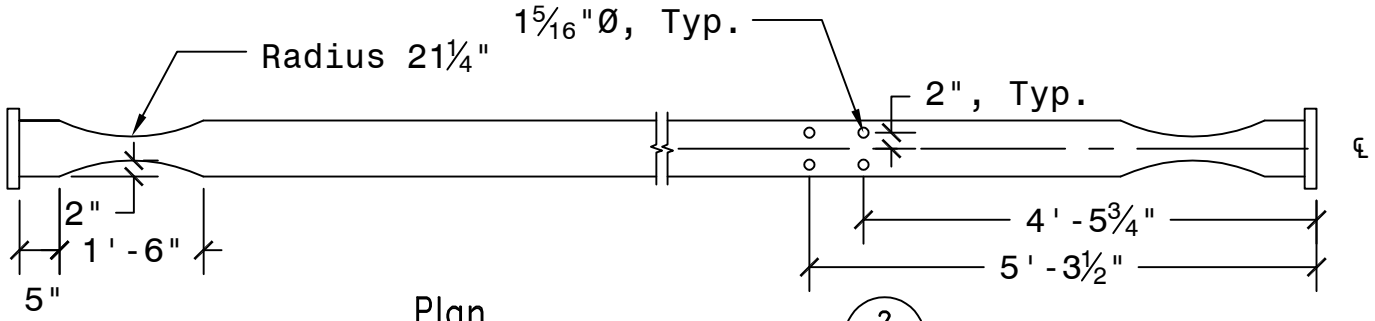

Plan

Scale: 1/2" = 1'-0"

2

S1

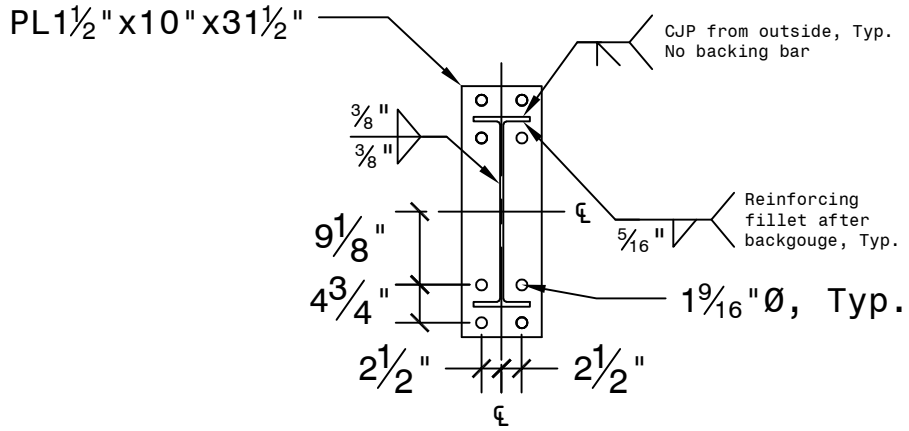

End-Plate

Scale: 1/2" = 1'-0"

3

S1

ADDITIONAL SHEET NOTES:

1. Weld metal shall have CVN toughness of 20 ft-lbs min. at 0 degrees F and 40 ft-lbs min. at 70 degrees F.
2. Beam material shall be A992; plate material shall be A572 Gr. 50.

VIRGINIA TECH

VIRGINIA TECH
CHARLES E. VIA JR. DEPARTMENT OF CIVIL & ENVIRONMENTAL ENGINEERING
200 PATTON HALL
BLACKSBURG, VA 24061
P: 540-231-6635

PROJECT:

MRF Protected Zone/Low-Cycle Fatigue

SHEET NOTES:

1. No weld access holes for beam flange welds.
2. The W24x62 beam shall be centered vertically and horizontally on the end-plate.

REVISIONS:

NO.	DATE	BY
1	5/8/2020	RS

DESIGNED BY:

DRAWN BY: R. Stevens

CHECKED BY:

DATE: 1/3/2019

PROJECT NO.:

SHEET TITLE:

W24x62 Specimens with Reduced Beam Section and 4-Bolt Extended Unstiffened Endplate

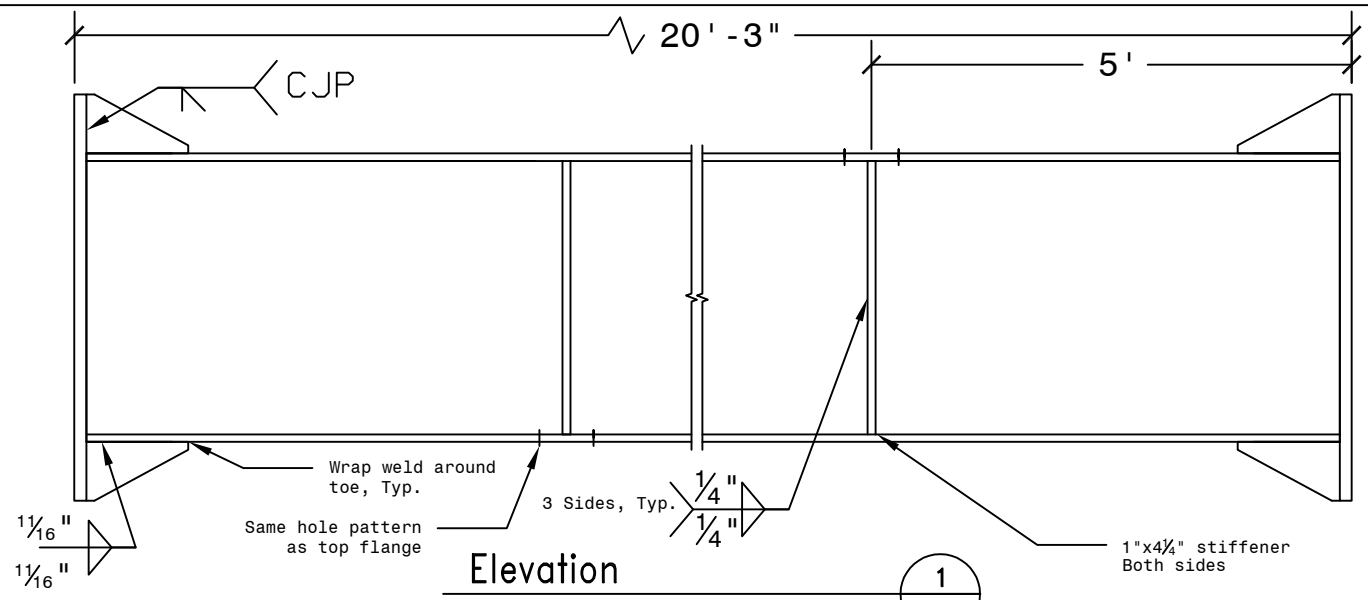

Elevation — 1 / S2

Scale: 1/2" = 1'-0"

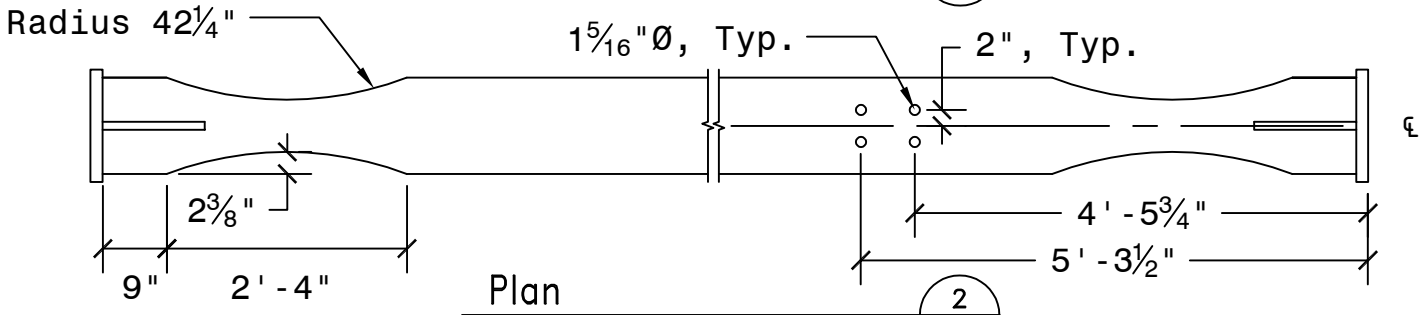

Plan — 2 / S2

Scale: 1/2" = 1'-0"

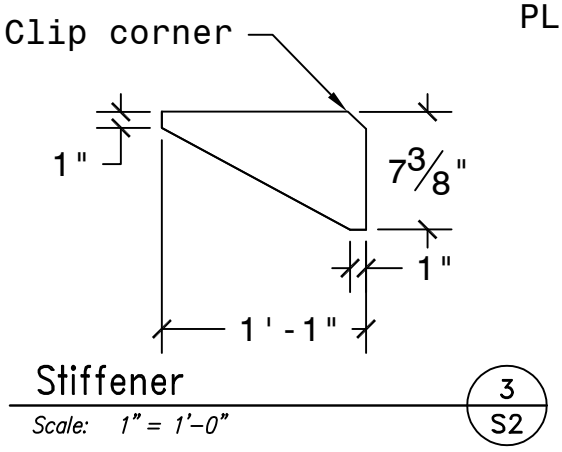

Stiffener — 3 / S2

Scale: 1" = 1'-0"

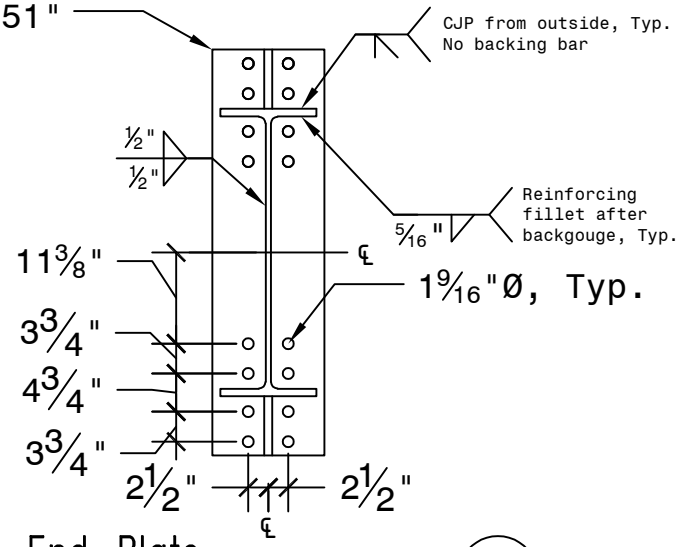

End-Plate — 4 / S2

Scale: 1/2" = 1'-0"

ADDITIONAL SHEET NOTES:

1. Weld metal shall have CVN toughness of 20 ft-lbs min. at 0 degrees F and 40 ft-lbs min. at 70 degrees F.
2. Beam material shall be A992; plate material shall be A572 Gr. 50.
3. Stiffener is 1" thick.

VIRGINIA TECH

VIRGINIA TECH
CHARLES E. VIA JR. DEPARTMENT OF CIVIL & ENVIRONMENTAL ENGINEERING
200 PATTON HALL
BLACKSBURG, VA 24061
P: 540-231-6635

PROJECT:

MRF Protected Zone/Low-Cycle Fatigue

SHEET NOTES:

1. No weld access holes for beam flange welds.
2. The W36x150 beam shall be centered vertically and horizontally on the end-plate.

REVISIONS:

NO.	DATE	BY
1	5/28/2020	RTS

DESIGNED BY:

DRAWN BY: R. Stevens

CHECKED BY:

DATE: 1/3/2019

PROJECT NO.:

SHEET TITLE:

W36x150 Specimens with Reduced Beam Section and 8-Bolt Extended Stiffened Endplate

SHEET NO.: 2 of 2

Appendix C. Weld Procedure Specification

This appendix includes the weld procedure specification used when welding the 0.25 in. deep notches. This section also includes the weld metal certificates from the manufacturer. Additional information about practice welds that were done to fine-tune the voltage and wire feed speed settings are given in Appendix X.

C.1 Weld Procedure Specification Steps

1. The base metal shall be ground to a depth of 0.25 in., $\pm$0.01 in. The finished taper shall not be greater than 1:5 parallel to the longitudinal axis of the member and 1:2.5 parallel to the transverse axis of the member (Section 6.18.5.1 in AWS D1.8).
2. The taper and surrounding base metal within 1 in. of the taper shall be ground and/or wire brushed to a bright metal finish.
3. Clean the taper and surrounding base metal with acetone or a nonchlorinated solvent and a clean rag to remove oil, grease, and dirt. The metal shall be dry before proceeding.
4. Weld tabs shall be tack welded to the base metal such that the tack weld is within the taper (see included drawings).
5. Preheat shall be applied using oxy-fuel torches held perpendicular to the plane of the taper.
6. A minimum preheat temperature of 150°F shall be established and maintained throughout the repair area until all welding is complete (Section 6.18.5.2 in AWS D1.8).
7. Upon attaining the required preheat temperature, commence welding in accordance with the included repair weld procedure specification.
8. The maximum interpass temperature shall be 550°F measured 3 in. from the edge of the weld, measured before each arc (Section 6.7.1 in AWS D1.8 and Section 5.6 in AWS D1.1).
9. Weld tabs shall be removed by grinding.
10. The completed weld shall be ground flush with surrounding base metal with a maximum remaining reinforcement of $\pm$0.063 in. (Section 6.18.5.2 of AWS D1.8).
11. The surface roughness of the ground weld shall not exceed 500 μin. (Section 6.18.5.2 of AWS D1.8).

12. Upon completion of grinding, the repaired area shall be allowed to cool to ambient temperature through natural means, and then examined by both visual and magnetic particle testing (Section 6.18.5.2 in AWS D1.8).

C.2 Filler Metal Notes

1. The filler metal used was E70C-6M H4 GMAW metal cored wire (Lincoln Electric MetalShield 706) that had been stored in a dry environment. See the included specification sheet and certificate from the manufacturer for more information.
2. The included AWS A5 Certificate of Conformance shall be adequate proof that the electrode meets diffusible hydrogen requirements (Section 6.1.2 in AWS D1.8).
3. The filler metal must have a minimum yield strength of 58 ksi, a minimum tensile strength of 70 ksi, and a minimum CVN toughness of 40 ft-lbf at 70°F (Table 6.2 in AWS D1.8).

Sample WPS Form (GMAW & FCAW)
WELDING PROCEDURE SPECIFICATION (WPS)

MRF Protected zone/low-cycle fatigue	Final	1	5/28/2019
Company Name	WPS No.	Rev. No.	Date
Authorized by / Date	Supporting PQR(s)	CVN Report	

BASE METALS	Specification	Type or Grade	AWS Group No.
Base Material	A992	Gr. 50	2
Welded To	N/A		
Backing Material	N/A		
Other			

BASE METAL THICKNESS	As-Welded	With PWHT
CJP Groove Welds		
CJP Groove w/CVN		
PJP Groove Welds		
Fillet Welds		
DIAMETER		

JOINT DETAILS	
Groove Type	Tapered
Groove Angle	1:5 in the longitudinal direction, 1:2.5 in the transverse direction
Root Opening	N/A
Root Face	N/A
Backgouging	None
Method	N/A

POSTWELD HEAT TREATMENT	
Temperature	
Time at Temperature	
Other	Natural cooling to ambient, time as required

JOINT DETAILS (Sketch)

See attached

PROCEDURE								
Weld Layer(s)	All							
Weld Pass(es)	All							
Process	GMAW							
Type *(Semiautomatic, Mechanized, etc.)*	Semiautomatic							
Position	1G							
Vertical Progression	N/A							
Filler Metal (AWS Spec.)	Fy = 58 ksi	Fu = 70 ksi	20 ft-lb at 0 F	40 ft-lb at 70 F	22% elongation	AWS D1.8 Table	6.1 and 6.2	
AWS Classification	E70C-6M H4							
Diameter	0.045"							
Manufacturer/Trade Name	Lincoln Electric	MetalShield	MC-706					
Shielding Gas (Composition)	92 Ar/8 CO2							
Flow Rate	35-50 CFM							
Nozzle Size	5/8"							
Preheat Temperature	>150 F	Measured 3 in.	from edge of weld.	AWS D1.8 6.18.5.2	AWS D1.1 5.6			
Interpass Temperature	Maximum 550 F	Checked before	each arc.	AWS D1.8 6.7.1				
Electrical Characteristics								
Current Type & Polarity	DCEP							
Transfer Mode	Globular							
Power Source Type (*cc, cv, etc.*)	CV							
Amps								
Volts	26.0							
Wire Feed Speed	195 in/min							
Travel Speed								
Maximum Heat Input								
Technique								
Stringer or Weave	Stringer							
Multi or Single Pass (per side)	Multi pass							
Oscillation (*Mechanized/Automatic*)	N/A							
Traverse Length	N/A							
Traverse Speed	N/A							
Dwell Time	N/A							
Number of Electrodes	Single							
Contact Tube to Work Distance	5/8" - 1"							
Peening	None							
Interpass Cleaning	Cleaned with	die grinder and	carbide burr	between each	pass.			
Other	See attached	sheet for step-by	step directions.					

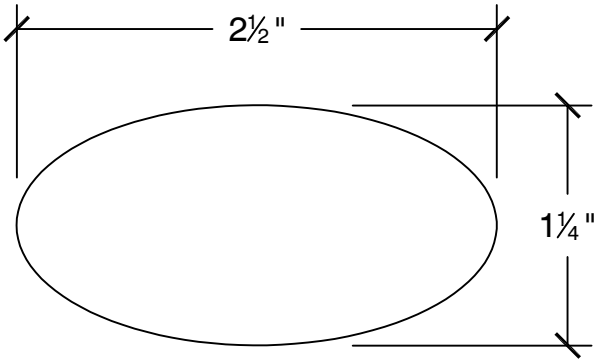

Actual dimensions (1 / S1)

Scale: 1" = 1"

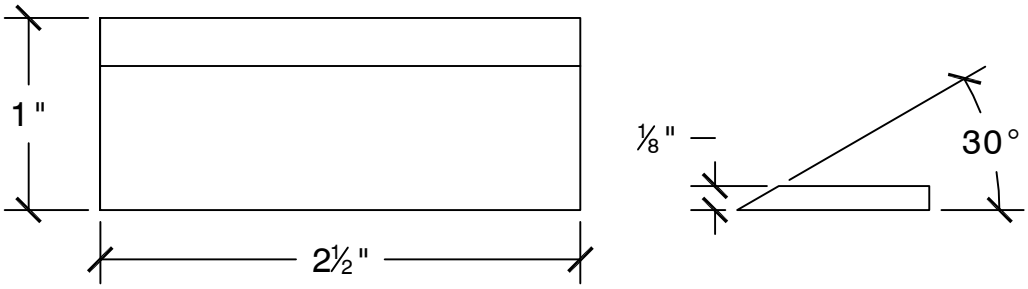

Runoff tab dimensions (2 / S1)

Scale: 1" = 1

VIRGINIA TECH

VIRGINIA TECH
CHARLES E. VIA JR. DEPARTMENT OF CIVIL & ENVIRONMENTAL ENGINEERING
200 PATTON HALL
BLACKSBURG, VA 24061
P: 540-231-6635

PROJECT:

MRF Protected Zone/Low-Cycle Fatigue

SHEET NOTES:

1. Artifact is 1/4" deep.

REVISIONS:

NO.	DATE	BY
0	5/13/2019	RTS
1	5/28/2019	RTS
1	6/6/2020	RTS

DESIGNED BY: R. STEVENS

DRAWN BY:

CHECKED BY:

DATE: 5/13/2019

PROJECT NO.:

SHEET TITLE:

1/4" Notch Ground to Taper and Filled with Weld Dimensions

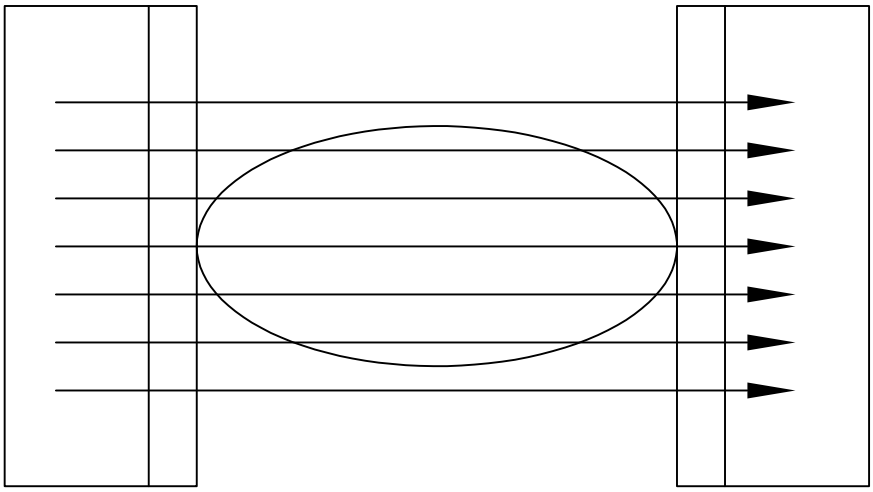

Weld direction

Scale: 1" = 1"

1
S2

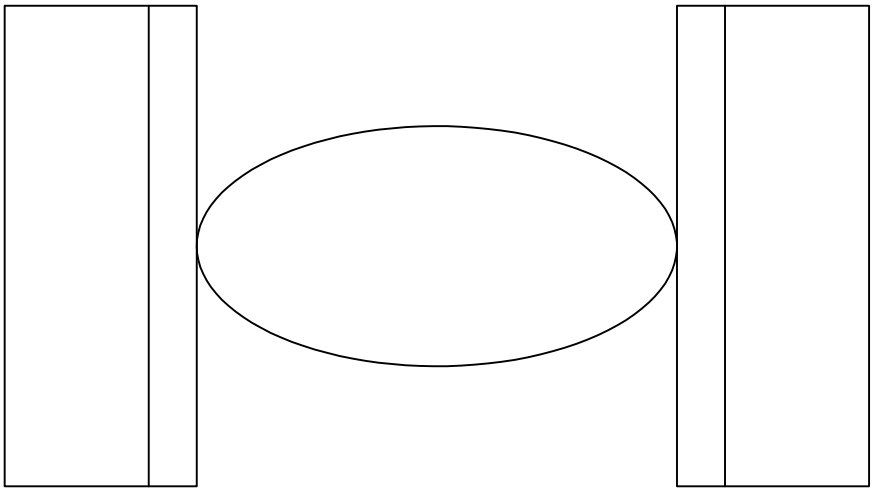

Runoff tab layout

Scale: 1" = 1"

2
S2

Runoff tab layout

Scale: 1" = 1"

3
S2

VIRGINIA TECH

VIRGINIA TECH
CHARLES E. VIA JR. DEPARTMENT OF CIVIL & ENVIRONMENTAL ENGINEERING
200 PATTON HALL
BLACKSBURG, VA 24061
P: 540-231-6635

PROJECT:

MRF Protected Zone/Low-Cycle Fatigue

SHEET NOTES:

1. Runoff tabs are removed after welding by grinding.

REVISIONS:

NO.	DATE	BY
0	5/28/2019	RTS
1	6/6/2020	RTS

DESIGNED BY: R. STEVENS

DRAWN BY:

CHECKED BY:

DATE: 5/13/2019

PROJECT NO.:

SHEET TITLE:

1/4" Notch Ground to Taper and Filled with Weld: Layout

The Lincoln Electric Company
22801 St. Clair Avenue
Cleveland, Ohio 44117-1199

CERTIFICATE OF CONFORMANCE

LINCOLN ELECTRIC
THE WELDING EXPERTS®

Product:	**Metalshield® MC®-706**
Classification:	**E70C-6M-H4**
	E70T15-M20A4-CS1-H4, E70T15-M21A4-CS1-H4
Specification:	**AWS A5.18:2005, ASME SFA-5.18**
	AWS A5.36:2016, ASME SFA-5.36
Date	**May 26, 2017**

This is to certify that the product named above is of the same classification(s) and design as the material used for the tests reported herein. The material was tested according to the specification(s) indicated and met all requirements. It was manufactured and supplied according to a Quality System Program that meets the requirements of ISO9001 among others as documented on The Lincoln Electric web page (*http://www.lincolnelectric.com/en-us/company/Pages/certifications.aspx*).

Operating Settings	**E70C-6M-H4 Requirements**	**E70T15-M21A4-CS1-H4 Requirements**	**RESULTS**
Required Size for Classification	1/16 inch	1/16 inch	1/16" (1.6 mm)
Current Type/Polarity	Not Specified	DC+ or DC-	DC+
Shielding Gas	75-80% Ar, balance CO2	M21-ArC	75% Ar, 25% CO2
Nominal Voltage, V	Not Specified		28
Wire Feed Speed, cm/min (in/min)	Not Specified		673 (265)
Nominal Current, A	Not Specified		350
Average Heat Input, kJ/mm (kJ/in)		(25 - 55)	1.5 (39)
Contact Tip to Work Distance, mm (in)	Not Specified		25 (1)
Travel Speed, cm/min (in/min)	Not Specified		41 (16)
Pass/Layers			14/7
Preheat Temperature, °C (°F)	(60 min.)	(60 min.)	20 (70)
Interpass Temperature, °C (°F)	(325 max.)	(325 max.)	165 (325)
Postweld Heat Treatment	As-welded	As-welded	As-welded

Mechanical properties of weld deposits

Tensile Strength, MPa (ksi)	(70 min.)	(70 - 95)	530 (77)
Yield Strength, 0.2% Offset, MPa (ksi)	(58 min.)	(58 min.)	450 (66)
Elongation %	22 min.	22 min.	30
Average Impact Energy Joules @ -40 °C (ft-lbs @ -40 °F)	(20 min.)	(20 min.)	60 (44) 56,60,64 (41,44,47)

Chemical composition of weld deposits (weight %)

C	0.12 max.	0.12 max.	0.05
Mn	1.75 max.	1.75 max.	1.31
Si	0.90 max.	0.90 max.	0.59
S	0.03 max.	0.030 max.	0.029
Cr	0.20 max.		0.07
P	0.03 max.	0.030 max.	0.01
Ni	0.50 max.		0.03
Mo	0.30 max.		0.02
V	0.08 max.		0.01
Cu	0.50 max.		0.07
B		Not Specified	0.0040
Ni+Cr+Mo+V	0.50 max.		0.13

Diffusible Hydrogen (per AWS A4.3)	**E70C-6M-H4 Requirements**	**E70T15-M21A4-CS1-H4 Requirements**	**RESULTS**
Required Size for Classification			1/16" (1.6 mm)
Current Type/Polarity			DC+
Shielding Gas			75% Ar, 25% CO2
Nominal Voltage, V			30
Diffusible Hydrogen, mL/100g	4.0 max.	4 max.	1.1
Abs. Humidity (gr moisture/lb dry air)			49

Cert. No. 95437

The Lincoln Electric Company
22801 St. Clair Avenue
Cleveland, Ohio 44117-1199

CERTIFICATE OF CONFORMANCE

LINCOLN ELECTRIC
THE WELDING EXPERTS®

Product: **Metalshield® MC®-706**
Classification: **E70C-6M-H4**
E70T15-M20A4-CS1-H4, E70T15-M21A4-CS1-H4
Specification: **AWS A5.18:2005, ASME SFA-5.18**
AWS A5.36:2016, ASME SFA-5.36
Date **May 26, 2017**

Operating Settings	E70T15-M20A4-CS1-H4 Requirements	RESULTS
Required Size for Classification	1/16 inch	1/16" (1.6 mm)
Current Type/Polarity	DC+ or DC-	DC+
Shielding Gas	M20-ArC	90% Ar, 10% CO2
Nominal Voltage, V		28
Wire Feed Speed, cm/min (in/min)		673 (265)
Nominal Current, A		350
Average Heat Input, kJ/mm (kJ/in)	(25 - 55)	1.7 (42.5)
Contact Tip to Work Distance, mm (in)		25 (1)
Travel Speed, cm/min (in/min)		38 (15)
Pass/Layers		14/7
Preheat Temperature, °C (°F)	(60 min.)	20 (70)
Interpass Temperature, °C (°F)	(325 max.)	165 (325)
Postweld Heat Treatment	As-welded	As-welded

Mechanical properties of weld deposits

Tensile Strength, MPa (ksi)	(70 - 95)	560 (81)
Yield Strength, 0.2% Offset, MPa (ksi)	(58 min.)	490 (71)
Elongation %	22 min.	30
Average Impact Energy Joules @ -40 °C (ft-lbs @ -40 °F)	(20 min.)	105 (78) 103,104,108 (76,77,80)

Chemical composition of weld deposits (weight %)

C	0.12 max.	0.04
Mn	1.75 max.	1.35
Si	0.90 max.	0.63
S	0.030 max.	0.023
P	0.030 max.	0.009
B	Not Specified	0.0040

Diffusible Hydrogen (per AWS A4.3)	E70T15-M20A4-CS1-H4 Requirements	RESULTS
Required Size for Classification		1/16" (1.6 mm)
Current Type/Polarity		DC+
Shielding Gas		90% Ar, 10% CO2
Nominal Voltage, V		29
Diffusible Hydrogen, mL/100g	4 max.	2
Abs. Humidity (gr moisture/lb dry air)		49

1. This document meets the requirements of EN10204, type 2.2, when a specific lot or order number is referenced. It does not meet the requirements of type 3.1.
2. The electrode size required to be tested for this classification is 1/16 inch. All other sizes manufactured will also meet these requirements.
3. Radiographic Inspection: Met requirements.
4. The strength and elongation properties were obtained from tensile specimens artificially aged at 105°C (220°F) for 48 hours.
5. Strength values in SI units are reported to the nearest 10 MPa converted from actual data. Preheat and interpass temperature values in SI units are reported to the nearest 5 degrees.

May 26, 2017

Gregory Mills, Supervisor, Testing and Certification — Date

May 26, 2017

Chris Hood, Manager, Quality Assurance — Date

Cert. No. 95437

The Lincoln Electric Company
22801 St. Clair Avenue
Cleveland, Ohio 44117-1199

CERTIFICATE OF CONFORMANCE

(APPLIES ONLY TO U.S. PRODUCTS)

LINCOLN ELECTRIC
THE WELDING EXPERTS®

Product: **Metalshield® MC®-706**
Electrode Lot Number: **14602191**
Classification: **E70C-6M-H4**
Specification: **AWS D1.8:2009**
Date **May 02, 2016**

This is to certify that the above listed product was manufactured to meet the Class T4 requirement of AWS A5.01 as required by clause 6.3.8.1 of AWS D1.8:2009.

The product stated herein was manufactured and supplied in accordance with the Quality System Program of The Lincoln Eletric Co., Cleveland, Ohio, U.S.A. as outlined in our Quality Assurance Manual. The Quality System Program of The Lincoln Electric Co. has been accepted by ASME, ABS and approved by VdTUV, and is certified to ISO 9001:2013

Operating Settings	AWS D1.8 Requirements	High Heat Input Results	Low Heat Input Results
Electrode Size		0.045 inch	0.045 inch
Polarity		DC+	DC+
Shielding Gas		90% Ar, 10% CO2	90% Ar, 10% CO2
Voltage, V		28	27
Wire Feed Speed, cm/min (in/min)		1143 (450)	953 (375)
Current, A		320	265
Average Heat Input, kJ/mm (kJ/in)		2.3 (59)	1.2 (30)
Contact Tip to Work Distance, mm (in)		22 (7/8)	22 (7/8)
Travel Speed, cm/min (in/min)		23 (9)	36 (14)
Pass/Layers		9/5	17/8
Preheat Temperature, °C (°F)		120 (250)	20 (70)
Interpass Temperature, °C (°F)		230 (450)	120 (250)
Weld Position		1G	1G
Mechanical properties of weld deposits			
Tensile Strength, MPa (ksi)	(70 min.)	530 (77)	580 (84)
Yield Strength, 0.2% Offset, MPa (ksi)	(58 min.)	430 (62)	520 (75)
Elongation %	22 min.	31	28
Average Impact Energy	(40 min.)	128 (95)	149 (110)
Joules @ 21 °C (ft-lbs @ 70 °F)		122,132,132 (90,97,97)	146,148,153 (108,110,113)
Average Impact Energy	(40 min.)	59 (43)	93 (68)
Joules @ -18 °C (ft-lbs @ 0 °F)		54,57,65 (40,42,48)	80,91,106 (59,67,78)

1. This product satisfies the requirements of AWS D1.8:2009, Annex E, after exposure for 72 hours at 80°F / 80% relative humidity.
2. The Charpy V-notch impact values reported at -18 °C (0 °F) are required when the Lowest Anticipated Service Temperature (LAST) is -29 °C (-20 °F).
3. The Charpy V-notch impact values reported at 21 °C (70 °F) are required when the Lowest Anticipated Service Temperature (LAST) is 10 °C (50 °F).
4. Test assembly constructed of ASTM A36 steel.
5. The strength and elongation properties reported here were obtained from tensile specimens artificially aged at 105°C (220°F) for 48 hours.
6. Strength values in SI units are reported to the nearest 10 MPa converted from actual data. Preheat and interpass temperature values in SI units are reported to the nearest 5 degrees.

Toronto Cunningham — May 02, 2016
Toronto Cunningham, Certification Supervisor — Date

Marie Quintana — May 02, 2016
Marie Quintana, Director, Consumable Compliance — Date

Cert. No. 17116

Metalshield® MC-6®

Mild Steel • AWS E70C-6M H4

Key Features

- Excellent performance in fast follow, high travel speed applications
- Optimal wetting action, even at low voltages
- H4 diffusible hydrogen level
- Use with Rapid-Arc® Waveform Control Technology®
- Deoxidizing arc action minimizes pre-weld work

Conformances

AWS A5.18/A5.18M: 2005	E70C-6M H4
ASME SFA-A5.18:	E70C-6M H4
CWB/CSA W48-06:	E491C-6MJ-H4

Welding Positions

All

Typical Applications

- Robotics/Hard automation
- Automotive
- Structural fabrication
- Process piping and pressure vessels
- General fabrication

Shielding Gas

75-95% Argon / Balance CO_2
Flow Rate: 40-60 CFH

DIAMETERS / PACKAGING

Diameter in (mm)	33 lb (15 kg) Steel Spool	50 lb (22.7 kg) Fiber Spool	60 lb (27.2 kg) Coil	500 lb (227 kg) Accu-Trak® Drum
0.045 (1.1)	ED030392	ED030554	ED030549	ED031011
0.052 (1.3)	ED030393	ED030556	ED030550	ED030946
1/16 (1.6)	ED030394	ED030555	ED030577	ED030947

MECHANICAL PROPERTIES[1] – *As Required per AWS A5.18/A5.18M: 2005*

	Yield Strength[2] MPa (ksi)	Tensile Strength MPa (ksi)	Elongation %	Charpy V-Notch J (ft•lbf) @ -29°C (-20°F)	Charpy V-Notch J (ft•lbf) @ -40°C (-40°F)
Requirements - AWS E70C-6M H4	400 (58) min.	480 (70) min.	22 min.	27 (20) min.	Not Specified
Typical Performance[3]					
As-Welded with 75% Argon / 25% CO_2[4]	450-510 (65-75)	510-590 (75-85)	24-28	81-122 (60-90)	47-75 (35-55)
As-Welded with 90% Argon / 10% CO_2	480-550 (70-80)	550-620 (80-90)	24-28	75-102 (55-75)	61-81 (45-60)

Metalshield® MC-6®

(AWS E70C-6M H4)

DEPOSIT COMPOSITION[1] – *As Required per AWS A5.18/A5.18M: 2005*

	%C	%Mn	%Si	%S	%P	%Cu
Requirements - AWS E70C-6M H4	0.12 max.	1.75 max.	0.90 max.	0.03 max.	0.03 max.	0.50 max.
Typical Performance[3]						
As-Welded with 75% Argon / 25% CO_2[4]	0.03-0.05	1.25-1.60	0.40-0.60	0.01-0.02	0.01-0.02	0.01-0.05
As-Welded with 90% Argon / 10% CO_2	0.03-0.05	1.25-1.70	0.40-0.70	0.01-0.02	0.01-0.02	0.01-0.05

	%Ni	%Cr	%Mo	%V	%Ni + %Cr + %Mo + %V	Diffusible Hydrogen (mL/100g weld deposit)
Requirements - AWS E70C-6M H4	0.50 max.	0.20 max.	0.30 max.	0.08 max.	0.50 max.	≤ 4
Typical Performance[3]						
As-Welded with 75% Argon / 25% CO_2[4]	0.02-0.05	0.01-0.04	0.01-0.02	0.01-0.02	0.05-0.10	2-4
As-Welded with 90% Argon / 10% CO_2	0.02-0.05	0.01-0.04	0.01-0.02	0.01-0.02	0.05-0.10	

TYPICAL OPERATING PROCEDURES

Diameter, Polarity Shielding Gas	CTWD[5] mm (in)	Wire Feed Speed m/min (in/min)	Voltage[6] (volts)	Approx. Current (amps)	Melt-Off Rate kg/hr (lb/hr)	Deposition Rate kg/hr (lb/hr)	Efficiency (%)
0.045 in (1.1 mm), DC+ 90% Argon / 10% CO_2	19-25 (3/4-1)	5.1 (200)	21-23	170	2.5 (5.6)	2.3 (5.2)	92
		6.4 (250)	22-25	190	2.9 (6.4)	2.7 (6.1)	95
		7.6 (300)	22-26	210	3.5 (7.8)	3.2 (7.1)	92
		8.9 (350)	22-27	245	4.1 (9.1)	3.9 (8.7)	95
		10.2 (400)	23-27	265	4.6 (10.2)	4.5 (9.9)	97
		12.7 (500)	23-28	300	5.7 (12.6)	5.6 (12.4)	98
		15.2 (600)	25-29	335	7.0 (15.4)	6.9 (15.3)	99
		17.8 (700)	26-30	370	8.1 (17.8)	7.9 (17.5)	98
0.052 in (1.3 mm), DC+ 90% Argon / 10% CO_2	19-25 (3/4-1)	5.1 (200)	22-24	220	3.2 (7.0)	2.9 (6.4)	92
		6.4 (250)	22-26	260	4.0 (8.7)	3.8 (8.3)	95
		7.6 (300)	22-27	300	4.9 (10.7)	4.7 (10.3)	96
		8.9 (350)	23-27	335	5.6 (12.3)	5.5 (12.0)	98
		10.2 (400)	24-28	360	6.3 (13.9)	6.3 (13.8)	99
		12.7 (500)	27-30	410	7.9 (17.4)	7.8 (17.3)	99
		15.2 (600)	27-31	455	9.5 (21.1)	9.4 (20.8)	99
1/16 in (1.6 mm), DC+ 90% Argon / 10% CO_2	25-32 (1-1 1/4)	2.5 (100)	21-24	175	2.1 (4.7)	2.0 (4.4)	93
		3.8 (150)	22-25	235	3.2 (7.1)	2.9 (6.4)	90
		5.1 (200)	22-26	290	4.3 (9.5)	4.0 (8.9)	94
		6.4 (250)	22-28	345	5.4 (11.9)	5.2 (11.4)	96
		7.6 (300)	23-29	360	6.4 (14.2)	6.3 (13.9)	98
		10.2 (400)	26-31	425	8.5 (18.7)	8.4 (18.5)	99
		12.7 (500)	27-32	485	10.8 (23.8)	10.7 (23.5)	99

[1]Typical all weld metal. [2]Measured with 0.2% offset. [3]See test results disclaimer below. [4]Required gas mixture 75-80% Argon/Balance CO_2 for AWS testing.
[5]To estimate ESO, subtract 3/16 in (4.8 mm) from CTWD. [6]For greater percentage of CO_2 shielding gas, increase voltage by 1-2 volts.

Material Safety Data Sheets (MSDS) and Certificates of Conformance are available on our website at www.lincolnelectric.com

TEST RESULTS

Test results for mechanical properties, deposit or electrode composition and diffusible hydrogen levels were obtained from a weld produced and tested according to prescribed standards, and should not be assumed to be the expected results in a particular application or weldment. Actual results will vary depending on many factors, including, but not limited to, weld procedure, plate chemistry and temperature, weldment design and fabrication methods. Users are cautioned to confirm by qualification testing, or other appropriate means, the suitability of any welding consumable and procedure before use in the intended application.

CUSTOMER ASSISTANCE POLICY

The Lincoln Electric Company is manufacturing and selling high quality welding equipment, consumables, and cutting equipment. Our challenge is to meet the needs of our customers and to exceed their expectations. On occasion, purchasers may ask Lincoln Electric for information or advice about their use of our products. Our employees respond to inquiries to the best of their ability based on information provided to them by the customers and the knowledge they may have concerning the application. Our employees, however, are not in a position to verify the information provided or to evaluate the engineering requirements for the particular weldment. Accordingly, Lincoln Electric does not warrant or guarantee or assume any liability with respect to such information or advice. Moreover, the provision of such information or advice does not create, expand, or alter any warranty on our products. Any express or implied warranty that might arise from the information or advice, including any implied warranty of merchantability or any warranty of fitness for any customers' particular purpose is specifically disclaimed.

Lincoln Electric is a responsive manufacturer, but the selection and use of specific products sold by Lincoln Electric is solely within the control of, and remains the sole responsibility of the customer. Many variables beyond the control of Lincoln Electric affect the results obtained in applying these types of fabrication methods and service requirements.

Subject to Change – This information is accurate to the best of our knowledge at the time of printing. Please refer to www.lincolnelectric.com for any updated information.

THE LINCOLN ELECTRIC COMPANY
22801 St. Clair Avenue • Cleveland, OH • 44117-1199 • U.S.A.
Phone: +1.216.481.8100 • www.lincolnelectric.com

LINCOLN® ELECTRIC
THE WELDING EXPERTS®

Issue Date 01/12

Appendix D. Artifact Layouts

This appendix includes drawings for the artifact layouts on the full-scale tests.

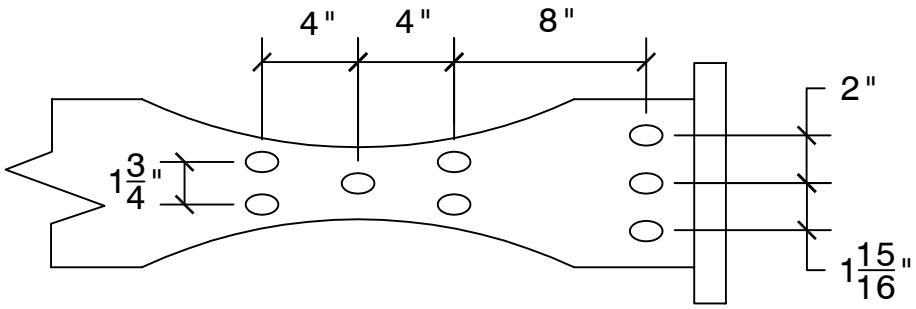

0.125NGT

Scale: 3" = 2'-0"

1 / S1

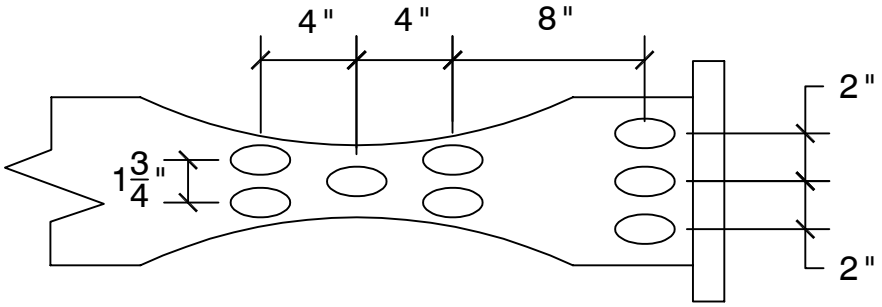

0.25NGTW

Scale: 3" = 2'-0"

2 / S1

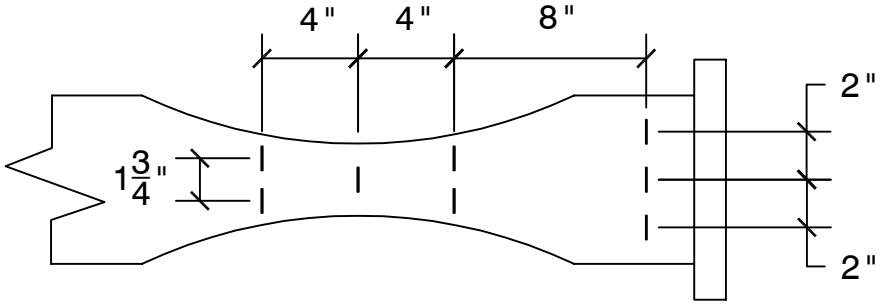

0.25N

Scale: 3" = 2'-0"

3 / S1

VIRGINIA TECH

VIRGINIA TECH
CHARLES E. VIA JR. DEPARTMENT OF CIVIL & ENVIRONMENTAL ENGINEERING
200 PATTON HALL
BLACKSBURG, VA 24061
P: 540-231-6635

PROJECT:

MRF Protected Zone/Low-Cycle Fatigue

SHEET NOTES:

REVISIONS:

NO.	DATE	BY

DESIGNED BY:

DRAWN BY: R. Stevens

CHECKED BY:

DATE: 5/8/2020

PROJECT NO.:

SHEET TITLE:

W24x62 Artifact Layouts

SHEET NO.: 1 of 2

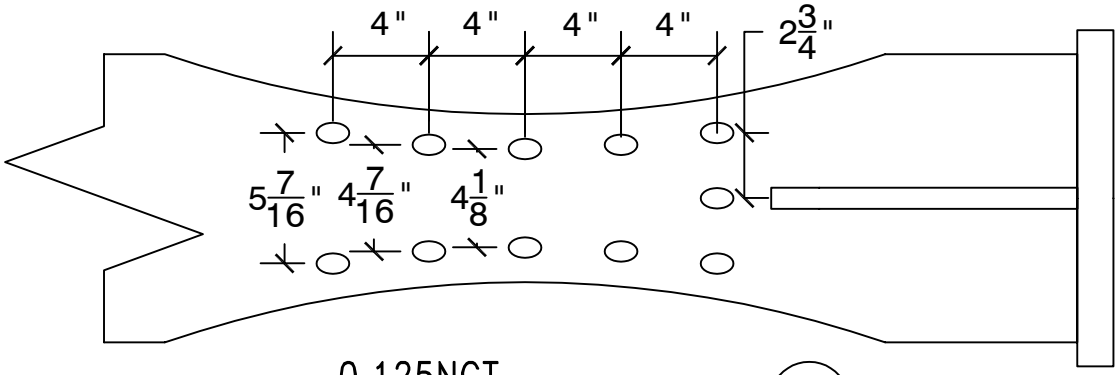

0.125NGT — 1 / S2

Scale: 3" = 2'-0"

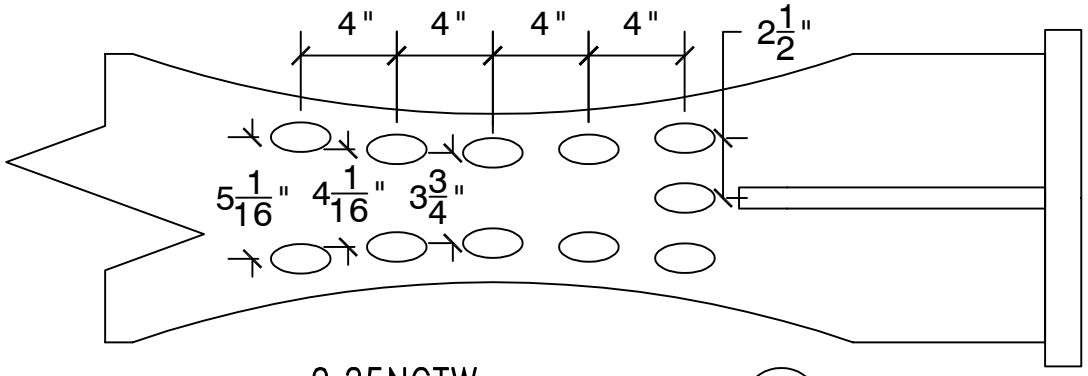

0.25NGTW — 2 / S2

Scale: 3" = 2'-0"

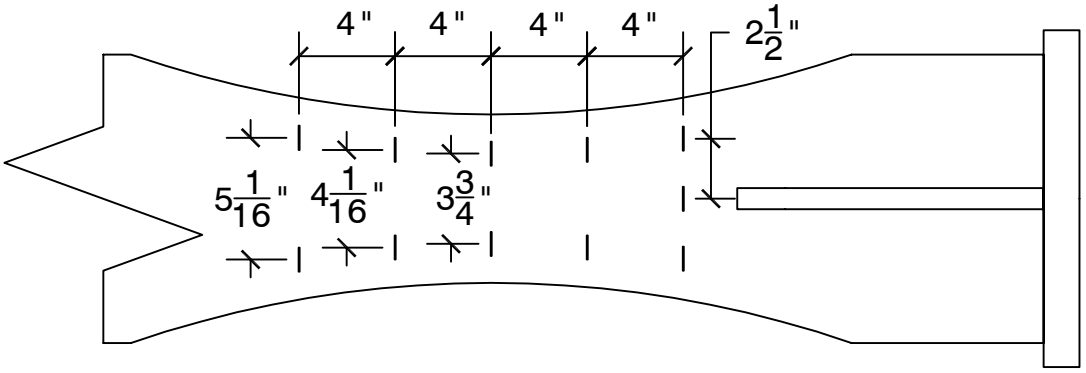

0.25N — 3 / S2

Scale: 3" = 2'-0"

VIRGINIA TECH

VIRGINIA TECH
CHARLES E. VIA JR. DEPARTMENT OF CIVIL & ENVIRONMENTAL ENGINEERING
200 PATTON HALL
BLACKSBURG, VA 24061
P: 540-231-6635

PROJECT:

MRF Protected Zone/Low-Cycle Fatigue

SHEET NOTES:

REVISIONS:

NO.	DATE	BY

DESIGNED BY:

DRAWN BY: R. Stevens

CHECKED BY:

DATE: 5/8/2020

PROJECT NO.:

SHEET TITLE:

W36x150 Artifact Layouts

SHEET NO.: 2 of 2

Appendix E. Story Drift Decomposition

This appendix presents equations for decomposing the applied story drift into components due to panel zone shear, column flexure, end-plate separation, elastic deformation, and plastic hinge rotation. This is necessary because the inelastic rotation developed in each element or member of the test specimen must be within 25% of the anticipate inelastic rotation developed in the same element or member of the prototype connection (AISC 2016b). Unless otherwise stated, these equations are adapted from Toellner (2013) and Szabo (2017).

E.1 Panel Zone Shear

The calculations for story drift due to panel zone shear and rigid body rotation of the panel zone are adapted from Uang and Bondad (1996). The average panel zone shear strain, $\bar{\gamma}$, was first calculated using Eq. (E.1),

$$\bar{\gamma} = \frac{\sqrt{(d_c - t_{cf})^2 + (d_b - t_{bf})^2}}{2(d_c - t_{cf})(d_b - t_{bf})}(\delta_{LP\_02} - \delta_{LP\_01}) \tag{E.1}$$

where: d_b = beam depth
d_c = column depth
t_{bf} = beam flange thickness
t_{cf} = column flange thickness
δ_{LP_01} = displacement of LP_01
δ_{LP_02} = displacement of LP_02.

Equation (E.1) assumes that the ends of LP_01 and LP_02 were placed at the intersections of the centerlines of the beam and column flanges. If this was not the case, $(d_c - t_{cf})$ and $(d_b - t_{bf})$ would be replaced with the actual horizontal and vertical distances, respectively, between the ends of the potentiometers. The deflection at the loading point, δ_{PZ}, due to the panel zone shear was calculated using Eq. (E.2), and the story drift due to panel zone shear, θ_{PZ}, was calculated using Eq. (E.3).

$$\delta_{PZ} = \bar{\gamma}(L_{cl} - \frac{d_c}{2}) - \frac{\bar{\gamma} d_b}{h_{col}} L_{cl} \tag{E.2}$$

$$\theta_{PZ} = \frac{\delta_{PZ}}{L_{cl}} \tag{E.3}$$

where: d_b = beam depth

d_c = column depth

h_{col} = distance between SP_01 and SP_08

L_{cl} = distance from the actuator centerline to the column centerline.

E.2 Column Flexure

Column deformations include rigid body rotations of the frame, panel zone shear, and column flexure. While rigid body rotation was accounted for during testing, it needs to be removed again to isolate the rotation due to column flexure. The story drift due to rigid body rotation of the column, θ_{RB}, was calculated using Eq. (E.4). The story drift due to column flexure, θ_{CF}, was then calculated using Eq. (E.5).

$$\theta_{RB} = \frac{\delta_{SP\_01} - \delta_{SP\_08}}{h_{col}} \tag{E.4}$$

$$\theta_{CF} = \frac{\delta_{SP\_02} - \delta_{SP\_03}}{L_{sp1}} - \theta_{RB} - \theta_{PZ} \tag{E.5}$$

where: h_{col} = distance between SP_01 and SP_08

L_{sp1} = distance between SP_02 and SP_03

δ_{SP_01} = displacement of SP_01

δ_{SP_02} = displacement of SP_02

δ_{SP_03} = displacement of SP_03

δ_{SP_08} = displacement of SP_08.

If SP_02 and SP_03 are placed at the centerlines of the beam flanges, L_{sp1} can be replaced with $d_b - t_{bf}$, where d_b is the depth of the beam and t_{bf} is the thickness of the beam flanges.

E.3 End-Plate Separation

The bolts were pretensioned when the test specimens were bolted to the reaction column, but during testing the moment created in the plastic hinge can create bolt forces that exceed the pretension. If this occurs, the end-plate will separate from the column flange, which contributes to the applied drift. This separation was measured by the spring calipers CLP_01 and CLP_02, placed at the centerlines of the top and bottom beam flanges. Since the spring calipers were not used on the first two tests, the story drift component due to end-plate separation was included in the plastic hinge

rotation. The story drift due to the end-plate separation, θ_{EP}, was calculated using Eq. (E.6),

$$\theta_{EP} = \frac{-\delta_{CLP}}{d_b - t_{bf}} \tag{E.6}$$

where: d_b = beam depth
t_{bf} = beam flange thickness
δ_{CLP} = displacement measured by the caliper.

Equation (E.6) assumes that small-angle theory applies, and that the beam is rotating about the centerline of the opposite flange. If the calipers were placed on the inside of the flange, as has been done in past moment connection tests, $(d_b - t_{bf})$ would be replaced with $(d_b - \frac{3}{2}t_{bf})$ (Szabo 2017).

E.4 Elastic Beam Deformation

Outside of the plastic hinge region, the beam is deforming elastically, which has flexure and shear components. The shear component was calculated by Timoshenko (1955). The elastic deflection at the loading point, δ_{el}, was calculated using Eq. (E.8), which required the shape factor α from Eq. (E.7). The story drift due to elastic beam deformation outside the plastic hinge region, θ_{EL}, was then calculated using Eq. (E.9).

$$\alpha = \frac{A}{8I_x t_w}(b_f d_b^2 - b_f h_w^2 + t_w h_w^2) \tag{E.7}$$

$$\delta_{el} = \frac{PL_{el}^3}{3EI_x} + \frac{PL_{el}\alpha}{AG} \tag{E.8}$$

$$\theta_{EL} = \frac{\delta_{el}}{L_{cl}} \tag{E.9}$$

where: A = cross-sectional area
b_f = flange width
d_b = beam depth
E = modulus of elasticity
G = shear modulus
h_w = clear distance between flanges
I_x = moment of inertia of the beam
L_{cl} = distance from the actuator centerline to the column centerline
L_{el} = distance from SP_04 to actuator centerline
P = applied load
t_w = web thickness.

E.5 Plastic Hinge Rotation

In these tests, deformation in the plastic hinge region was expected to be the greatest story drift component. To measure this rotation, string potentiometers SP_06 and SP_07 were attached to the column flange above and below the beam. The end of the string potentiometers were attached to the beam at the same location as SP_04. The rotation due to deformation in the plastic hinge region, θ_{PH}, was then calculated using Eq. (E.10),

$$\theta_{PH} = -(\frac{\delta_{SP\_06} - \delta_{SP\_07}}{L_{sp2}}) - \theta_{EP} \tag{E.10}$$

where: L_{sp2} = distance between SP_06 and SP_07

δ_{SP_06} = displacement of SP_06

δ_{SP_07} = displacement of SP_07.

It is important to note that Eq. (E.10) also includes elastic beam rotation. Thus, in the early cycles when no plastic deformation is expected, θ_{PH} will be nonzero.

E.6 Total Story Drift

The total story drift is calculated using Eq. (E.11).

$$\theta_{total} = \theta_{CF} + \theta_{PZ} + \theta_{EP} + \theta_{EL} + \theta_{PH} \tag{E.11}$$

If the calculated total story drift is checked against the applied story drift, discrepancies will be found. This is due to simplifying assumptions made in the decomposition and drift components that were not captured by this instrumentation plan.

Appendix F. Instrumentation Wiring Diagram

This appendix includes the wiring diagram for the full-scale tests.

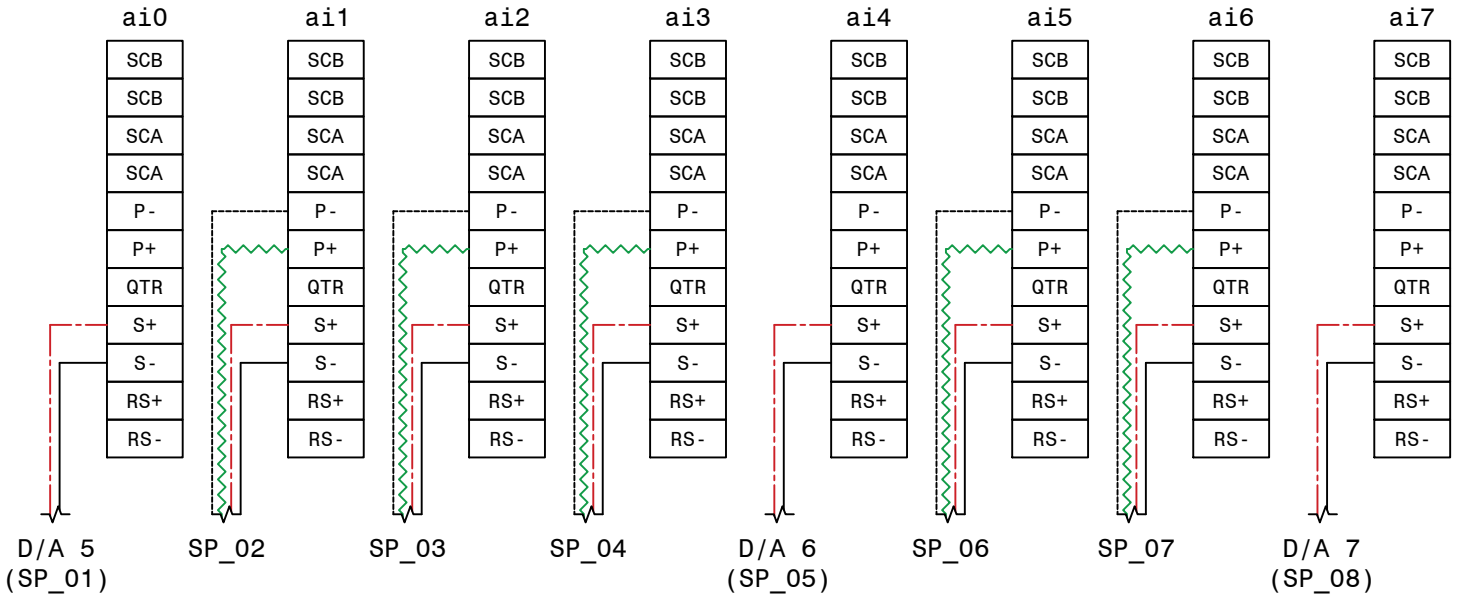

SC1 Mod1

Scale: NTS

1 / S1

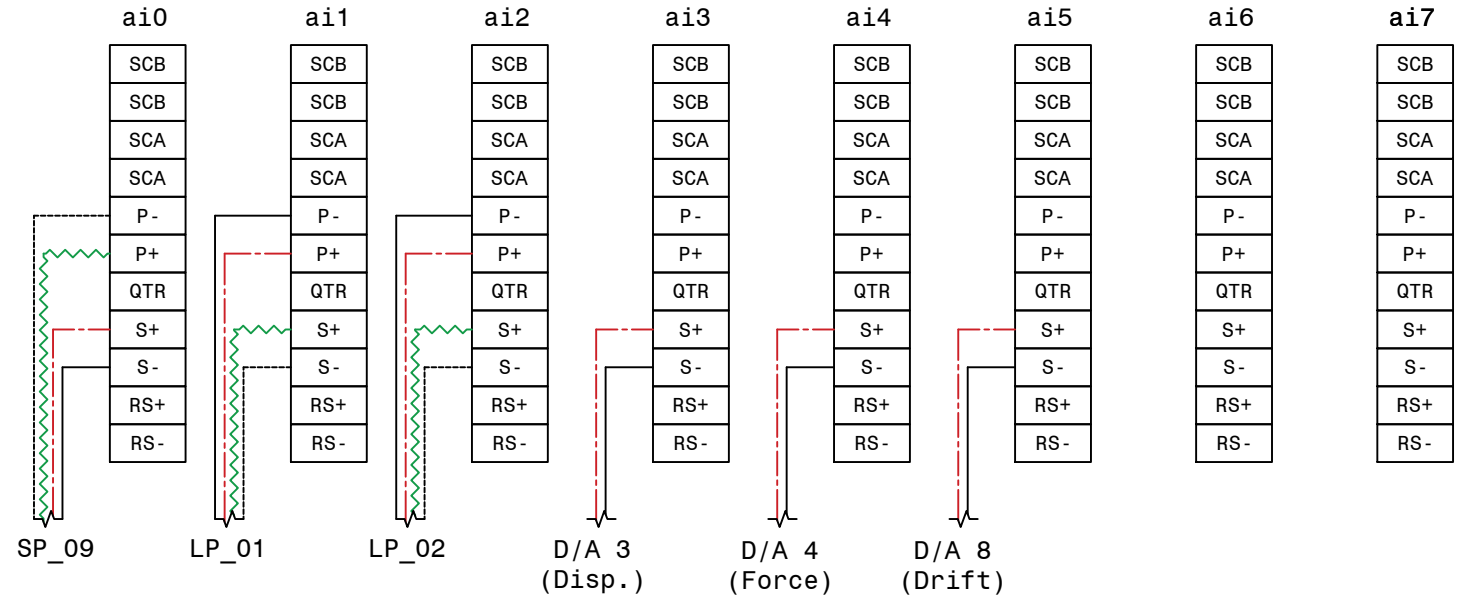

SC1 Mod2

Scale: NTS

2 / S1

Red
Black
Green
White

VIRGINIA TECH

VIRGINIA TECH
CHARLES E. VIA JR. DEPARTMENT OF CIVIL & ENVIRONMENTAL ENGINEERING
200 PATTON HALL
BLACKSBURG, VA 24061
P: 540-231-6635

PROJECT:

MRF Protected Zone/Low-Cycle Fatigue

SHEET NOTES:

1. D/A 3-8 are digital to analog outputs from the MTS FlexTest 60 controller.

REVISIONS:

NO.	DATE	BY

DESIGNED BY:

DRAWN BY: R. Stevens

CHECKED BY:

DATE: 6/6/2020

PROJECT NO.:

SHEET TITLE:

1314 Terminal Block Wiring Diagram for SCXI 1001 Chassis

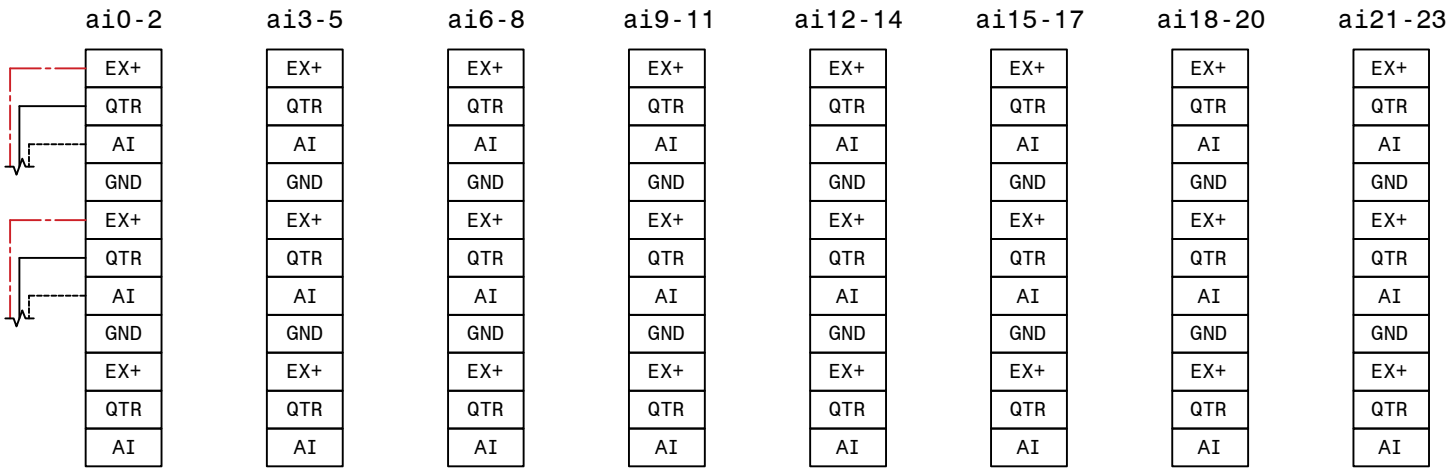

SC1 Mod4

Scale: NTS

1
S2

Red
Black
Green
White

VIRGINIA TECH
CHARLES E. VIA JR. DEPARTMENT OF CIVIL & ENVIRONMENTAL ENGINEERING
200 PATTON HALL
BLACKSBURG, VA 24061
P: 540-231-6635

PROJECT:
MRF Protected Zone/Low-Cycle Fatigue

SHEET NOTES:

REVISIONS:

NO.	DATE	BY

DESIGNED BY:
DRAWN BY: R. Stevens
CHECKED BY:
DATE: 6/6/2020
PROJECT NO.:

SHEET TITLE:
1317 Terminal Block Wiring Diagram for SCXI 1001 Chassis

Appendix G. Small-Scale Test Setup Drawings

This appendix includes drawings for the small-scale test setup, which encompasses the fixed assembly, the rollers, the moveable assembly, and the bracing.

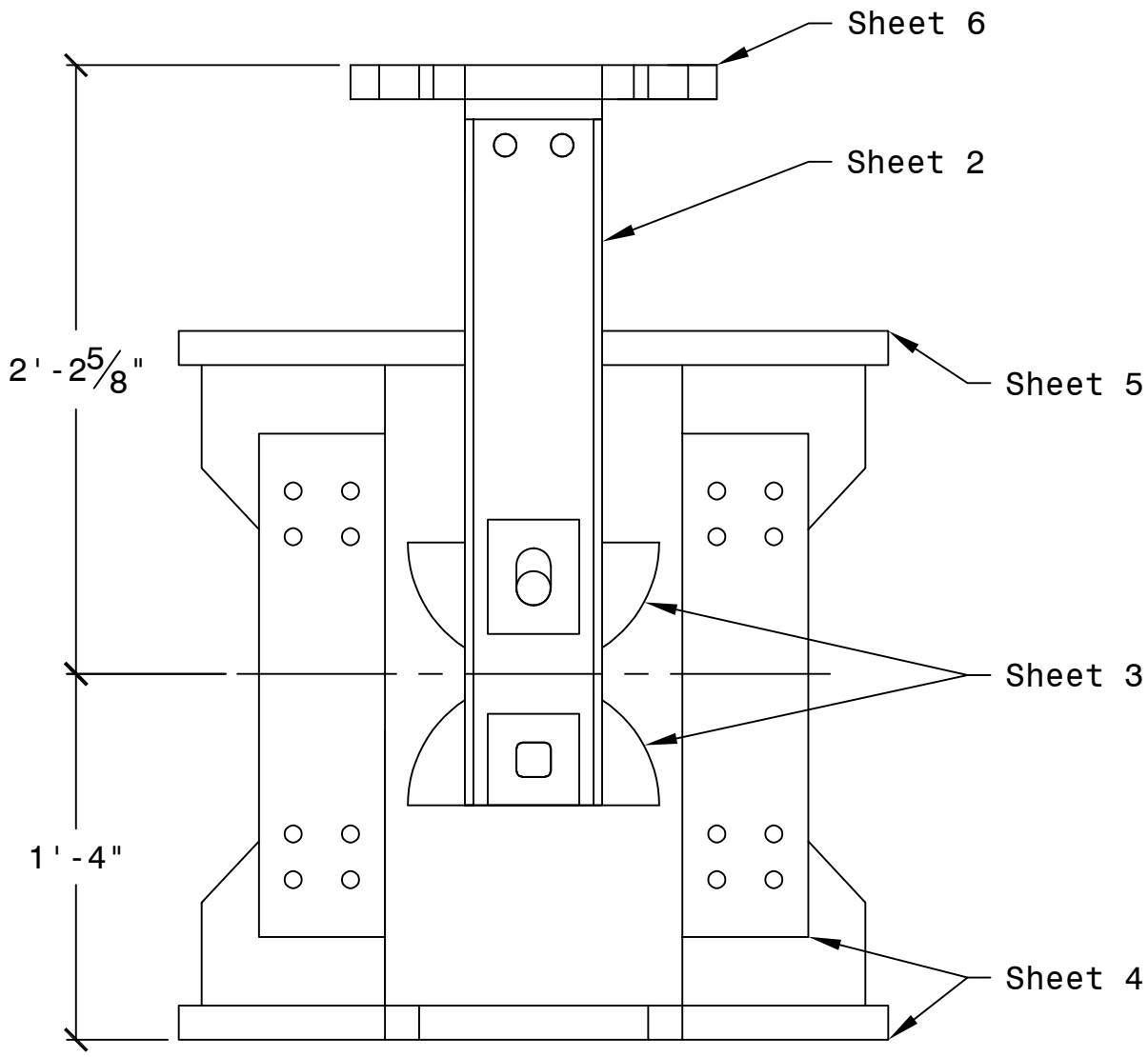

VIRGINIA TECH
CHARLES E. VIA JR. DEPARTMENT OF CIVIL & ENVIRONMENTAL ENGINEERING
200 PATTON HALL
BLACKSBURG, VA 24061
P: 540-231-6635

PROJECT:

MRF Protected Zone/Low-Cycle Fatigue

SHEET NOTES:

1. The setup is shown with the actuator at the neutral position

REVISIONS:

NO.	DATE	BY

DESIGNED BY:

DRAWN BY: R. Stevens

CHECKED BY:

DATE: 8/2/2020

PROJECT NO.:

SHEET TITLE:

Overall view

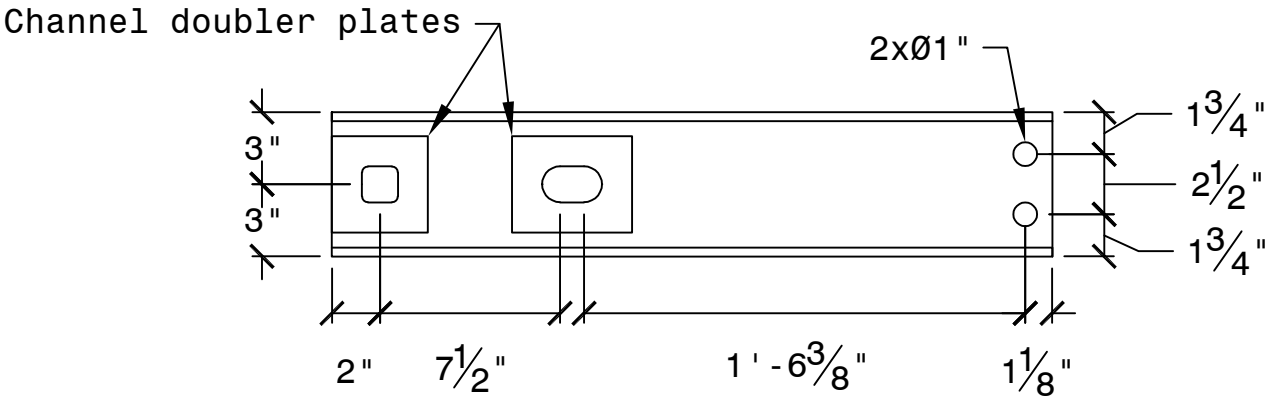

Channel Plan — Scale: 3" = 2'-0" — 1 / S2

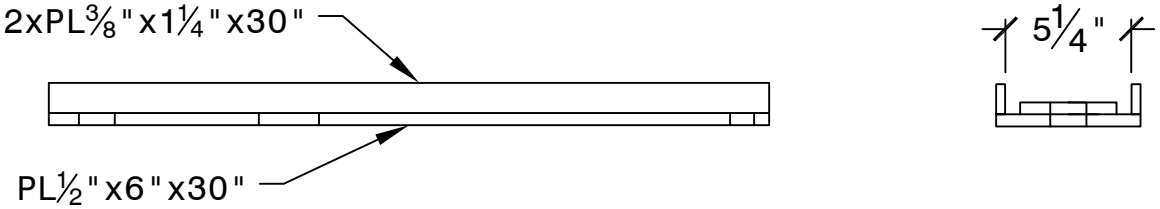

Channel Elevation — Scale: 3" = 2'-0" — 2 / S2

Channel End — Scale: 3" = 2'-0" — 3 / S2

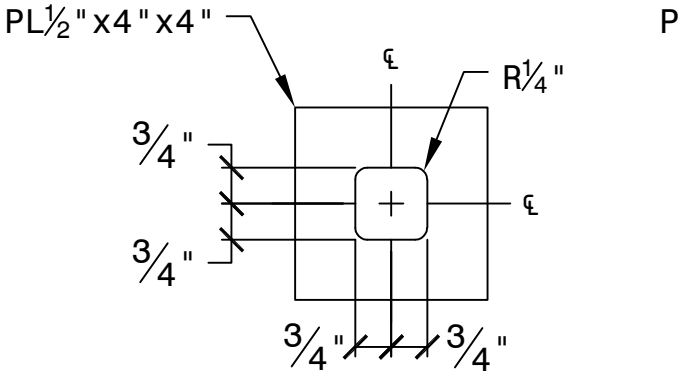

Square Doubler Plate — Scale: 3" = 1'-0" — 4 / S2

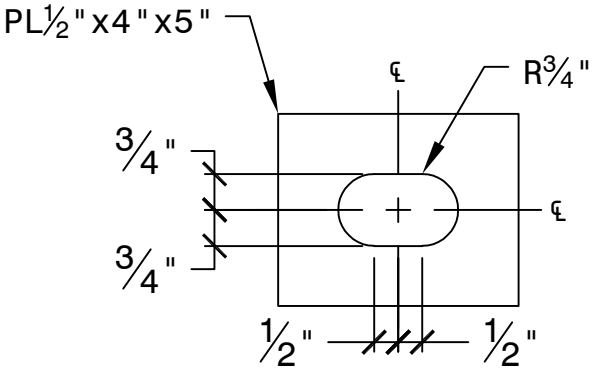

Oval Doubler Plate — Scale: 3" = 1'-0" — 5 / S2

VIRGINIA TECH
VIRGINIA TECH
CHARLES E. VIA JR. DEPARTMENT OF CIVIL & ENVIRONMENTAL ENGINEERING
200 PATTON HALL
BLACKSBURG, VA 24061
P: 540-231-6635

PROJECT:
MRF Protected Zone/Low-Cycle Fatigue

SHEET NOTES:

REVISIONS:

NO.	DATE	BY

DESIGNED BY:
DRAWN BY: R. Stevens
CHECKED BY:
DATE: 7/31/2020
PROJECT NO.:

SHEET TITLE:
Moveable channels

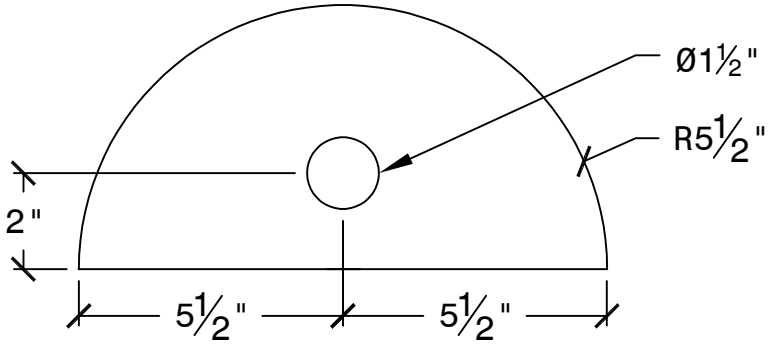

Top Roller

Scale: 3" = 1'-0"

1
S3

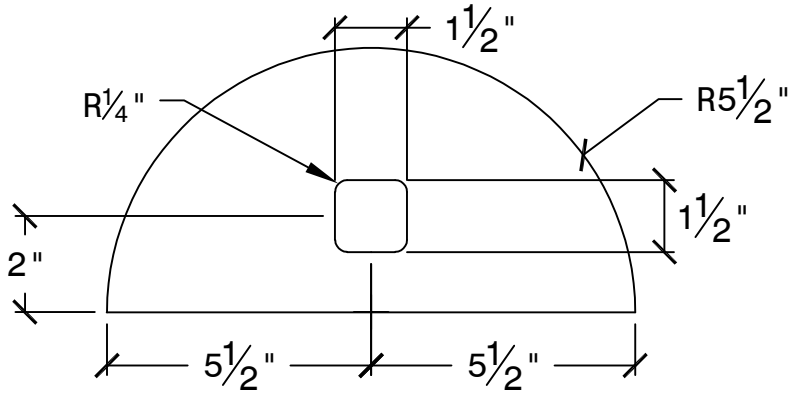

Bottom Roller

Scale: 3" = 1'-0"

2
S3

VIRGINIA TECH

VIRGINIA TECH
CHARLES E. VIA JR. DEPARTMENT OF CIVIL & ENVIRONMENTAL ENGINEERING
200 PATTON HALL
BLACKSBURG, VA 24061
P: 540-231-6635

PROJECT:

MRF Protected Zone/Low-Cycle Fatigue

SHEET NOTES:

1. Rollers are 3" thick

REVISIONS:

NO.	DATE	BY

DESIGNED BY:

DRAWN BY: R. Stevens

CHECKED BY:

DATE: 7/31/2020

PROJECT NO.:

SHEET TITLE:

Rollers

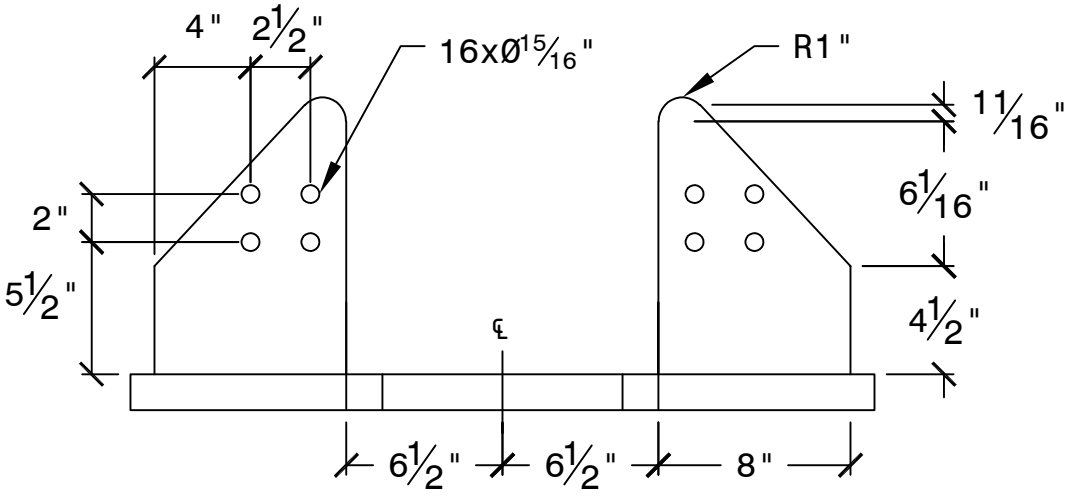

Bottom Guide Elevation — 1 / S4

Scale: 3" = 2'-0"

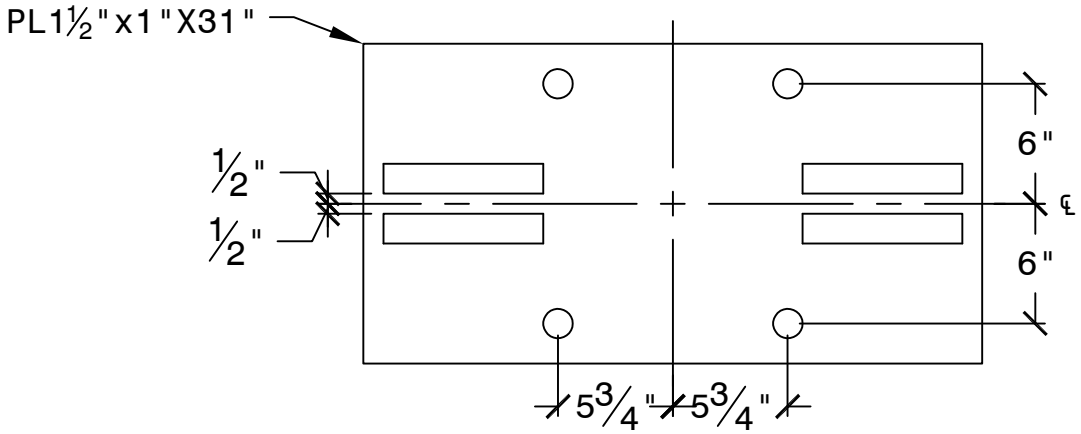

Bottom Guide Elevation — 2 / S4

Scale: 3" = 2'-0"

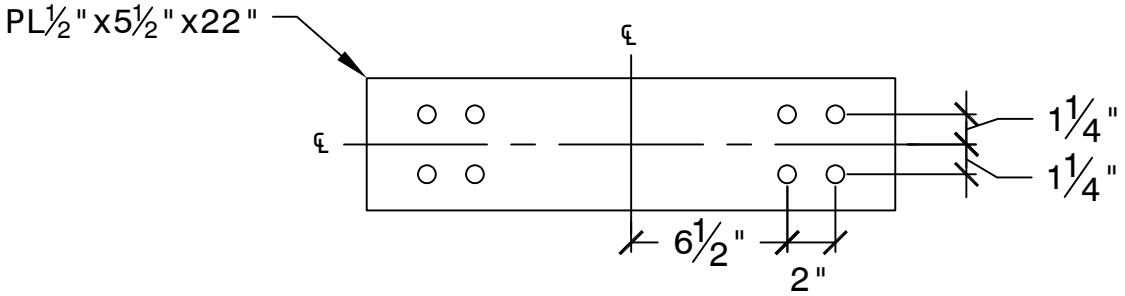

Connecting Plate — 3 / S4

Scale: 3" = 2'-0"

VIRGINIA TECH

VIRGINIA TECH
CHARLES E. VIA JR. DEPARTMENT OF CIVIL & ENVIRONMENTAL ENGINEERING
200 PATTON HALL
BLACKSBURG, VA 24061
P: 540-231-6635

PROJECT:

MRF Protected Zone/Low-Cycle Fatigue

SHEET NOTES:

1. Guide plates are 1 1/2" thick

REVISIONS:

NO.	DATE	BY

DESIGNED BY:

DRAWN BY: R. Stevens

CHECKED BY:

DATE: 7/31/2020

PROJECT NO.:

SHEET TITLE:

Bottom guide and connecting plate

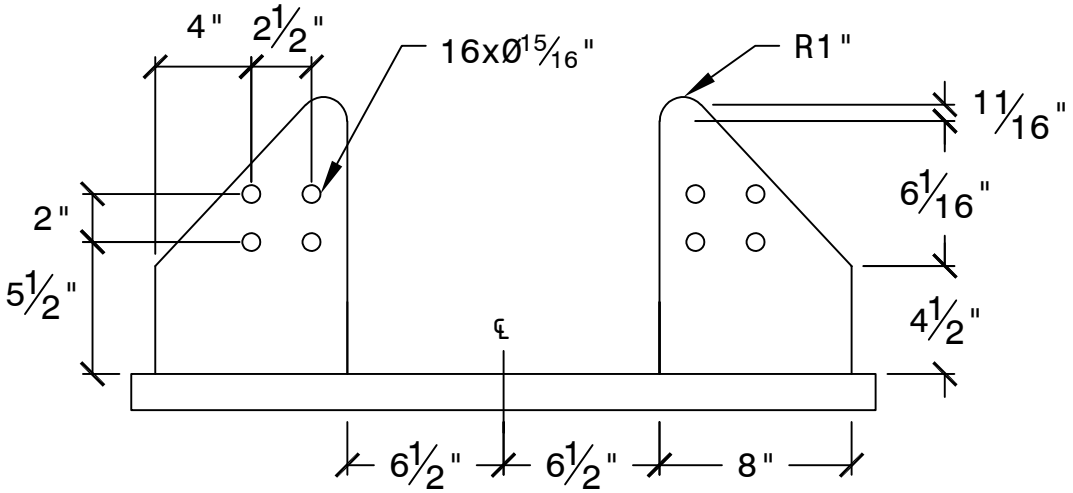

Top Guide Elevation — 1 / S5

Scale: 3" = 2'-0"

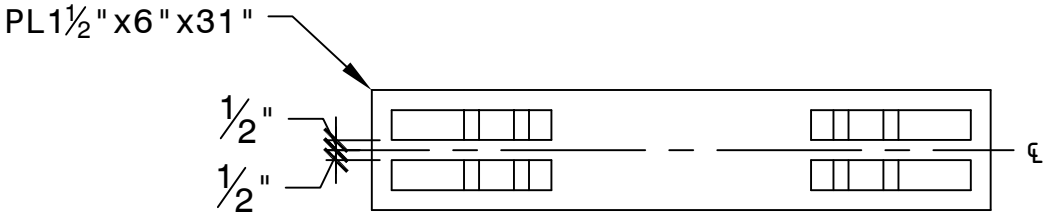

Top Guide Plan — 2 / S5

Scale: 3" = 2'-0"

VIRGINIA TECH

VIRGINIA TECH
CHARLES E. VIA JR. DEPARTMENT OF CIVIL & ENVIRONMENTAL ENGINEERING
200 PATTON HALL
BLACKSBURG, VA 24061
P: 540-231-6635

PROJECT:

MRF Protected Zone/Low-Cycle Fatigue

SHEET NOTES:

1. Guide plates are 1 1/2" thick

REVISIONS:

NO.	DATE	BY

DESIGNED BY:

DRAWN BY: R. Stevens

CHECKED BY:

DATE: 8/2/2020

PROJECT NO.:

SHEET TITLE: Top guide

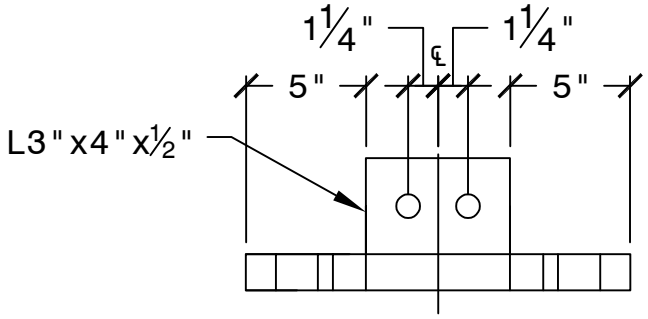

Actuator Plate Elevation (1 / S6)

Scale: 3" = 2'-0"

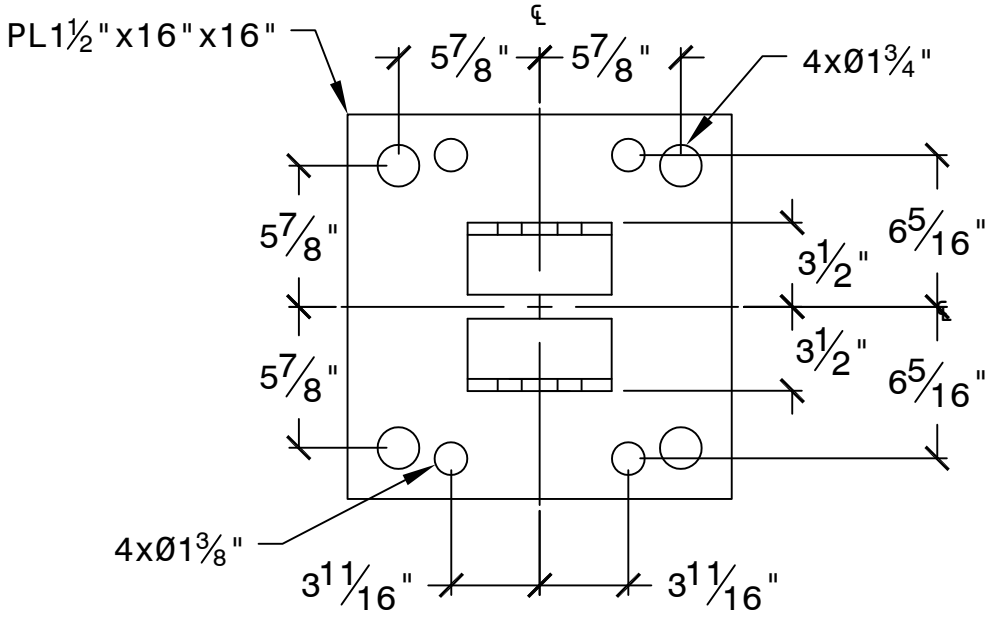

Actuator Plate Plan (2 / S6)

Scale: 3" = 2'-0"

VIRGINIA TECH

VIRGINIA TECH
CHARLES E. VIA JR. DEPARTMENT OF CIVIL & ENVIRONMENTAL ENGINEERING
200 PATTON HALL
BLACKSBURG, VA 24061
P: 540-231-6635

PROJECT:

MRF Protected Zone/Low-Cycle Fatigue

SHEET NOTES:

1. Holes in angles are 4xØ1"

REVISIONS:

NO.	DATE	BY

DESIGNED BY:

DRAWN BY: R. Stevens

CHECKED BY:

DATE: 8/2/2020

PROJECT NO.:

SHEET TITLE:

Actuator plate

SHEET NO.: 6 of 6

Appendix H. Small-Scale Coupon Dimensions

This appendix presents the actual dimensions of the small-scale coupons in Tables H.1 to H.3. The width and thickness was measured at each end of the coupon and averaged.

Table H.1. Actual dimensions of coupons with power actuated fasteners and puddle welds.

Specimen Name	Average Width, in.	Average Thickness, in.
W24-PAF-T50-R11.02	3.00	0.50
W24-PAF-T50-R11.03	2.99	0.50
W36-PAF-T100-R11.01	5.02	1.00
W36-PAF-T100-R11.02	5.02	0.99
W24-0.625PnAF-T50-R11.01	2.99	0.50
W24-0.625PnAF-T50-R11.02	2.99	0.50
W36-0.625PnAF-T100-R11.01	5.02	0.99
W36-0.625PnAF-T100-R11.02	5.02	0.99
W24-0.75PnAF-T50-R11.01	2.99	0.50
W24-0.75PnAF-T50-R11.02	2.99	0.50
W36-0.75PnAF-T100-R11.01	5.01	1.00
W36-0.75PnAF-T100-R11.02	5.01	0.99
W24-PW-T50-R11.01	2.99	0.50
W24-PW-T50-R11.02	2.98	0.50
W36-PW-T100-R11.01	5.02	1.00
W36-PW-T100-R11.02	5.02	1.00

Table H.2. Actual dimensions of coupons with repairs and defects.

Specimen Name	Average Width, in.	Average Thickness, in.
W24-0.125NGT-T50-R11.01	2.98	0.50
W24-0.125NGT-T50-R11.02	2.98	0.53
W24-0.125NGT-T59-R11.01	3.02	0.61
W24-0.125NGT-T59-R11.02	2.97	0.60
W36-0.125NGT-T94-R11.01	4.47	0.84
W36-0.125NGT-T94-R11.02	4.43	0.82
W36-0.125NGT-T100-R11.01	5.02	1.01
W36-0.125NGT-T100-R11.02	5.03	1.01
W24-0.25NGTW-T50-R11.01	2.98	0.51
W24-0.25NGTW-T50-R11.02	2.96	0.52
W24-0.25NGTW-T59-R11.01	2.98	0.60
W24-0.25NGTW-T59-R11.02	2.99	0.62
W36-0.25NGTW-T94-R11.01	4.57	0.94
W36-0.25NGTW-T94-R11.02	4.56	1.00
W36-0.25NGTW-T100-R11.01	5.02	1.03
W36-0.25NGTW-T100-R11.02	5.02	1.05
W24-0.25N-T50-R11.02	2.97	0.52
W24-0.25N-T50-R11.03	2.96	0.51
W24-0.25N-T59-R11.02	3.01	0.61
W24-0.25N-T59-R11.03	3.01	0.62
W36-0.25N-T94-R11.01	4.62	0.97
W36-0.25N-T94-R11.02	4.60	0.96
W36-0.25N-T100-R11.01	5.02	1.02
W36-0.25N-T100-R11.02	5.02	1.00
W24-0.375N-T50-R11.01	2.99	0.50
W24-0.375N-T50-R11.02	2.98	0.50
W24-0.375N-T59-R11.01	2.99	0.60
W24-0.375N-T59-R11.02	3.03	0.59
W36-0.375N-T94-R11.01	4.65	0.97
W36-0.375N-T94-R11.02	4.55	1.00
W36-0.375N-T100-R11.01	5.02	0.99
W36-0.375N-T100-R11.02	5.03	1.00

Table H.3. Actual dimensions of bare steel coupons.

Specimen Name	Average Width, in.	Average Thickness, in.
W24-BAR STOCK-T40-R11.02	2.98	0.39
W24-FLANGE MATERIAL-T40-R11.02	2.99	0.39
W24-STEEL-T50-R11.02	2.97	0.52
W24-STEEL-T50-R11.03	2.99	0.52
W36-STEEL-T100-R11.01	5.03	1.02
W36-STEEL-T100-R11.02	5.02	1.00

Appendix I. Small Scale Specimen Drawings

This appendix includes drawings for small-scale cyclic bend coupons cut from beam flange material and bar stock.

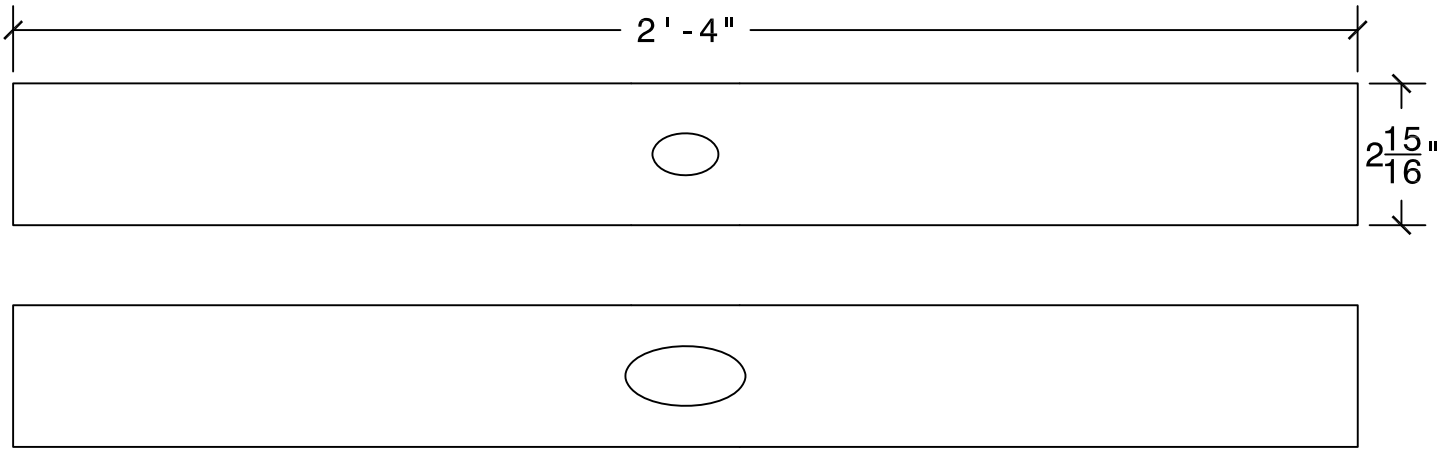

W24x62 Flange Material (1 / S1)

Scale: 3" = 1'–0"

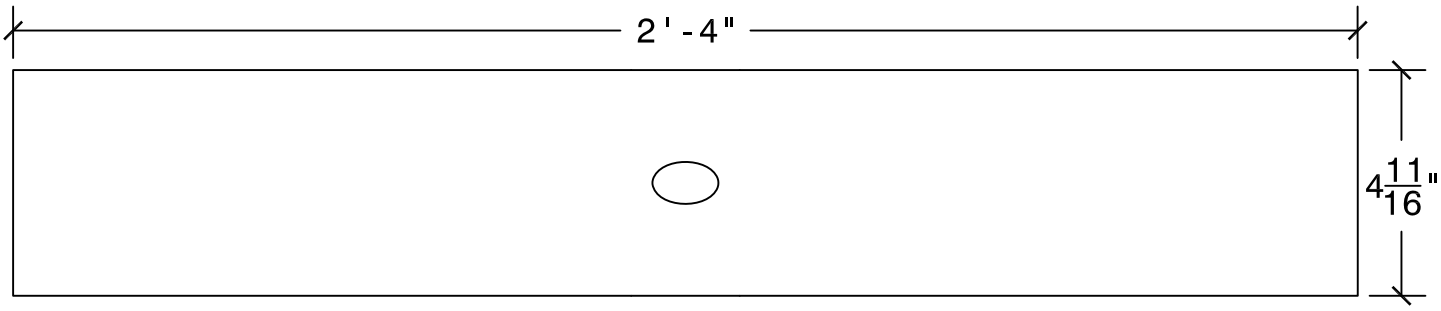

W36x150 Flange Material (2 / S1)

Scale: 3" = 1'–0"

VIRGINIA TECH

VIRGINIA TECH
CHARLES E. VIA JR. DEPARTMENT OF CIVIL & ENVIRONMENTAL ENGINEERING
200 PATTON HALL
BLACKSBURG, VA 24061
P: 540-231-6635

PROJECT:

MRF Protected Zone/Low-Cycle Fatigue

SHEET NOTES:

1. Artifacts are centered on the coupons in both directions.

REVISIONS:

NO.	DATE	BY
1	5/7/2020	RS

DESIGNED BY:

DRAWN BY: R. Stevens

CHECKED BY:

DATE: 2/18/2019

PROJECT NO.:

SHEET TITLE:

Small-Scale Bend Coupons cut from Flange Material

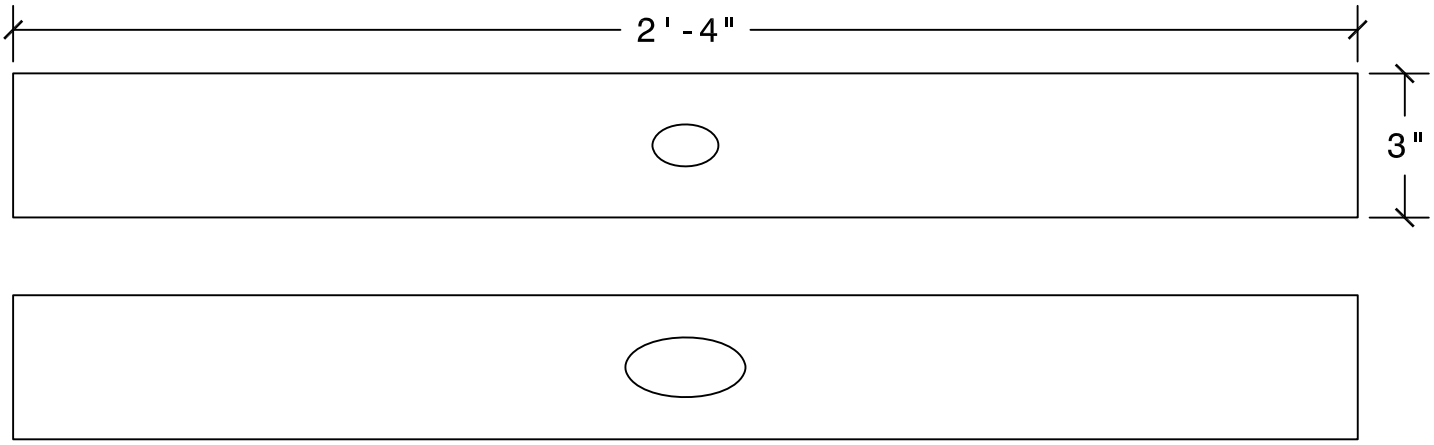

1/2" Bar Stock

Scale: 3" = 1'-0"

1
S2

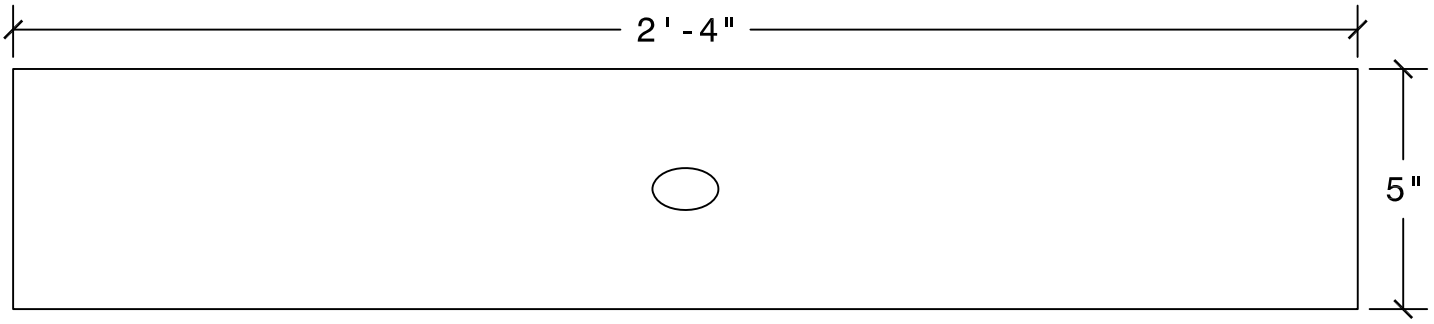

1" Bar Stock

Scale: 3" = 1'-0"

2
S2

VIRGINIA TECH

VIRGINIA TECH
CHARLES E. VIA JR. DEPARTMENT OF CIVIL & ENVIRONMENTAL ENGINEERING
200 PATTON HALL
BLACKSBURG, VA 24061
P: 540-231-6635

PROJECT:

MRF Protected Zone/Low-Cycle Fatigue

SHEET NOTES:

1. Artifacts are centered on the coupons in both directions.

REVISIONS:

NO.	DATE	BY
1	5/7/2020	RS

DESIGNED BY:

DRAWN BY: R. Stevens

CHECKED BY:

DATE: 2/18/2019

PROJECT NO.:

SHEET TITLE:

Small-Scale Bend Coupons cut from Bar Stock

Appendix J. Finite Element Data Analysis

This appendix describes the data analysis for the finite element models. The principal stress histories were extracted from the models for the worst-case locations, usually at the edge of an artifact, but the Lode angle parameter, ζ, and stress triaxiality, η were needed to compare the behavior of the models. The Lode angle parameter was calculated using Eq. (J.3), which required calculating the J_2 invariant, J_3 invariant using Eqs. (J.1) to (J.2).

$$J_2 = \frac{1}{6}[(\sigma_1 - \sigma_2)^2 + (\sigma_2 - \sigma_3)^2 + (\sigma_3 - \sigma_1)^2] \tag{J.1}$$

$$J_3 = (\sigma_1 - \sigma_m)(\sigma_2 - \sigma_m)(\sigma_3 - \sigma_m) \tag{J.2}$$

$$\zeta = \frac{3\sqrt{3}J_3}{2J_2^{\frac{3}{2}}} \tag{J.3}$$

$$\theta = \frac{\arccos\zeta}{3} \tag{J.4}$$

where: σ_m = mean principal stress

σ_1 = first principal stress

σ_2 = second principal stress

σ_3 = third principal stress.

The stress triaxiality was calculated using Eq. (J.6), which required calculating the von Mises stress, σ_{vm}, using Eq. (J.5),

$$\sigma_{vm} = \sqrt{3J_2} \tag{J.5}$$

$$\eta = \frac{\sigma_m}{\sigma_{vm}} \tag{J.6}$$

where J_2 was calculated using Eq. (J.1) and σ_m was previously defined.

Appendix K. Elastic-Plastic Fracture Mechanics Calculations

This appendix presents the equations used to create the Failure Assessment Diagrams (FAD) given in Chapter 5.

K.1 K_I Stress-Intensity Factor

The Mode I stress-intensity factor, K_I, was calculated using Eq. (K.1), taken from Newman and Raju (1984) and Anderson (2017). The stress-intensity factor has units of $ksi * in^{0.5}$.

$$K_I = (\sigma_m + H\sigma_b)F\sqrt{\frac{\pi a}{Q}} \tag{K.1}$$

where: a = crack depth
σ_m = axial stress
σ_b = bending stress.

This equation requires F from Eq. (K.2), which in turn requires M_1, M_2, M_3, f_ϕ, f_w, and g, from Eqs. (K.3) to (K.8), respectively.

$$F = (M_1 + M_2(\frac{a}{t})^2 + M_3(\frac{a}{t})^4)f_\phi f_w g \tag{K.2}$$

$$M_1 = 1.13 - 0.09(\frac{a}{c}) \tag{K.3}$$

$$M_2 = -0.54 + \frac{0.89}{0.2 + \frac{a}{c}} \tag{K.4}$$

$$M_3 = 0.5 - \frac{1}{0.65 + \frac{a}{c}} + 14(1 - \frac{a}{c})^2 4 \tag{K.5}$$

$$f_\phi = ((\frac{a}{c})^2 \cos^2\phi + \sin^2\phi)^0.25 \tag{K.6}$$

$$f_w = (\sec(\frac{\pi c}{2W}\sqrt{\frac{a}{t}}))^0.5 \tag{K.7}$$

$$g = 1 + (0.1 + 0.35(\frac{a}{c})^2)(1 - \sin^2\phi) \tag{K.8}$$

where: a = crack depth

c = half the width of the crack on the flange face

t = thickness of the beam flange

W = half the width of the flange at the center of the RBS

ϕ = parametric angle of the crack.

Equation (K.1) also requires H, which is given by Eq. (K.9), which in turn requires H_1, H_2, G_1, G_2, and p from Eqs. (K.10) to (K.14), respectively.

$$H = H_1 + (H_2 - H_1)\sin^p \phi \tag{K.9}$$

$$H_1 = 1 - 0.34(\frac{a}{t}) - 0.11(\frac{a}{c})(\frac{a}{t}) \tag{K.10}$$

$$H_2 = 1 + G_1(\frac{a}{t}) + G_2(\frac{a}{t})^2 \tag{K.11}$$

$$G_1 = -1.22 - 0.12(\frac{a}{c}) \tag{K.12}$$

$$G_2 = 0.55 - 1.05(\frac{a}{c})^{0.75} + 0.47(\frac{a}{c})^{1.5} \tag{K.13}$$

$$p = 0.2 + \frac{a}{c} + 0.6(\frac{a}{t}) \tag{K.14}$$

where: a = crack depth

c = half the width of the crack on the flange face

t = thickness of the beam flange

ϕ = parametric angle of the crack.

The equation for Q in Eq. (K.1) is given by Eq. (K.15)

$$Q = 1 + 1.464(\frac{a}{c})^{1.65} \tag{K.15}$$

where: a = crack depth

c = half the width of the crack on the flange face.

K.2 J Integral

The equation for the total J integral is given by Eq. (K.16), from (Anderson 2017).

$$J = J_{el} + J_{pl} \tag{K.16}$$

where J_{el} is the elastic J integral from Eq. (K.17) and J_{pl} is the plastic J integral, from Eq. (K.18).

$$J_{el} = \frac{K_I^2}{\frac{E}{1-\nu^2}} \tag{K.17}$$

$$J_{pl} = \frac{\mu K_I^2}{E}\left(\frac{E\epsilon_{ref}}{\sigma_{ref}} - 1\right) \tag{K.18}$$

where: E = modulus of elasticity, 29000 ksi

K_I = Mode I stress-intensity factor

ϵ_{ref} = reference strain

μ = 0.75 for plane strain conditions

ν = Poisson's ratio, 0.3

σ_{ref} = reference stress.

The reference stress is from (Goodall and Webster 2001) and is given by Eq. (K.19). When the reference stress was derived, (Goodall and Webster 2001) modeled the semi-elliptical crack as a rectangle with depth a and with $2c$, that circumscribes the semi-elliptical crack. This is a conservative approximation.

$$\sigma_{ref} = \frac{(\sigma_b + 3\gamma\sigma_m) + ((\sigma_b + 3\gamma\sigma_m)^2 + 9\sigma_m^2((1-\gamma)^2 + 2\gamma(\alpha - \gamma)))^{0.5}}{3((1-\gamma)^2 + 2\gamma(\alpha - \gamma))} \tag{K.19}$$

where: σ_b = bending stress

σ_m = axial stress

α is equal to $\frac{a}{t}$ and γ is equal to $\frac{ac}{Wt}$, where a is the depth of the crack, c is half the width of the crack on the flange face, t is the flange thickness, and W is half of the width of the flange at the center of the RBS.

The reference strain, ϵ_{ref}, a related to the reference stress, σ_{ref}, by the constitutive model, such as the Ramberg-Osgood relationship given by Eq. (K.20) (Dowling 2013)

$$\epsilon_{ref} = \frac{\sigma_{ref}}{E} + \left(\frac{\sigma_{ref}}{H}\right)^{\frac{1}{n}} \tag{K.20}$$

where H and n are constants derived by fitting the equation to a log-log plot of true stress and true plastic strain (Toellner 2013).

K.3 Failure Assessment Diagram

The y-axis of the failure assessment diagram (FAD) is normalized as $K_r = \frac{K_I}{K_J}$, where K_I is the Mode I stress-intensity factor and K_j is given by Eq. (K.21)

$$K_J = \sqrt{\frac{JE}{1-\nu^2}} \tag{K.21}$$

where: E = modulus of elasticity, 29,000 ksi

J = applied J integral from Eq. (K.16)

ν = Poisson's ratio, 0.3.

The x-axis of the FAD is normalized by the load ratio $L_r = \frac{\sigma_{ref}}{\sigma_y}$, where σ_y is the yield stress of the material. The maximum load ratio is

$$L_{rmax} = \frac{\sigma_y + \sigma_u}{2\sigma_y} \tag{K.22}$$

where σ_u is the ultimate stress of the material.

K.4 Evaluating an Assessment Point

For a given applied load, the assessment point can be plotted with an x-coordinate of $\frac{\sigma_{ref}}{\sigma_y}$ and a y-coordinate of $\frac{K_I}{K_{mat}}$. K_{mat} is the fracture toughness of the material, and can be approximated using Eq. (K.23) (Rolfe and Novak 1970; Barsom and Rolfe 1999)

$$K_{mat} = \sigma_y \sqrt{\frac{5}{\sigma_y}(CVN - \frac{\sigma_y}{20})} \tag{K.23}$$

where: CVN = absorbed energy from a CVN test

σ_y = yield stress of the material.

Appendix L. Sensor Plots for W24RBS-0.125NGT-T59

This section includes modified sensor plots for the W24RBS-0.125NGT-T59 test. A discussion of any data modifications is given in Appendix Y.

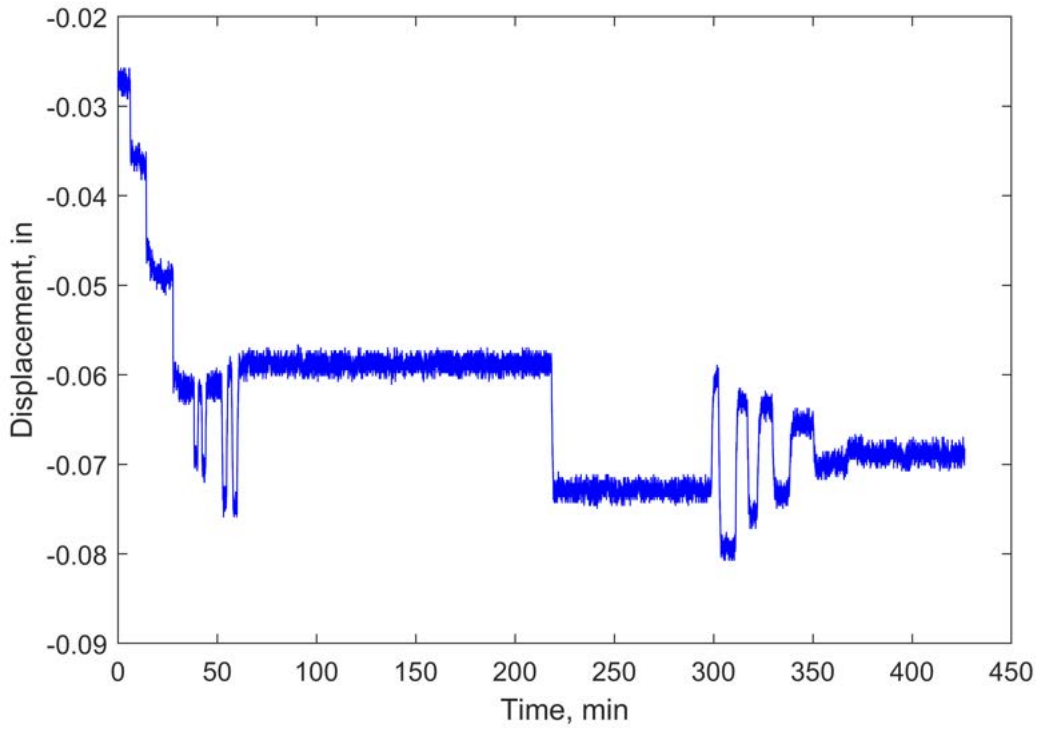

Figure L.1. Displacement-time plot of SP_01 for W24RBS-0.125NGT-T59.

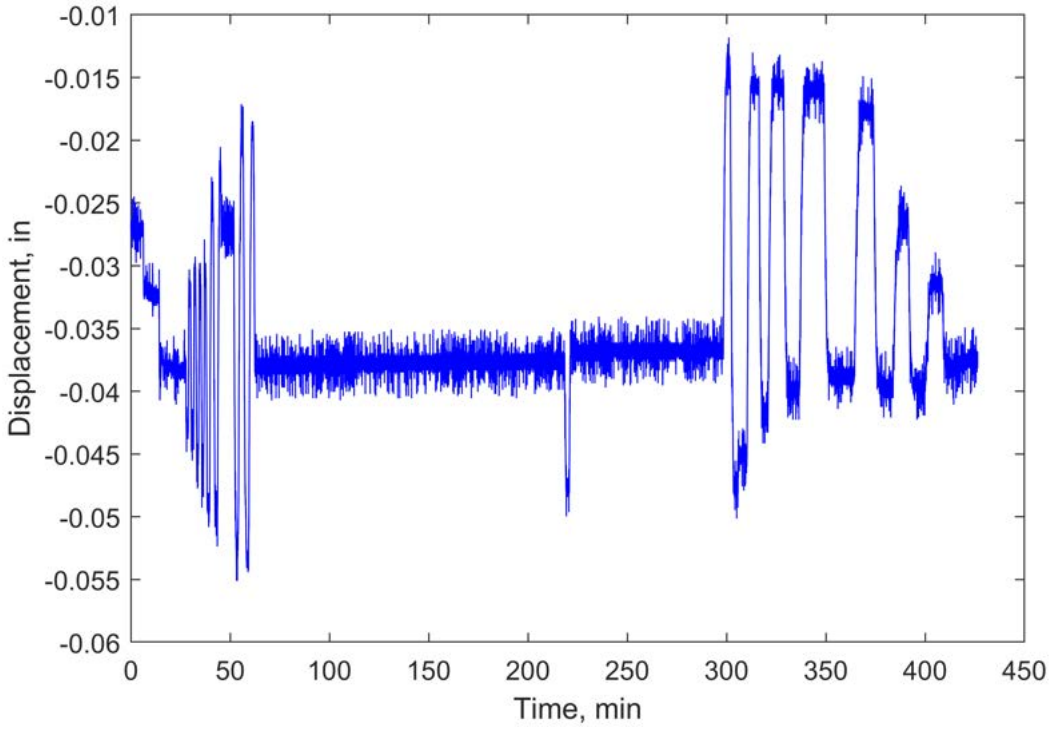

Figure L.2. Displacement-time plot of SP_02 for W24RBS-0.125NGT-T59.

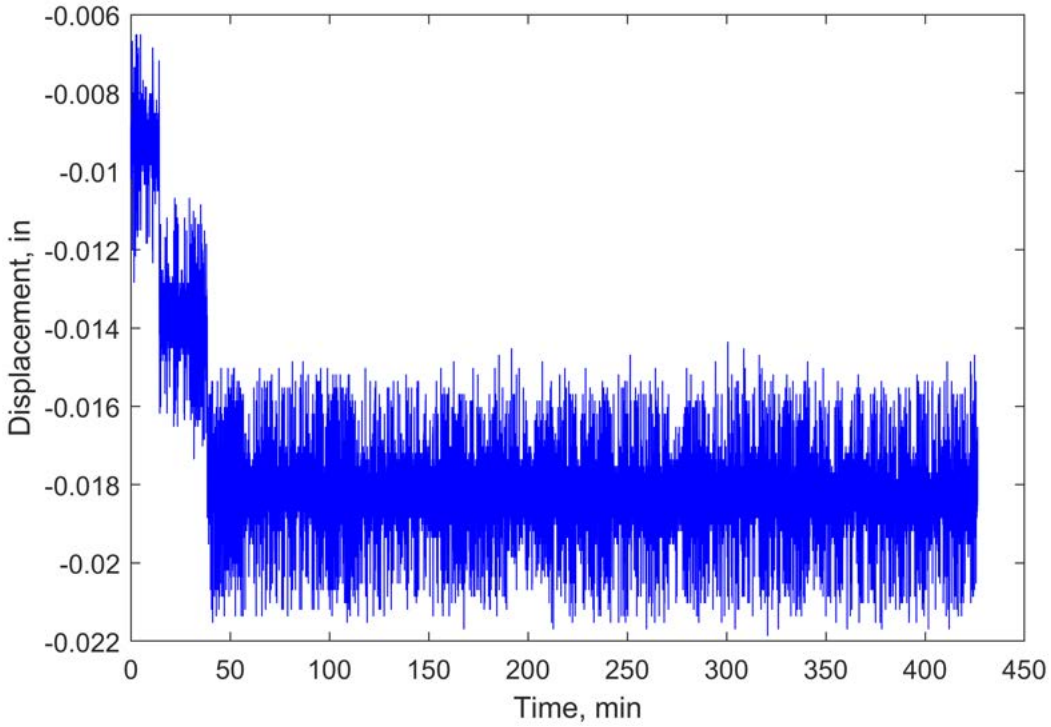

Figure L.3. Displacement-time plot of SP_03 for W24RBS-0.125NGT-T59.

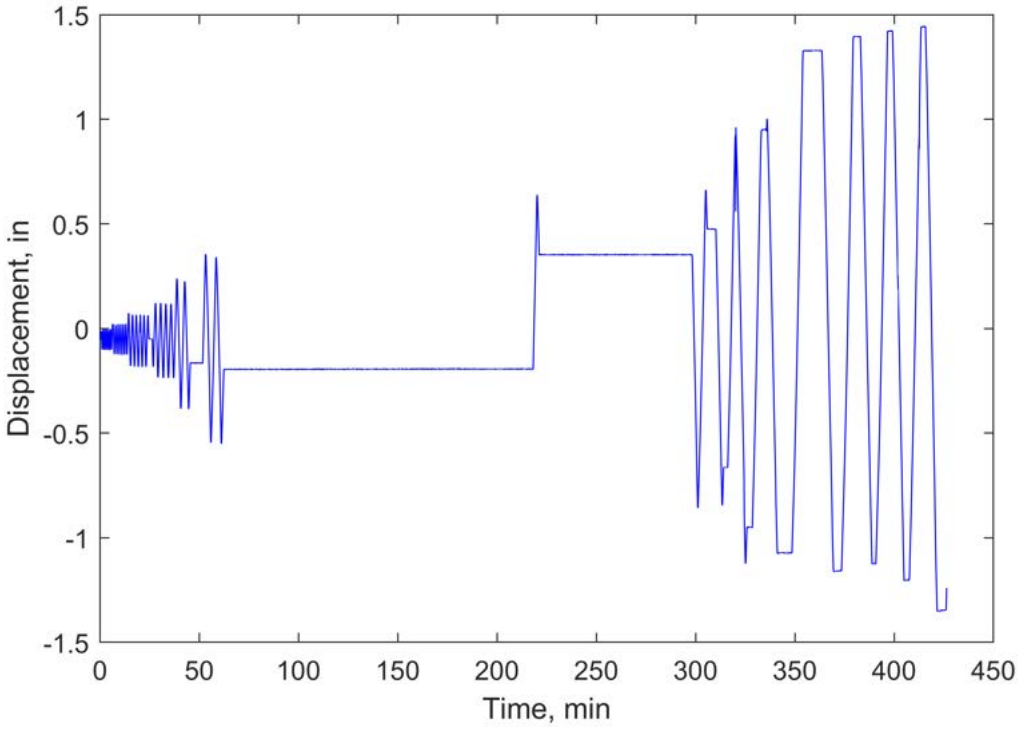

Figure L.4. Displacement-time plot of SP_04 for W24RBS-0.125NGT-T59.

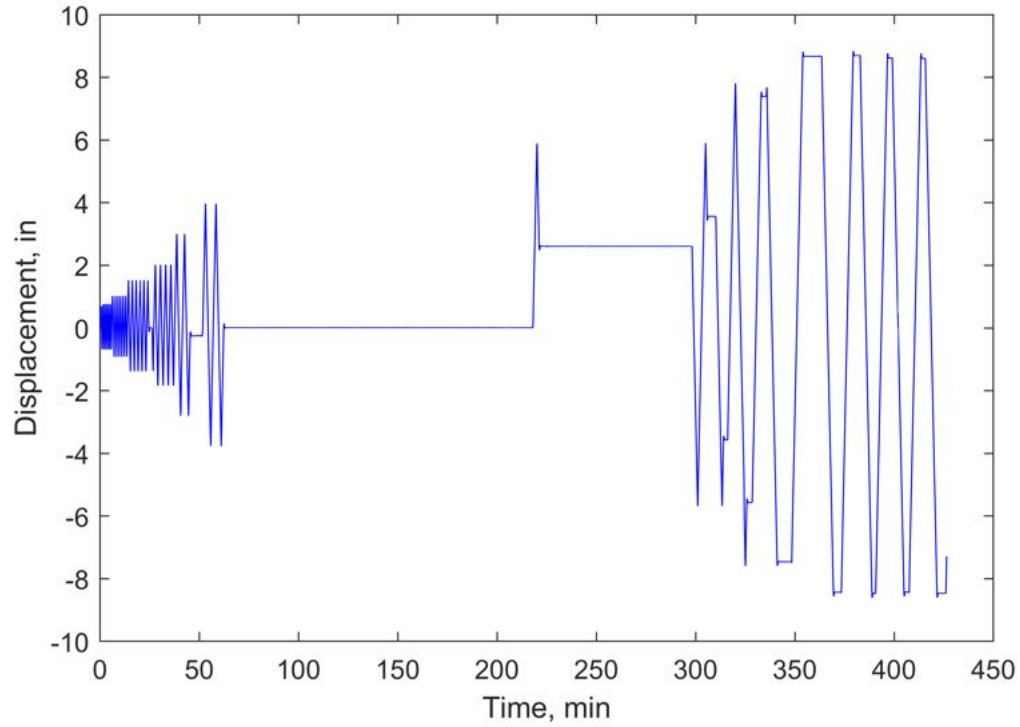

Figure L.5. Displacement-time plot of SP_05 for W24RBS-0.125NGT-T59.

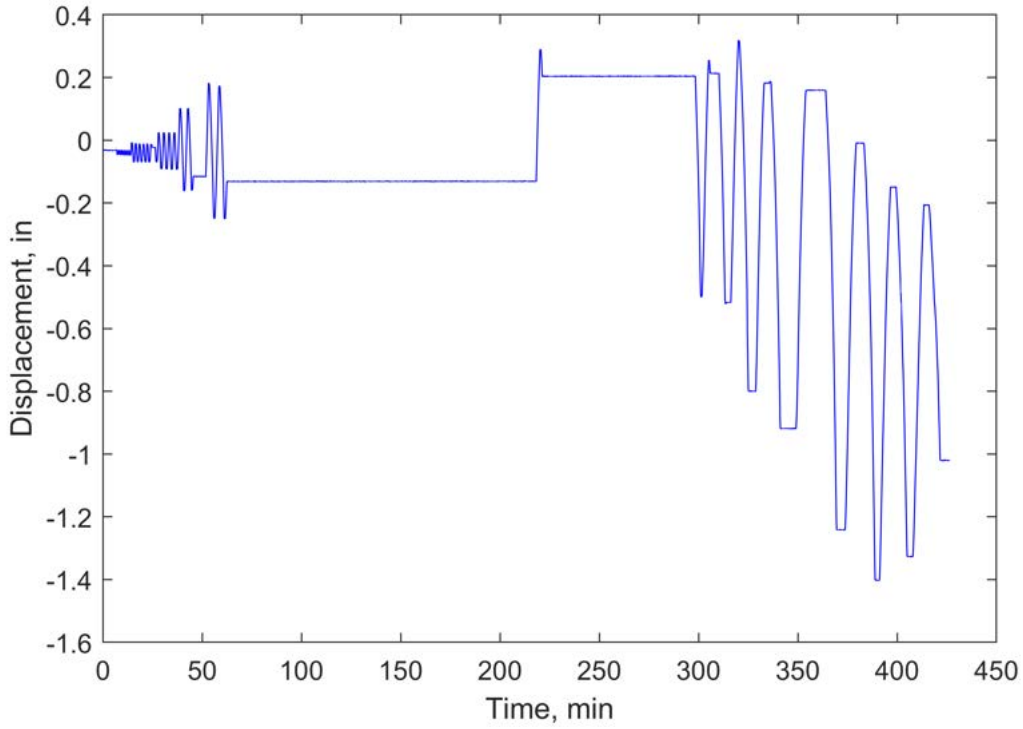

Figure L.6. Displacement-time plot of SP_06 for W24RBS-0.125NGT-T59.

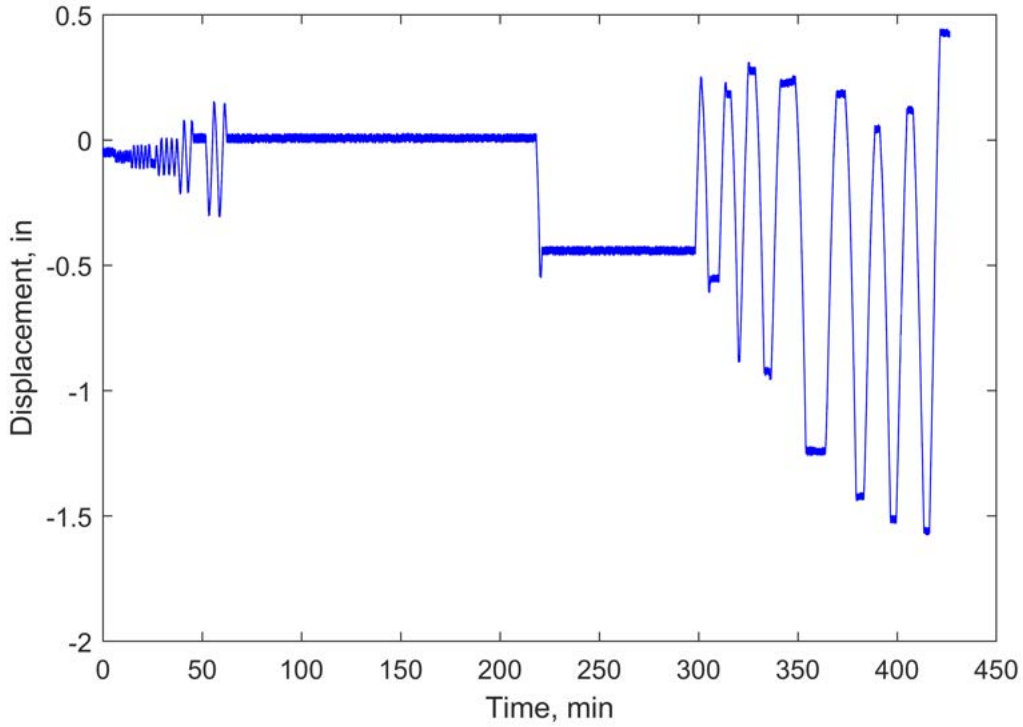

Figure L.7. Displacement-time plot of SP_07 for W24RBS-0.125NGT-T59.

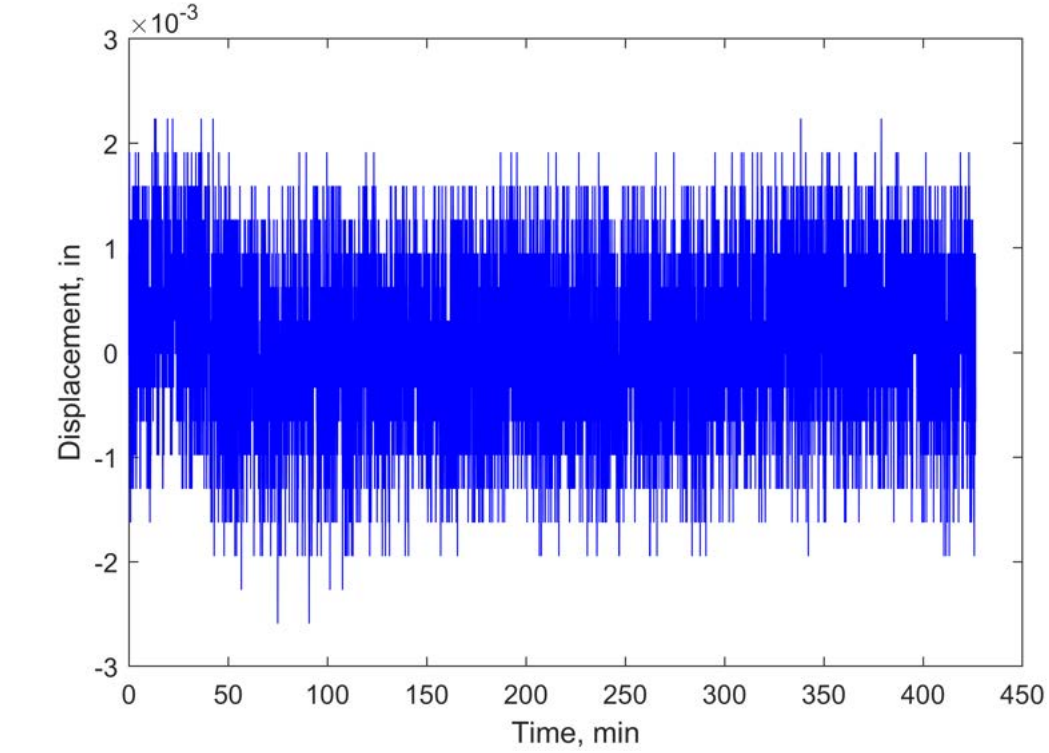

Figure L.8. Displacement-time plot of SP_08 for W24RBS-0.125NGT-T59.

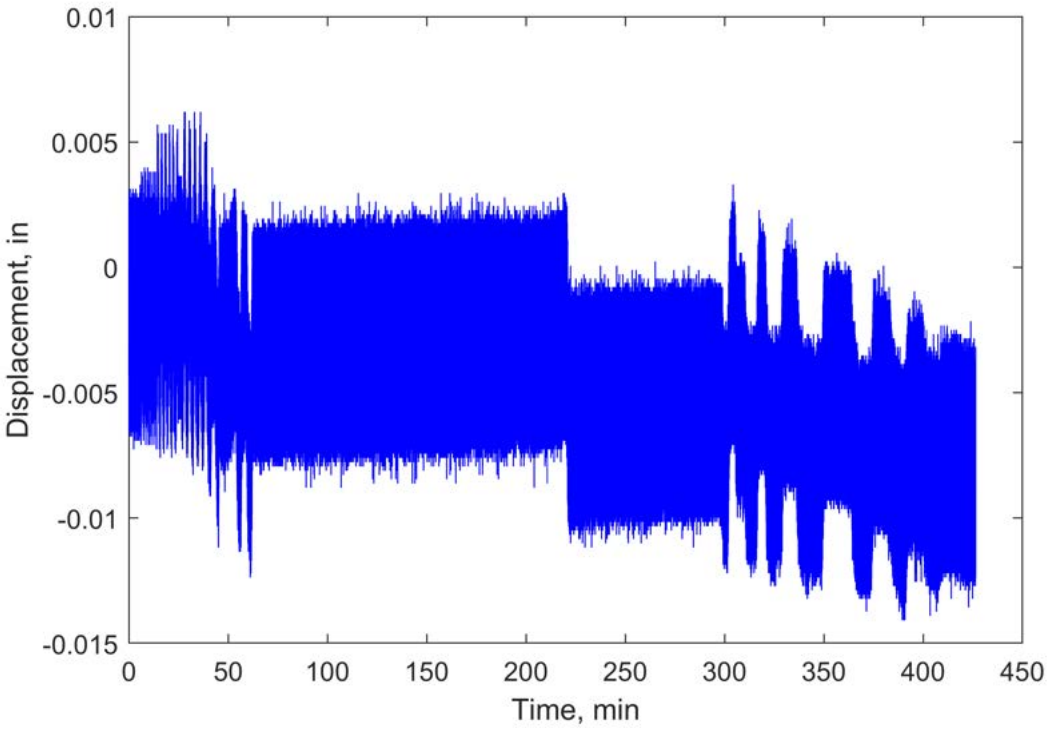

Figure L.9. Displacement-time plot of SP_09 for W24RBS-0.125NGT-T59.

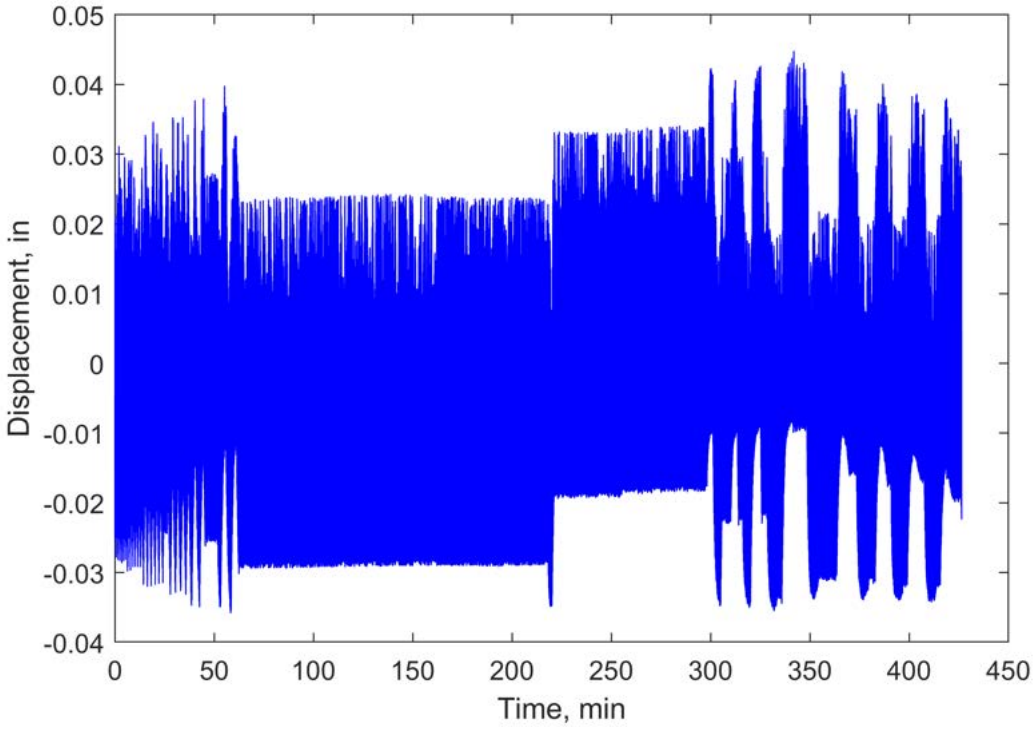

Figure L.10. Displacement-time plot of LP_01 for W24RBS-0.125NGT-T59.

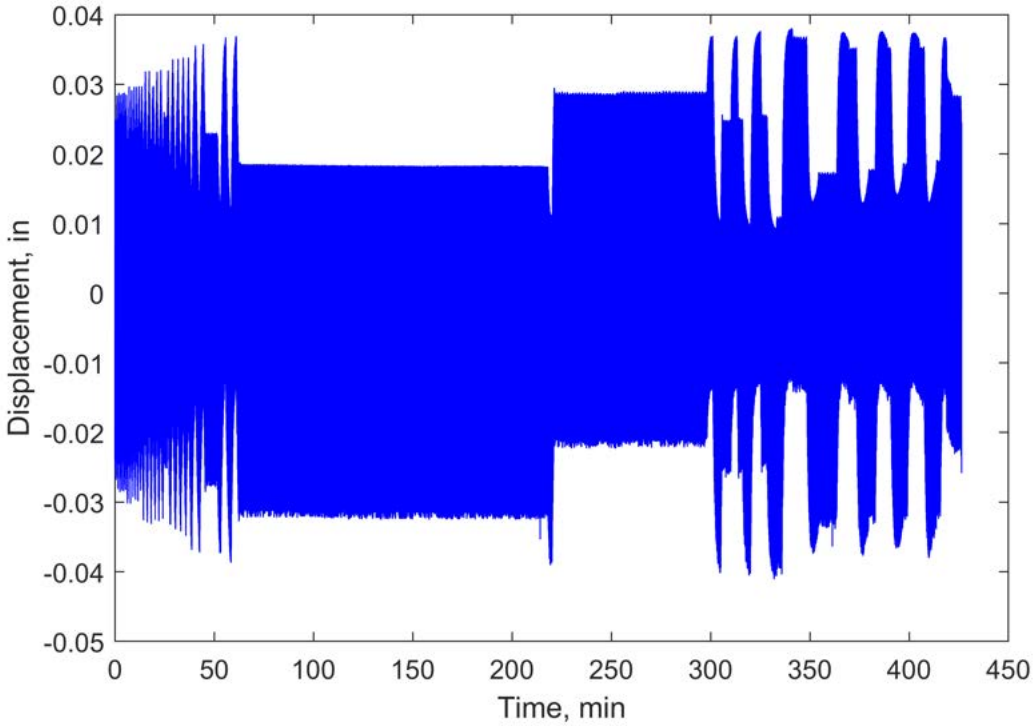

Figure L.11. Displacement-time plot of LP_02 for W24RBS-0.125NGT-T59.

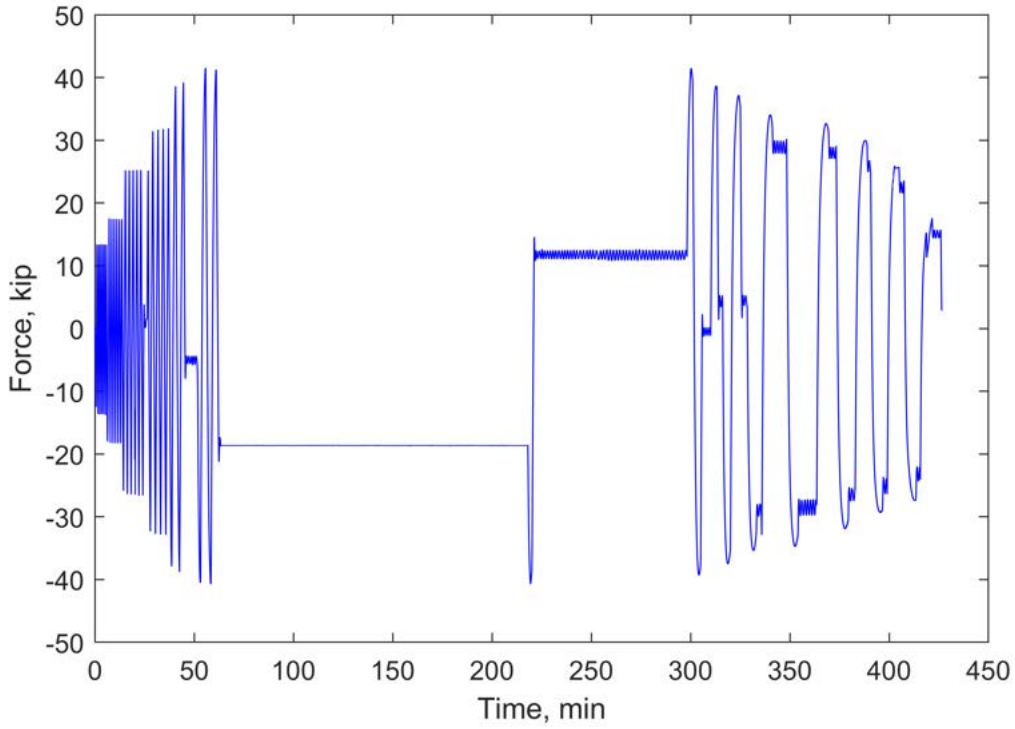

Figure L.12. Force-time plot for W24RBS-0.125NGT-T59.

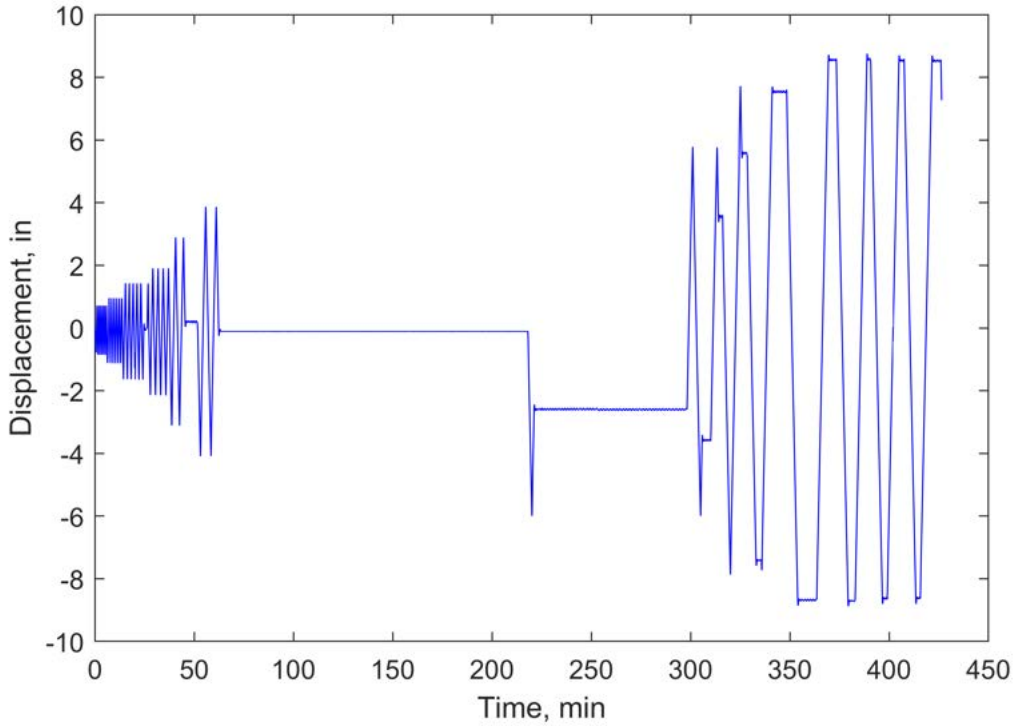

Figure L.13. Actuator displacement-time plot for W24RBS-0.125NGT-T59.

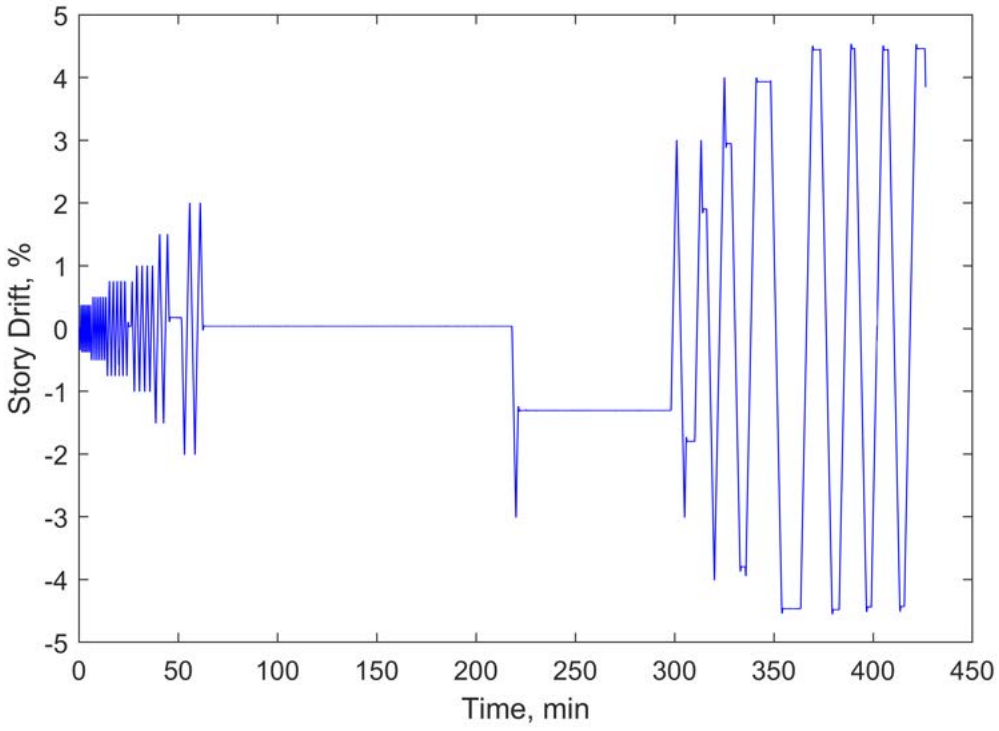

Figure L.14. Drift-time plot for W24RBS-0.125NGT-T59.

Appendix M. Sensor Plots for W36RBS-0.125NGT-T94

This section includes modified sensor plots for the W36RBS-0.125NGT-T94 test. A discussion of any data modifications is given in Appendix Y.

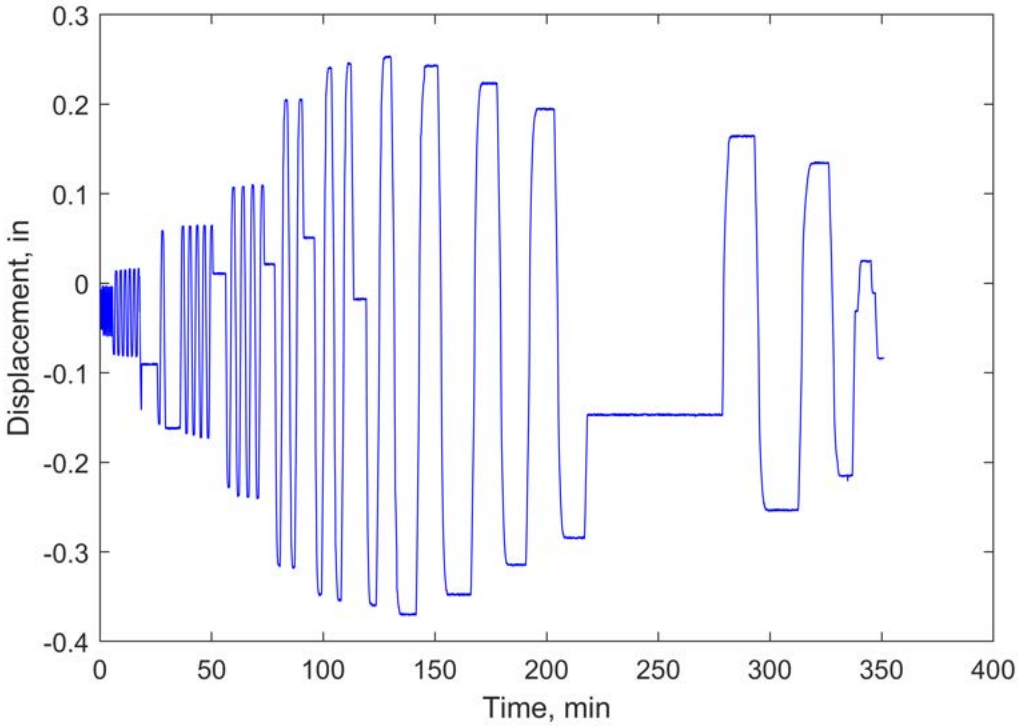

Figure M.1. Displacement-time plot of SP_01 for W36RBS-0.125NGT-T94.

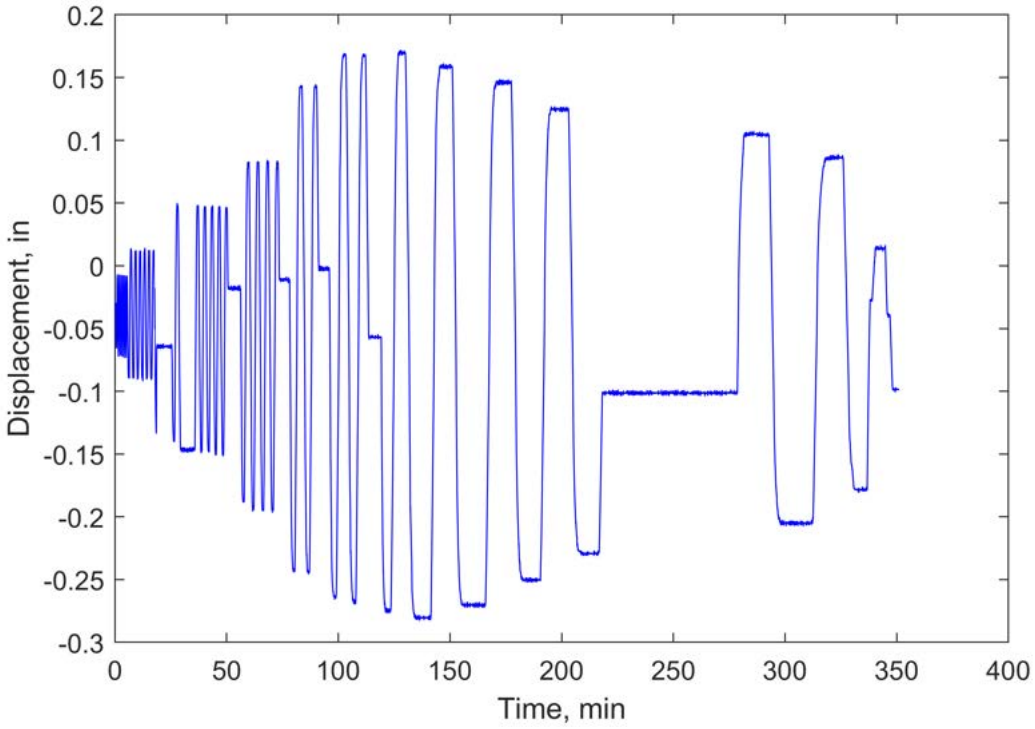

Figure M.2. Displacement-time plot of SP_02 for W36RBS-0.125NGT-T94.

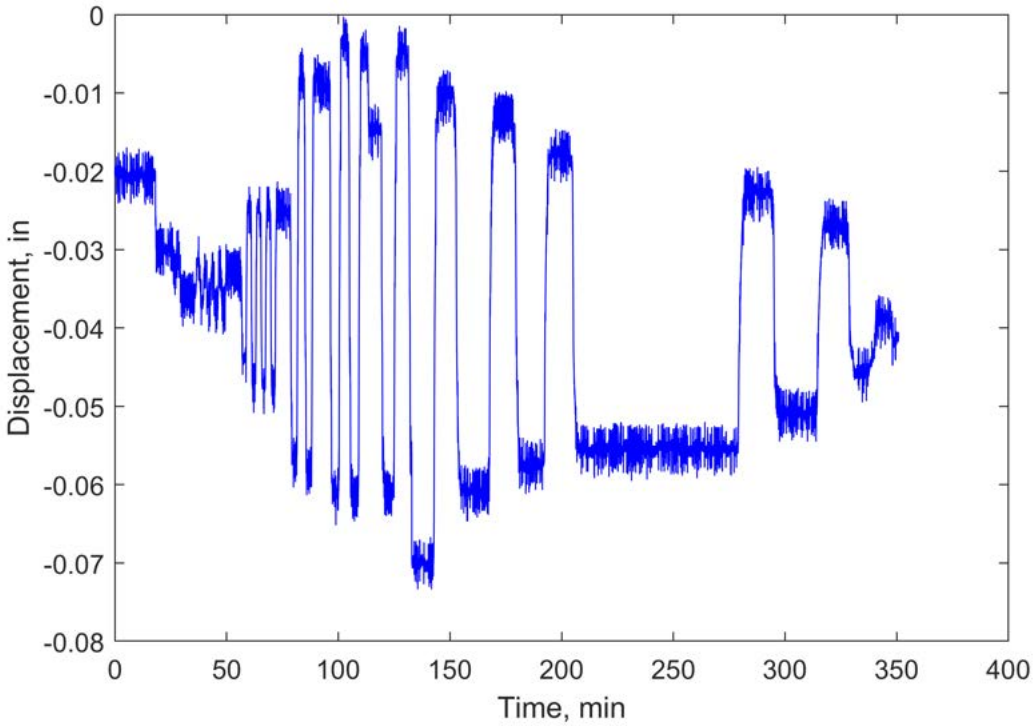

Figure M.3. Displacement-time plot of SP_03 for W36RBS-0.125NGT-T94.

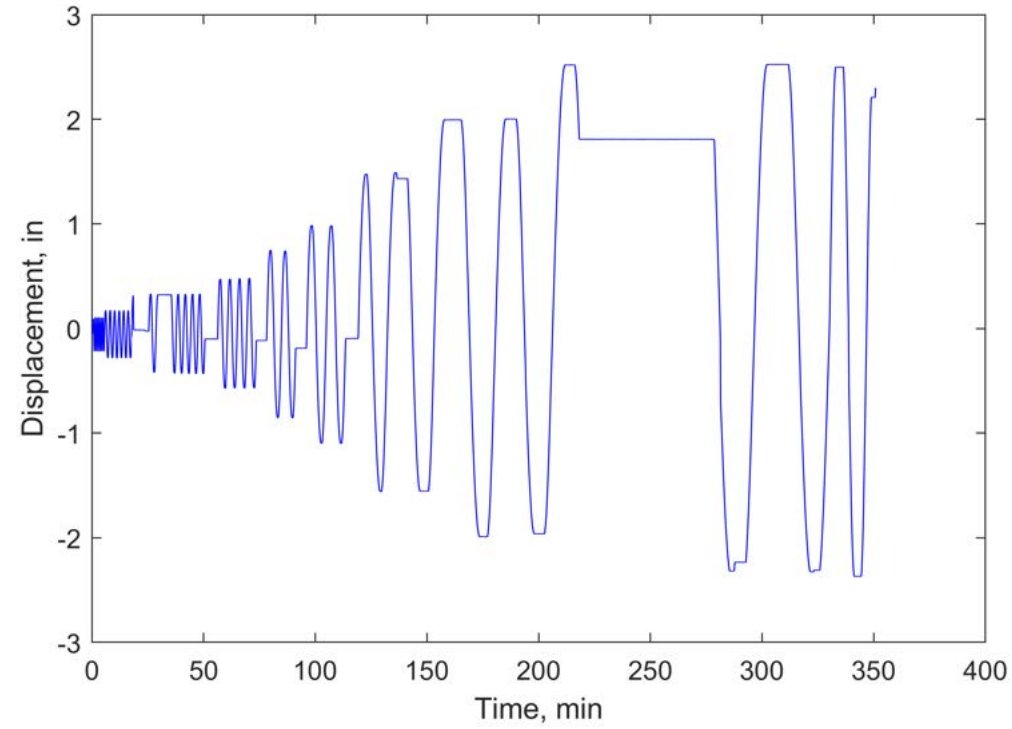

Figure M.4. Displacement-time plot of SP_04 for W36RBS-0.125NGT-T94.

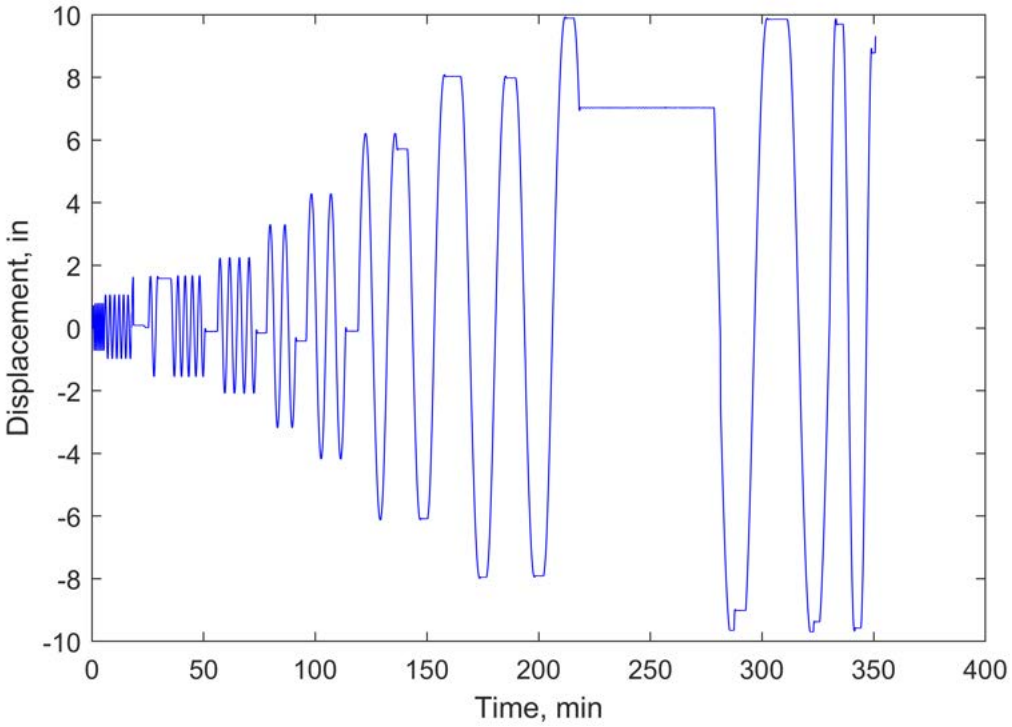

Figure M.5. Displacement-time plot of SP_05 for W36RBS-0.125NGT-T94.

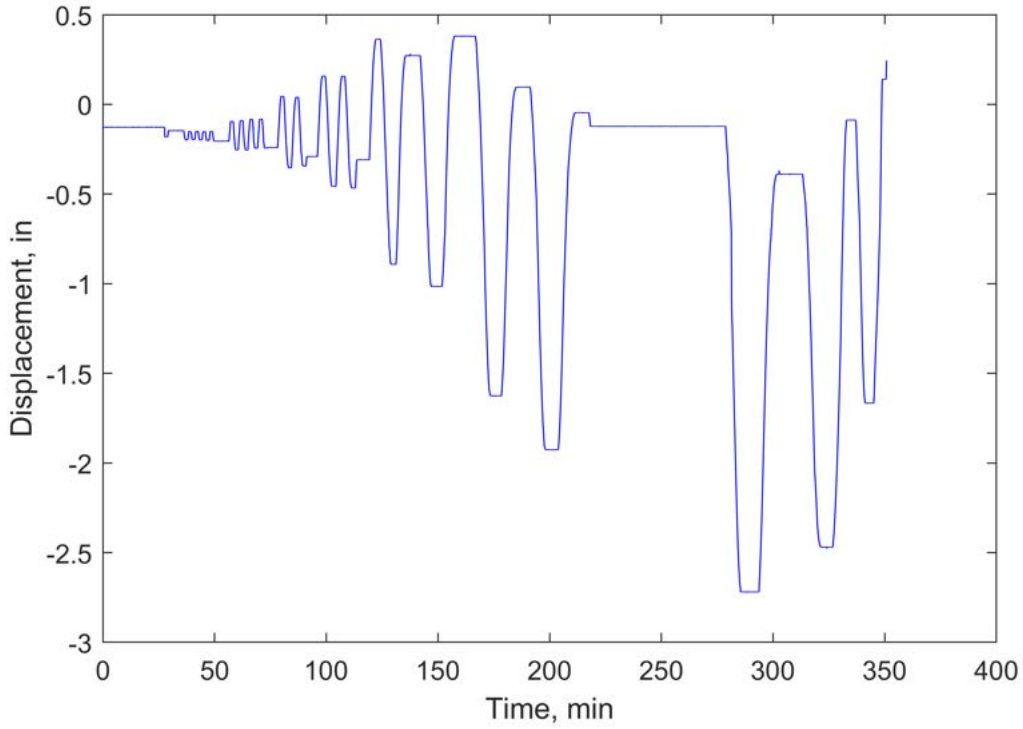

Figure M.6. Displacement-time plot of SP_06 for W36RBS-0.125NGT-T94.

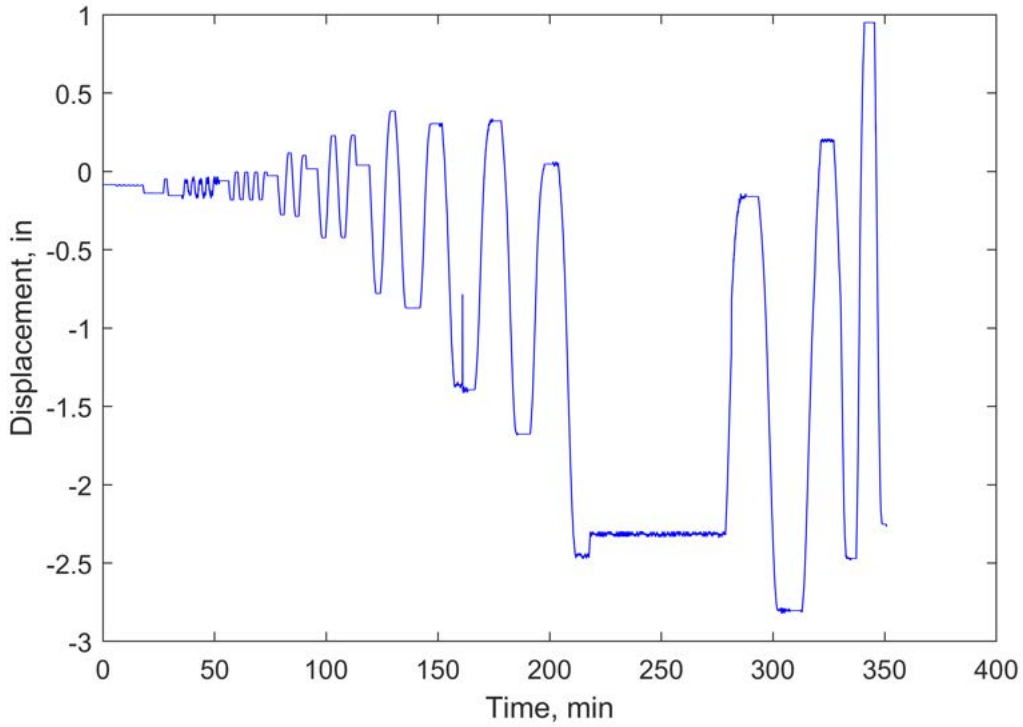

Figure M.7. Displacement-time plot of SP_07 for W36RBS-0.125NGT-T94.

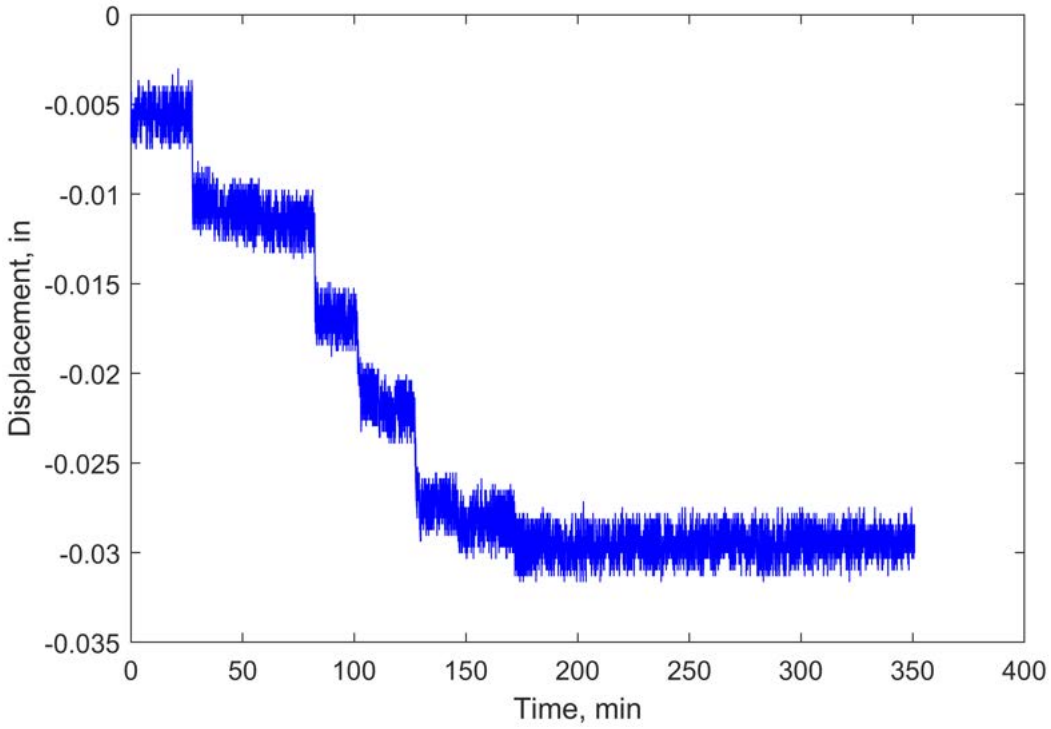

Figure M.8. Displacement-time plot of SP_08 for W36RBS-0.125NGT-T94.

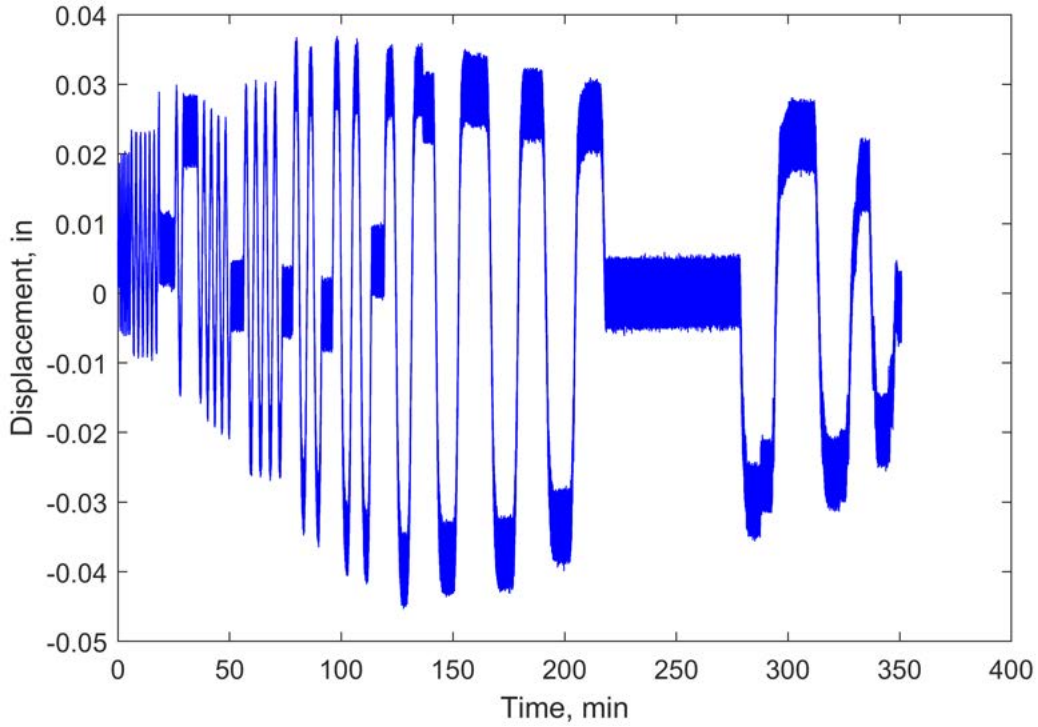

Figure M.9. Displacement-time plot of SP_09 for W36RBS-0.125NGT-T94.

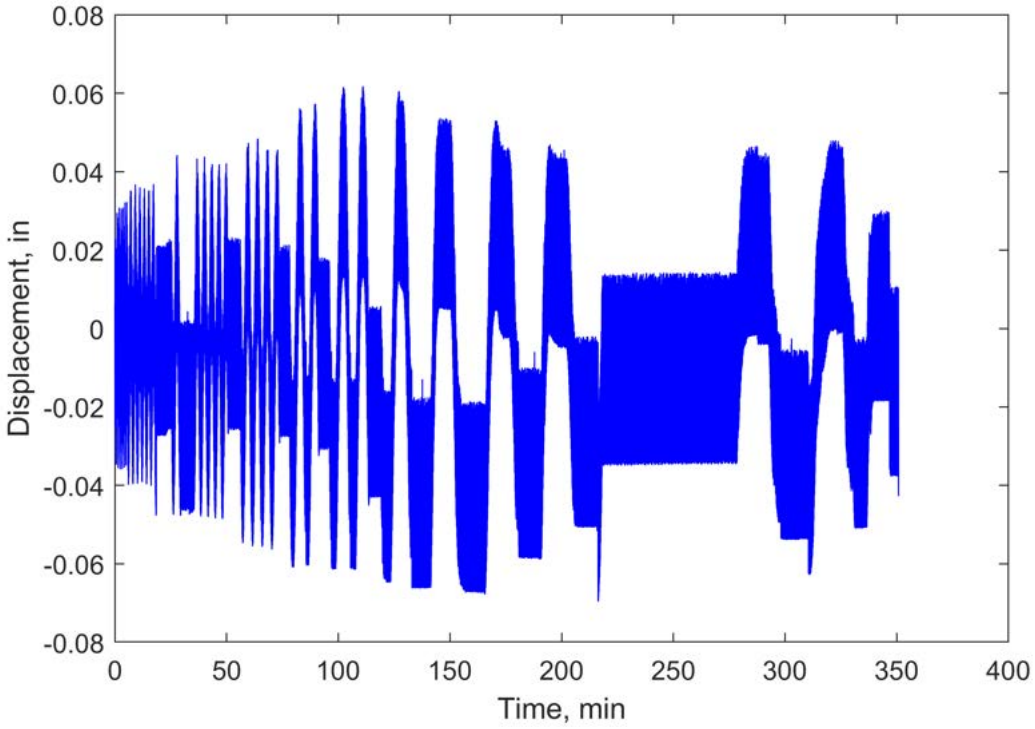

Figure M.10. Displacement-time plot of LP_01 for W36RBS-0.125NGT-T94.

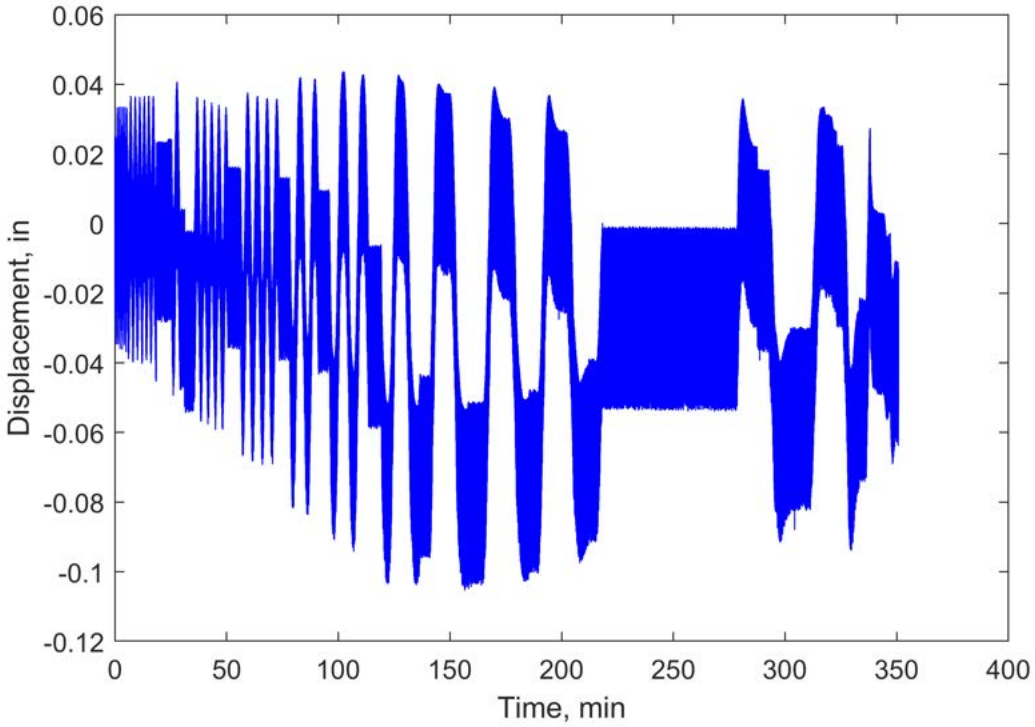

Figure M.11. Displacement-time plot of LP_02 for W36RBS-0.125NGT-T94.

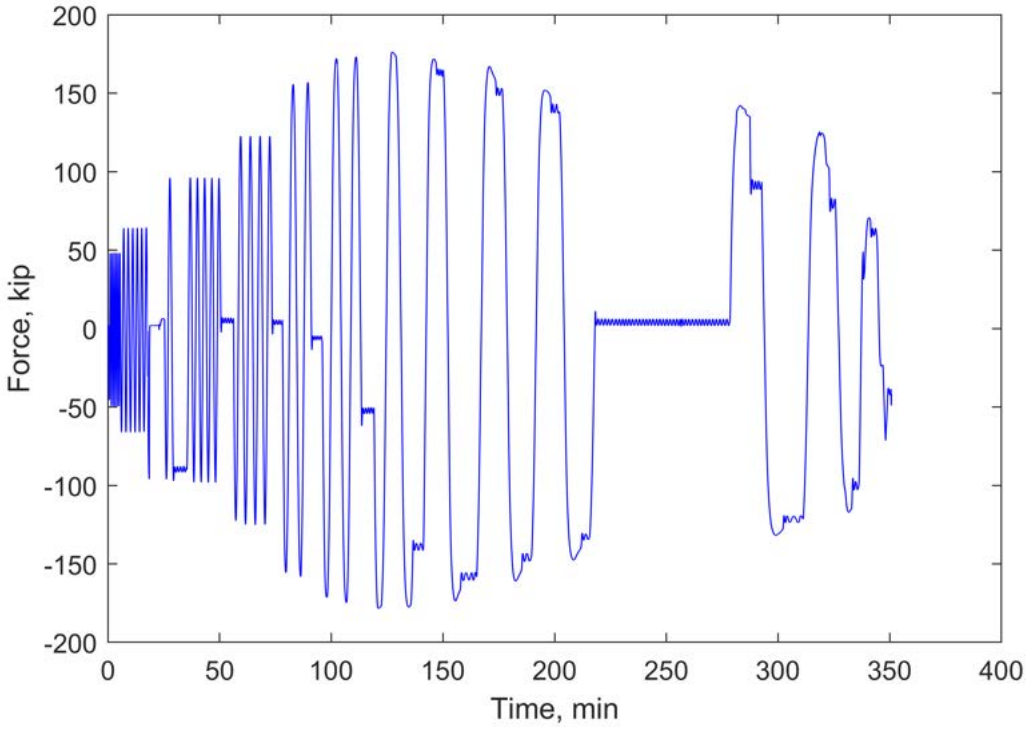

Figure M.12. Force-time plot for W36RBS-0.125NGT-T94.

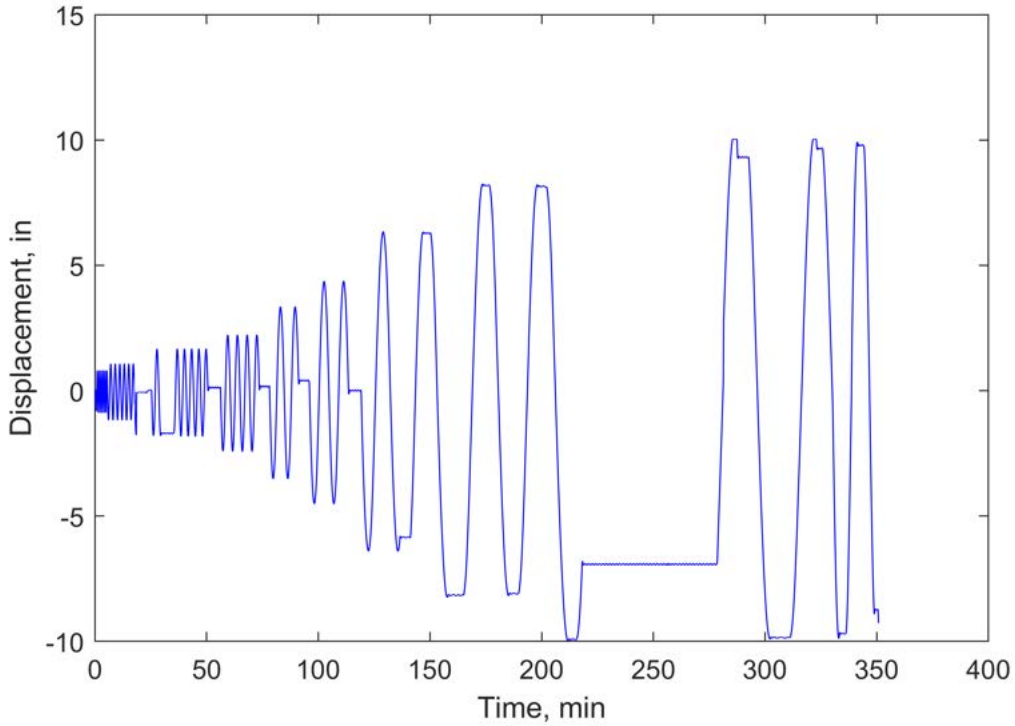

Figure M.13. Actuator displacement-time plot for W36RBS-0.125NGT-T94.

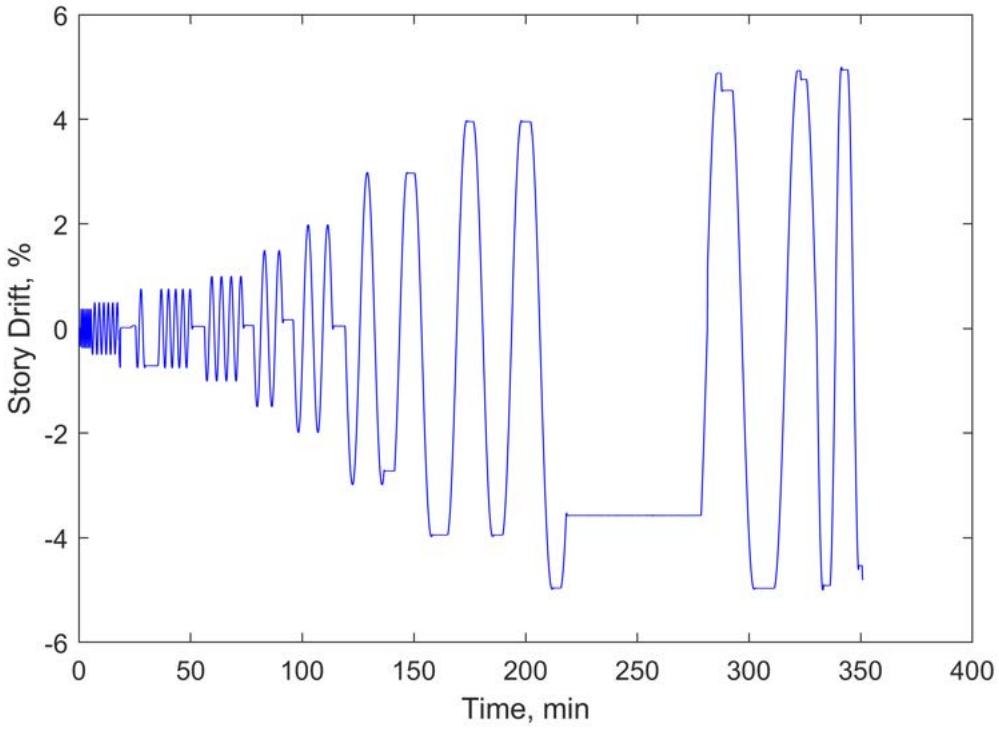

Figure M.14. Drift-time plot for W36RBS-0.125NGT-T94.

Appendix N. Sensor Plots for W24RBS-0.25NGTW-T59

This appendix includes modified sensor plots for the W24RBS-0.25NGTW-T59 test. A discussion of any data modifications is given in Appendix Y.

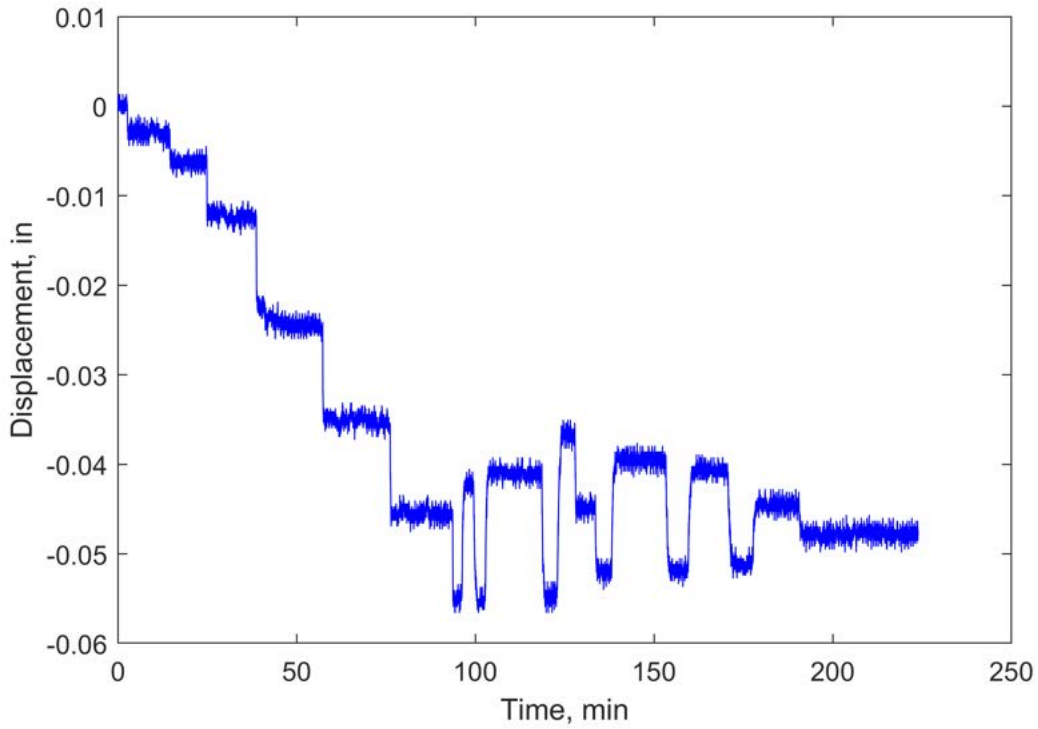

Figure N.1. Displacement-time plot of SP_01 for W24RBS-0.25NGTW-T59.

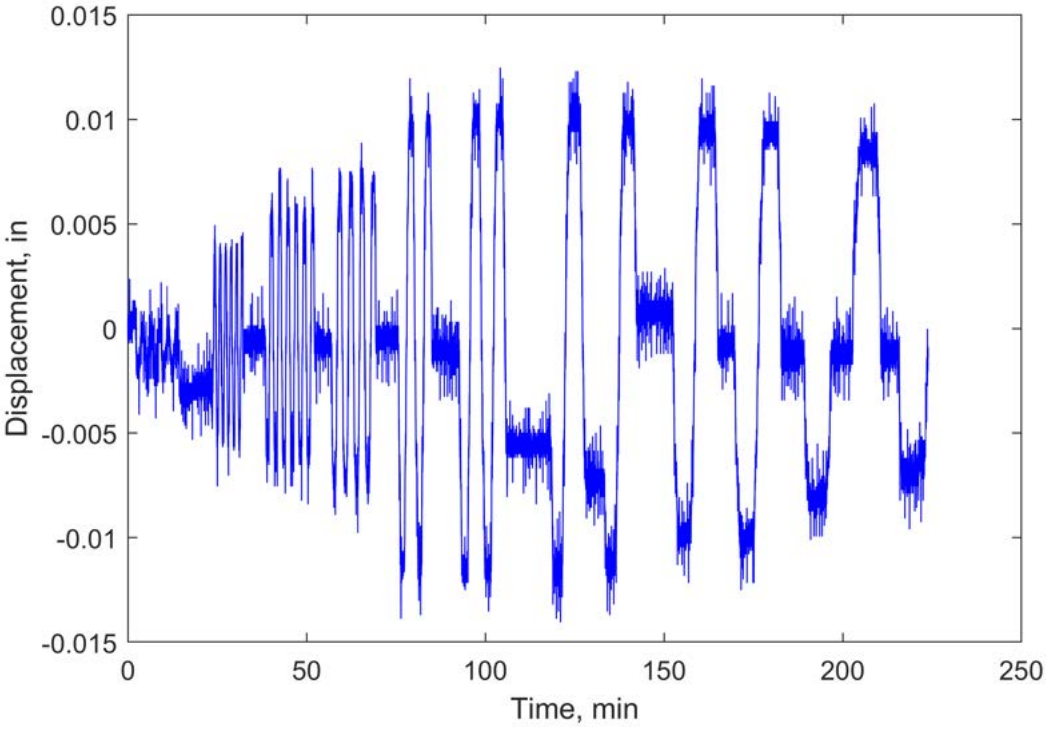

Figure N.2. Displacement-time plot of SP_02 for W24RBS-0.25NGTW-T59.

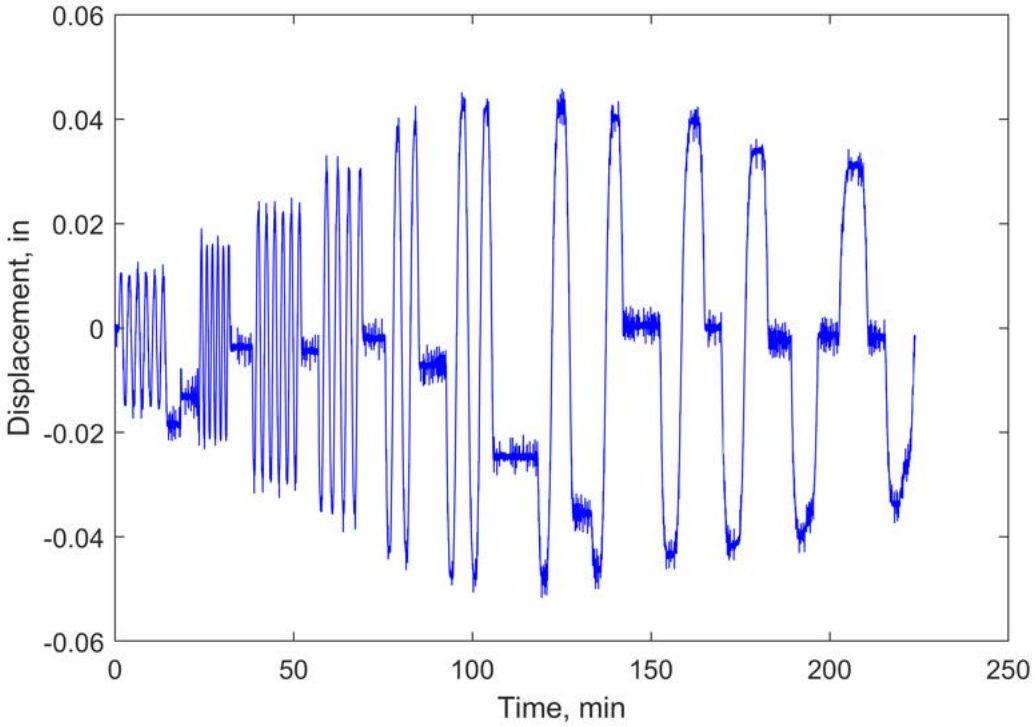

Figure N.3. Displacement-time plot of SP_03 for W24RBS-0.25NGTW-T59.

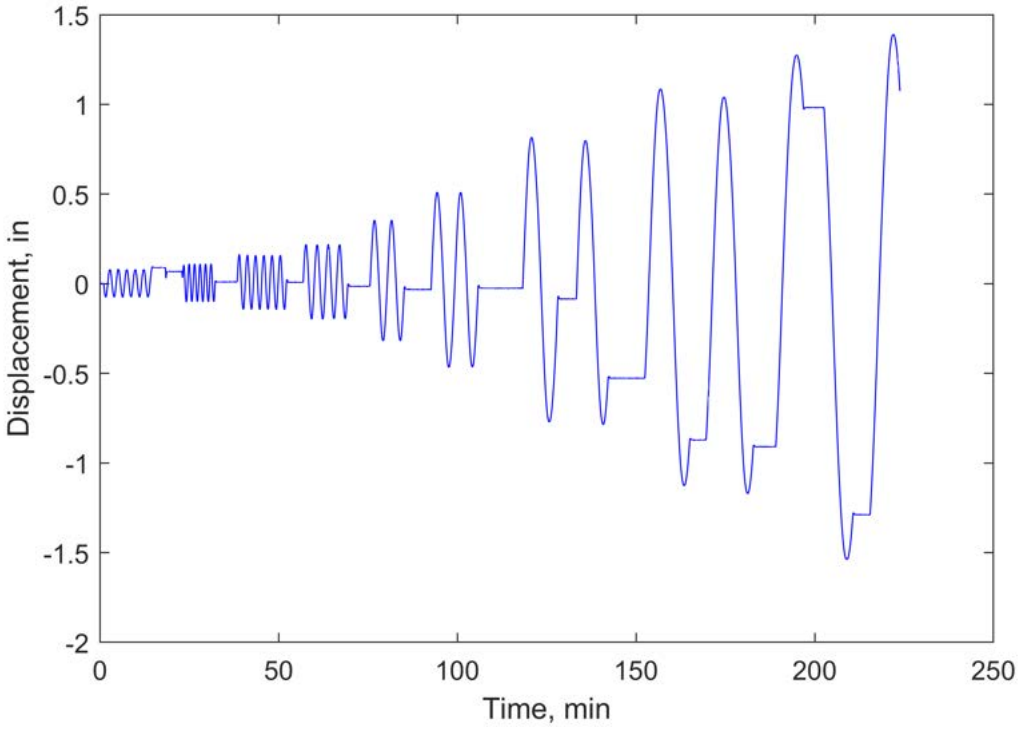

Figure N.4. Displacement-time plot of SP_04 for W24RBS-0.25NGTW-T59.

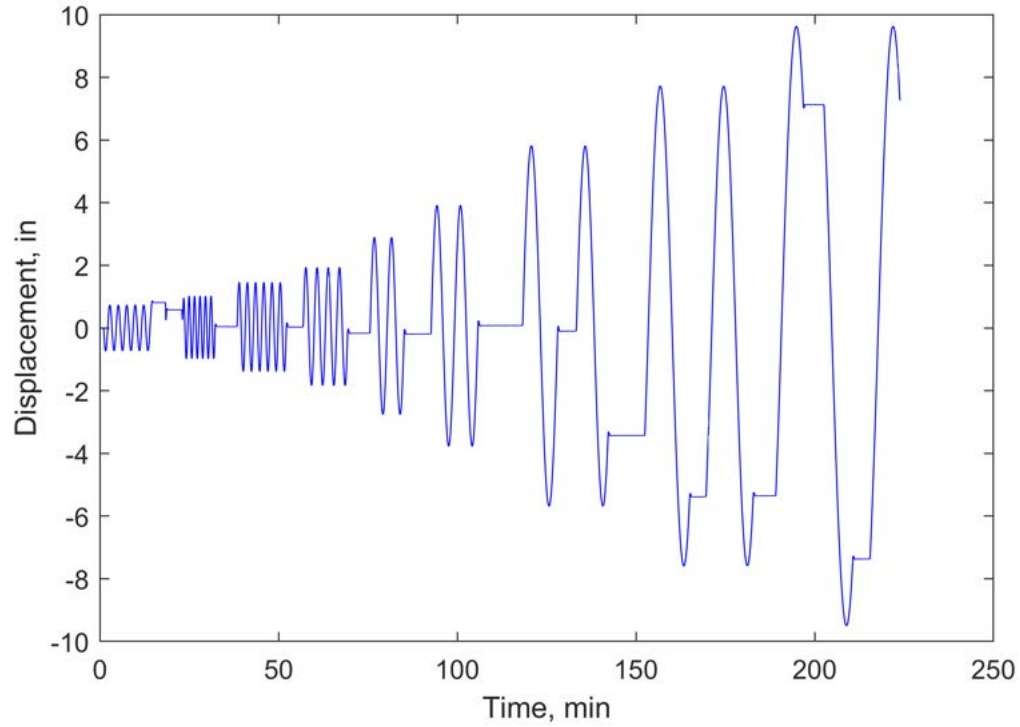

Figure N.5. Displacement-time plot of SP_05 for W24RBS-0.25NGTW-T59.

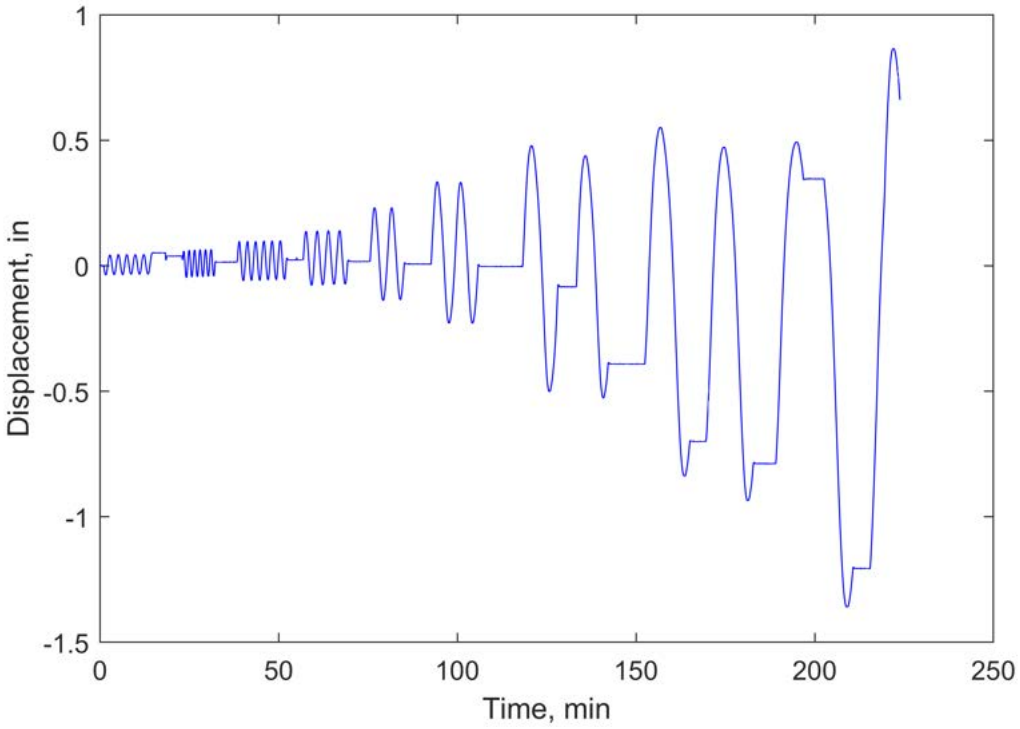

Figure N.6. Displacement-time plot of SP_06 for W24RBS-0.25NGTW-T59.

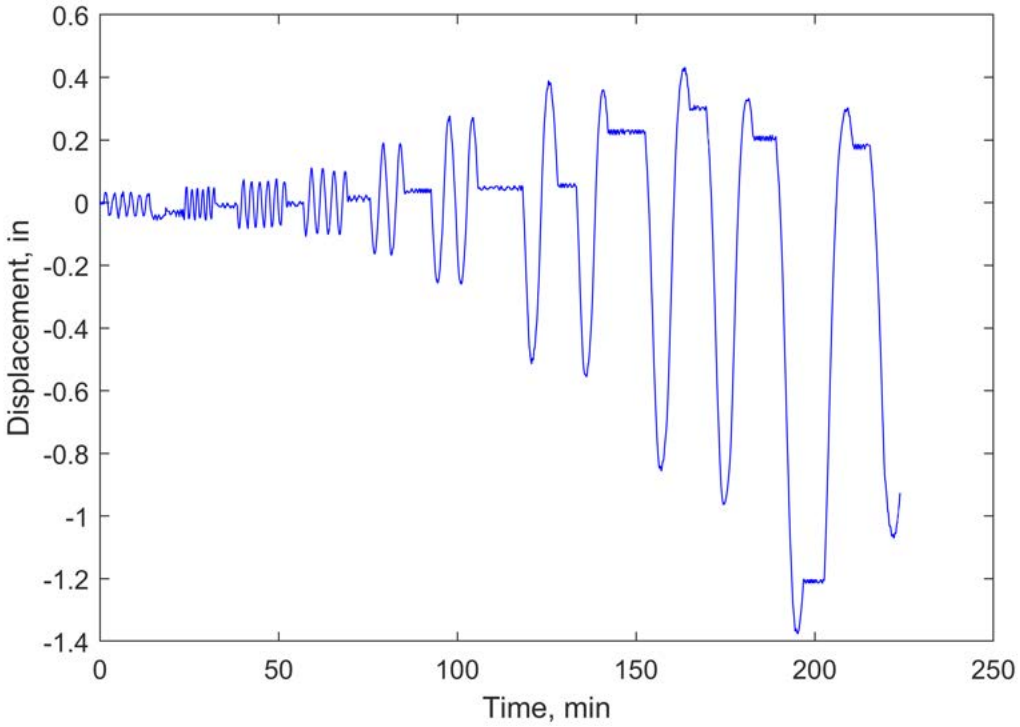

Figure N.7. Displacement-time plot of SP_07 for W24RBS-0.25NGTW-T59.

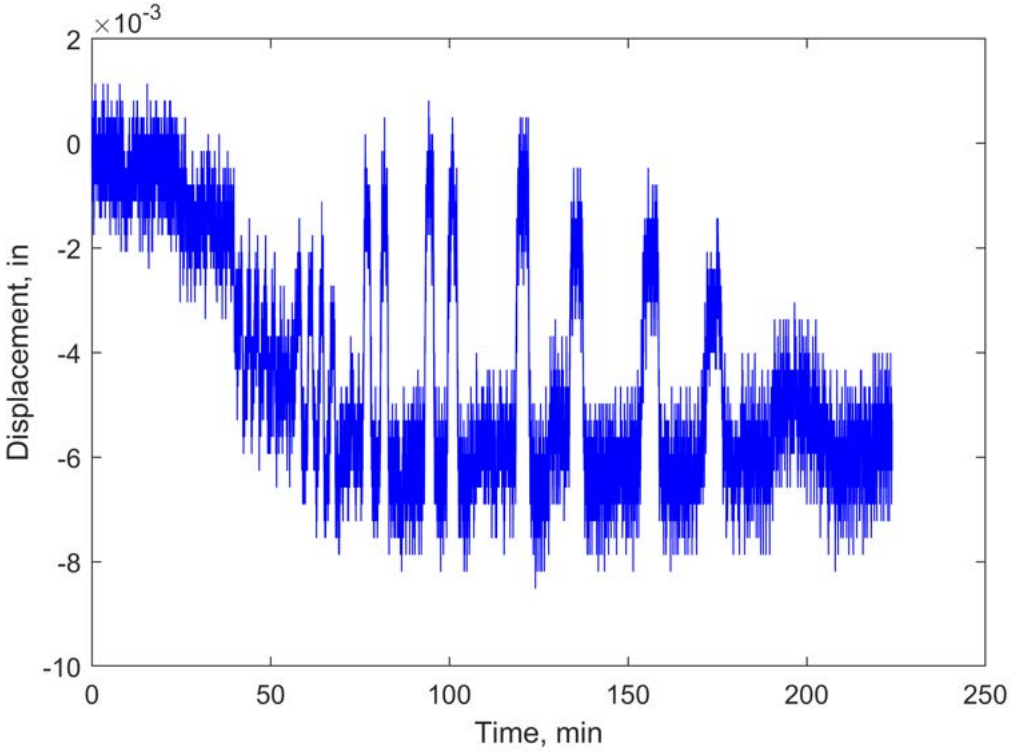

Figure N.8. Displacement-time plot of SP_08 for W24RBS-0.25NGTW-T59.

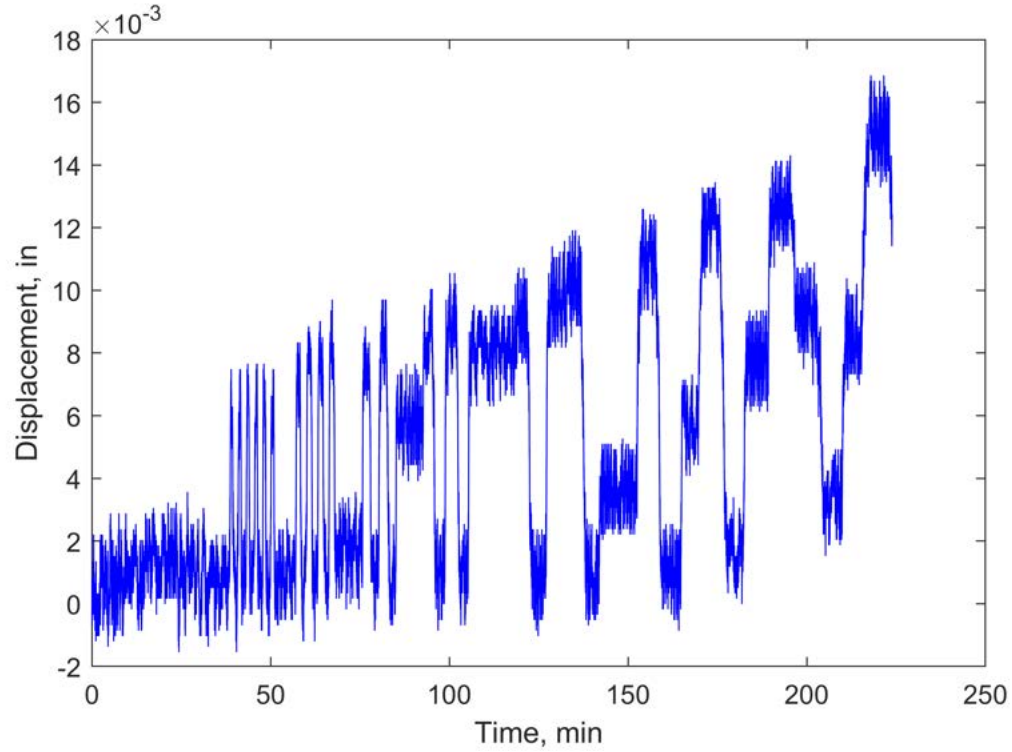

Figure N.9. Displacement-time plot of SP_09 for W24RBS-0.25NGTW-T59.

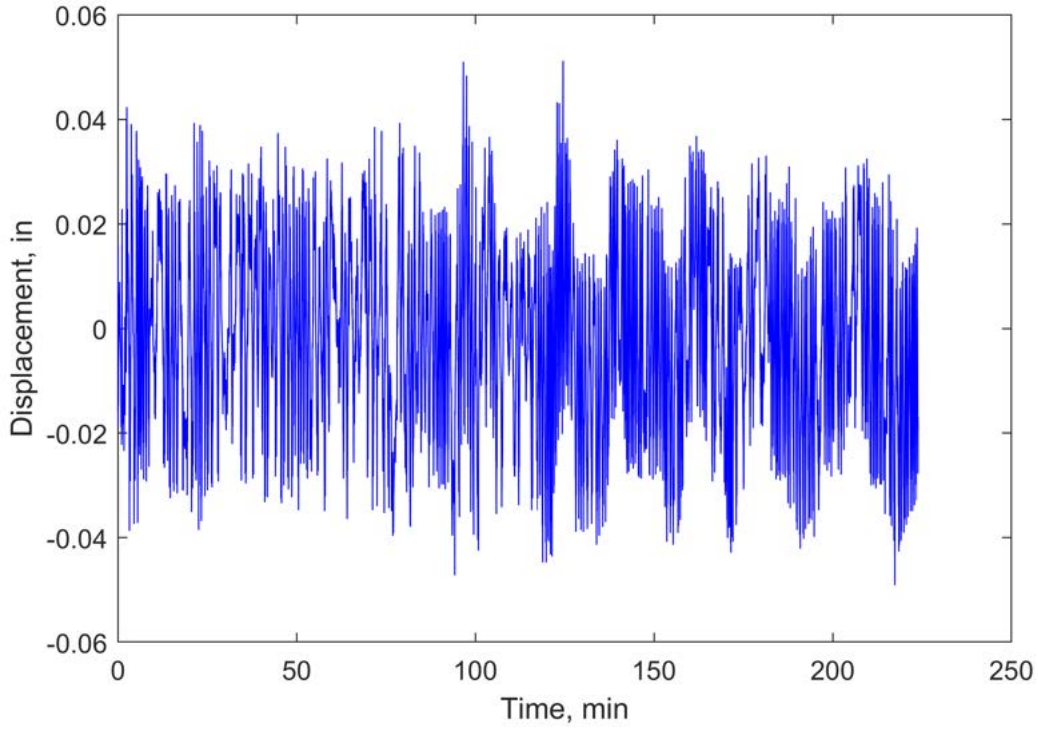

Figure N.10. Displacement-time plot of LP_01 for W24RBS-0.25NGTW-T59.

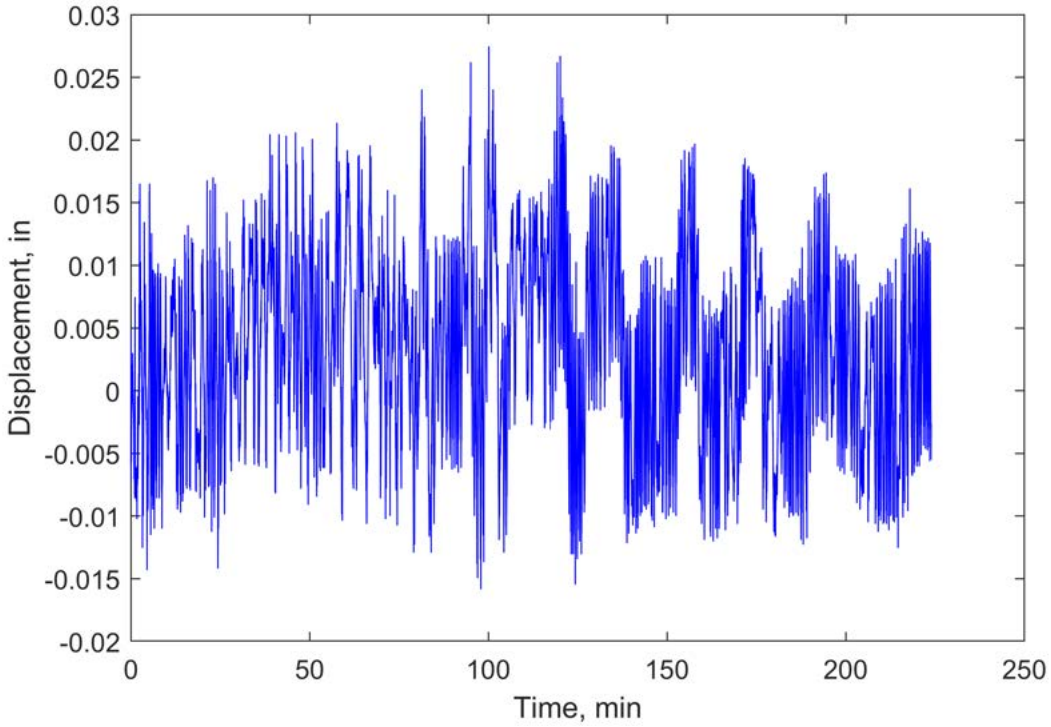

Figure N.11. Displacement-time plot of LP_02 for W24RBS-0.25NGTW-T59.

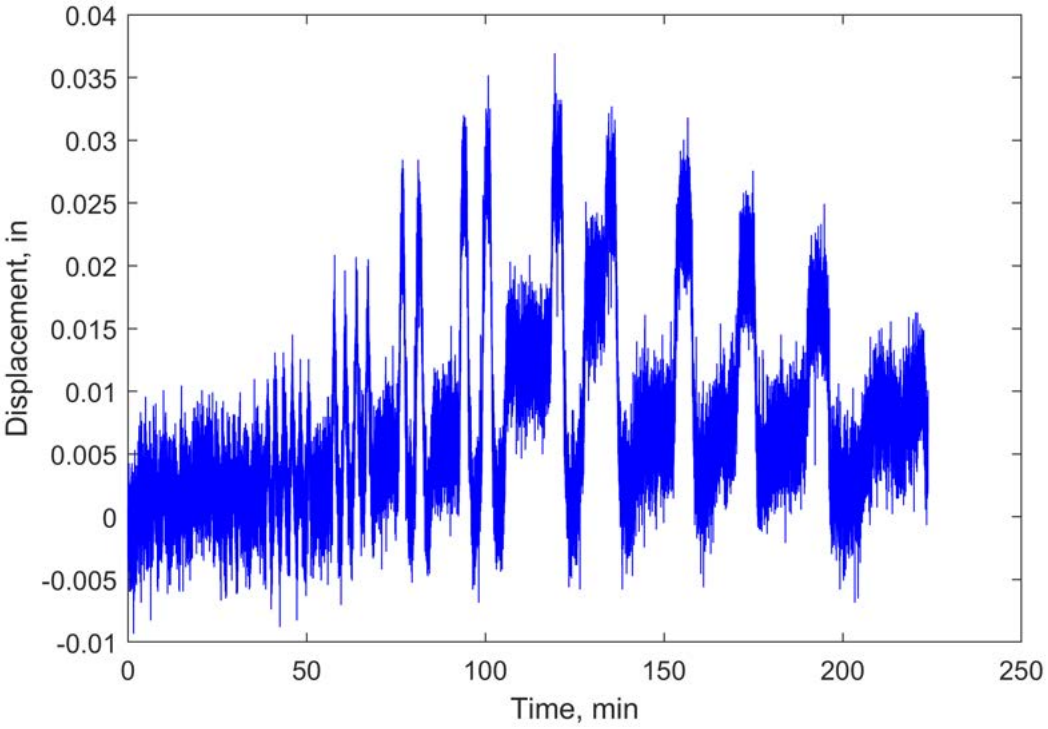

Figure N.12. Displacement-time plot of CLP_01 for W24RBS-0.25NGTW-T59.

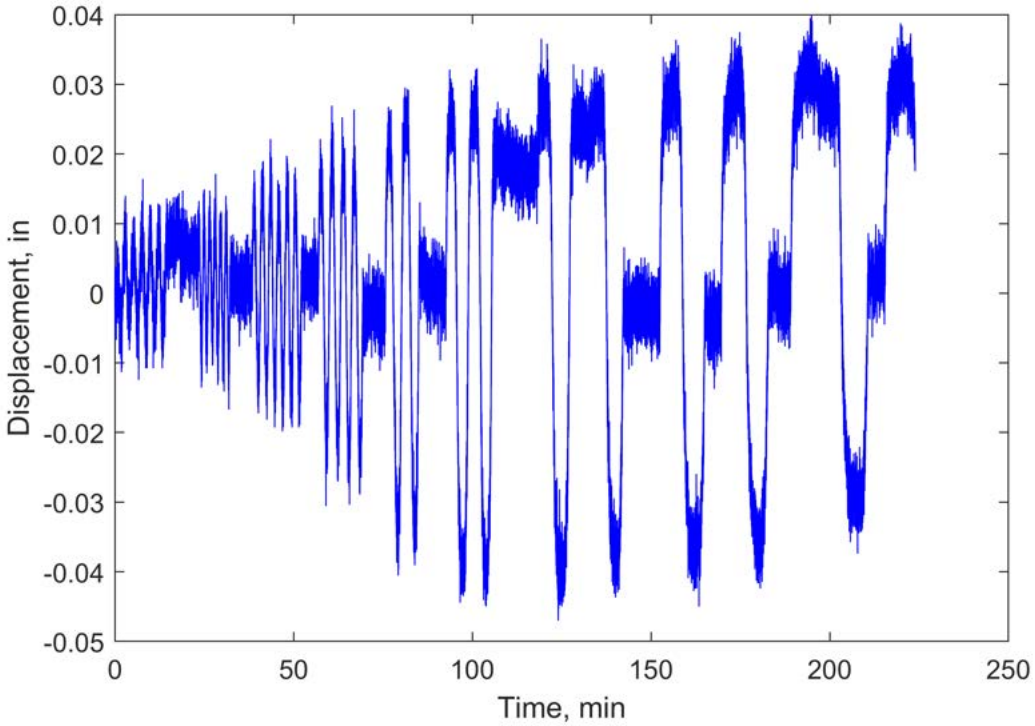

Figure N.13. Displacement-time plot of CLP_02 for W24RBS-0.25NGTW-T59.

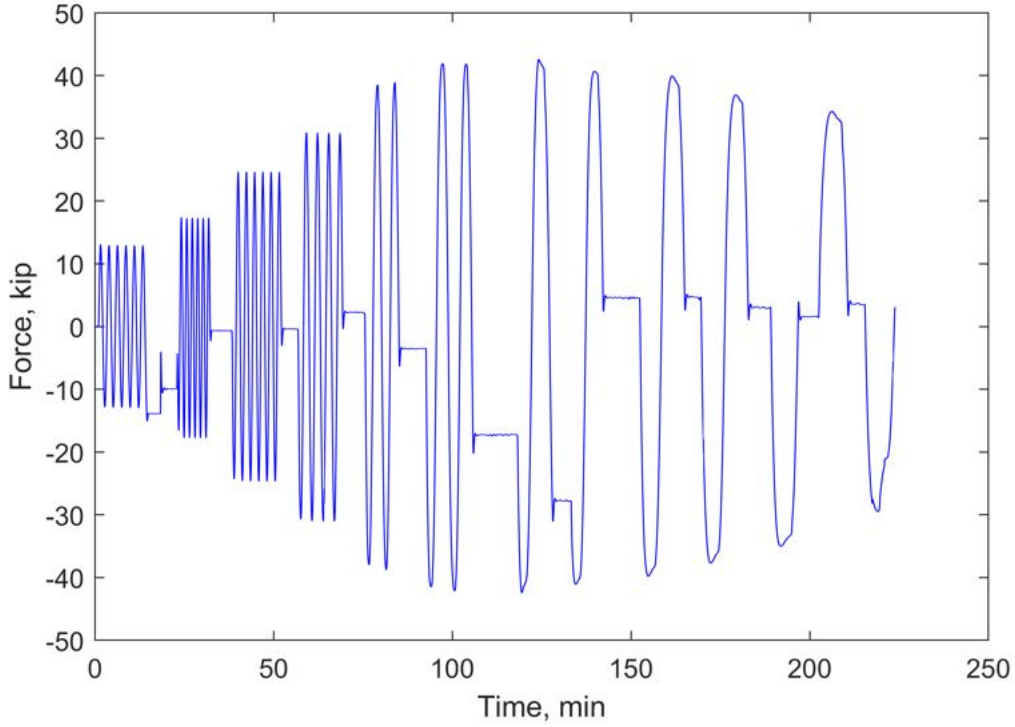

Figure N.14. Force-time plot for W24RBS-0.25NGTW-T59.

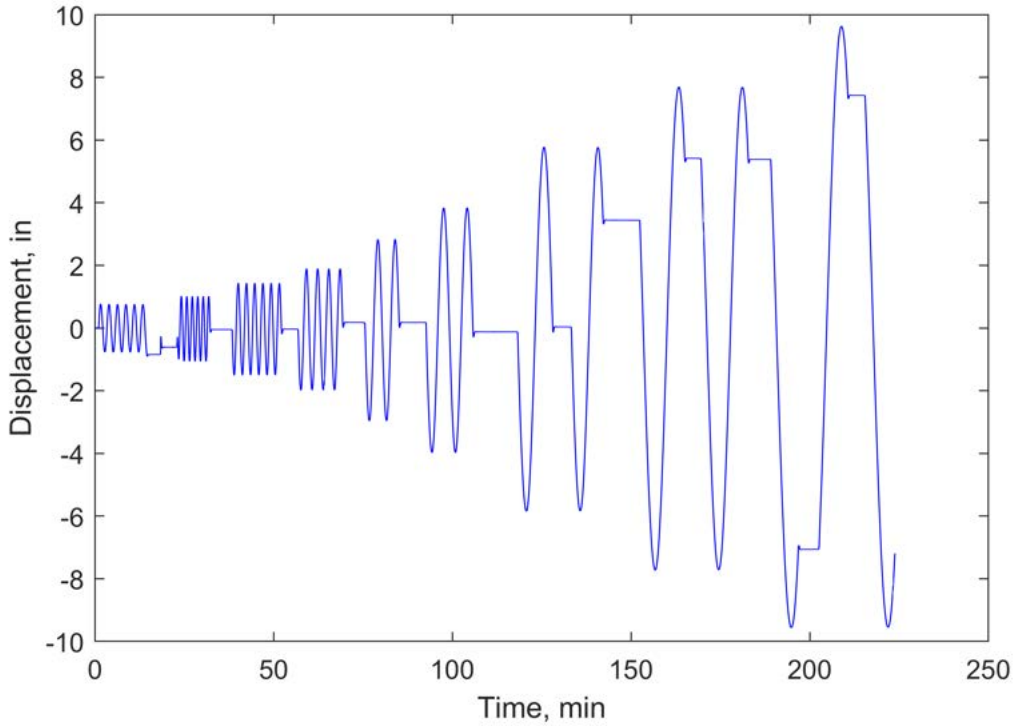

Figure N.15. Actuator displacement-time plot for W24RBS-0.25NGTW-T59.

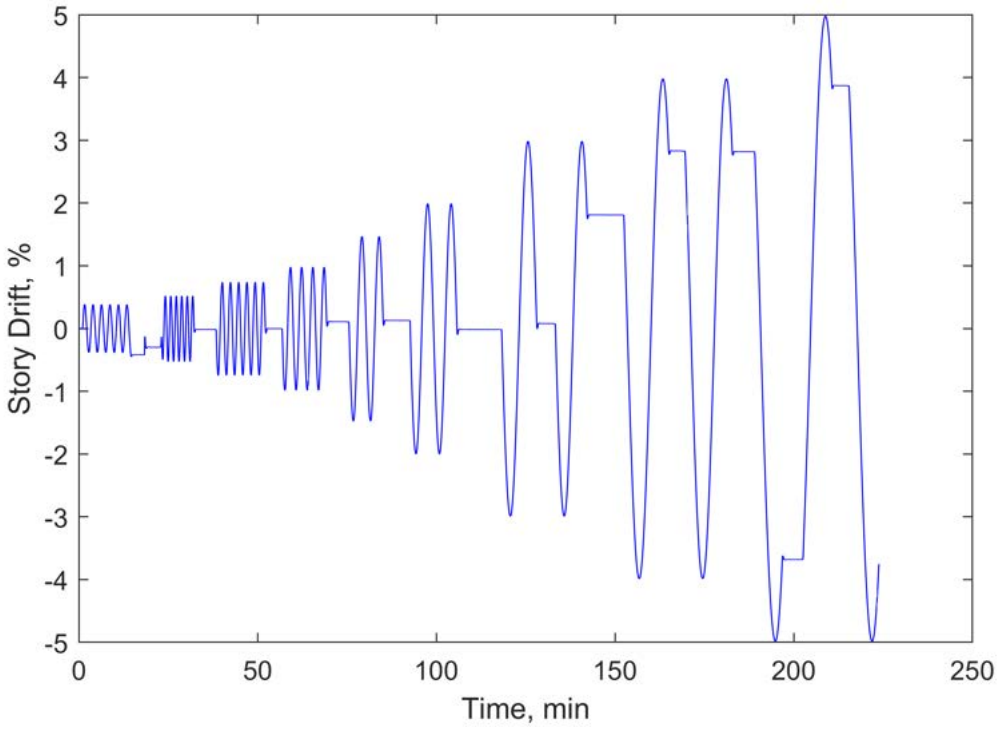

Figure N.16. Drift-time plot for W24RBS-0.25NGTW-T59.

Appendix O. Sensor Plots for W36RBS-0.25NGTW-T94

This appendix includes modified sensor plots for the W36RBS-0.25NGTW-T94 test. A discussion of any data modifications is given in Appendix Y.

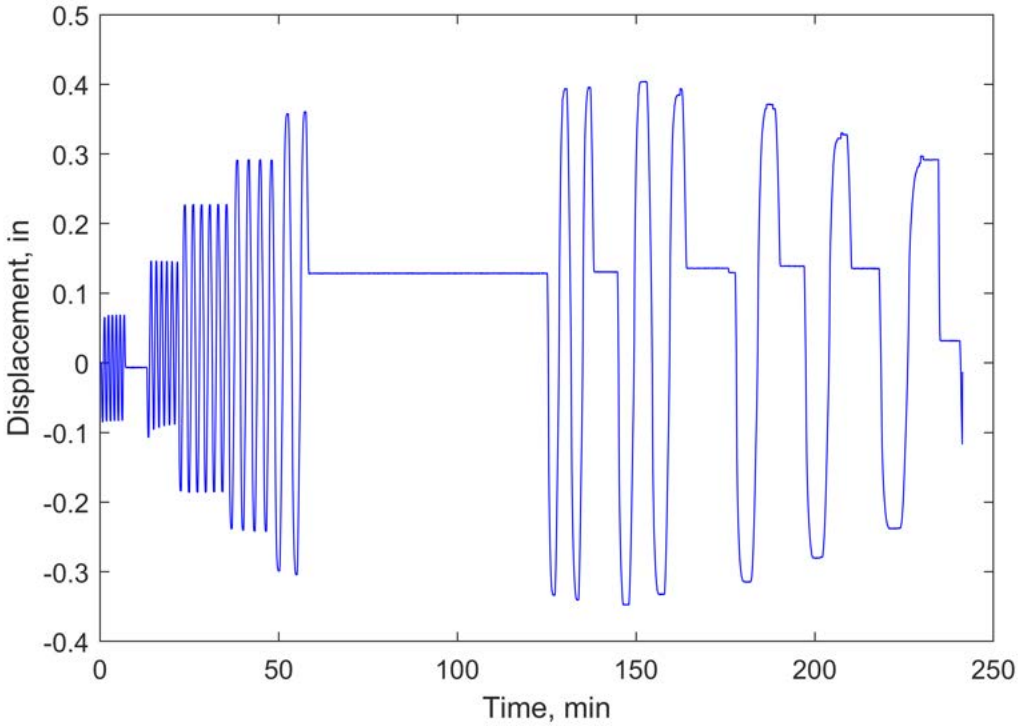

Figure O.1. Displacement-time plot of SP_01 for W36RBS-0.25NGTW-T94.

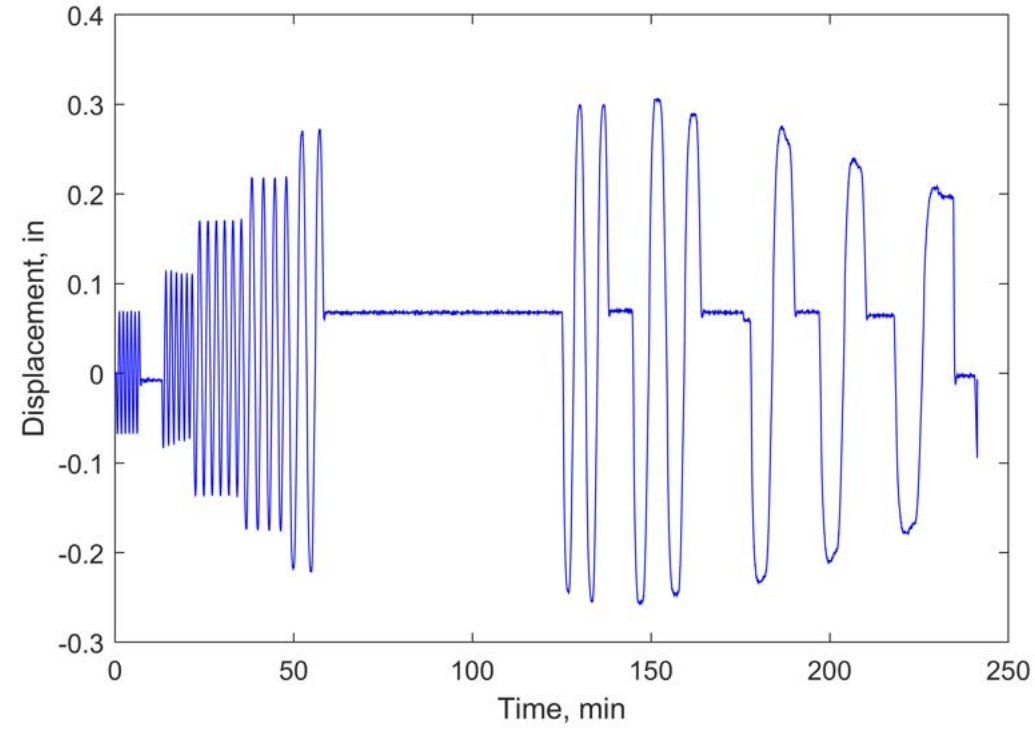

Figure O.2. Displacement-time plot of SP_02 for W36RBS-0.25NGTW-T94.

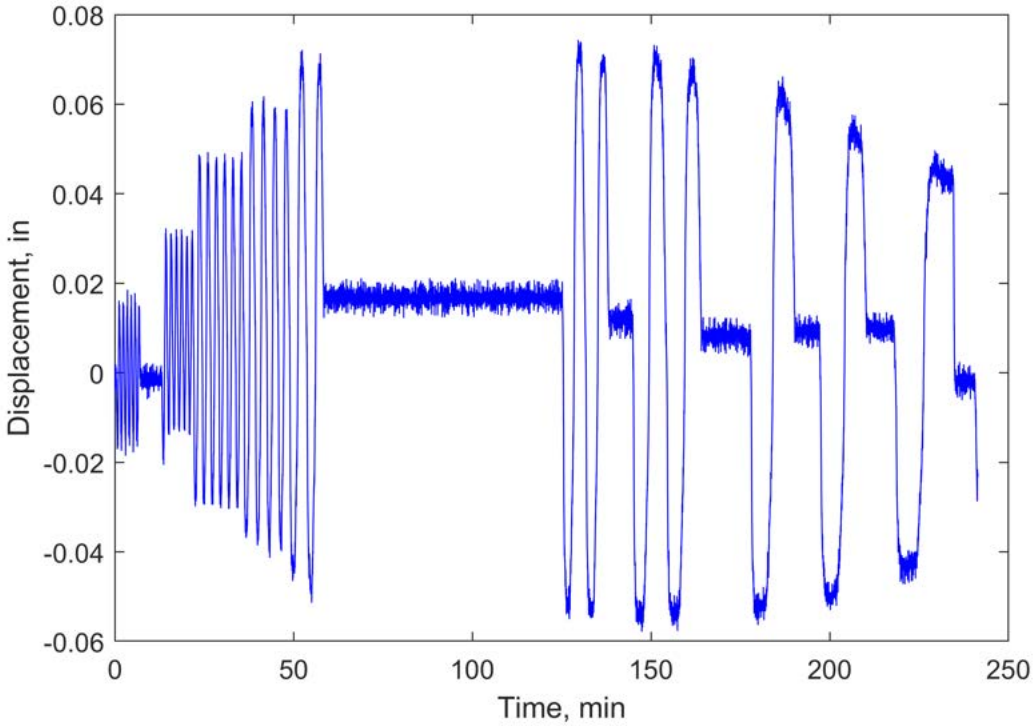

Figure O.3. Displacement-time plot of SP_03 for W36RBS-0.25NGTW-T94.

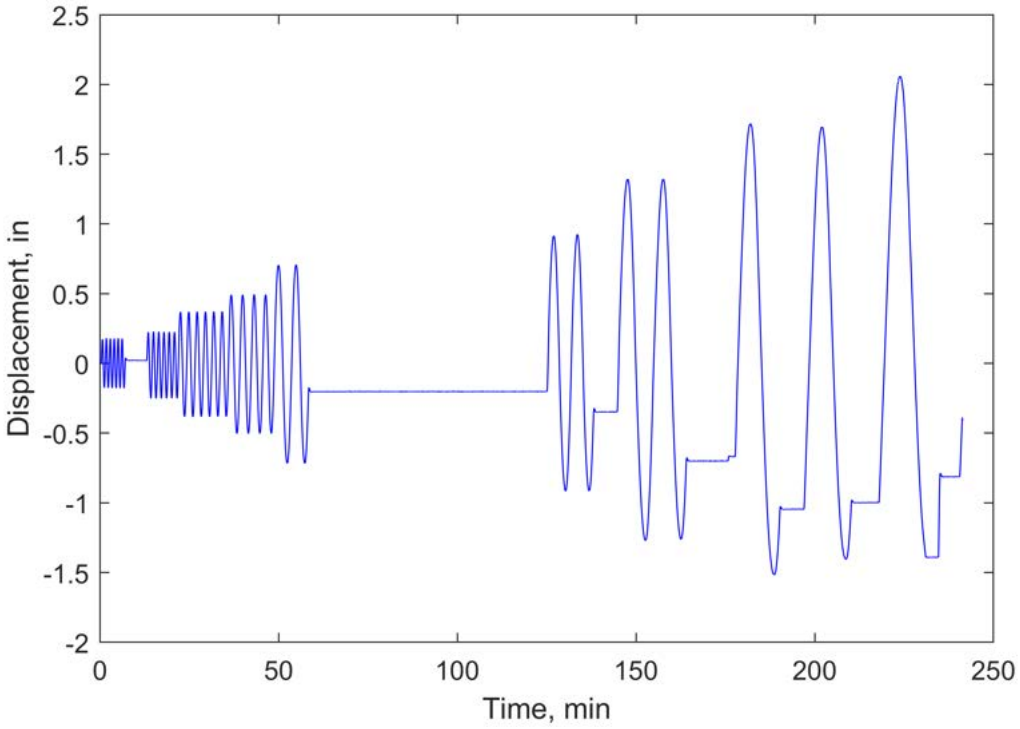

Figure O.4. Displacement-time plot of SP_04 for W36RBS-0.25NGTW-T94.

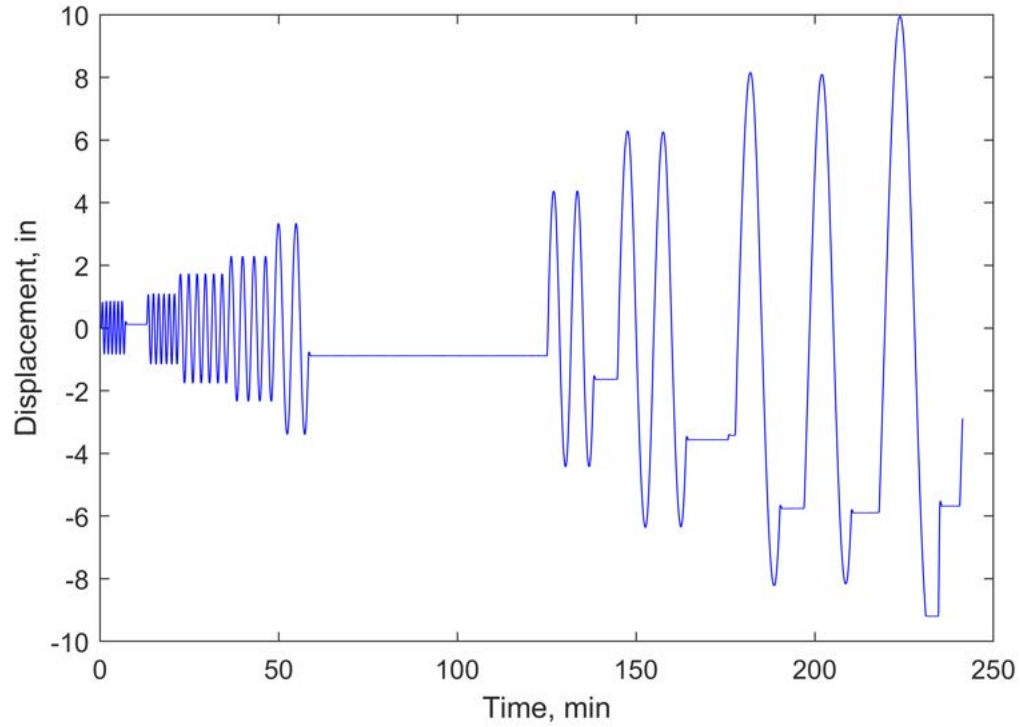

Figure O.5. Displacement-time plot of SP_05 for W36RBS-0.25NGTW-T94.

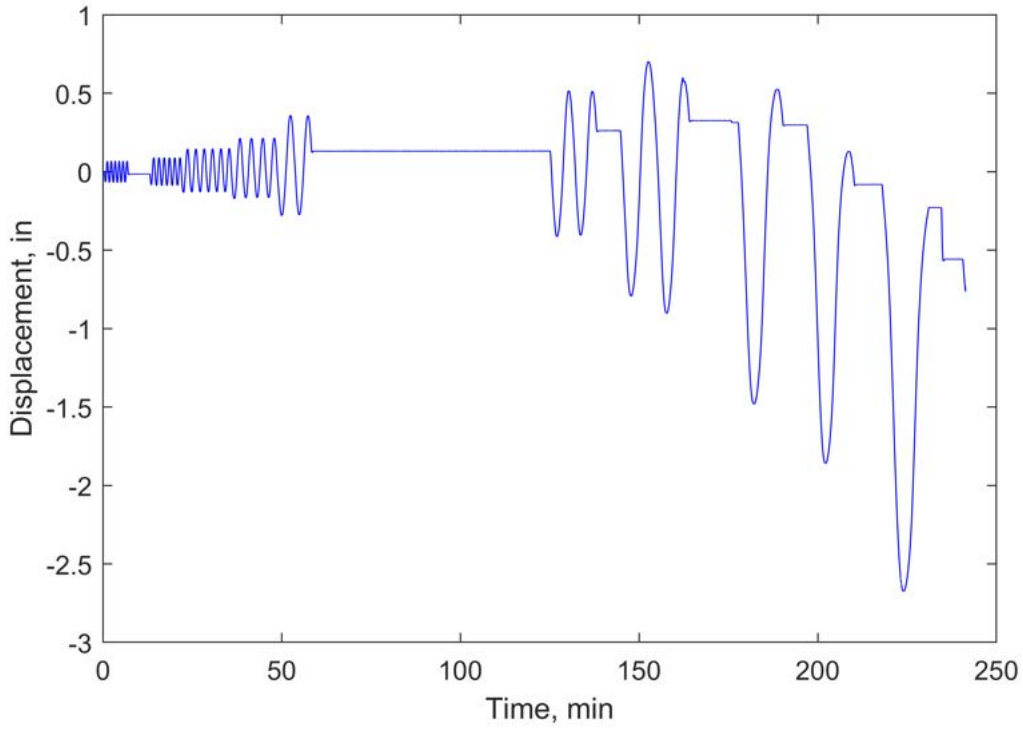

Figure O.6. Displacement-time plot of SP_06 for W36RBS-0.25NGTW-T94.

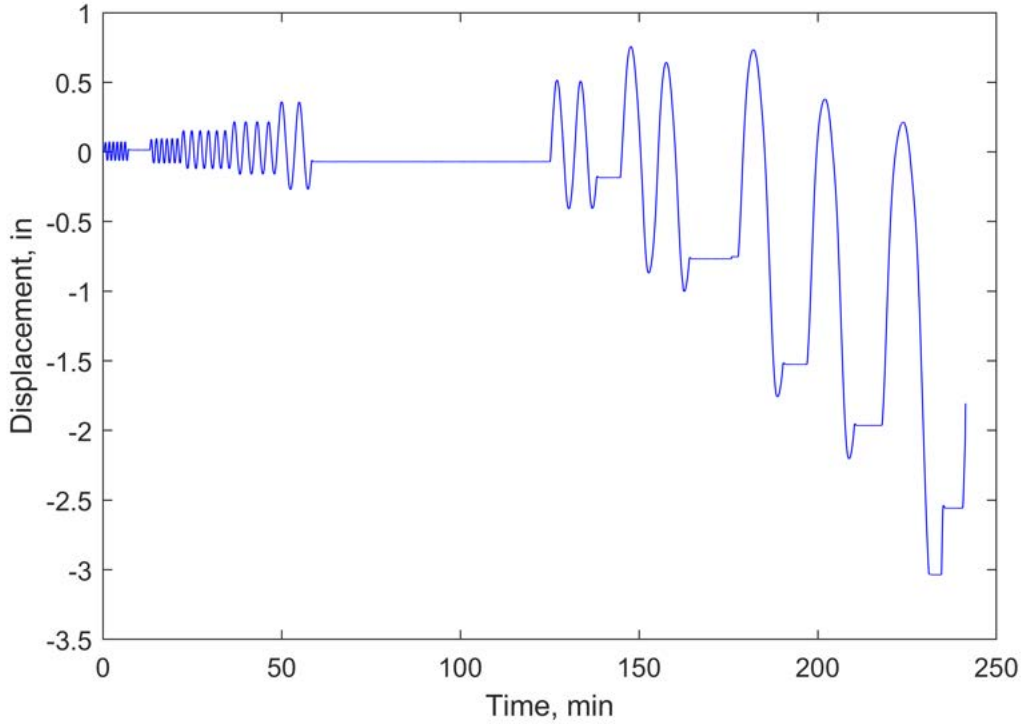

Figure O.7. Displacement-time plot of SP_07 for W36RBS-0.25NGTW-T94.

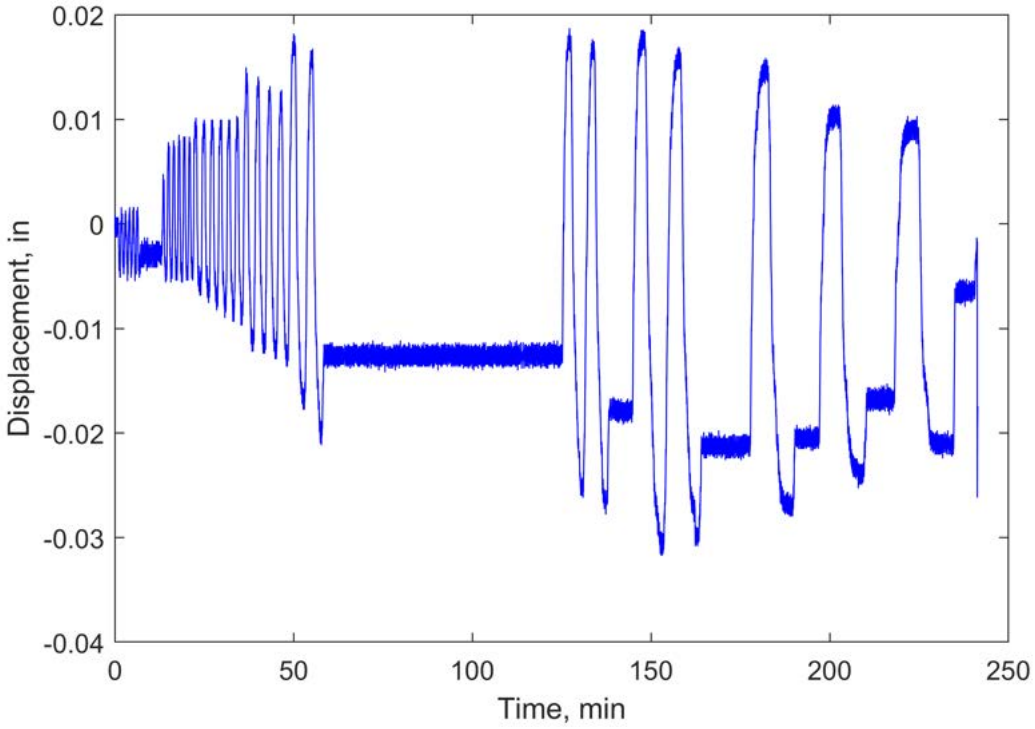

Figure O.8. Displacement-time plot of SP_08 for W36RBS-0.25NGTW-T94.

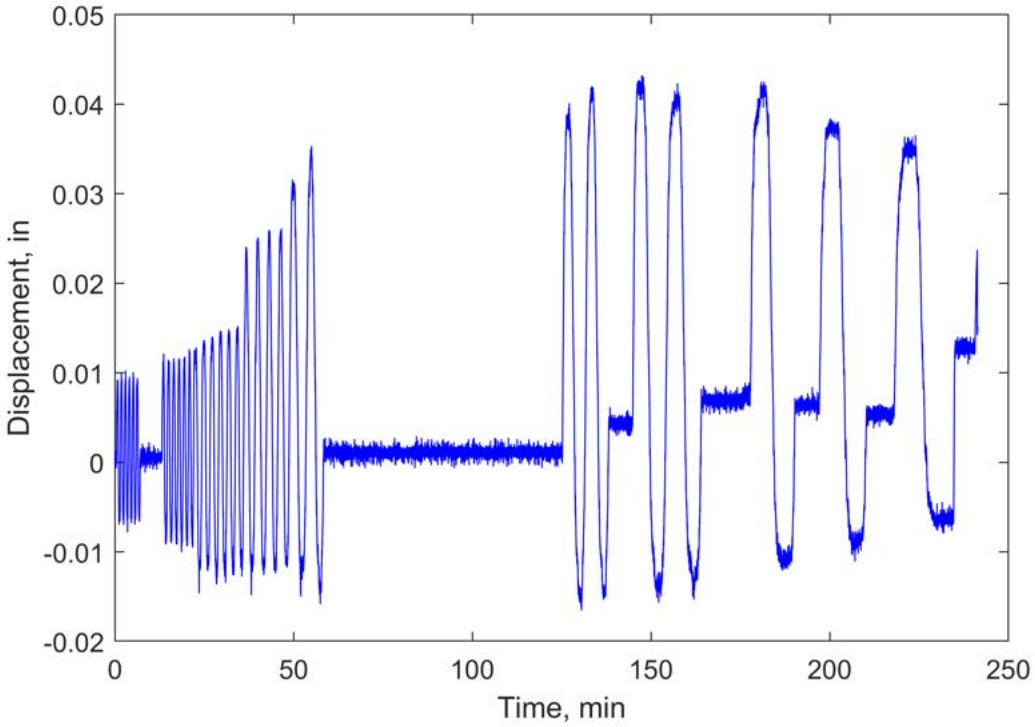

Figure O.9. Displacement-time plot of SP_09 for W36RBS-0.25NGTW-T94.

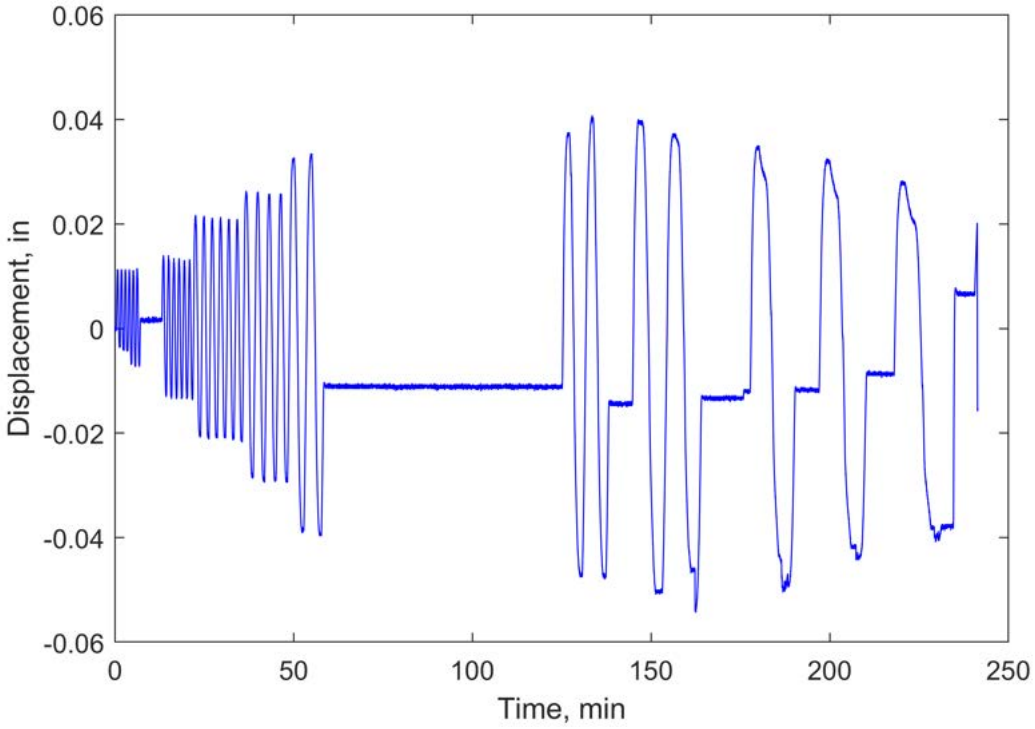

Figure O.10. Displacement-time plot of LP_01 for W36RBS-0.25NGTW-T94.

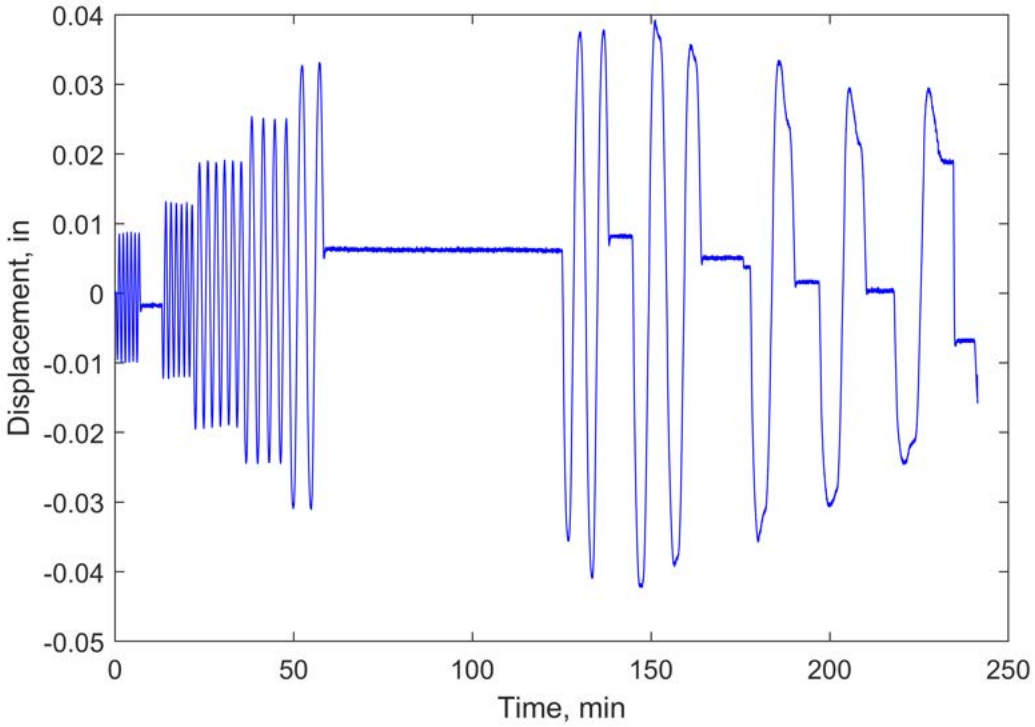

Figure O.11. Displacement-time plot of LP_02 for W36RBS-0.25NGTW-T94.

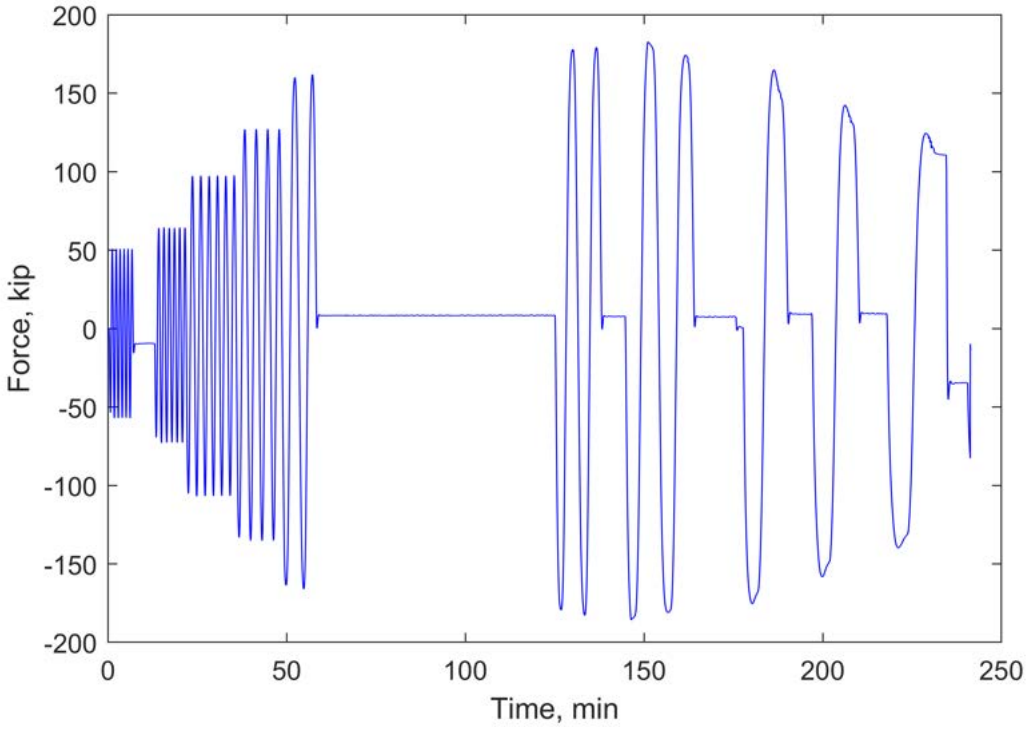

Figure O.12. Force-time plot for W36RBS-0.25NGTW-T94.

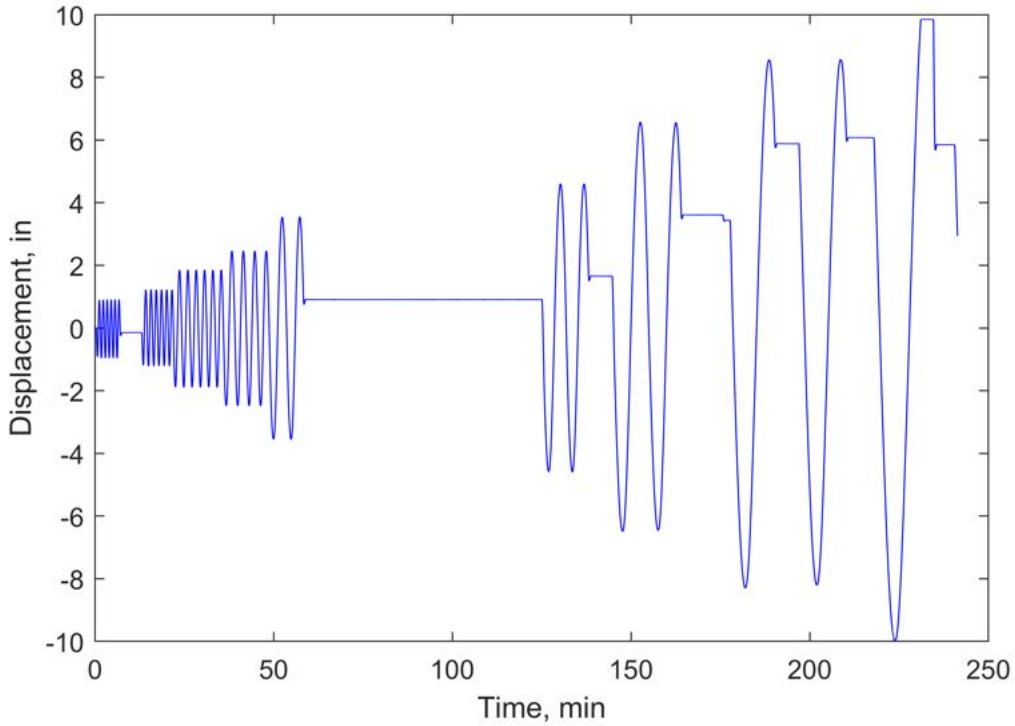

Figure O.13. Actuator displacement-time plot for W36RBS-0.25NGTW-T94.

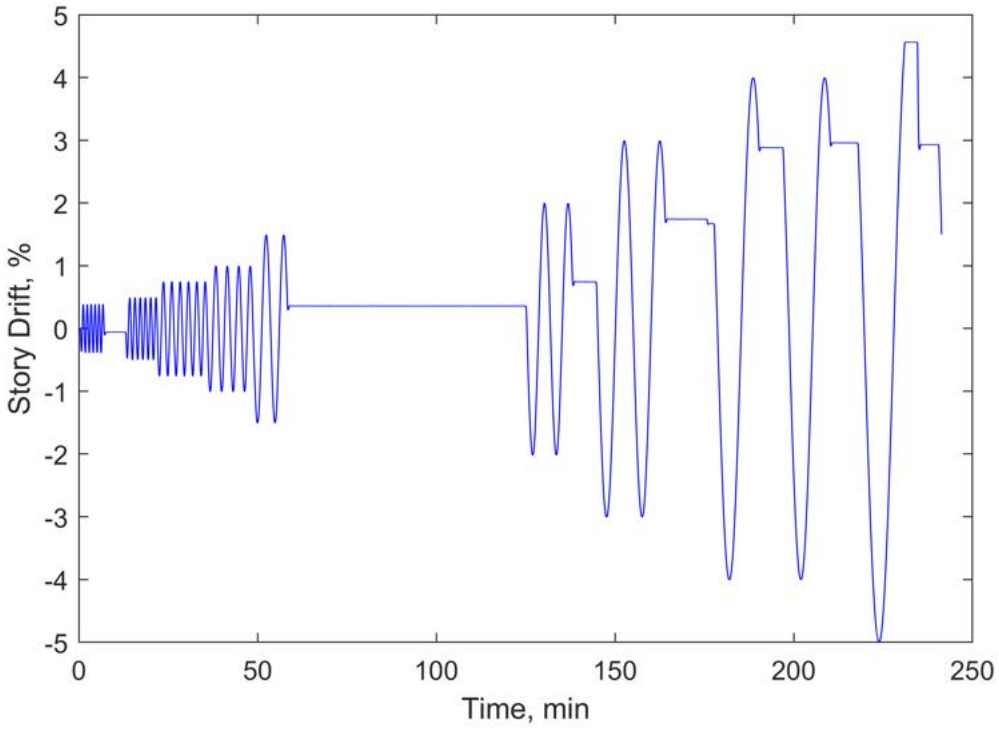

Figure O.14. Drift-time plot for W36RBS-0.25NGTW-T94.

Appendix P. Sensor Plots for W24RBS-0.375N-T59

This appendix includes modified sensor plots for the W24RBS-0.375N-T59 test. A discussion of any data modifications is given in Appendix Y.

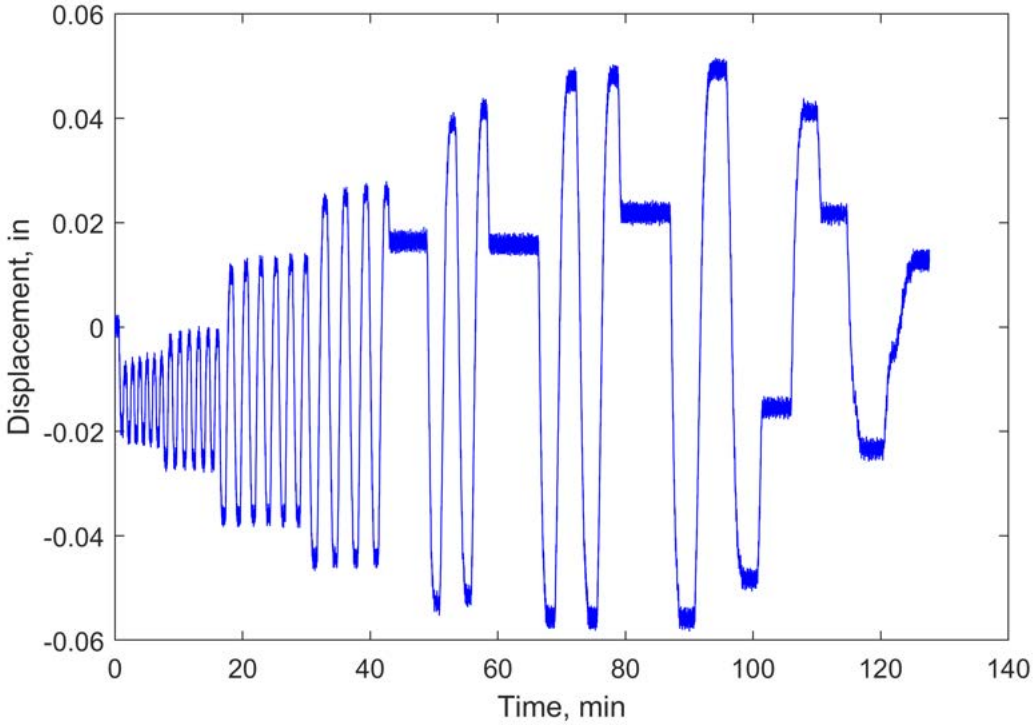

Figure P.1. Displacement-time plot of SP_01 for W24RBS-0.375N-T59.

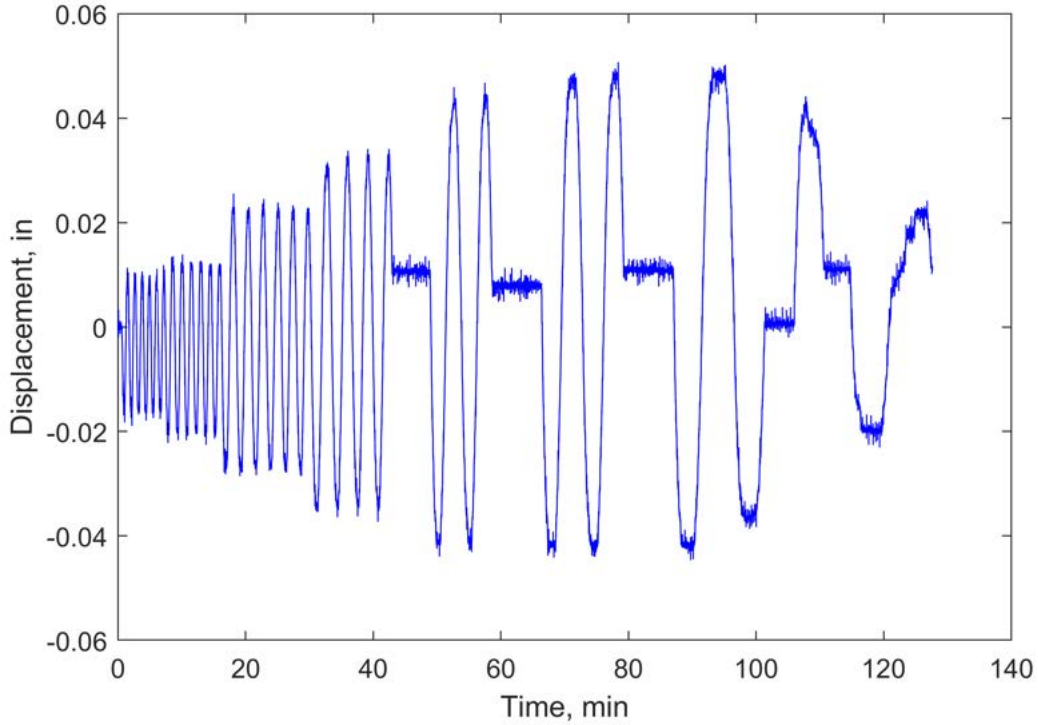

Figure P.2. Displacement-time plot of SP_02 for W24RBS-0.375N-T59.

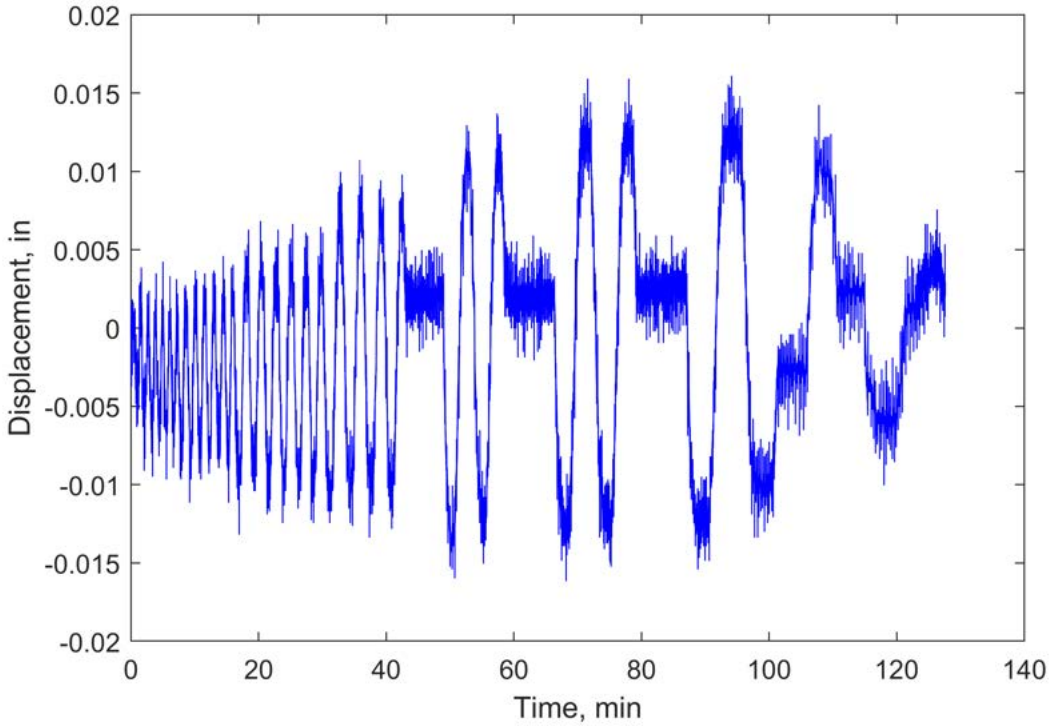

Figure P.3. Displacement-time plot of SP_03 for W24RBS-0.375N-T59.

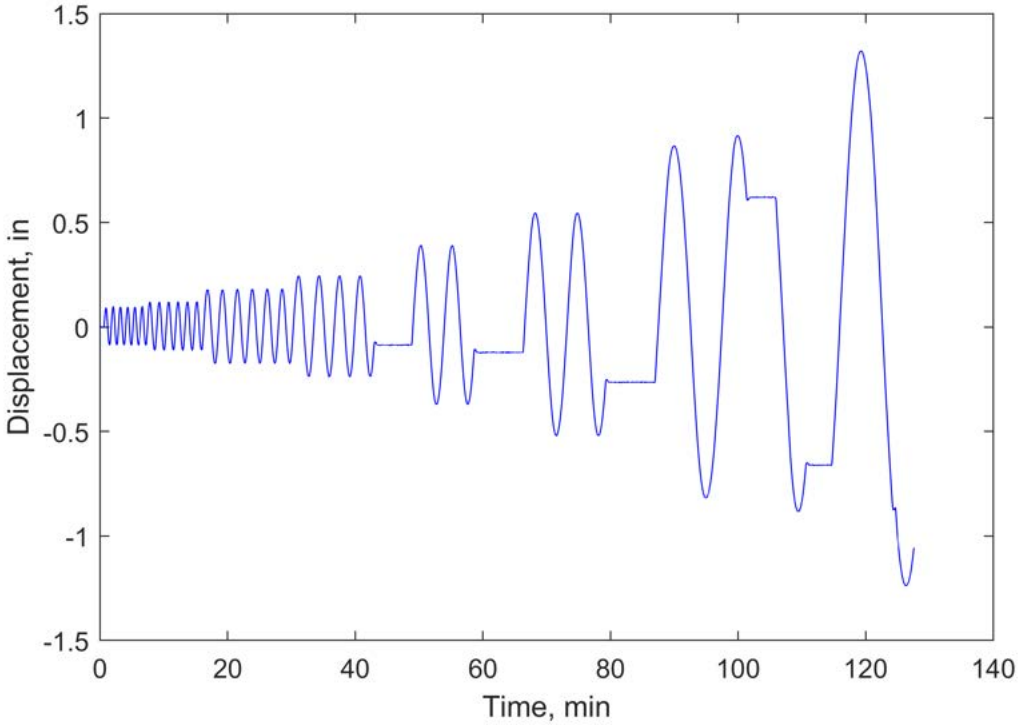

Figure P.4. Displacement-time plot of SP_04 for W24RBS-0.375N-T59.

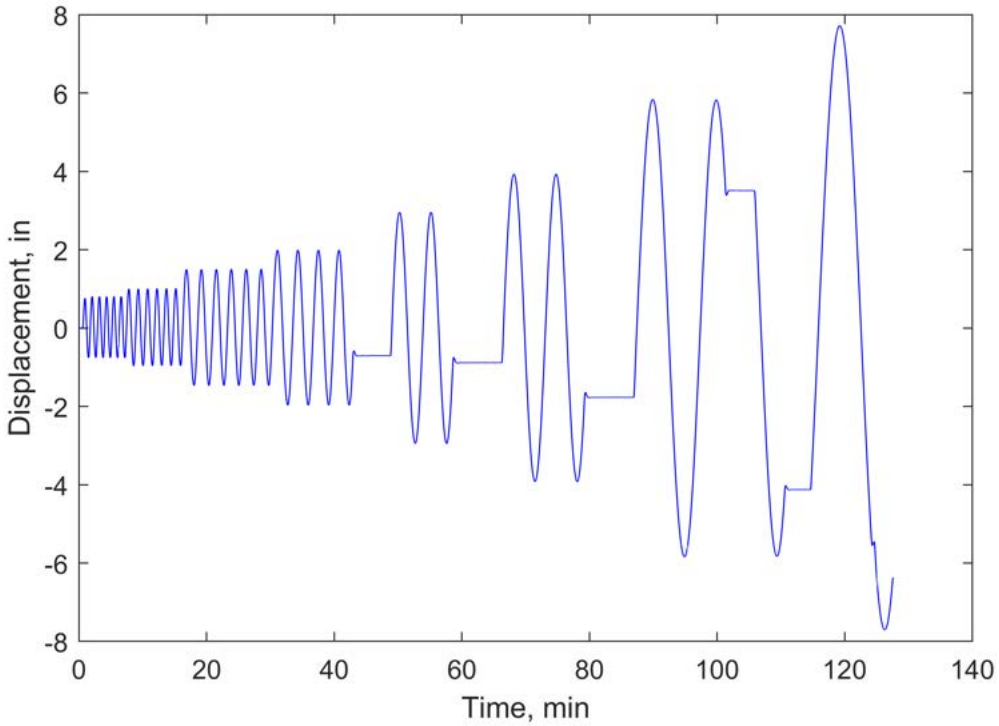

Figure P.5. Displacement-time plot of SP_05 for W24RBS-0.375N-T59.

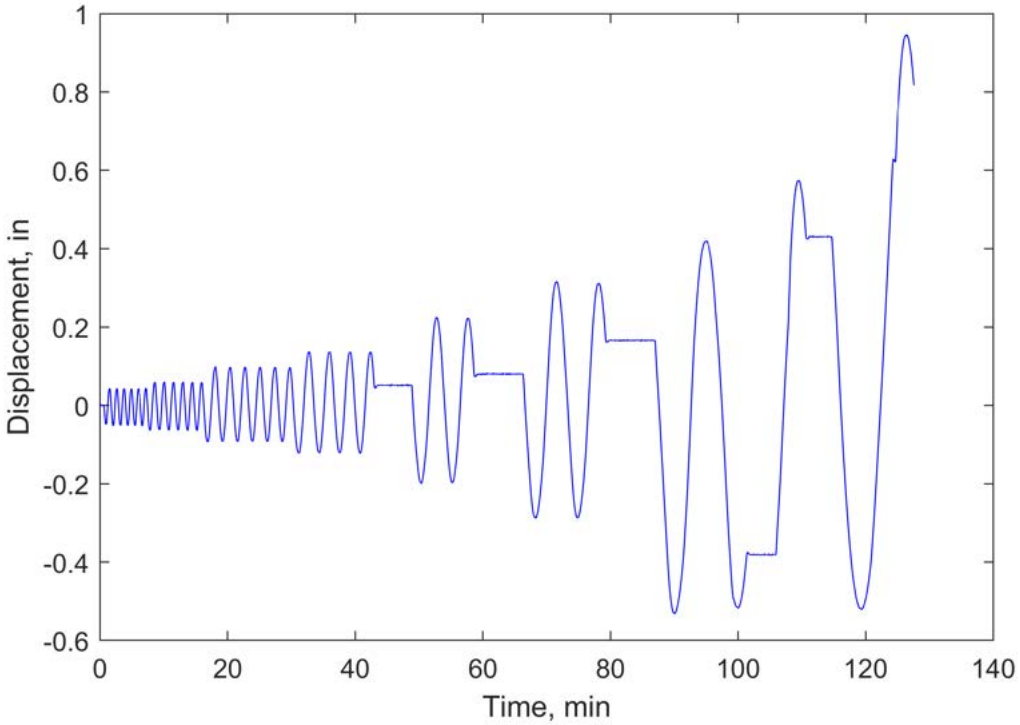

Figure P.6. Displacement-time plot of SP_06 for W24RBS-0.375N-T59.

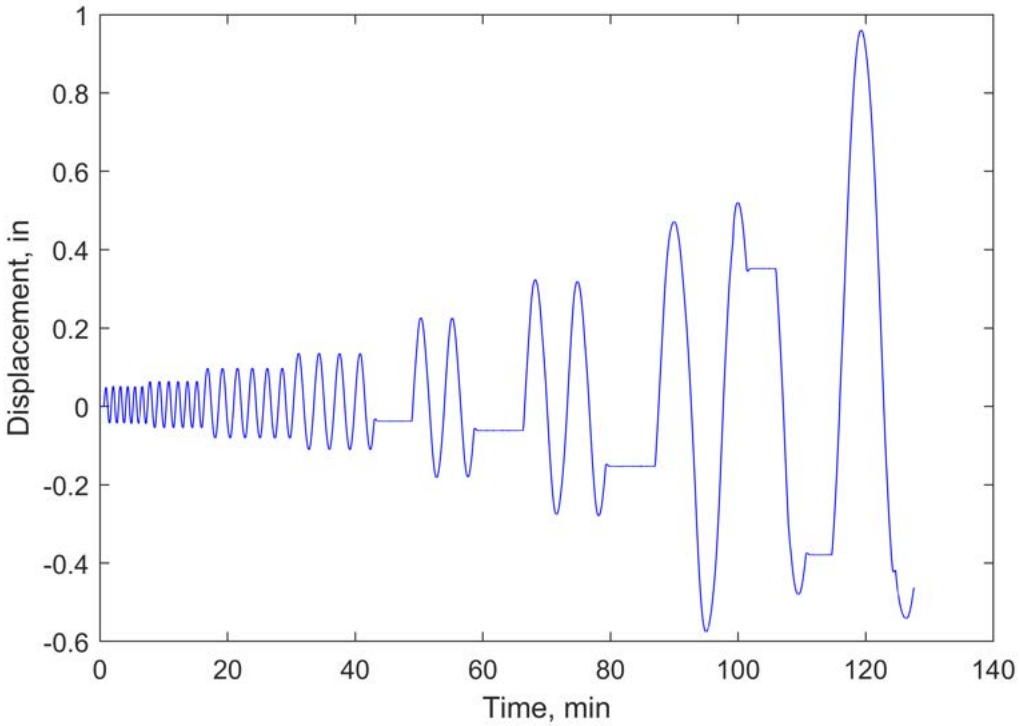

Figure P.7. Displacement-time plot of SP_07 for W24RBS-0.375N-T59.

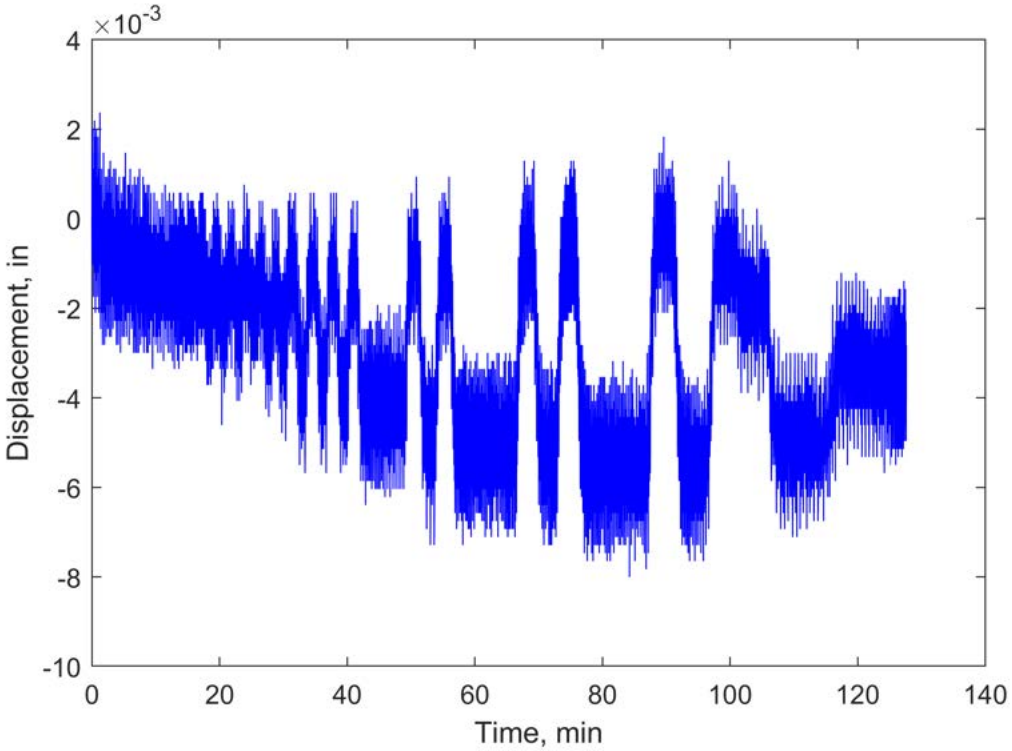

Figure P.8. Displacement-time plot of SP_08 for W24RBS-0.375N-T59.

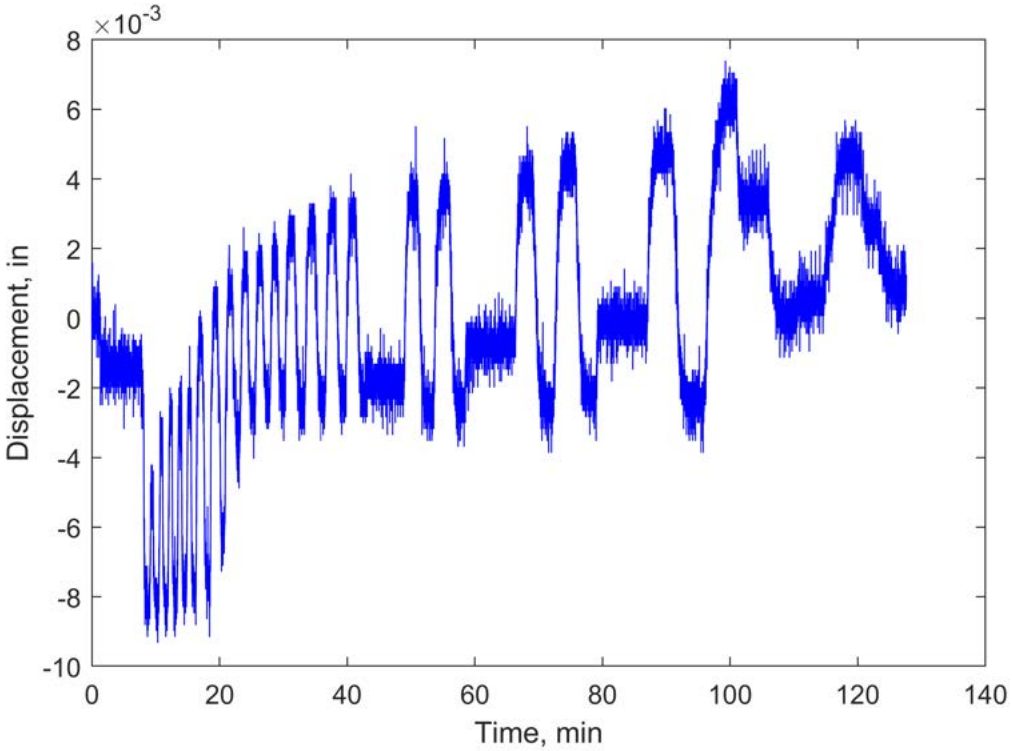

Figure P.9. Displacement-time plot of SP_09 for W24RBS-0.375N-T59.

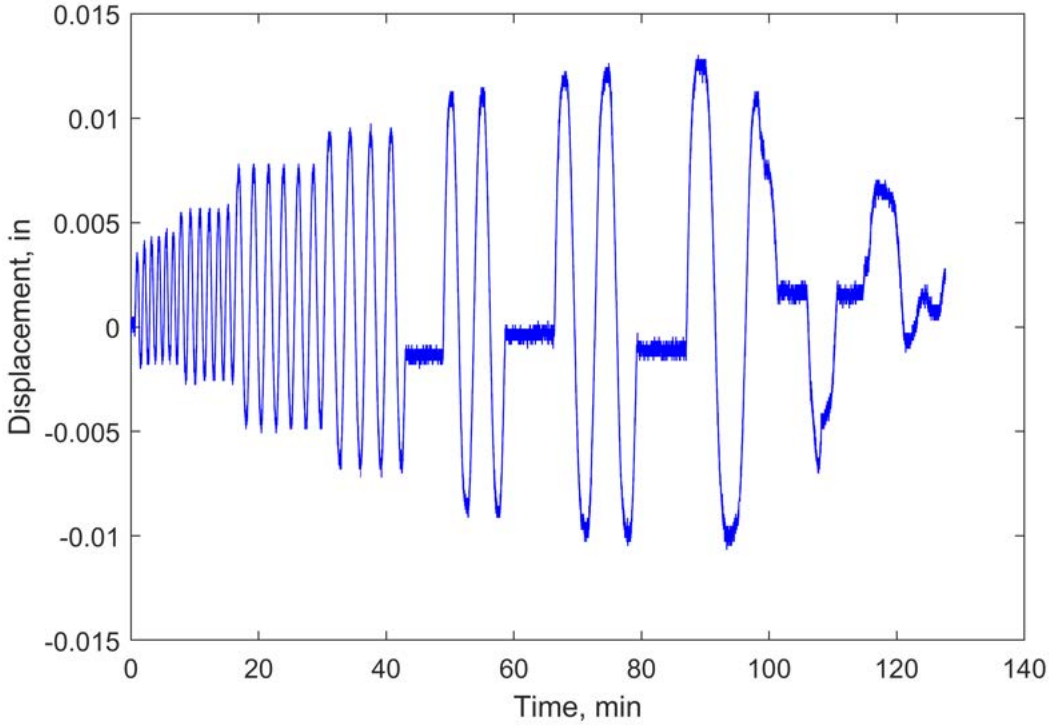

Figure P.10. Displacement-time plot of LP_01 for W24RBS-0.375N-T59.

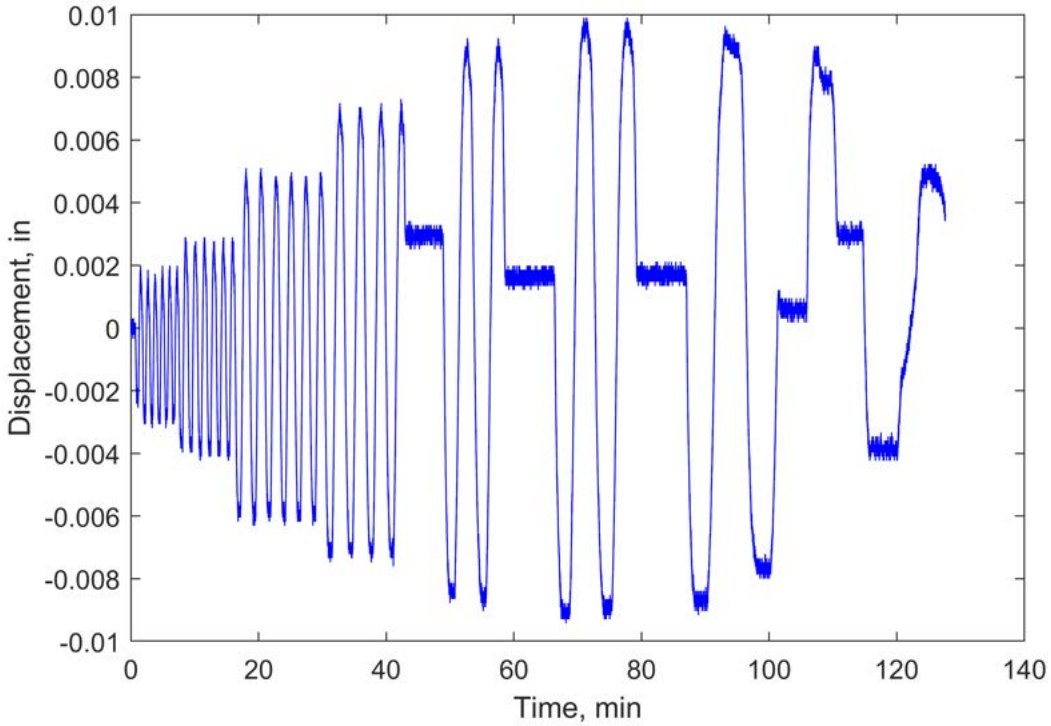

Figure P.11. Displacement-time plot of LP_02 for W24RBS-0.375N-T59.

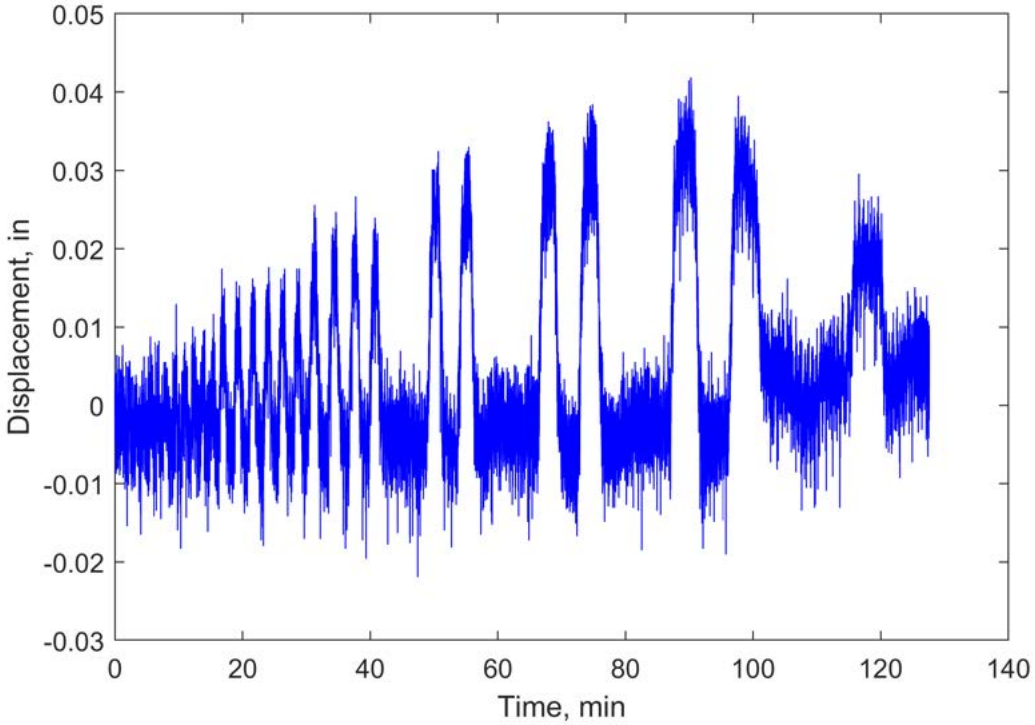

Figure P.12. Displacement-time plot of CLP_01 for W24RBS-0.375N-T59.

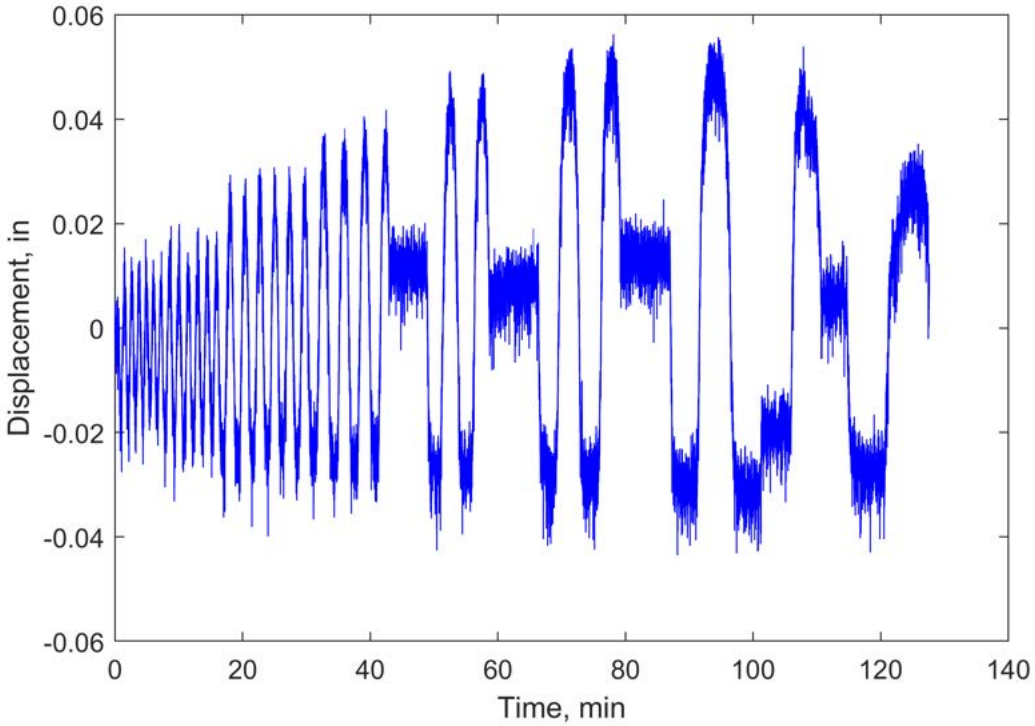

Figure P.13. Displacement-time plot of CLP_02 for W24RBS-0.375N-T59.

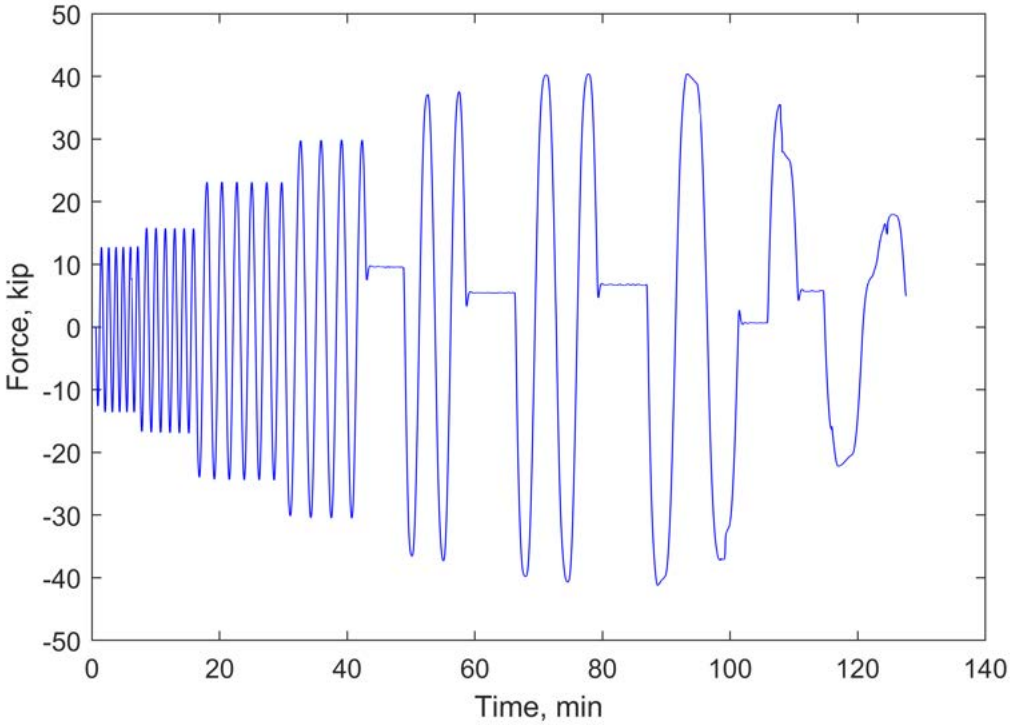

Figure P.14. Force-time plot for W24RBS-0.375N-T59.

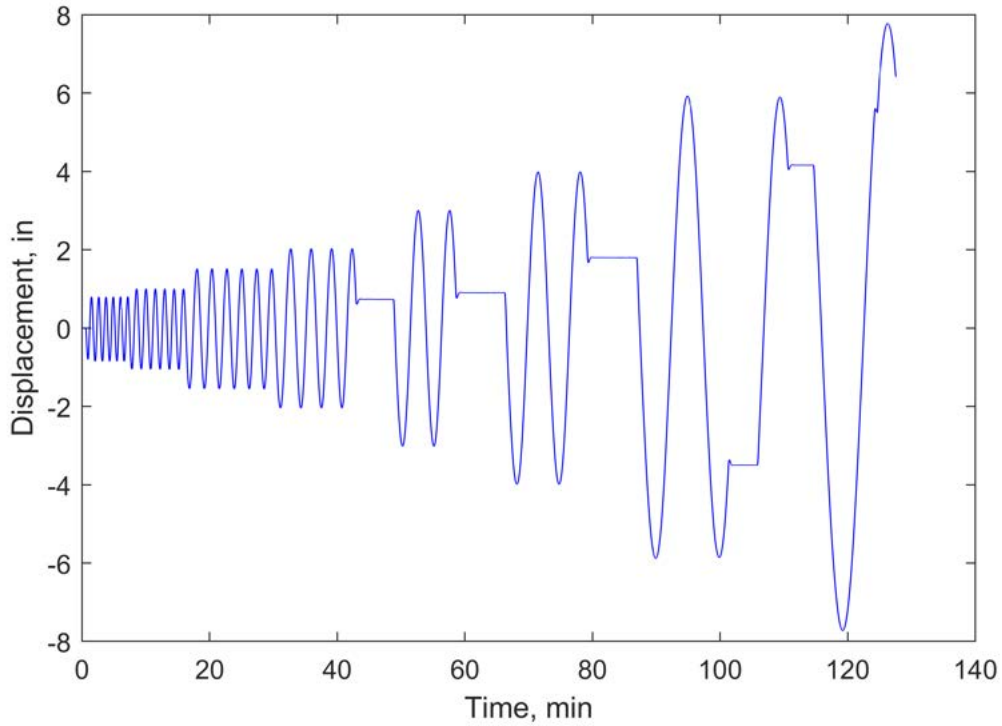

Figure P.15. Actuator displacement-time plot for W24RBS-0.375N-T59.

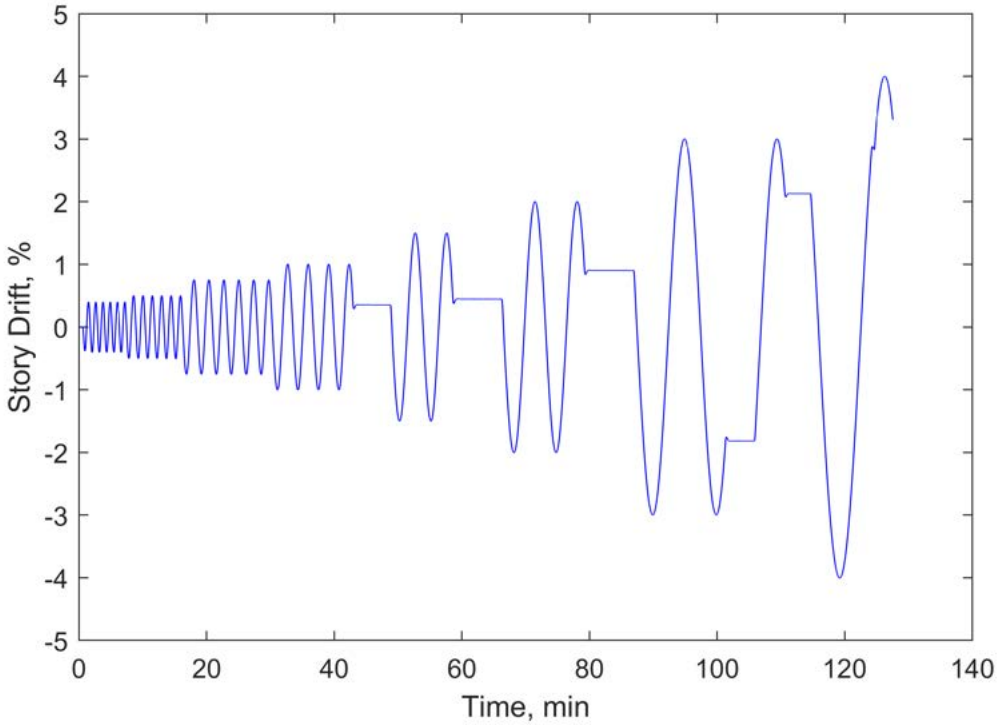

Figure P.16. Drift-time plot for W24RBS-0.375N-T59.

Appendix Q. Sensor Plots for W36RBS-0.25N-T94

This appendix includes modified sensor plots for the W36RBS-0.25N-T94 test. A discussion of any data modifications is given in Appendix Y.

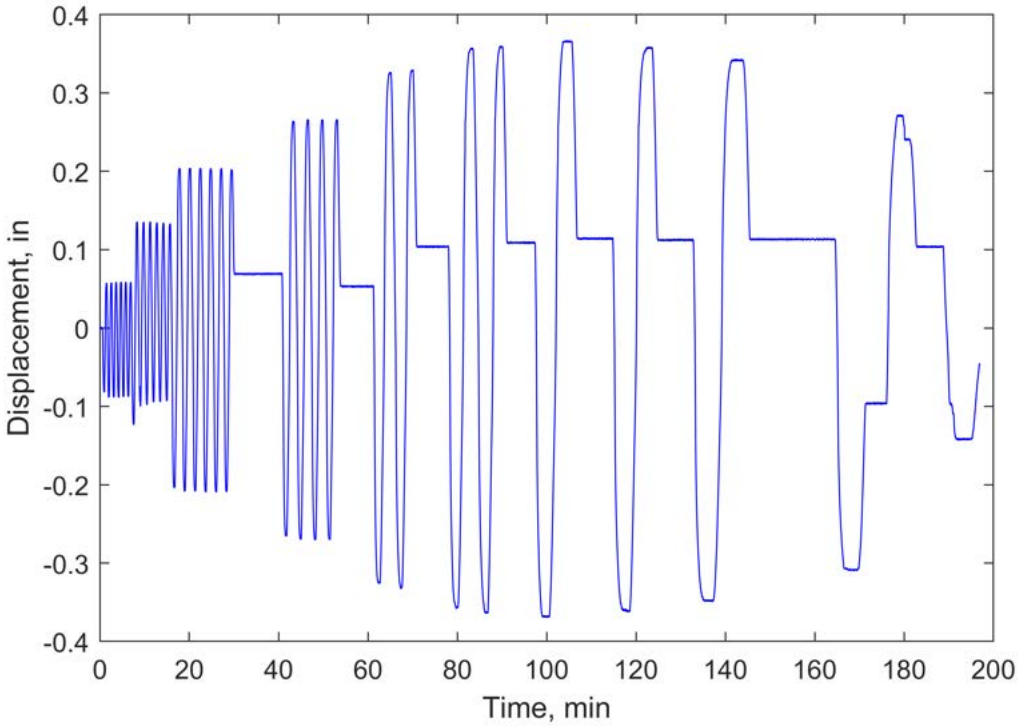

Figure Q.1. Displacement-time plot of SP_01 for W36RBS-0.25N-T94.

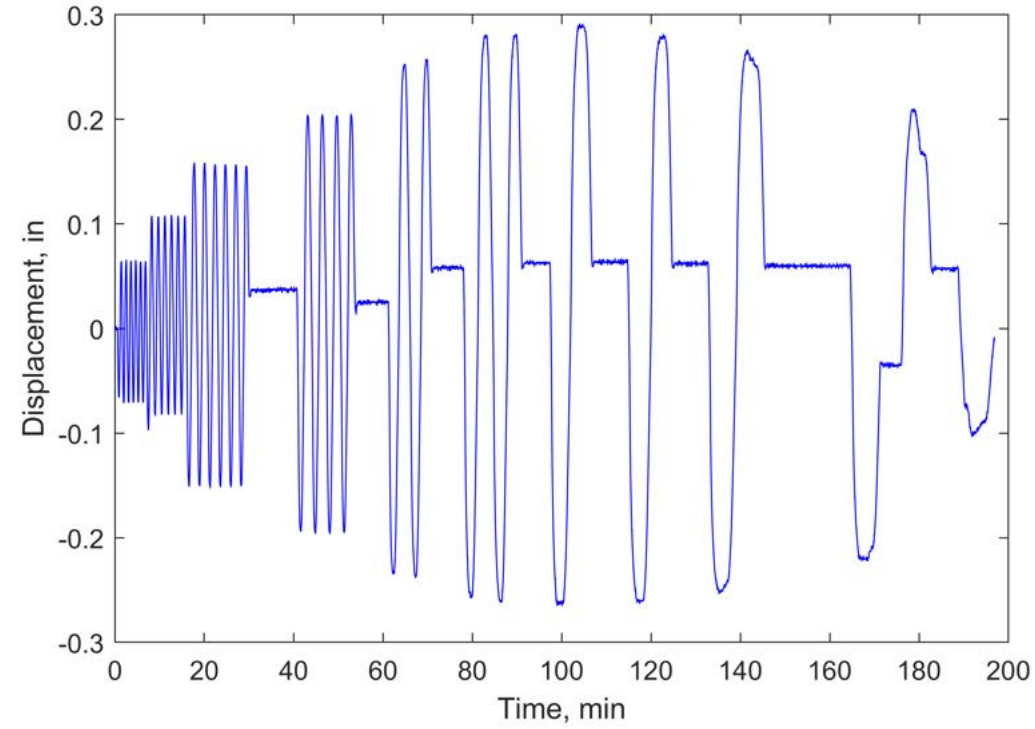

Figure Q.2. Displacement-time plot of SP_02 for W36RBS-0.25N-T94.

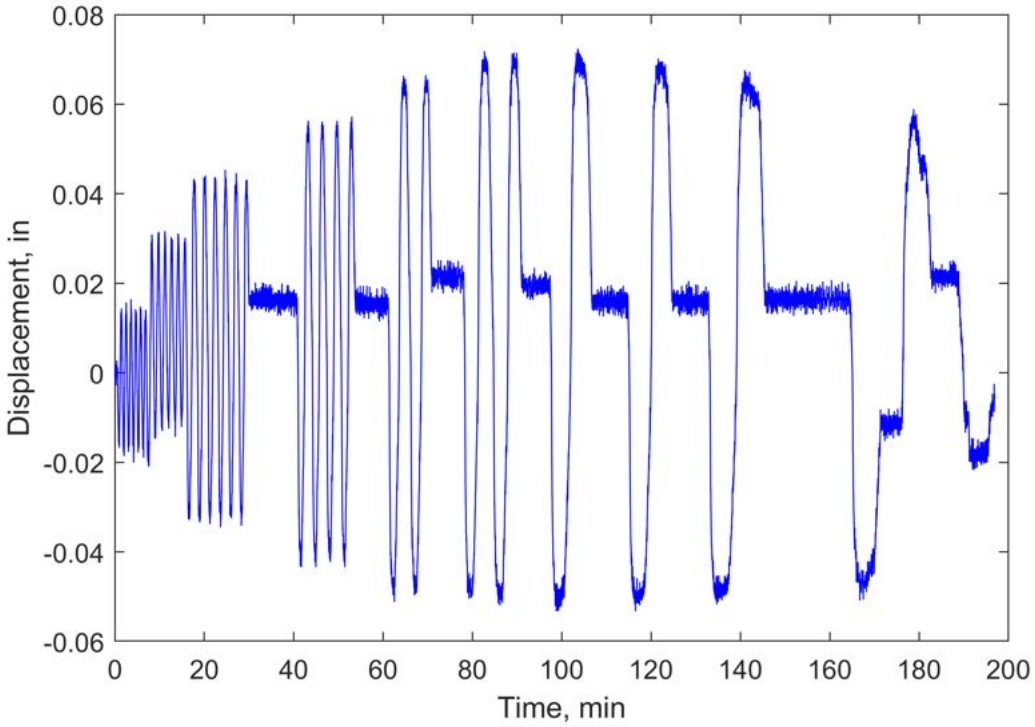

Figure Q.3. Displacement-time plot of SP_03 for W36RBS-0.25N-T94.

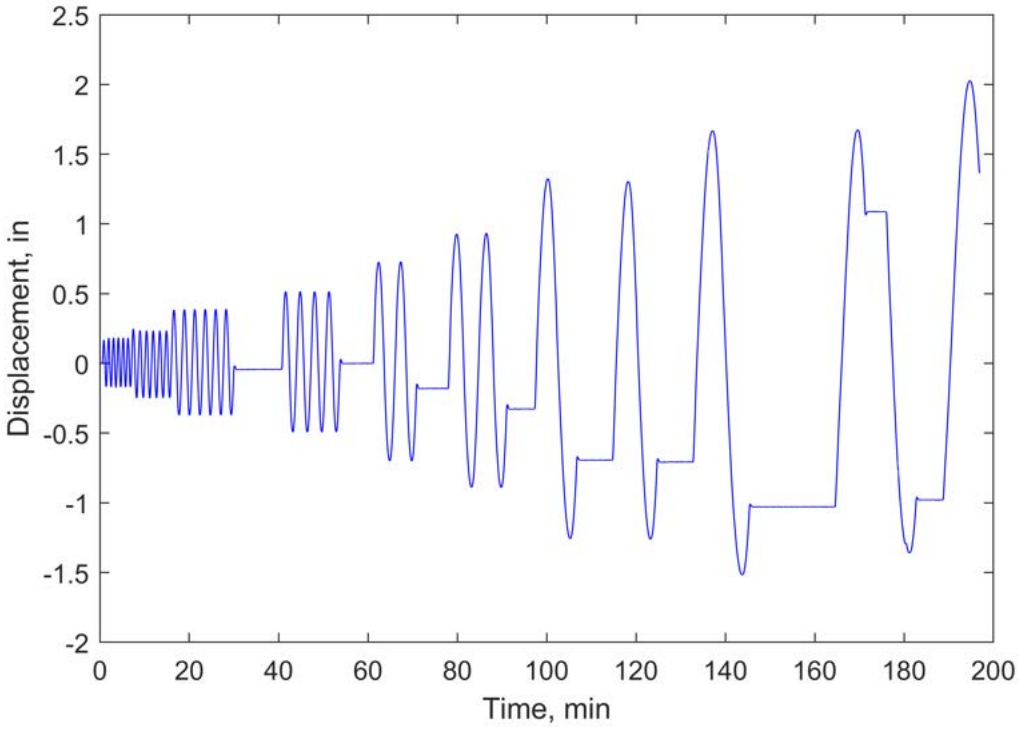

Figure Q.4. Displacement-time plot of SP_04 for W36RBS-0.25N-T94.

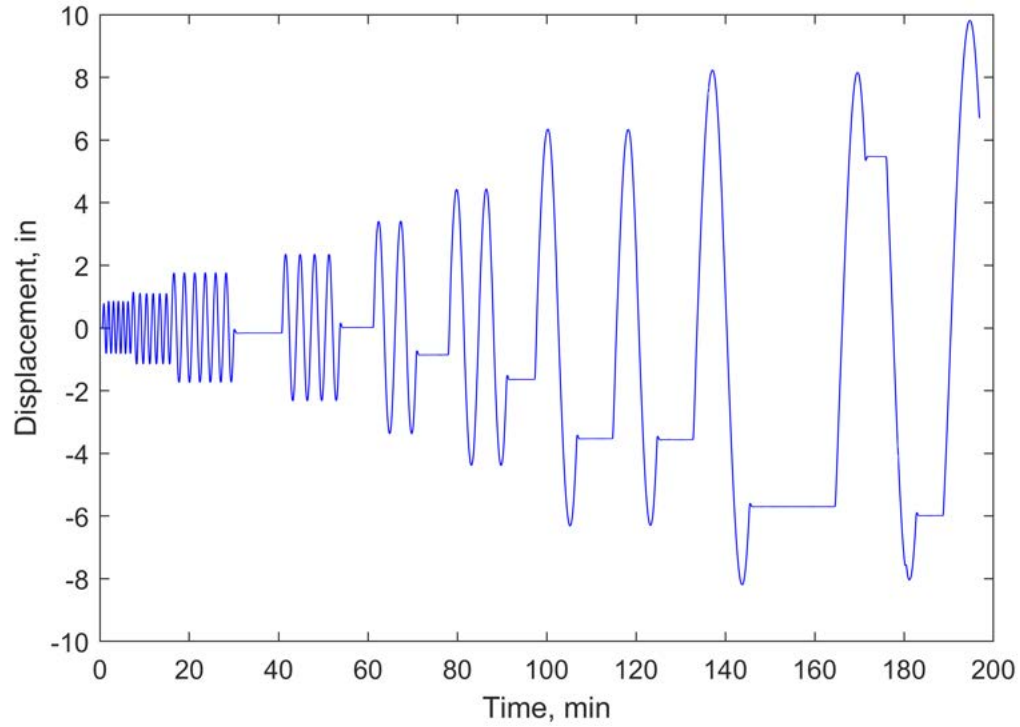

Figure Q.5. Displacement-time plot of SP_05 for W36RBS-0.25N-T94.

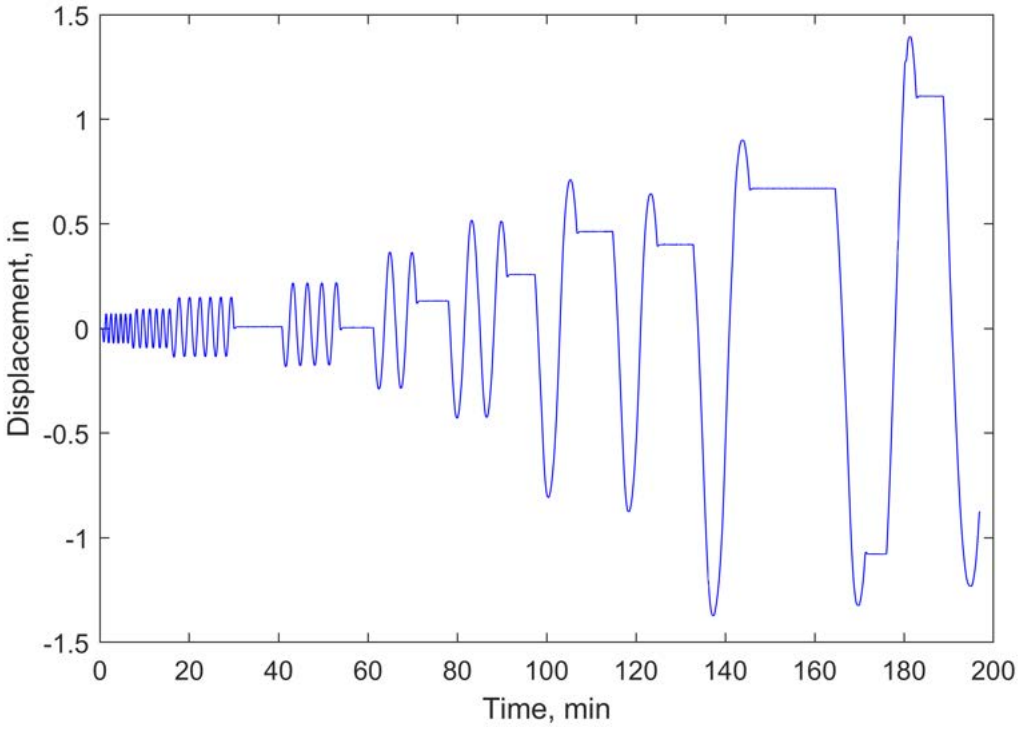

Figure Q.6. Displacement-time plot of SP_06 for W36RBS-0.25N-T94.

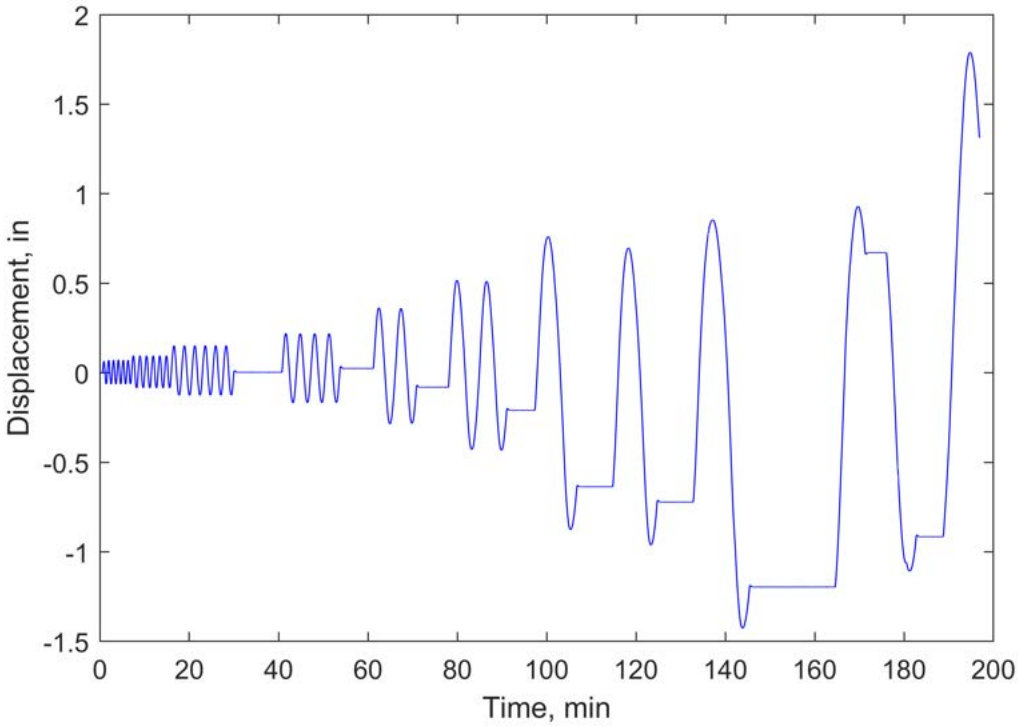

Figure Q.7. Displacement-time plot of SP_07 for W36RBS-0.25N-T94.

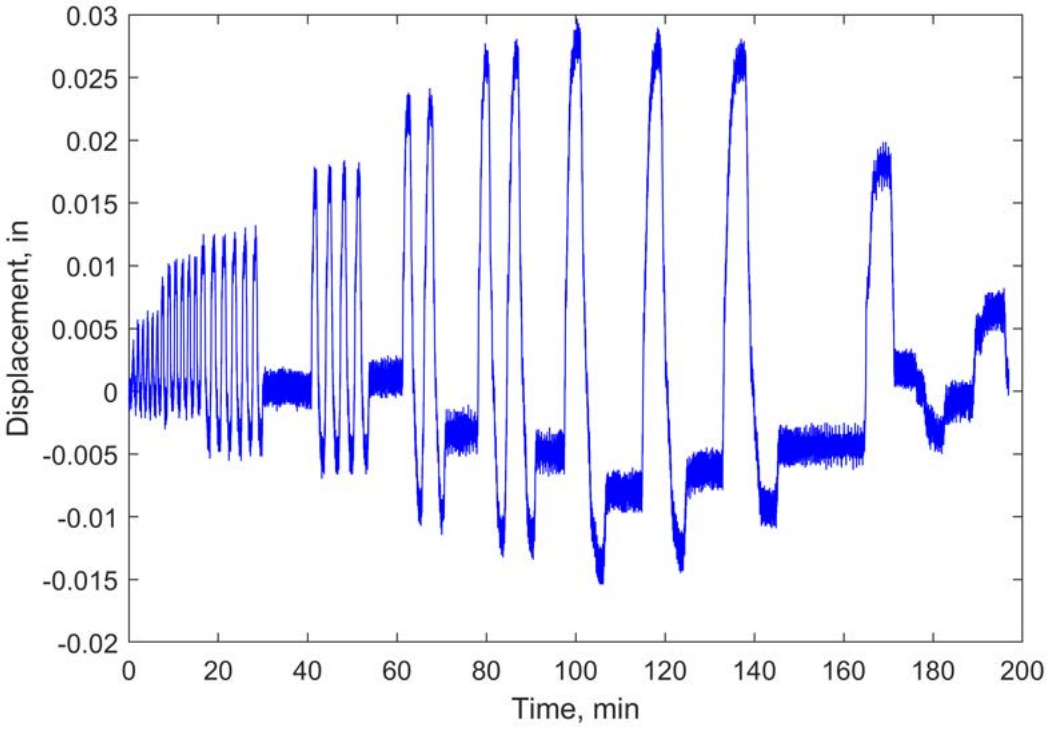

Figure Q.8. Displacement-time plot of SP_08 for W36RBS-0.25N-T94.

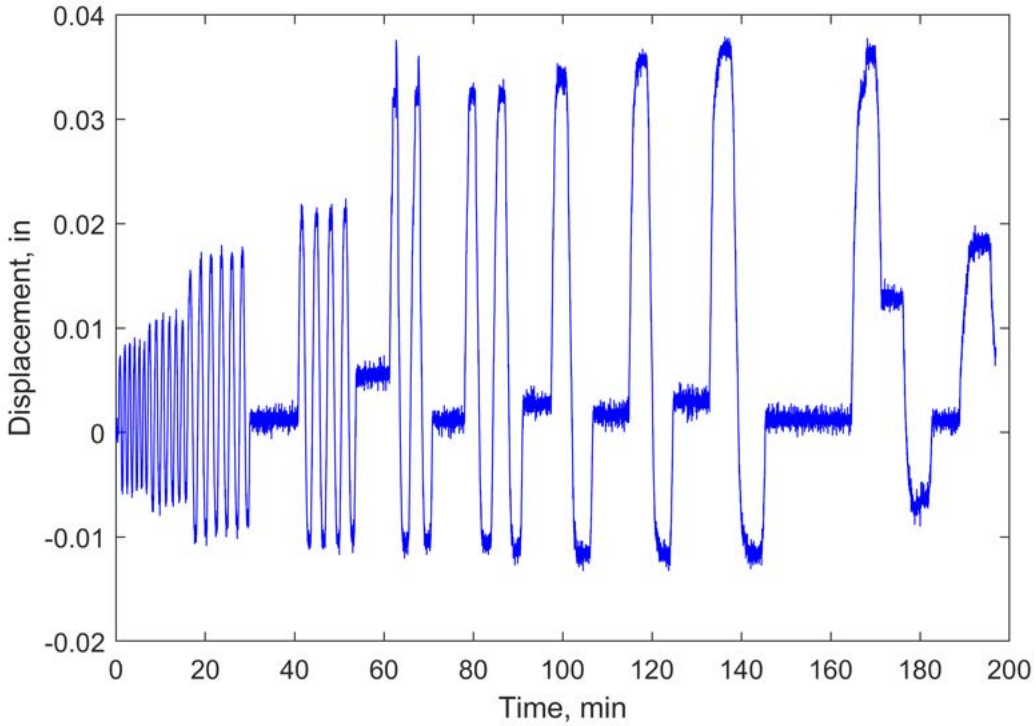

Figure Q.9. Displacement-time plot of SP_09 for W36RBS-0.25N-T94.

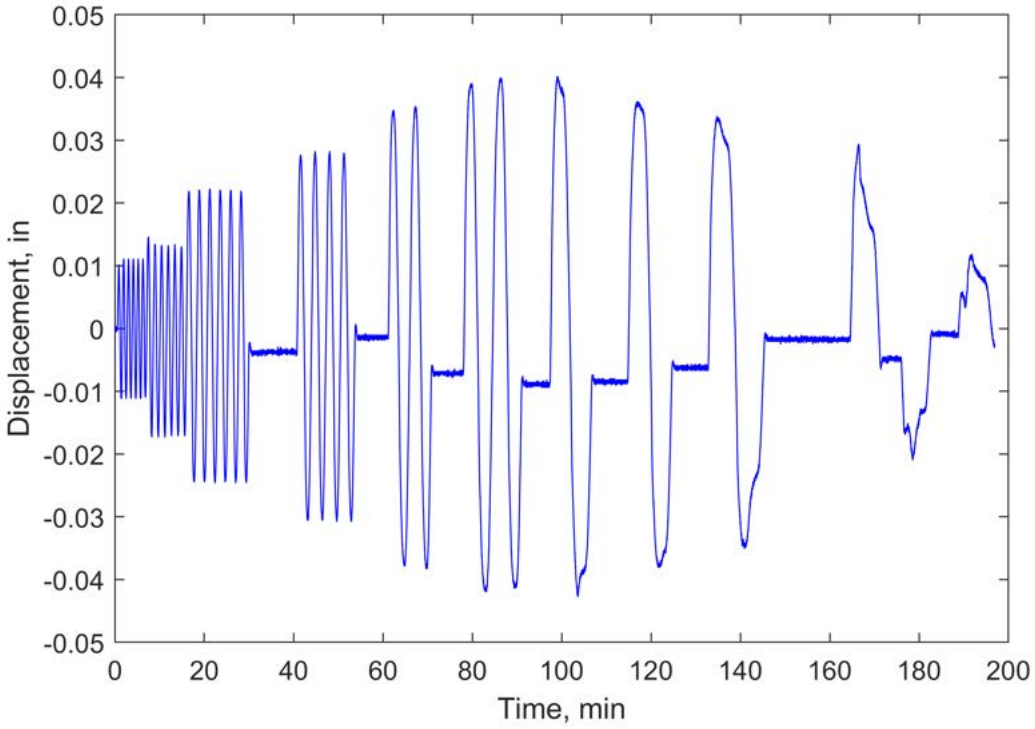

Figure Q.10. Displacement-time plot of LP_01 for W36RBS-0.25N-T94.

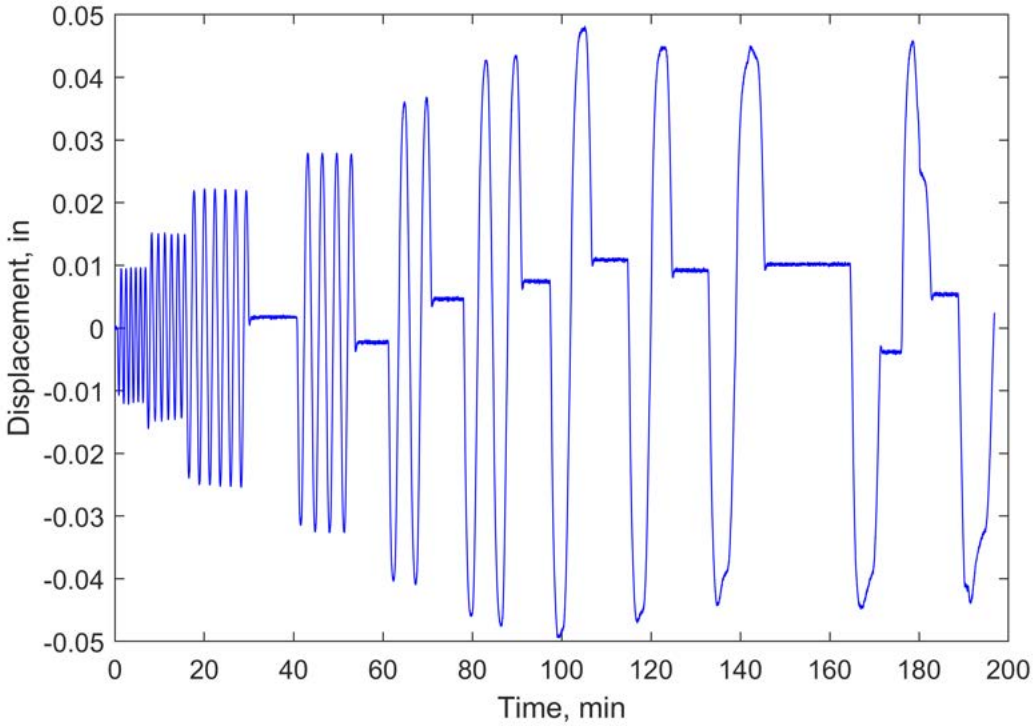

Figure Q.11. Displacement-time plot of LP_02 for W36RBS-0.25N-T94.

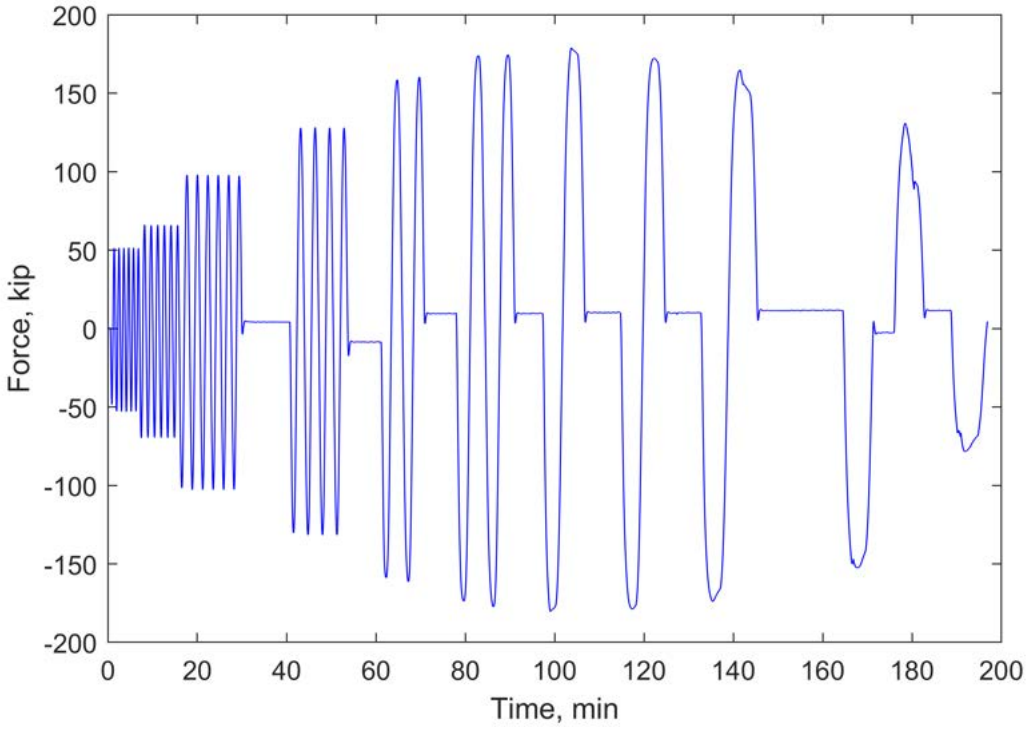

Figure Q.12. Force-time plot for W36RBS-0.25N-T94.

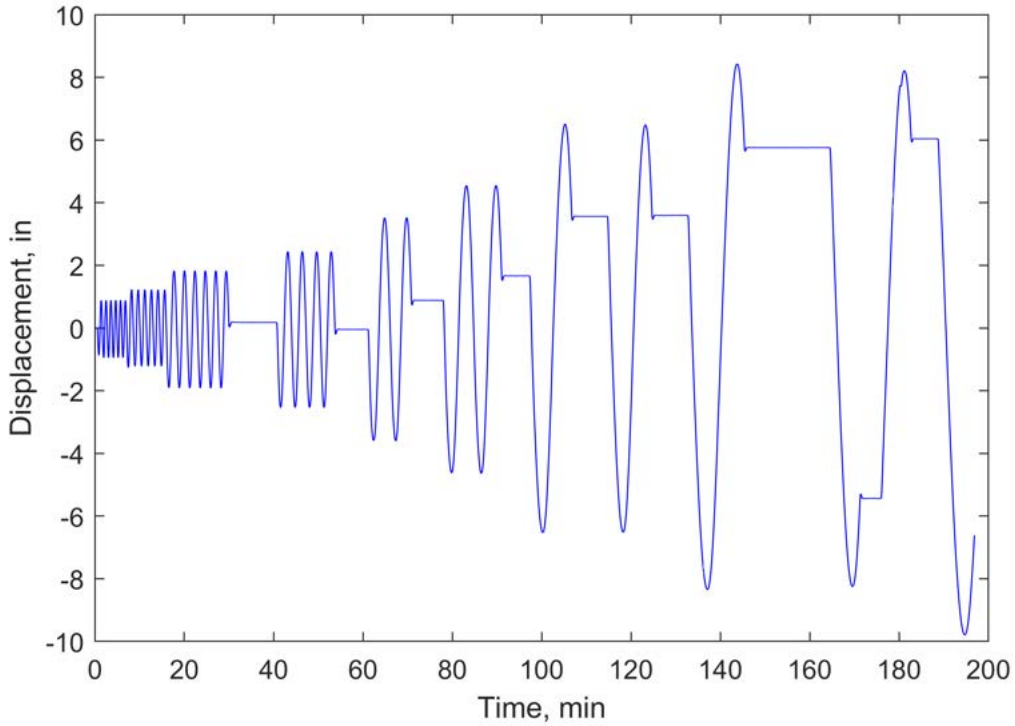

Figure Q.13. Actuator displacement-time plot for W36RBS-0.25N-T94.

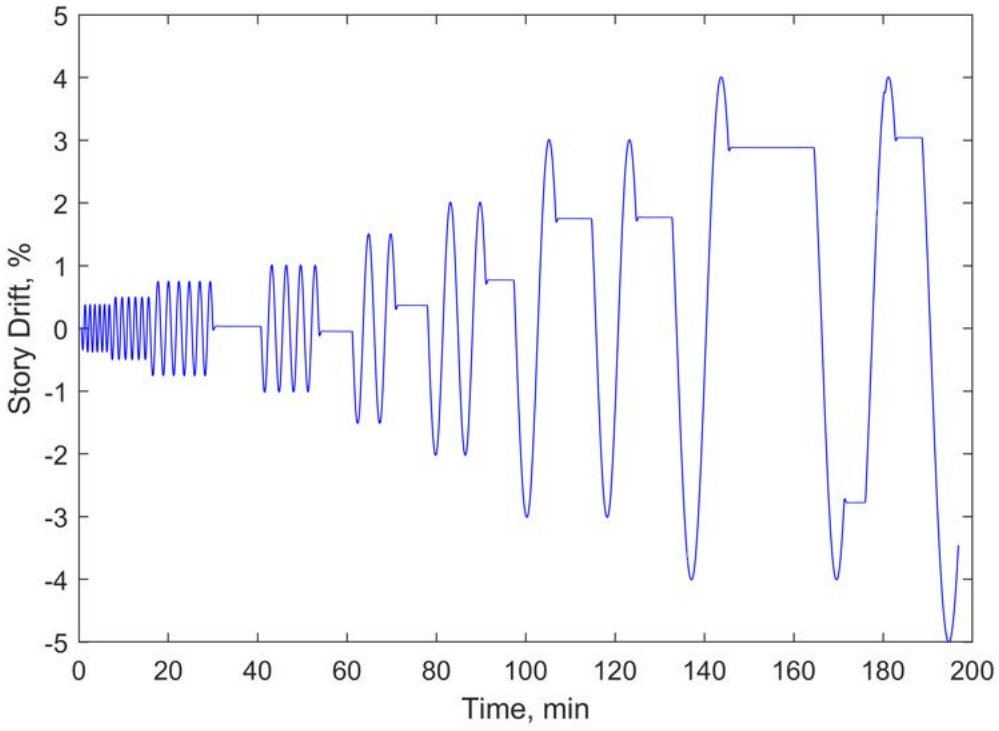

Figure Q.14. Drift-time plot for W36RBS-0.25N-T94.

Appendix R. Force-Displacement Plots for Small-Scale Specimens

This appendix includes force-displacement plots for the small-scale specimens, organized by coupon thickness. The data used to create the plots has not been modified.

R.1 0.4 in. Coupons

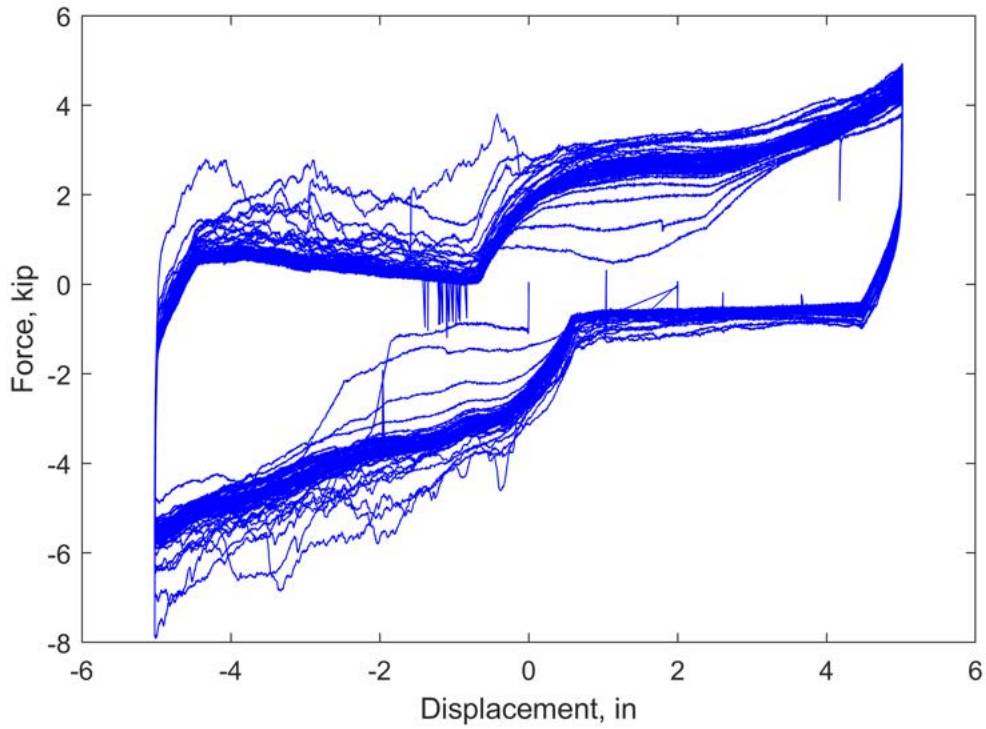

Figure R.1. Force-displacement plot of W24-BAR STOCK-T40-R11.02.

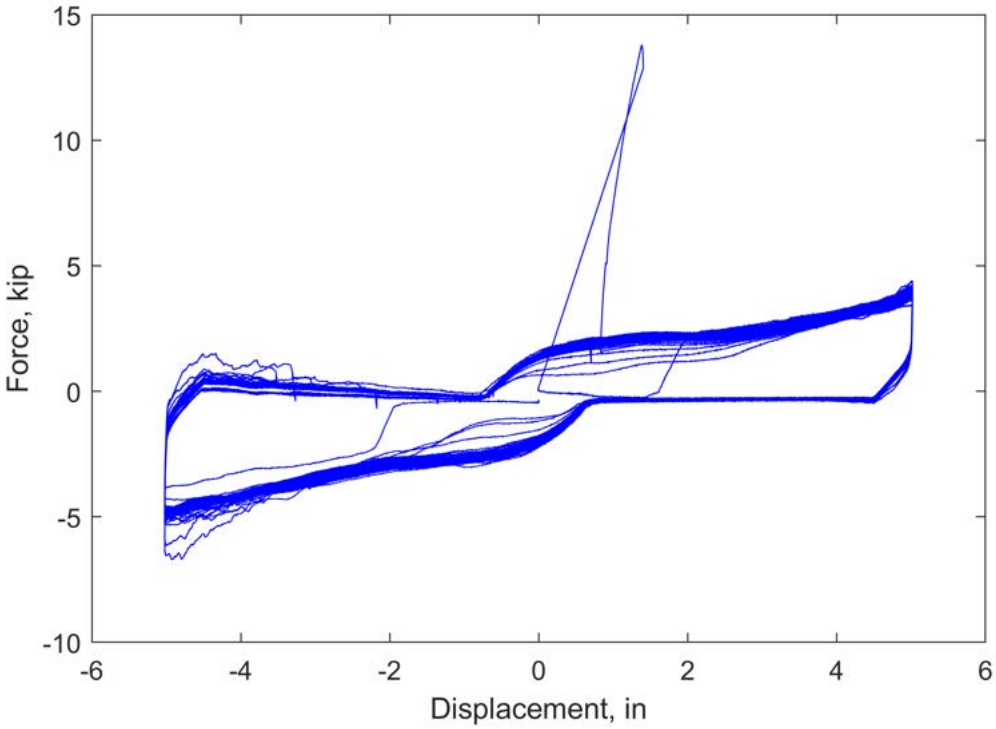

Figure R.2. Force-displacement plot of W24-FLANGE MATERIAL-T40-R11.01.

R.2 0.5 in. Coupons

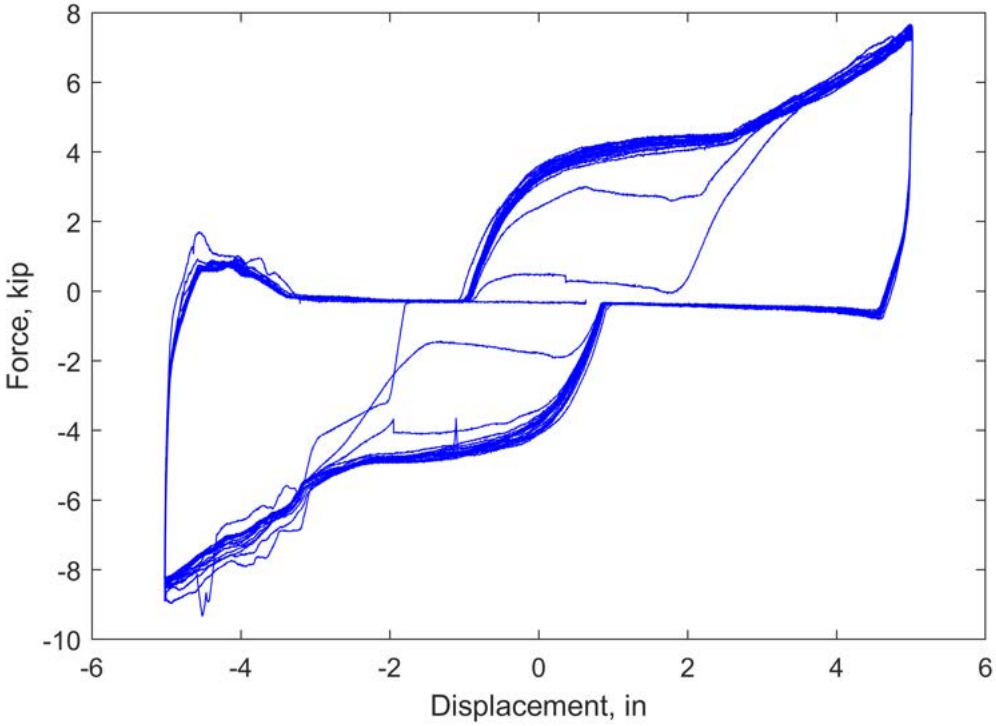

Figure R.3. Force-displacement plot of W24-0.125NGT-T50-R11.01.

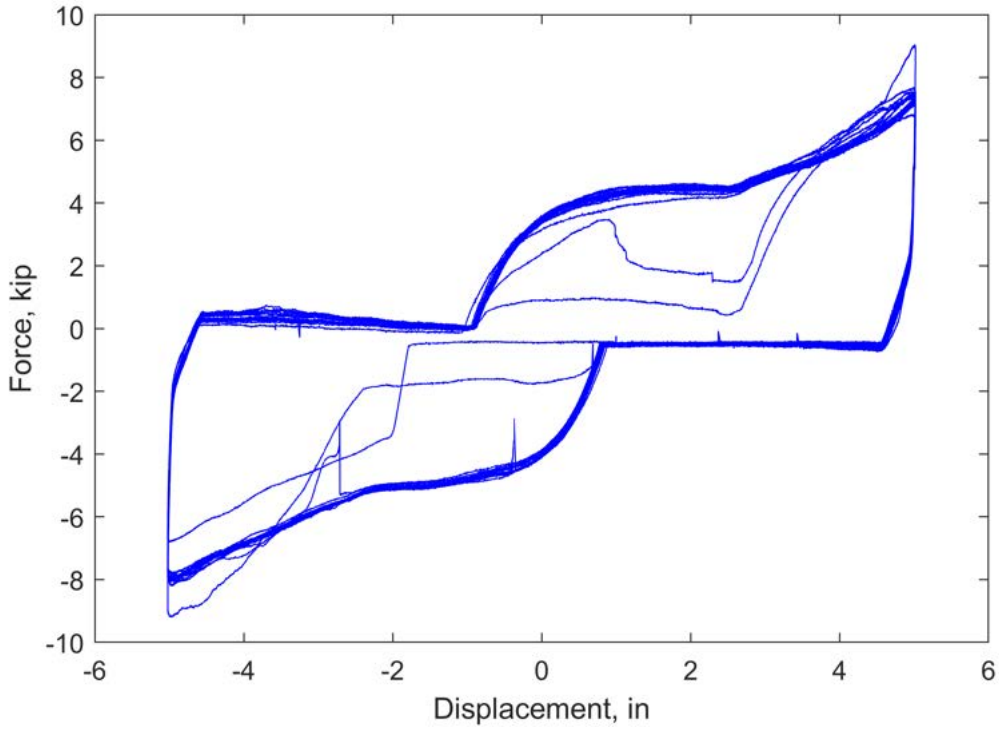

Figure R.4. Force-displacement plot of W24-0.125NGT-T50-R11.02.

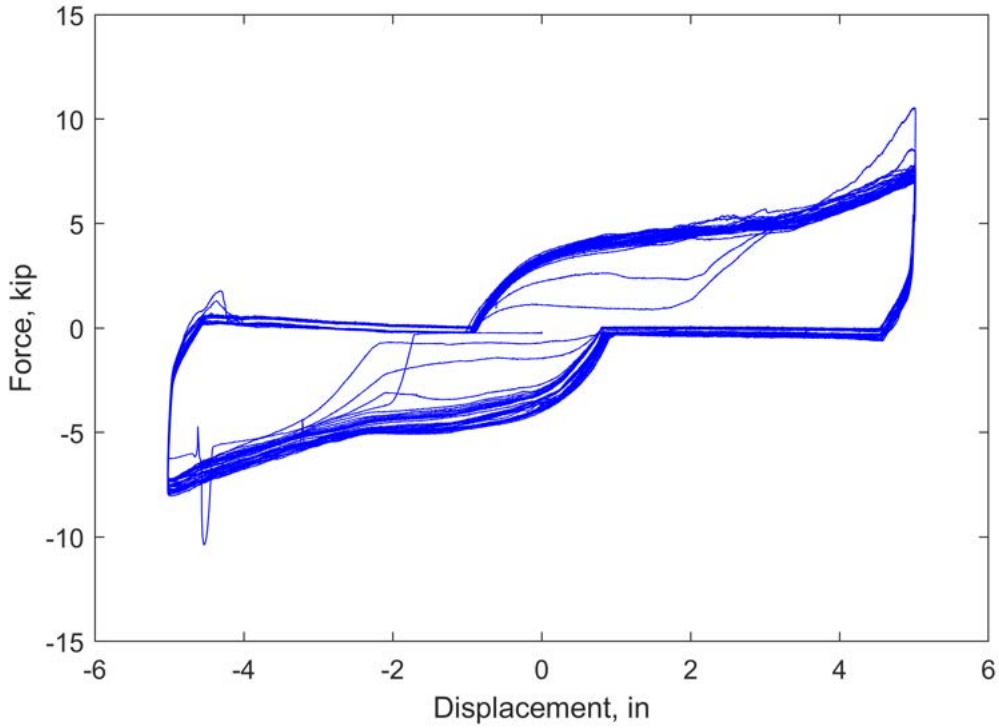

Figure R.5. Force-displacement plot of W24-0.25NGTW-T50-R11.01.

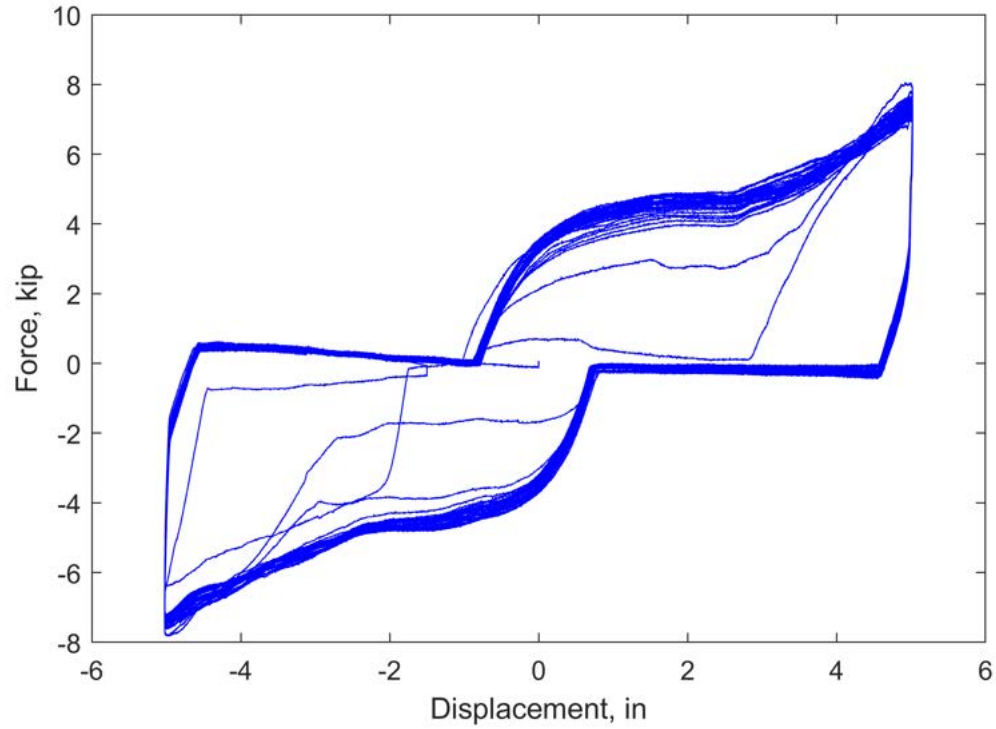

Figure R.6. Force-displacement plot of W24-0.25NGTW-T50-R11.02.

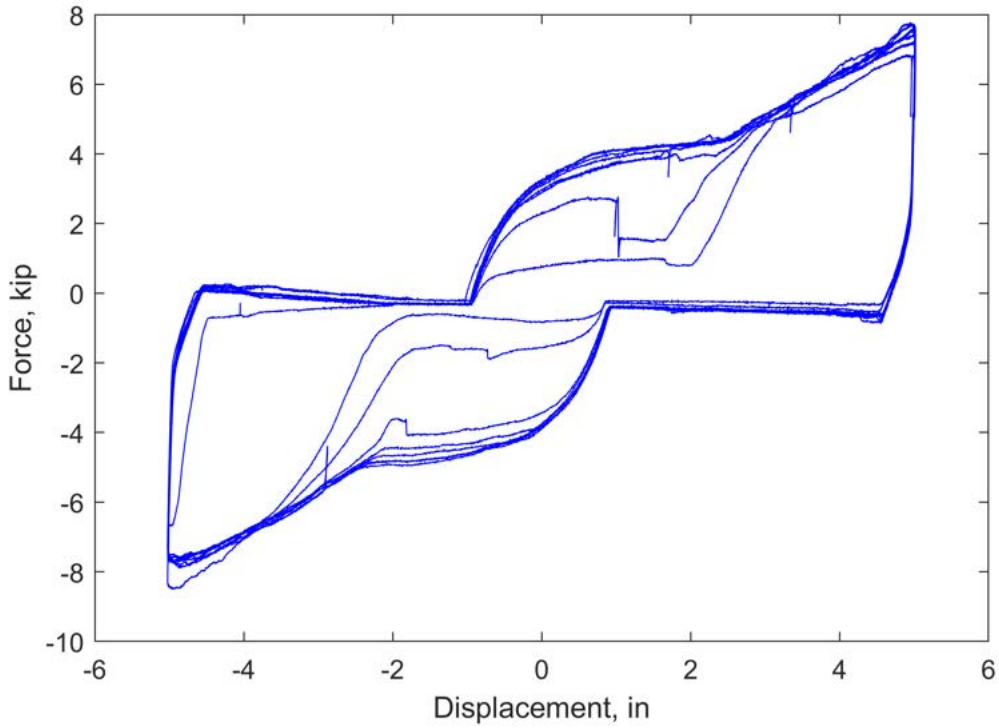

Figure R.7. Force-displacement plot of W24-0.25N-T50-R11.02.

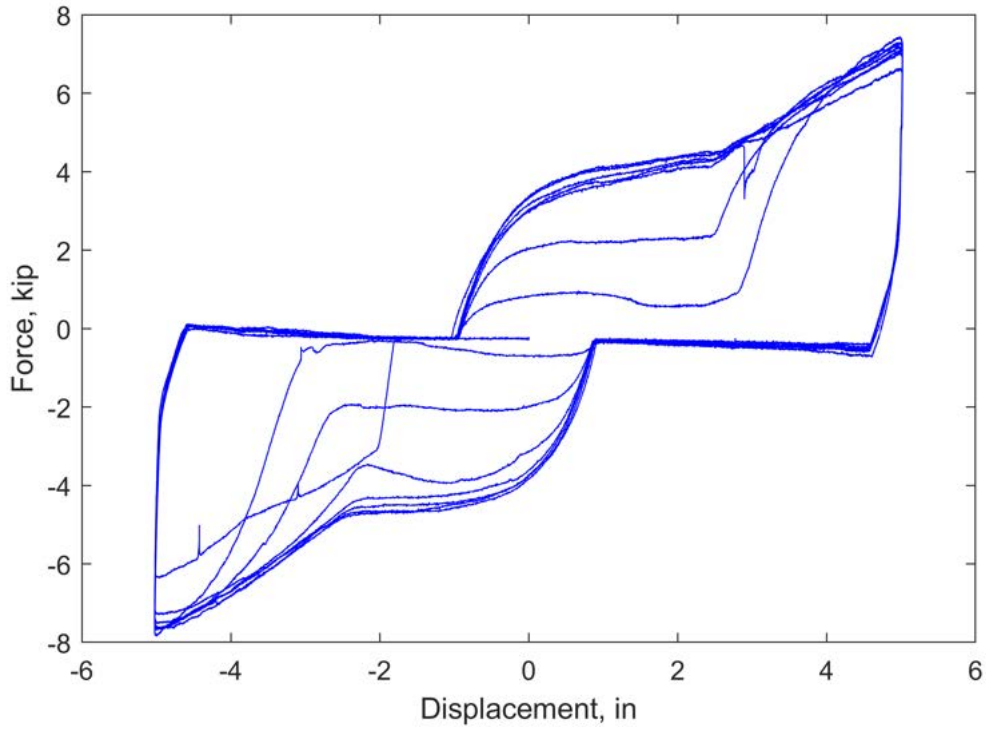

Figure R.8. Force-displacement plot of W24-0.25N-T50-R11.03.

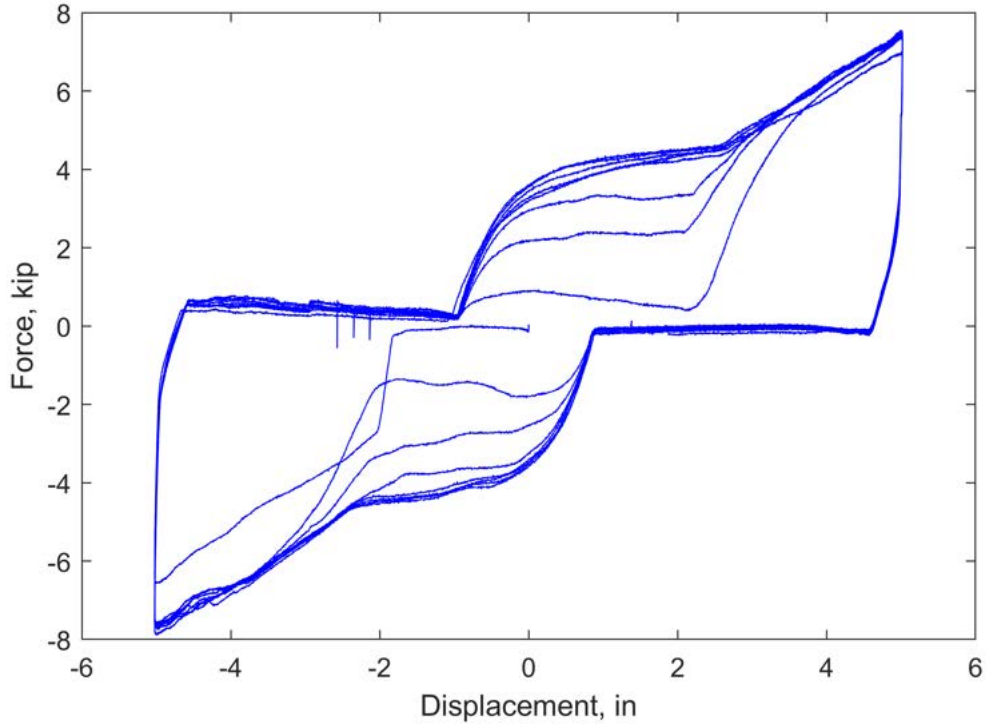

Figure R.9. Force-displacement plot of W24-0.375N-T50-R11.01.

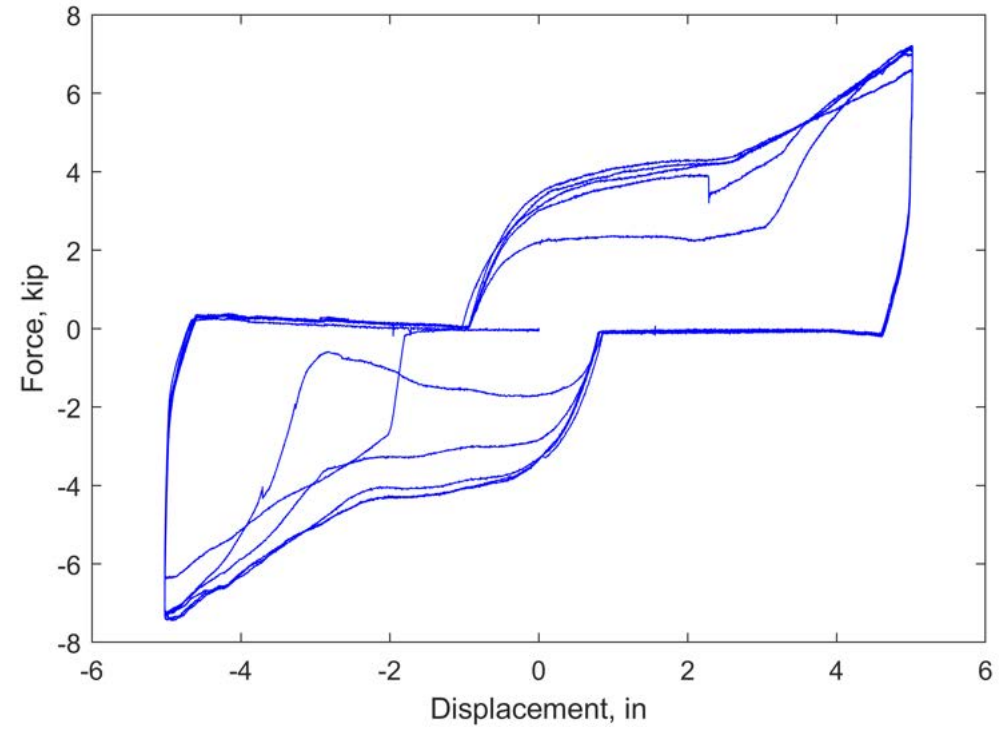

Figure R.10. Force-displacement plot of W24-0.375N-T50-R11.02.

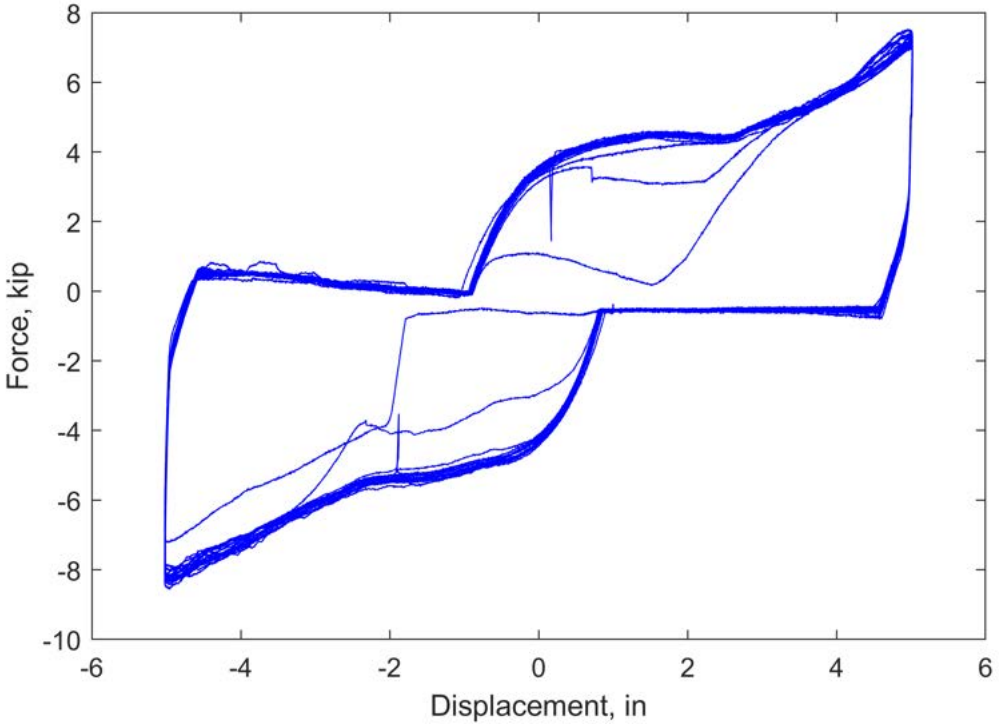

Figure R.11. Force-displacement plot of W24-STEEL-T50-R11.01.

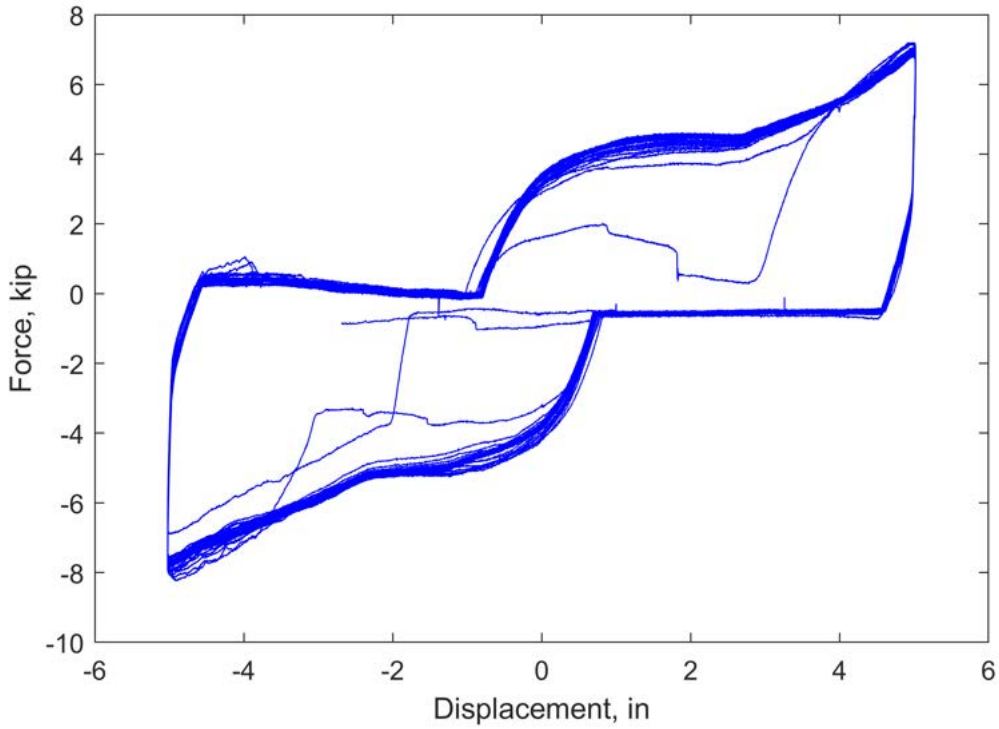

Figure R.12. Force-displacement plot of W24-STEEL-T50-R11.02.

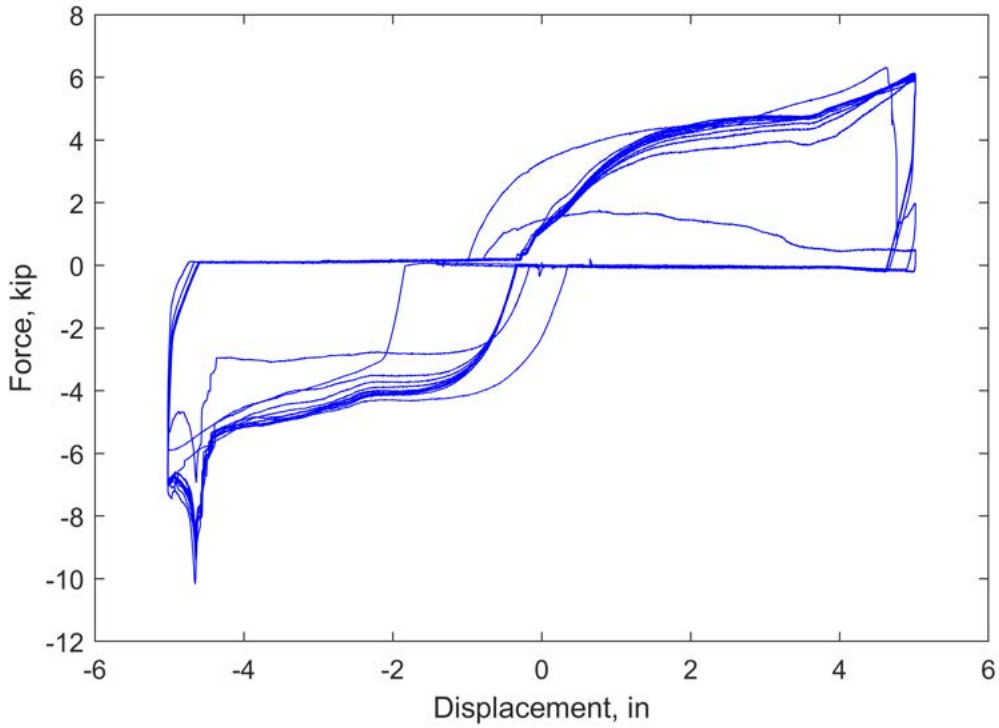

Figure R.13. Force-displacement plot of W24-0.625PnAF-T50-R11.01.

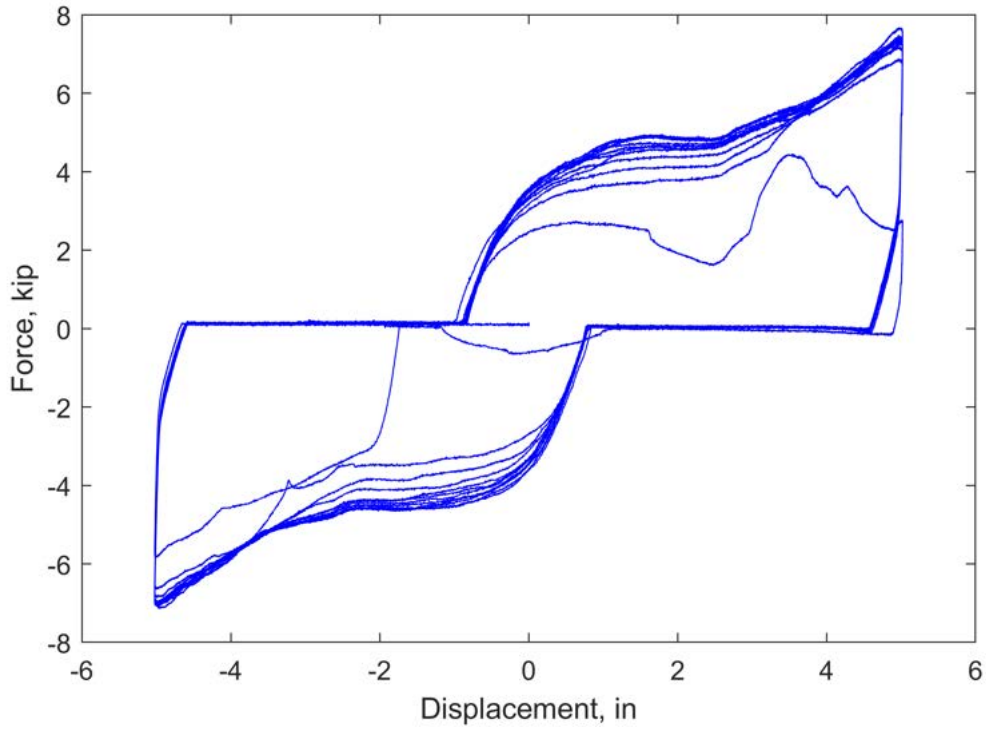

Figure R.14. Force-displacement plot of W24-0.625PnAF-T50-R11.02.

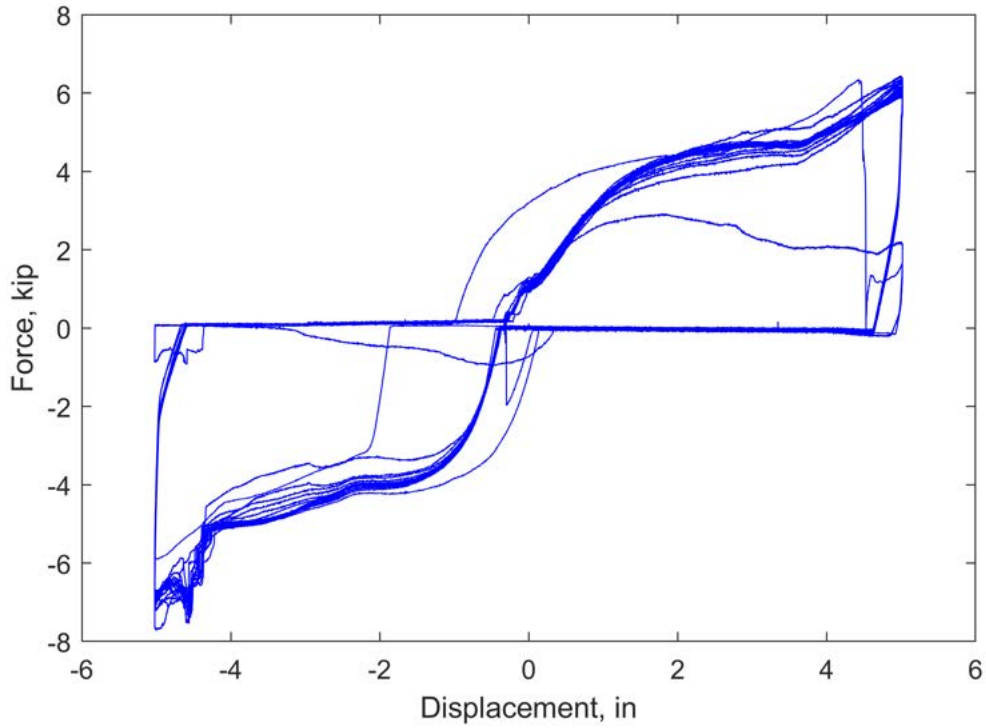

Figure R.15. Force-displacement plot of W24-0.75PnAF-T50-R11.01.

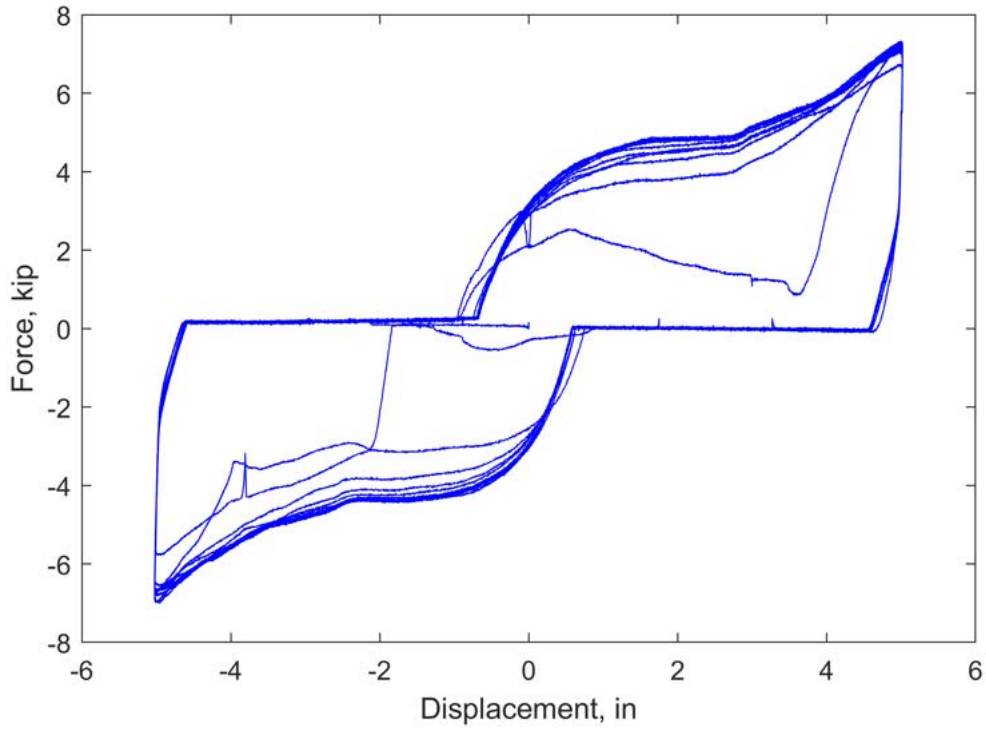

Figure R.16. Force-displacement plot of W24-0.75PnAF-T50-R11.02.

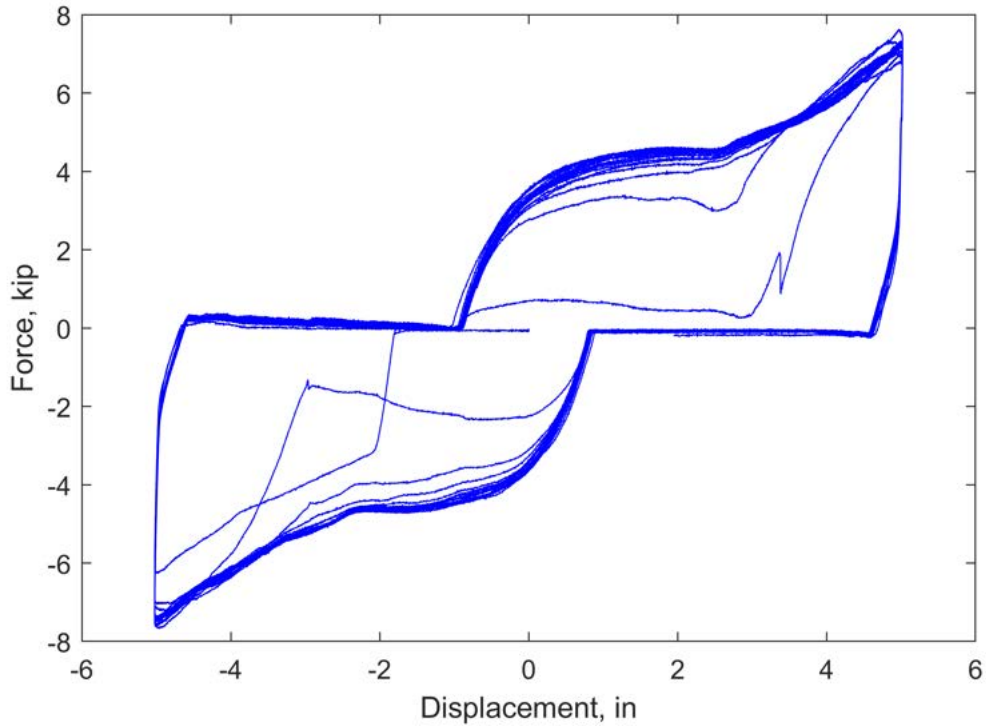

Figure R.17. Force-displacement plot of W24-PAF-T50-R11.01.

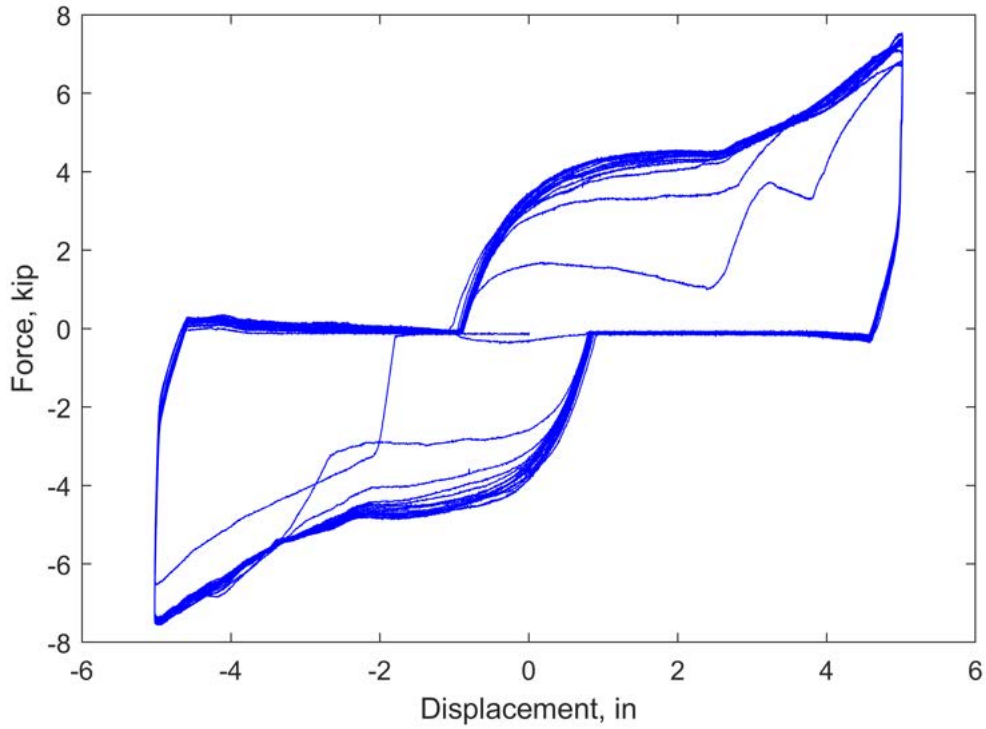

Figure R.18. Force-displacement plot of W24-PAF-T50-R11.02.

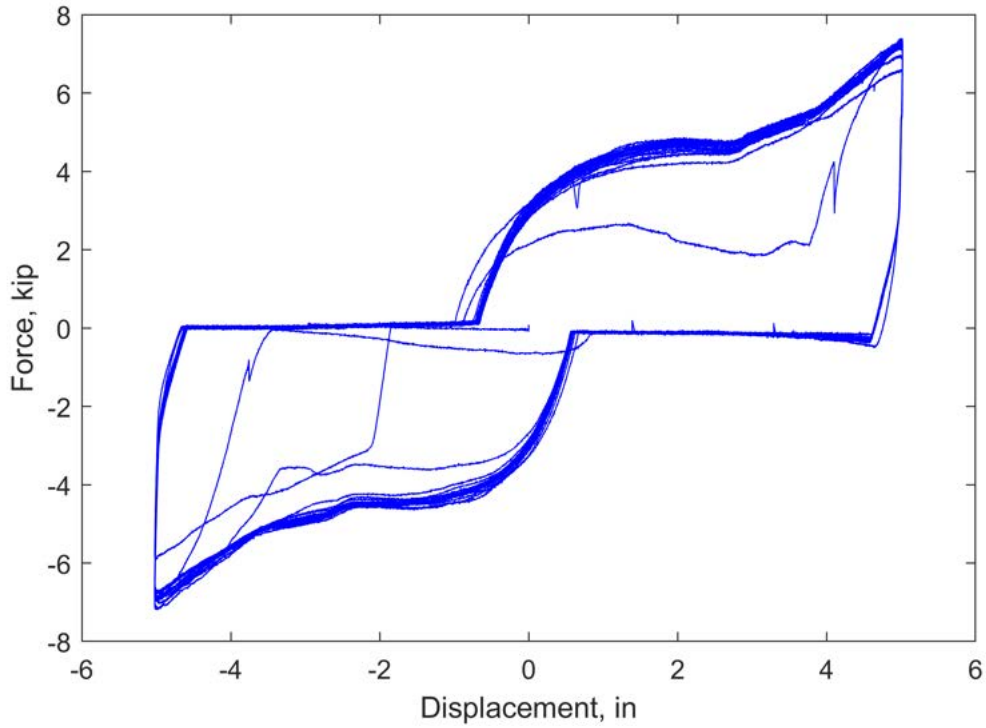

Figure R.19. Force-displacement plot of W24-PW-T50-R11.01.

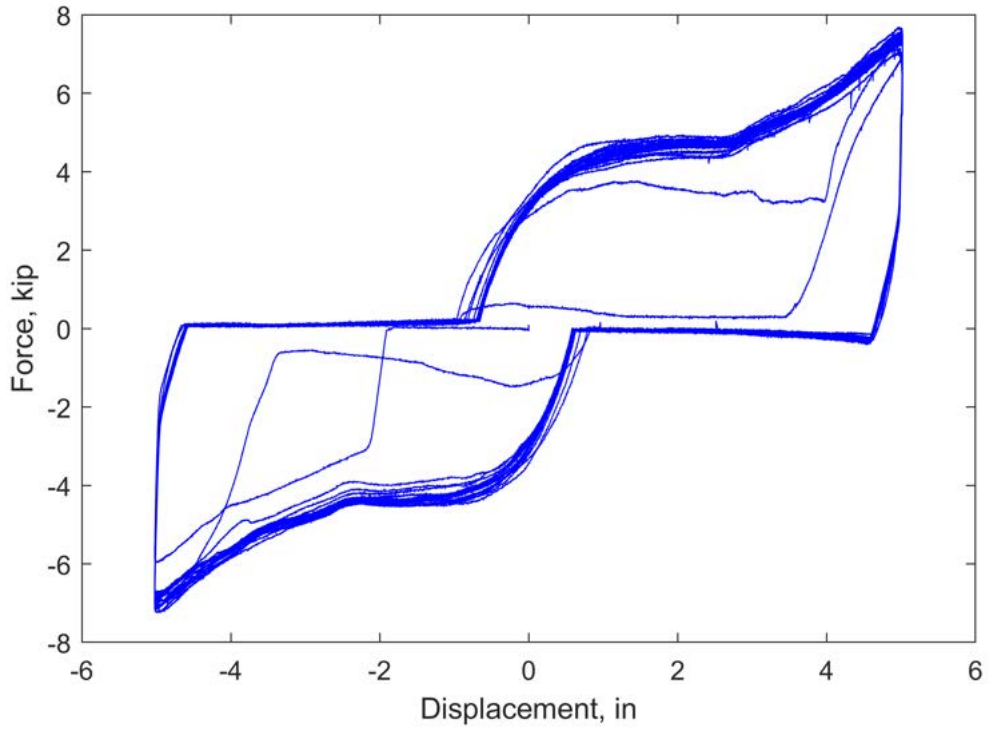

Figure R.20. Force-displacement plot of W24-PW-T50-R11.02.

R.3 0.59 in. Coupons

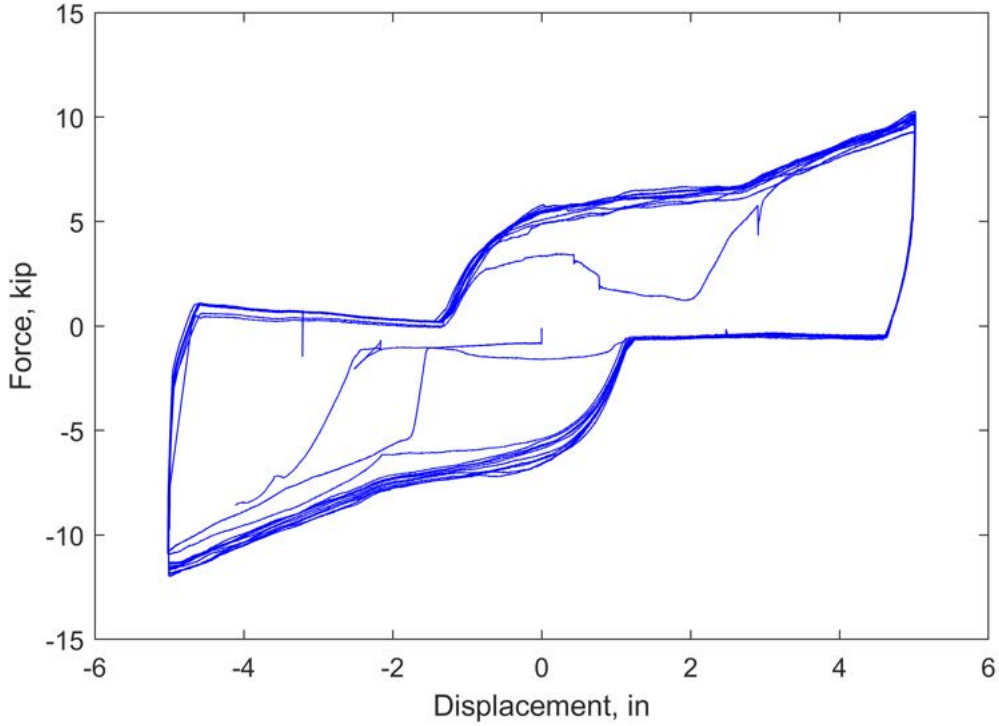

Figure R.21. Force-displacement plot of W24-0.125NGT-T59-R11.01.

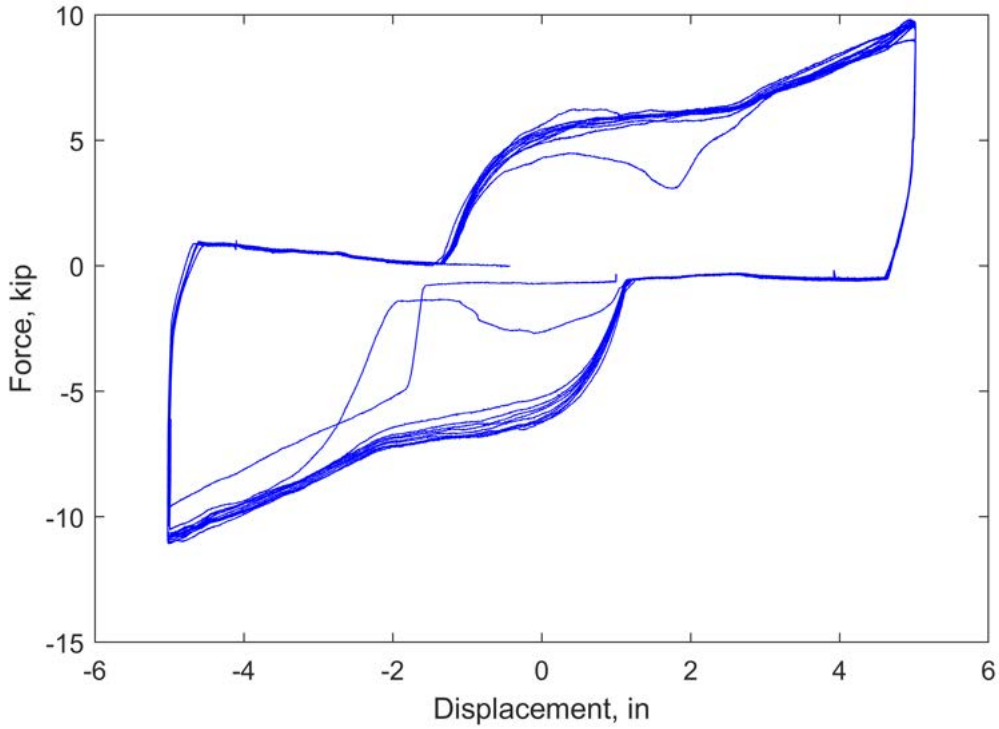

Figure R.22. Force-displacement plot of W24-0.125NGT-T59-R11.02.

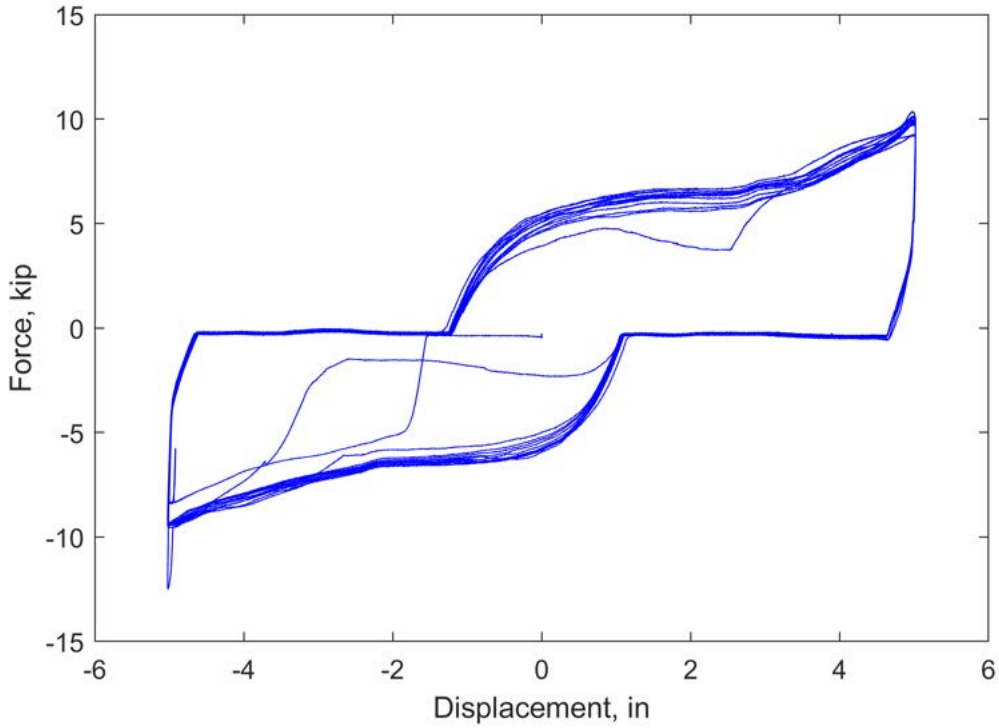

Figure R.23. Force-displacement plot of W24-0.25NGTW-T59-R11.01.

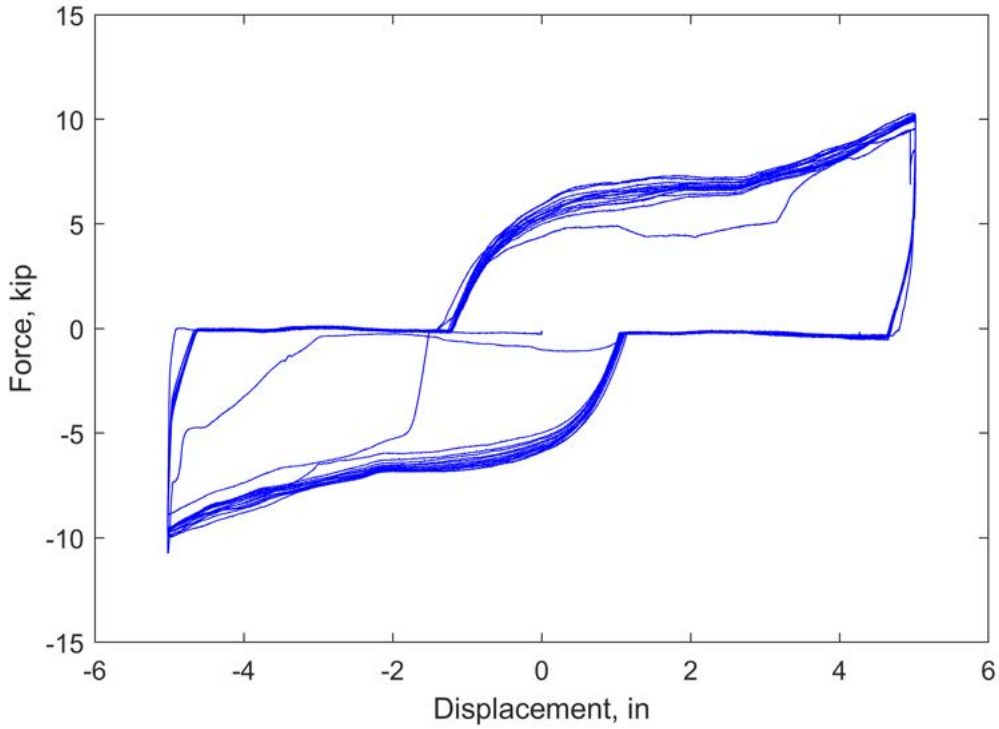

Figure R.24. Force-displacement plot of W24-0.25NGTW-T59-R11.02.

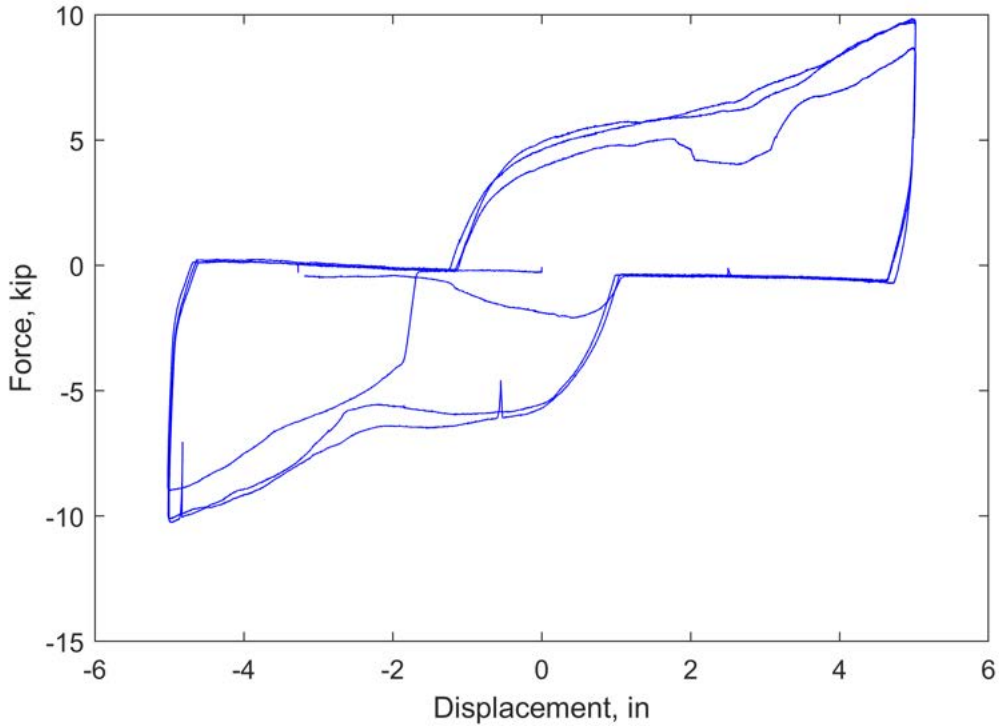

Figure R.25. Force-displacement plot of W24-0.25N-T59-R11.02.

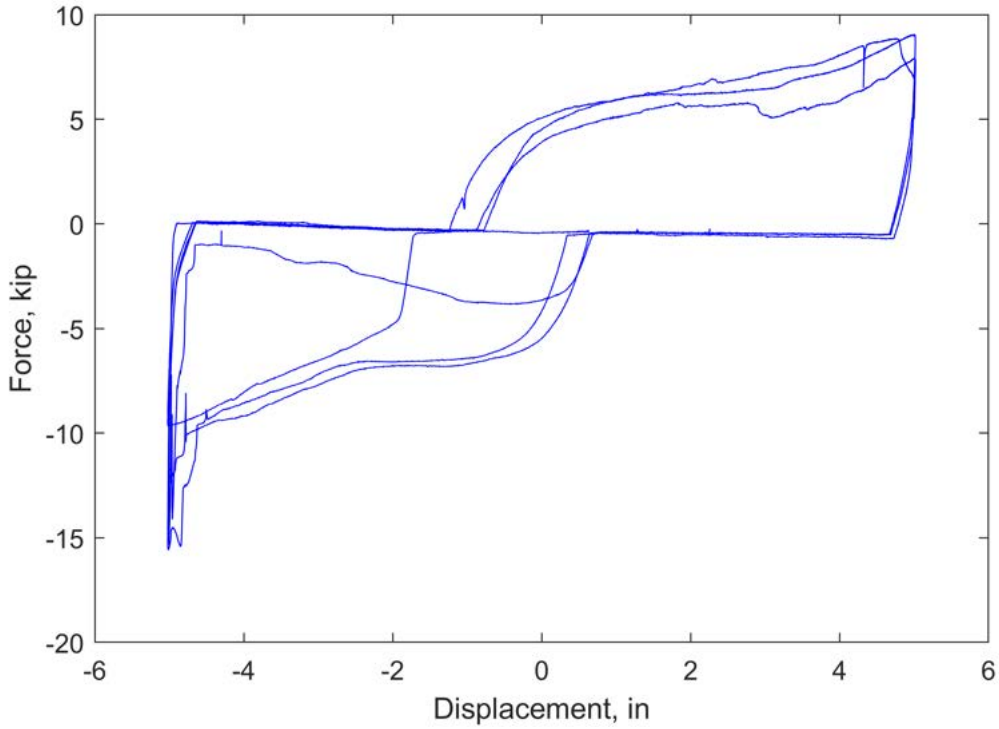

Figure R.26. Force-displacement plot of W24-0.25N-T59-R11.03.

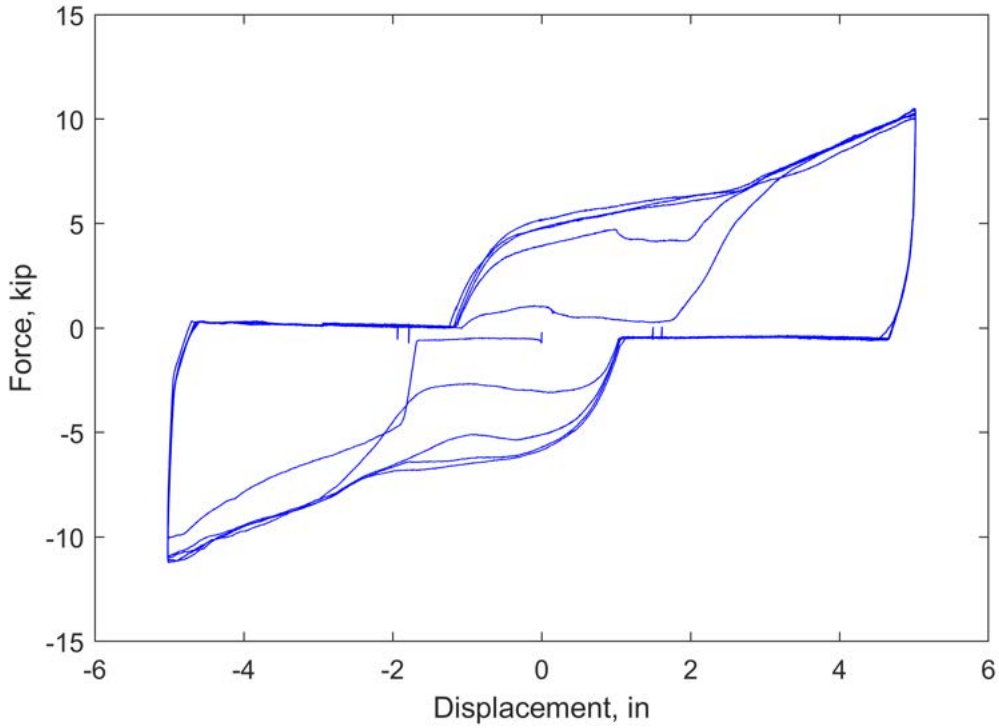

Figure R.27. Force-displacement plot of W24-0.375N-T59-R11.01.

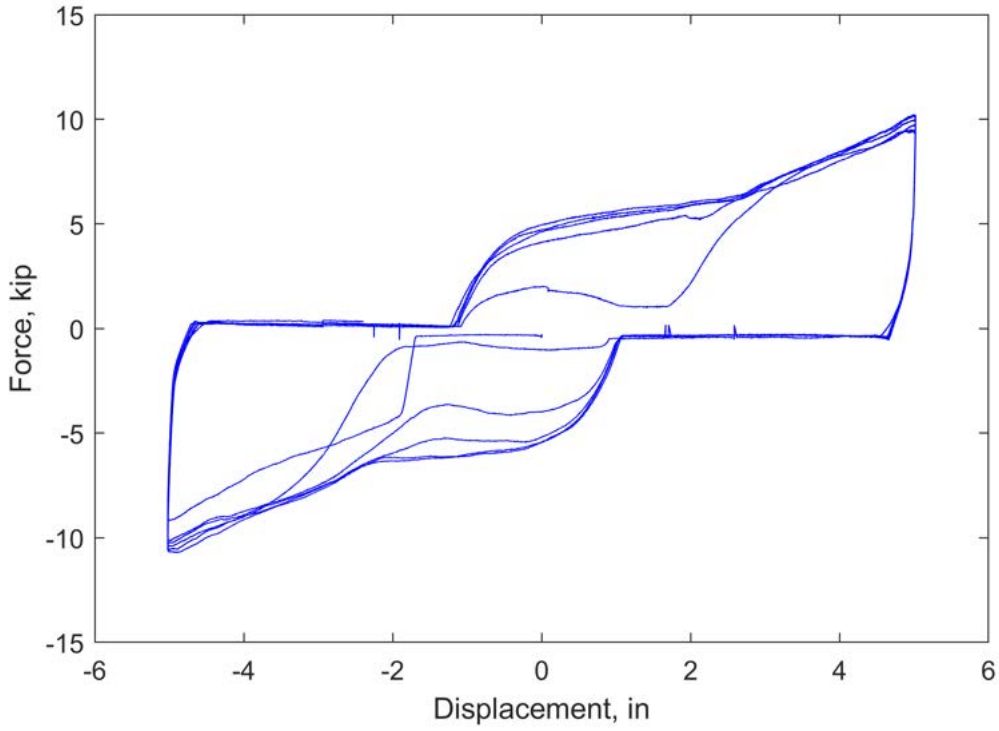

Figure R.28. Force-displacement plot of W24-0.375N-T59-R11.02.

R.4 0.94 in. Coupons

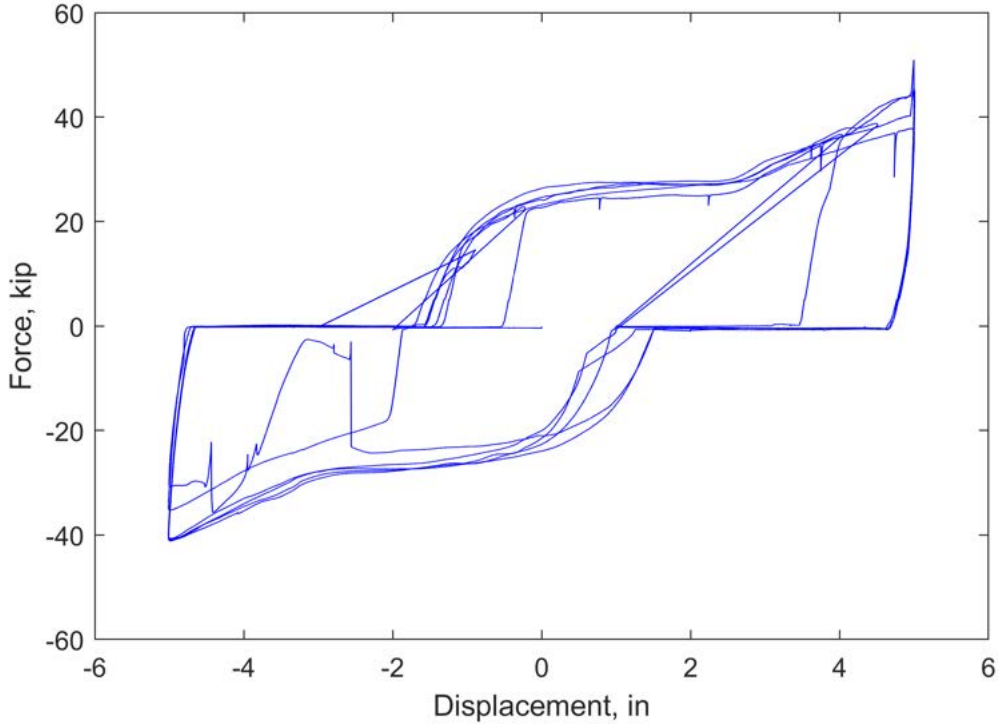

Figure R.29. Force-displacement plot of W36-0.125NGT-T94-R11.01.

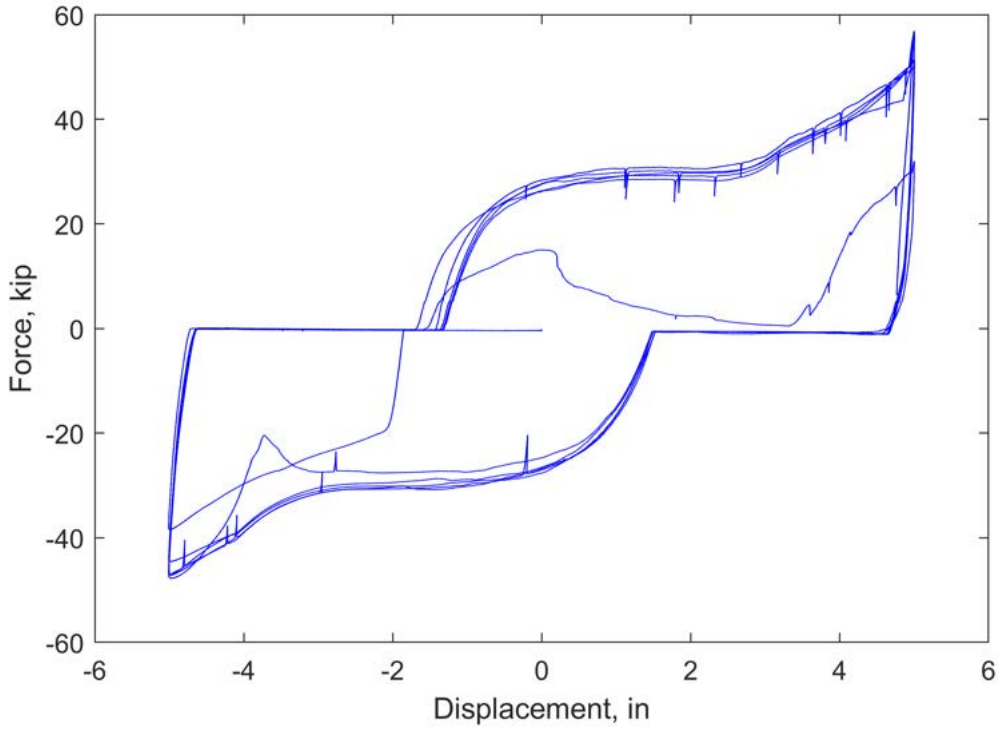

Figure R.30. Force-displacement plot of W36-0.125NGT-T94-R11.02.

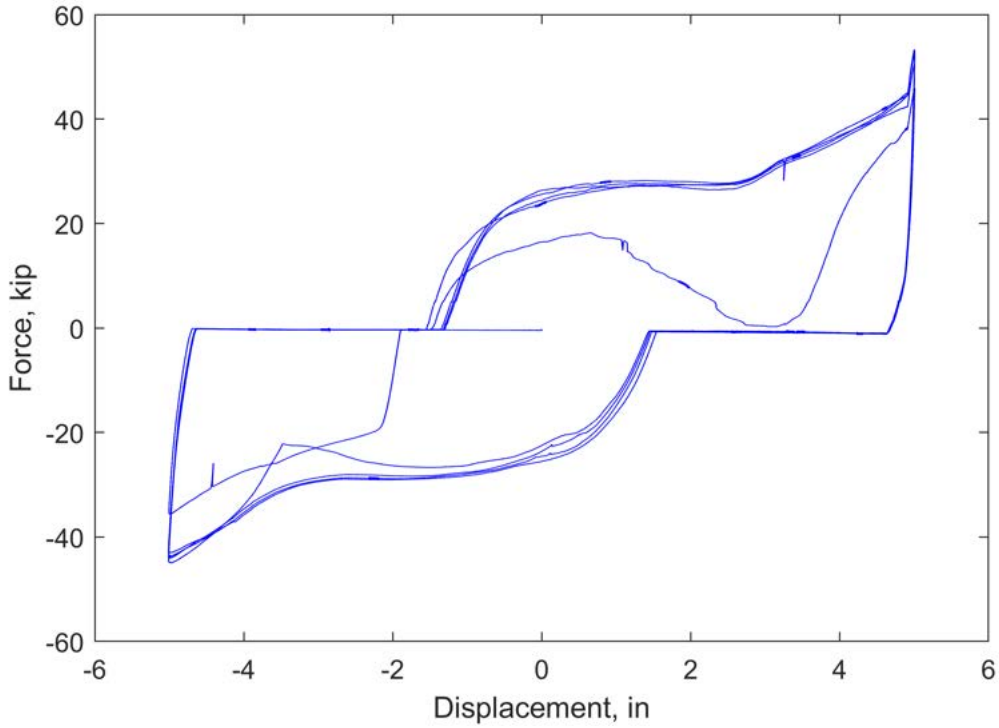

Figure R.31. Force-displacement plot of W36-0.25NGTW-T94-R11.01.

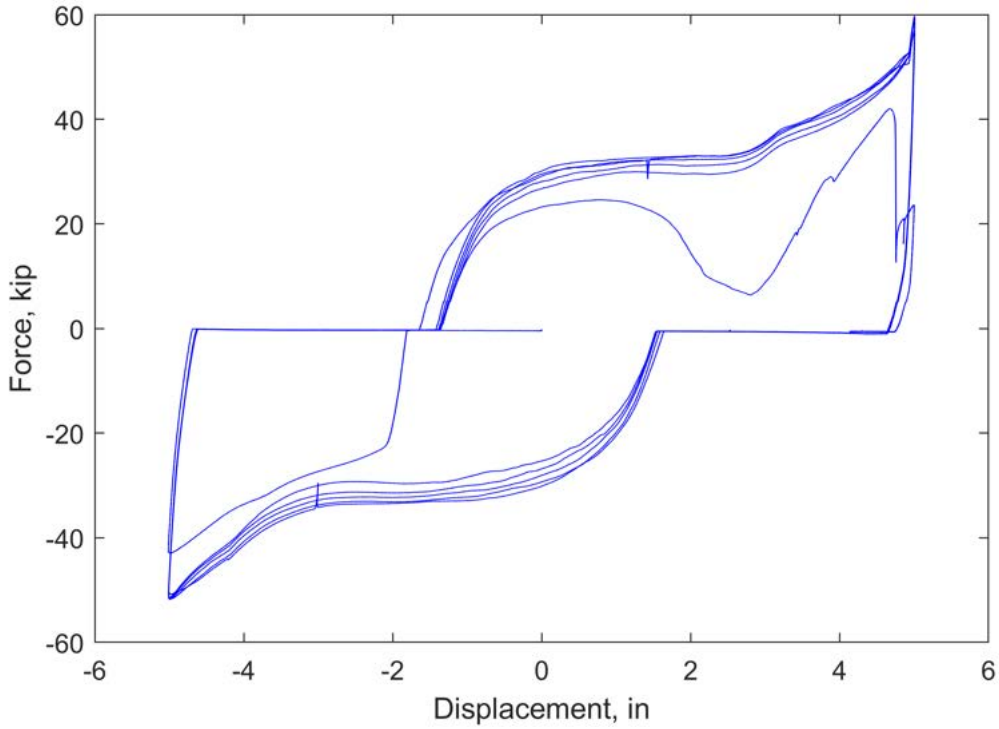

Figure R.32. Force-displacement plot of W36-0.25NGTW-T94-R11.02.

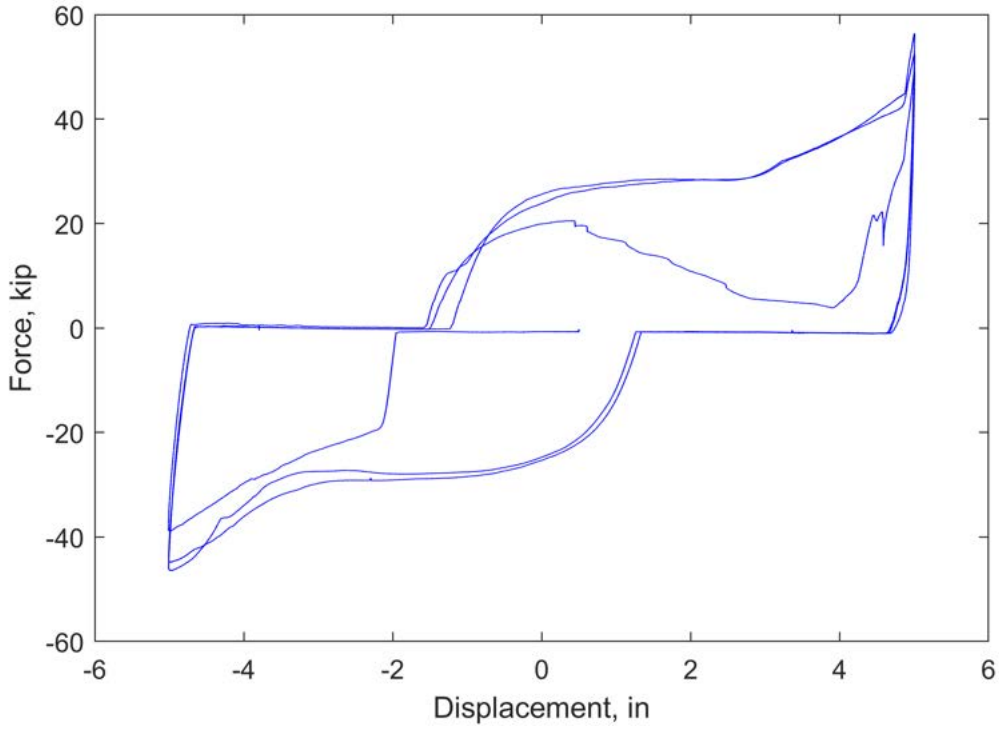

Figure R.33. Force-displacement plot of W36-0.25N-T94-R11.01.

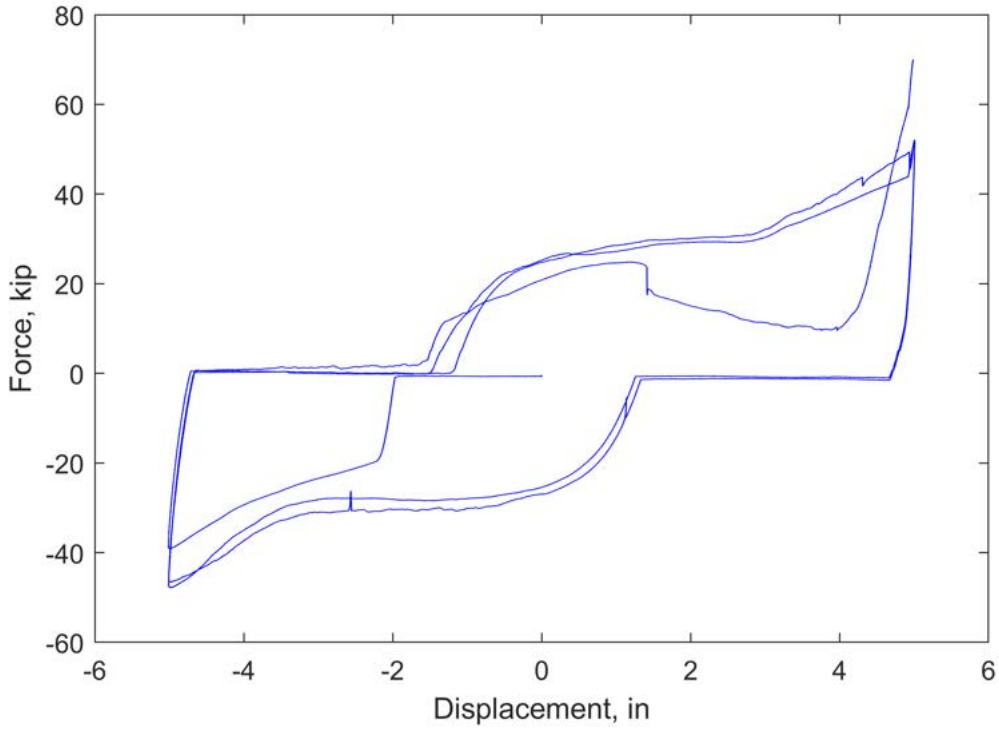

Figure R.34. Force-displacement plot of W36-0.25N-T94-R11.02.

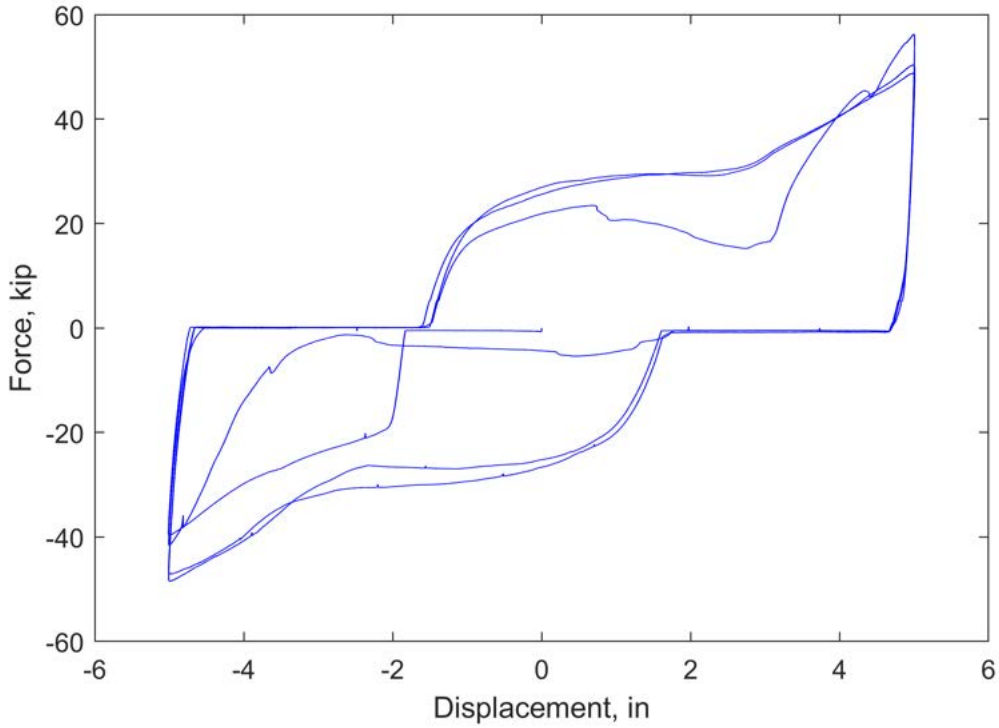

Figure R.35. Force-displacement plot of W36-0.375N-T94-R11.01.

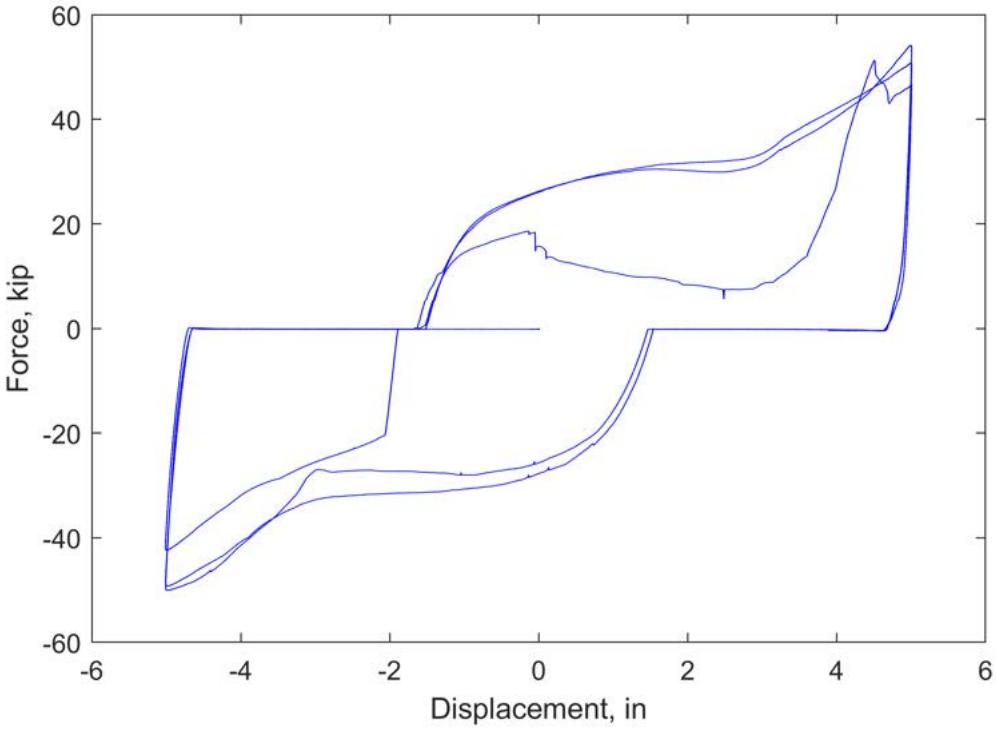

Figure R.36. Force-displacement plot of W36-0.375N-T94-R11.02.

R.5 1.0 in. Coupons

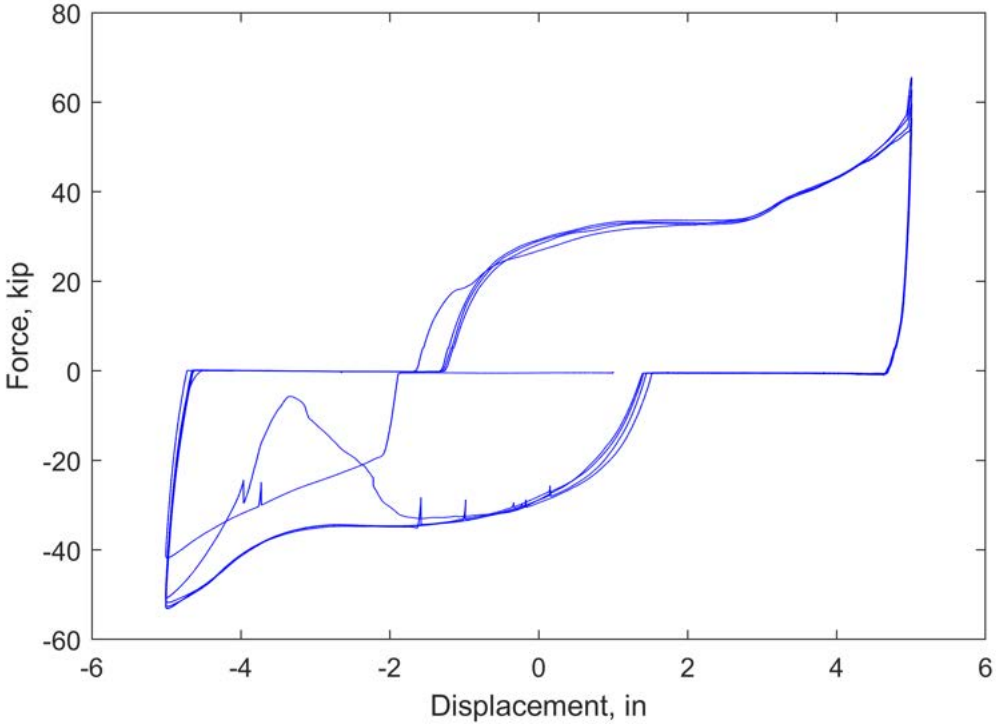

Figure R.37. Force-displacement plot of W36-0.125NGT-T100-R11.01.

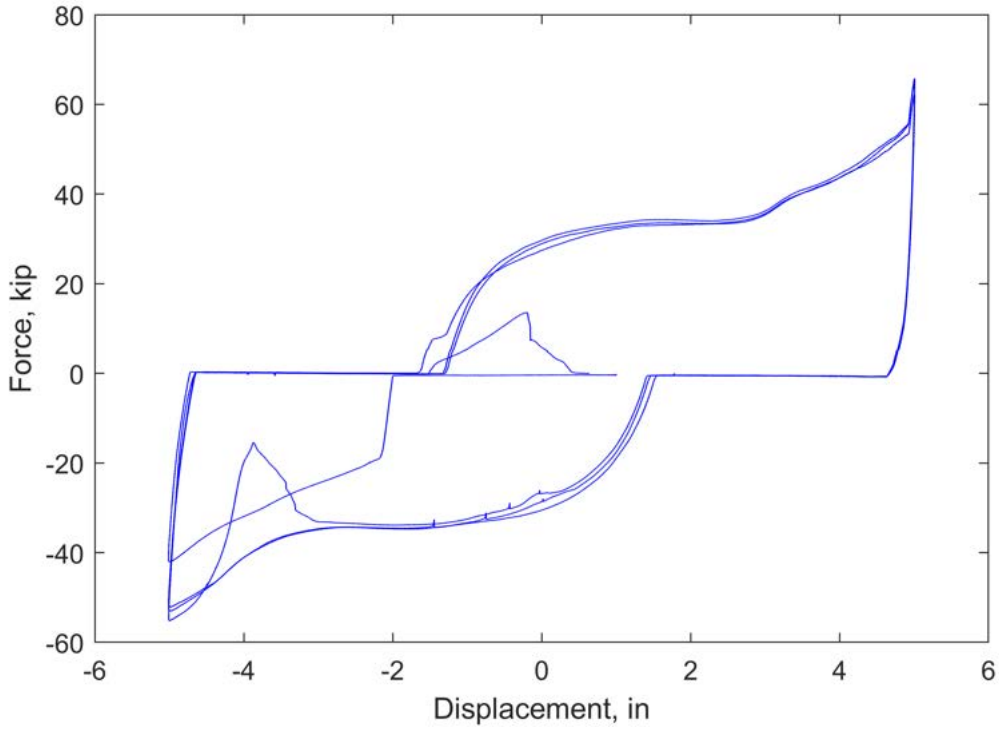

Figure R.38. Force-displacement plot of W36-0.125NGT-T100-R11.02.

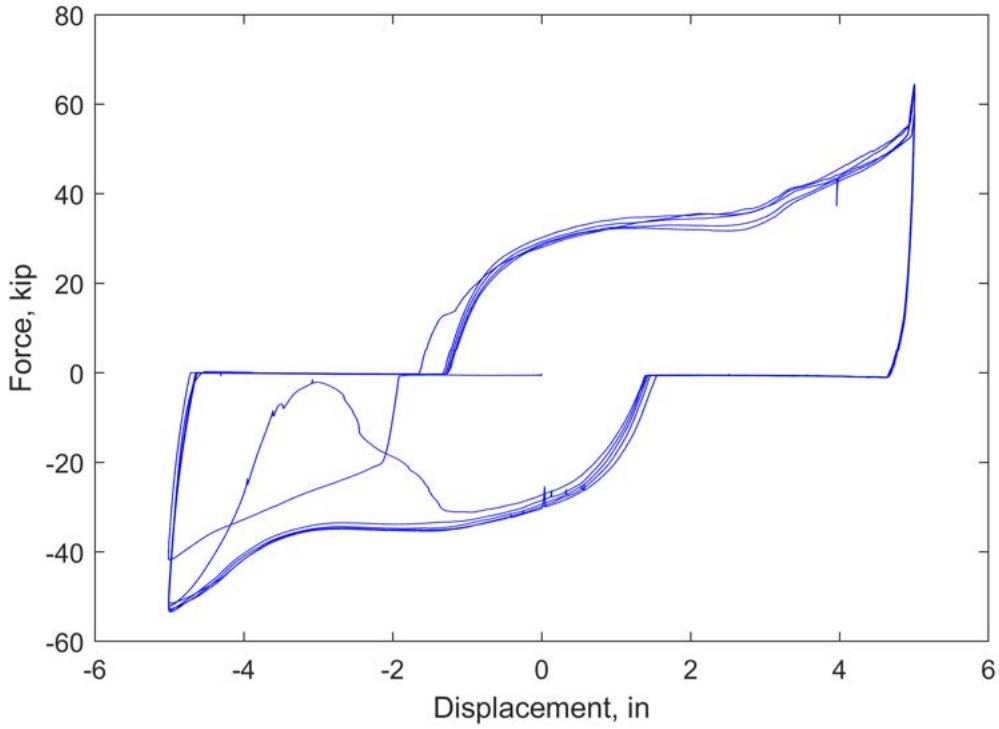

Figure R.39. Force-displacement plot of W36-0.25NGTW-T100-R11.01.

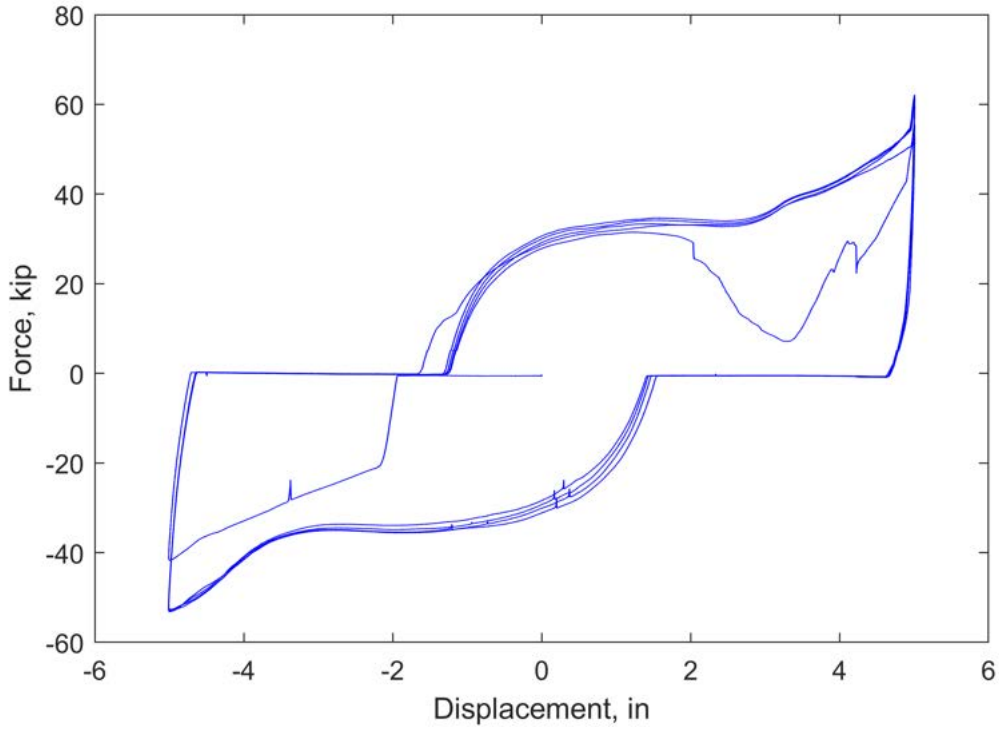

Figure R.40. Force-displacement plot of W36-0.25NGTW-T100-R11.02.

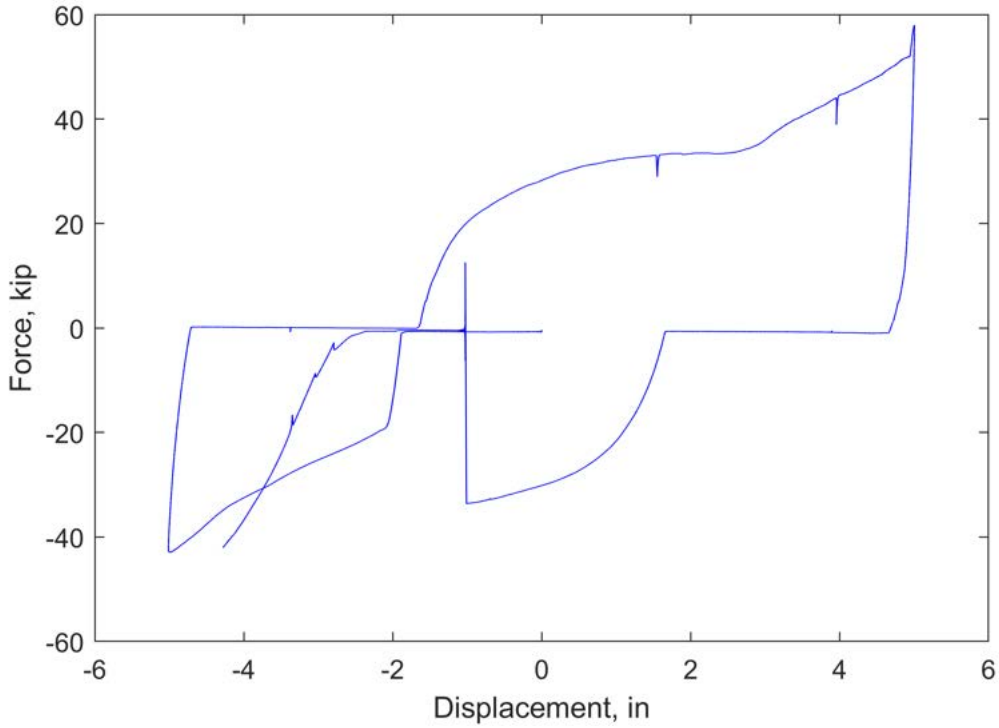

Figure R.41. Force-displacement plot of W36-0.25N-T100-R11.01.

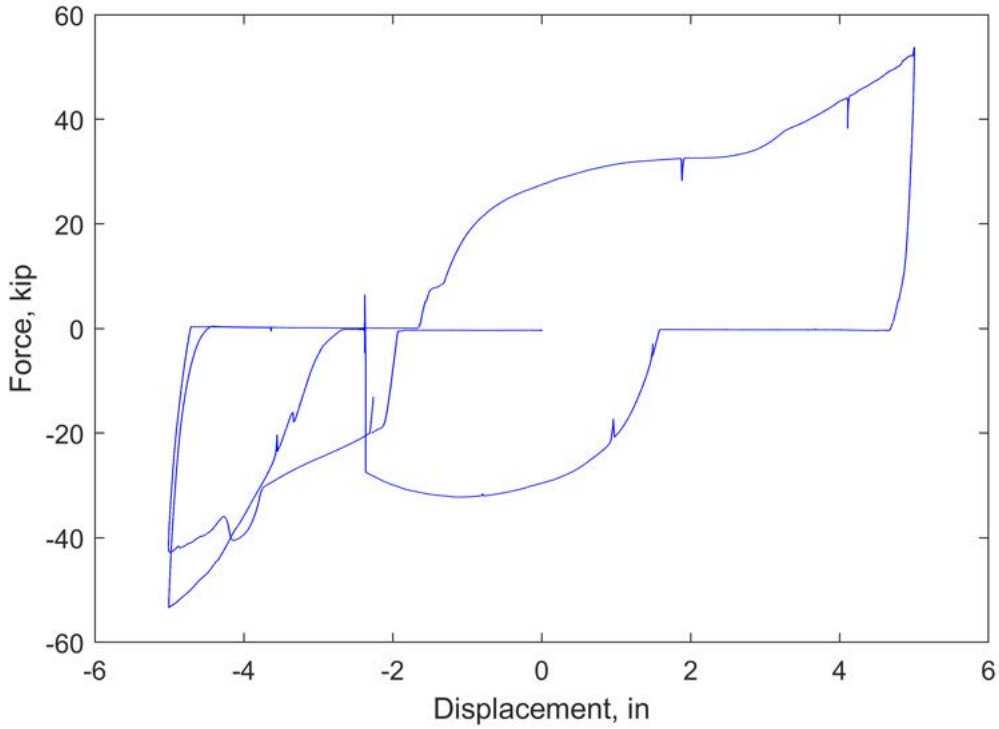

Figure R.42. Force-displacement plot of W36-0.25N-T100-R11.02.

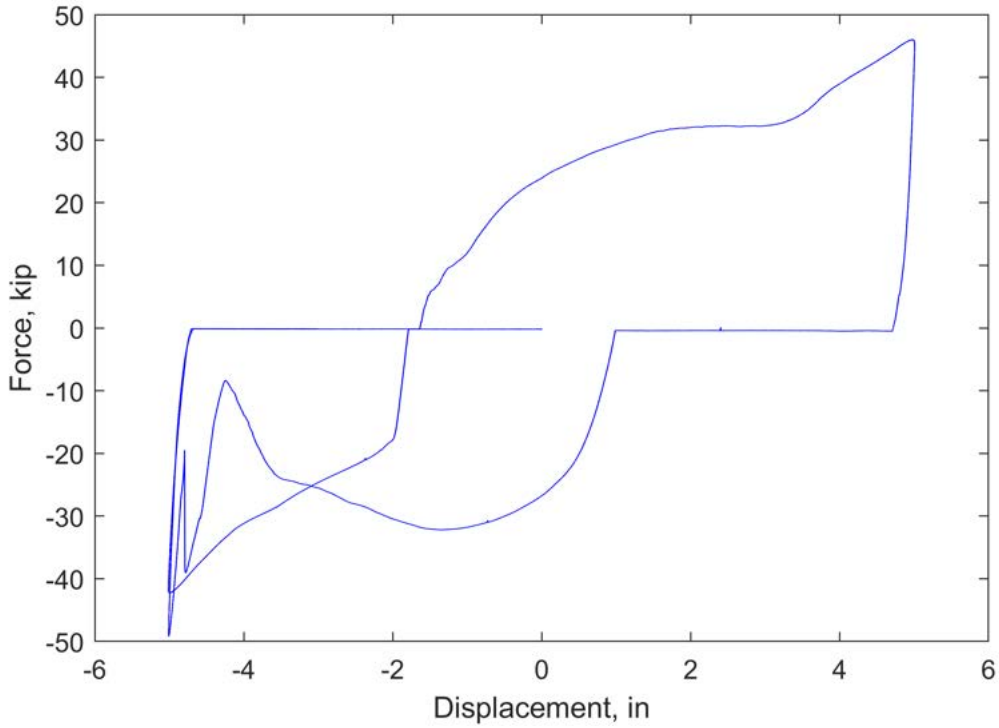

Figure R.43. Force-displacement plot of W36-0.375N-T100-R11.01.

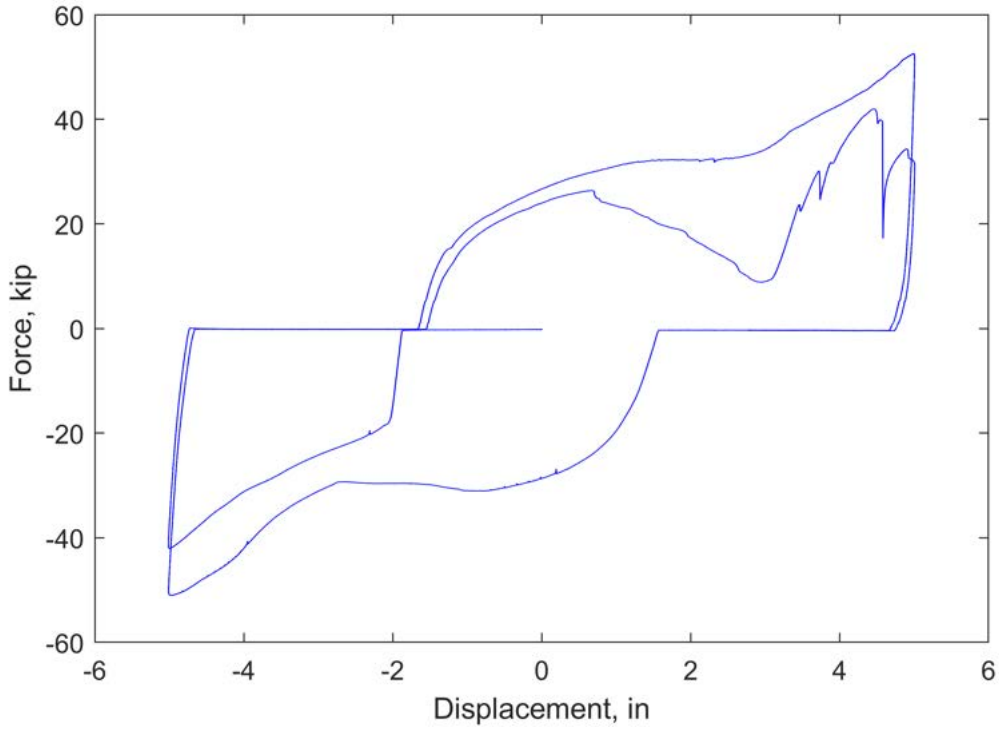

Figure R.44. Force-displacement plot of W36-0.375N-T100-R11.02.

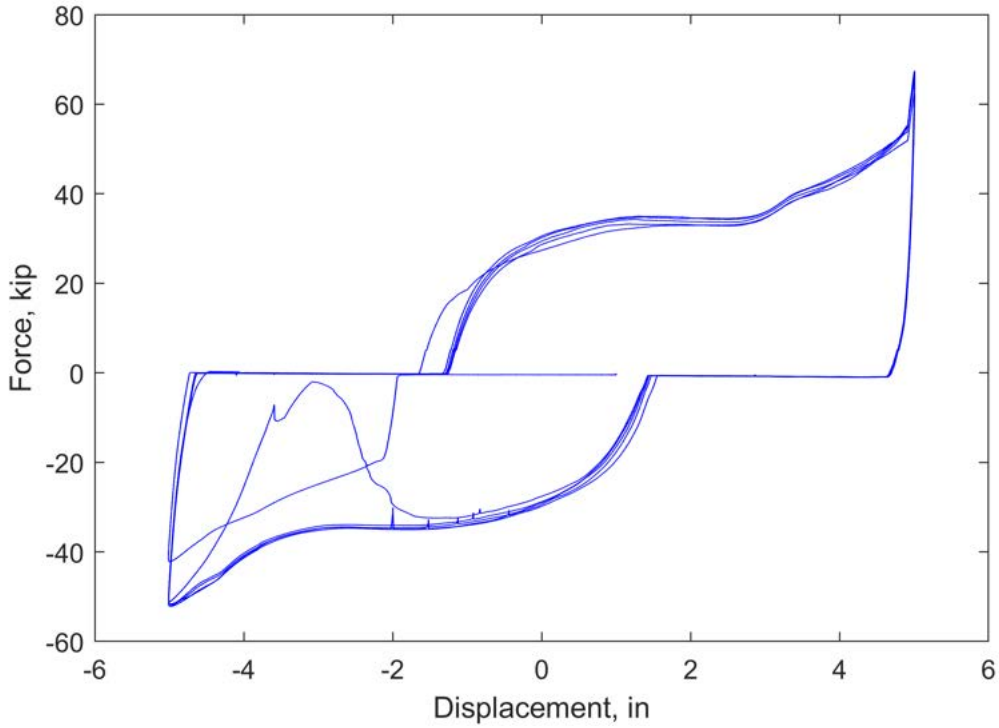

Figure R.45. Force-displacement plot of W36-STEEL-T100-R11.01.

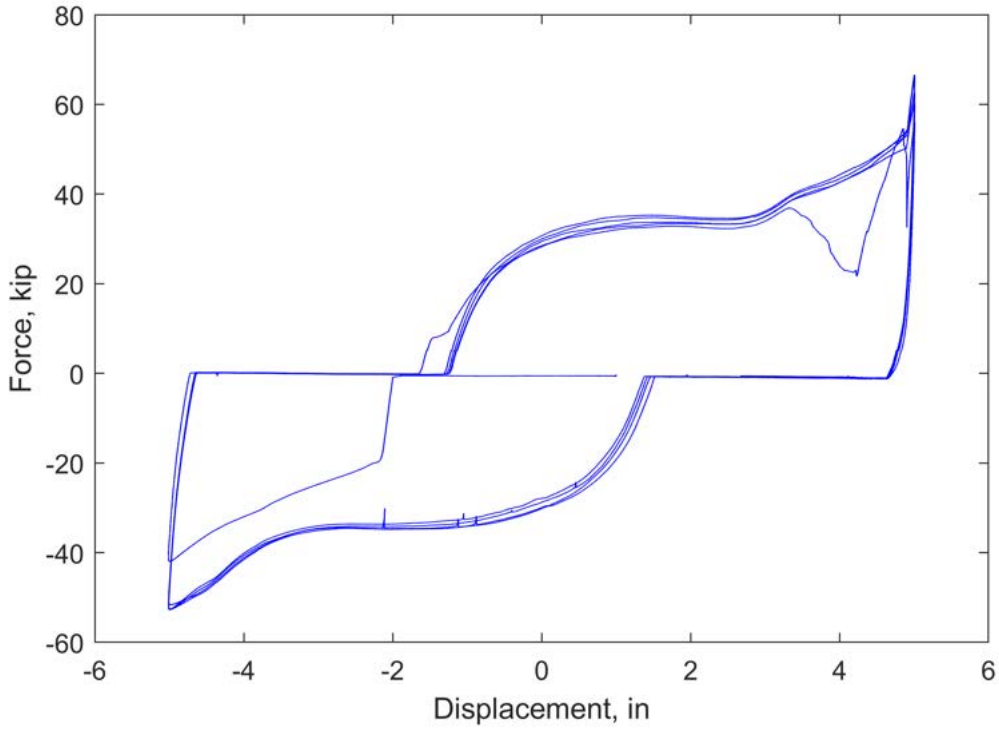

Figure R.46. Force-displacement plot of W36-STEEL-T100-R11.02.

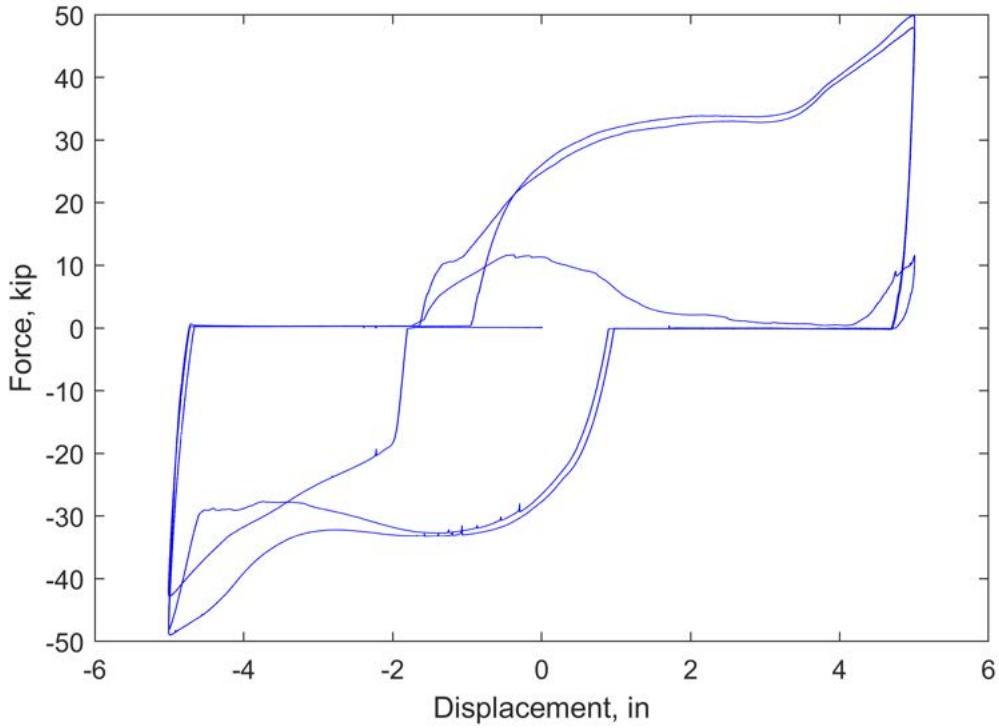

Figure R.47. Force-displacement plot of W36-0.625PnAF-T100-R11.01.

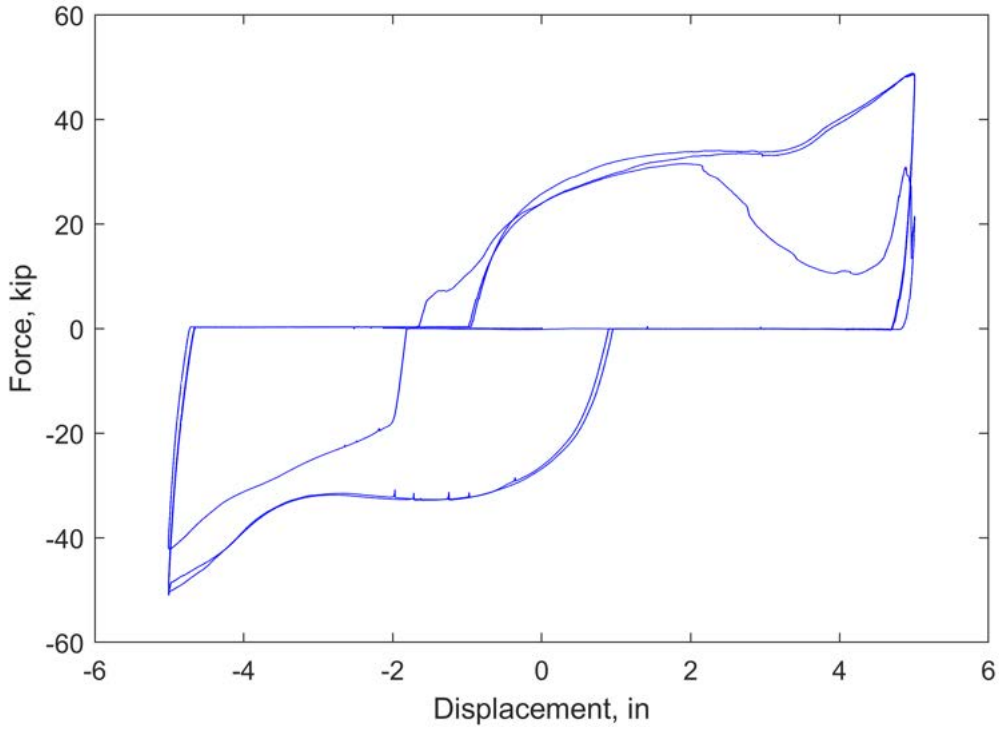

Figure R.48. Force-displacement plot of W36-0.625PnAF-T100-R11.02.

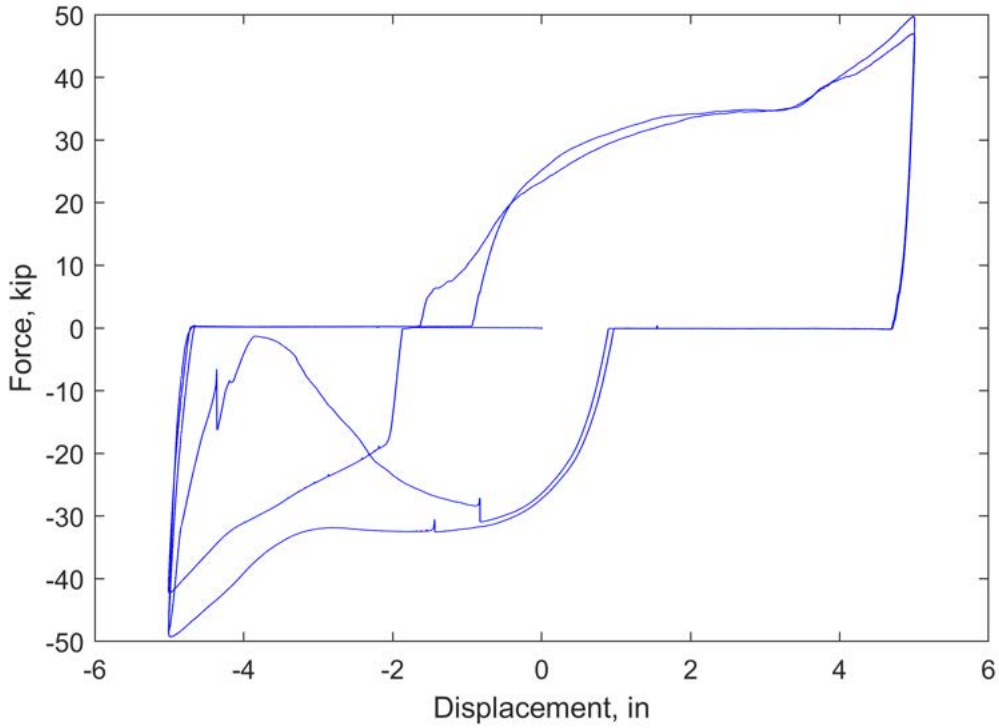

Figure R.49. Force-displacement plot of W36-0.75PnAF-T100-R11.01.

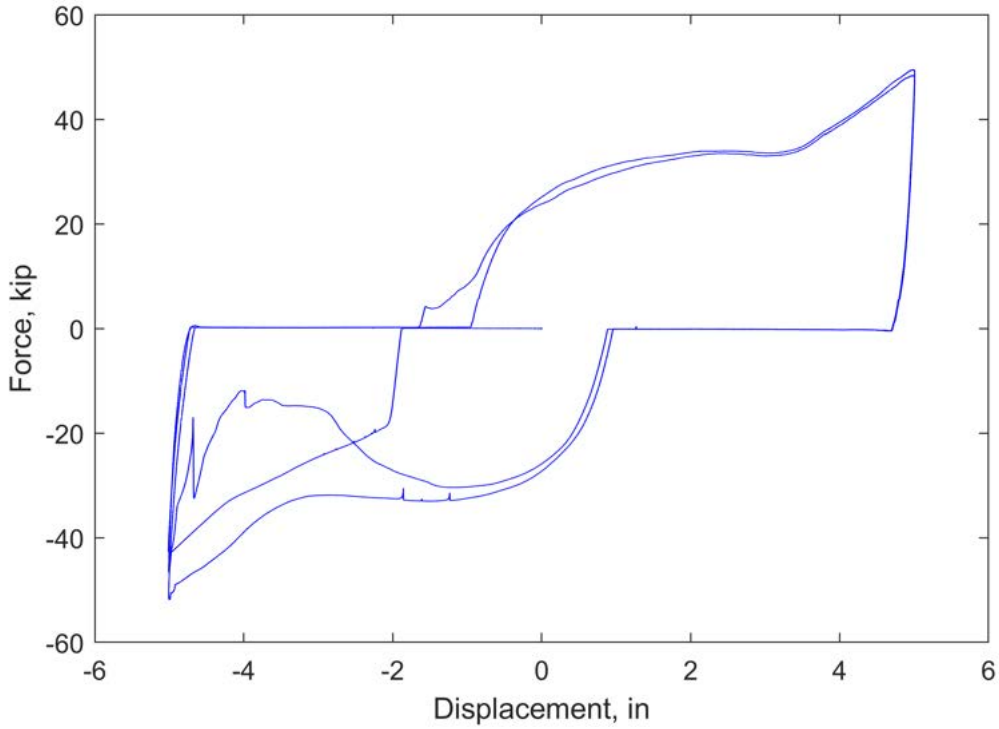

Figure R.50. Force-displacement plot of W36-0.75PnAF-T100-R11.02.

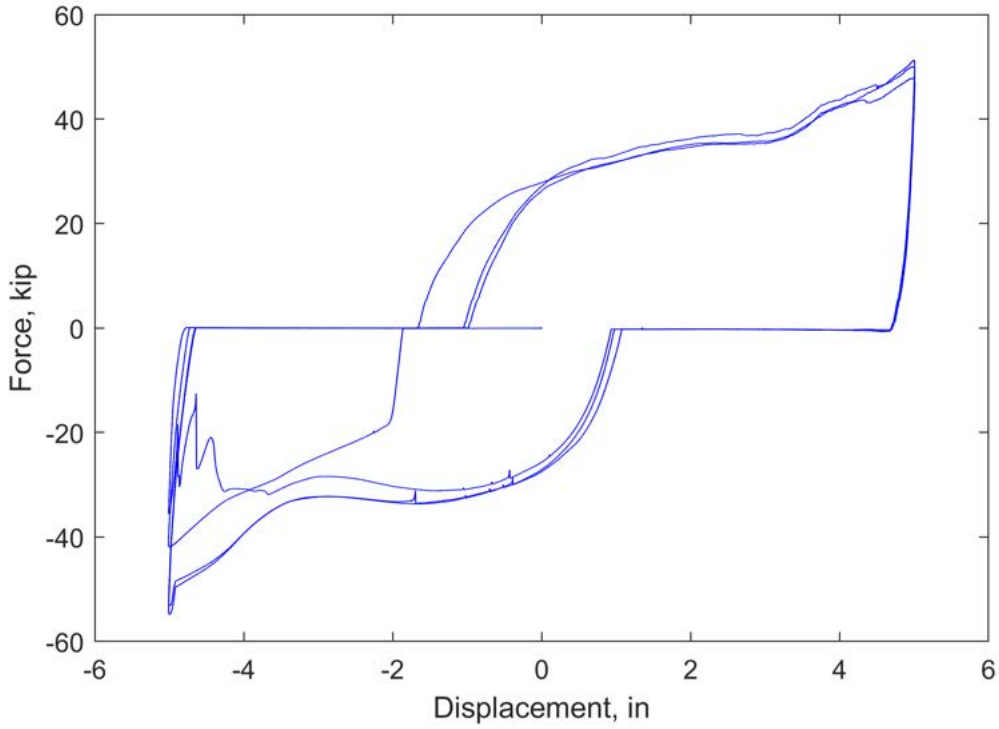

Figure R.51. Force-displacement plot of W36-PAF-T100-R11.01.

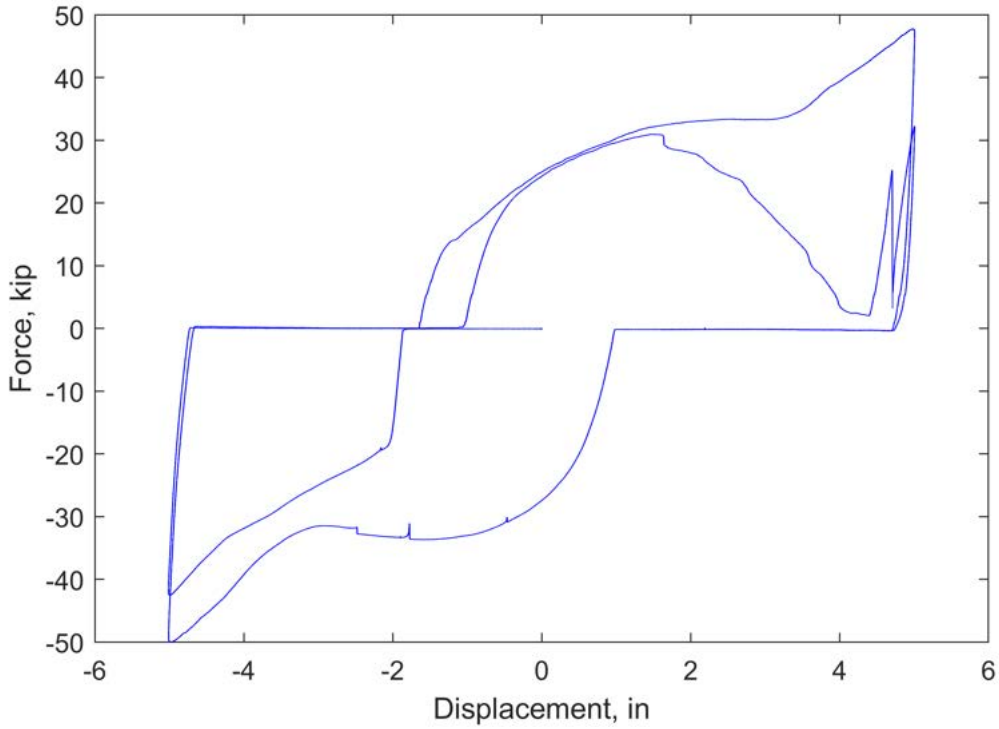

Figure R.52. Force-displacement plot of W36-PAF-T100-R11.02.

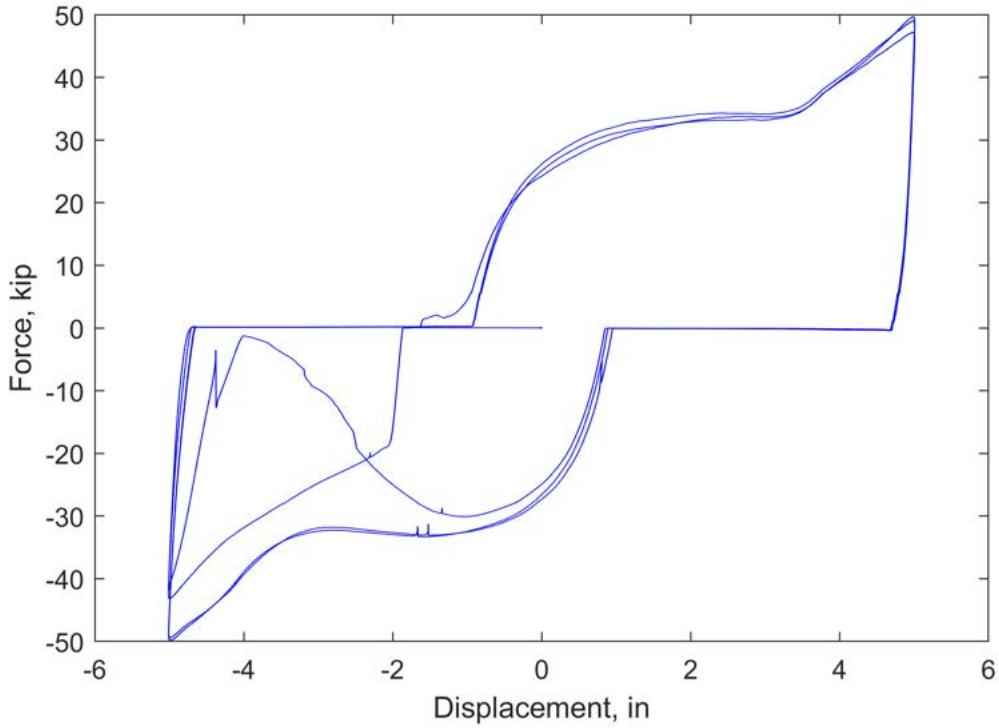

Figure R.53. Force-displacement plot of W36-PW-T100-R11.01.

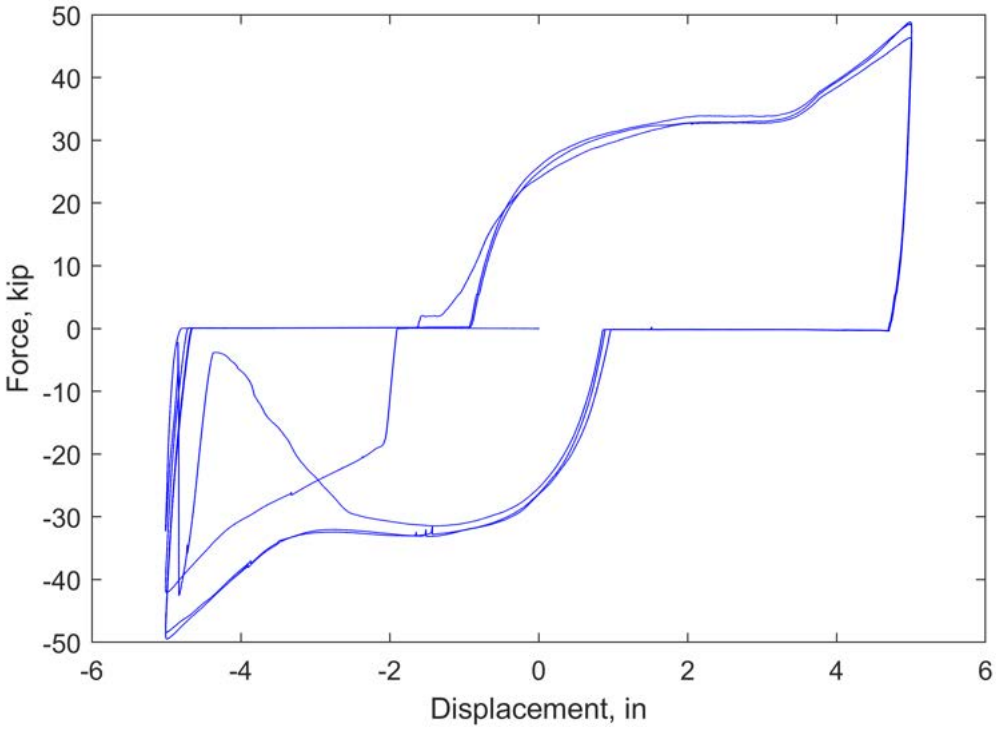

Figure R.54. Force-displacement plot of W36-PW-T100-R11.02.

Appendix S. Additional Repairs for Full-Scale Specimens with Welded Artifacts

This appendix describes additional repairs that were needed after the runoff tabs were removed from the W24RBS-0.25NGTW-T59 and W36RBS-0.25NGTW-T94 specimens.

S.1 W24RBS-0.25NGTW-T59

Two surface cracks were found on this specimen when the ground welds were inspected with the magnetic particle test. These cracks were ground out and then rewelded following the weld procedure specification. The first bottom flange surface crack is shown in Figure S.1 and the first top flange surface crack is shown in Figure S.2. Before welding, the new bottom flange notch was ground to 0.125 in. deep and the new top flange notch was ground to 0.063 in. deep.

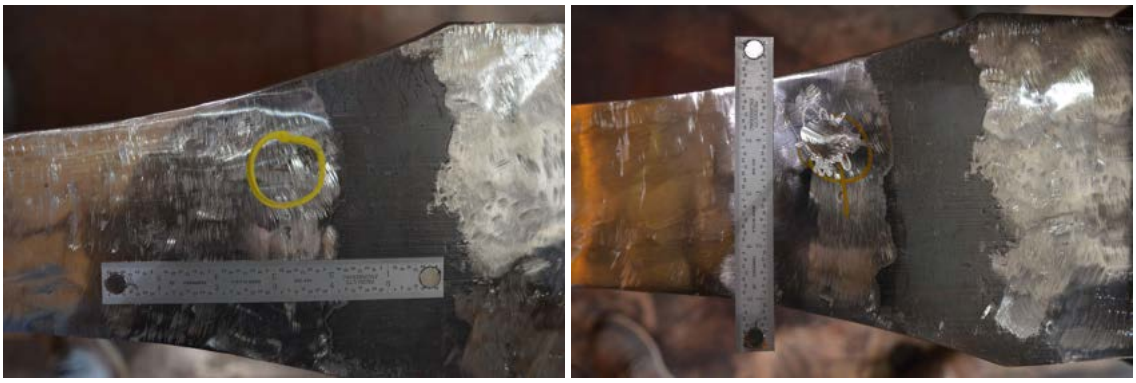

(a) Surface crack. **(b)** After surface crack was removed.

Figure S.1. First bottom flange surface crack and repair .

(a) Surface crack. **(b)** After surface crack was removed.

Figure S.2. First top flange surface crack and repair.

After the welds were ground flush and reinspected, two additional surface cracks were found in the same locations. The second bottom flange surface crack is shown in Figure S.3 and the second top flange surface crack is shown in Figure S.4. The crack on the bottom flange was ground out to a depth of 0.125 in. and the crack on the top flange was ground out to less than 0.06 in. deep. Only the new bottom flange notch was rewelded, as the new top flange notch was within the thickness tolerance given in AWS D1.8.

(a) Surface crack. **(b)** After surface crack was removed.

Figure S.3. Second bottom flange surface crack and repair.

Figure S.4. Second top flange surface crack.

S.2 W36RBS-0.25NGTW-T94

Numerous surface defects were found when the weld runoff tabs were removed. These included errant gouges from the angle grinder and areas where the base metal was removed when the tabs were pried off. These defects are shown in Figure S.5 and Figure S.6. After documenting the location, size, and depth, the defects were ground to a smooth taper in every direction and rewelded. The rewelding followed the same weld procedure specification except runoff tabs were not used. The included drawings show the approximate location of each defect. The depth of the defects before and after grinding are given in Table S.1. The depth of the defects on the top flange before grinding are given in Table S.2, but the depth after grinding was inadvertently not recorded.

Figure S.5. Bottom flange defects.

Figure S.6. Top flange defects.

Table S.1. Depth of bottom flange defects on W36RBS-0.25NGTW-T94.

Defect No.	Before grinding, in.	After grinding, in.
1	0.032	0.042
2	0.021	0.014
3	0.076	0.046
4	0.026	0.025
5	0.01	0.028
6	0.031	0.033
7	0.013	0.02
8	0.01	0.01
9	0.028	0.025
10	0.013	0.01
11	0.053	0.021
12	0.016	0.04
13	0.031	0.063
14	0.029	0.069
15	0.023	0.096
16	0.027	0.023
17	0.029	0.014
18	0.013	0.017
19	0.017	0.019
20	0.062	0.03
21	0.026	0.047
22	0.01	0.073
23	0.014	0.028
24	0.028	0.03
25	0.05	0.064
26	0.01	0.03
27	0.017	0.025
28	0.01	0.069
29	0.045	0.104
30	0.028	0.038
31	0.013	0.066
32	0.025	0.054
33	0.047	0.082

Table S.2. Depth of top flange defects on W36RBS-0.25NGTW-T94.

Defect No.	Before grinding, in.
1	0.034
2	0.012
3	0.005
4	0.02
5	0.079
6	0.01
7	0.063
8	0.013
9	0.022
10	0.03
11	0.028
12	0.025
13	0.01
14	0.044
15	0.031
16	0.013
17	0.0
18	0.012

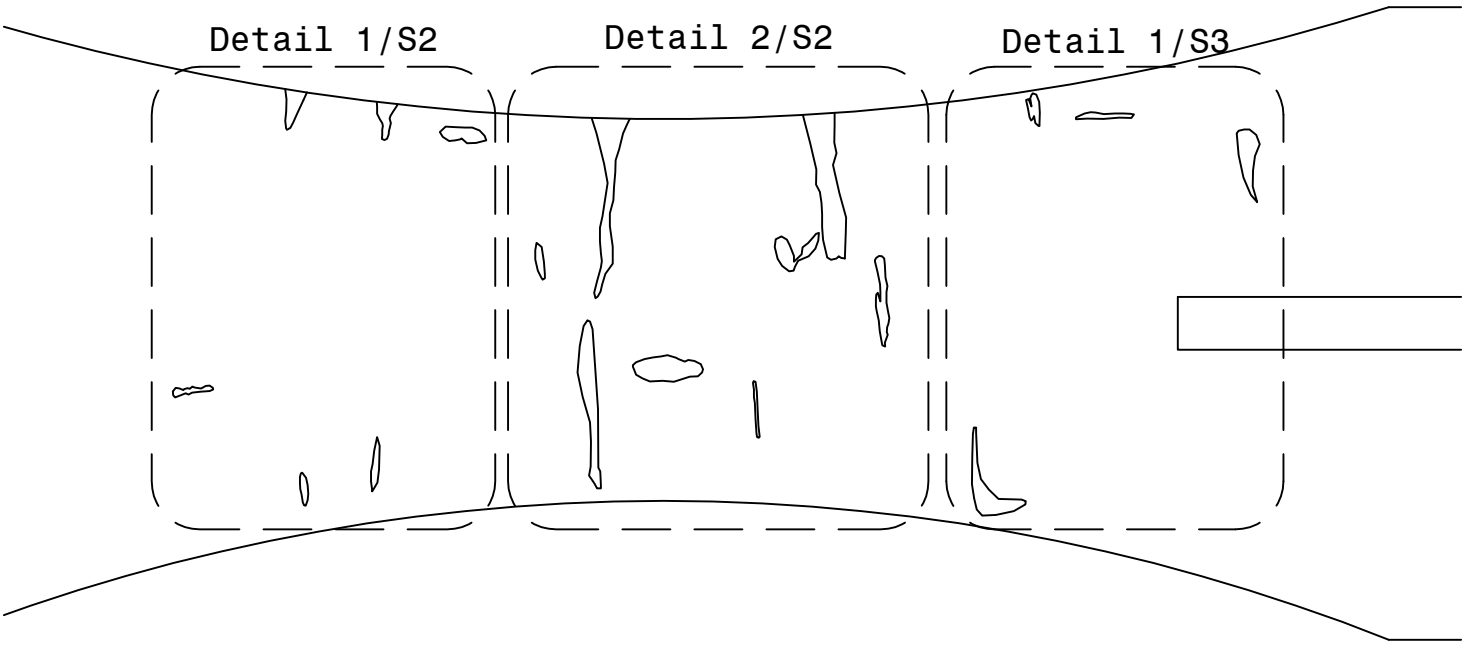

Top flange defects

Scale: NTS

1/S1

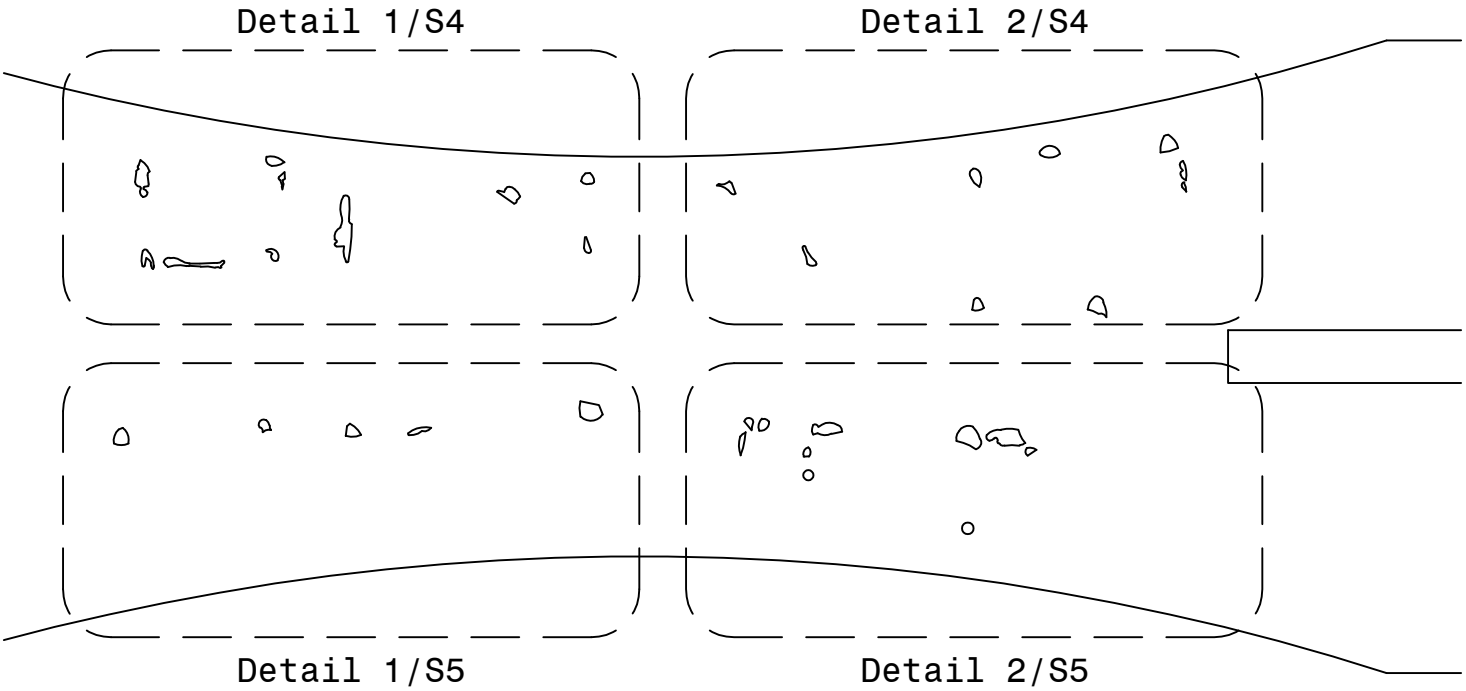

Bottom flange defects

Scale: NTS

2/S1

VIRGINIA TECH

VIRGINIA TECH
CHARLES E. VIA JR. DEPARTMENT OF CIVIL & ENVIRONMENTAL ENGINEERING
200 PATTON HALL
BLACKSBURG, VA 24061
P: 540-231-6635

PROJECT:

MRF Protected Zone/Low-Cycle Fatigue

SHEET NOTES:

REVISIONS:

NO.	DATE	BY

DESIGNED BY:

DRAWN BY: R. Stevens

CHECKED BY:

DATE: 6/7/2020

PROJECT NO.:

SHEET TITLE:

W36RBS-0.25NGTW-T94 Defects

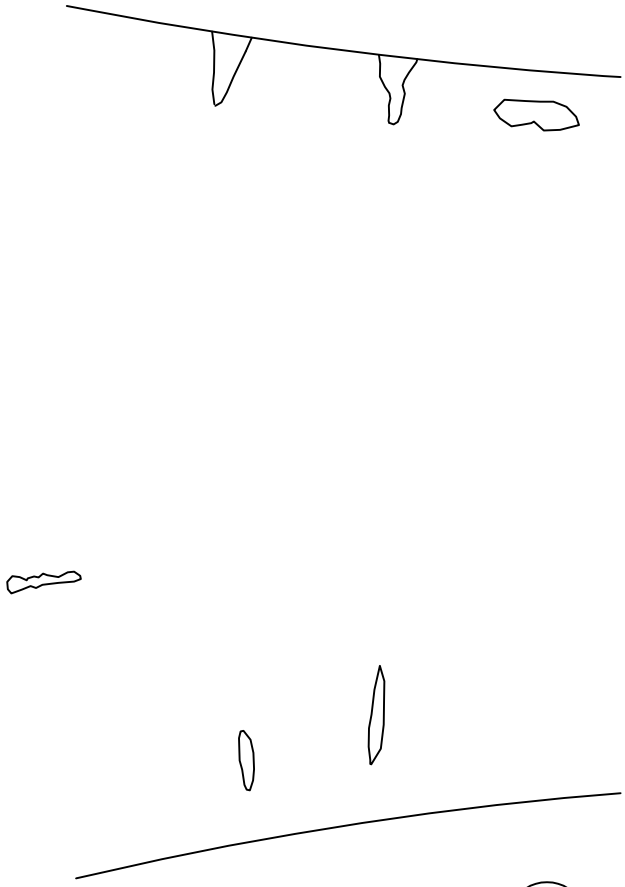

Scale: 6" = 1'

1
S2

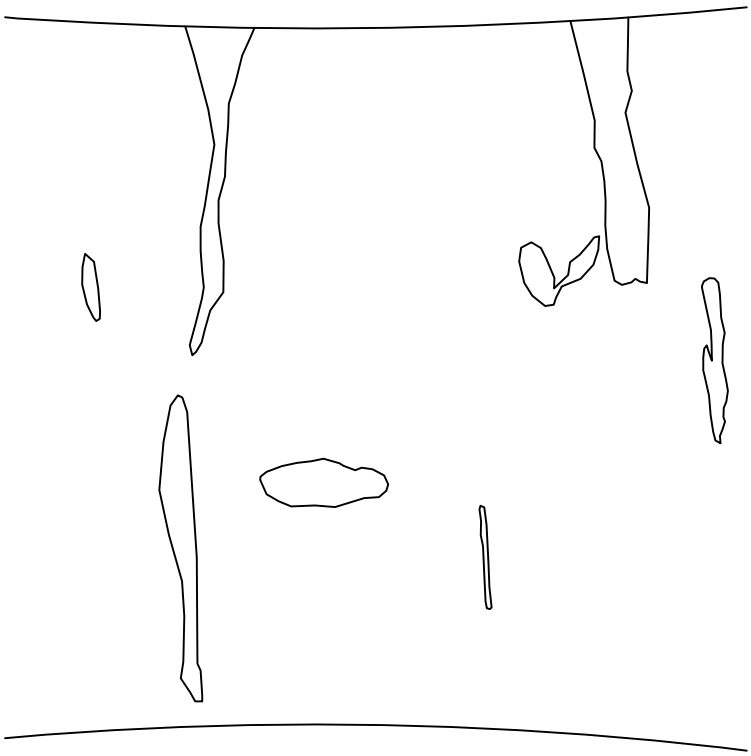

Scale: 6" = 1'

2
S2

VIRGINIA TECH
CHARLES E. VIA JR. DEPARTMENT OF CIVIL & ENVIRONMENTAL ENGINEERING
200 PATTON HALL
BLACKSBURG, VA 24061
P: 540-231-6635

PROJECT:
MRF Protected Zone/Low-Cycle Fatigue

SHEET NOTES:

REVISIONS:

NO.	DATE	BY

DESIGNED BY:
DRAWN BY: R. Stevens
CHECKED BY:
DATE: 6/7/2020
PROJECT NO.:

SHEET TITLE:
Top Flange Defects Detail Sheet

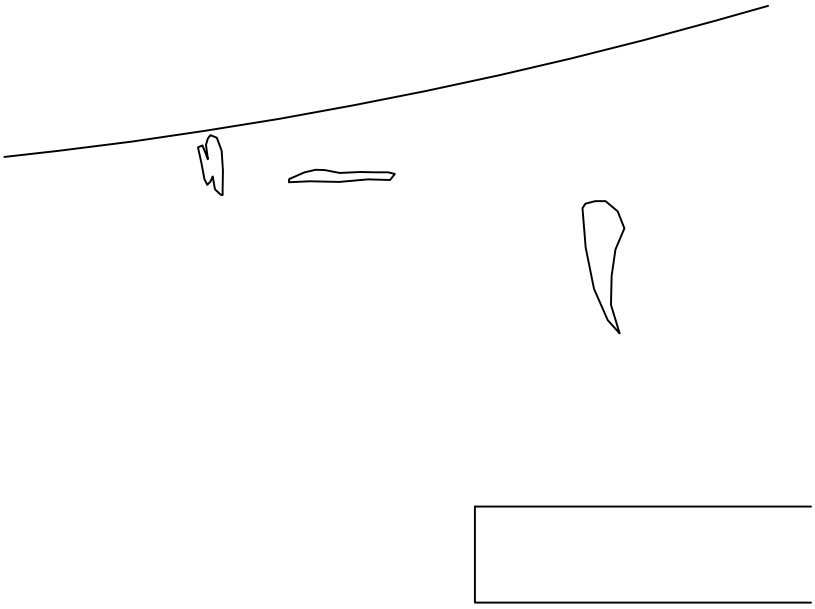

Scale: 6" = 1'

1
S3

VIRGINIA TECH
CHARLES E. VIA JR. DEPARTMENT OF CIVIL & ENVIRONMENTAL ENGINEERING
200 PATTON HALL
BLACKSBURG, VA 24061
P: 540-231-6635

PROJECT:
MRF Protected Zone/Low-Cycle Fatigue

SHEET NOTES:

REVISIONS:

NO.	DATE	BY

DESIGNED BY:
DRAWN BY: R. Stevens
CHECKED BY:
DATE: 6/7/2020
PROJECT NO.:

SHEET TITLE:
Top Flange Defect Detail Sheet

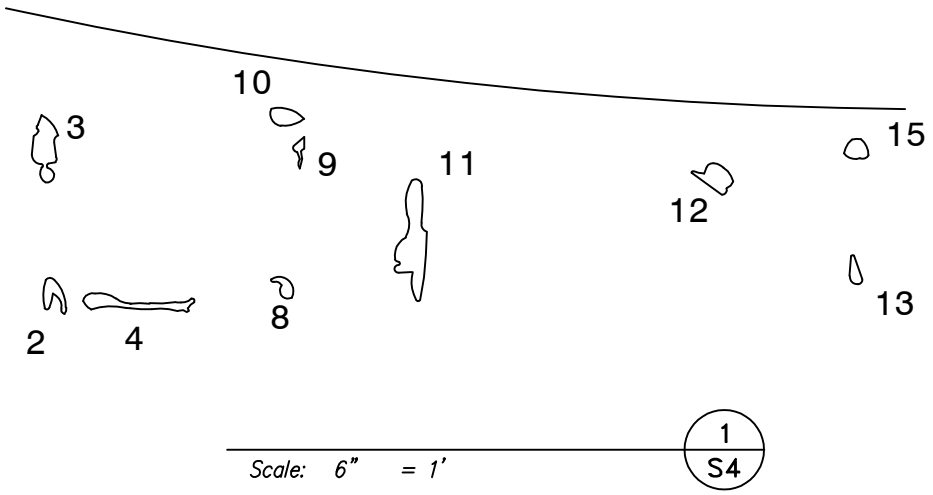

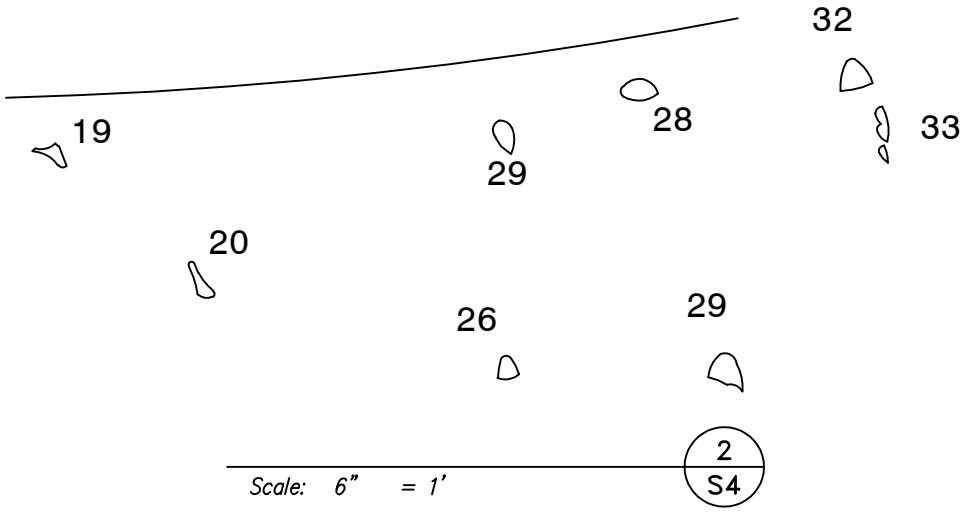

VIRGINIA TECH
CHARLES E. VIA JR. DEPARTMENT OF CIVIL & ENVIRONMENTAL ENGINEERING
200 PATTON HALL
BLACKSBURG, VA 24061
P: 540-231-6635

PROJECT:
MRF Protected Zone/Low-Cycle Fatigue

SHEET NOTES:

REVISIONS:

NO.	DATE	BY

DESIGNED BY:
DRAWN BY: R. Stevens
CHECKED BY:
DATE: 6/7/2020
PROJECT NO.:

SHEET TITLE:
Bottom Flange Defect Detail Sheet

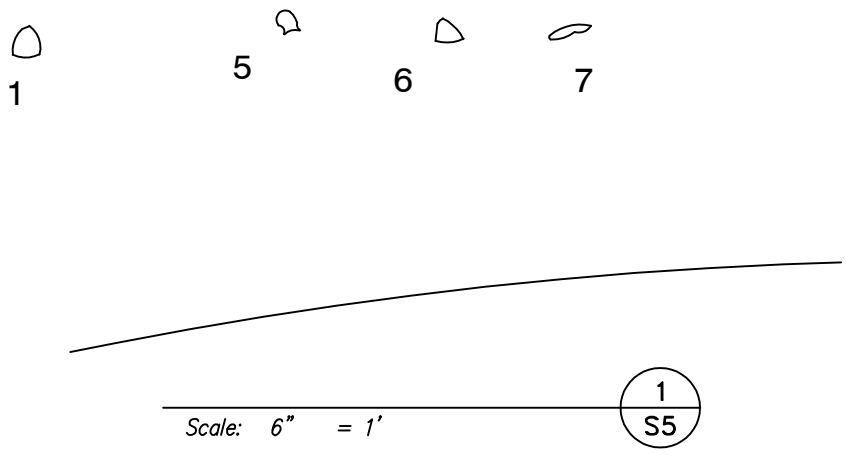

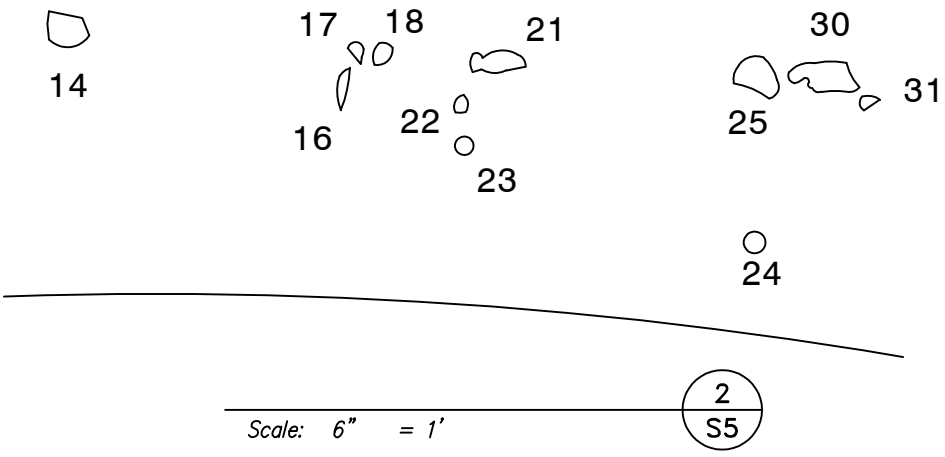

VIRGINIA TECH
CHARLES E. VIA JR. DEPARTMENT OF CIVIL & ENVIRONMENTAL ENGINEERING
200 PATTON HALL
BLACKSBURG, VA 24061
P: 540-231-6635

PROJECT:
MRF Protected Zone/Low-Cycle Fatigue

SHEET NOTES:

REVISIONS:

NO.	DATE	BY

DESIGNED BY:
DRAWN BY: R. Stevens
CHECKED BY:
DATE: 6/7/2020
PROJECT NO.:

SHEET TITLE:
Bottom Flange Defect Detail Sheet

Appendix T. Mill Certificates

This appendix includes mill certificates for the beams used in the full-scale tests and the bar stock used in the small-scale tests. Both W24×62 full-scale specimens were fabricated from heat no. 485104, while the flange material for the small-scale tests was cut from heat no. 485101.

Invoice No.	931746
Bill of Lading	360829
Customer No.	3094
Customer P.O	HOLD TOM

NUCOR-YAMATO STEEL CO.

P.O. BOX 1228: BLYTHEVILLE, AR 72316

CERTIFIED MILL TEST REPORT

100% Melted and Manufactured in U.S.A

All Shapes produced by Nucor-Yamato Steel are cast and rolled to a fully killed and fine grain practice

Date 2018-12-27

SOLD TO
AISC
130 E RANDOLPH ST STE 2000
CHICAGO IL 60601-2001
USA

SHIP TO
CIVES STEEL COMPANY VA
540-667-3480
210 CIVES LN
WINCHESTER VA 22604-1978
USA

ASTM A992/A992M-11 A572/A572M GR50-15
ASTM A709/A709M-15 GR50 (345)
ASTM A709/A709M-15 GR50S (345S)
CSA G40.21-13 50WM (345WM)
ASTM A6/A6M-14

Item	# Item Description	QTY	Heat#	Mechanical Properties								Chemical Properties														
				Yield to Tensile Ratio	Yield Strength	Tensile Strength	ELONG	Charpy Impact				C	Mn	P	S	Si	Cu	Ni	Cr	Mo	V	Cb	CE	Sn	Pcm	CI
								Temp	Impact Energy		Loc															
					KSI	KSI	%	° F	ft• lbf																	
					MPa	MPa	%	° C	J																	
1	W14X398.0 25 ft 0 in W360X592 (7.62 m)	1	499493	0.77 0.78	54 55 375 377	70 70 484 484	31 30					.06	1.47	.013	.020	.27	.33	.12	.16	.04	.06	.005	.39	.01	.18	
2	W24X062.0 46 ft 0 in W610X92 (14.02 m)	1	485101	0.74 0.74	51 51 348 353	68 69 471 478	22 26					.07	1.14	.014	.030	.25	.27	.11	.13	.03	.04	.001	.33	.01	.17	
3	W24X062.0 46 ft 0 in W610X92 (14.02 m)	1	485104	0.75 0.75	54 54 374 370	72 72 496 495	25 25					.07	1.15	.012	.029	.26	.25	.08	.09	.03	.04	.002	.31	.01	.16	
4	W36X150.0 46 ft 0 in W920X223 (14.02 m)	1	496451	0.77 0.77	56 55 389 381	73 72 507 497	27 26					.07	1.30	.018	.025	.24	.26	.10	.15	.03	.04	.001	.36	.01	.17	

ELONGATION BASED ON 8.00 INCH GAUGE LENGTH

Pcm= C+Si/30+Mn/20+Cu/20+Ni/60+Cr/20+Mo/15+V/10+5B(B=Approx .0005)

Corrosion Index= 26.01(%Cu)+3.88(%Ni)+1.2(%Cr)+1.49(%Si)+17.28(%P)-7.29(%Cu)(%Ni)-9.10(%Ni)(%P)-33.39(%Cu)^2

ISO 9001:2015 certified (Registration # 0985-07).

Meets mechanical lab independence requirements of EN10204 type 3.1.

The Charpy machine striker geometry used by Nucor-Yamato Steel is the 8 mm (0.315")striker (KV_8) per ASTM A370 Section 22.1.2 and ISO 148-1 Section 7.3.

CARBON EQUIVALENT CE= C+Mn/6+(Cr+Mo+V)/5+(Ni+Cu)/15

Mercury has not been used in the direct manufacturing of this material

This material was produced in accordance with the Nucor-Yamato Steel Quality Manual.

I hereby certify that the contents of this report are accurate and correct. All test results and operations performed by this material manufacturer are in compliance with the requirements of the material specifications, and when designated by the purchaser, meet the applicable specifications.

Chief Metallurgist

State of Arkansas
County of Mississippi
Sworn to and subscribed before me

on 2018-12-27
My commission expires on 07/17/2023

DEBORAH ANN RHODES
Commission # 12394533
NOTARY PUBLIC
My Commission Expires 7-17-2023
STATE OF ARKANSAS–MISSISSIPPI COUNTY

Customer Name CONCENTRIC STEEL
Customer PO# 1776 19.444
Shipper No 1511585
Heat Number 63190859

CERTIFIED MATERIAL TEST REPORT

GERDAU

US-ML-JACKSON TN
801 GERDAU AMERISTEEL ROAD
JACKSON, TN 38305
USA

CUSTOMER SHIP TO	CUSTOMER BILL TO
INFRA METALS CO 1 STURGILLS WAY NEW BOSTON,OH 45662 USA	INFRA METALS CO 1 STURGILLS WAY NEW BOSTON,OH 45662 USA

GRADE	SHAPE / SIZE	DOCUMENT ID:
GGMULTI	Flat Bar / 1 X 5	0000219369

LENGTH	WEIGHT	HEAT / BATCH
20'00"	4,760 LB	**63190859**/03

SALES ORDER	CUSTOMER MATERIAL N°
7764281/000020	

SPECIFICATION / DATE or REVISION
ASTM A529-14, A572-15
ASTM A6-17,A36-14, ASME SA-36
ASTM A709-17, AASHTO M270-15
CSA G40.20-13/G40.21-13

CUSTOMER PURCHASE ORDER NUMBER	BILL OF LADING	DATE
OH-572951	1333-0000128816	05/22/2019

CHEMICAL COMPOSITION

C %	Mn %	P %	S %	Si %	Cu %	Ni %	Cr %	Mo %	V %	Nb %	Al %	CEqvA529 %
0.16	0.78	0.011	0.047	0.23	0.28	0.12	0.10	0.037	0.022	0.001	0.000	0.39

CHEMICAL COMPOSITION

Sn %
0.014

MECHANICAL PROPERTIES

Elong. %	G/L Inch	G/L mm	UTS PSI	UTS MPa	YS PSI
27.00	8.000	200.0	72215	498	50198
29.00	8.000	200.0	71415	492	50088

MECHANICAL PROPERTIES

YS MPa
346
345

GEOMETRIC CHARACTERISTICS

R:R
6.95

COMMENTS / NOTES

This grade meets the requirements for the following grades:
ASTM Grades: A36; A529-50; A572-50; A709-36; A709-50
CSA Grades: 44W; 50W
AASHTO Grades: M270-36; M270-50
ASME Grades: SA36

The above figures are certified chemical and physical test records as contained in the permanent records of company. We certify that these data are correct and in compliance with specified requirements. This material, including the billets, was melted and manufactured in the USA. CMTR complies with EN 10204 3.1.

BHASKAR YALAMANCHILI
QUALITY DIRECTOR
Phone: (409) 267-1071 Email: Bhaskar.Yalamanchili@gerdau.com

BEN LOVELL
QUALITY ASSURANCE MGR.
Phone: (731) 423-5213 Email: benjamin.lovell@gerdau.com

Customer Name	Customer PO#	Shipper No	Heat Number
CONCENTRIC STEEL	1776	1511585	DL19101503

NUCOR
NUCOR CORPORATION
NUCOR STEEL SOUTH CAROLINA

Mill Certification
4/13/2019

MTR #: C1-465148
300 Steel Mill Road
DARLINGTON, SC 29540
(843) 393-5841
Fax: (843) 395-8701

Sold To: INFRA METALS CO
1 STURGILLS WAY
NEW BOSTON, OH 45662
(203) 294-2980
Fax: (740) 351-1770

Ship To: INFRA METALS CO
1 STURGILLS WAY
NEW BOSTON, OH 45662
(877) 741-8806
Fax: (740) 351-1770

Customer P.O.	OH-570657	Sales Order	310451.40
Product Group	Merchant Bar Quality	Part Number	53A0050024010W0
Grade	NUCOR MULTIGRADE	Lot #	DL1910150302
Size	1x5" Flat	Heat #	DL19101503
Product	1x5" Flat 20' NUCOR MULTIGRADE	B.L. Number	C1-783290
Description	NUCOR MULTIGRADE	Load Number	C1-465148
Customer Spec		Customer Part #	

I hereby certify that the material described herein has been manufactured in accordance with the specifications and standards listed above and that it satisfies those requirements.

Roll Date: 3/13/2019 **Melt Date: 3/9/2019** **Qty Shipped LBS: 4,763** **Qty Shipped Pcs: 14**

Melt Date: 3/9/2019

C	Mn	P	S	Si	Cu	Ni	Cr	Mo	V	Cb	Sn
0.12%	0.82%	0.005%	0.021%	0.18%	0.48%	0.19%	0.18%	0.022%	0.0050%	0.027%	0.009%

Ti	CE4020	CEA529
0.002%	0.34%	0.38%

CE4020: C. E. CSA G4020, AASHTO M270
CEA529: A529 CARBON EQUIVALENT

Roll Date: 3/13/2019

Yield 1: 58,000psi	Tensile 1: 75,000psi	Elongation: 31% in 8"(% in 203.3mm)
Yield 2: 57,000psi	Tensile 2: 75,000psi	Elongation 29% in 8"(% in 203.3mm)

Specification Comments: NUCOR MULTIGRADE MEETS THE REQUIREMENTS OF: ASTM A36/A36M-08, A529/529M-05(2009) GR50(345), A572/572M-07 GR50(345), A709/709M-10 GR36(250) & GR50(345), CSA G40.21-04 GR44W(300W) & GR50W(350W) AASHTO M270/M270M-10 GR36(270) & GR50(345), ASME SA36/SA36M-07, QQ-S-741D PRODUCED TO A FULLY KILLED, FINE GRAIN PRACTICE

1. WELDING OR WELD REPAIR WAS NOT PERFORMED ON THIS MATERIAL
2. MELTED AND MANUFACTURED IN THE USA
3. MERCURY, RADIUM, OR ALPHA SOURCE MATERIALS IN ANY FORM HAVE NOT BEEN USED IN THE PRODUCTION OF THIS MATERIAL

James H. Blew
Division Metallurgist

NUCOR
NUCOR CORPORATION
NUCOR STEEL SOUTH CAROLINA

Mill Certification
5/15/2019

MTR #: C1-468147
300 Steel Mill Road
DARLINGTON, SC 29540
(843) 393-5841
Fax: (843) 395-8701

Sold To: INFRA METALS CO
1 STURGILLS WAY
NEW BOSTON, OH 45662
(203) 294-2980
Fax: (740) 351-1770

Ship To: INFRA METALS CO
1 STURGILLS WAY
NEW BOSTON, OH 45662
(877) 741-8806
Fax: (740) 351-1770

Customer P.O.	OH-573163	Sales Order	313483.3
Product Group	Merchant Bar Quality	Part Number	5350030024010W0
Grade	NUCOR MULTIGRADE	Lot #	DL1910226501
Size	1/2x3" Flat	Heat #	DL19102265
Product	1/2x3" Flat 20' NUCOR MULTIGRADE	B.L. Number	C1-785990
Description	NUCOR MULTIGRADE	Load Number	C1-468147
Customer Spec		Customer Part #	

I hereby certify that the material described herein has been manufactured in accordance with the specifications and standards listed above and that it satisfies those requirements.

Roll Date: 4/16/2019 **Melt Date: 4/11/2019** **Qty Shipped LBS: 4,899** **Qty Shipped Pcs: 48**

Melt Date: 4/11/2019

C	Mn	P	S	Si	Cu	Ni	Cr	Mo	V	Cb	Sn
0.12%	0.95%	0.010%	0.021%	0.20%	0.21%	0.08%	0.17%	0.016%	0.0040%	0.024%	0.008%

Ti	CE4020	CEA529
0.001%	0.34%	0.37%

CE4020: C. E. CSA G4020, AASHTO M270
CEA529: A529 CARBON EQUIVALENT

Roll Date: 4/16/2019

Yield 1: 57,000psi	Tensile 1: 76,000psi	Elongation: 28% in 8"(% in 203.3mm)
Yield 2: 58,000psi	Tensile 2: 76,000psi	Elongation 29% in 8"(% in 203.3mm)

Specification Comments: NUCOR MULTIGRADE MEETS THE REQUIREMENTS OF: ASTM A36/A36M-14, A529/529M-05(2009) GR50(345), A572/572M-13A GR50(345), A709/709M-13A GR36(250) & GR50(345), CSA G40.21-04 GR44W(300W) & GR50W(350W) AASHTO M270/M270M-10 GR36(270) & GR50(345), ASME SA36/SA36M-07, QQ-S-741D PRODUCED TO A FULLY KILLED, FINE GRAIN PRACTICE

1. WELDING OR WELD REPAIR WAS NOT PERFORMED ON THIS MATERIAL
2. MELTED AND MANUFACTURED IN THE USA
3. MERCURY, RADIUM, OR ALPHA SOURCE MATERIALS IN ANY FORM HAVE NOT BEEN USED IN THE PRODUCTION OF THIS MATERIAL

James H. Blew
Division Metallurgist

Appendix U. Charpy V-Notch Test Reports

This appendix includes test reports for the Charpy V-notch tests done to characterize the notch toughness of the beam flange material and bar stock.

CHICAGO SPECTRO SERVICE LABORATORY, INC.

Spectrographic and Chemical Analysts
Metallurgists

ACCREDITED
#0781-01

6245 S. OAK PARK AVE · CHICAGO, IL 60638-4015
TELEPHONE: 773-229-0099 · FAX: 773-229-0313
EMAIL: office@chicagospectro.com · WEB: chicagospectro.com

ANALYSIS REPORT FOR:

Virginia Tech
Attention: Ryan Stevens
200 Patton Hall
Blacksburg, VA 24061

Date 08/18/2020
PO #

Report/Lab Number 200814K003

SUBJECT: Sample Received on 08/14/2020

CHARPY V-NOTCH IMPACT TEST @Charpy Temperature 70°F

SPECIMEN SIZE: 0.394" x 0.394"

	ENERGY ABSORBED(FT·LBS)
1.)	86
2.)	40
3.)	34
Average	53

%SHEAR: 75, 35, 40%

LATERAL EXPANSION: 84, 48, 43 mils

TEST METHOD: ASTM E23

CHICAGO SPECTRO SERVICE LABORATORY, Inc.
BY Michael Landon

CHICAGO SPECTRO SERVICE LABORATORY, INC.

Spectrographic and Chemical Analysts
Metallurgists

ACCREDITED
#0781-01

6245 S. OAK PARK AVE · CHICAGO, IL 60638-4015
TELEPHONE: 773-229-0099 · FAX: 773-229-0313
EMAIL: office@chicagospectro.com · WEB: chicagospectro.com

ANALYSIS REPORT FOR:

Virginia Tech
Attention: Ryan Stevens
200 Patton Hall
Blacksburg, VA 24061

Date 08/18/2020
PO #

Report/Lab Number 200814K004

SUBJECT: Sample Labeled 2, Received on 08/14/2020

CHARPY V-NOTCH IMPACT TEST @Charpy Temperature 70°F

SPECIMEN SIZE: 0.394" x 0.394"

ENERGY ABSORBED(FT·LBS)

1.) 234
2.) 206
3.) 200
Average 213

%SHEAR: 100 H, 100 H, 100 H%

LATERAL EXPANSION: 87, 92, 97 mils

TEST METHOD: ASTM E23

CHICAGO SPECTRO SERVICE LABORATORY, Inc.
BY Michael Landon

CHICAGO SPECTRO SERVICE LABORATORY, INC.

Spectrographic and Chemical Analysts
Metallurgists

ACCREDITED
#0781-01

6245 S. OAK PARK AVE · CHICAGO, IL 60638-4015
TELEPHONE: 773-229-0099 · FAX: 773-229-0313
EMAIL: office@chicagospectro.com · WEB: chicagospectro.com

ANALYSIS REPORT FOR:

Virginia Tech
Attention: Ryan Stevens
200 Patton Hall
Blacksburg, VA 24061

Date 08/18/2020
PO #

Report/Lab Number 200814K005

SUBJECT: Sample Labeled 3, Received on 08/14/2020

CHARPY V-NOTCH IMPACT TEST @Charpy Temperature 70°F

SPECIMEN SIZE: 0.394" x 0.394"

ENERGY ABSORBED(FT·LBS)

1.) 104
2.) 113
3.) 119
Average 112

%SHEAR: 70, 85, 90%

LATERAL EXPANSION: 90, 84, 96 mils

TEST METHOD: ASTM E23

CHICAGO SPECTRO SERVICE LABORATORY, Inc.
BY Michael Landon

CHICAGO SPECTRO SERVICE LABORATORY, INC.

Spectrographic and Chemical Analysts
Metallurgists

ACCREDITED
#0781-01

6245 S. OAK PARK AVE · CHICAGO, IL 60638-4015
TELEPHONE: 773-229-0099 · FAX: 773-229-0313
EMAIL: office@chicagospectro.com · WEB: chicagospectro.com

ANALYSIS REPORT FOR:

Virginia Tech
Attention: Ryan Stevens
200 Patton Hall
Blacksburg, VA 24061

Date 08/18/2020
PO #

Report/Lab Number 200814K006

SUBJECT: Sample Labeled 4, Received on 08/14/2020

CHARPY V-NOTCH IMPACT TEST @Charpy Temperature 70°F

SPECIMEN SIZE: 0.394" x 0.394"

	ENERGY ABSORBED(FT·LBS)
1.)	59
2.)	68
3.)	35
Average	54

%SHEAR: 35, 45, 25%

LATERAL EXPANSION: 60, 70, 41 mils

TEST METHOD: ASTM E23

CHICAGO SPECTRO SERVICE LABORATORY, Inc.
BY Michael Landon

Appendix V. Small-Scale Bend Test Fractures

This appendix describes the behavior of each small-scale bend test with regards to fracture initiation and propagation. The discussion is first grouped by artifact type and then ordered by the coupon thickness.

V.1 0.125 in. Notches Repaired by Grinding

V.1.1 W24-0.125NGT-T50-R11.01

Fracture initiation occurred in the eleventh cycle, at the edge of the notch. Complete fracture occurred in the eighteenth cycle, when the bottom was in tension. Fracture initiation is shown in Figure V.1 and the fracture surfaces of both halves are shown in Figure V.2.

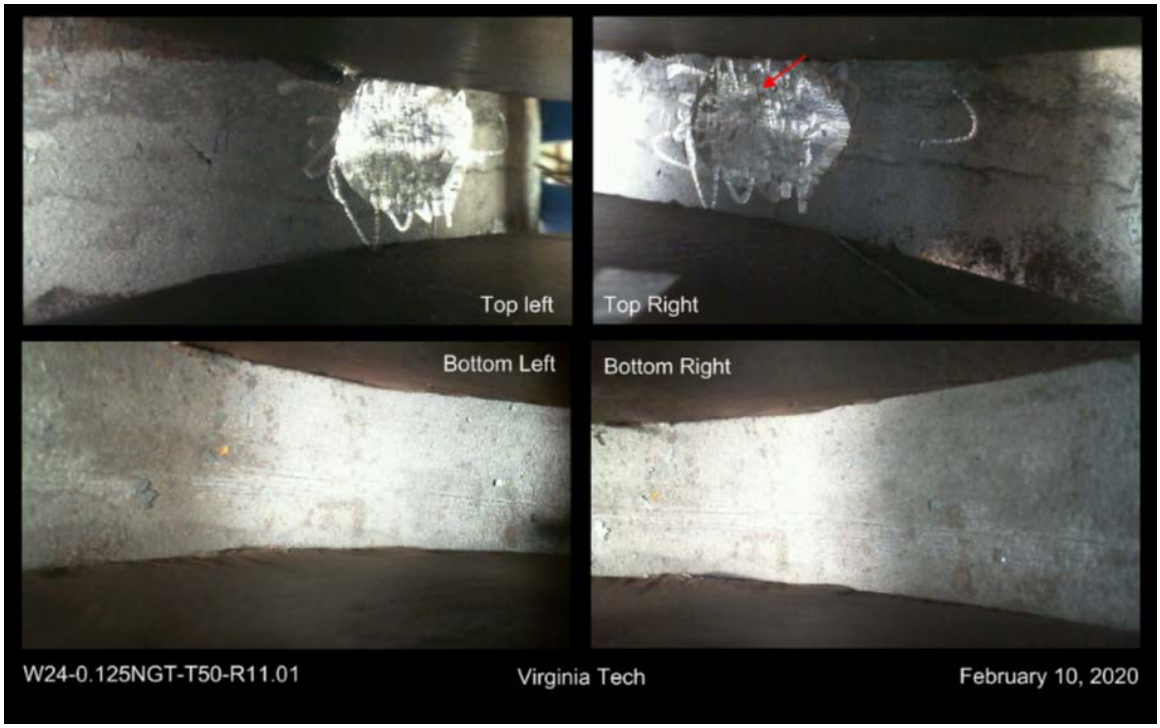

Figure V.1. Fracture initiation of W24-0.125NGT-T50-R11.01.

Figure V.2. Fracture surfaces of W24-0.125NGT-T50-R11.01.

V.1.2 W24-0.125NGT-T50-R11.02

Fracture initiation occurred in the eleventh cycle, at the edge and within the notch. Complete fracture occurred in the seventeenth cycle while the bottom was in tension. Fracture initiation is shown in Figure V.3 and the fracture surfaces of both halves are shown in Figure V.4.

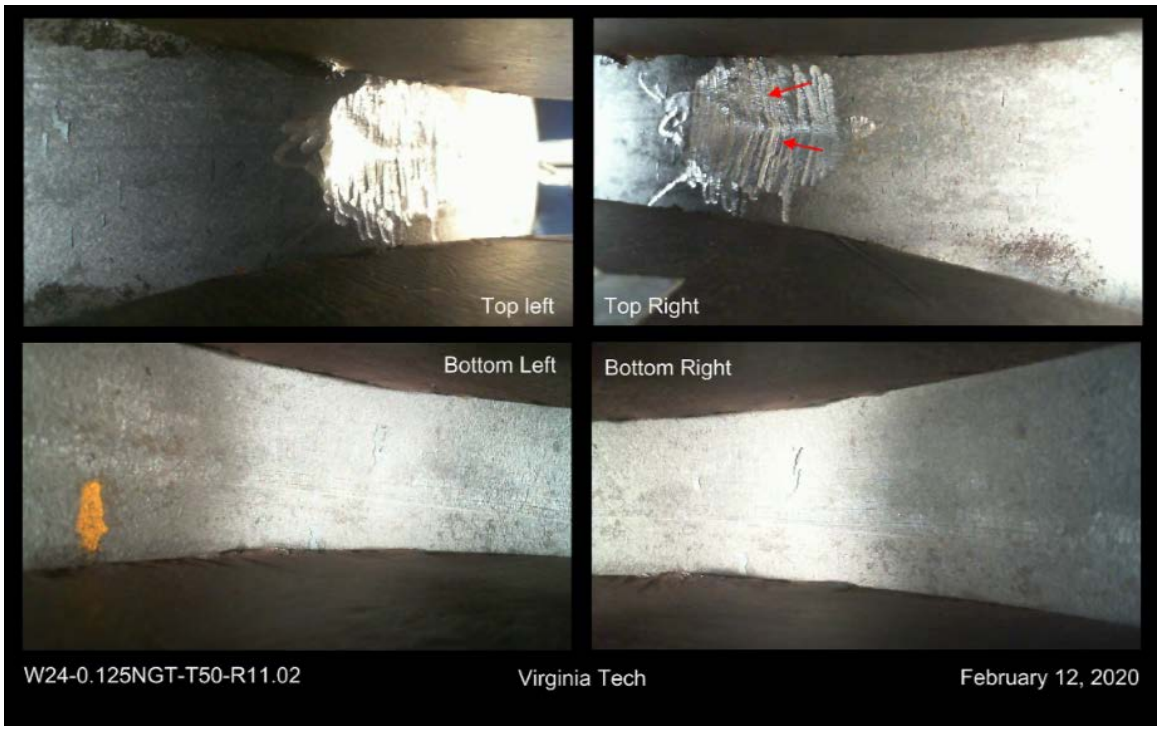

Figure V.3. Fracture initiation of W24-0.125NGT-T50-R11.02.

Figure V.4. Fracture surfaces of W24-0.125NGT-T50-R11.02.

V.1.3 W24-0.125NGT-T59-R11.01

Fracture initiation occurred in the eighth cycle at the edge of the notch. Complete fracture occurred in the twelfth cycle while the top was in tension. Fracture initiation is shown in Figure V.5 and the fracture surfaces of both halves are shown in Figure V.6.

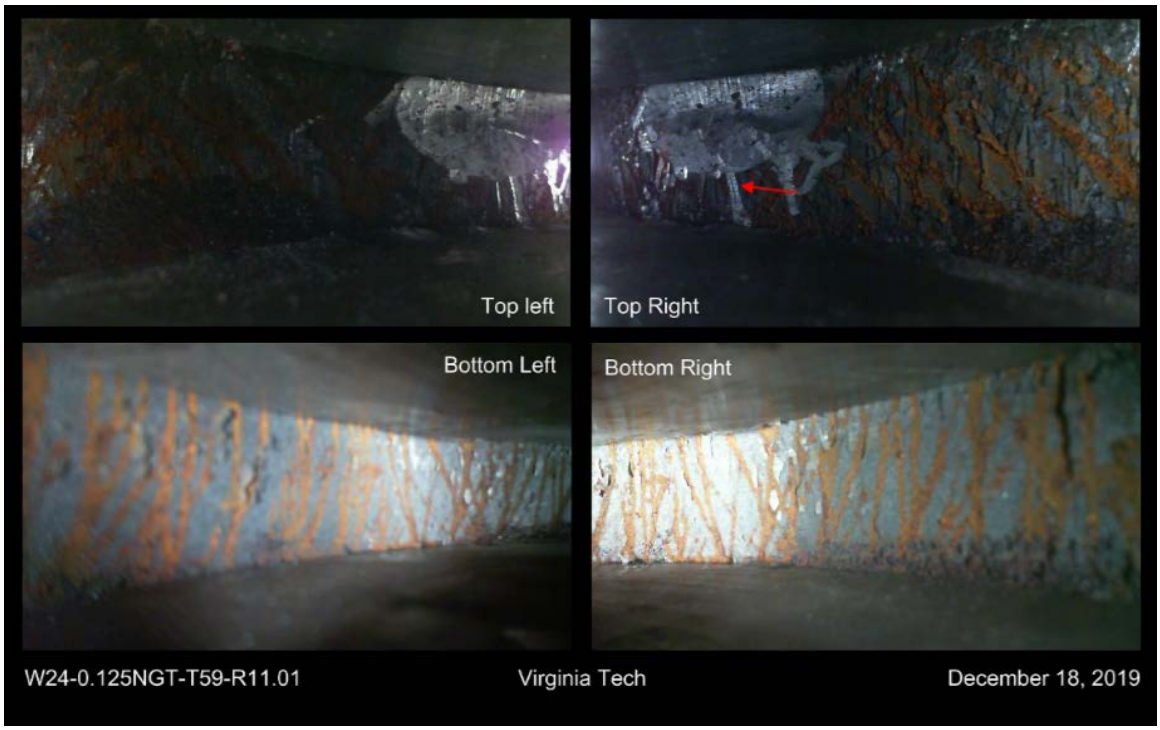

Figure V.5. Fracture initiation of W24-0.125NGT-T59-R11.01.

Figure V.6. Fracture surfaces of W24-0.125NGT-T59-R11.01.

V.1.4 W24-0.125NGT-T59-R11.02

Fracture initiation occurred in the seventh cycle at the edge of the notch. Complete fracture occurred in the eleventh cycle while the top was in tension. Fracture initiation is shown in Figure V.7 and the fracture surfaces of both halves are shown in Figure V.8.

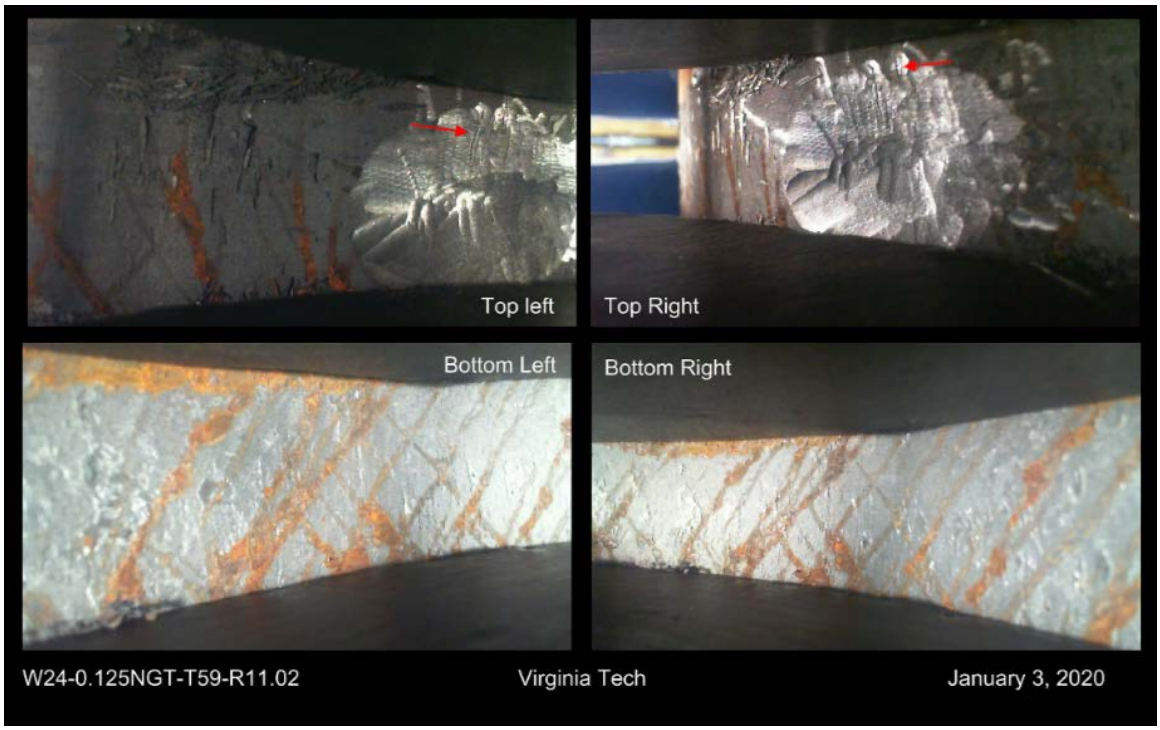

Figure V.7. Fracture initiation of W24-0.125NGT-T59-R11.02.

Figure V.8. Fracture surfaces of W24-0.125NGT-T59-R11.02.

V.1.5 W36-0.125NGT-T94-R11.01

Fracture initiation occurred in the notch in the fourth cycle. Complete fracture occurred in the sixth cycle while the top was in tension. Fracture initiation is shown in Figure V.9 and the fracture surfaces of both halves are shown in Figure V.10.

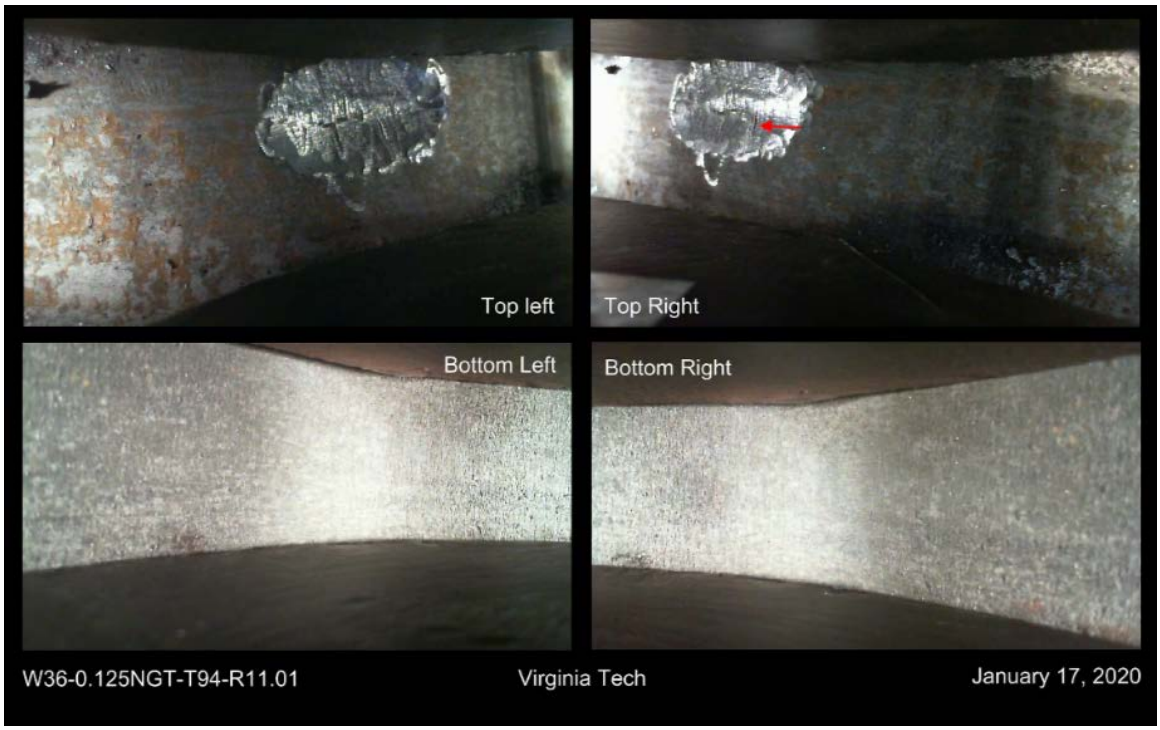

Figure V.9. Fracture initiation of W36-0.125NGT-T94-R11.01.

Figure V.10. Fracture surfaces of W36-0.125NGT-T94-R11.01.

V.1.6 W36-0.125NGT-T94-R11.02

Fracture initiation occurred in the notch in the fourth cycle. Complete fracture occurred in the sixth cycle when the bottom was in tension. Fracture initiation is shown in Figure V.11 and the fracture surfaces of both halves are shown in Figure V.12.

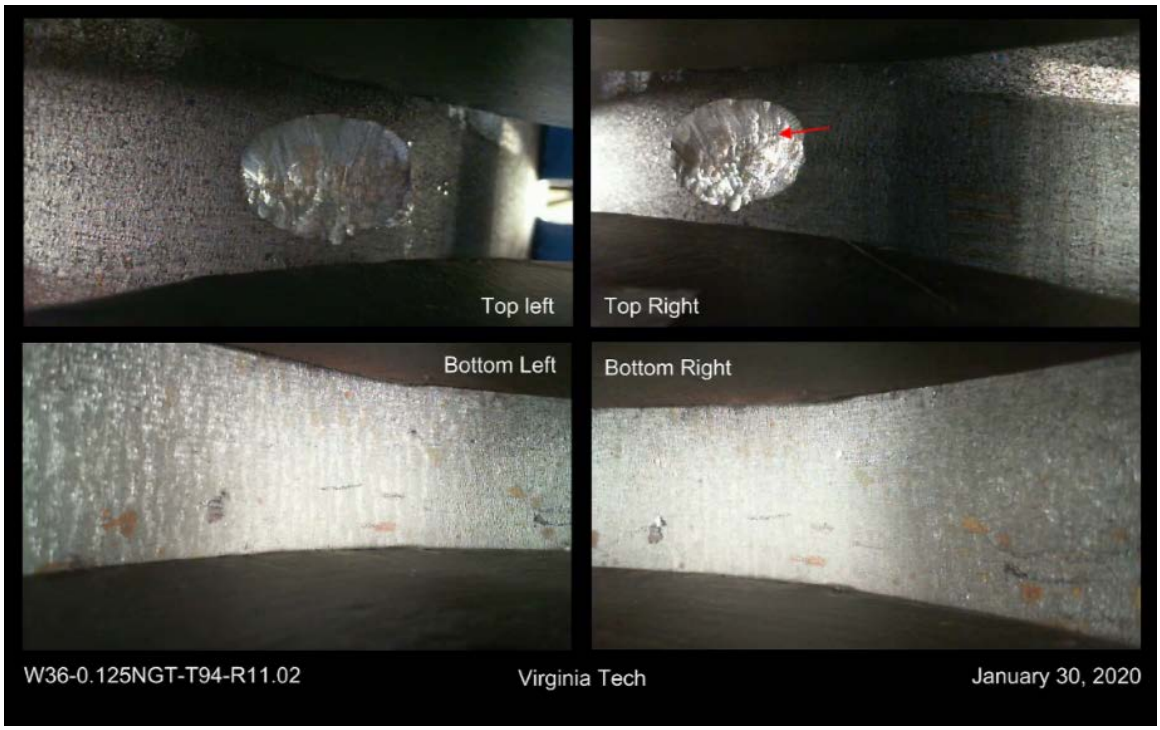

Figure V.11. Fracture initiation of W36-0.125NGT-T94-R11.02.

Figure V.12. Fracture surfaces of W36-0.125NGT-T94-R11.02.

V.1.7 W36-0.125NGT-T100-R11.01

Fracture initiation occurred in the notch in the third cycle. Complete fracture occurred in the fifth cycle while the top was in tension. Fracture initiation is shown in Figure V.13 and the fracture surfaces of both halves are shown in Figure V.14.

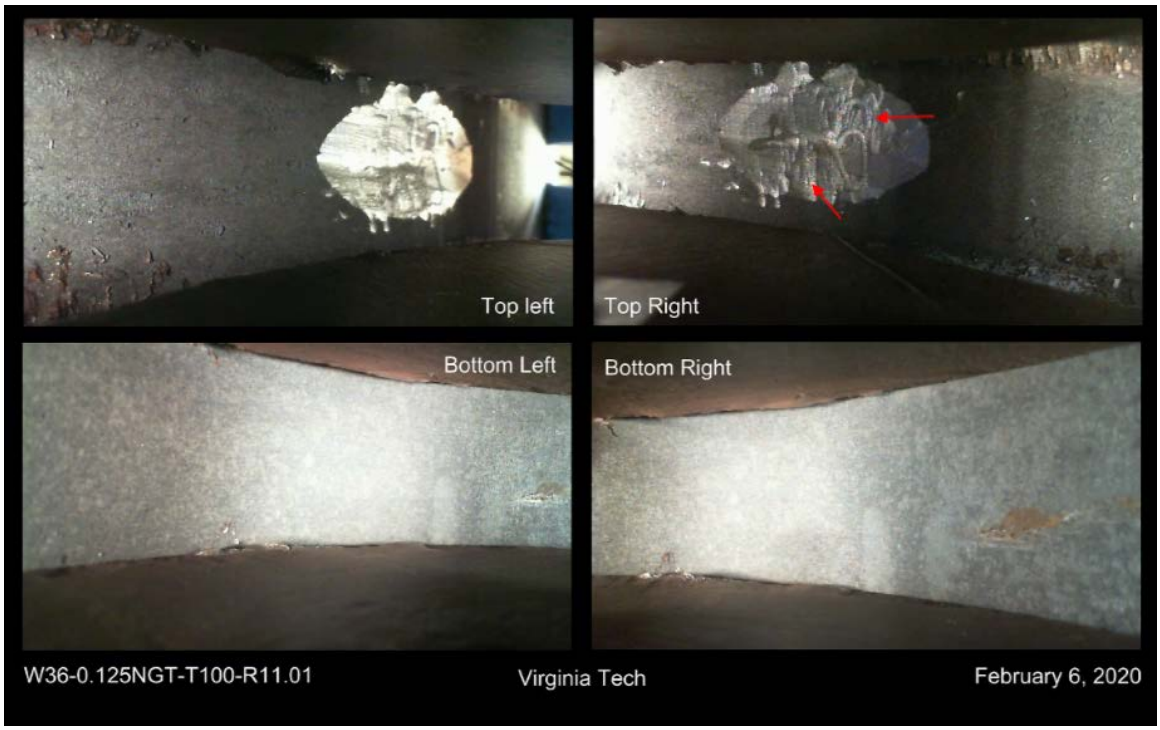

Figure V.13. Fracture initiation of W36-0.125NGT-T100-R11.01.

Figure V.14. Fracture surfaces of W36-0.125NGT-T100-R11.01.

V.1.8 W36-0.125NGT-T100-R11.02

Fracture initiation occurred in the notch in the second cycle. Complete fracture occurred in the fourth cycle while the bottom was in tension. Fracture initiation is shown in Figure V.15 and the fracture surfaces of both halves are shown in Figure V.16.

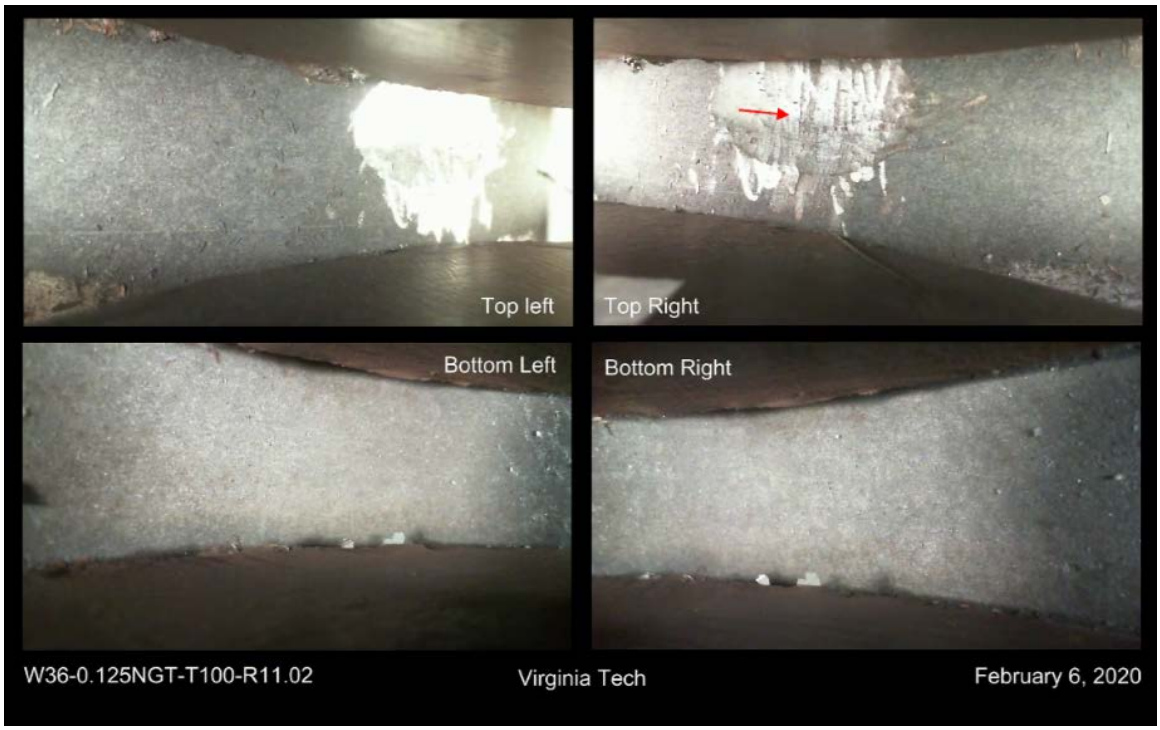

Figure V.15. Fracture initiation of W36-0.125NGT-T100-R11.02.

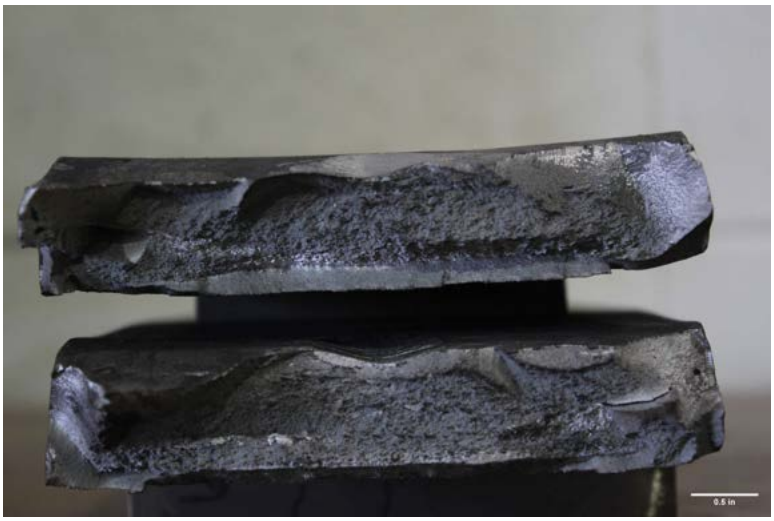

Figure V.16. Fracture surfaces of W36-0.125NGT-T100-R11.02.

V.2 0.25 in. Notches Repaired by Welding

V.2.1 W24-0.25NGTW-T50-R11.01

The first visible defect appeared in the second cycle, and the first folded steel defect appeared in the eighth cycle. Complete fracture occurred in the thirty-fifth cycle while the top was in tension. The first folded steel defect is shown in Figure V.17 and the fracture surfaces of both halves are shown in Figure V.18.

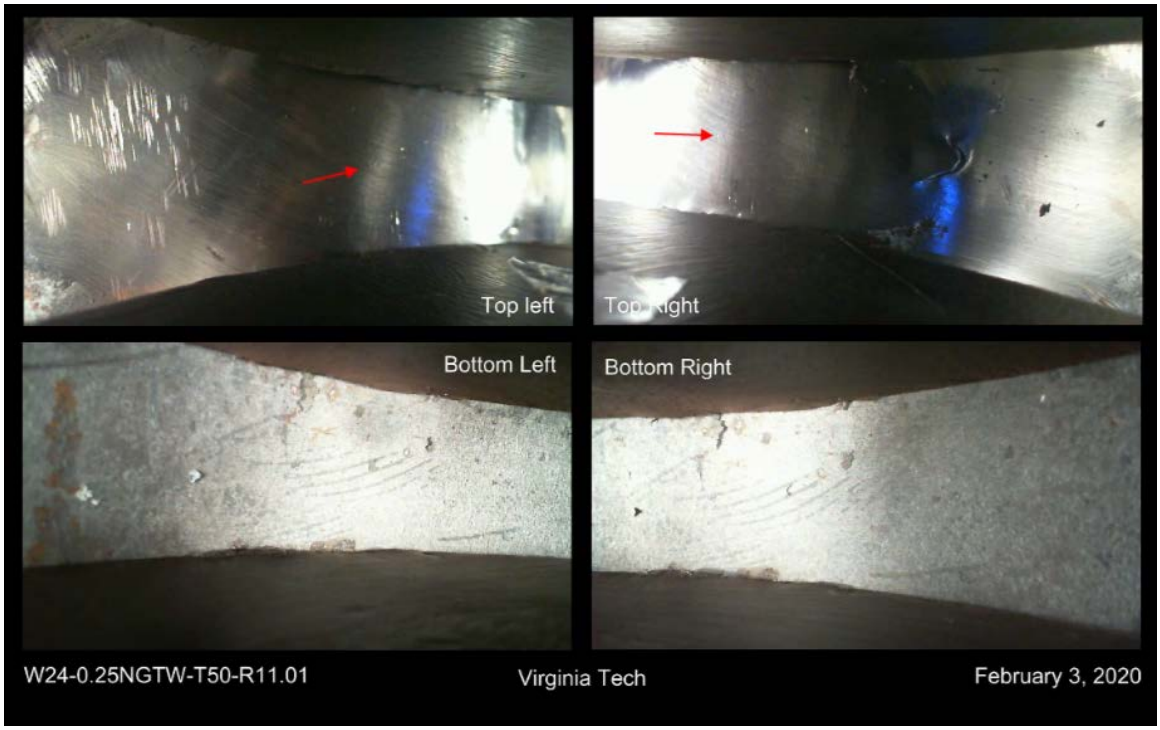

Figure V.17. Fracture initiation of W24-0.25NGTW-T50-R11.01.

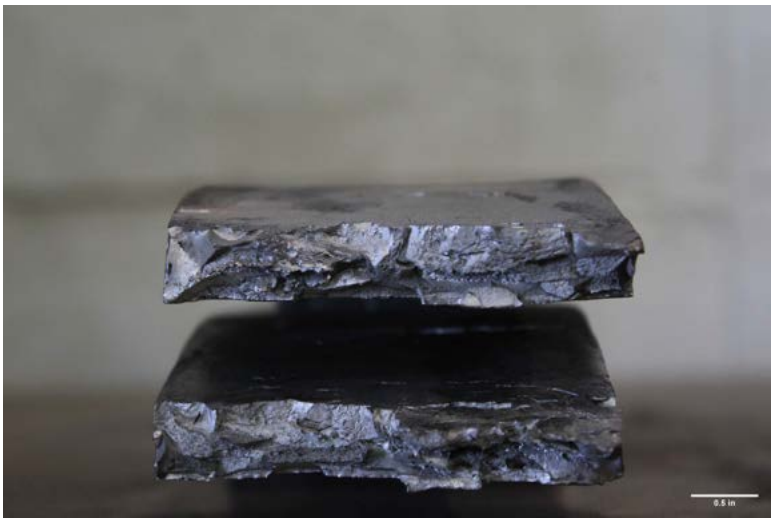

Figure V.18. Fracture surfaces of W24-0.25NGTW-T50-R11.01.

V.2.2 W24-0.25NGTW-T50-R11.02

The first visible defect appeared in the fourth cycle and the first folded steel defect appeared in the seventh cycle. Complete fracture occurred in the thirty-third cycle when the bottom was in tension. The first folded steel defect is shown in Figure V.19 and the fracture surfaces of both halves are shown in Figure V.20.

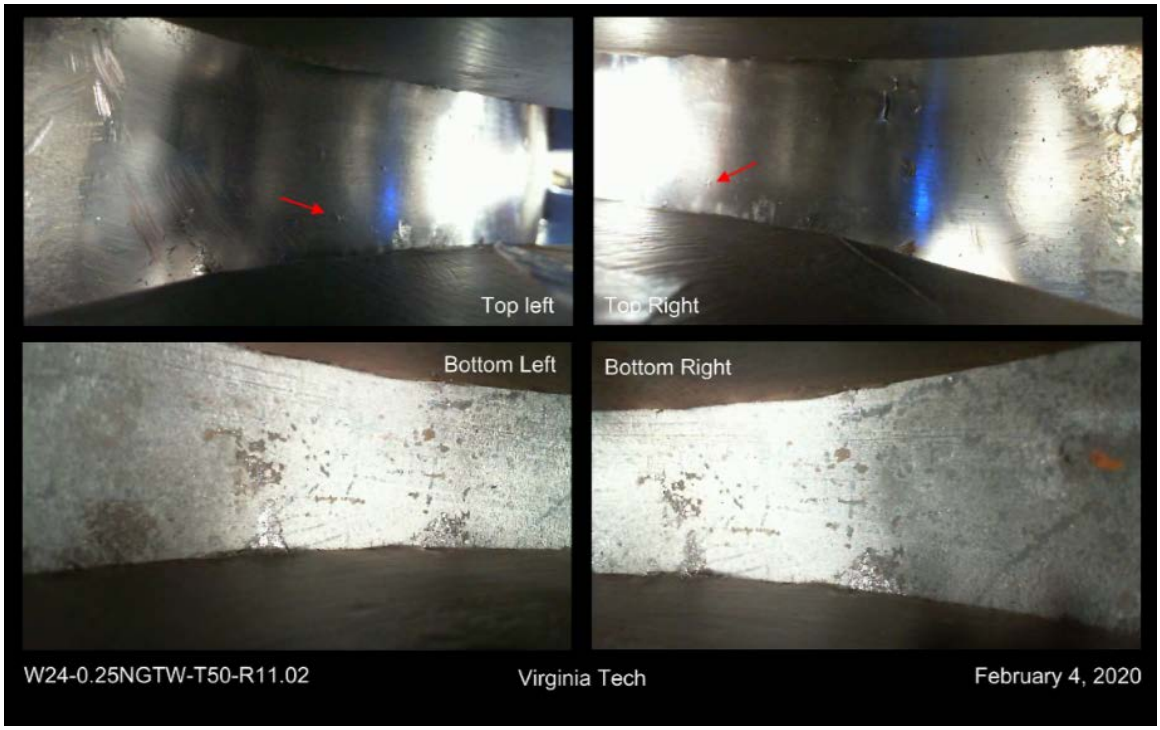

Figure V.19. Fracture initiation of W24-0.25NGTW-T50-R11.02.

Figure V.20. Fracture surfaces of W24-0.25NGTW-T50-R11.02.

V.2.3 W24-0.25NGTW-T59-R11.01

The first visible defect appeared in the second cycle and the first folded steel defect appeared in the fifth cycle. Complete fracture occurred in the thirteenth cycle when the top was in tension. The first folded steel defect is shown in Figure V.21 and the fracture surfaces of both halves are shown in Figure V.22.

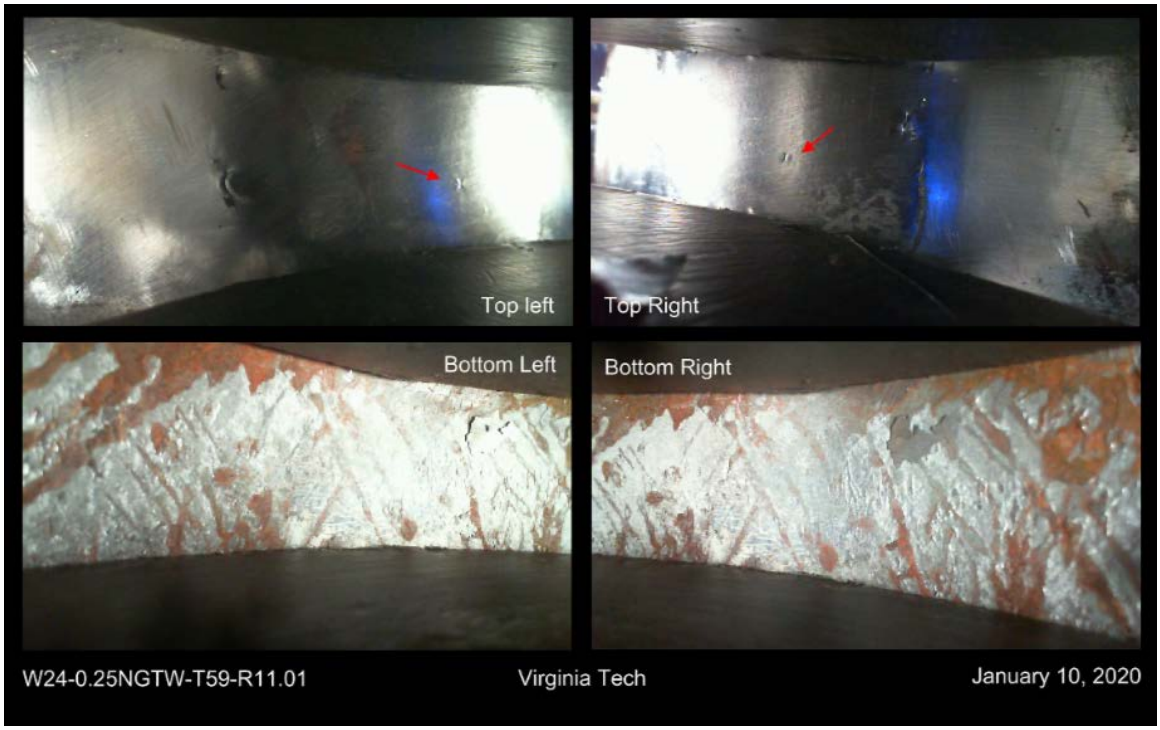

Figure V.21. Fracture initiation of W24-0.25NGTW-T59-R11.01.

Figure V.22. Fracture surfaces of W24-0.25NGTW-T59-R11.01.

V.2.4 W24-0.25NGTW-T59-R11.02

The first visible defect appeared in the first cycle and the first folded steel defect appeared in the sixth cycle. Complete fracture occurred in the thirteenth cycle when the bottom was in tension. The first folded steel defect is shown in Figure V.23 and the fracture surfaces of both halves are shown in Figure V.24.

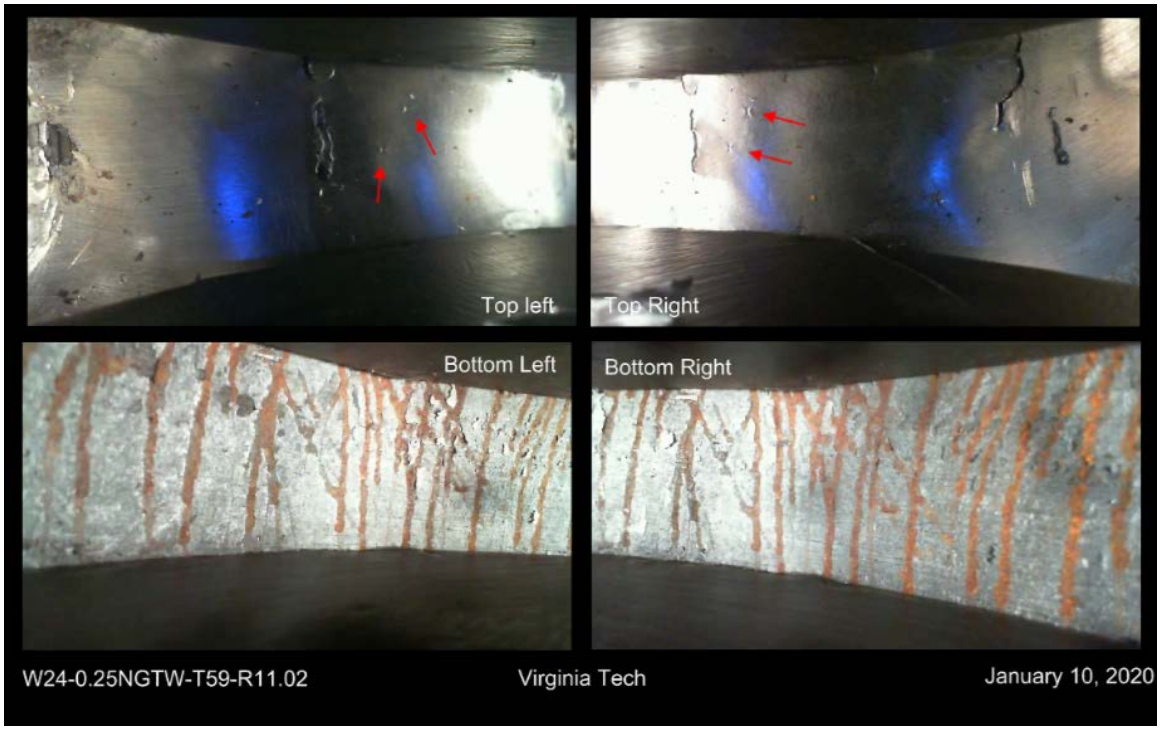

Figure V.23. Fracture initiation of W24-0.25NGTW-T59-R11.02.

Figure V.24. Fracture surfaces of W24-0.25NGTW-T59-R11.02.

V.2.5 W36-0.25NGTW-T94-R11.01

The first visible defect appeared in the second cycle, and there were no visible folded steel defects. Complete fracture occurred in the fifth cycle when the bottom was in tension. The first visible fractures are shown in Figure V.25 and the fracture surfaces of both halves are shown in Figure V.26.

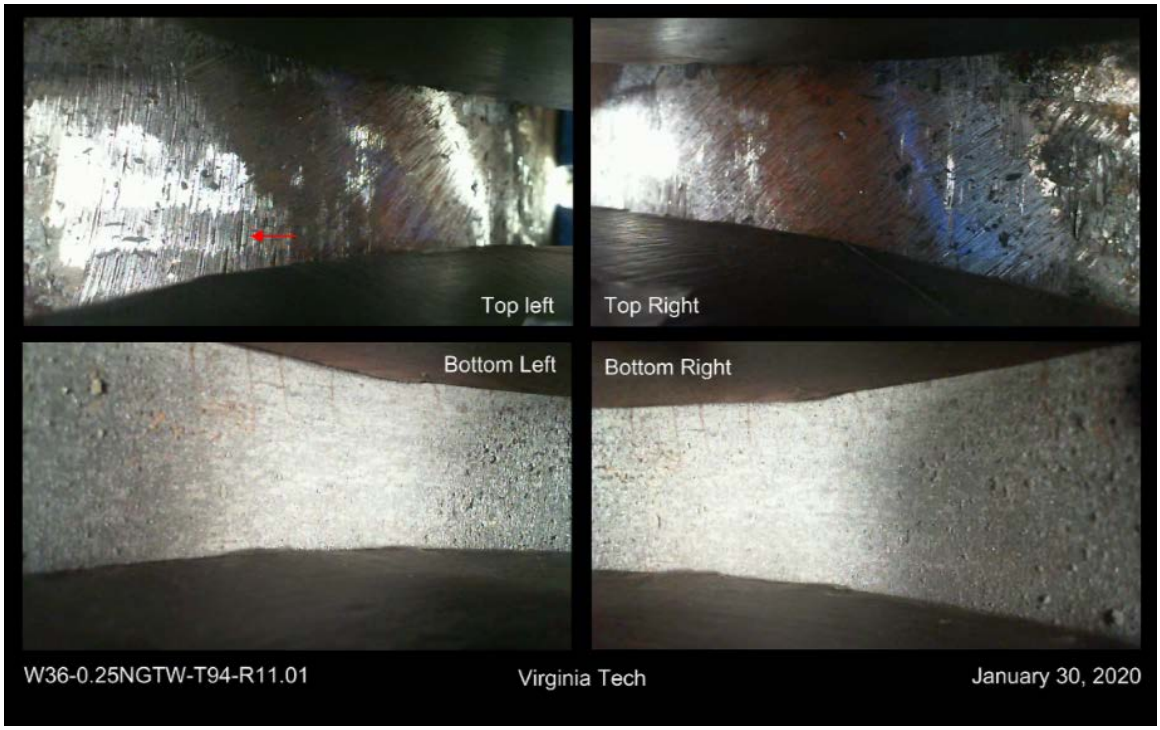

Figure V.25. Fracture initiation of W36-0.25NGTW-T94-R11.01.

Figure V.26. Fracture surfaces of W36-0.25NGTW-T94-R11.01.

V.2.6 W36-0.25NGTW-T94-R11.02

The first visible defect appeared in the first cycle and the first folded steel defect appeared in the third cycle. Complete fracture occurred in the sixth cycle when the top was in tension. The first folded steel defect is shown in Figure V.27 and the fracture surfaces of both halves are shown in Figure V.28.

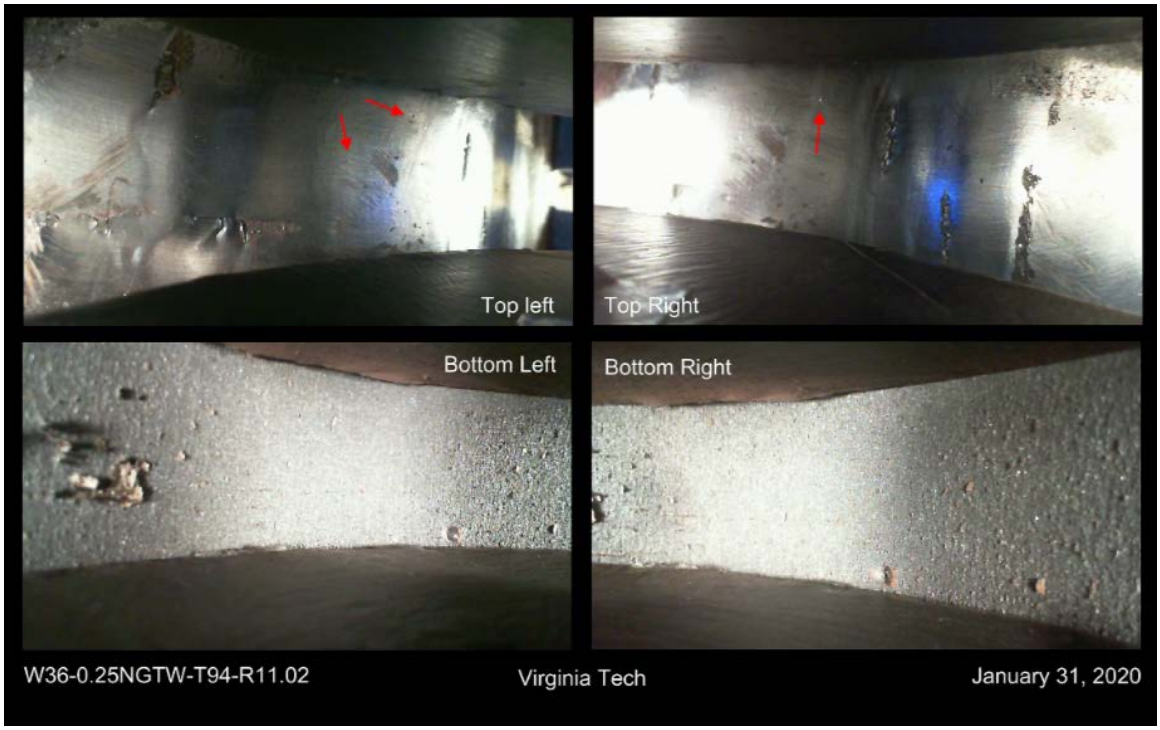

Figure V.27. Fracture initiation of W36-0.25NGTW-T94-R11.02.

Figure V.28. Fracture surfaces of W36-0.25NGTW-T94-R11.02.

V.2.7 W36-0.25NGTW-T100-R11.01

The first folded steel defect appeared in the third cycle, and there were no visible defects prior to this point. Complete fracture occurred in the sixth cycle, when the top was in tension. The first folded steel defect is shown in Figure V.29 and the fracture surfaces of both halves are shown in Figure V.30.

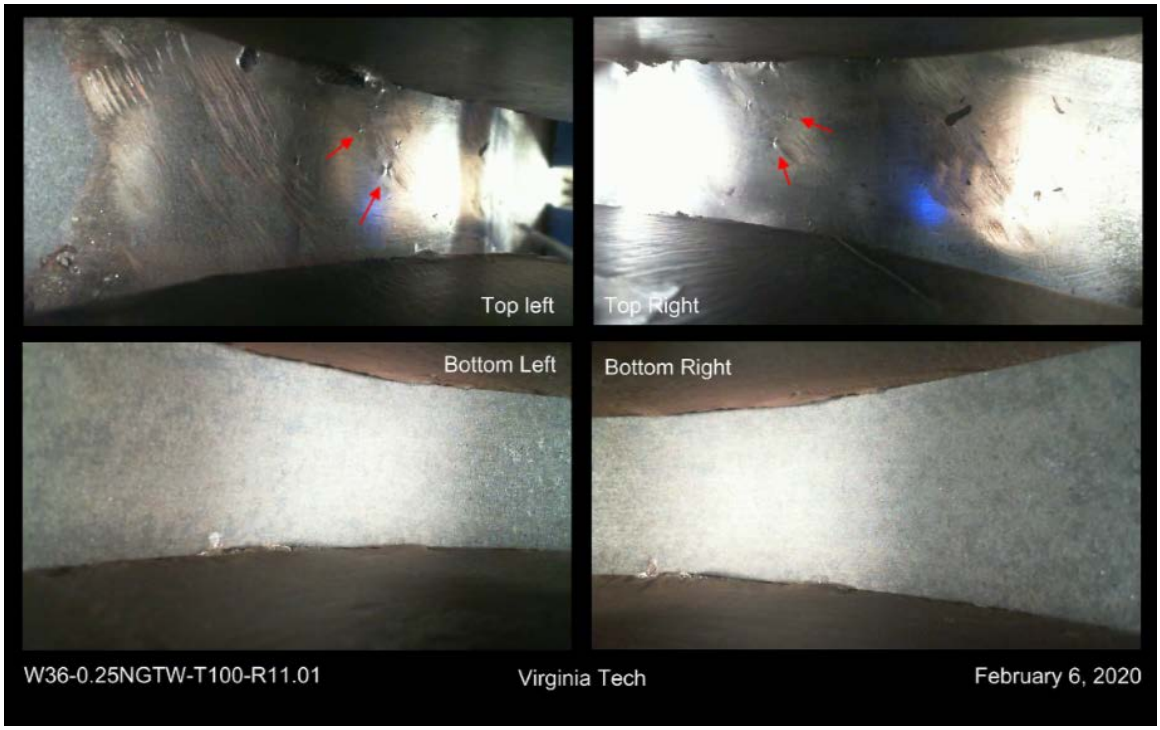

Figure V.29. Fracture initiation of W36-0.25NGTW-T100-R11.01.

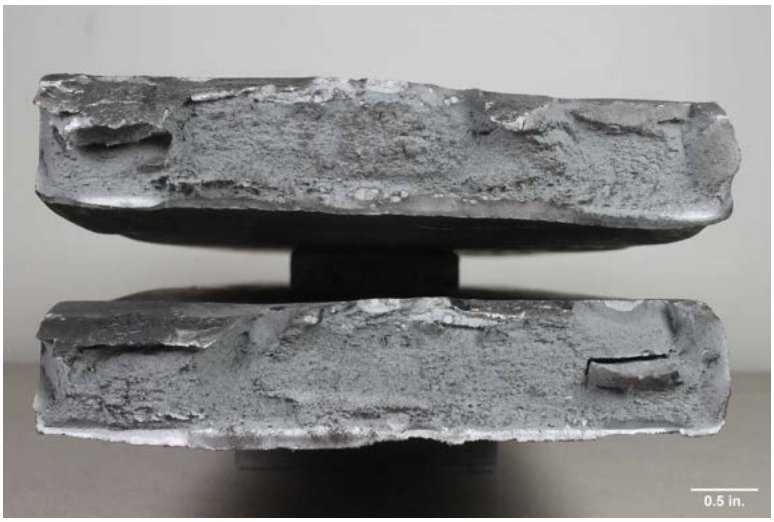

Figure V.30. Fracture surfaces of W36-0.25NGTW-T100-R11.01.

V.2.8 W36-0.25NGTW-T100-R11.02

The first folded steel defect appeared in the third cycle, and there were no visible defects prior to this point. Complete fracture occurred in the fifth cycle when the bottom was in tension. The first folded steel defects are shown in Figure V.31 and the fracture surfaces of both halves are shown in Figure V.32.

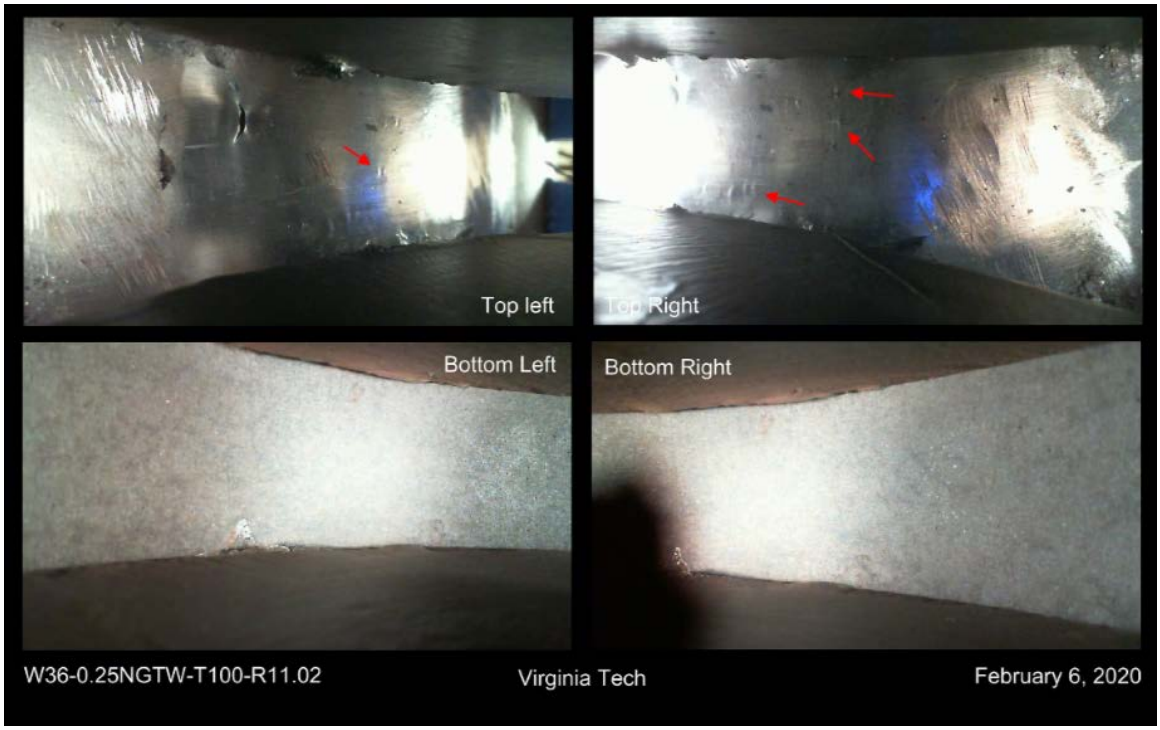

Figure V.31. Fracture initiation of W36-0.25NGTW-T100-R11.02.

Figure V.32. Fracture surfaces of W36-0.25NGTW-T100-R11.02.

V.3 Sharp 0.25 in. Notches

Due to the nature of this defect, fracture initiation was always assumed to occur in the first cycle. Final fracture also always occurred when the top side was in tension.

V.3.1 W24-0.25N-T50-R11.02

Fracture initiation on the bottom side occurred in the fifth cycle, shown in Figure V.33, and final fracture occurred in the ninth cycle. The fracture surfaces of both halves are shown in Figure V.34.

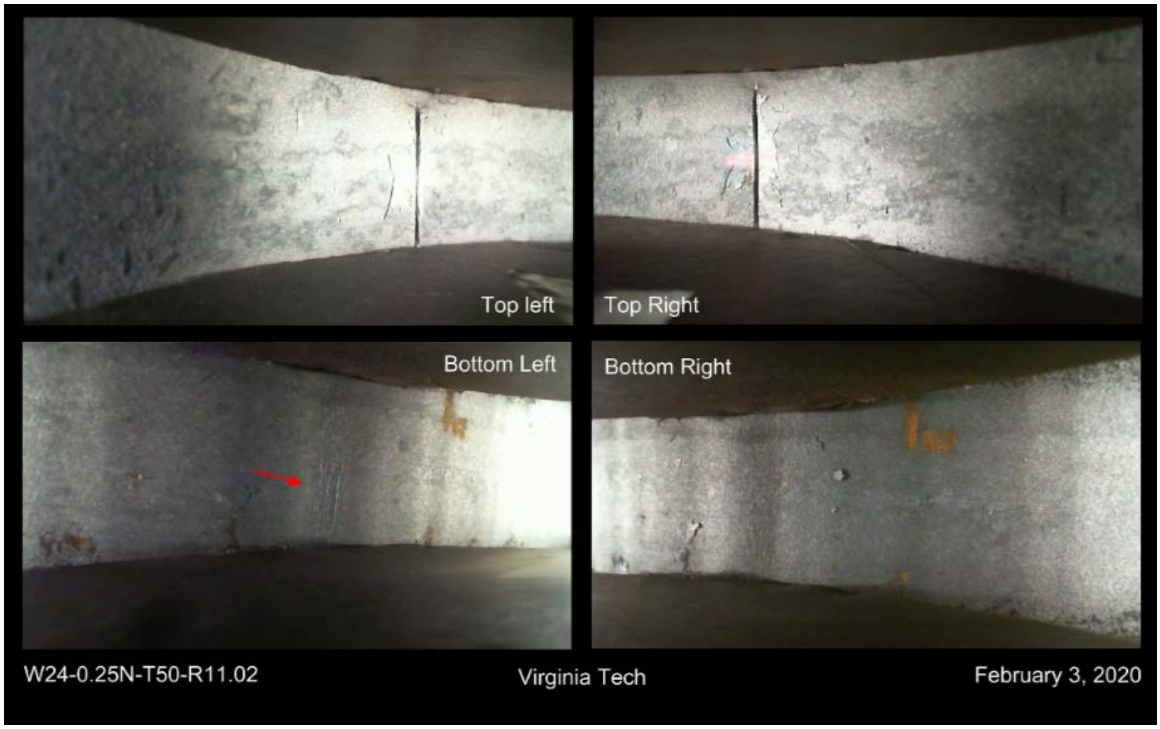

Figure V.33. Fracture initiation of W24-0.25N-T50-R11.02.

Figure V.34. Fracture surfaces of W24-0.25N-T50-R11.02.

V.3.2 W24-0.25N-T50-R11.03

Fracture initiation occurred on the bottom side in the fifth cycle, shown in Figure V.35, and complete fracture occurred in the eighth cycle. The fracture surfaces of both halves are shown in Figure V.36.

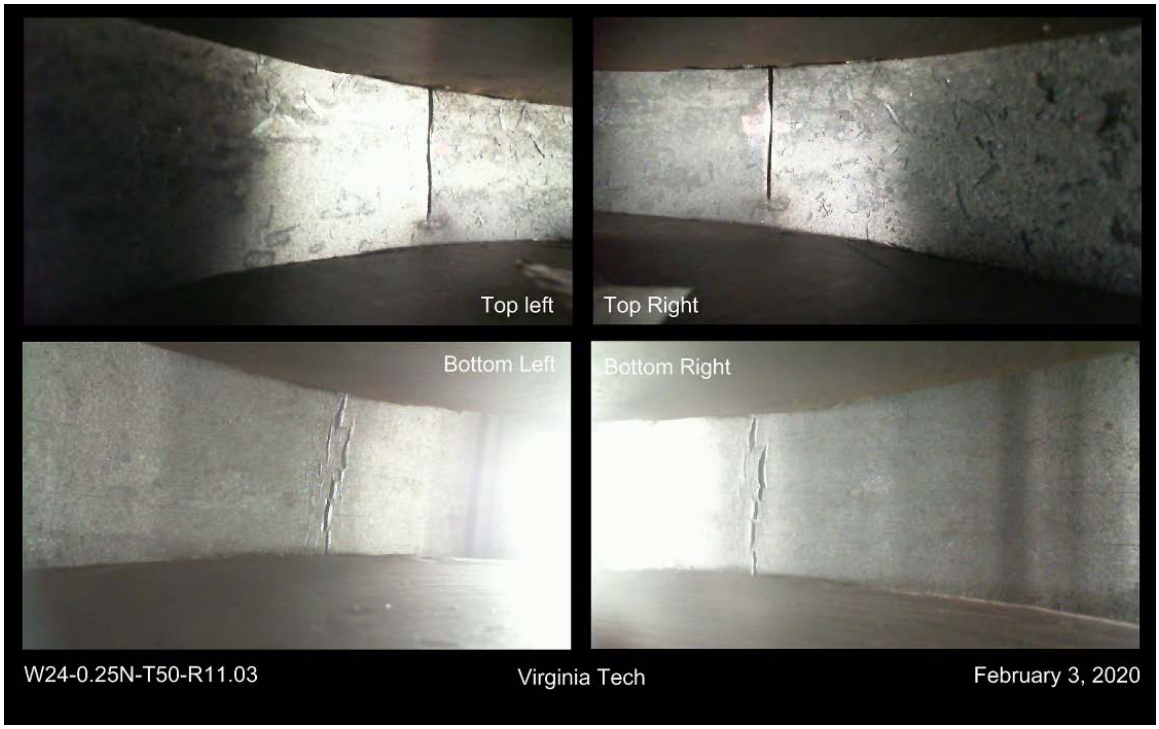

Figure V.35. Fracture initiation of W24-0.25N-T50-R11.03.

Figure V.36. Fracture surfaces of W24-0.25N-T50-R11.03.

V.3.3 W24-0.25N-T59-R11.02

Fracture initiation on the bottom side occurred in the third cycle, shown in Figure V.37, and complete fracture occurred in the fourth cycle. The fracture surfaces of both halves are shown in Figure V.38.

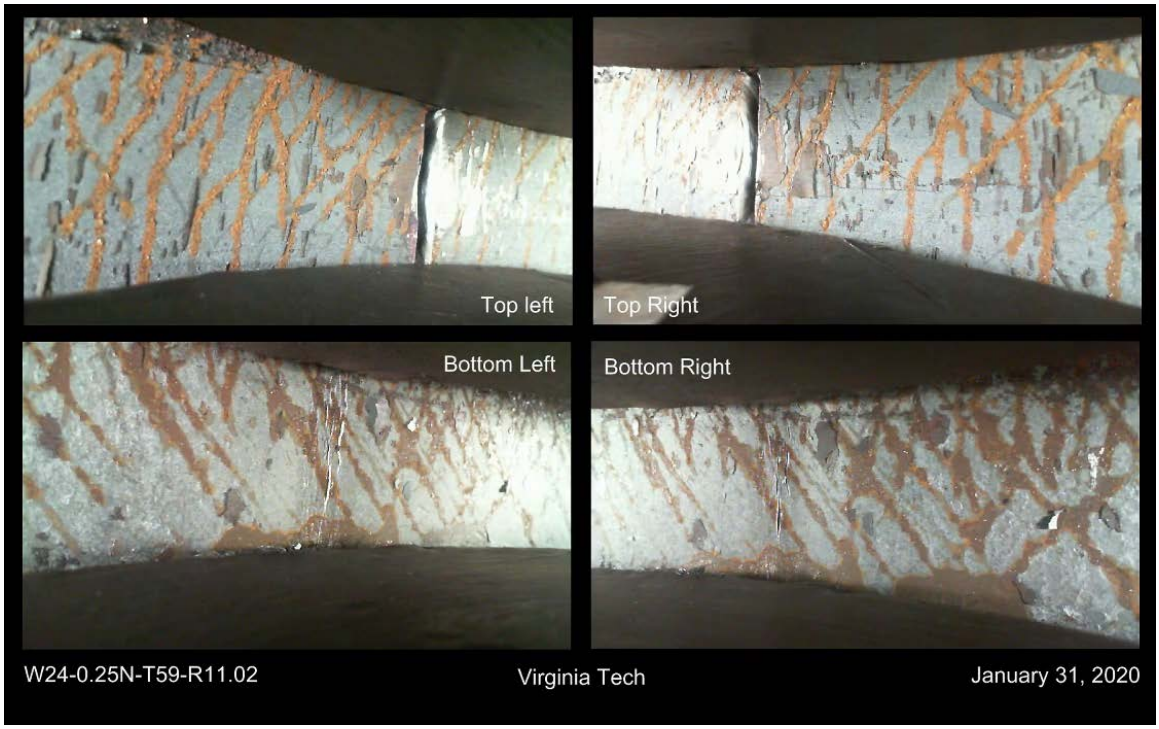

Figure V.37. Fracture initiation of W24-0.25N-T59-R11.02.

Figure V.38. Fracture surfaces of W24-0.25N-T59-R11.02.

V.3.4 W24-0.25N-T59-R11.03

Fracture initiation on the bottom side occurred in the third cycle, shown in Figure V.39, and complete fracture occurred in the fourth cycle. The fracture surfaces of both halves are shown in Figure V.40.

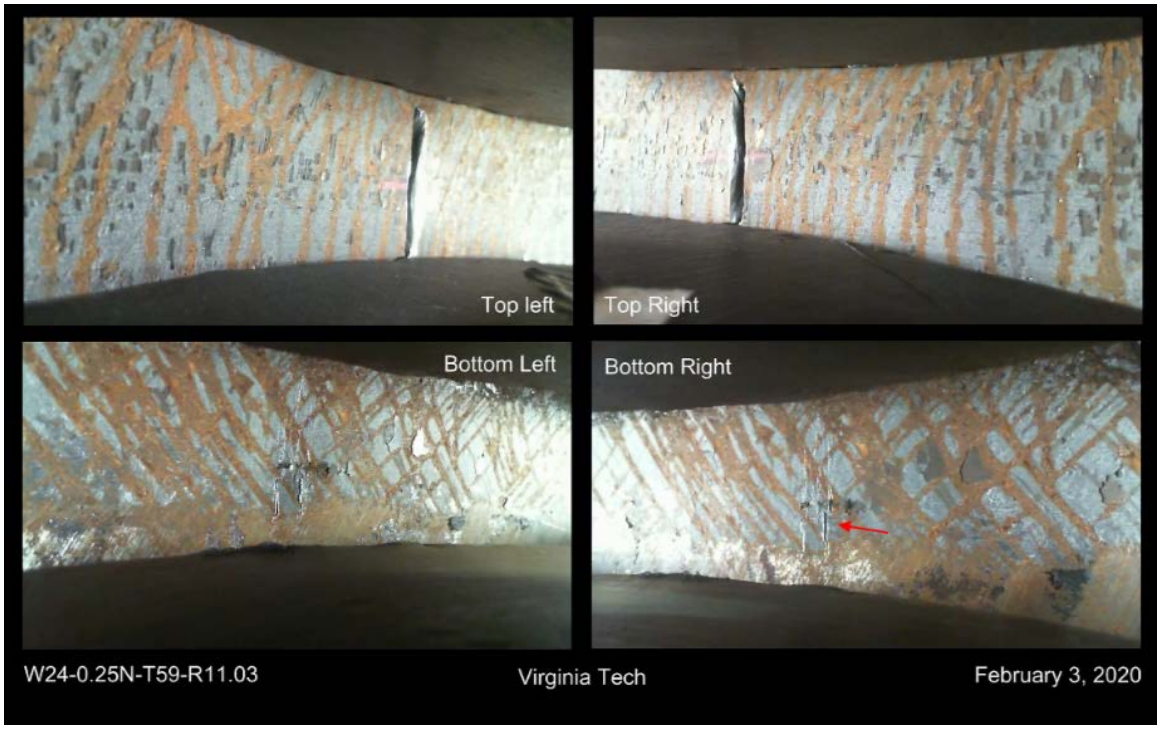

Figure V.39. Fracture initiation of W24-0.25N-T59-R11.03.

Figure V.40. Fracture surfaces of W24-0.25N-T59-R11.03.

V.3.5 W36-0.25N-T94-R11.01

Fracture initiation on the bottom side and complete fracture both occurred in the third cycle, shown in Figure V.41. The fracture surfaces of both halves are shown in Figure V.42.

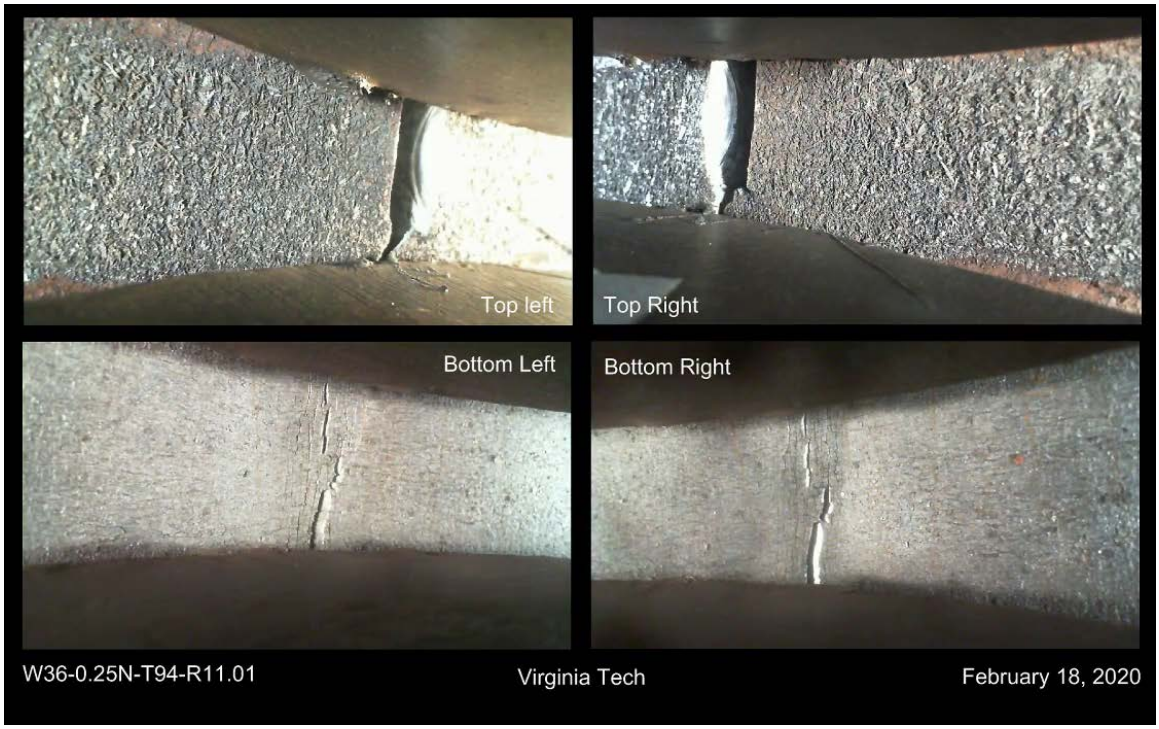

Figure V.41. Fracture initiation of W36-0.25N-T94-R11.01.

Figure V.42. Fracture surfaces of W36-0.25N-T94-R11.01.

V.3.6 W36-0.25N-T94-R11.02

Fracture initiation on the bottom side occurred in the third cycle, shown in Figure V.43, and complete fracture occurred in the fourth cycle. The fracture surfaces of both halves are shown in Figure V.44.

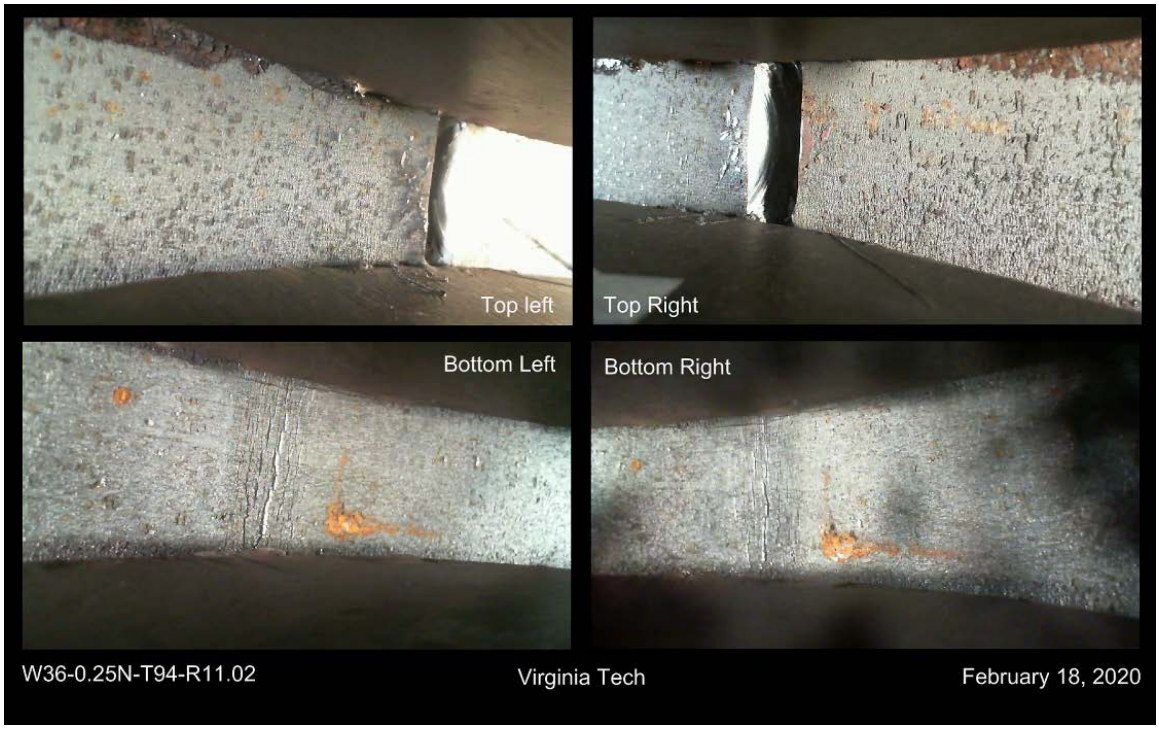

Figure V.43. Fracture initiation of W36-0.25N-T94-R11.02.

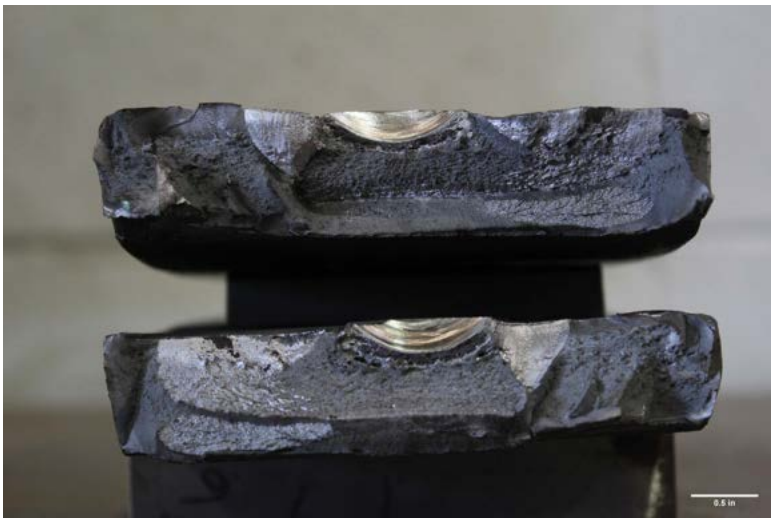

Figure V.44. Fracture surfaces of W36-0.25N-T94-R11.02.

V.3.7 W36-0.25N-T100-R11.01

There was no fracture initiation on the bottom side before the brittle fracture in the second cycle. The fracture surfaces of both halves are shown in Figure V.45.

Figure V.45. Fracture surfaces of W36-0.25N-T100-R11.01.

V.3.8 W36-0.25N-T100-R11.02

There was no fracture initiation on the bottom side before the brittle fracture in the second cycle. The fracture surfaces of both halves are shown in Figure V.46.

Figure V.46. Fracture surfaces of W36-0.25N-T100-R11.02.

V.4 Sharp 0.375 in. Notches

Due to the nature of this defect, fracture initiation was always assumed to occur in the first cycle.

V.4.1 W24-0.375N-T50-R11.01

Fracture initiation on the bottom side occurred in the fourth cycle, shown in Figure V.47, and complete fracture occurred in the eighth cycle while the bottom was in tension. The fracture surfaces of both halves are shown in Figure V.48.

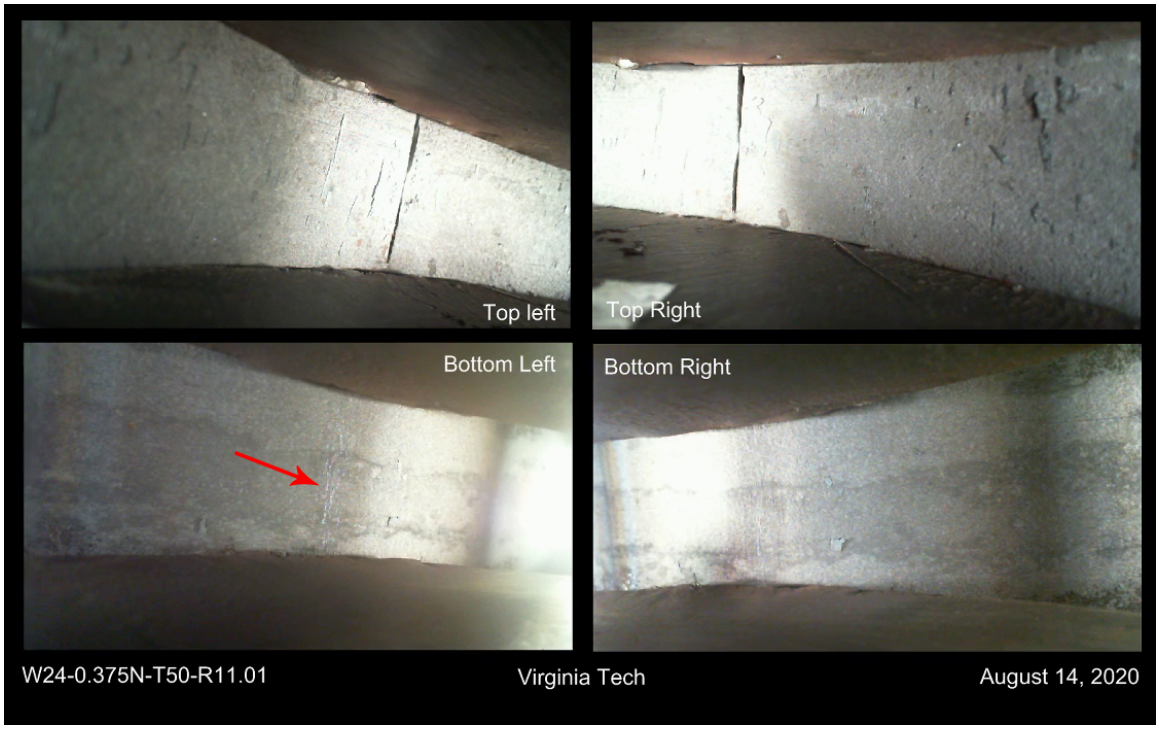

Figure V.47. Fracture initiation of W24-0.375N-T50-R11.01.

Figure V.48. Fracture surfaces of W24-0.375N-T50-R11.01.

V.4.2 W24-0.375N-T50-R11.02

Fracture initiation on the bottom side occurred in the third cycle, shown in Figure V.49, and complete fracture occurred in the sixth cycle while the top was in tension. The fracture surfaces of both halves are shown in Figure V.50.

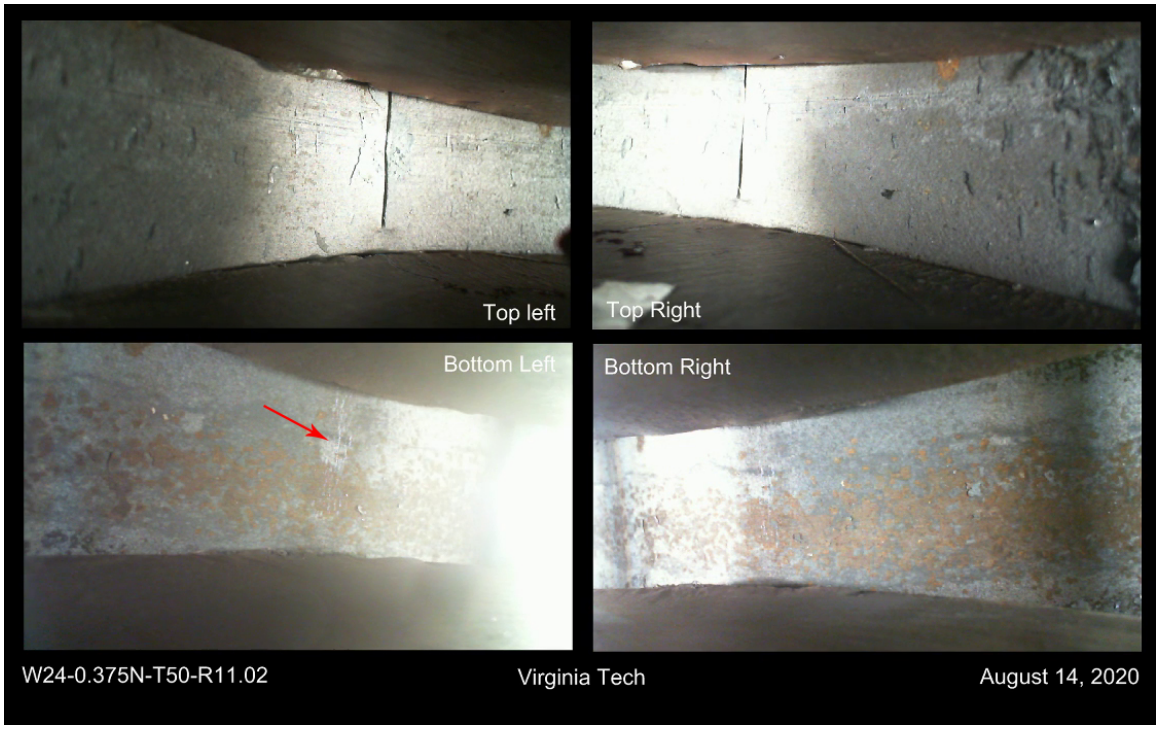

Figure V.49. Fracture initiation of W24-0.375N-T50-R11.02.

Figure V.50. Fracture surfaces of W24-0.375N-T50-R11.02.

V.4.3 W24-0.375N-T59-R11.01

Fracture initiation on the bottom side occurred in the third cycle, shown in Figure V.51, and final fracture occurred in the fifth cycle while the bottom was in tension. The fracture surfaces of both halves are shown in Figure V.52.

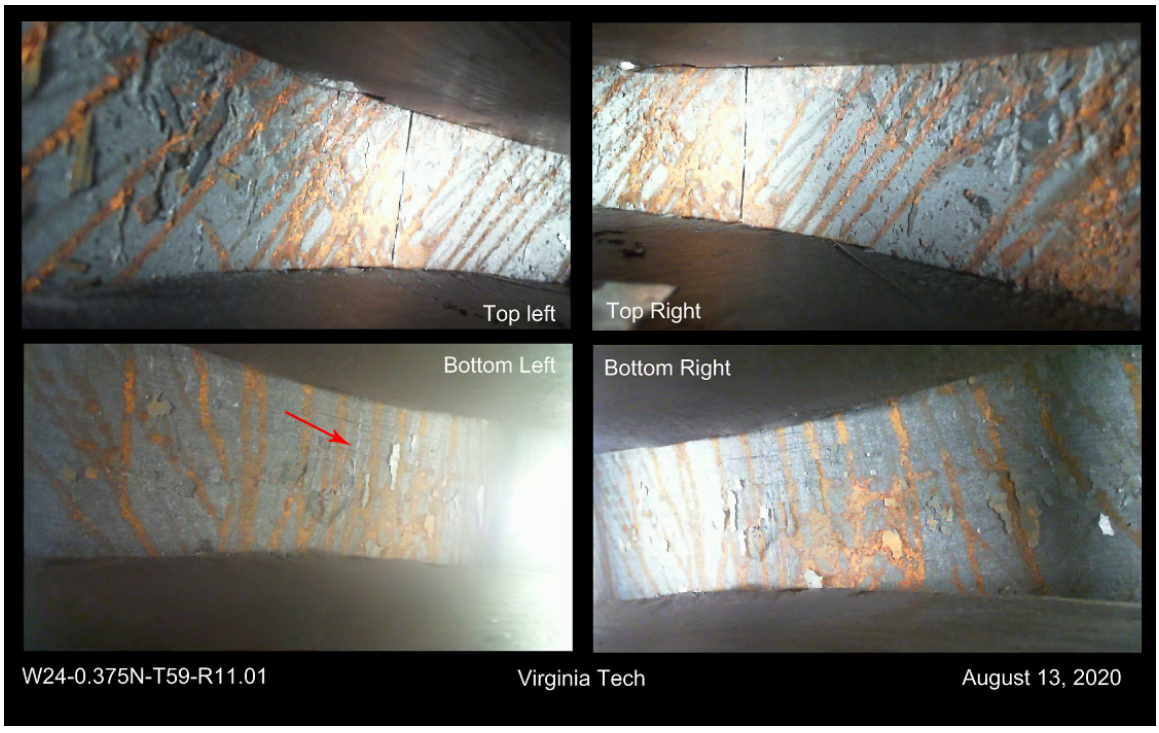

Figure V.51. Fracture initiation of W24-0.375N-T59-R11.01.

Figure V.52. Fracture surfaces of W24-0.375N-T59-R11.01.

V.4.4 W24-0.375N-T59-R11.02

Fracture initiation on the bottom side occurred in the third cycle, shown in Figure V.53, and final fracture occurred in the sixth cycle while the top was in tension. The fracture surfaces of both halves are shown in Figure V.54.

Figure V.53. Fracture initiation of W24-0.375N-T59-R11.02.

Figure V.54. Fracture surfaces of W24-0.375N-T59-R11.02.

V.4.5 W36-0.375N-T94-R11.01

Fracture initiation on the bottom side occurred in the second cycle, shown in Figure V.55, and final fracture occurred in the fourth cycle while the top was in tension. The fracture surfaces of both halves are shown in Figure V.56.

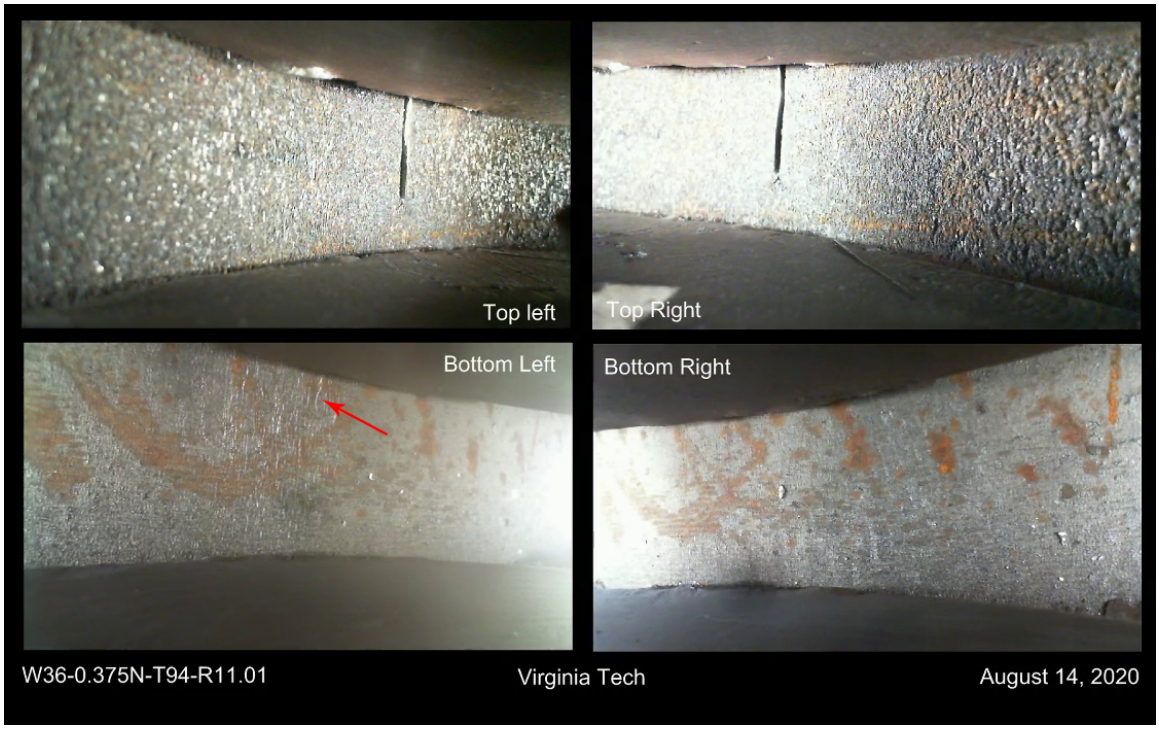

Figure V.55. Fracture initiation of W36-0.375N-T94-R11.01.

Figure V.56. Fracture surfaces of W36-0.375N-T94-R11.01.

V.4.6 W36-0.375N-T94-R11.02

Fracture initiation on the bottom side occurred in the second cycle, shown in Figure V.57, and final fracture occurred in the third cycle while the bottom was in tension. The fracture surfaces of both halves are shown in Figure V.58.

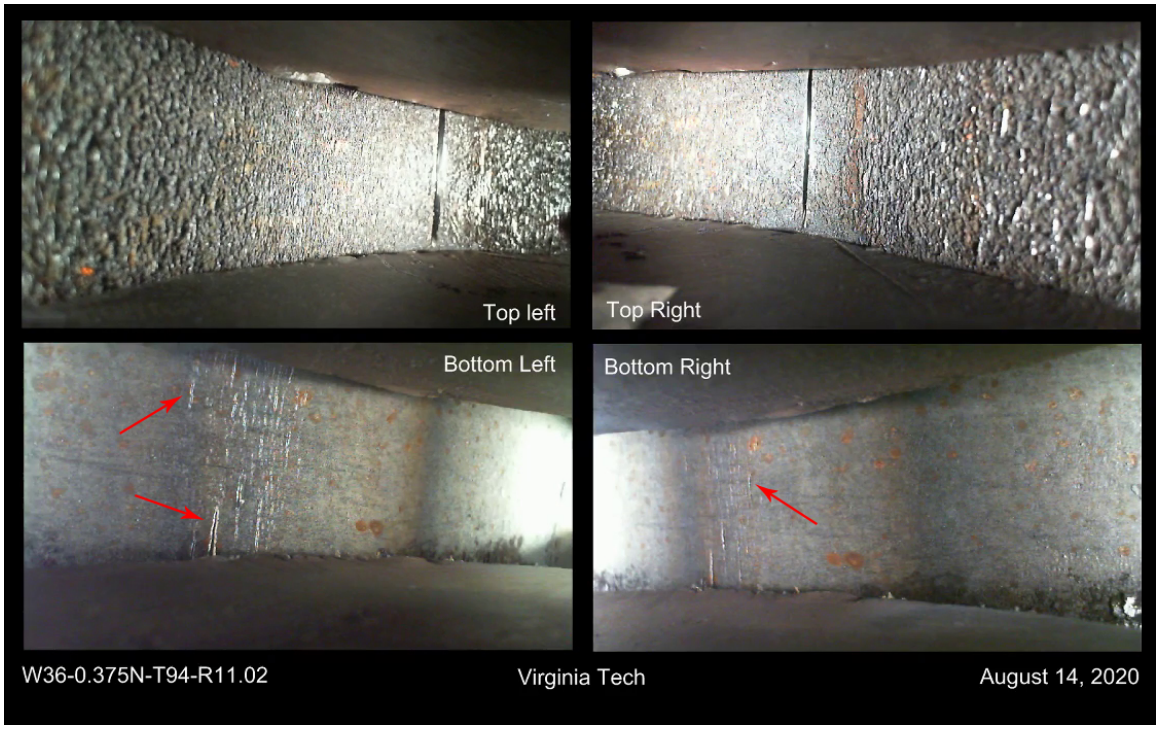

Figure V.57. Fracture initiation of W36-0.375N-T94-R11.02.

Figure V.58. Fracture surfaces of W36-0.375N-T94-R11.02.

V.4.7 W36-0.375N-T100-R11.01

Fractures formed on the bottom side in the second cycle, shown in Figure V.59, when the top flange fracture propagated through the thickness of the coupon. Complete fracture occurred in the second cycle while the top was in tension. The fracture surfaces of both halves are shown in Figure V.60.

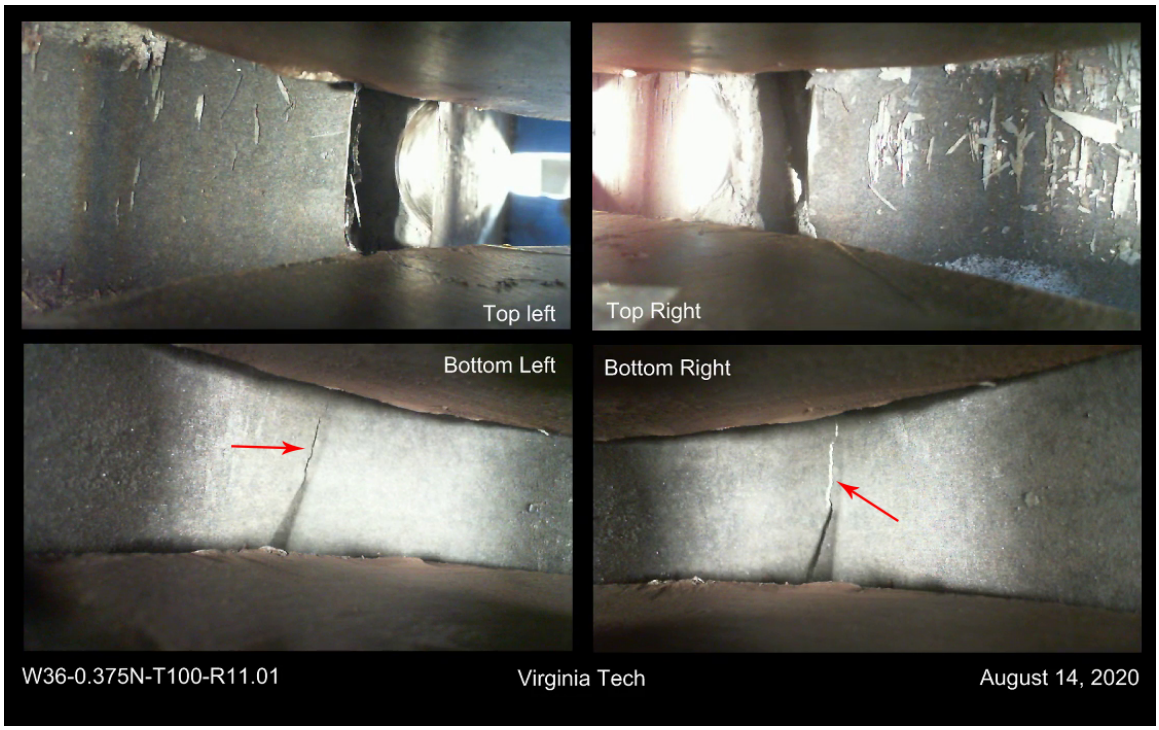

Figure V.59. Fracture surfaces of W36-0.375N-T100-R11.01.

Figure V.60. Fracture surfaces of W36-0.375N-T100-R11.01.

V.4.8 W36-0.375N-T100-R11.02

Fracture initiation on the bottom side is not known due to issues with the video recording. The fracture surfaces of both halves are shown in Figure V.61. Complete fracture occurred in the second cycle.

Figure V.61. Fracture surfaces of W36-0.375N-T100-R11.02.

V.5 Bare Steel

V.5.1 W24-BAR STOCK-T40-R11.02

Fracture initiation occurred in the twenty-eighth cycle while the bottom was in tension and final fracture occurred in the sixty-seventh cycle, also while the bottom was in tension. Fracture initiation is shown in Figure V.62 and the fracture surfaces of both halves are shown in Figure V.63.

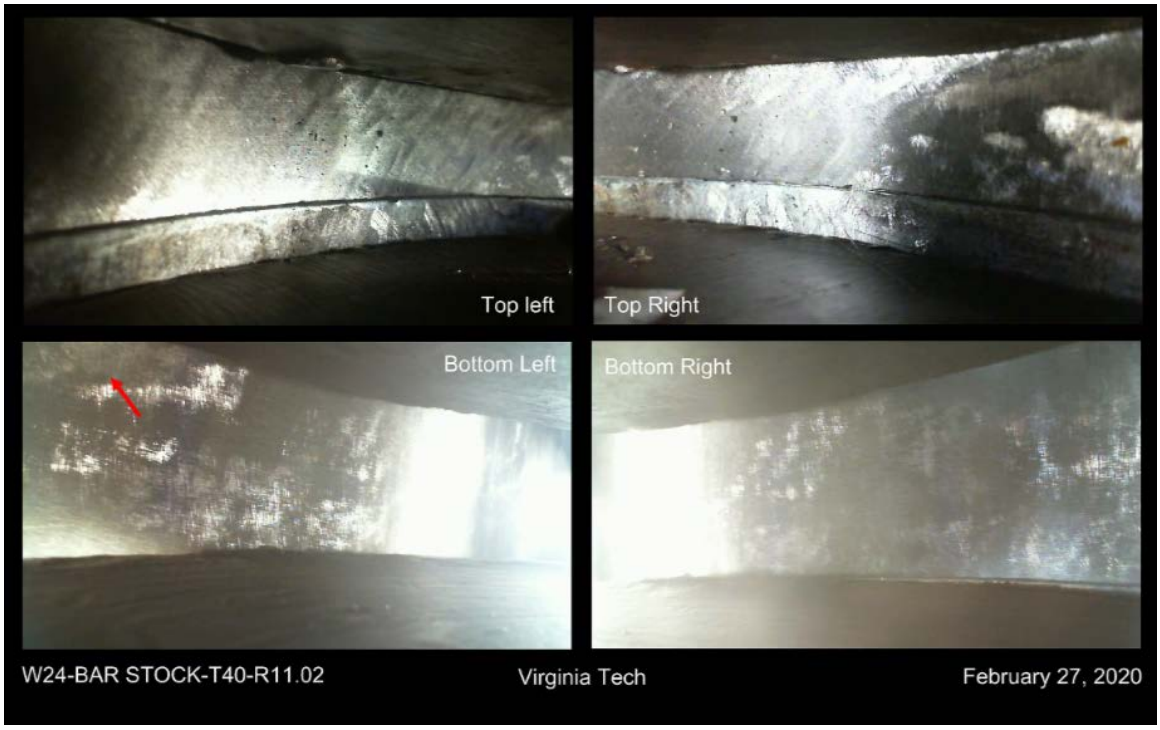

Figure V.62. Fracture initiation of W24-BAR STOCK-T40-R11.02.

Figure V.63. Fracture surfaces of W24-BAR STOCK-T40-R11.02.

V.5.2 W24-FLANGE MATERIAL-T40-R11.01

Fracture initiation occurred in the thirteenth cycle, shown in Figure V.64, and final fracture occurred in the sixty-ninth cycle when the bottom was in tension. The fracture surfaces of both halves are shown in Figure V.65.

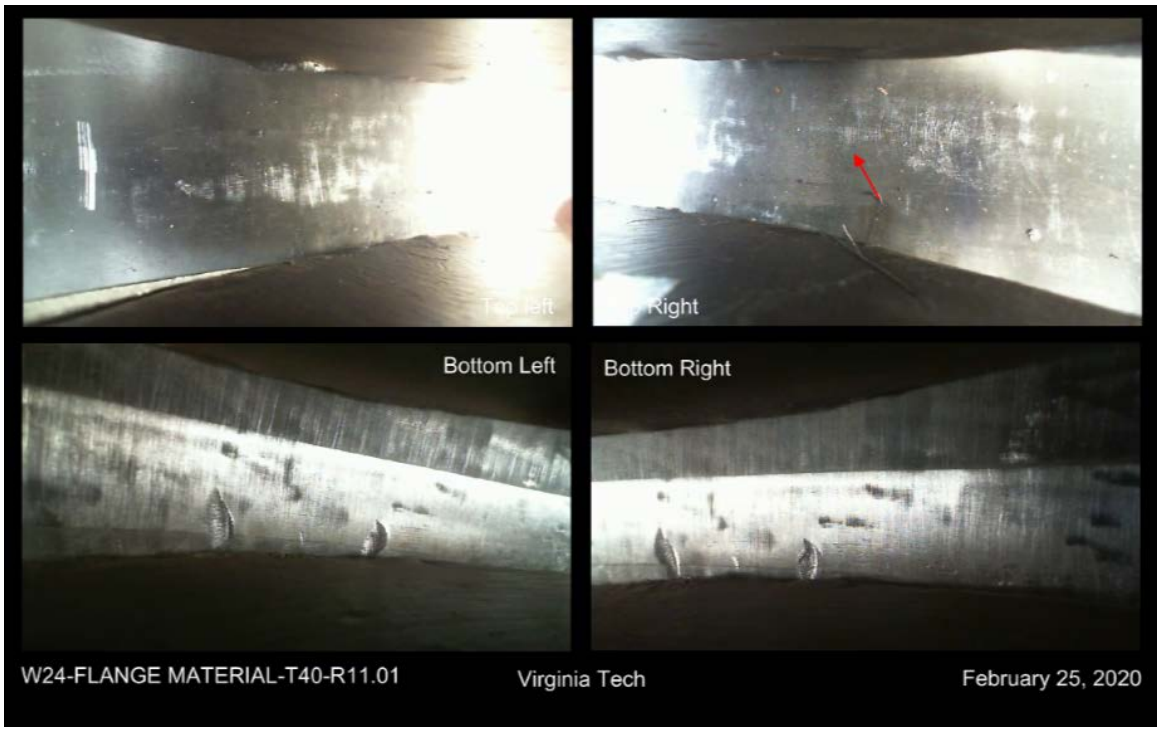

Figure V.64. Fracture initiation of W24-FLANGE MATERIAL-T40-R11.01.

Figure V.65. Fracture surfaces of W24-FLANGE MATERIAL-T40-R11.01.

V.5.3 W24-STEEL-T50-R11.02

Fracture initiation occurred in the thirty-first cycle, shown in Figure V.66, and complete fracture occurred in the thirty-third cycle while the top was in tension. The fracture surfaces of both halves are shown in Figure V.67.

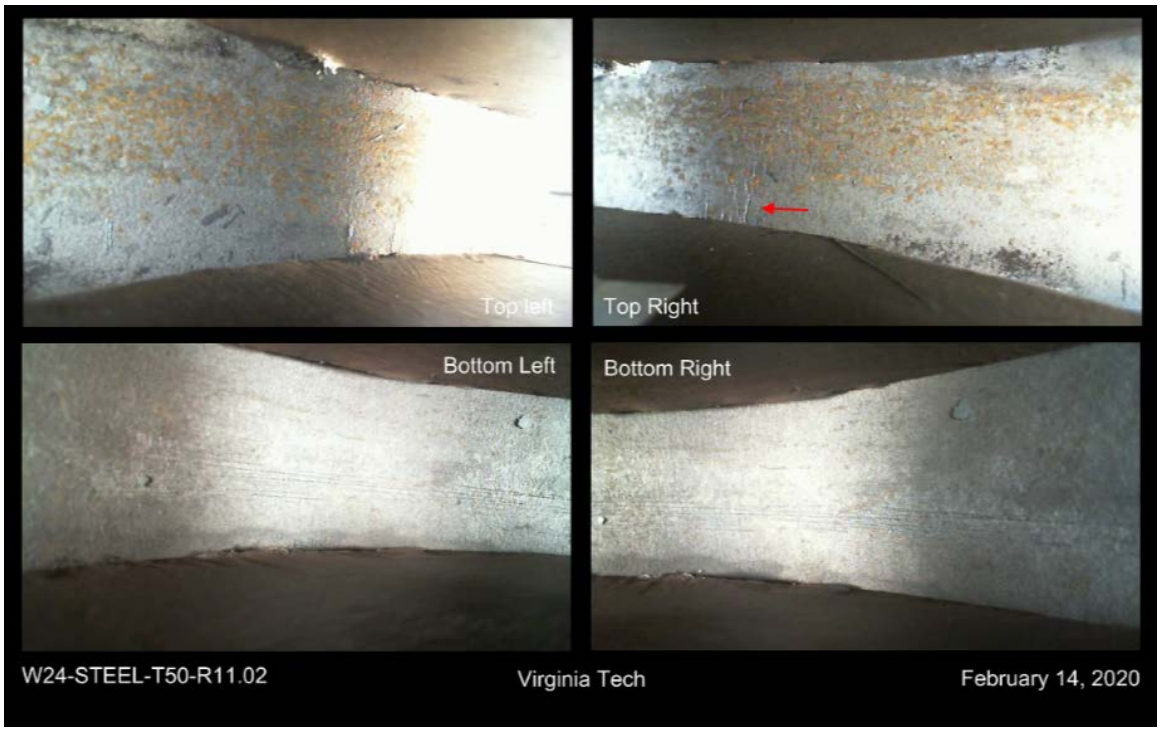

Figure V.66. Fracture initiation of W24-STEEL-T50-R11.02.

Figure V.67. Fracture surfaces of W24-STEEL-T50-R11.02.

V.5.4 W24-STEEL-T50-R11.03

Fracture initiation occurred in the thirty-fifth cycle, shown in Figure V.68, and complete fracture occurred in the thirty-seventh cycle while the bottom was in tension. The fracture surfaces of both halves are shown in Figure V.69.

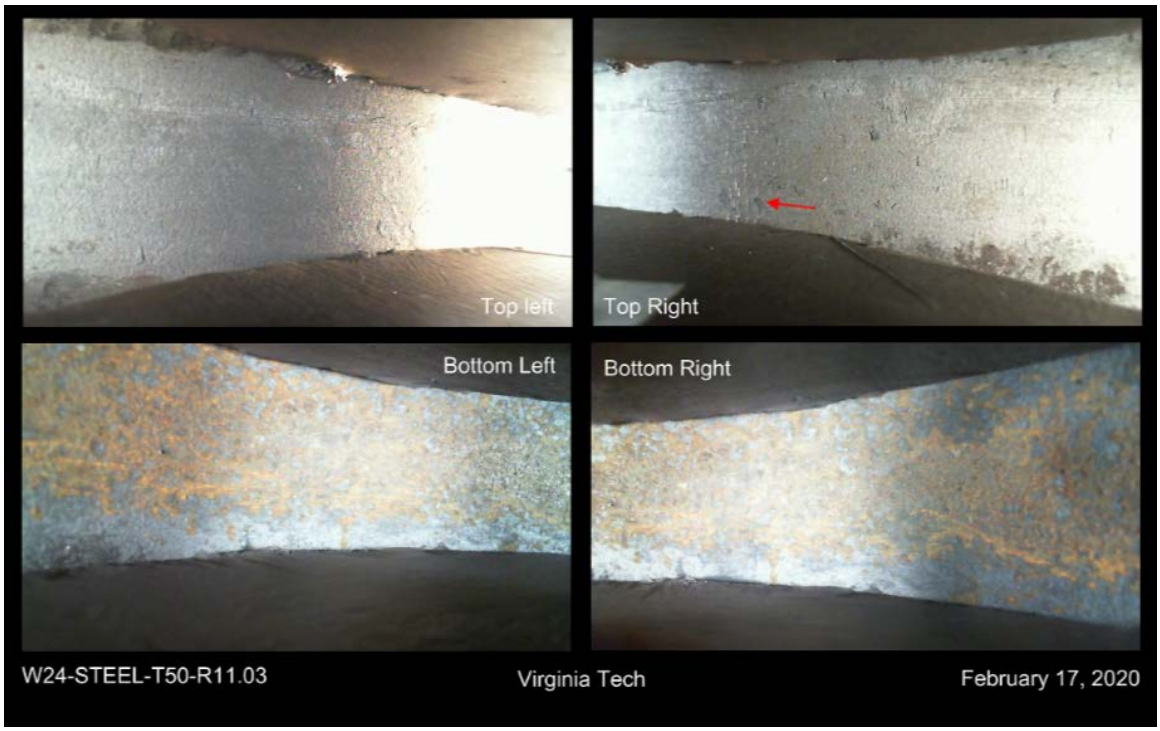

Figure V.68. Fracture initiation of W24-STEEL-T50-R11.03.

Figure V.69. Fracture surfaces of W24-STEEL-T50-R11.03.

V.5.5 W36-STEEL-T100-R11.01

Fracture initiation occurred in the fifth cycle, shown in Figure V.70, and complete fracture occurred in the sixth cycle while the top was in tension. The fracture surfaces of both halves are shown in Figure V.71.

Figure V.70. Fracture initiation of W36-STEEL-T100-R11.01.

Figure V.71. Fracture surfaces of W36-STEEL-T100-R11.01.

V.5.6 W36-STEEL-T100-R11.02

Fracture initiation occurred in the fourth cycle, shown in Figure V.72, and complete fracture occurred in the fifth cycle while the bottom was in tension. The fracture surfaces of both halves are shown in Figure V.73.

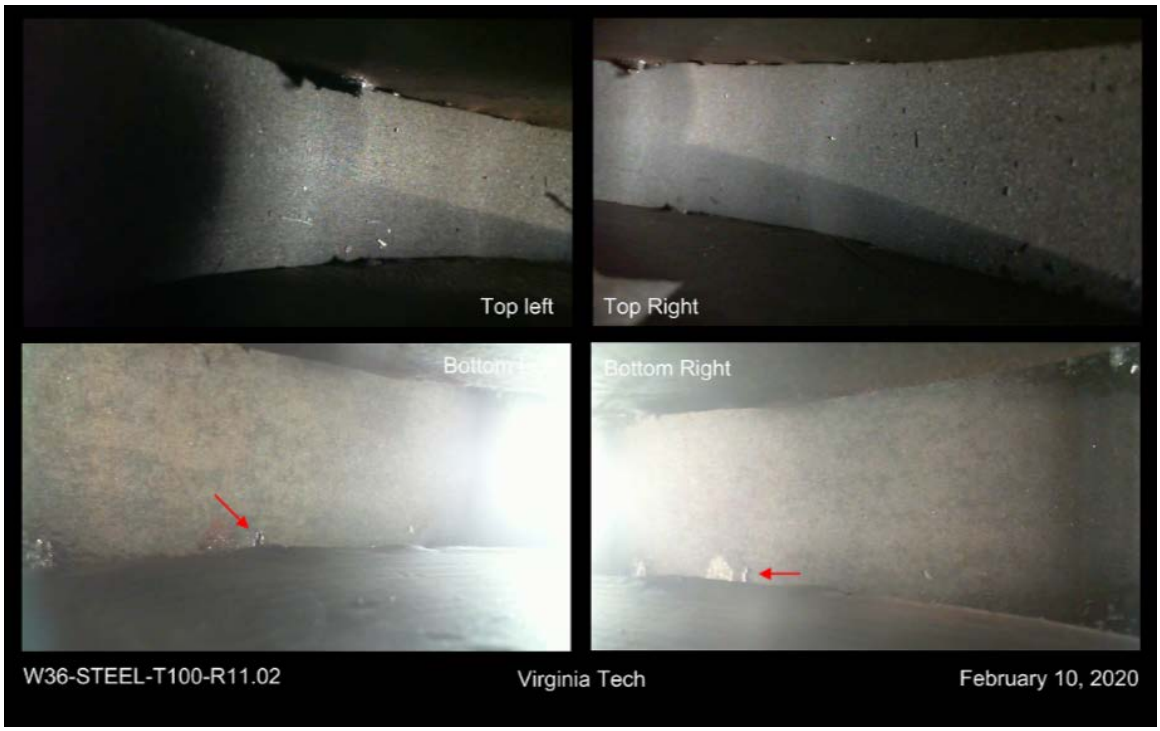

Figure V.72. Fracture initiation of W36-STEEL-T100-R11.02.

Figure V.73. Fracture surfaces of W36-STEEL-T100-R11.02.

V.6 Power Actuated Fasteners

V.6.1 W24-0.625PnAF-T50-R11.01

Fracture initiation occurred on the bottom side around the point formed by the fastener in the second cycle, shown in Figure V.74. Complete fracture occurred in the thirteenth cycle while the bottom was in tension. The fracture surfaces of both halves are shown in Figure V.75.

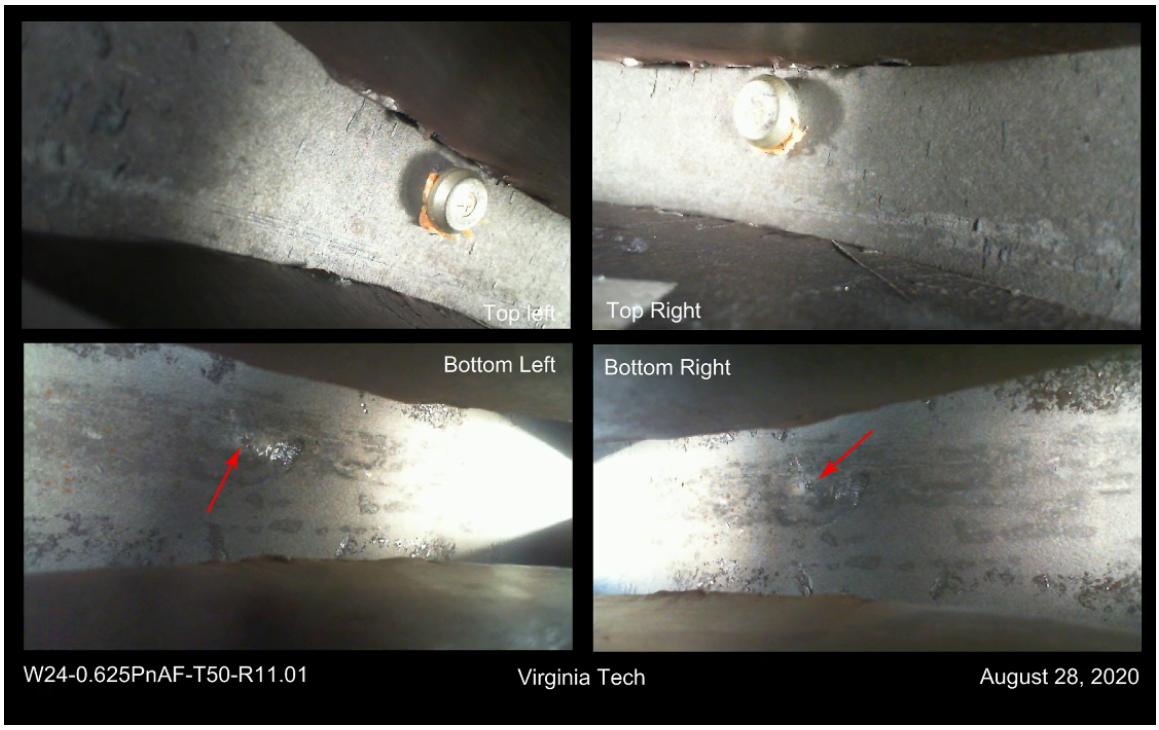

Figure V.74. Fracture initiation of W24-0.625PnAF-T50-R11.01.

Figure V.75. Fracture surfaces of W24-0.625PnAF-T50-R11.01.

V.6.2 W24-0.625PnAF-T50-R11.02

Fracture initiation occurred on the bottom side around the point formed by the fastener in the second cycle, shown in Figure V.76. Complete fracture occurred in the twelfth cycle while the bottom was in tension. The fracture surfaces of both halves are shown in Figure V.77.

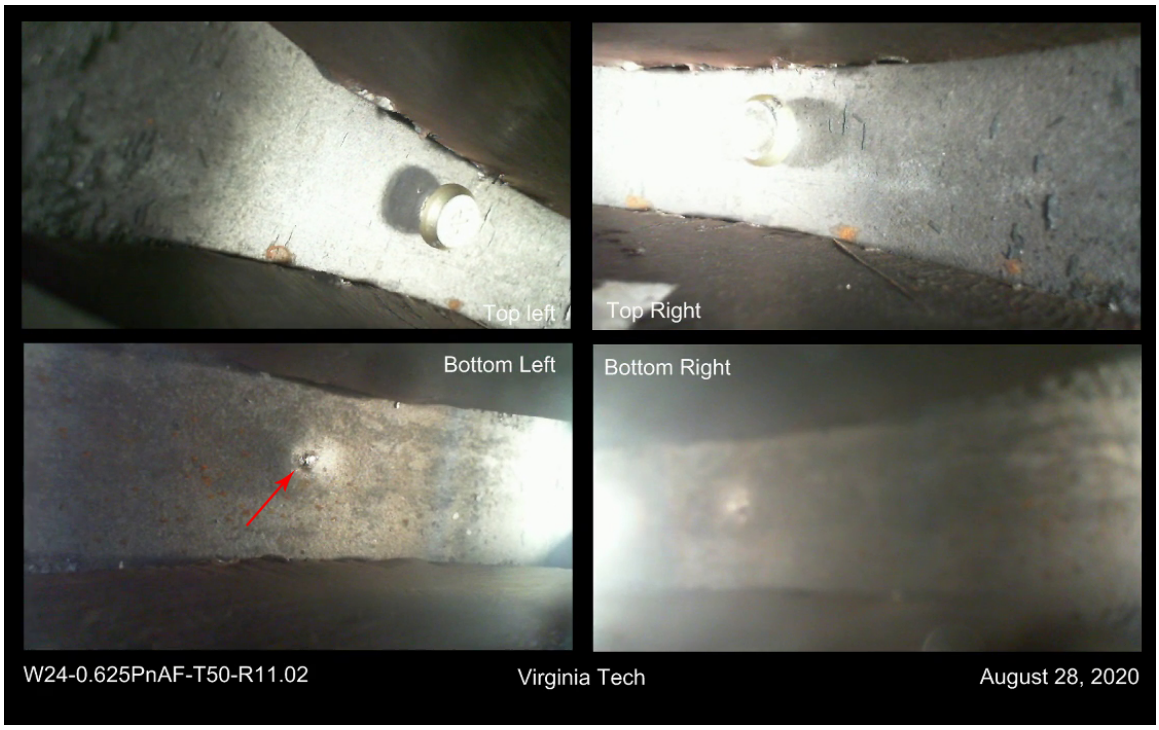

Figure V.76. Fracture initiation of W24-0.625PnAF-T50-R11.02.

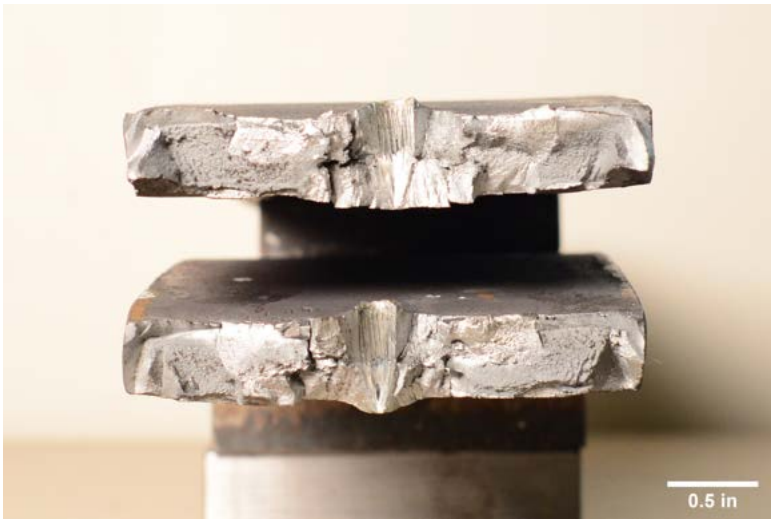

Figure V.77. Fracture surfaces of W24-0.625PnAF-T50-R11.02.

V.6.3 W24-0.75PnAF-T50-R11.01

Fracture initiation occurred on bottom side in the first cycle around the hole formed by the fastener, shown in Figure V.78. Complete fracture occurred in the eighteenth cycle while the top was in tension. The fracture surfaces of both halves are shown in Figure V.79.

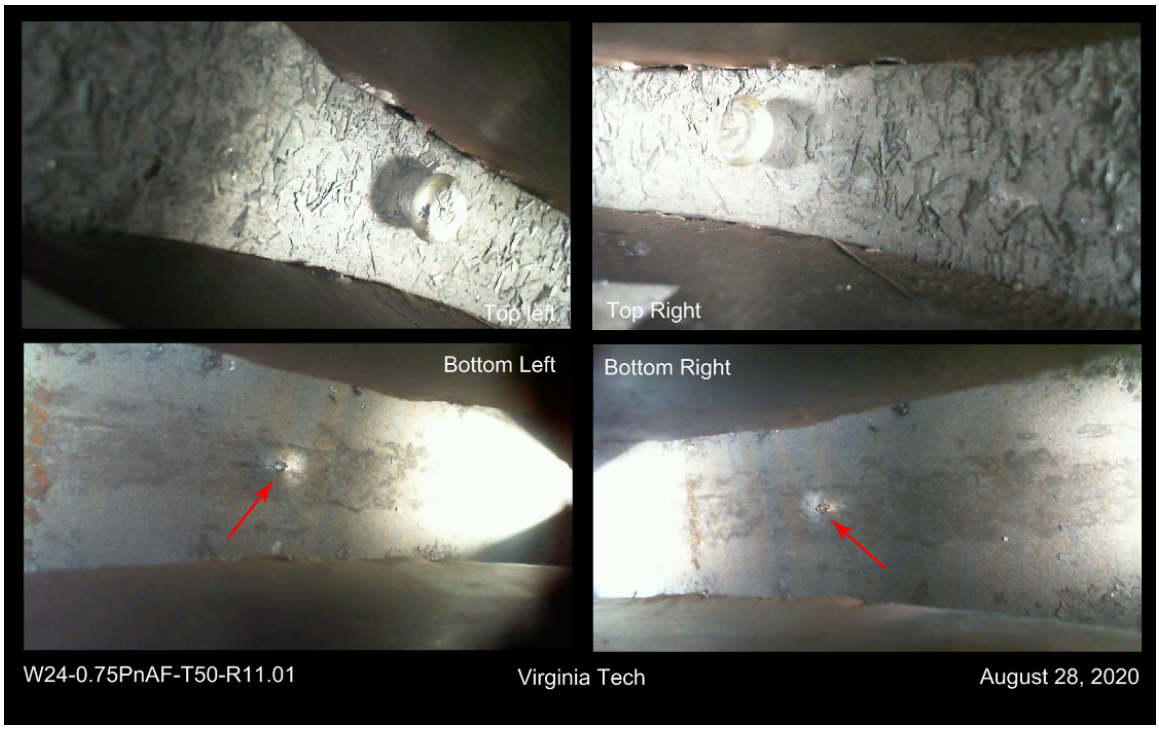

Figure V.78. Fracture initiation of W24-0.75PnAF-T50-R11.01.

Figure V.79. Fracture surfaces of W24-0.75PnAF-T50-R11.01.

V.6.4 W24-0.75PnAF-T50-R11.02

Fracture initiation occurred on the bottom side in the first cycle around the hole formed by the fastener, shown in Figure V.80. Complete fracture occurred in the eleventh cycle while the bottom was in tension. The fracture surfaces of both halves are shown in Figure V.81.

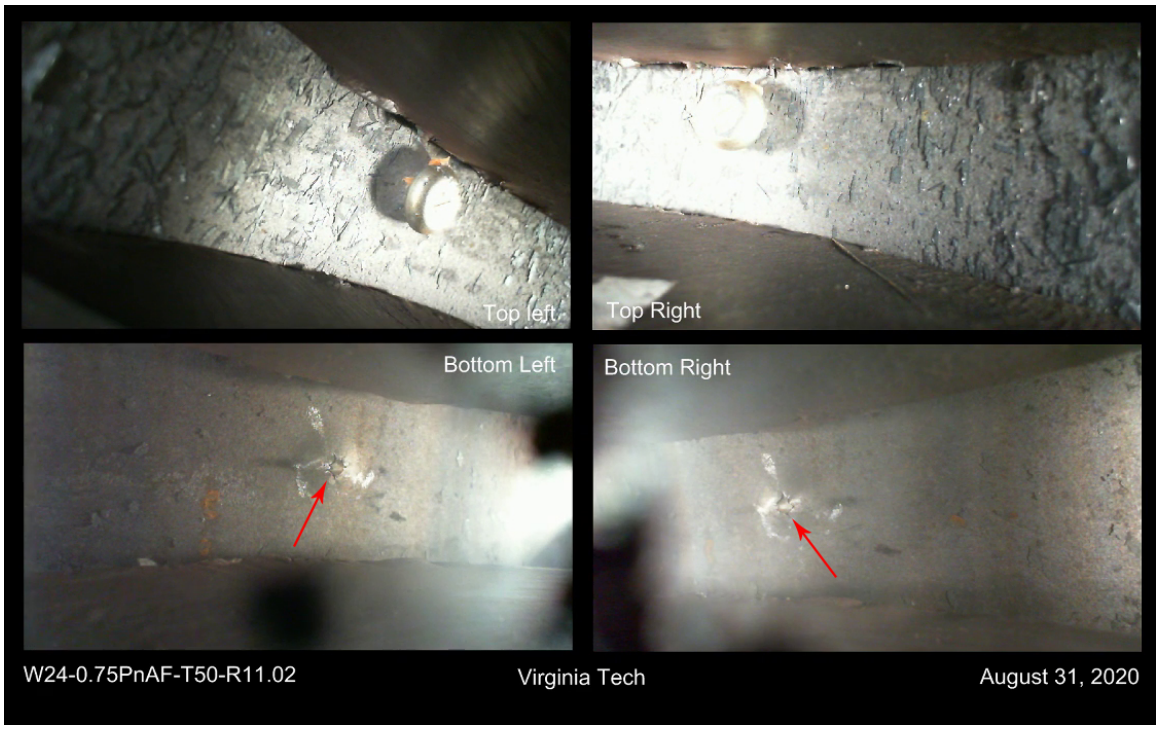

Figure V.80. Fracture initiation of W24-0.75PnAF-T50-R11.02.

Figure V.81. Fracture surfaces of W24-0.75PnAF-T50-R11.02.

V.6.5 W24-PAF-T50-R11.01

Fracture initiation occurred on the bottom side around the end of the fastener in the seventh cycle, shown in Figure V.82. Complete fracture occurred in the seventeenth cycle while the bottom was in tension. The fracture surfaces of both halves are shown in Figure V.83.

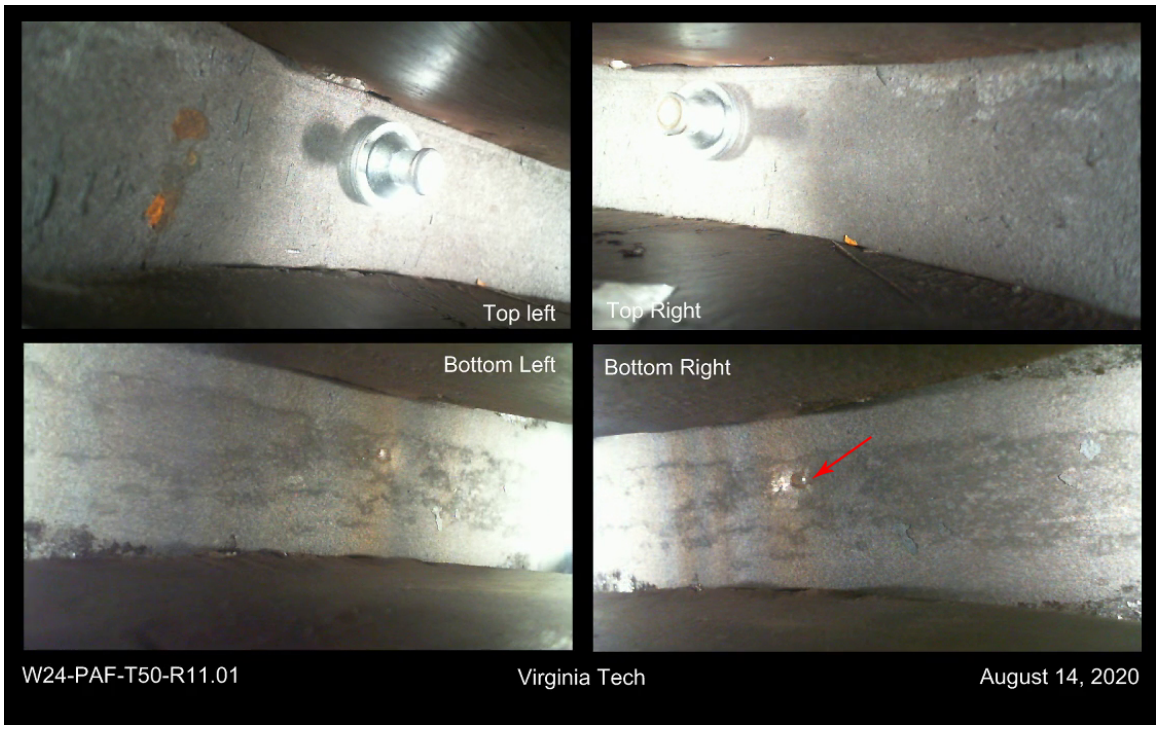

Figure V.82. Fracture initiation of W24-PAF-T50-R11.01.

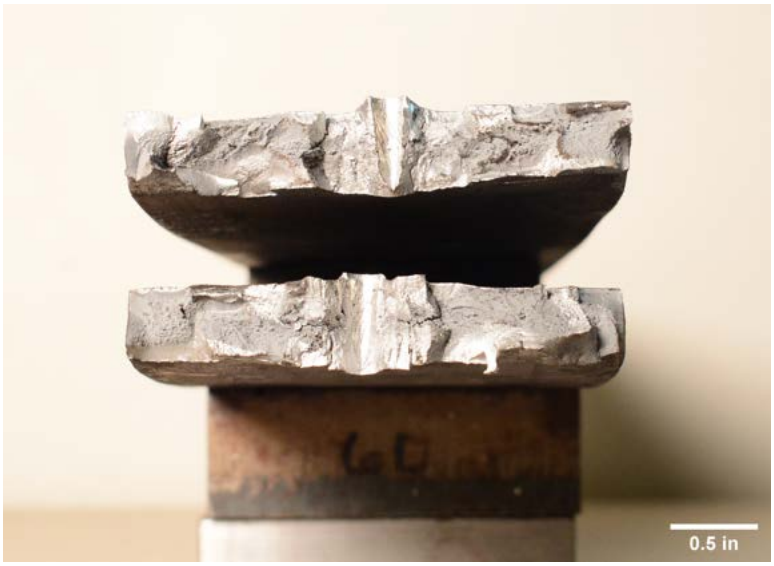

Figure V.83. Fracture surfaces of W24-PAF-T50-R11.01.

V.6.6 W24-PAF-T50-R11.02

Fracture initiation occurred on the bottom side in the fifth cycle, shown in Figure V.84. Complete fracture occurred in the seventeenth cycle while the bottom was in tension. The fracture surfaces of both halves are shown in Figure V.85.

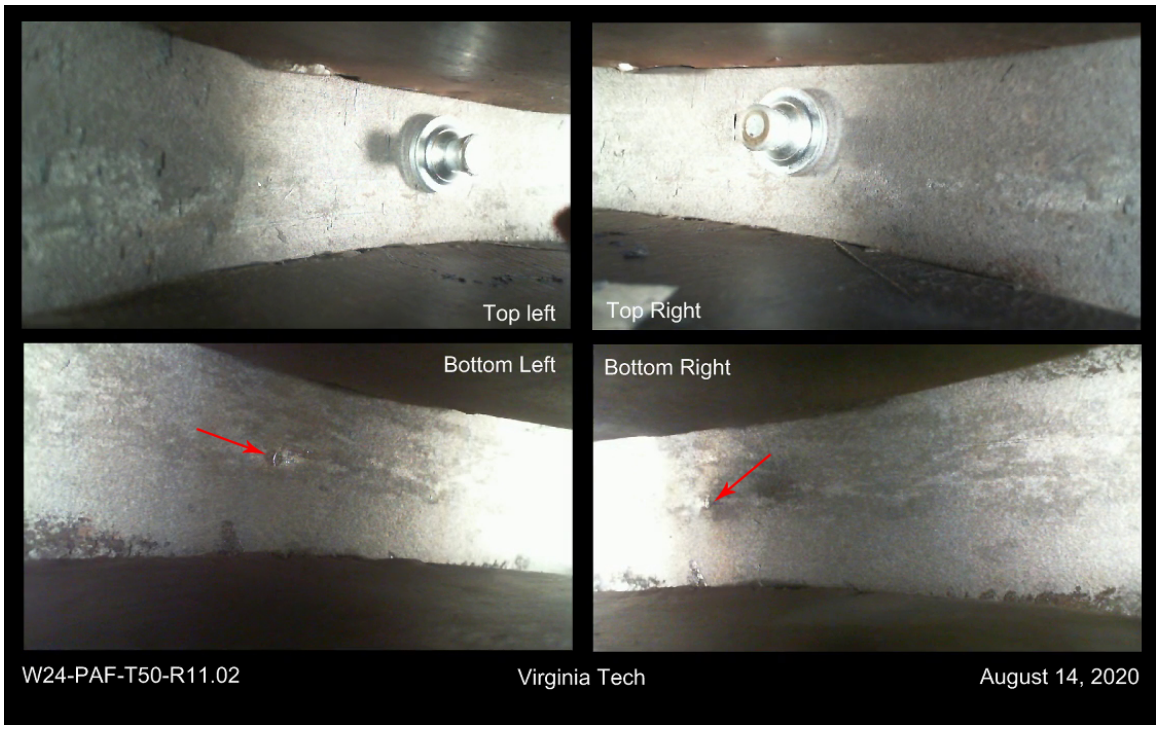

Figure V.84. Fracture initiation of W24-PAF-T50-R11.02.

Figure V.85. Fracture surfaces of W24-PAF-T50-R11.02.

V.6.7 W36-0.625PnAF-T100-R11.01

Fracture initiation occurred on the top side around the fastener hole in the second cycle, shown in Figure V.86. Complete fracture occurred in the third cycle when the bottom was in tension. The fracture surfaces of both halves are

shown in Figure V.87.

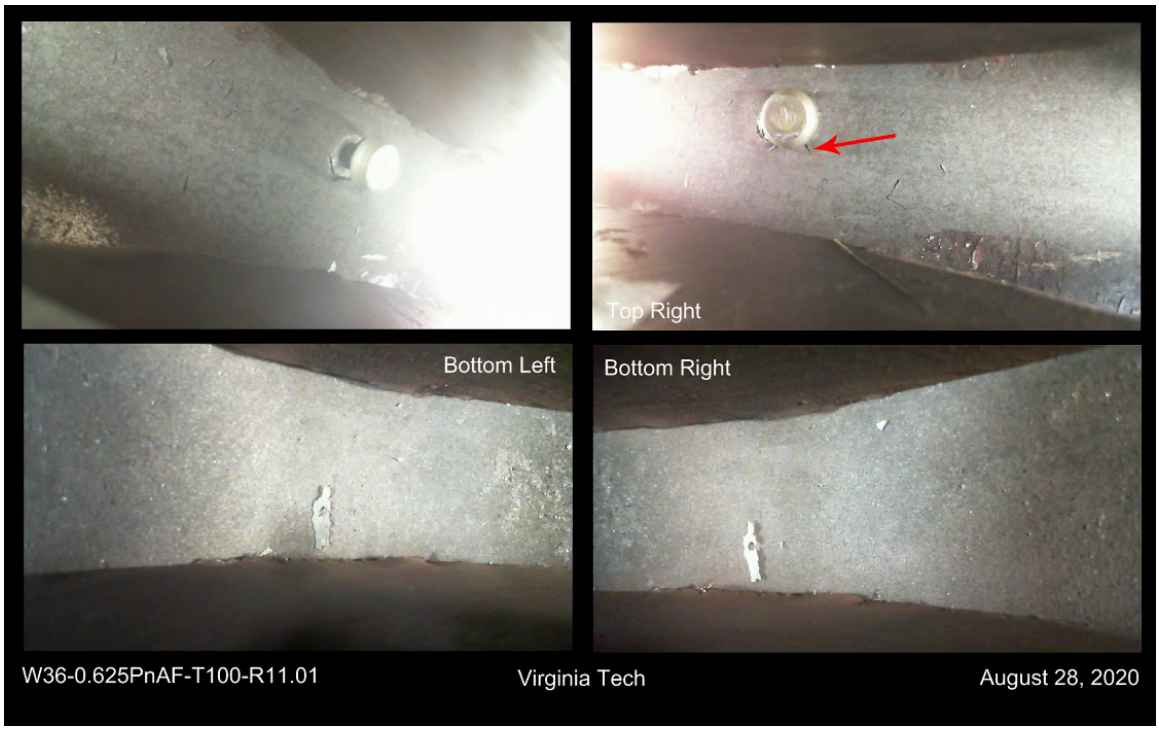

Figure V.86. Fracture initiation of W36-0.625PnAF-T100-R11.01.

Figure V.87. Fracture surfaces of W36-0.625PnAF-T100-R11.01.

V.6.8 W36-0.625PnAF-T100-R11.02

Fracture initiation occurred on the top side around the fastener hole in the third cycle, shown in Figure V.88. Complete fracture occurred in the fourth cycle when the top was in tension. The fracture surfaces of both halves are shown in Figure V.89.

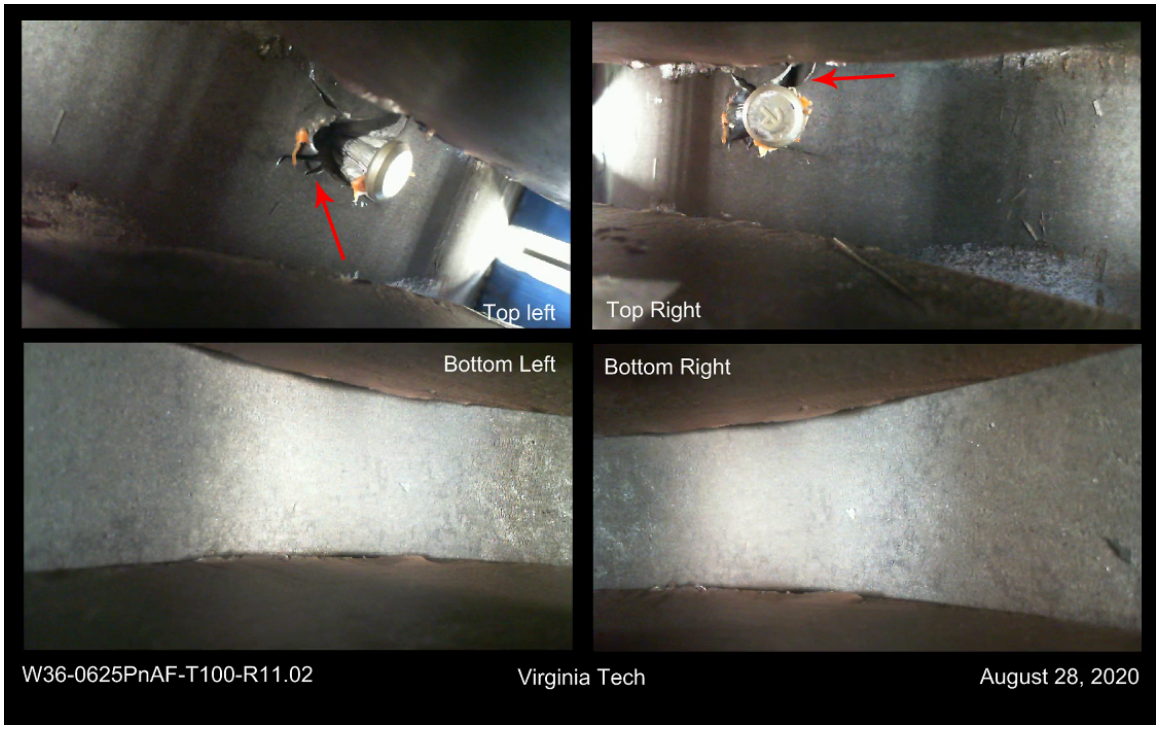

Figure V.88. Fracture initiation of W36-0.625PnAF-T100-R11.02.

Figure V.89. Fracture surfaces of W36-0.625PnAF-T100-R11.02.

V.6.9 W36-0.75PnAF-T100-R11.01

Fracture initiation occurred on the top side in the second cycle, shown in Figure V.90. Complete fracture occurred in the third cycle when the top was in tension. The fracture surfaces of both halves are shown in Figure V.91.

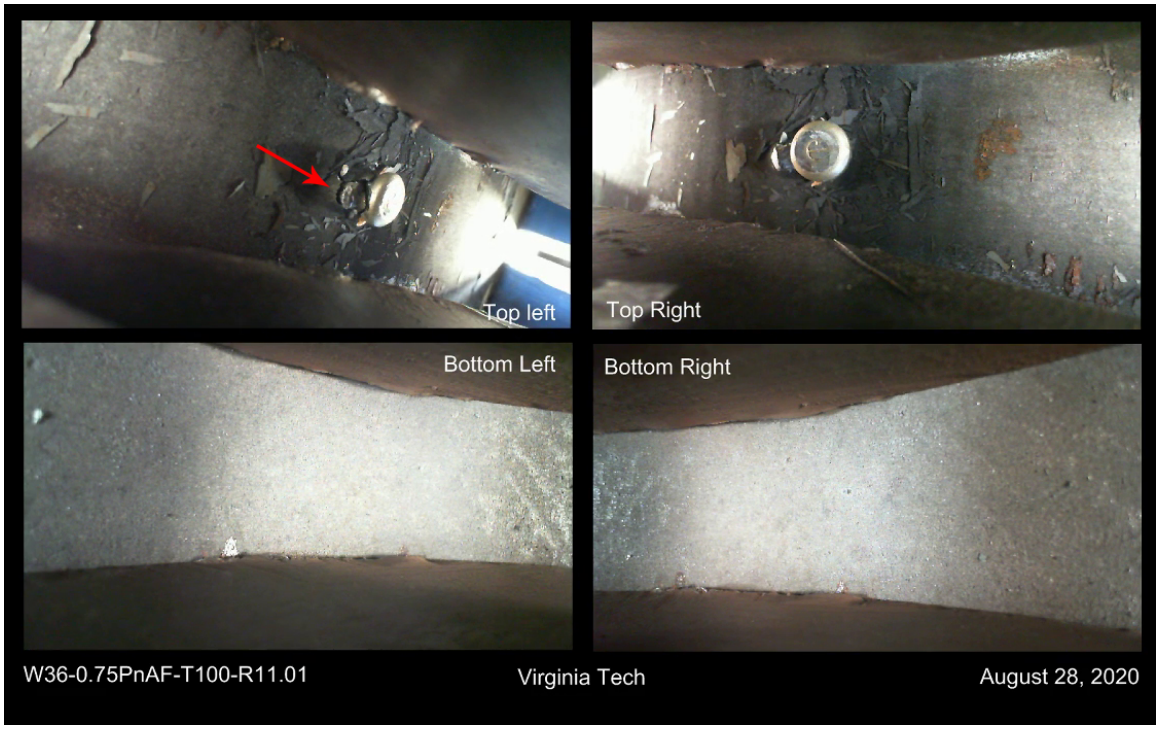

Figure V.90. Fracture initiation of W36-0.75PnAF-T100-R11.01.

Figure V.91. Fracture surfaces of W36-0.75PnAF-T100-R11.01.

V.6.10 W36-0.75PnAF-T100-R11.02

Fracture initiation occurred on the top side in the second cycle, shown in Figure V.92. Complete fracture occurred in the third cycle when the top was in tension. The fracture surfaces of both halves are shown in Figure V.93.

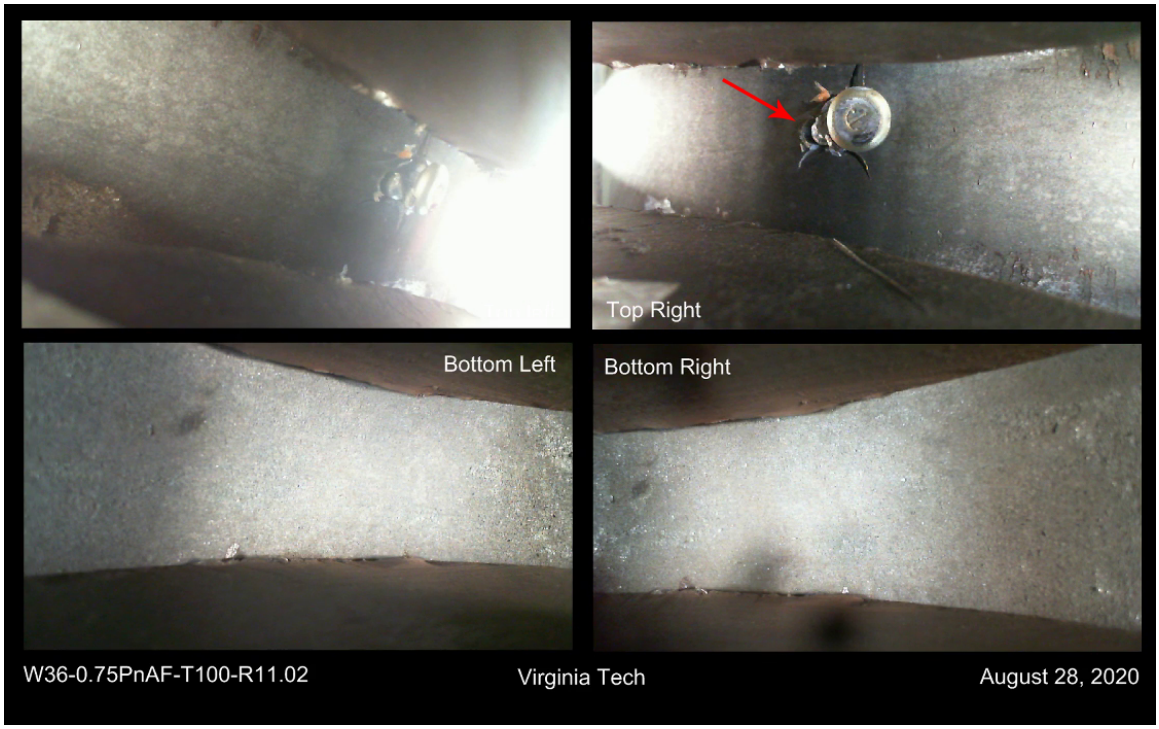

Figure V.92. Fracture initiation of W36-0.75PnAF-T100-R11.02.

Figure V.93. Fracture surfaces of W36-0.75PnAF-T100-R11.02.

V.6.11 W36-PAF-T100-R11.01

Fracture initiation occurred on the top side in the third cycle, shown in Figure V.94. Complete fracture occurred in the fourth cycle when the top was in tension. The fracture surfaces of both halves are shown in Figure V.95.

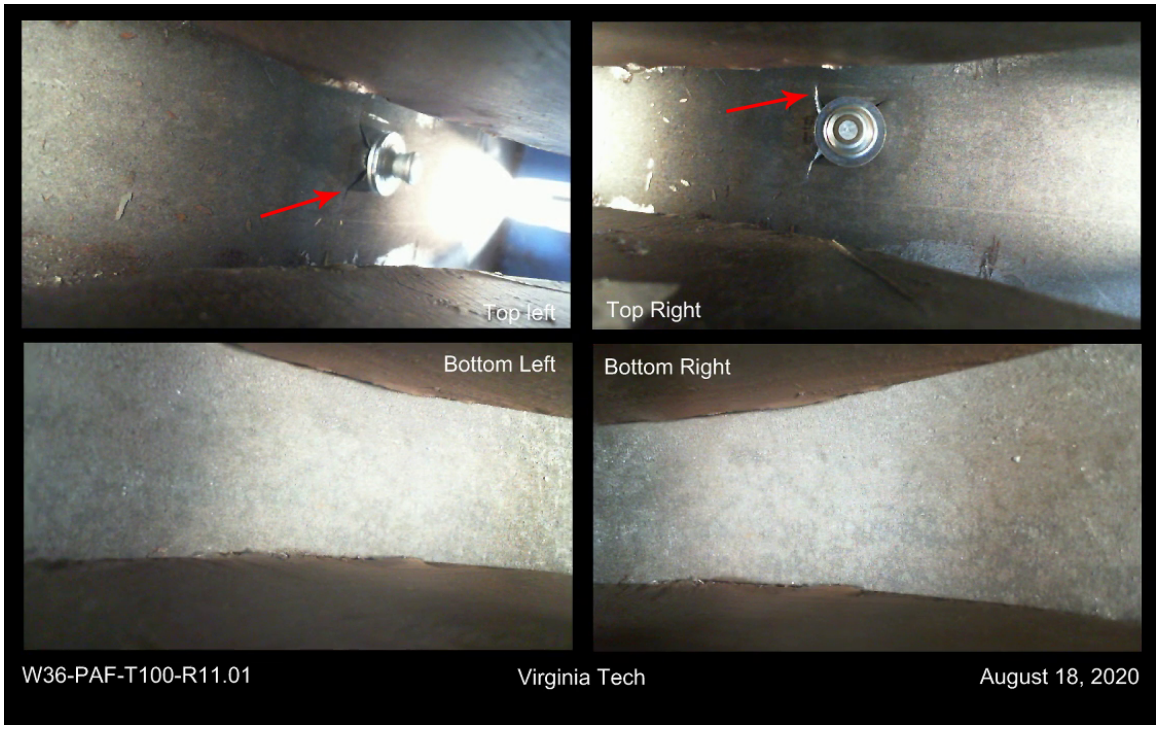

Figure V.94. Fracture initiation of W36-PAF-T100-R11.01.

Figure V.95. Fracture surfaces of W36-PAF-T100-R11.01.

V.6.12 W36-PAF-T100-R11.02

Fracture initiation occurred on the top side in the second cycle, shown in Figure V.96. Complete fracture occurred in the second cycle when the bottom was in tension. The fracture surfaces of both halves are shown in Figure V.97.

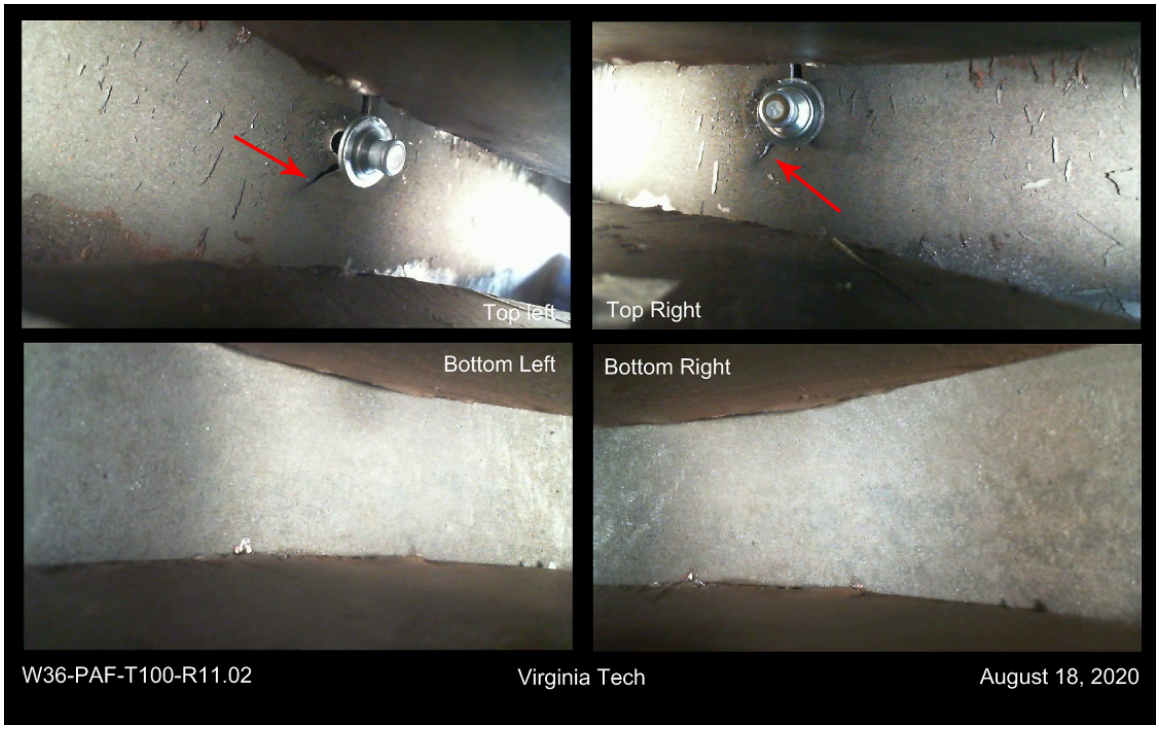

Figure V.96. Fracture initiation of W36-PAF-T100-R11.02.

Figure V.97. Fracture surfaces of W36-PAF-T100-R11.02.

V.7 Puddle Welds

V.7.1 W24-PW-T50-R11.01

Fracture initiation occurred in the third cycle at the edge of the puddle weld, shown in Figure V.98, while the top was in tension. Complete fracture occurred in the eighteenth cycle while the top was in tension. The fracture surfaces of both halves are shown in Figure V.99.

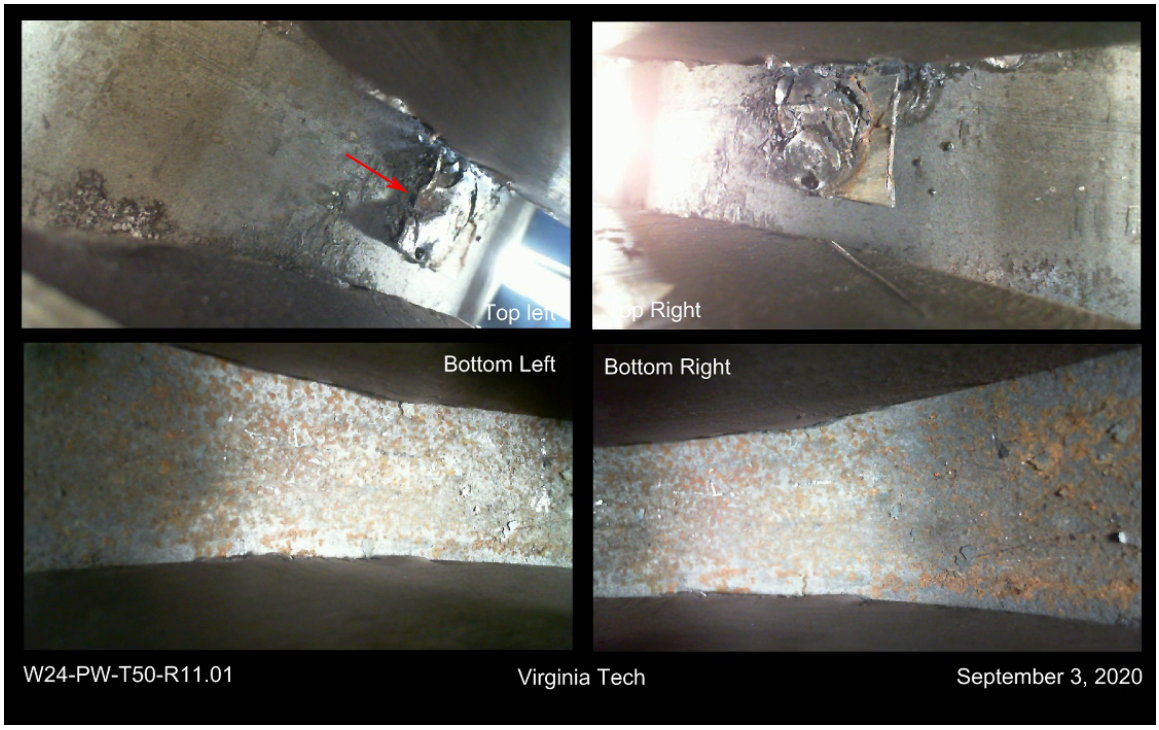

Figure V.98. Fracture initiation of W24-PW-T50-R11.01.

Figure V.99. Fracture surfaces of W24-PW-T50-R11.01.

V.7.2 W24-PW-T50-R11.02

Fracture initiation occurred in the fourth cycle at the edge of the puddle weld, shown in Figure V.100, while the top was in tension. Complete fracture occurred in the twenty-second cycle while the bottom was in tension. The fracture surfaces of both halves are shown in Figure V.101.

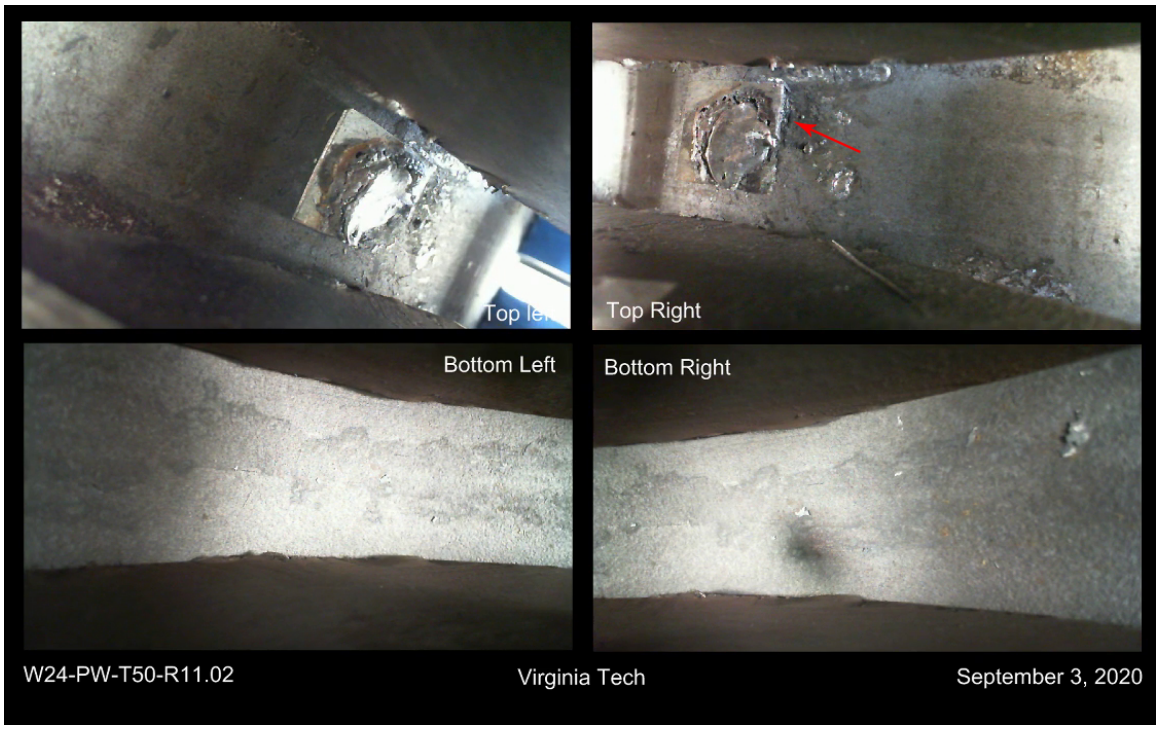

Figure V.100. Fracture initiation of W24-PW-T50-R11.02.

Figure V.101. Fracture surfaces of W24-PW-T50-R11.02.

V.7.3 W36-PW-T100-R11.01

Fracture initiation occurred in the second cycle at the edge of the puddle weld, shown in Figure V.102, while the top was in tension. Complete fracture occurred in the fourth cycle while the top was in tension. The fracture surfaces of

both halves are shown in Figure V.103.

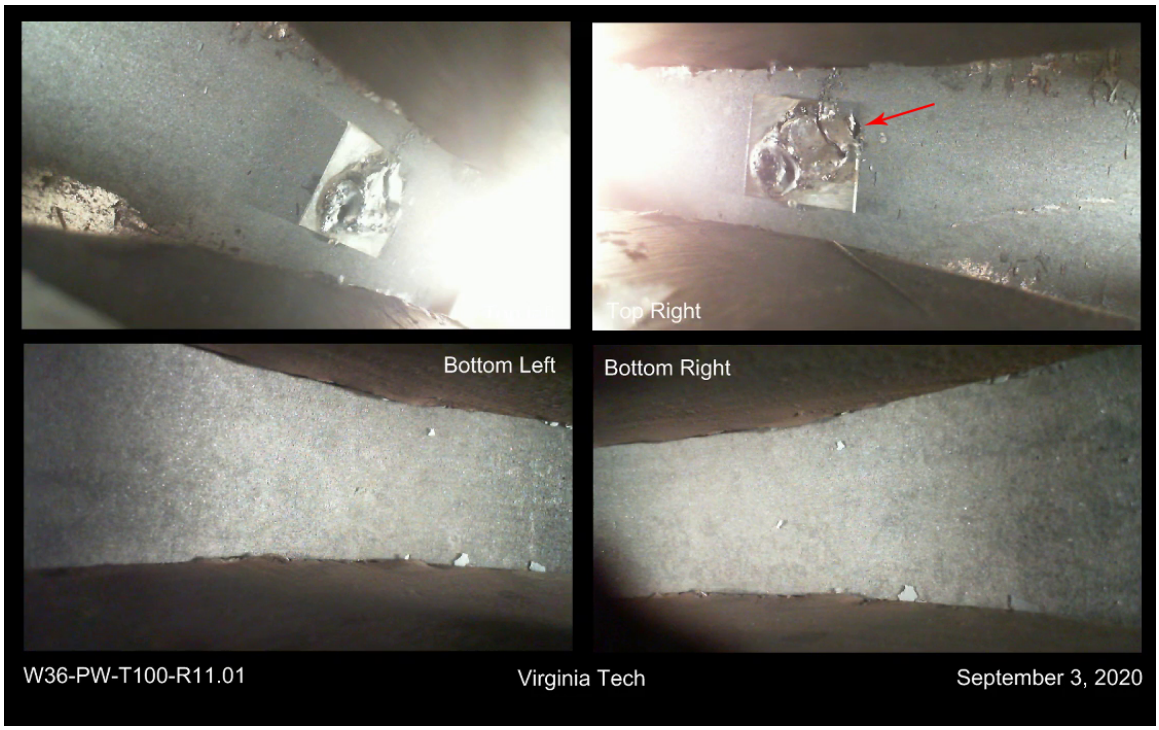

Figure V.102. Fracture initiation of W36-PW-T100-R11.01.

Figure V.103. Fracture surfaces of W36-PW-T100-R11.01.

V.7.4 W36-PW-T100-R11.02

Fracture initiation occurred in the third cycle, at the edge of the puddle weld, shown in Figure V.104, while the top was in tension. Complete fracture occurred in the fourth cycle while the top was in tension. The fracture surfaces of

both halves are shown in Figure V.105.

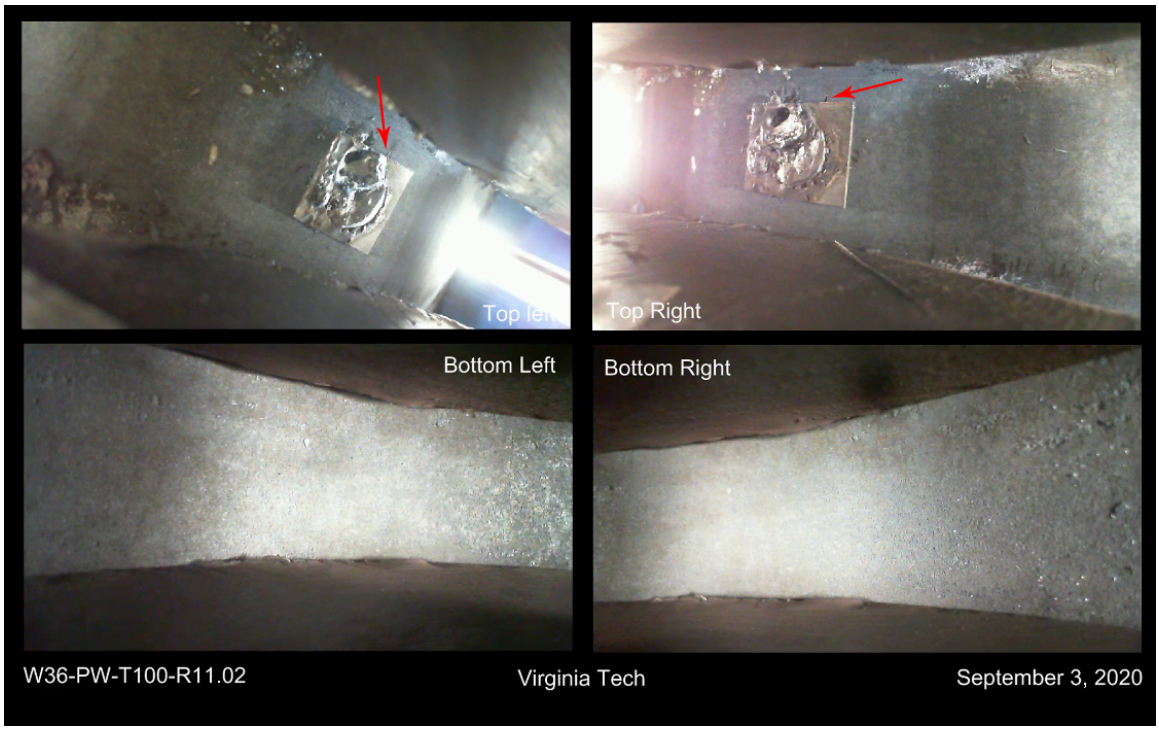

Figure V.104. Fracture initiation of W36-PW-T100-R11.02.

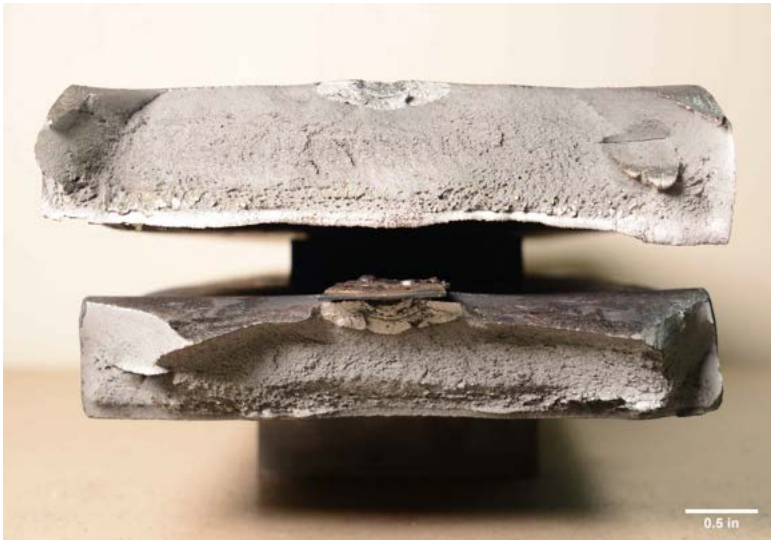

Figure V.105. Fracture surfaces of W36-PW-T100-R11.02.

Appendix W. Correlation for Fracture Initiation

As discussed in Section 7.2.1, the focus was on correlating final fracture between the full-scale moment connections and small-scale flat bar specimens. Determining when final fracture occurred was more objective than fracture initiation, and the estimates of plastic strain amplitudes in Table 7.3 were calibrated for final fracture. Despite these limitations, a correlation was still attempted for fracture initiation to determine if the same method for predicting fracture described in Section 7.3 could be applied.

Coffin-Mason relationships were calibrated for fracture initiation for flat bar specimens with each artifact, except the sharp 0.25 in. and 0.375 in. notches. The coefficients for ϵ'_f and c are given in Table W.1. A relationship was not calibrated for the sharp notches because fracture initiation did not follow the inverse power law of the Coffin-Mason relationship. For coupons with these two artifacts, fracture initiation was assumed to occur in the first cycle, regardless of the coupon thickness. Plots of the individual relationships with data points are given in Figures W.1a to W.1g.

Table W.1. Coffin-Manson coefficients for fracture initiation.

Artifact	ϵ'_f	c
0.125 in. notch repaired by grinding	0.1623	-0.4177
0.25 in. notch repaired by welding	0.1841	-0.5255
Pneutek K66062	0.0249	0.5696
Pneutek K66075	0.0493	0.1768
Hilti X-ENP-19 L15	0.1681	-0.5098
0.63 in. puddle weld	0.1586	-0.4998
Bare steel	0.1768	-0.3717

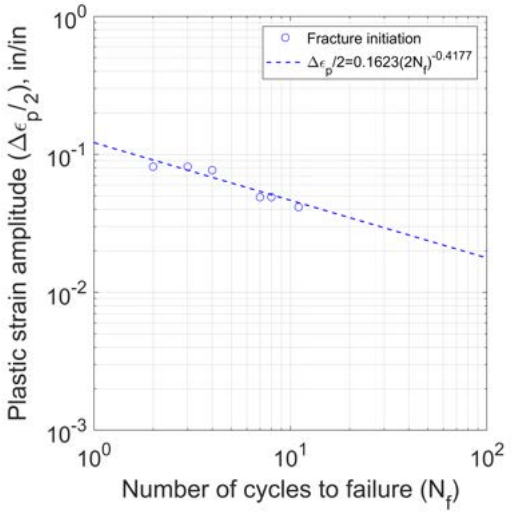

(a) 0.125 in. notch repaired by grinding.

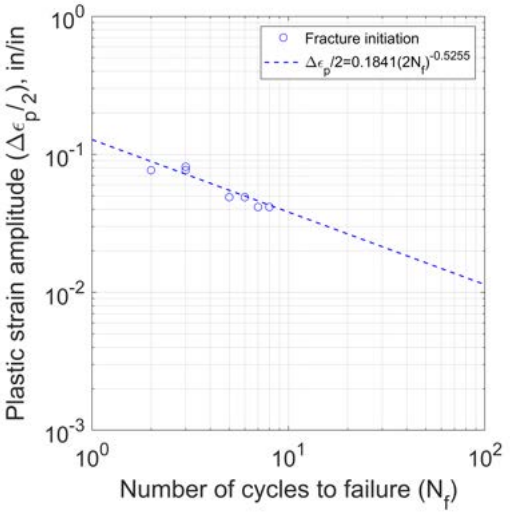

(b) 0.25 in. notch repaired by welding.

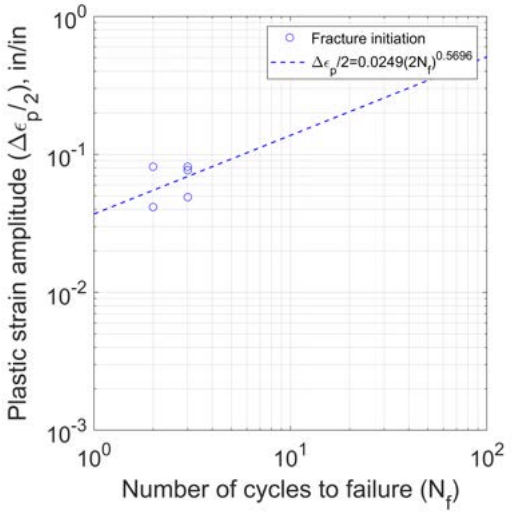

(c) Pneutek K66062 fastener.

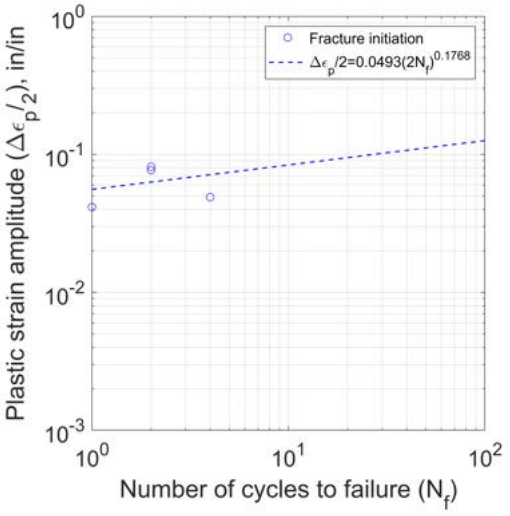

(d) Pneutek K66075 fastener.

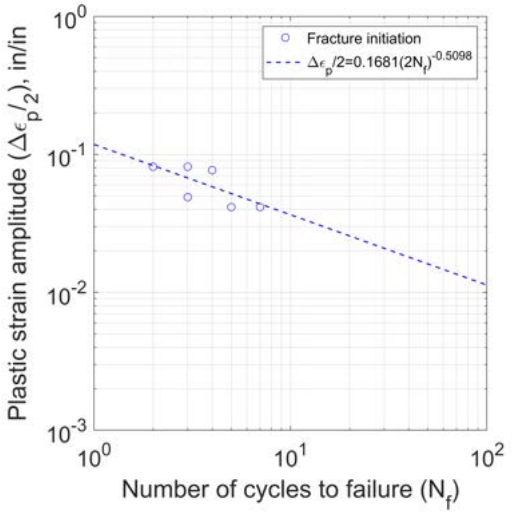

(e) Hilti X-ENP-19 L15 fastener.

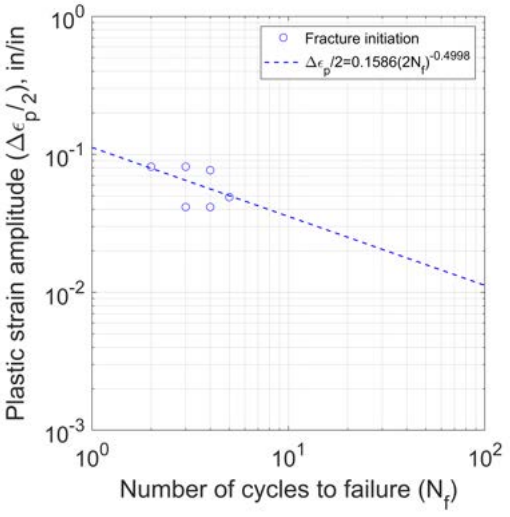

(f) 0.63 in. puddle weld.

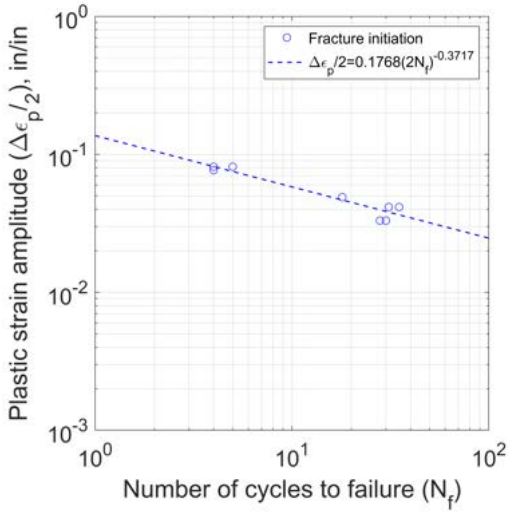

(g) Bare steel specimens.

Figure W.1. Coffin-Manson relationships for fracture initiation of flat bar specimens.

It is evident from Figure W.1c and Figure W.1d that the Coffin-Manson relationship did not apply to specimens with Pneutek K66062 and K66075 fasteners. For the Pneutek fasteners, fractures initiated sooner than an inverse power relationship would imply because the fasteners created stress concentrations on the back side of the thinner coupons. The K66062 fasteners created a bump on the back side of the 0.5 in. and 0.59 in. thick coupons, while the tip of the K66075 fasteners protruded from the back side of the 0.5 in. thick coupons and created a bump on the back of the 0.59 in. coupons.

The same method used for predicting final fracture described in Section 7.3 was applied to fracture initiation of the W24×62 reduced beam section (RBS) specimen with an array of 0.125 in. notches repaired by grinding. The Coffin-Manson relationship for fracture initiation is given in Eq. (W.1).

$$\frac{\Delta\epsilon_p}{2} = 0.1623(2N_f)^{-0.4177} \tag{W.1}$$

Like predicting final fracture, the process for predicting fracture initiation was iterative, with the final results shown in Table W.2. Using this method, fracture initiation is predicted to occur after 1.3 cycles of 4.5% story drift. This means fracture initiation is expected to occur in the second cycle of 4.5% story drift at a cumulative story drift of 1.62 radians. On the full-scale test, fracture initiation was first observed in the second cycle of 4% story drift, two cycles before the prediction.

Table W.2. Prediction of fracture initiation for W24RBS-0.125NGT-T59.

Story Drift, rad	Plastic Strain Amplitude, in./in.	Theoretical Fatigue Life (cycles)	Applied Cycles	Fatigue Life Used	Cumulative Fatigue Life Used
0.0075	0.0031	6520	6	0.001	0.001
0.01	0.0045	2672	4	0.001	0.002
0.015	0.0075	786	2	0.003	0.005
0.02	0.0113	295	2	0.007	0.012
0.03	0.0202	73	2	0.027	0.039
0.04	0.0530	7	2	0.274	0.313
0.045	0.0930	2	1.3	0.686	1.000

This process was repeated for the full-scale moment connections with 0.125 in. notches repaired by grinding, 0.25 in. notches repaired by welding, Hilti X-ENP-19 L15 sheet metal nails, puddle welds, and no artifacts. The results are shown in Table W.3. This method overpredicted fracture initiation for four specimens, underpredicted fracture initiation for three specimens, and predicted the same cycle of fracture initiation for three specimens. The actual cumulative story drift at fracture initiation is not reported in Table W.3 because the exact moment of fracture initiation is unknown. Rather, fractures were first observed when the test was paused after completing a set of loading cycles.

Table W.3. Fracture initiation prediction for full-scale RBS specimens.

Specimen Name	Artifact	Actual Result		Predicted Result	
		Fracture Cycle	Cumulative Story Drift, rad.	Fracture Cycle	Cumulative Story Drift, rad.
RBS24[1]	None	2nd cycle of 4.7% drift	N/A	2nd cycle of 4.7% drift	1.67
RBS24-PW12[1]	4 puddle welds at 12 in. spacing	3rd cycle of 4.7% drift	N/A	1st cycle of 4.7% drift	1.48
RBS24-PAF12[1]	4 PAFs at 12 in. spacing	1st cycle of 3% drift	N/A	1st cycle of 4.7% drift	1.50
W24RBS-0.125NGT-T59	0.125 in. notch ground to a taper	2nd cycle of 4% drift	N/A	2nd cycle of 4.5% drift	1.62
W24RBS-0.25NGTW-T59	0.25 in. notch ground to a taper and welded	1st cycle of 3% drift	N/A	1st cycle of 5% drift	1.49
RBS36[1]	None	2nd cycle of 4% drift	N/A	1st cycle of 4.7% drift	1.40
RBS36-PW12[1]	4 puddle welds at 12 in. spacing	1st cycle of 4% drift	N/A	1st cycle of 4% drift	1.12
RBS36-PAF_ARRAY[1]	Grid of PAFs	2nd cycle of 4% drift	N/A	1st cycle of 4% drift	1.15
W36RBS-0.125NGT-T94	0.125 in. notch ground to a taper	2nd cycle of 4% drift	N/A	1st cycle of 4% drift	1.23
W36RBS-0.25NGTW-T94	0.25 in. notch ground to a taper and welded	1st cycle of 4% drift	N/A	1st cycle of 4% drift	1.18

[1] From Eatherton et al. (2013).

Appendix X. Weld Etchings

This appendix describes the weld etchings that were done to refine the voltage and wire feed speed settings for the weld procedure specification. This involved cutting a thin cross section, polishing the cut surfaces, and etching with acid to show the weld passes and heat-affected zone. Etching the welds also showed that cleaning the toe of the weld between passes was needed to remove inclusions. Figures X.1 to X.5 show the etched cross sections.

Five 0.25 in. notches repaired by welding were prepared and welded following the same steps described in Chapter 3 and Appendix C. After welding, a transverse or longitudinal cross section about 0.125 in. thick was cut from each weld using a bandsaw. The process for polishing and etching the sections was as follows:

1. Bandsaw marks on one or both sides were removed using a surface grinder.
2. The section was polished using 240, 320, 400, 600, 1000, 1500, and 2000 grit silicon carbide sandpaper and water until the section had a mirror-like finish. The section was polished with each grit until the scratches from the previous grit were removed.
3. The section was cleaned with acetone and dried.
4. The section was etched using a 10% Nital solution applied with a cotton swab until the section changed from a mirror finish to a dull finish. It was important that the Nital was not allowed to dry on the section because it will discolor the surface and require starting over from Step 2.
5. The section was rinsed in acetone.
6. The section was etched with Fry's Reagent applied with a cotton swab or immersed in a dish. When the desired etch was reached, the section was rinsed with acetone. Water cannot be used to rinse the section because it will leave copper deposits.
7. The section was dried and sprayed with a clear lacquer finish to preserve the etch.

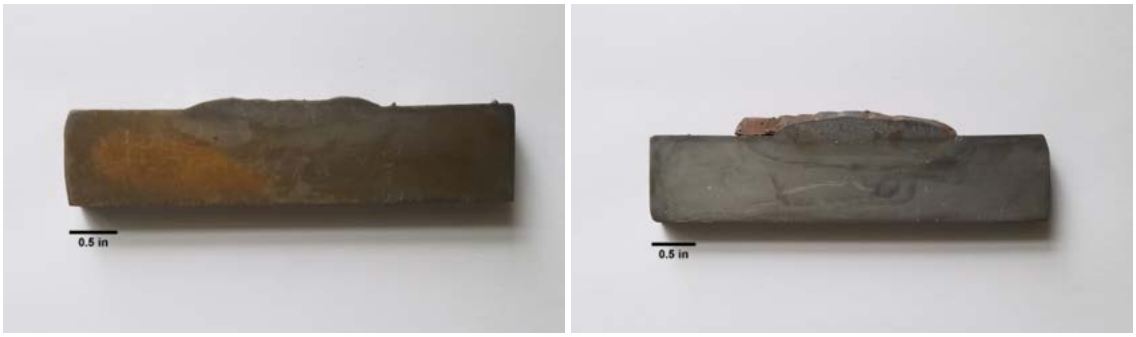

(a) Transverse through the middle. **(b)** Transverse through the tack weld.

Figure X.1. Etchings from the first weld (26.1 volts and 355 ipm).

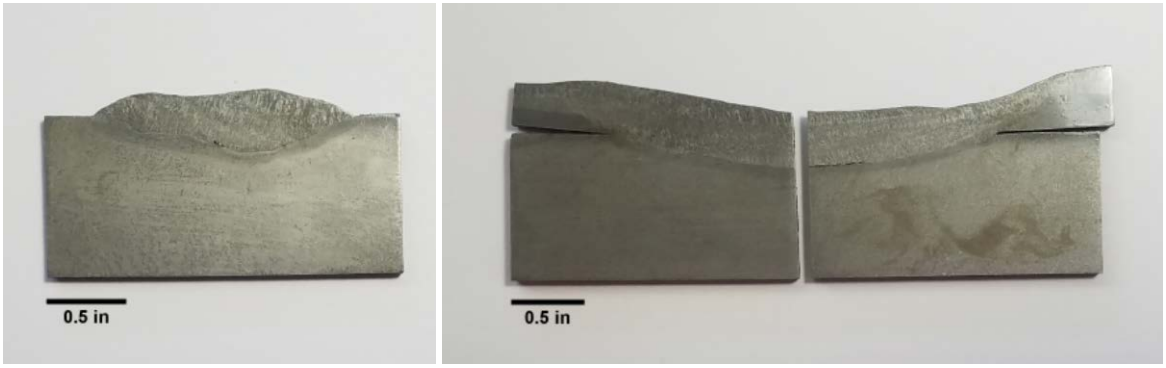

(a) Transverse cross-section from the middle. **(b)** Longitudinal cross section through the middle.

Figure X.2. Etchings from the second weld (27.3 volts and 350 ipm).

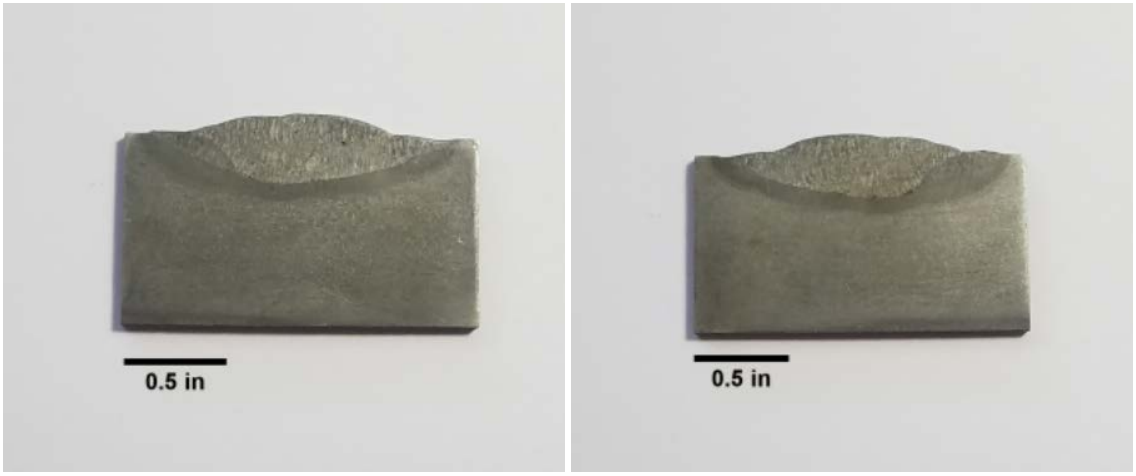

(a) Front. **(b)** Back.

Figure X.3. Etchings from transverse cross-sections through the middle of the third weld (26.0 volts and 185 ipm).

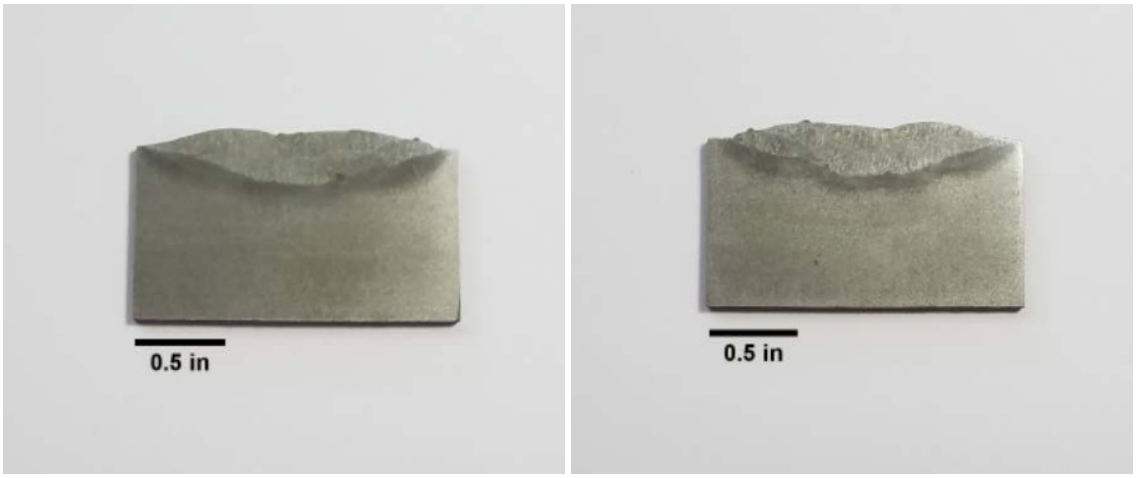

(a) Front. **(b)** Back.

Figure X.4. Etchings from transverse cross-sections through the middle of the fourth weld (28.0 volts and 198 ipm).

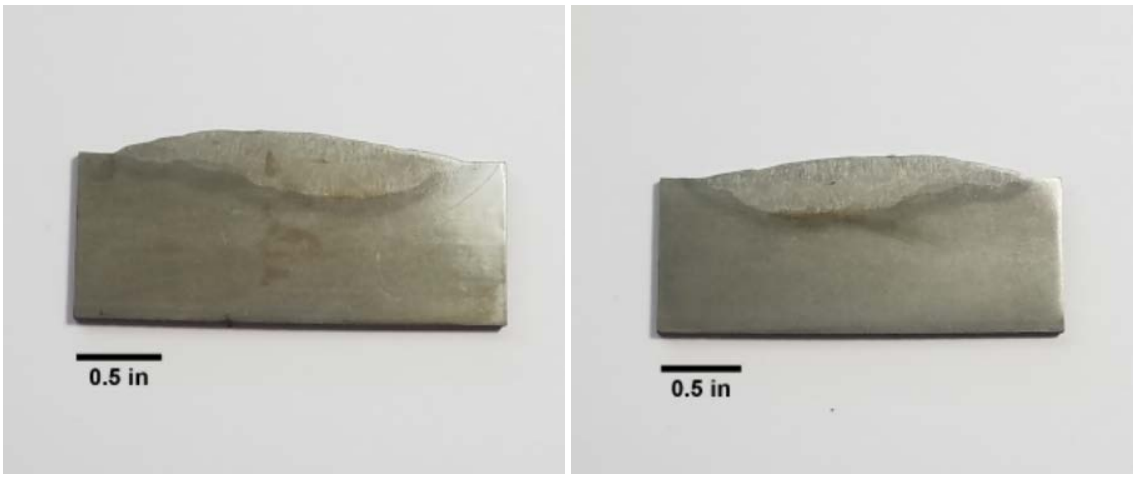

(a) Front. **(b)** Back.

Figure X.5. Etchings from transverse cross-sections through the middle of the fifth weld (26.0 volts and 190 ipm).

Appendix Y. Data Adjustments for Full-Scale Tests

This appendix describes adjustments made to the test data before it was used for the story drift decomposition. Data modifications fell into two categories: general adjustments applied to all data from all tests and specific adjustments for times when the instrumentation was disturbed.

General adjustments included removing any data recorded after fracture occurred and shifting all sensor measurements to zero, except for the force measurement, which was handled separately for each test. At the start of each test, the actuator was moved until the load cell measured a force equal to the weight of the actuator clevis plus half of the specimen weight. This removed any load on the connection that would not be present in a real structure, where the self-weight of the beam is distributed equally between the connections at either end. The initial force was then used in the data analysis as a load adjustment factor when zeroing the force measurements. The load adjustment factor was 2.82 kips for the W24×62 beams and 4.1 kips for the W36×150 beams.

Y.1 W24RBS-0.125NGT-T59

Specific data adjustments for this specimen were:

1. Modified SP_04 data to remove two spikes that were not attributed to the behavior of the specimen. The unmodified and modified plots are shown in Figure Y.1.

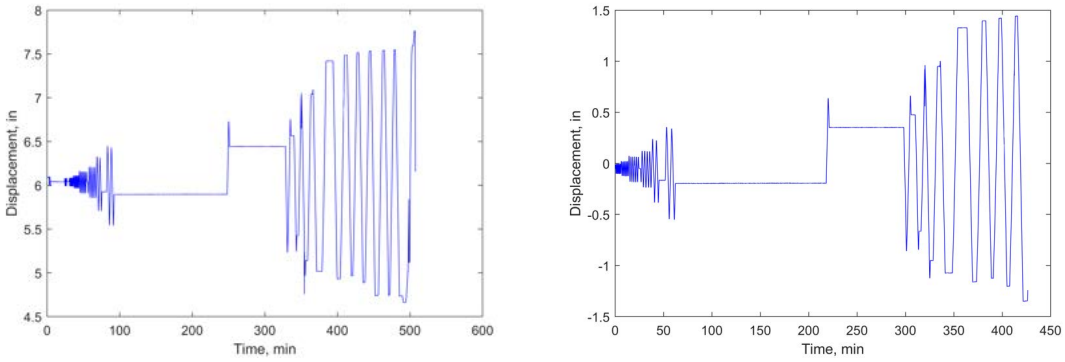

(a) Unmodified. **(b)** Modified.

Figure Y.1. SP_04 data adjustments for W24RBS-0.125NGT-T59.

Y.2 W36RBS-0.125NGT-T94

Specific data adjustments for this specimen were:

1. Modified SP_04 data to remove four spikes that were not attributed to the behavior of the specimen. The unmodified and modified plots are shown in Figure Y.2.
2. Modified SP_07 data to remove a spike that occurred when the string was bumped during a pause in the test. After the string was bumped, data was offset by 0.03 in. for the remainder of the test. The unmodified and modified plots are shown in Figure Y.3.

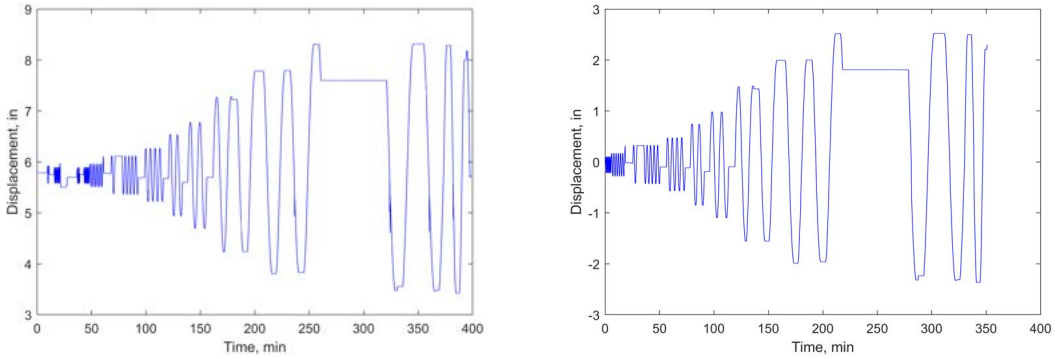

(a) Unmodified. **(b)** Modified.

Figure Y.2. SP_04 data adjustments for W36RBS-0.125NGT-T94.

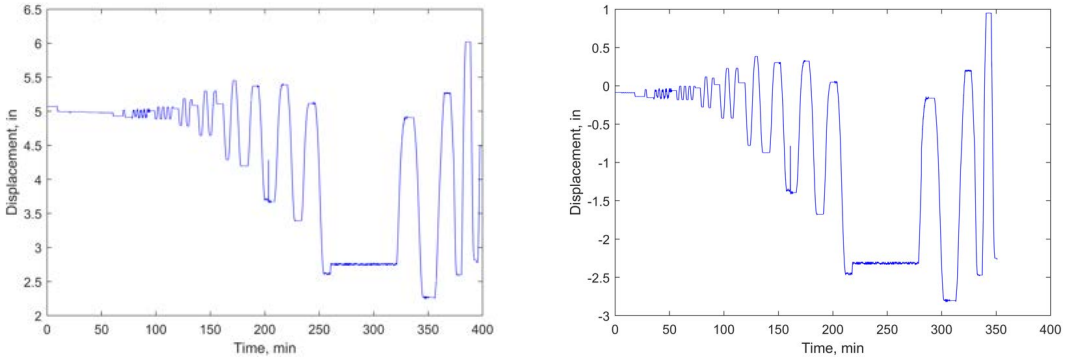

(a) Unmodified. **(b)** Modified.

Figure Y.3. SP_07 data adjustments for W36RBS-0.125NGT-T94.

Y.3 W24RBS-0.25NGTW-T59

There were no specific data adjustments for this specimen.

Y.4 W36RBS-0.25NGTW-T94

There were no specific data adjustments for this specimen.

Y.5 W24RBS-0.375N-T59

There were no specific data adjustments for this specimen.

Y.6 W36RBS-0.25N-T94

There were no specific data adjustments for this specimen.